Incorporation of Fault Rock Properties into Production Simulation Models

Bader Al-Busafi

Submitted in accordance with the requirements for the degree of

Doctor of Philosophy

The University of Leeds
School of Earth and Environment

September 2005

The candidate confirms that the work submitted is his own and that appropriate credit has been given where reference has been made to the work of others.

Acknowledgements

The list would go on forever if I were to mention every single person that contributed in the production of this thesis. However, my thanks must first go to all my supervisors for their sound advice and careful attention to detail. I am very thankful to all of them for enthusing me to do this PhD project, despite being a different area from my first degree. First of all, I thank my supervisor Dr. Quentin Fisher for his continual guidance and help with the SEM. I am grateful to my supervisor Dr. Simon Harris for his constant help with the programming parts. I also express my appreciation to my co-supervisor Prof. Michael Kendall for his valuable advice on the seismic models. I am very grateful for the financial support from my sponsor the Petroleum Development Oman (PDO).

Further, I must mention a number of people who either directly or indirectly helped me during this research. I appreciate the invaluable discussions I had with my colleagues Attila Vaszi and Suleiman Al-Hinai. I would like to thank the whole RDR group members for welcoming me and for every help they have given. Thanks also go to Steve Jolley and Sam Carter from Shell for acting as focal communication points in Shell EP Europe throughout this work and for their constructive comments and suggestions.

My family have been wonderful with their priceless emotional support. My mother, six brothers and two sisters in Oman, though words cannot express how much they have helped, all have played a tangible role in supporting me while I am abroad. Most of all and in the time honoured way, I owe my success in this life-changing step of my academic life to my wonderful wife Sabra who has given me every glimmer of hope and all the possible encouragement and emotional help to complete this project.

Abstract

Abstract

This thesis has two aims. First, to investigate the importance of incorporating the multiphase flow properties of faults into production simulation models. Second, to investigate methodologies to incorporate the multiphase flow properties of faults into production simulation models. Tests using simple simulation models suggest that in some situations it is not particularly important to take into account the multiphase flow properties of faults, whereas in other situations the multiphase properties have proved very important. The differences depend on drive mechanism, well position, and the capillary pressure distribution along the fault as well on the parameters that need to be modelled (*e.g.* bottom-hole pressures, hydrocarbon production rates, water cuts, *etc.*). The results show that it is possible for hydrocarbons to flow across a sealing fault (*i.e.* 100% water saturation) as a result of its threshold pressure being overcome. The relative permeability of fault rocks may be one of the largest unknowns in simulating fluid in structurally complex petroleum reservoirs.

Microstructural and petrophysical measurements are conducted on faults from core within the Pierce Field, North Sea. The results are used to calculate transmissibility multipliers (*TMs*) required to take into account the effect of faults on fluid flow within the Pierce production simulation model. The fault multiphase flow behaviour is approximated by varying the *TMs* as a function of height above the free water level. This methodology results in an improved history match of production data. Further, the improved model is then used to plan the optimal time to conduct a follow-up 3D seismic survey to identify unswept compartments. Further, an alternative model was proposed to overcome some of the possible limitations that the previous *TM* treatments may have at certain stages of a reservoir life. The similar behaviour of the different proposed fault models for the Pierce Field indicate that the current faulting system in this model is not largely responsible for the history mismatch in water production.

Multiphase flow properties of faults can be incorporated into production simulation models using dynamic pseudofunctions. In this thesis, different dynamic pseudofunctions are generated by conducting high-resolution fluid flow models at the scale of the reservoir simulation grid block, using flow rates similar to those that are likely to be encountered within petroleum reservoirs. In these high-resolution models, both the fault and reservoir rock are given their own capillary pressure and relative permeability curves. The results of the simulations are used to create pseudocurves that are then incorporated into the up-scaled production simulation model to account for the presence of both the fault and undeformed reservoir. Different flow regimes are used to compare the performance of each pseudoisation method with the conventional, single-phase *TM* fault representations.

The results presented in this thesis show that it is more important to incorporate fault multiphase properties in capillary dominated flow regimes than in those that are viscosity dominated. It should, however, be emphasised that the Brooks–Corey relations used to estimate relative permeability and capillary pressure curves of the fault rock in this study have a significant influence on some of these conclusions. In other words, these conclusions may not be valid if the relative permeability curves of fault rocks are very different to those calculated using the aforementioned relationships. Finally, an integrated workflow is outlined showing how dynamic pseudofunctions can be generated in fault juxtaposition models by taking advantage of the dynamic flux preservation feature in **Eclipse 100™** simulator.

Publications

List of publications

Al-Busafi, B., Fisher, Q.J. and Harris, S.D. (2005). The importance of incorporating the multi-phase flow properties of fault rocks into production simulation models. *Marine and Petroleum Geology*, **22**, 365-374. (**Chapter 3**)

Al-Busafi, B., Fisher, Q.J. and Harris, S.D., and Kendall, M. (2005). The impact of faults representations on history match and future generated seismic impedance response in reservoir models—Case study for the Pierce Field, North Sea. *Society of Petroleum Engineering*, SPE 93429. (**Chapters 4 and 5**)

Al-Busafi, B., Vaszi, A.Z., Fisher, Q.J. and Harris, S.D. (2005). Incorporating the multi-phase flow properties of fault rocks in simulation models using in-situ generated pseudofunctions. Presented during the *EAGE 67th Conference and Exhibition*—Madrid, Spain, 13 – 16 June. (**Chapters 6 and 7**)

Contents

Table of contents

Units

Thesis units conversion table

Unit Name	Symbol	Field Units (English)	SI Units	Multiplier factor (Field to SI)
Length	L	ft	m	0.3048*
Area	A	ft^2	m^2	0.092903*
Volume	V	ft^3	m^3	0.0283168466
Liquid volume	V_l	stb	m^3	1.589873×10^{-1}
Gas volume	V_g	$Mscf$	m^3	28.31685
Mass	m	lb	kg	4.535234×10^{-1}
Density	ρ	lb/ft^3	kg/m^3	16.01846
Time	t	hr	s	3600*
Compressibility	C	$1/psi$	$1/Pa$	1.450377×10^{-4}
Pressure	P	psi	Pa	6894.757
Reservoir Pore volume	v	rb	rm^3	1.589873×10^{-1}
Liquid formation volume factor	B_l	rb/stb	rm^3/sm^3	1*
Gas formation volume factor	B_g	$rb/Mscf$	rm^3/sm^3	5.61458×10^{-3}
Permeability	k	mD	m^2	9.869233×10^{-16}
Viscosity	μ	cP	$Pa.s$	1×10^{-3}*
Velocity	υ	ft/s	m/s	0.3048*
Liquid volumetric rate	q_l	stb/day	m^3/s	1.84013×10^{-6}
Gas volumetric rate	q_g	$Mscf/day$	m^3/s	3.2774205×10^{-4}
Gas-oil ratio	GOR	scf/stb	rm^3/sm^3	0.178108
Mobility	λ	mD/cP	$m^2/Pa.s$	9.869233×10^{-13}
Surface tension	σ	$dyne/cm$	N/m	1×10^{-3}*

* Conversion factor is exact.

Chapter 1 Introduction

"Anytime a fault is involved, I try to at least qualitatively evaluate fault seal, if not quantitatively. One rule of thumb I have is if the proportion of sand to shale is greater than .5, it raises a flag for me. In a section with greater than 50 percent sand where you have sand-on-sand juxtaposition, you know you have to worry about fault seal because of leakage. If a prospect is on the margin of commerciality because of the fault, you may want to do full-blown fault seal evaluation."

Robert Merrill

Exploration manager at Samson International in Houston

1.1. The effects of faults on fluid flow in the subsurface

Faults are localised shear deformations within rocks and are widely believed to have a significant impact on fluid flow within petroleum-bearing sequences on both geological and production time-scales. Two end-member behaviours have been suggested. The first is where faults act as high permeability conduits, which enhance the rate of fluid flow. The second is where faults act as seals[1], barriers[2] or baffles[3] decreasing the rate of fluid flow.

Faults that have sealed petroleum over geological time can be a potential target for exploration geologists. There are numerous examples all around the world where faults have sealed and enhanced the petroleum column over geological times. Classic examples of such faults can be found in the late Jurassic faulting system in the Gullfaks Field, North Sea (Evans *et al.*, 2003). **Figure 1.1** shows a top structure of some Brent fields, North Sea. The figure also shows an interpreted E-W seismic cross-section of the Gullfaks Field with the initial distribution of the petroleum. The sealing faults, numbered 1 and 2, have enhanced the height of the accumulated petroleum. With sufficient petroleum charge from lower formations, fault 1 has allowed a maximum column height of petroleum accumulation, *i.e.* up to the low structure spill point.

---

[1] **Petroleum seals** are defined here as rocks that have such low effective permeability that petroleum can accumulate over geological time where trapping geometry and charge are present.
[2] **Flow barriers** are defined here as structures within a reservoir that prevent fluid flow production on a production time-scale.
[3] **Flow baffles** are defined here as structures that impede but do not totally restrict fluid flow on a production time-scale.

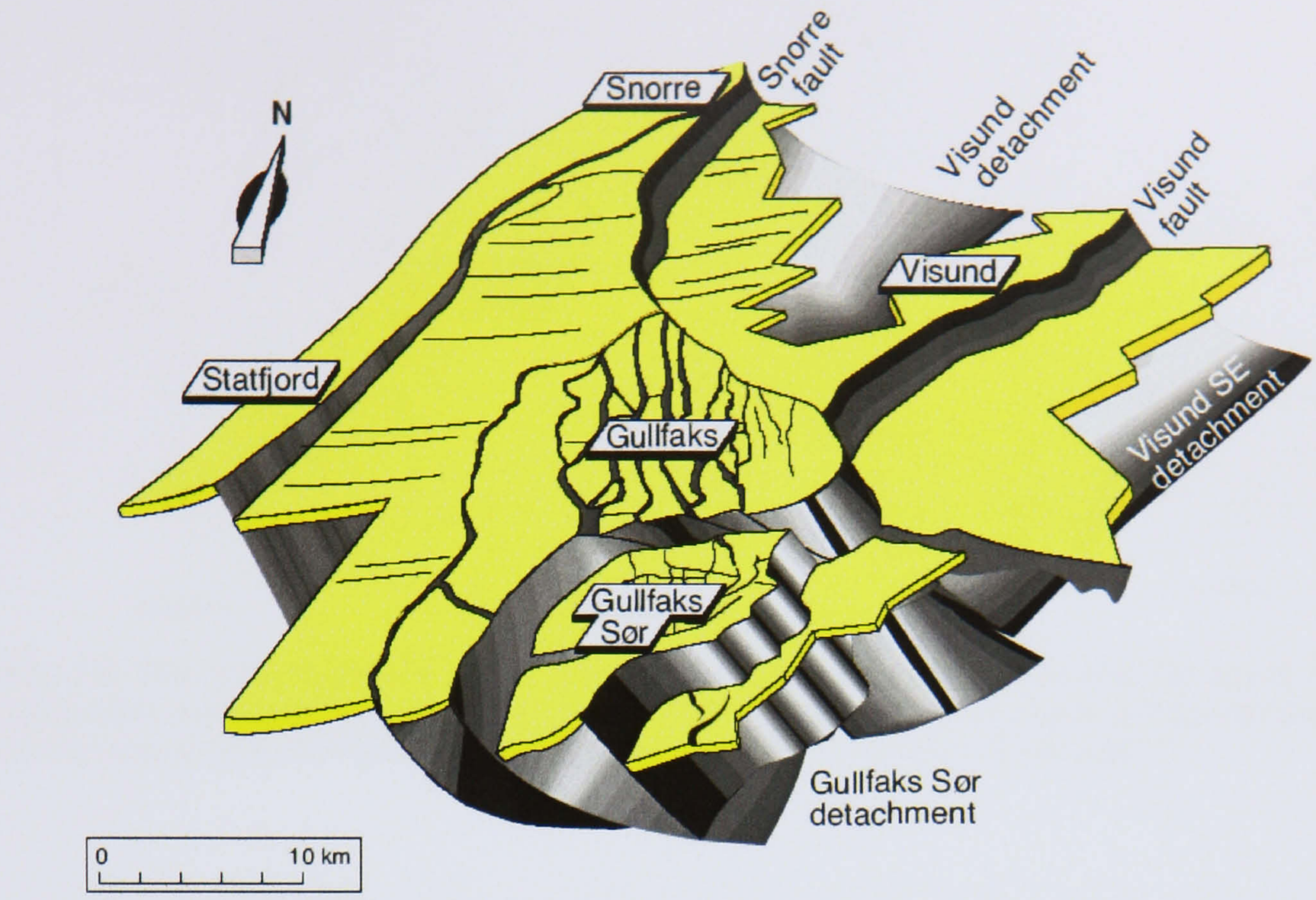

Fig. 1.1. Top: Top Brent Structure map showing fault compartments in the Gullfaks Field, North Sea. Bottom: an interpreted E-W seismic cross-section of the Gullfaks Field with the initial distribution of the petroleum (green highlights). The sealing faults, numbered 1 and 2, have enhanced the height of the accumulated petroleum. Modified from Evans *et al.* (2003).

Sealing faults are not always, however, a benefit to explorationists; sometimes their presence can lead to the drilling of costly dry holes. The Hudson Field, North Sea, is an excellent example of the latter case (Hardman and Booth, 1991). The map and cross-section in **Fig. 1.2** show that the first well, marked **1**, was located in the crest of an obvious structural high. This well encountered water-saturated Brent Group sands. A second well on the flank, marked **2**, encountered oil shows suggestive of a local stratigraphic trap. Thirteen years after the initial well, a third well, marked **3**, discovered the Hudson Field: a fault dependent trap. The sealing fault trapped petroleum in a flank fault compartment and prevented petroleum from migrating into the more obvious structural high to the west. Pre-drill fault seal analysis and a migration pathway map may have correctly identified the sealing fault and would have placed a much greater risk on the success of well **1**. Petroleum does not always migrate into the crest of the obvious structural highs, because of barrier-acting faults over geological time-scale.

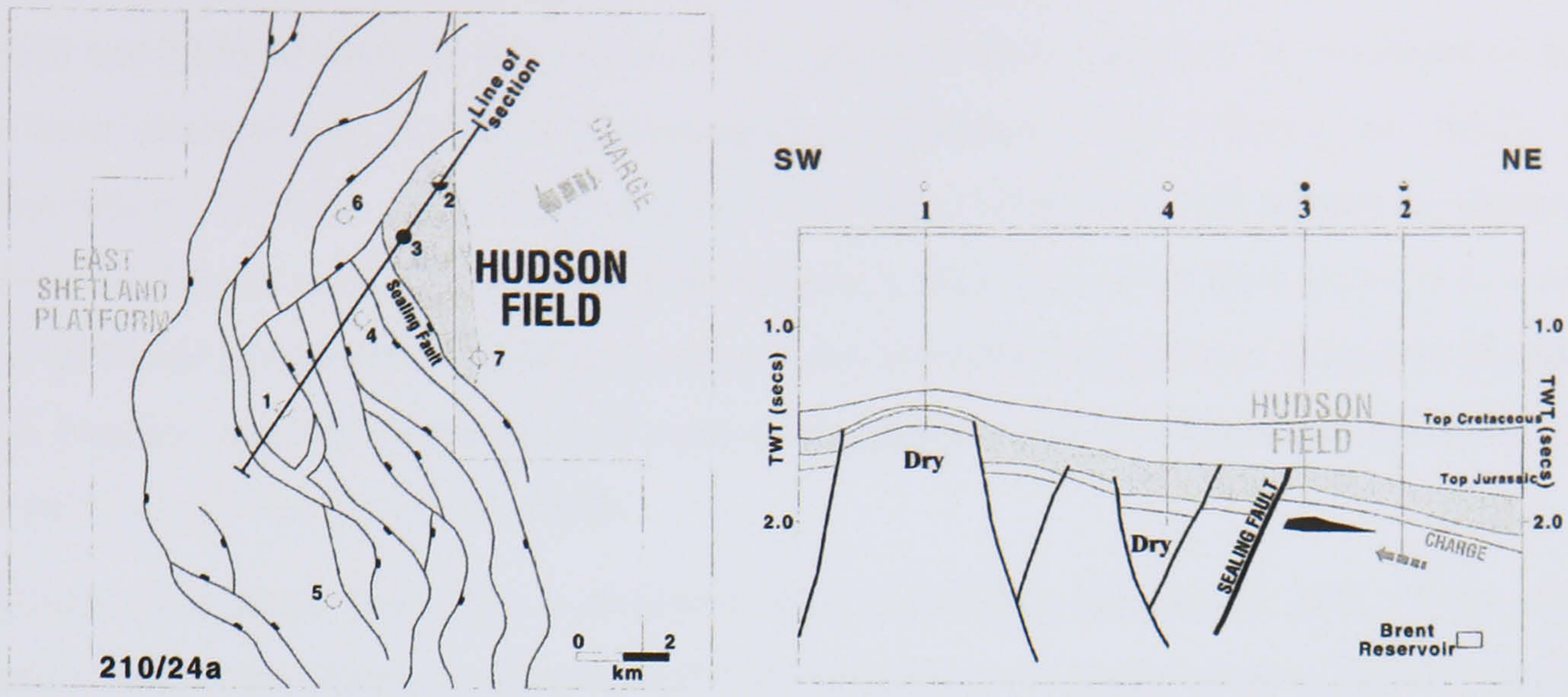

Fig. 1.2. The fault dependent trap in the Hudson Field, North Sea, discovered by well **3**, thirteen years after the structural high well **1**. Oil did not migrate to the west structural high because of a barrier-acting fault over geological time-scale. After Hardman and Booth (1991).

Faults are frequently observed to have leaked over geological time but act as barriers or baffles over production time-scales; the G3/G4 fault in the Gullfaks Field, North Sea, appears to be an example of such behaviour (Yielding, 1999). Fault blocks G2 and G3, **Fig. 1.3**, originally had the same oil-water contact. Therefore, on a geological time-scale, the G2/G3 fault probably did not constitute a 'sealing' fault. However, the two fault blocks underwent differential depletion once production had started, implying that the fault was a barrier or baffle to flow on the production time-scale.

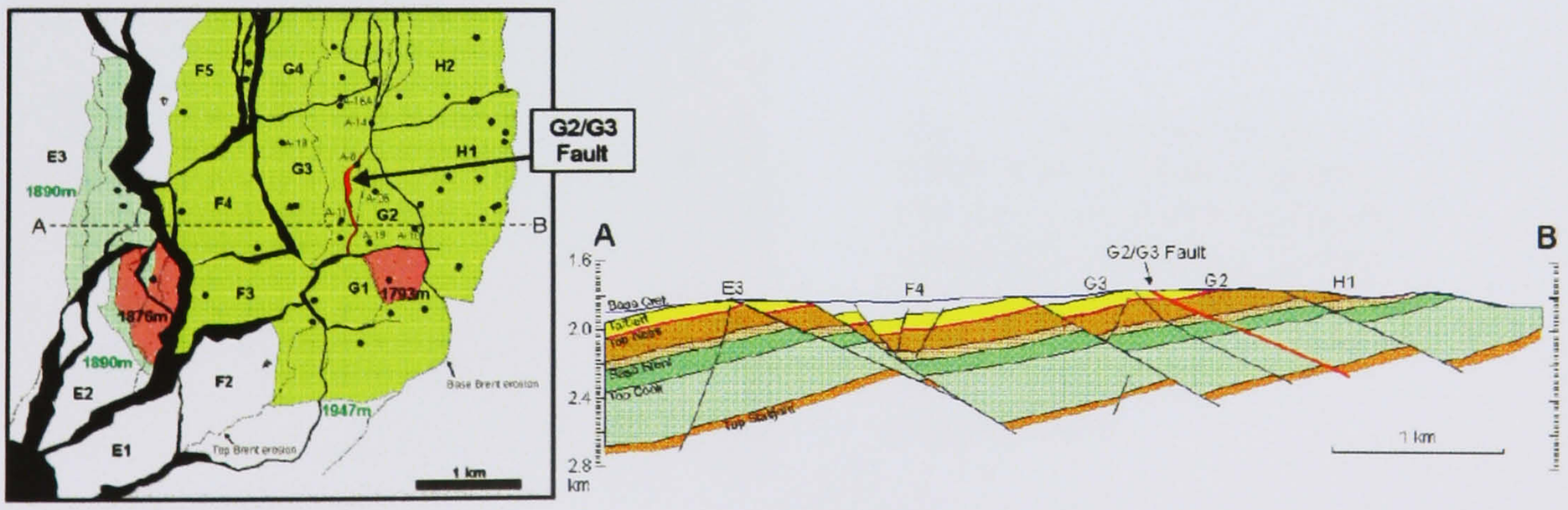

Fig. 1.3. Left: Top Brent Structure map showing fault compartments (*e.g.* G3, G2) and well locations (dots). Green area is oil-bearing Brent Group (pink areas are gas caps). Fault highlighted in Red is the G2/G3 fault. Right: Cross-section along line A-B. Modified from Yielding (1999).

It is frequently argued within industry that a fault may undergo a transition from sealing behaviour to conducting behaviour during production time-scale as a result of two different processes: a structural related process or a multiphase behaviour related process. Inactive faults

may undergo mechanical rupturing as a result of rapid pressure depletion and start to leak. The Valhall and Ekofisk fields in the central North Sea have been suggested as examples of faults that have mechanically broken down during the production period (Chan *et al.* 2002). This interpretation, however, was based on production data, which are still subject to arguments because of their non-uniqueness. On the other hand, a fault may allow flow across it as a result of its threshold pressure been exceeded, without any mechanical rupturing. A fault in the Akaso Field, Nigeria, may have undergone this type of breakdown with a differential pressure of about 600 psi (~ 41.37 bar) (Jev *et al.*, 1993).

Faults can conduct fluid flow at different times scales. The **Juba**rte oil field, 77 km off the Espirito Santo state coast in southeastern Brazil, provides an example where a fault has acted as a conduit to fluid flow and helped oil migration over geological time from underlying early Cretaceous source rocks (Gontijo, 2005). Traces of oil in some core samples collected from the fault zone provide some evidence for such behaviour. On the other hand, there are numerous examples where faults have acted as conduits over production time-scales, thus being able to allow fluid to move from one compartment to its adjacent, assuming up-structure movement, in 10–100 years. Detecting such faults that act as conduits is a crucial step in field development. Mud losses during drilling are often used to indicate the presence of fluid-conductive fractures and faults (**Fig. 1.4**). Examples of mud loss tracking during drilling as an indicator of conductive faults include some fractured carbonate reservoirs in Oman (Ozkaya and Minton, 2005).

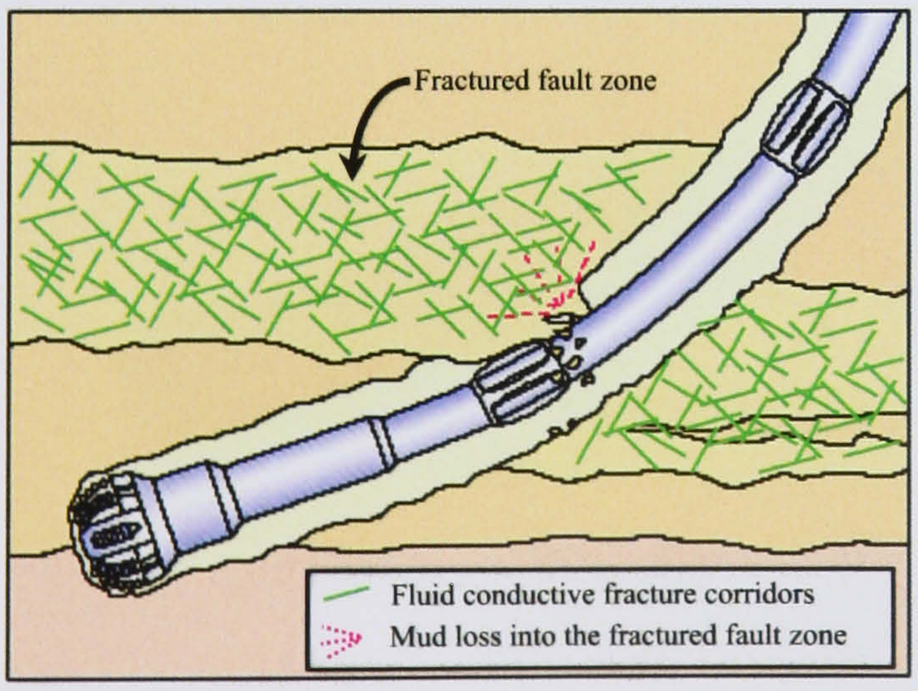

Fig. 1.4. Mud loss during drilling can be used to detect conductive fractures and faults. Locating conductive fractures and faults is a crucial step that plays a major role in field well planning and future developments.

It has often been suggested that the observed paradoxical behaviour of faults, *i.e.* as sealing or conducting, is related to fluid activity: active faults are often regarded as being conduits for flow, whereas inactive faults are regarded as being barriers to fluid flow. However, factors such as stress conditions and stress history of the reservoir at the time of faulting often have a more important influence on whether a fault acts as a conduit or a barrier to fluid flow than whether or not it is active (Fisher *et al.*, 2003). Faults, generally, increase in permeability when the rocks being deformed have low porosity and are brittle or overconsolidated (*e.g.* deformation of deep

carbonate rocks). A decrease in permeability, on the other hand, is inferred for deformation bands that form in poorly consolidated rocks of high porosity under high effective stress conditions. In this situation, grain sliding and rotation leads to porosity reduction without any significant grain breakage. This thesis concentrates on faults as partial flow barriers and conduits will not be discussed further.

1.2. Fault seal mechanisms

Faults restrict fluid flow in several ways depending on the lithologies present, the types of fluid present and the phase pressure distributions. Watts (1997) suggested that faults could restrict fluid flow either because: (i) they juxtapose permeable strata against less permeable horizons; Watts (1987) referred to such situations as juxtaposition seals; (ii) the products of faulting (hereinafter referred to as fault rocks) restrict fluid flow; Watts (1987) referred to such situations as fault seals *sensu stricto*. The Barque Field, Blocks 48/13a and 48/14, in the southern North Sea, may present an example that illustrates the difference between these two types of seals (Farmer and Hillier, 1991). The fault numbered 1 in **Fig. 1.5** is a possible example of a fault rock seal, whereas the fault numbered 2 is an example of a juxtaposition seal, where the Rotliegendes Group Leman Sandstone Formation of Lower Permian age, occurs between Carboniferous Coal Measures, which source the gas and Zechstein evaporates, which form an excellent seal, juxtapose this latter formation.

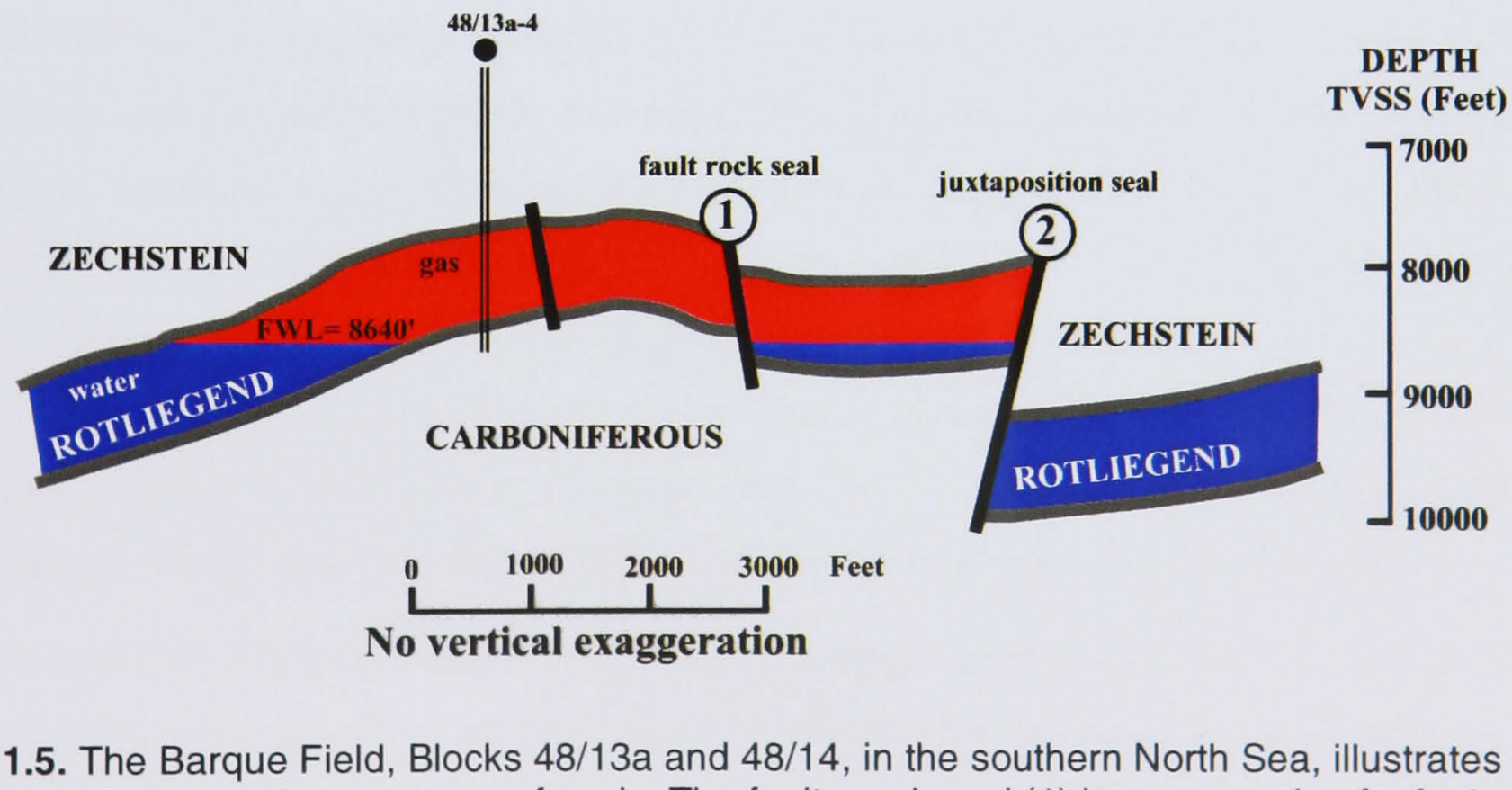

Fig. 1.5. The Barque Field, Blocks 48/13a and 48/14, in the southern North Sea, illustrates the difference between the two types of seals. The fault numbered (1) is an example of a fault rock seal, whereas the fault numbered (2) is an example of a juxtaposition seal, where the Rotliegend Group Leman Sandstone Formation of Lower Permian age occurs between Carboniferous Coal Measures, which source the gas, and Zechstein evaporates, which form an excellent seal, juxtapose this latter formation. Adapted from Farmer and Hillier (1991).

It should be emphasised that a considerable controversy remains throughout the industry regarding the importance of fault rocks as whether they can seal petroleum over geological time.

For example, recent papers, especially from the ExxonMobil group (*e.g.* Vroliijk *et al.*, 2005), argue that only the juxtaposition of reservoir against non-reservoir can seal substantial quantities of petroleum over geological time. On the other hand, other groups (*e.g.* Naruk *et al.*, 2002), argue that there are many examples where faults at reservoir–reservoir juxtapositions have sealed enhanced petroleum columns over geological time. It might seem odd that there remains such controversy regarding such issues, especially given that the latter two papers are from ExxonMobil and Shell, respectively, who are partners in much of the same acreage around the world and therefore have access to similar data. This paradox may be explained by the fact that the interpretation of much static data is non-unique and therefore interpretations often come down to individual bias. For example, the difference in gas–water contacts across fault 2 in **Fig. 1.5** may either be explained by the fault rock acting as a seal over geological time or alternatively the brine between faults 1 and 2 may have been unable to escape. In other words, the gas–water contact between faults 1 and 2 is perched.

Faults restrict fluid flow in physically different ways depending upon whether there is a single fluid phase present (*i.e.* brine) or whether two or more immiscible fluids are present (*i.e.* brine, oil and/or gas). If only brine is present resistance to flow comes mainly from viscous forces. On the other hand, if immiscible fluids are present capillary forces can further inhibit fluid flow.

Single-phase flow can be restricted because fault rocks have lower permeability than their surrounding rocks. Faults can also restrict single-phase flow if they juxtapose reservoir rocks against horizons with lower permeability. However, the restriction of multiphase flow by faults can also be due to capillary effects. For example, sealing can develop on an interface between water-wet sandstone and shale because the shales have much higher threshold pressures than sands due to their small pore throats. The different capillary function of the shale causes the water contact to be elevated and the resulting water saturation presents a barrier to petroleum flow through the shale. To drive oil, for example, through the shale a minimum pressure differential across the interface is required. Once this threshold pressure has been exceeded, flow occurs. These types of seals are called capillary or membrane seals (Watts, 1987).

For a non-wetting phase to pass through a pore throat its phase pressure needs to be higher than the phase pressure of the wetting fluid by an amount known as the threshold pressure. The threshold pressure can be estimated from the rock pore size and interfacial tension using Washburn's (1921) equation:

$$P_t = 2\sigma\cos(\theta)/r_c \qquad \textbf{1.1}$$

where P_t is the threshold pressure in dynes/cm^2, σ is the interfacial tension in dynes/cm between hydrocarbon and water, θ is the contact angle between the fluid and rock surface, and

r_c is the capillary radius measured in μm. This capillary radius is defined as the minimum pore throat radius along the path joining the largest connected pore throats in the rock and can be estimated using data obtained by mercury injection porosimetry analysis (**Chapter 4**). The contact angle is a measure of wettability (see **Appendix B** for a discussion of wettability); $\theta = 0^\circ$ for a strongly water-wet rock, whereas a strongly oil-wet rock tends to have a contact angle of $\theta = 180^\circ$ (Berg, 1975). Petroleum/brine interfacial tension values typically range from 15–72 dynes/cm (Schowalter, 1979; Watts, 1987; Vavra *et al.*, 1992). Laboratory studies provide interfacial tension values for a range of gas and oil compositions (Firoozabadi and Ramey, 1988).

Phase pressure differentials between wetting and non-wetting phases may be generated due to buoyancy effects. These arise because petroleum tends to be less dense than brine. The pressure differential due to buoyancy forces (P_b) exerted by a petroleum column can be related to the densities of the hydrocarbon (ρ_h) and the aqueous phase (ρ_w), the vertical height of the petroleum column (H) and the acceleration due to gravity (g) by the following equation:

$$P_b = gH(\rho_w - \rho_h) \qquad \textbf{1.2}$$

or in terms of field units:

$$P_b = 0.433H(\rho_w - \rho_h) \qquad \textbf{1.3}$$

where 0.433 is a conversion constant which takes into account the effect of g, densities are measured in g/cm^3, and H is in feet (Schowalter, 1979; Watts, 1987).

In a water-wet reservoir, petroleum can only move if P_b exceeds P_t. The maximum column of petroleum ($H = H_{cp}$) that can accumulate under a seal supported by a fault can be estimated by combining **equation-1.1** and **equation-1.2** in the limiting situation for which $P_b = P_t$. Thus,

$$H_{cp} = \frac{P_t}{0.443(\rho_w - \rho_h)} \qquad \textbf{1.4}$$

The sealing capacity of a fault is more complicated than being only related to the measured threshold pressure of the faulted rock material. Once a fault has been breached and petroleum forced through, theoretically, the fault-supported petroleum column will shrink until the buoyancy pressure becomes slightly less than the threshold pressure and the fault zone again

seals. In practice, however, hydrocarbons continue to flow through the fault zone until there is no longer a continuous hydrocarbon filament. Although the process is not fully understood, laboratory studies suggest that flow continues until the hydrocarbon column shrinks to half its original height (Roof, 1970; Schowalter, 1979).

The maximum sealable petroleum column is also affected by the hydrodynamic flow (Schowalter, 1979; Dahlberg, 1982; Lerche and Thomsen, 1994). Flow in the direction of the buoyancy vector decreases the seal capacity, *i.e.* petroleum column height, and vice versa. Gibson (1996) presented examples from different petroleum fields in the US Gulf of Mexico and Columbus Basin (offshore Trinidad) reflecting the complex interplay of several column-height limiting factors, including hydraulic fracturing of the seal, capillary pressure phenomena, and hydrodynamic flow conditions. Petroleum columns in these field examples are trapped in sand against sand juxtaposition in the footwall of normal faults. Fluid pressure differences of 700–5000 psi (~ 48–345 bar) are observed across some portions of these faults. Column heights are several times larger in reservoirs that are underpressured relative to juxtaposed strata than along fault segments that juxtapose reservoirs with equivalent datum fluid pressures. In contrast, sandstones that are juxtaposed against lower-pressure sandstone units contain anomalously short oil or gas columns. In all cases examined, the buoyancy pressures generated by the petroleum columns are insufficient to elevate the reservoir pressures to those necessary for hydraulic fracturing of the seal. These data are most consistent with a model in which 'pressure sealing' faults are capillary seals with a superimposed hydrodynamic influence. Seal capacity is either enhanced or degraded relative to that of a capillary seal, depending on the relative conditions of potential hydrocarbon migration and changes in datum water pressure across the fault zone. Some studies on fields that are not affected by regional hydrodynamic gradients appear to show that the trapped column heights match the predicted height from trapping fault threshold pressures. Benton Field, Illinois, is one example in which the theory correctly predicted the reality (Sneider and Neasham, 1993).

1.3. Fault rock properties—controls and implications

In recent years a large amount of data has been collected on the microstructural and petrophysical properties (permeability and threshold pressure) of fault rocks (Fisher and Knipe, 1998, 2001). Based on the detailed microstructural and petrophysical property analysis of over 2000 fault rocks within cores retrieved from petroleum reservoirs, Fisher and Knipe (2001) summarised the factors that control the flow properties of fault rocks as follows:

- clay content of the prolith at the time of faulting;
- pre-syn- and post-deformation temperature and stress history;
- porosity at the time of faulting;

- grain size of the protolith.

Based on such a detailed quantitative analysis, fault rocks have been subdivided depending on the clay content of the protolith at the time of faulting. It is important to emphasise that the following classification applies to rocks and sediments deformed in a ductile manner or high porosity rocks deformed in a brittle manner; the brittle deformation of low porosity rocks tends to create flow conduits.

- **Clean sandstones** (<15% clay) deform to produce either disaggregation zones or cataclastic faults depending on the stress conditions at the time of faulting. Disaggregation zones (**Fig. 1.6a**) form in poorly lithified sands under low effective stress conditions. Faulting occurs without grain fracturing and simply involves the movement and rearrangement of sand grains. These fault rocks usually have similar flow properties to the undeformed reservoir and do not affect fluid flow. Cataclastic faults (**Fig. 1.6b**) form under higher effective stress conditions. These experience a reduction in permeability and increase in threshold pressure as a result of two processes. First, grains are fractured during faulting, resulting in a porosity collapse. Second, following faulting, the grain fragments can become preferentially cemented by quartz once the reservoir is sufficiently hot (>90^{o}C). Cataclastic faults that we have analyzed have permeabilities of >1 to <0.0001 mD and Hg-threshold pressures of 10 to 2000 psi (around 0.7 to 138 bar).

- **Impure sands** (15 to 40% clay) deform to produce phyllosilicate-framework fault rocks (**Fig. 1.6c**). These faults have lower permeability and increased threshold pressures compared to the undeformed reservoir as a result of two processes. First, during faulting, clay is mixed with the framework grains, resulting in a replacement of macroporosity with clay and microporosity. Second, following faulting, such fault rocks experience enhanced grain-contact quartz dissolution ('pressure solution') once the temperature of the reservoir rises above 90^{o}C. The phyllosilicate-framework fault rocks that we have analysed have permeabilities of <0.1 to <0.0001 mD and Hg-threshold pressures of 50 to 3000 psi (around 3.5 to 207 bar).

- **Clay-rich sediments** (>40% clay) are often smeared along the fault plane to produce clay smears (**Fig. 1.6d**), which are extremely effective barriers to fluid flow. The majority of clay smears that we have analysed have permeabilities of <0.0001 mD and Hg-threshold pressures of >3000 psi (around >207 bar).

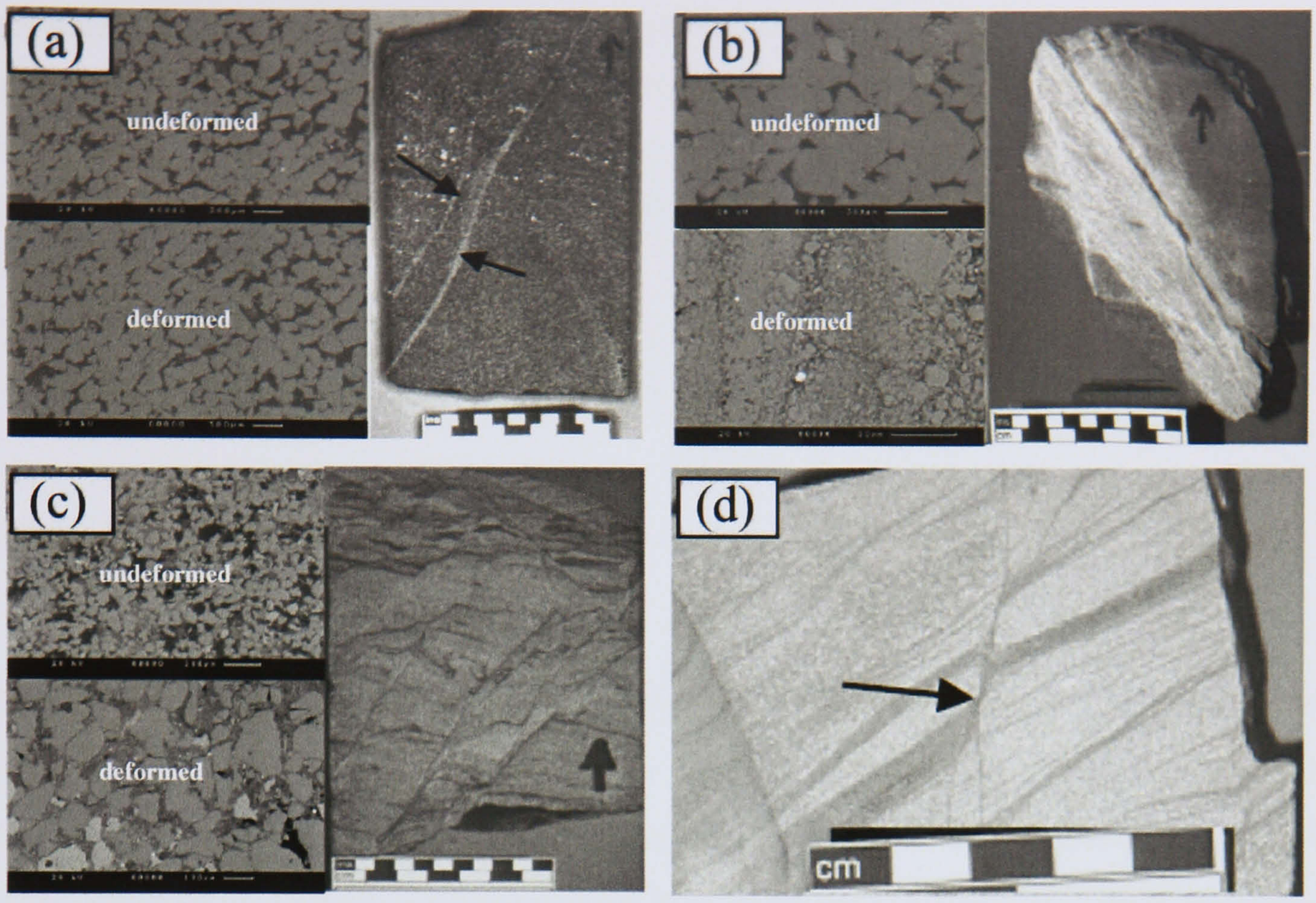

Fig. 1.6. (a) Back-scattered electron microscopy (BSEM) images for a disaggregation (deformed) zone and the adjacent undeformed sandstone. Right in (a) shows a hand specimen containing two dissaggregation zones (arrows). (b) BSEM images of an undeformed Rotliegendes sandstone and the adjacent cataclastic deformed zone (fault). Right in (b) is a hand specimen containing a zone of cataclastic faults. (c) BSEM images of undeformed impure Brent sandstone and the adjacent deformed phyllosilicate-framework fault rock. Right in (c) is a hand specimen containing several phyllosilicate-framework fault rocks. (d) a hand specimen containing a clay smear (arrow). Modified from Fisher and Knipe (2001). BSEM images scale is 300 μm.

1.4. History of fault seal analysis

Early work on fault seal concentrated on the theoretical aspects (*e.g.* Hubbert, 1953; Smith, 1966; Downey, 1984). Faults were regarded as either completely sealing or completely non-sealing (Smith, 1980). One of the early qualitative attempts at fault seal analysis was published by Bouvier *et al.* (1989), who adapted a method first introduced by Brown *et al.* (1987) to illustrate juxtaposition of lithology, in which a method called 'fault slicing' was used to evaluate juxtaposition along fault planes in the Nun River Field in Nigeria. A fault slice is an extraction of seismic amplitudes from 3D seismic along a surface parallel and adjacent to a fault plane, either in the footwall or hanging wall, and is displayed as a projection onto a vertical surface. Fault slices provide continuous, unfaulted, strike sections within narrow fault blocks of complexly faulted fields. The fault slices are useful for deriving fault throw and juxtaposition of sandstones and shales along fault planes.

Bouvier *et al.* (1989) also used another fault seal analysis method called clay smear potential (CSP), originally developed by Shell, based on laboratory and experimental studies (Weber *et al.*, 1978) to investigate fault sealing in the Nun River Field in Nigeria. Clay smear is a

geological process that involves entrapment of clay or shale within the fault zone, thereby giving the fault a high threshold pressure. Lower values of CSP equate to increased chances of fault sealing. Essentially, the CSP is a measure of the likelihood that a clay smear will be continuous along a fault. CSP represents a measure of the relative amount of clay that has been smeared from individual shale source beds at certain points along the fault plane. Input data required to calculate the CSP is the stratigraphy taken from seismic analysis or wireline logs. CSP has been defined by Fulljames *et al.* (1996) as:

$$CSP = \sum \frac{(t_{sh})^2}{D} \qquad \textbf{1.5}$$

where t_{sh} is the thickness of the shale layer which has been faulted, and D is the distance of the reference point of interest from the source bed, assumed to be less than fault offset (see **Fig. 1.7a**). The summation is over all faulted source beds. Note that in this equation t_{sh} is raised to the power of 2. This has been justified by fluid dynamics arguments by Lehner and Pilaar (1996), who stated that the outflux from the ductile shale or clay layer should be proportional to the square of its thickness if the material undergoes Newtonian flow. Note that this outflux has nothing to do with brine or oil flow across the fault; it is strictly related to the movement of the shale. CSP, as defined by **equation-1.5**, has a dimension of distance.

Subsurface data has been used to calibrate CSP in different fields. For example, Bouvier *et al.* (1989) calibrated their CSP calculations against known sealing and non-sealing faults, and divided the observed range into high, medium, and low CSP. Low CSP represents little chance for the presence of continuous clay smear seals that can trap petroleum. Jev *et al.* (1993) used the same technique on the Akaso Field (in the Niger Delta) and quoted a CSP of more than 30 as sealing for faults bounding undrilled prospects. Bentley and Barry (1991) varied the CSP of faults in their simulation model for the Cormorant Field (Brent province, northern North Sea) until a history match was achieved. They found that on a production time-scale a CSP of five marked the general threshold of fault sealing.

In 1989, Allan (Allan, 1989) introduced an important fault seal analysis method known as 'fault-plane section'. Allan began work on this method in 1967 for a Texas offshore lease sale, after which it received further testing and development at Shell's Offshore Division in New Orleans. A fault-plane section (also termed 'fault section' or 'fault-surface section') is a display of the geometry of the stratigraphy brought into contact by fault displacement, *i.e.* two sides of a fault juxtaposed. Two sections are made to the same scale and have a common line of section, which is the strike of the fault plane being investigated. The plane of the section is not vertical, as in normal cross sections, but is the plane of the fault. The bedding dips in the sections are the apparent dips of the beds at the fault in each fault block. If faults did not change throw along

strike and if stratigraphic geometry and character remained uniform, fault-plane sections would not be needed and a single conventional cross-section, perpendicular to the fault strike, would be sufficient. However, because fault throw almost always changes along strike, the only substitute for a fault-plane section would be a very inconveniently large number of conventional cross-sections. Many of the software products now available make use of fault plane maps because they can accommodate changes in fault throw and sediment stratigraphy (*e.g.* Knipe, 1997; James *et al.*, 2004).

Shale smear factor (SSF) or clay smear factor (CSF) was another fault seal analysis algorithm defined by Lindsay *et al.* (1993) to constrain the likelihood of shale smear continuity. To estimate the SSF or CSF, it is necessary to know fault throw and stratigraphic data:

$$SSF = \frac{Throw}{t_{sh}}, \qquad \textbf{1.6}$$

where 'Throw' is the vertical distance between the source beds (see **Fig. 1.7b**). Threshold values are calculated for the SSF which allow sealing potential to be assessed. From a study of 80 faults, Lindsay *et al.* (1993) suggest that faults will leak when SSF is greater than seven. Unpublished data by Rock Deformation Research (RDR) suggests that where the SSF is below three the smears are continuous and form a low permeability barrier to flow. With increasing SSF, the probability of discontinuous smears with high permeability leak points increases.

Knott (1993) approached fault seal analysis from quite a different angle in that he analysed a large dataset comprising over 400 faults from 101 exploration targets and 20 oil and gas fields in a regional study of the North Sea to provide an empirical database for determining whether faults are likely to seal or not. The emphasis of the study was on fault-related seals that act as pressure or migration barriers over geological time. Knott plotted fault strike and throw, reservoir thickness, depth, net-to-gross, porosity, and net sand connectivity to predict fault seal characteristics. He found that a correlation appeared to exist between fault orientation and sealing, but this relationship is not statistically significant. It was argued that the seal potential of a fault is proportional to fault throw normalised as a fraction of the reservoir thickness. Knott (1993) found that great a majority of faults with throw greater than the thickness of the reservoir interval were sealing faults; in many ways this is little more than saying that the juxtaposition of reservoir against non-reservoir produces far more effective barriers to fluid flow than the fault rocks themselves. Further, Knott concluded that the most useful parameters in fault seal prediction are fault displacement, net-to-gross ratio, and net-sand connectivity. Two problems exist with the approach of Knott *et al.* (1993). First, the evidence used to distinguish between sealing and non-sealing faults was not properly critically appraised and therefore many faults

were probably assigned to the wrong category. Second, faults were simply treated as sealing or non-sealing, whereas some measure of sealing capacity would have been more helpful.

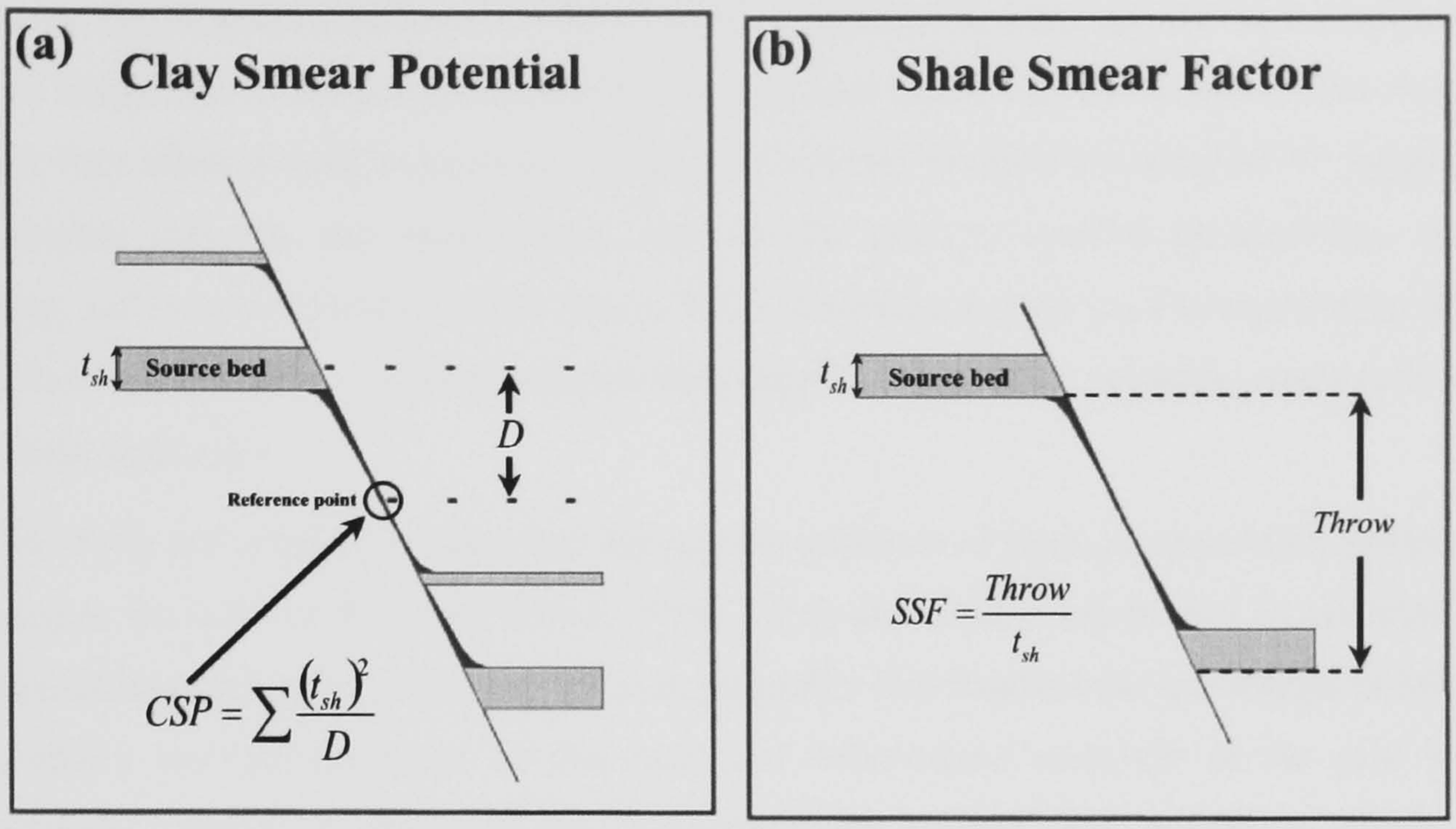

Fig. 1.7. Smear factor algorithms for estimating likelihood of clay smear on a fault plane. (a) Clay smear potential (CSP) (Bouvier *et al.*, 1989; Fulljames *et al.*, 1996) given by the square of faulted-shale thickness (source bed) divided by smear distance to a reference point. (b) shale smear factor (SSF) (Lindsay *et al.*, 1993) given by fault throw divided by the faulted-shale thickness (source bed). Method (a) models the distance-tapering of shear-type smears, whereas method (b) models the form of abrasion smears. Modified from Yielding *et al.* (1997).

Yielding *et al.* (1997) noted that the approaches of the CSP and SSF algorithms described above depend upon a consideration of the thickness and offset of individual shale beds. They stated that such an approach may be difficult to apply directly in thick heterogeneous sequences because it is often not feasible to map every shale bed and consider its effect at the fault surface. A key problem with the CSP method is that it only provides information on the continuity of clay smears and does not by itself provide an estimate of the clay content along the fault zone when the smear is discontinuous and other fault rocks are important. In such cases, Yielding *et al.* (1997) defined a simpler approach called the shale gouge ratio (SGR) that is applicable at the seismic scale where detailed information relative to individual shale beds is not available. The SGR provides an estimate of the clay content and distribution along a fault plane. SGR is calculated by estimating the cumulative shale and sand contents that have moved past a particular point along a fault (see **Chapter 2** for details). A fault may leak if it has a low SGR. It is important to mention that Yielding *et al.* (1997) actually tried to calibrate their data, *i.e.* they considered plots of SGR versus cross-fault pressure difference. The use of pressure difference, instead of the phase pressure difference in the fault, does not produce a reliable calibration for capillary seals. Furthermore, their data does not appear to contain example from fields where

cataclasis is an important fault seal process (*e.g.* Rotliegendes reservoirs from the UK southern North Sea).

To aid in the analysis of fault juxtaposition and sealing, Knipe (1997) presented a set of diagrams. The diagrams are based on the interaction of rock lithology and the fault displacement (throw) magnitude to control juxtaposition and fault seal types. The advantages of the diagrams are that they allow a rapid evaluation of fault seal without the need for detailed 3D mapping of stratigraphic horizons and fault planes, and can be used to contour permeability, sealing capacity, and transmissibility of fault zones. Those diagrams may be used to repeatedly identify the critical fault throw and juxtaposition that require mapping to identify compartments in petroleum reservoirs.

One of the first attempts to take into account the presence of faults in simulation models was reflected in the work of Knai and Knipe (1998). They used core analysis data to calculate fault transmissibility multiplier; a simulation input parameter that requires the knowledge of both the permeability and the thickness of the fault and undeformed reservoir in the grid blocks immediately adjacent to the fault (see **Chapter 2** for details). The models in which fault properties are incorporated using transmissibility multipliers allow flow across the fault according to the normal Darcy law, in which the interblock transmissibility is scaled by the fault transmissibility multiplier.

Manzocchi *et al.* (1999) use the established method of SGR by Yielding *et al.* (1997) to determine the shale content and distribution along faults for more geologically-reasonable transmissibility multiplier calculations. Unlike the CSP method, the SGR method can be used to estimate the presence of other fault rock types, *e.g.* catalasites or phyllosilicate- framework fault rock. It is possible to combine these two algorithms by using CSP to predict the distribution of clay smears and then SGR to predict the distribution of other fault rock types. The method of Manzocchi *et al.* (1999) was one of the first to provide geologically-reasonable transmissibility multipliers as input for production simulation modelling. Indeed, the algorithms have now even been incorporated into mainstream production simulation packages (*e.g.* **Eclipse 100**^{TM}, Geoquest, 2003) to generate transmissibility multipliers for complicated (in terms of properties and distribution) fault planes.

Recently, RDR (Knipe *et al.*, 2004; Freeman *et al.*, 2005) introduced the concept of the effective shale gouge ratio (ESGR) algorithm, as an improved method over the SGR, to predict the clay content and distribution in fault zones. The ESGR at a point along the fault zone is defined as the weighted running average of the SGRs calculated at increasing incremental distances away from the point in the slipped interval. A weighting factor along the throw distance is used to capture the influence of stratigraphic units at different positions along this distance. The weighting function can be any function, but RDR uses Gaussian distribution function as a weighting function based on some conducted outcrop studies (Freeman *et al.*,

2005). The ESGR can be weighted towards the clay content of units close to the point of interest. In contrast, the SGR provides an average (unweighted) of the clay in the total slipped interval, *i.e.* the SGR is one member of the series defined by the ESGR.

In the case of the footwall (FW) ESGR, for a normal fault, the stratigraphy above the point of interest that may contribute to the fault rock clay content at the point of interest, is considered to span the height equal to the throw. However, the stratigraphic units closest to the point of interest, (immediately above the point of interest) are considered most likely to influence the clay content. One way this can be viewed is, to consider a fault rock becoming thicker with increasing throw; then the stratigraphic unit, in the FW, just above the point of interest is the closest one to be incorporated into the fault as it widens. It will thus act as the main source of material for the fault rock which is then 'moved down' the fault during offset on the normal fault to be adjacent to the point of interest. Thus, the units above and closest to the point of interest in the FW are weighted to have the largest impact on the predicted ESGR value. The stratigraphic units furthest away form the point of interest (*i.e.* at a height equal to the throw above the point of interest in the FW) are considered to have the least impact and thus have a low weighting factor). That is, the FW units closest to the point of interest have the best chance to contribute material to the fault rock at the point of interest as the fault rock widens, so influence the ESGR most.

The opposite is true for the hanging wall (HW) ESGR, where the stratigraphic unit just underneath the point of interest is the one most likely to contribute material to the fault rock at the point of interest. *i.e.* think of it – as the fault widens, it incorporates the material in the unit just under the reference point, which is then sheared/'moved' to become next the point of interest as the throw is increased. Thus, for the HW ESGR the weighting used for the ESGR clay prediction is maximum for the unit just under the point of interest and decreases down the stratigraphic column until it is a minimum for the unit one throw height/depth below the point of interest.

So the FW ESGR will be different to the HW ESGR as the two have different weightings on the stratigraphic units in the throw interval even if the stratigraphy is the same in both HW and FW. This means that the FW ESGR will focus on the units just above and in the FW, while the HW ESGR will focus on the units in the HW and just below the point of interest. In an attempt to compare the SGR and the ESGR for some fault rocks, Freeman *et al.* (2005) found that predicted values in the clay contents vary by up to 20% for individual points when derived using SGR function. The difference between the measured and ESGR predicted clay values is usually less than 5%, while the average difference between measured and SGR predicted is approximately 9% (**Fig. 1.8**).

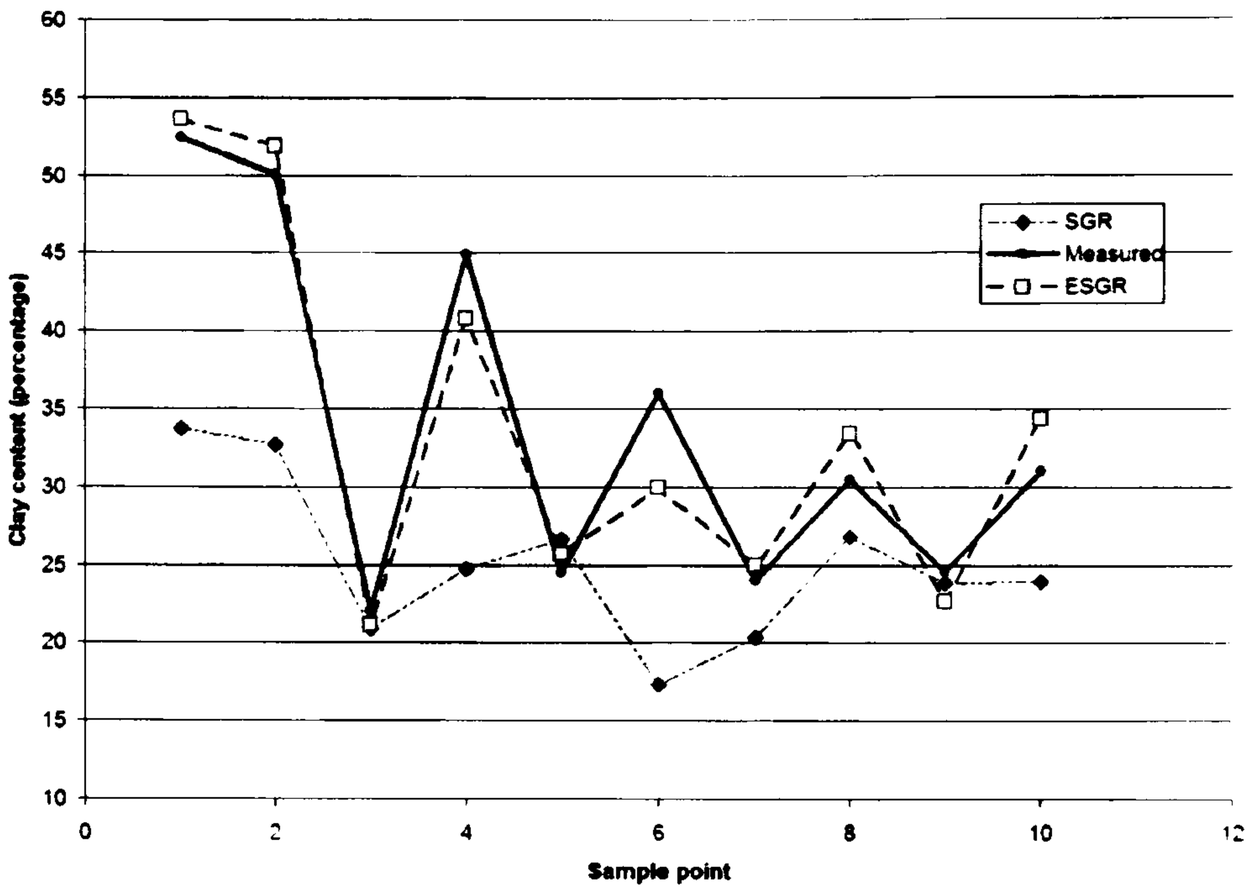

Fig. 1.8. Comparison of predicted fault-rock clay contents with measured values. Note the ESGR provides a closer fit to the measured clay content than the SGR. After Freeman *et al.* (2005).

Although it is becoming increasingly common practise to calculate geologically-reasonable transmissibility multipliers (*e.g.* Knai and Knipe, 1998; Manzocchi *et al.*, 1999), it is a long way from becoming routine. This may, however, be about to change. Many software products are now available that allow a rapid assessment of the fluid flow behaviour of faults to be made (*e.g.* TRANSGEN, TRAPTESTER, RDR FAULTSEAL TOOLBOX, PETREL, RMS, ECLIPSE, *etc.*). A certain amount of caution should, however, be exercised when using such products because, although they produce visually convincing diagrams of complex fault plane properties, it is not clear what level of accuracy that can be achieved by the application of any of these methodologies. This is for two reasons: first, there are never many post-mortem studies to see if predictions have been good; second, the interpretation of subsurface data is non-unique.

More attempts are, however, being made to establish the accuracy of fault seal analyses. For example, Fisher (2005), after reviewing around 13 production simulation models, argues that faults have tended to be made scapegoats when existing models fail to explain reservoir behaviour. A particular problem is that fault transmissibility multipliers have tended to be applied in an *ad hoc* manner without scientific justification. However, although the exact details have yet to be published, Fisher (2005) argued that initial history matches of production simulation models where fault rock properties have been incorporated are encouraging. Also, it was argued that, even if the accuracy of modern fault seal analyses could not be unequivocally proven, it is unquestionable that modern databases on the fluid flow properties of fault rocks significantly removed the 'wriggle room' in simulation by limiting the range of fault properties that could legitimately be argued to be valid.

The advances in fault seal analysis described above appear to be very positive; stumbling blocks do, however, keep arising. For example, it has recently been suggested that the problem with the way that the transmissibility multipliers are conventionally calculated is that they do not take into account the multiphase flow behaviour of fault rocks and they only represent a single-phase treatment (Fisher and Knipe, 2001; Manzocchi *et al.*, 2002). It has been suggested that it would be possible to incorporate the multiphase flow properties of faults into production simulation models using dynamic pseudofunctions (Ringrose and Corbett, 1994; Fisher and Knipe, 2001; Manzocchi *et al.*, 2002). Unfortunately, at present there have been only a few attempts to incorporate the multiphase flow properties of faults in simulation models and these are not yet in the public domain. There are several reasons why such technology is not yet being applied more often:

- There have not been sufficient studies conducted by industry to demonstrate the value of taking into account multiphase flow across fault rocks.
- The construction of pseudofunctions greatly adds to the complexity of simulation and without more evidence pointing to the benefits is difficult to justify.
- Multiphase relative permeability measurements from fault rocks are very scarce (almost non-existent, Fisher (2005)) and limited to faulted sand–shale sequences. No such measurements were reported for carbonate or interbedded shale-carbonate fault rocks.
- Limitations still exist in our understanding of the macrophysical/electrical effects of wettability alteration and its effects on fault sealing capacity.
- Most importantly is that automated ways of handling faults, *e.g.* refinements and upscaling, are only now becoming available.

1.5. Aims of thesis

The review presented above has highlighted many problems with fault seal analysis, but it has also highlighted many interesting recent developments that may in a few years revolutionise the way that the fluid flow behaviour along and across deformed materials (*i.e.* faults) is modelled. In this thesis I concentrate on one of these areas and investigate (I) the importance of incorporating the multiphase flow properties of faults into simulation models by comparing different representations of faults in both synthetic and real models, and (II) the methods that are available to incorporate the multiphase flow properties of faults into simulation models.

The initial focus of this work was to use 4D seismic data of a simulated field to validate fault seal analyses. The ideal field for this project was envisaged to have both a simulation model with long-term reliable history data and a 4D seismic data set. The first chosen field had been modelled in the MoRes simulator, which is not available for academic researchers. There was not enough time under the scope of this project to convert the commercial code of the MoRes

simulator to the academically available simulator **Eclipse 100**^{TM}. Therefore, an alternative field was sought, which happened to be a field with an **Eclipse 100**^{TM} simulation model, but unfortunately without 4D seismic data. With such a limited dataset, the initial plan of the project was altered and work was conducted on more theoretical aspects regarding the incorporation of multiphase flow properties into production simulation models.

The thesis presents different approaches, some of which are based on previous ideas, to practically account for fault multiphase fluid flow behaviour in production simulation models. The thesis is divided into seven further chapters covering various aspects of this research.

Chapter 2 introduces the concept of transmissibility multipliers that are routinely used in conventional simulation models to account for flow across faults, either for single-phase or multiphase flows. Using simple illustrative examples, the chapter compares the different ways that transmissibility multipliers are calculated. **Chapter 3**, based on a published paper, gives a detailed description of the problems associated with the use of transmissibility multipliers to model two-phase flow across faults. The chapter compares different flow scenarios to provide an answer to the question '*under what circumstances is it better to incorporate the multiphase flow properties of faults into production simulation models than to accurately account for fault rock thickness?*' The aim of **Chapters 4** and **5** is to account for faults multiphase fluid flow in the Pierce Field, North Sea, through the use of relative transmissibility multipliers, *i.e.* transmissibility multipliers are varied at certain points along the fault depth depending on the position relative to the free water level. **Chapter 4** summarises some of the microstructural and petrophysical property measurements of fault rocks within the Pierce Field. **Chapter 5**, based on a published paper, implements those measurements into the Pierce black oil simulation model. **Chapter 6** presents a simple two-cell model that can be easily used to test various parameters that can affect the shape of the generated dynamic pseudo-curves. This simple model is used to test the effects of fault thickness, fault permeability and across-fault Darcy flow rates on the general shape of the pseudo-relative permeability curves. In this chapter, this simple model is used to generate a library of pseudo-curves. The validity of these curves is tested by comparing different faults representations for 3D models with an assumed high-resolution true model, for different degrees of complexity. **Chapter 7** addresses some weaknesses with the approach used in **Chapter 6**, and presents an alternative model for pseudo-curve generation. Using an analogous validation technique to that used in **Chapter 6**, the approach in this chapter is validated. Finally, **Chapter 8** presents conclusions from this thesis and recommendations for possible further work in this area.

Chapter 2

Interblock transmissibilities and fault transmissibility multipliers

"The goal of successful production is to maximise flow by exploiting or applying pressure gradients. The resistance to flow is the viscosity of the fluid, and the coefficients relating viscosity and pressure gradients to flow rates, are permeability and length. Hence the most important fault properties for production are the permeability and thickness of the fault-rock, and these properties are captured in the flow simulator as transmissibility multipliers."

Tom Manzocchi

Fault Analysis Group, Department of Geology, University College Dublin

2.1. Introduction

In production simulation models, transmissibility is defined as the conductance that appears in mass transfer problems, *i.e.* mass flow of the oil, water and gas in a porous media. Transmissibility depends only on block geometry, permeability and net-to-gross ratio (Hegre *et al.*, 1986). Interblock transmissibility calculations differ depending on the geometry used, *i.e.* traditional block centred, flexible corner point or radial. In this chapter, transmissibility in a corner point geometry is presented (Ponting, 1989). A corner point geometry defines a distorted grid with cells assumed to have edges defined as straight lines between the corner points, and the cell faces may be bilinear surfaces, **Fig. 2.1**. Pore volumes may be calculated exactly for such a shape. The implementation of this type of geometry was first described by Goldthrope and Chow (1985). They applied this technique on a highly faulted field utilising a non-rectangular grid in the horizontal plane, variable layer thickness and non-standard connections across sloping faults.

The calculation of interblock transmissibility is illustrated here for a pair of grid blocks as shown in **Fig. 2.1c**. Although slightly varying formulae are presented in the literature for interblock transmissibility calculations (*cf.* Ponting, 1989; Sammon, 2000; Cordazzo *et al.*, 2002), this chapter follows the way they are calculated in the **Eclipse 100™** simulator for distorted corner point geometries following the derivation of Ponting (1989), see **Eclipse 100™** manual, Geoquest (2003). Examples will be presented to compare the way interblock transmissibilities are calculated in **Eclipse 100™** and the way they are calculated in some reported formulae in the literature.

This chapter is divided into two parts. In the first part, **§ 2.2**, expressions used by **Eclipse 100™** to calculate corner point transmissibility calculations are described. In the second part,

§ **2.3-2.4**, steps for accounting for the resistance to fluid flow of a fault in simulations models through absolute transmissibility multiplier calculations are outlined.

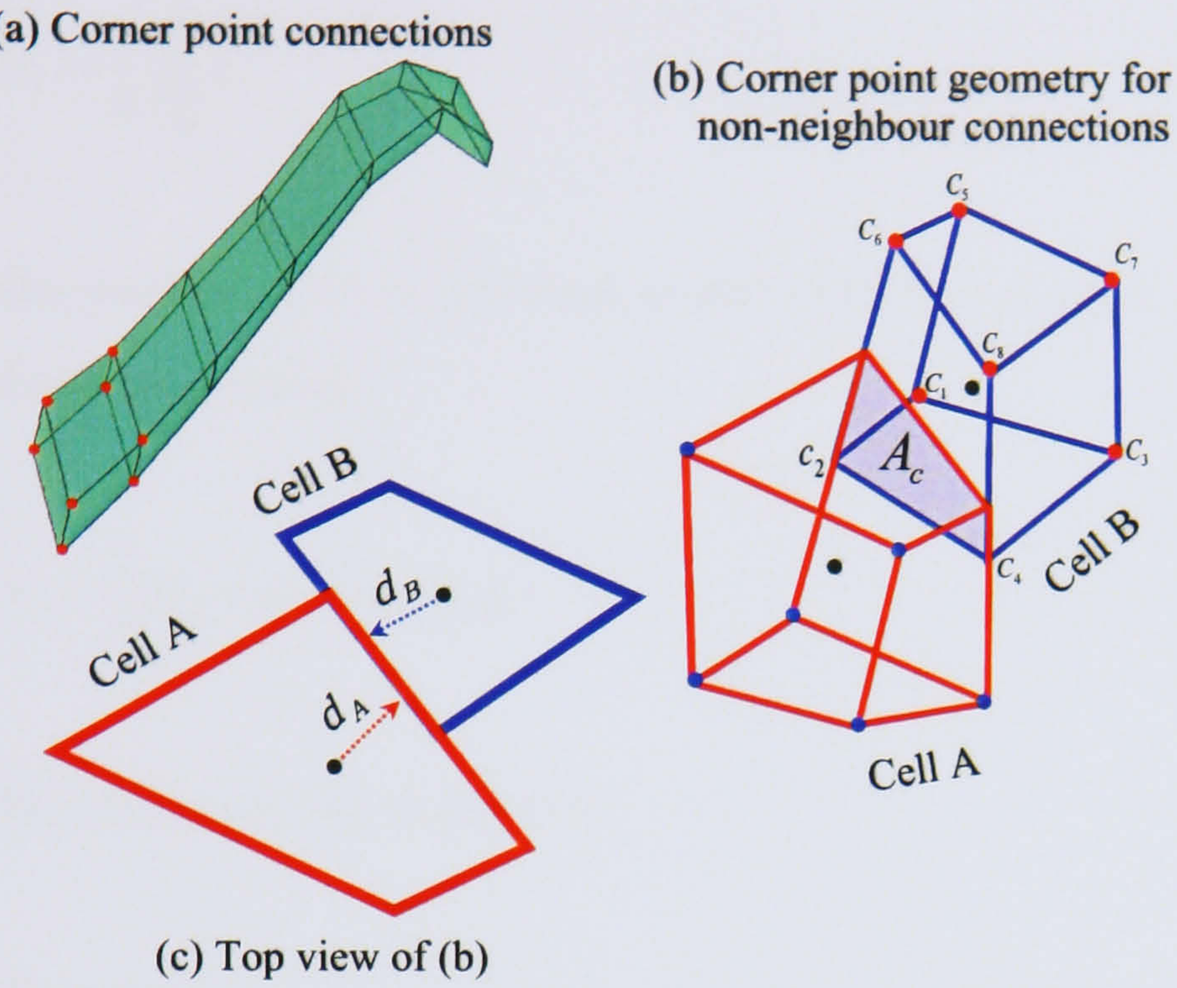

Fig. 2.1. Corner point grid blocks are defined by their eight corners in the coordinate system. Each corner is represented by a vector ($\mathbf{c}_i$). The corner point geometry gives flexibility when representing dipping beds (**a**) or faults (**b**). $\mathbf{d}_A$ and $\mathbf{d}_B$ in **(c)** are vectors from the cell centre to the centre of the relevant cell face.

2.2. Corner point interblock transmissibility calculations

This section presents the interblock transmissibility calculation as performed in the **Eclipse 100™** simulator (**Eclipse 100™** manual, Geoquest, 2003). Different formulations reported in the literature will also be presented. A simple numerical example will be given to compare different interblock transmissibility calculations.

2.2.1. Corner point interblock transmissibility calculations in the Eclipse 100™ simulator

This method of interblock transmissibility calculations is based upon the use of cell corner points, which are available to the **Eclipse 100™** simulator when using the *COORD* and *ZCORN* keywords (see Schlumberger Geoquest, 2003, manual for an overview of **Eclipse 100™** data file). In this case it is possible to distinguish unambiguously between the cell dip and the fault displacement. For corner point grid geometry, the transmissibility values between adjacent gridblocks are calculated from the *x*-, *y*- and *z*-projections of the mutual interface area of the two cells. An inner product is taken with the vector from the cell centre to the centre of the cell face, so that the dip correction is automatically incorporated.

Consider the corner point geometry shown in **Fig. 2.1b-c**. The distance between the centre of cell B and the centre of the relevant face of cell B is given by the magnitude of the vector $\mathbf{d}_B$.

The position vector of the centre of the volume of cell B, $\mathbf{v}_1$, is determined by averaging its eight corner position vectors:

$$\mathbf{v}_1 = \frac{1}{8}\sum_{i=1}^{8}\mathbf{c}_i \qquad \textbf{2.1}$$

The position vector of the centre of the frontal face of cell B, $\mathbf{v}_2$, is determined by averaging its four corner vectors:

$$\mathbf{v}_2 = \frac{1}{4}(\mathbf{c}_2 + \mathbf{c}_4 + \mathbf{c}_6 + \mathbf{c}_8) \qquad \textbf{2.2}$$

Thus the vector $\mathbf{d}_B$ is given by:

$$\mathbf{d}_B = \mathbf{v}_2 - \mathbf{v}_1 \qquad \textbf{2.3}$$

The vector $\mathbf{d}_A$ is determined in the same way. The true mutual interface area, or contact area, between cell A and cell B is denoted by A_c, see **Fig. 2.1b**. When flow occurs from the centre of one cell to the centre of its relevant face, it 'sees' A_c projected on a plane perpendicular to the flow direction. The projected area normal to the flow direction is generally different to the actual area A_c. To illustrate the differences between the projected and the actual contact areas, consider the 2D illustration in **Fig. 2.2**.

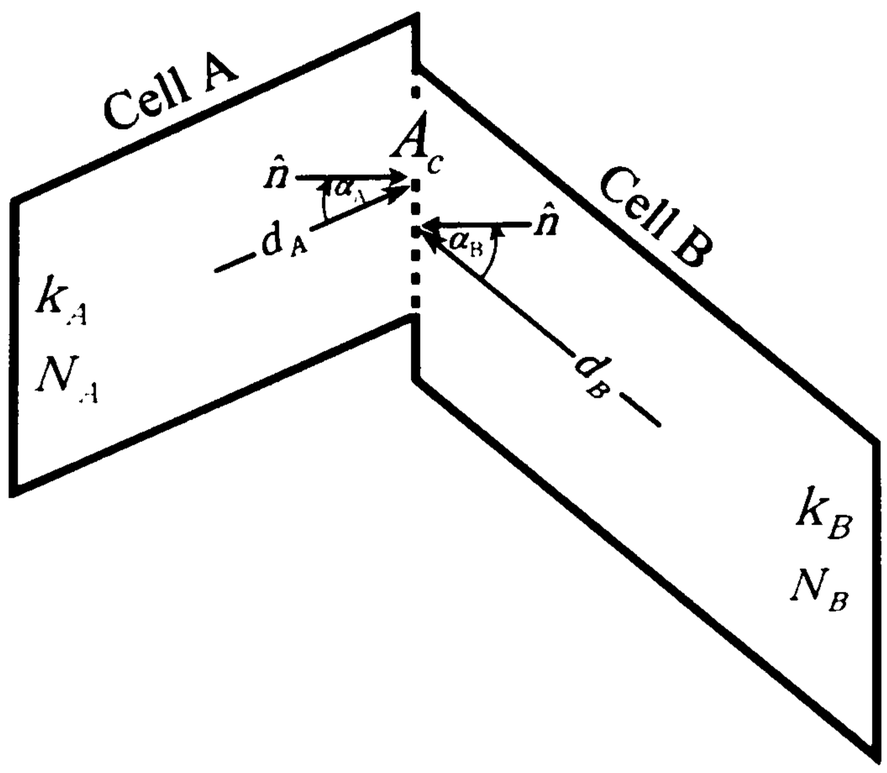

Fig. 2.2. Distorted, sheared, grid block connection illustrating that the contact areas, A_A and A_B, projected on planes normal to the flow direction (from cell centre to face centre) are different from the actual contact area (A_c). k and N are cell permeability and net-to-gross ratio.

The flow direction projected areas A_A and A_B are given by:

$$A_A = A_c(\hat{\mathbf{n}}.\hat{\mathbf{d}}_\mathbf{A}) = A_c\cos(\alpha_A) \qquad \textbf{2.4}$$

$$A_B = A_c(\hat{\mathbf{n}}.\hat{\mathbf{d}}_\mathbf{B}) = A_c\cos(\alpha_B) \qquad \textbf{2.5}$$

where $\hat{\mathbf{n}}$ is the unit vector normal to the true contact area A_c. Here α_A and α_B are the angles that the vectors $\mathbf{d}_\mathbf{A}$ and $\mathbf{d}_\mathbf{B}$, respectively, make with the normal vector $\mathbf{n}$, $\hat{\mathbf{d}}_\mathbf{A}$ and $\hat{\mathbf{d}}_\mathbf{B}$ are unit vectors of the vectors $\mathbf{d}_\mathbf{A}$ and $\mathbf{d}_\mathbf{B}$, respectively, given by:

$$\hat{\mathbf{d}}_\mathbf{A} = \frac{\mathbf{d}_\mathbf{A}}{d_A} \qquad \textbf{2.6}$$

$$\hat{\mathbf{d}}_\mathbf{B} = \frac{\mathbf{d}_\mathbf{B}}{d_B} \qquad \textbf{2.7}$$

and d_A and d_B are the magnitudes of the vectors $\mathbf{d}_\mathbf{A}$, and $\mathbf{d}_\mathbf{B}$, respectively.

After defining all the required geometry, the interblock transmissibility between cell A and cell B, T_{AB}, is defined in the **Eclipse 100™** simulator from these geometries and cell properties as follows:

$$T_{AB} = \frac{C_d.T_{mult}}{\frac{1}{T_A} + \frac{1}{T_B}} \qquad \textbf{2.8}$$

where

C_d = Darcy's constant

= 0.00852702 (Metric units)

= 0.00112712 (Field units)

T_{mult} = absolute transmissibility multiplier that enables the user to change the transmissibility to account for features that enhance or resist the flow (*e.g.* fractures, faults, *etc.*).

T_A and T_B are the transmissibilities of cell A and cell B, respectively, defined as follows:

$$T_A = k_A.N_A.\frac{A_A}{d_A} \qquad \textbf{2.9}$$

$$T_B = k_B.N_B.\frac{A_B}{d_B} \qquad \textbf{2.10}$$

where k is the absolute permeability and N is the net-to-gross ratio of each cell.

2.2.2. Different formulation for interblock transmissibility calculations

The expression for calculating interblock transmissibility presented in **equation-2.8** is the most widely reported expression in the literature (Hegre *et al.*, 1986; Ponting, 1989). Cordazzo *et al.* (2002) argued that, but without giving a detailed derivation, inner block transmissibilities, *i.e.* T_A and T_B in **equation-2.8**, must be weighted by an area factor for the general case when $A_A \neq A_B \neq A_c$. This factor is the contact area divided by the gridblock area, *i.e.*:

$$T_{AB} = \frac{C_d.T_{mult}}{\frac{1}{\frac{A_c}{A_A}T_A} + \frac{1}{\frac{A_c}{A_B}T_B}} = \frac{C_d.T_{mult}.A_c}{\frac{A_A}{T_A} + \frac{A_B}{T_B}} \qquad \textbf{2.11}$$

Equation-2.11 gives different results to **equation-2.8** if the angles α_A and α_B, see **Fig. 2.2**, are different. To demonstrate this difference, consider the grid connection shown in **Fig. 2.3**.

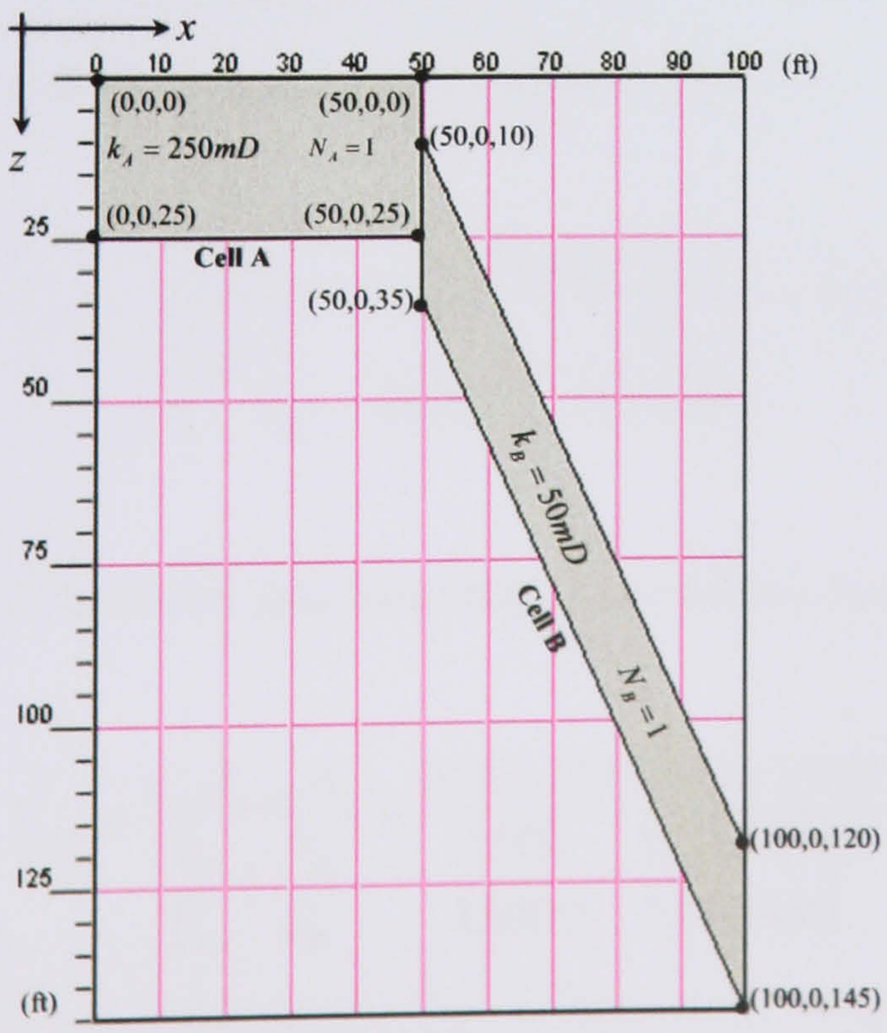

Fig. 2.3. Grid connection example to demonstrate the differences in cells interblock transmissibility calculations, see text.

Both cells in **Fig. 2.3** extend 100 ft along the y-direction. Using the geometry shown, the following areas can be easily determined:

$$A_c = (100 \times 15) = 1500 \text{ ft}^2$$

$$A_A = A_c = 1500 \text{ ft}^2$$

$$A_B = A_c(\hat{\mathbf{n}}.\hat{\mathbf{d}}_\mathbf{B}) = A_c\left(\frac{\hat{\mathbf{n}}.\mathbf{d}_\mathbf{B}}{d_B}\right)$$

$$2\mathbf{d}_\mathbf{B} = (50,50,22.5) - (100,50,132.5) = (-50,0,-110)$$

$$\hat{\mathbf{n}}.\mathbf{d}_\mathbf{B} = (-1,0,0).(-25,0,-55) = 25$$

$$d_B = \tfrac{1}{2}\sqrt{(50)^2 + (0)^2 + (110)^2} \approx 60.4152 \text{ ft}$$

$$\therefore A_B = A_c\left(\frac{\hat{\mathbf{n}}.\mathbf{d}_\mathbf{B}}{d_B}\right) = 1500\frac{25}{60.41523} \approx 620.7044 \text{ ft}^2$$

Note the considerable difference between A_B and A_c.

The inner transmissibility of each cell can be determined as follows (with $N_A = N_B = 1$):

$$T_A = k_A.N_A.\frac{A_A}{d_A} = 250\frac{1500}{25} = 15000 \text{ mD.ft}$$

$$T_B = k_B.N_B.\frac{A_B}{d_B} = 50\frac{620.7044}{60.41523} \approx 513.6986 \text{ mD.ft}$$

As calculated by the **Eclipse 100™** simulator, the interblock transmissibility multiplier, in field units and T_{mult} given its default value of 1, is:

$$T_{AB} = \frac{C_d.T_{mult}}{\frac{1}{T_A} + \frac{1}{T_B}} = \frac{0.00112712 \times 1}{\frac{1}{15000} + \frac{1}{513.6986}} \approx 0.5598 \text{ cP.rb/day/psi}$$

If, however, area weighting is considered, see **equation-2.11**, then T_{AB} will become:

$$T_{AB} = \frac{C_d.T_{mult}.A_c}{\frac{A_A}{T_A} + \frac{A_B}{T_B}} = \frac{0.00112712 \times 1 \times 1500}{\frac{1500}{15000} + \frac{620.7044}{513.6986}} \approx 1.2923 \text{ cP.rb/day/psi}$$

This difference in the interblock transmissibility calculations is very considerable. However it is only apparent on highly distorted connections where α_A and α_B are very different. Note that this difference is not only for cells with partial connection, as Cordazzo *et al.* (2002) stated, but it is still possible for cells with full contact where α_A and α_B are different. To avoid such complications in this chapter, and the proceeding chapters, we follow the **Eclipse 100**^{TM} simulator calculations, and we will avoid grid connections where α_A and α_B are significantly different.

2.3. Fault transmissibility multipliers

Faults are key features that control the flow regime in petroleum reservoirs. Faults often reduce the rate of petroleum production within petroleum reservoirs (*e.g.* Bunn and Yaxley, 1986; Bentley and Barry, 1992; Knai and Knipe, 1998). They are mainly classified into two groups: static and dynamic. A seal which has the capacity to maintain a pressure drop over millions of years (geological time scale) is deemed to have a static sealing capacity. A seal that can maintain a pressure drop only over the lifetime of a single field (5-100 years) is deemed to have a dynamic sealing capacity.

A fault represents a 3D zone with independent properties from the reservoir host rocks. With the aid of high resolution 3D seismic studies, fault zone extensions and geometries can be inferred in complex faulted reservoirs. In the world of reservoir simulation, engineers had to provide an alternative representation for these faulted zones. The reason for this is that most reservoir simulators were designed to handle 1D flow barriers instead of the complicated 3D faulted zones found in nature. Representing faults using the concept of a 3D zone is still possible in simple reservoir models, *i.e.* reservoirs with a well-defined geometry and a few faults that can be assumed vertical and straight. However, real situations are far from being simple and 3D fault zone inclusion in reservoir simulation is far more complicated in highly faulted reservoirs. For this reason, reservoir engineers use the concept of 'fault transmissibility multipliers'. In this transmissibility multiplier representation the static properties of the real 3D fault zones, *e.g.* fault permeability and geometry, are captured and represented as a single and absolute value. This value is termed an absolute transmissibility multiplier and it is multiplied with the interblock transmissibility, **equation-2.8**, to give the overall flow resistance that accounts for faults.

A transmissibility multiplier is a simple ratio between 'faulted transmissibility' and 'unfaulted transmissibility' (Manzocchi *et al.*, 1999). Within a reservoir model, 'unfaulted transmissibility' is the flow potential across a fault that has no fault rock, such as clay smear, cataclasis or diagenetic alteration. The primary control on flow potential will be reservoir connectivity across the fault, *i.e.* the position and surface area of the reservoir connections. The

'faulted transmissibility' implicitly incorporates the permeability, *e.g.* using an estimate of clay or shale concentration within fault gouge and thickness of fault rock products in the calculation of the potential flow across reservoir connections. The transmissibility multiplier therefore expresses the extent to which fault rock products will reduce flow across reservoir connections.

To capture the static properties of fault zones using transmissibility multipliers, knowledge of both the permeability and thickness of the fault rock and the undeformed reservoir of the grid blocks immediately adjacent to the fault are required.

2.3.1. Fault displacement

The primary parameter used to estimate fault thickness is fault displacement. The fault displacement calculation determines which cells have been offset across a fault and defines the distance between the cell face centres across the fault. The displacement magnitude across a fault between cell A and cell B (**Fig. 2.4**) is given by:

$$d_{AB} = \sqrt{(x_A - x_B)^2 + (y_A - y_B)^2 + (z_A - z_B)^2} \qquad \textbf{2.12}$$

The symbol d for fault displacement should not be confused with the vector $\mathbf{d}$ that appears in the interblock transmissibility calculations, see § **2.2.1**. Here (x_A, y_A, z_A) are the coordinates of the face centre on cell A adjacent to the fault and (x_B, y_B, z_B) are the coordinates of the face centre on cell B adjacent to the fault. The face centre on a grid cell is calculated using the average position vectors of the four corners of the face (Note that the two considered cells need not to be in the same layer):

$$(x_A, y_A, z_A) = \left(\frac{x_{A1} + x_{A2} + x_{A3} + x_{A4}}{4}, \frac{y_{A1} + y_{A2} + y_{A3} + y_{A4}}{4}, \frac{z_{A1} + z_{A2} + z_{A3} + z_{A4}}{4} \right) \qquad \textbf{2.13}$$

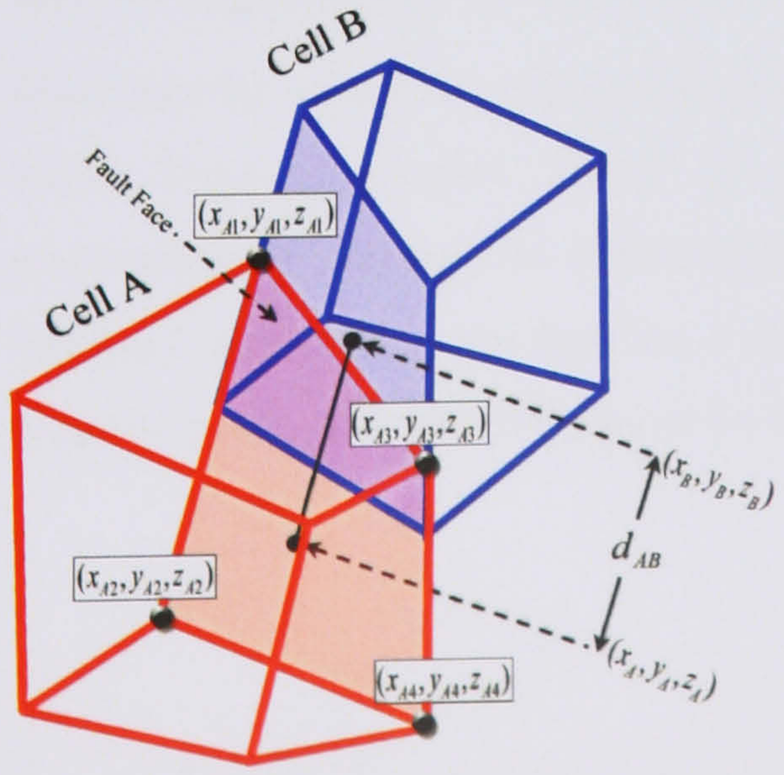

Fig. 2.4. Displacement magnitude across a fault between two non-neighbouring connected cells in a corner point geometry.

2.3.2. Fault thickness

Outcrop studies of faults reveal that there is a relationship between fault displacement and fault thickness. Depending on the scale of observation, this relationship may be linear:

$$t_f = b_0 \times d \qquad \textbf{2.14}$$

or logarithmic:

$$\log t_f = b_0 \times \log d \qquad \textbf{2.15}$$

where t_f is the fault thickness, d is the fault displacement, and b_0 is an empirical constant fit to observed data, typically derived from outcrop or core.

Detailed observations of faulted outcrops often reveal that the thickness of the fault zone is highly dependent on the mechanical strength of the rocks at the time of deformation (*e.g.* Hull, 1988; Knott *et al.*, 1996; and Foxford *et al.*, 1998). For example, poorly lithified sands, where the high porosity promotes deformation band and damage zones, are likely to produce thicker fault zones than thick, well-lithified sands, where the high lithification should induce a focused fault zone. For this reason, a lithology-based 'brittleness' weighting factor can be introduced for the fault thickness. This brittleness factor is applied to all rock units that have slid past a given point on the fault as a weighting factor to calculate the fault thickness. Thus **equation-2.14** can be generalised to the form:

$$t_f = \sum (b_i \times d_i) \qquad \textbf{2.16}$$

where the sum includes all the rock units that have slid past a given point on the fault with a specific displacement d_i and a brittleness b_i. **Figure 2.5** is a schematic block diagram that illustrates the calculation of the fault thickness incorporating the brittleness of the different rock units. These brittleness values of units can be derived from empirical observations, geomechanical analogs, or estimations of relative rock brittleness. Typically, each different lithology displaced by the fault has a distinct brittleness weighting factor. In practice, the values used for brittleness should be those for the rock units at the time of faulting.

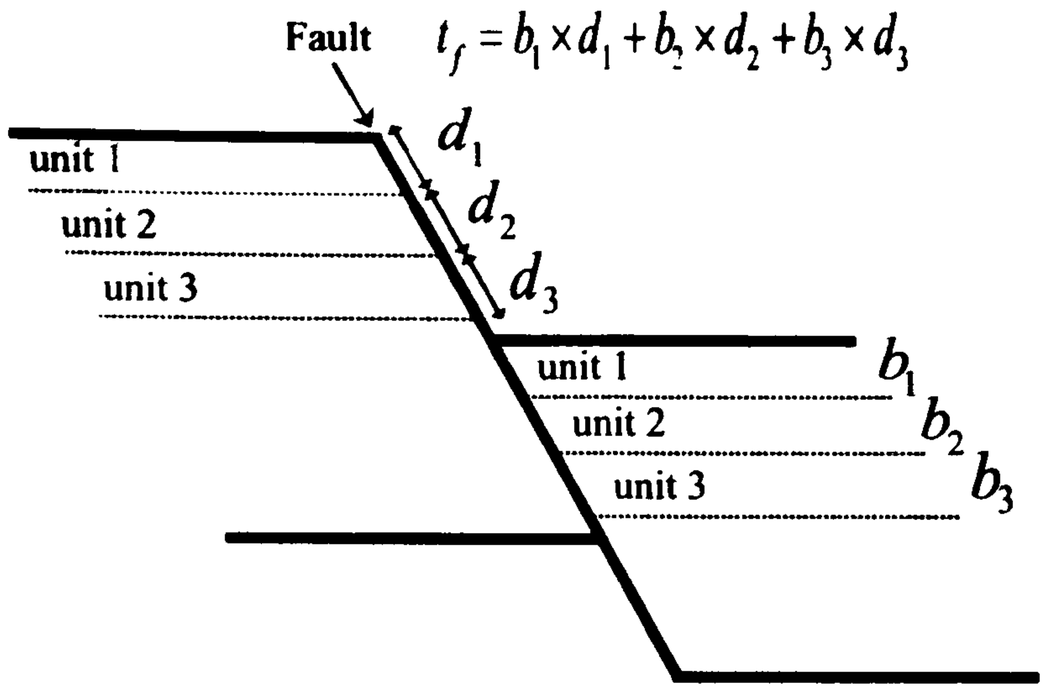

Fig. 2.5. Schematic block diagram illustrating the calculation of the fault thickness incorporating the brittleness of different rock units.

The thickness of the fault zone is defined as either the separation between the outermost slip surfaces (where more than one are present) minus the thickness of undeformed lenses, or the thickness of the slip surface itself in a lacuna. **Figure 2.6**, after Manzocchi *et al.* (1999) summarises the data compiled by Hull (1988), and data from faults in mixed sandstone/shale sequences in Sinai (Knott *et al.*, 1996), SE Utah (Foxford *et al.*, 1998) and Lancashire, UK (Walsh *et al.*, 1998a). Also plotted for several displacements are synthetic thickness values generated using the relationship $t_f = d/66$ to define a median thickness value, and a standard deviation for $\log t_f$ of 0.9 to define a log-normal thickness distribution. The data populate closely the envelopes defined by the outcrop studies for displacements over about 1 m. The relation $t_f = d/66$ tends to under-predict the thickness of smaller faults but, as fault displacements less than 1 m are seldom incorporated in production flow simulation models, there is no need to accurately predict their thickness for this application. In general, for the 200 log-normally distributed thickness data shown in **Fig. 2.6**, there are two main relationships between fault thickness and displacement:

Median value following the relationship:

$$t_f = \frac{d}{66} \qquad \textbf{2.17}$$

and the harmonic averages of these data follow the relationship:

$$t_f = \frac{d}{170} \qquad \textbf{2.18}$$

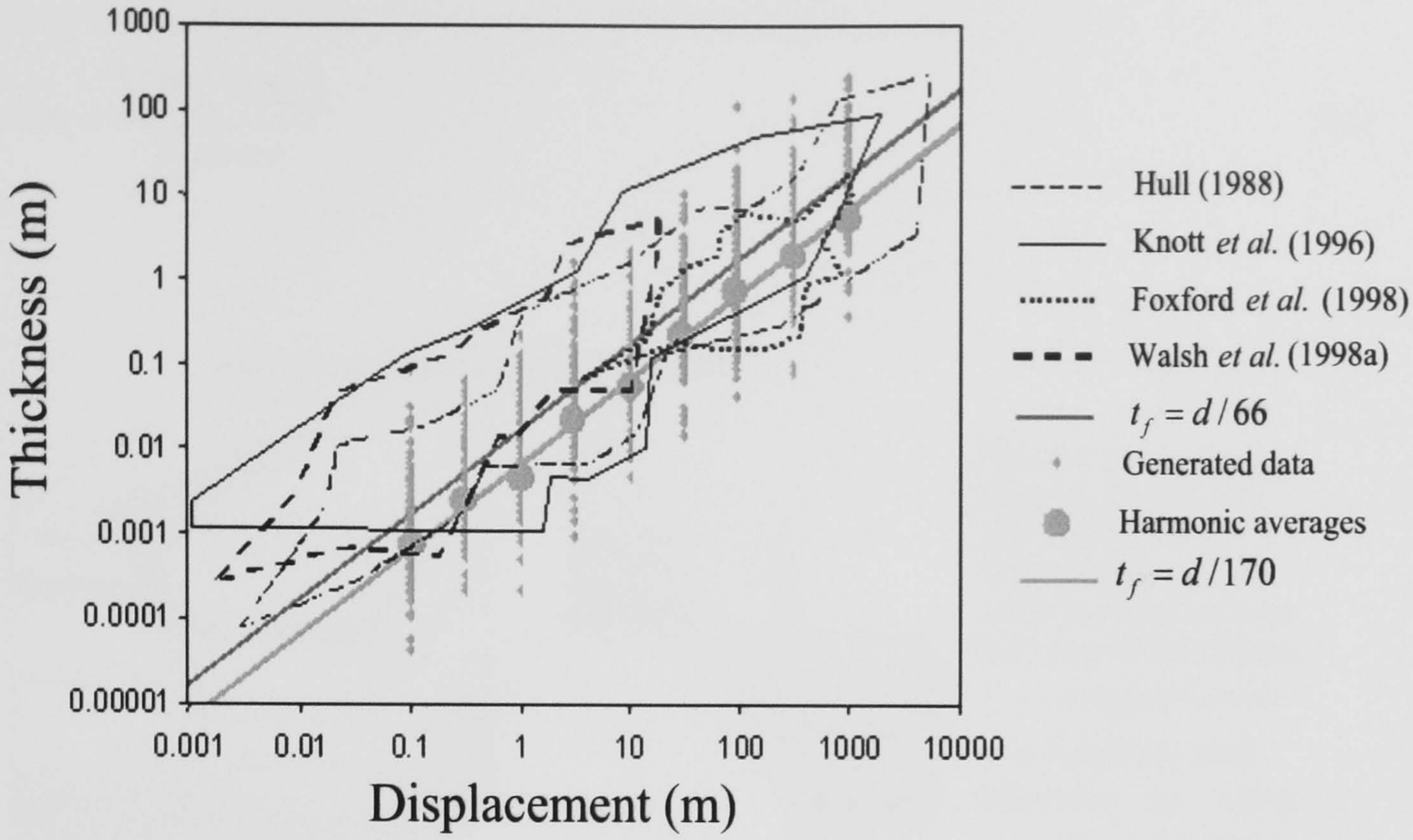

Fig. 2.6. Fault thickness (log scale) as a function of displacement (log scale). Summaries of outcrop measurements are given as envelopes containing measurements from a variety of sources (Hull, 1988), from faults in Nubian Sandstone in Western Sinia (Knott *et al.*, 1996), from the Moab Fault in SE Utah (Foxford *et al.*, 1998) and from faults in a Westphalian sandstone/shale sequence from Lancashire, UK (Walsh *et al.*, 1998a). 200 log-normally distributed thickness data (small grey dots) have been generated at various displacements with median value following the relationship $t_f = d/66$. The harmonic average of these data (large circles) follow the relationship $t_f = d/170$. Modified from Manzocchi *et al.* (1999).

2.3.3. Shale gouge ratio

Before showing how fault permeability is derived, we introduce the definition of the shale gouge ratio or SGR as a fault seal attribute that gives an estimate of the clay or shale concentration within fault gouge, mapped across the central surface of the fault. Shale forms an external effective capillary seal and permeability barrier due to the very small size of the pore throats and pore spaces. Faults can incorporate shale from the surrounding sequence during slip (*e.g.* Yielding *et al.*, 1997). The process of shale incorporation has been modelled using algorithms such as the clay smear potential (CSP; Bouvier *et al.*, 1989), shale smear factor (SSF; Lindsay *et al.*, 1993) and the shale gouge ratio (SGR; Yielding *et al.*, 1997; Freeman *et al.*, 1998). In the petroleum industry, the most commonly applied of these is the shale gouge ratio, see **Fig. 2.7**. The value of the SGR for a single cell face can be found as a weighting average of the effects of all other cells that have slid past that particular cell during the fault's displacement. For example, Yielding *et al.* (1997) gave a general definition for SGR for cases where the stratigraphic breakdown is by reservoir zone (**Fig. 2.7**). In such cases, the net contribution of fine-grained material from each reservoir zone can be related to the shale content (V_{sh_i}), or clay content, and individual zone thickness (Δz_i):

$$SGR = \frac{\sum \left(V_{sh_i} \times \Delta z_i \right)}{\sum throw} \qquad \textbf{2.19}$$

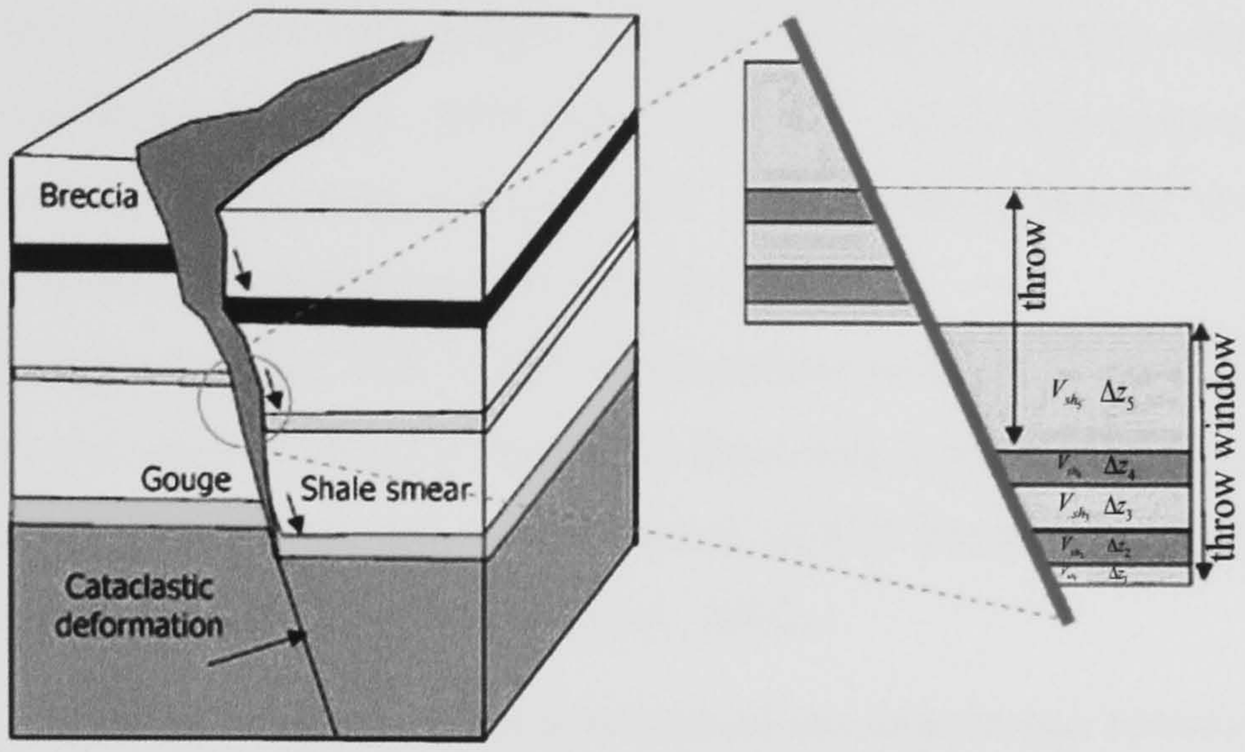

Fig. 2.7. A schematic diagram shows how shale gouge ratio (SGR) is calculated within a throw window from the shale volume, V_{sh_i} , in every horizon and individual zone thickness, Δz_i , using **equation-2.19**. After Yielding *et al.* (1997).

A high SGR value for a particular region of a fault would indicate that rock units with a high percentage of shale have slipped past that part of the fault. Pressure differences across faults of known SGR, derived from repeat formation tester (RFT) measurements, or different hydrocarbon column heights across a fault can be used to calibrate the results of the shale gouge algorithm (*e.g.* Yielding *et al.*, 1997). Fristad *et al.* (1997), Ottesen Ellevest *et al.* (1998), and Yielding *et al.* (1999a,b) have determined that the onset of static seal, *i.e.* seal over geological time, occurs when the fault gouge reaches 18-20% SGR. The pressure drop (hydrocarbon column height) that the fault can support increases as the calculated clay content of the fault increases (Yielding, 2002). Foxford *et al.* (1998) concluded that field observations support using an SGR of approximately 20% to distinguish between the presence or absence of a continuous clay smear and, implicitly, to distinguish those parts of faults which are sealing and non-sealing. Yielding (2002) suggested than an SGR of more than 15-20% indicates that a shaley or clay-rich gouge predominates in the fault, whereas an SGR of less than 15-20% indicates a clay-poor fault gouge, *e.g.* a cataclastic or disaggregation zone (see Fisher and Knipe, 1998, 2001).

Using dynamic pressure data across faults in the Strathspey and Gullfaks fields, Harris *et al.* (2002) showed that there is a link between composition of fault zone material and permeability by demonstrating a positive relationship between SGR and dynamic pressure drop across faults. These studies confirm that SGR can be used as a scalable permeability attribute. This 'scalability' of SGR as an indicator of fault permeability within a field could provide hitherto

unachievable flexibility in the systematic modelling of the hydraulic behaviour of faults during fluid flow simulations.

2.3.4. Fault permeability

The value of SGR is assumed to be related to the percentage of clay in the fault zone (Yielding *et al.*, 1997). Thus SGR can be converted to permeability using experimental determinations of permeability for fault gouges with varying clay content and the appropriate geological history (see Manzocchi *et al.*, 1999; Sperrevik *et al.*, 2002). The calibration by Manzocchi *et al.* (1999) indicates that a fault gouge with a clay content of around 20% will be expected to have a permeability of between 0.03 and 0.3 mD.

A single value of SGR is likely to represent several different values of permeability, depending on the depth of burial or degree of diagenetic alteration. Thus, at greater depths of burial, fault zone material with the same value of SGR is likely to be less permeable than at a shallower depth of burial (see Sperrevik *et al.*, 2002).

Manzocchi *et al.* (1999) summarised the relationship between volumetric shale fraction and fault rock permeability using different sources (**Fig. 2.8**). The figure shows plug and probe permeability data for various reservoirs and outcrop fault rock samples (Antonellini and Aydin, 1994; Knai, 1996; Gibson, 1998; Ottesen Ellevest *et al.*, 1998). The data in **Fig. 2.8** show a general decrease in fault zone permeability with increasing shale content, and a large variation in permeability at a particular shale content. At a very low shale content it has been suggested that there is an apparent bimodal distribution governed by fault displacement, demonstrated by the data from Antonellini and Aydin (1994). These data are probe permeameter measurements from samples of the Moab ($V_{shale} = 0$) and Slickrock ($V_{shale} = 0.09$) members of the Entrada Sandstone formation. The clean Moab Sandstone shows a clean distinction between the permeability of the deformation bands (displacements in the range 1 mm to a few centimetres and average fault rock permeabilities of about 10 mD) and the slip surface (displacements greater than about 1 m and average permeabilities of less than 0.01 mD). In the more shaley rock member, the permeabilities of the deformation bands and the slip surfaces are similar with average values of around 0.8 mD. A decrease in the influence of displacement on fault permeability with increasing shale content is caused by these differences in deformation style. In pure sandstone, cataclastic intensity increases with displacement (*e.g.* Crawford, 1989), ultimately resulting in highly polished, intensely cataclastic slip surfaces with exceptionally low permeabilities. However, Fisher and Knipe (2001) argued that grain size and permeability reductions on major slip planes (*i.e.* those with ten of metres of displacement) on number of fields, *e.g.* 90 Fathom Fault in England and Moab Fault in the USA) are often similar to those on the small-scale features examined in the surrounding damage zone. They have attributed the similarity between the microstructure of seismic-sacle faults and the smaller scale features to

two reasons. First, the total stain accommodated by a fault may be less important in controlling its grain-size distribution that the effective stress at the time of faulting. Second, each movement of seismic-scale faults results in small-offset faults of the surrounding reservoir. These latter deformations can be seen in cores and their examination can actually provide a good representation of the fault rock types present along larger offset features. As will be seen in **Chapters 4** and **5**, small-scale features preserved in core samples will be used to estimate some simulation properties of the larger scale features, relying on the finding of these experimental studeis. Deformation bands in more shaley sandstone are less cataclastic, as displacement is accommodated by small-scale smearing of the phyllosilicates (*e.g.* Antonellini and Aydin, 1994), and the main control on fault permeability is the shale content of the fault (Manzocchi *et al,* 1999).

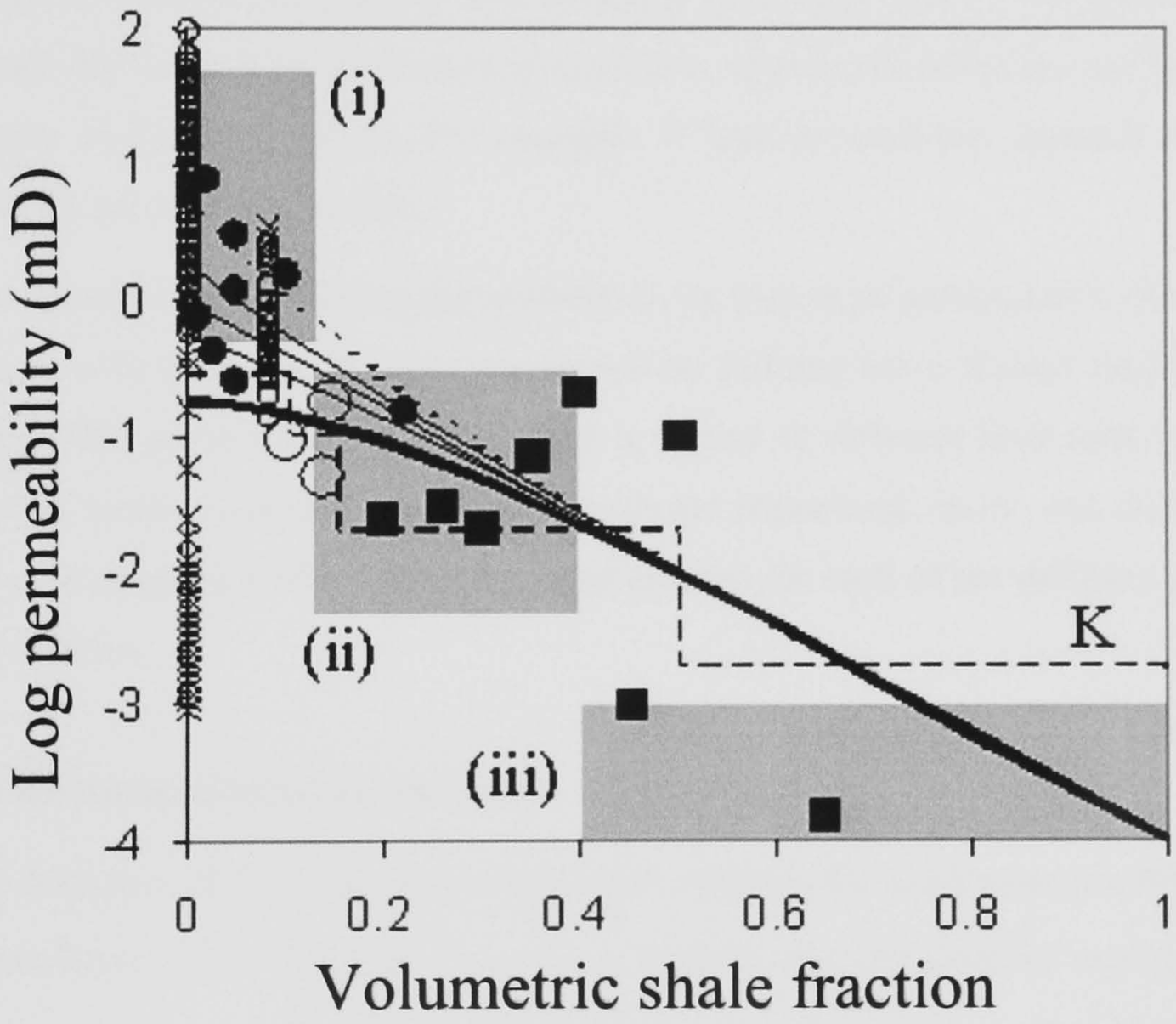

Fig. 2.8. Log permeability (mD) as a function of the volumetric shale fraction for fault rocks. Large data points are plug permeability measurements from core and outcrop samples from a variety of locations (Gibson, 1998). Filled circles: cataclastic deformation bands. Open circles: solution deformation bands. Filled squares: clay gouge. Small data points are probe permeability measurements of deformation bands (open circles) and slip surfaces (crosses) from sandstones in SE Utah (Antonellini and Aydin, 1994). The large grey boxes are summaries of data from the Sleipner Field (Ottesen Ellevest *et al.*, 1998): (i) cataclastic deformation bands, (ii) Phyllosilicate framework fault rocks, (iii) Shale smears. The line labelled 'K' represent average values, based on core samples from the Heidrun Field, used in a full-field flow simulation (Knai, 1996). The curves (**Equation 2-20**) represent the relationship used in this work for permeability as a function of SGR (assumed equivalent to the fault rock volumetric shale fraction) and displacement. Curves are given for d = 1 mm (dashed line), d = 10 cm, d = 1 m, d = 10 m and d = 1 km (thickest line). After Manzocchi *et al.* (1999).

The curves in **Fig. 2.8** show an empirical prediction of fault zone permeability as a function of shale content and displacement. The best fit to these curves is given by the general equation:

$$\log k_f = A1 \times SGR - A2 \times \log(d) \times (1 - SGR)^{A3} \qquad \textbf{2.20}$$

where k_f is fault permeability (in mD) and d is fault displacement (in metres). The numbers *A1*, *A2* and *A3* are empirical constants obtained by fitting to observed data and are typically derived from outcrop and core data. In practice, it would be best to apply constant factors that are appropriate for the local field, play or basin. Manzocchi *et al.* (1999) suggest values for *A1*, *A2* and *A3* of -4, 0.25 and 5, respectively. In the permeability equation (**equation-2-20**) the first term reflects permeability loss due to shale smear along the fault plane and the second term reflects permeability reduction due to non-smearing behaviour (that is, for lithologies with low shale content). By modifying the numerical constants, appropriate relations can be obtained that treat a variety of fault behaviours. For example, if fault permeability depends only on offset, then *A1* and *A3* are set equal to zero.

Another approach to calculating permeability is by rock-type juxtaposition (Knipe, 1997). In this approach, each pair of rock types juxtaposed by faulting has a distinct fault rock type and permeability. This approach could incorporate a variety of different fault rock types including disaggregation faults, cataclastic faults, phyllosilicate framework faults, and clay smear faults. Fault rock properties are derived from core and outcrop for each of the different potential rock-type juxtapositions.

2.3.5. Fault transmissibility multiplier

Once fault thickness and permeability have been defined, the fault transmissibility multiplier can be determined. This multiplier is used to replace the user-defined multiplier, T_{mult}, in **equation-2.8** and accounts for fault resistance to flow when calculating interblock transmissibility between faulted cells without the need to include the fault zone discretely.

Suppose that two cells, A and B, shown in **Fig. 2.9**, are separated by a fault with permeability k_f and thickness t_f.

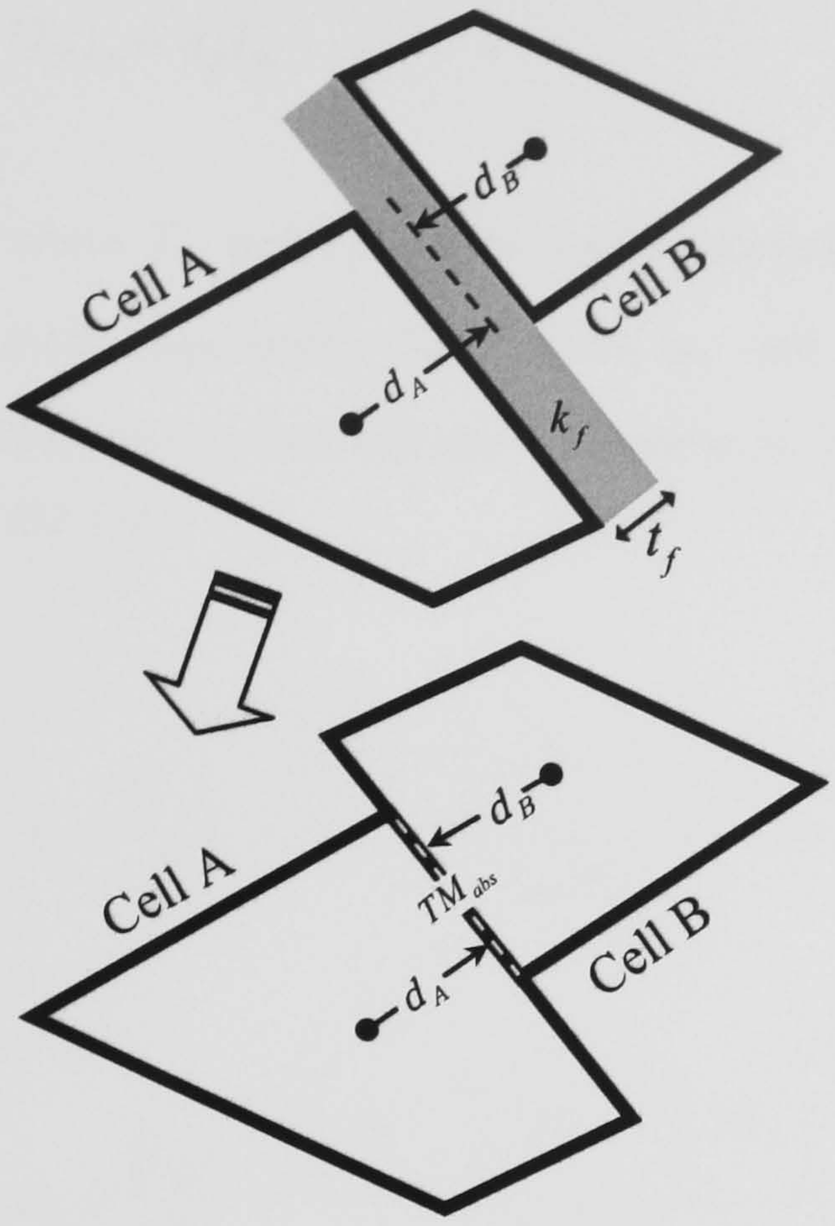

Fig. 2.9. A schematic diagram showing two non-neighbour connected cells separated by a fault with a thickness t_f and permeability k_f. This discrete representation of faults can be reduced to a simple representation using an absolute transmissibility multiplier (TM_{abs}) to account for the fault's existence in simulation models, see text.

The fault absolute transmissibility multiplier, TM_{abs}, is defined as the ratio of the interblock transmissibility between two cells with the fault present to the transmissibility without the fault:

$$TM_{abs} = \frac{(T_{AB})_f}{T_{AB}} \qquad \textbf{2.21}$$

where T_{AB} is the interblock transmissibility between cells A and B given by **equation-2.8** and $(T_{AB})_f$ is the analogous definition to T_{AB} when fault static properties, *i.e.* t_f and k_f, are taken into account:

$$(T_{AB})_f = \frac{C_d . T_{mult}}{\frac{1}{(T_A)_f} + \frac{1}{(T_B)_f}} \qquad \textbf{2.22}$$

here $(T_A)_f$ and $(T_B)_f$ are the transmissibilities of each cell incorporating half of the fault thickness and they are calculated as follows:

$$(T_A)_f = a_A T_A \qquad \textbf{2.23}$$

$$(T_B)_f = a_B T_B \tag{2.24}$$

where T_A and T_B are the cell transmissibilities without the fault given by **equation-2.9** and **2.10**, respectively. The factors a_A and a_B are calculated by attributing half of the fault thickness to each cell and calculating the harmonic average permeability across the merged cell and fault:

$$a_A = \frac{(T_A)_f}{T_A} = \frac{\left[\left(d_A - \frac{t_f}{2}\right)/k_A + \frac{t_f}{2}/k_f\right]^{-1}}{k_A/d_A} \tag{2.25}$$

$$a_B = \frac{(T_B)_f}{T_B} = \frac{\left[\left(d_B - \frac{t_f}{2}\right)/k_B + \frac{t_f}{2}/k_f\right]^{-1}}{k_B/d_B} \tag{2.26}$$

which each simplify to:

$$a_A = \left[1 + \frac{t_f}{2d_A}\left(\frac{k_A}{k_f} - 1\right)\right]^{-1} \tag{2.27}$$

$$a_B = \left[1 + \frac{t_f}{2d_B}\left(\frac{k_B}{k_f} - 1\right)\right]^{-1} \tag{2.28}$$

Combining **equation-2.8** with equations **2.21** to **2.24** yields an equation for the absolute transmissibility multiplier between two fault-juxtaposed cells:

$$TM_{abs} = \frac{1/T_A + 1/T_B}{1/(T_A)_f + 1/(T_B)_f} \tag{2.29}$$

or

$$TM_{abs} = \frac{T_A + T_B}{\frac{T_A}{a_B} + \frac{T_B}{a_A}} \tag{2.30}$$

Equation-2-29 gives an absolute number determining the resistance or conductance of a fault. For example, a value for the transmissibility multiplier of one indicates an 'invisible' fault and a value of zero indicates the existence of a sealing fault. Conducting faults, *i.e.* faults with permeability larger than those of their surrounding host rocks, result in transmissibility multiplier values larger than one.

2.4. Transmissibility multiplier calculations and representations in the Eclipse 100™ simulator

2.4.1. Example: simple 2D faulted model

To demonstrate the calculation of the transmissibility multiplier factor between non-neighbour connections, i.e. connected grid blocks with different z-coordinates, consider the simple 2D model shown in **Fig. 2.10**. We want to calculate the TM_{abs} factor between cell (3,1,1) and cell (2,1,2) due to a fault with $t_f = 1$ ft and $k_f = 0.1$ mD (note that in this example the relationship between fault thickness and displacement, **equation-2.17** or **2.18**, does not apply).

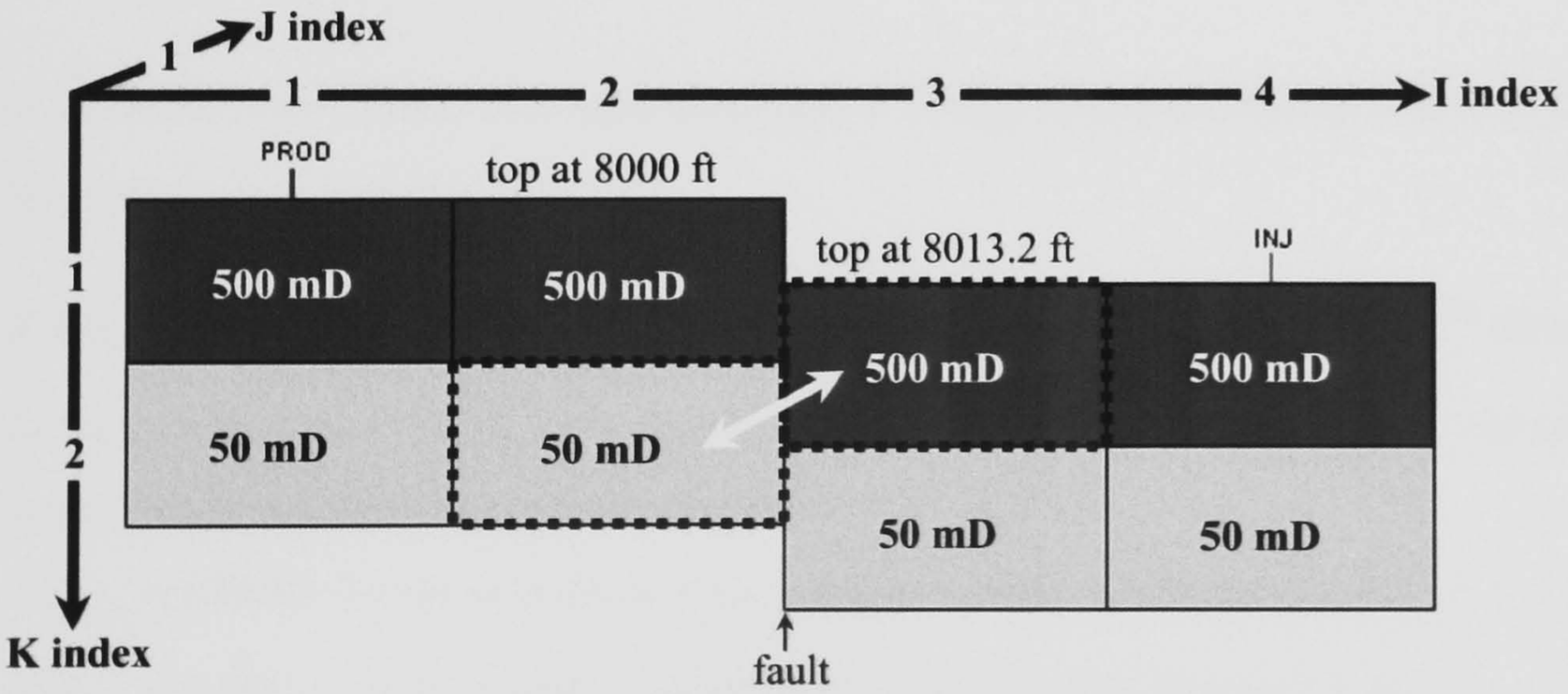

Fig. 2.10. A 2D model used to demonstrate the calculation of the transmissibility multiplier factor between non-neighbour connections (highlighted cells) with the existence of a low-permeability fault.

All of the cells are identical in size with (dx, dy, dz) = (50 ft,50 ft,25 ft). As the cells in this model are not distorted, the common contact area between cells (3,1,1) and (2,1,2) does not depend on the projection area resolved in the flow direction (see § 2.2), *i.e.* $A_{(2,1,2)} = A_{(3,1,1)} = A_c$, where A_c is the true contact area between the two cells. Similarly, the

distance between the centre of each cell and the centre of its relevant face is equal for each cell, *i.e.* $d_{(2,1,2)} = d_{(3,1,1)}$.

The cell permeability, k, is 500 mD for cell (3,1,1) and 50 mD for cell (2,1,2). The net-to-gross ratio, N, is unity for all cells. The mutual contact area between the two cells can be easily determined from their geometry and tops to be $A_c = 660$ ft^2 and in each cell d is simply $d_x/2 = 25$ ft. The inner transmissibility of cells (3,1,1) and (2,1,2) are calculated using **equation-2.9** and **equation-2.10** to be 13200 mD.ft and 1320 mD.ft, respectively.

The factor a for cell (3,1,1) is determined from the fault and host rock properties and geometries using **equation-2.27** to be:

$$a_{(3,1,1)} = \left[1 + \frac{1}{2\times 25}\left(\frac{500}{0.1} - 1\right)\right]^{-1} = 0.0099$$

and similarly for cell (2,1,2) we have,

$$a_{(2,1,2)} = \left[1 + \frac{1}{2\times 25}\left(\frac{50}{0.1} - 1\right)\right]^{-1} = 0.0920$$

Substituting these values into **equation-2.29**, a TM_{abs} of approximately 0.0521 is determined between the two non-neighbour cells.

2.4.2. Transmissibility multiplier representation in the Eclipse 100^{TM} simulator

In the model shown in **Fig. 2.10**, there are three x-directional transmissibility multipliers to be applied to the model to account for the existence of the fault:

$TM_{abs} = 0.0099$ for the normal connection between cells (2,1,1) and (3,1,1);

$TM_{abs} = 0.0920$ for the normal connection between cells (2,1,2) and (3,1,2);

$TM_{abs} = 0.0521$ for the non-neighbour connection between cells (3,1,1) and (2,1,2).

There are three different keywords that can be used in the **Eclipse 100^{TM}** simulator to represent these x-directional transmissibility multipliers for neighbour connections: *MULTFLT*, *MULTX*, and *TRANX* (see Schlumberger Geoquest, 2003, manual for the rules of using these keywords). These keywords can be used either in the **GRID** or **EDIT** section of the **Eclipse 100^{TM}** data file deck. When editing the transmissibility between non-neighbour connections, the keyword *EDITNNC* is used in the **EDIT** section of the data file deck. The three transmissibilities in the example presented in **§2.4.1** can be included using the following three representations:

Representation-1: Using the *MULTFLT* and *EDITNNC* keywords

In the **GRID** section

```
FAULTS

 ---Fault Name------------ FaultX Segments (I1 I2  J1 J2  K1 K2) ---------Face------------
   FAULTX1                                 2  2   1  1   1  1              x  /
   FAULTX2                                 3  3   1  1   2  2              x-  /
/

MULTFLT
--Fault Name              TMabs
 FAULTX1                  0.0099  /
 FAULTX2                  0.0920  /
/
```

In the **EDIT** section

```
-- Each line following the EDITNNC keyword specifies a non-neighbour connection to be
modified
EDITNNC
-- cell1          cell2          TMabs
  3 1 1           2 1 2          0.0521  /
/
```

Representation-2: Using the *MULTX* and *EDITNNC* keywords

In the **GRID** section

```
EQUALS
-- Array          Value (TMabs)       Box (I1 I2  J1 J2  K1 K2)
  MULTX            0.0099                    2 2   1 1   1 1 /
  MULTX-           0.0920                    3 3   1 1   2 2 /
/
```

In the **EDIT** section

```
-- Each line following the EDITNNC keyword specifies a non-neighbour connection to be
modified
EDITNNC
-- cell1          cell2          TMabs
  3 1 1           2 1 2          0.052  /
/
```

Representation-3: Using the *TRANX* and *EDITNNC* keywords

In the **EDIT** section

```
MULTIPLY
-- Array          Value (TMabs)       Box (I1 I2  J1 J2  K1 K2)
  TRANX            0.0099                    2 2   1 1   1 1 /
  TRANX            0.0920                    2 2   1 1   2 2 /
/
-- Each line following the EDITNNC keyword specifies a non-neighbour connection to be
modified
EDITNNC
-- cell1          cell2          TMabs
  3 1 1           2 1 2          0.0521  /
/
```

Note that the first two representations are complicated for simulation modelling because they require directional transmissibilities and, therefore, may require careful editing when applied to more complicated 3D models. Representation 3 is the one adopted in this study when simulating complex 3D models.

2.5. Conclusion

This chapter presented two methods of calculating interblock transmissibities for reservoir simulators. There is no general guideline for evaluating each method. Cordazzo *et al* (2002) conducted a transmissibility study, using a 2D heat transfer problem, to evaluate the method of interblock transmissibility calculations proposed by Sammon (2002) and which is similar to the one being used in **Eclipse 100™** simulator. When they compared Sammon's results with the analytical solution for the problem they used, a very close match was observed. However, no tests were done to support their arguments about the use of areal weighting for distorted cells, **equation-2.11**. If areal weighting has been proved to be necessary, the conventional calculations of *TMs*, that are being used to account for faults, will also be different. The different **Eclipse 100™** *TM* representations presented in this chapter should give equivalent output. The **Eclipse 100™** EDITNNC must be used in *TM* representations whenever there are non-neighbour connected cells in the model used. It is important to note that the *TM* calculations presented in this chapter are 'phase independent', and thus they represent a pure single-phase treatment. The next chapters will, however, show that this conventional treatment of faults may not always be valid to simulation multiphase runs.

Chapter 3

The importance of incorporating the multiphase flow properties of fault rocks into production simulation models

"As an integrated major, we would not drill a prospect without considering full fault seal risk. It's part and parcel of every subsurface study, and it goes beyond the exploration realm. In development projects, we consider the impact of fault seal on development plans and well completion design. In fact, exploration and development are co-key aspects to fault analysis/characterization. Fault seal studies do require an additional investment in time (read: money), but we feel it's worth it because there are other intangibles that are by-products of the analysis, like improved mapping accuracy, better incorporation of stratigraphic detail into the geologic model and things that are usually of benefit to all aspects of the project - not just the fault seal. Doing fault seal work requires that you pursue those things to a level of detail you might not otherwise perform. It requires you know your system well"

Peter Hennings

Senior Scientist-Upstream Technology at ConocoPhilips

3.1. Introduction

Faults often reduce the rate of petroleum production within petroleum reservoirs (*e.g.* Bunn and Yaxley, 1986; Bentley and Barry, 1992; Knai and Knipe, 1998). For accurate predictions of reservoir performance, it is therefore important to take into account the effects that faults have on fluid flow in production simulation models (*e.g.* Lia *et al.*, 1997; Knai and Knipe, 1998). It is becoming increasingly common practice to incorporate the fluid flow properties of faults into production simulation models using transmissibility multipliers (*e.g.* Knai and Knipe, 1998; Manzocchi *et al.*, 1999). The calculation of transmissibility multipliers requires knowledge of both the permeability and thickness of the fault rock and the undeformed reservoir in the grid blocks immediately adjacent to the fault (see **chapter 2** for more details). Recently, it has been suggested that a problem with the way that transmissibility multipliers are conventionally calculated is that no account is taken of the multiphase flow behaviour of fault rocks (Fisher and Knipe, 2001; Manzocchi *et al.*, 2002).

It has been proposed that a possible way of incorporating the multiphase flow properties of faults into simulation models is to use dynamic pseudofunctions (Fisher and Knipe, 2001; Manzocchi *et al.*, 2002). Essentially, dynamic pseudofunctions are generated by conducting high-resolution fluid flow models at the scale of the reservoir simulation grid block, using flow rates that are similar to those that are likely to be encountered within the reservoir. In these high-resolution models, both the fault and reservoir rock are given their own capillary pressure and relative permeability curves. The results of the simulations are then used to create a relative permeability and capillary pressure curve that is then incorporated into the upscaled production simulation model to account for the presence of both the fault and undeformed reservoir. There are many ways to calculate such pseudofunctions; the reader is referred to Barker and Thibeau

(1996) or Barker and Dupouy (1999) for comprehensive reviews of the subject. A quick review of the formulation of different dynamic pseudofunctions will be given in the remaining scope of this thesis (**Chapter 6**).

One of the problems with the use of pseudofunctions is that fault rock thickness is likely to vary significantly as a function of fault throw (*e.g.* Hull, 1988). A large number of pseudo-functions may therefore need to be created to account for the range of fault rock thicknesses present within a typical reservoir. At present, such a methodology would be unmanageable. A simplification would be to assume that only a small number (or even one) of fault rock thicknesses existed within the reservoir, thus limiting the number of pseudofunctions necessary to model the reservoir.

A key question raised by such arguments is "*under what circumstances is it better to incorporate the multiphase flow properties of faults into production simulation models than to accurately account for fault rock thickness?*" In this chapter we present some initial results from some simple, yet informative, numerical modelling that has been conducted to answer this question. The question is answered through simulating simple cases with extreme cases of fault thicknesses and capillary pressure characteristics. To aid the lay reader in understanding the capillary pressure concept as the main parameter addressed in this chapter to account for multiphase behaviour within fault materials, the chapter begins by giving a brief background about capillary pressure and its control in phase distributions within an oil/water system (**§3.2**). In **§3.2**, a detailed description of the multiphase flow behaviour across deformed rocks, *i.e.* rocks with different capillary characteristics from their surrounding undeformed rocks, is outlined. Simple simulation tests will be run to show various cases, or flow regimes, where accounting for multiphase flow properties of faults rocks in simulation models has various degrees of importance. The answer to the key question asked earlier will be addressed in depth in **§3.4**. The answer will be sought through running and comparing various simple models with different fault rock thicknesses, capillary characteristics and drive mechanisms. The results are then presented and their implications discussed. Finally, conclusions are provided to summarise the main output of the study and why such simple tests should provide 'rules of thumb' and 'quality controls' when simulating two-phase flows across faults in real faulted models.

3.2. Capillary pressure in an oil/water system

Capillary pressure, P_c, is defined as the pressure difference between two immiscible phases known as wetting phase and non-wetting phase, with different intermolecular forces between the molecules comprising the phase (Stegemeier, 1977). The dissimilarity of these forces causes a tension between the two immiscible fluid phases known as the surface or interfacial tension. For example, when oil and water are placed together on a surface, a curved interface between the oil and water is formed, with a contact angle, (which by convention is measured through the

water phase), at the surface that can range from 0° to 180° (see **Appendix B** for wettability review). Whenever the oil/water interface is curved, the pressure will abruptly increase across the interface to balance the interfacial tension forces. This pressure jump, which is the capillary pressure, P_c, is given by the Laplace's equation (Adamson, 1982):

$$P_c = P_o - P_w = \sigma_{wo}\left(\frac{1}{r_1} + \frac{1}{r_2}\right) \qquad \textbf{3.1}$$

Where σ_{wo} is the interfacial tension between oil and water, P_o is the oil-phase pressure, P_w is water-phase pressure, r_1 and r_2 are the radii of curvature of the interface, measured perpendicular to each other.

The capillary pressure can be positive or negative, depending on the curvature of the interface. By convention, the curvature directed into the petroleum in positive, as shown in **Fig. 3.1**, while one directed into the water is negative. The capillary pressure is zero when the interface is flat (Anderson, 1987). Note that, P_c can be negative if the water is forced in the tube until $P_w > P_o$. In general, P_c is defined as:

$$P_c = P_{NW} - P_{WET} \qquad \textbf{3.2}$$

where P_{NW} is the pressure in the non-wetting fluid, in this case is oil, and P_{WET} is pressure in the wetting fluid, in this case is water. **Figure 3.1** shows an interface between oil and water, having a contact angle of θ in a capillary tube with radius r_t. When the capillary tube is small enough, the interface can be approximated as a portion of a sphere with radius r_s. The relationship between r_s and r_t is:

$$\frac{1}{r_s} = \frac{\cos\theta}{r_t} \qquad \textbf{3.3}$$

Substituting **equation-3.3** is **equation-3.1**, and noting that the two radii of curvature are equal to r_s, gives an expression for P_c is term of the tube radius and the interfacial tension between oil and water, σ_{wo}:

$$P_c = \frac{2\sigma_{wo}\cos\theta}{r_t} \qquad \textbf{3.4}$$

Equation-3.4 shows that P_c is inversely proportional to the capillary tube radius.

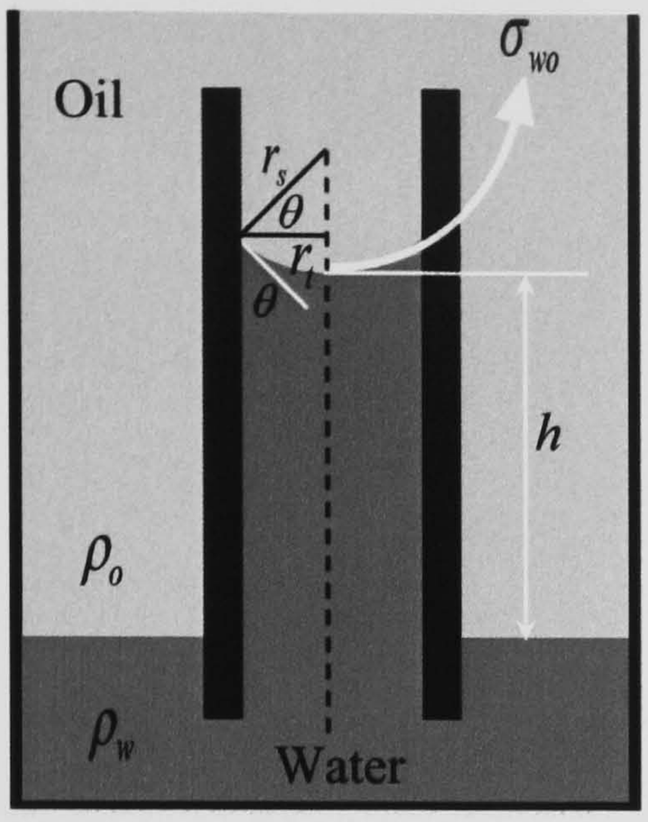

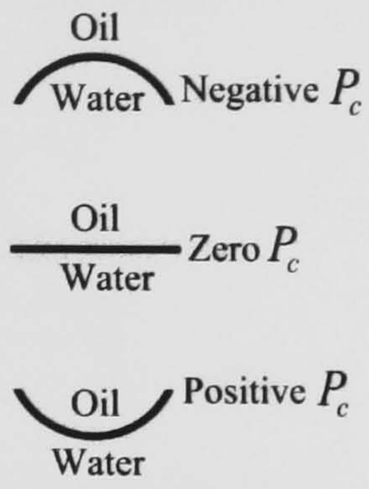

Fig. 3.1. Wetting phase, water, imbibes in a capillary tube and displaces the non-wetting phase, oil, as a result of capillary forces. The curvature of the immiscible phases interface, inferred from the size of the contact angle measured from the wetting phase, indicates the sign of the capillary pressure.

Figure 3.2 illustrates the concept of capillary force for an oil/water system filled with different grains: small, medium and coarse to allow different pore throats, analogous to capillary radius in the tube system in **Fig. 3.1**, for the fluid movements. If the separator between the two immiscible fluids is removed, water displaces oil upwards as a result of capillary forces. Water rises to the highest level in the smallest pore throats because capillary forces are more dominant in small tubes (see **equation-3.4**). If the rock is water wet, *i.e.* its rock surface is coated with a thin layer of water and its small pore throats are likely to be initially blocked with water, then water does not encounter any capillary resistance to enter the smallest pore throats. On the other hand, if the rock is oil wet, *i.e.* its rock surface is coated with a thin layer of oil and its small pore throats are likely to be initially blocked with oil, capillary forces prevent water from entering the small pores. Instead, water enters the larger pores leaving oil trapped within the small pores. Consequently, water rises to a lower height in an oil-wet rock than in a water-wet rock under the same conditions. The oil phase is less dense than the brine and therefore has a steeper pressure gradient. The point at which both oil and water pressure gradients intersect is known as the free water level, FWL. At this point, P_c vanishes.

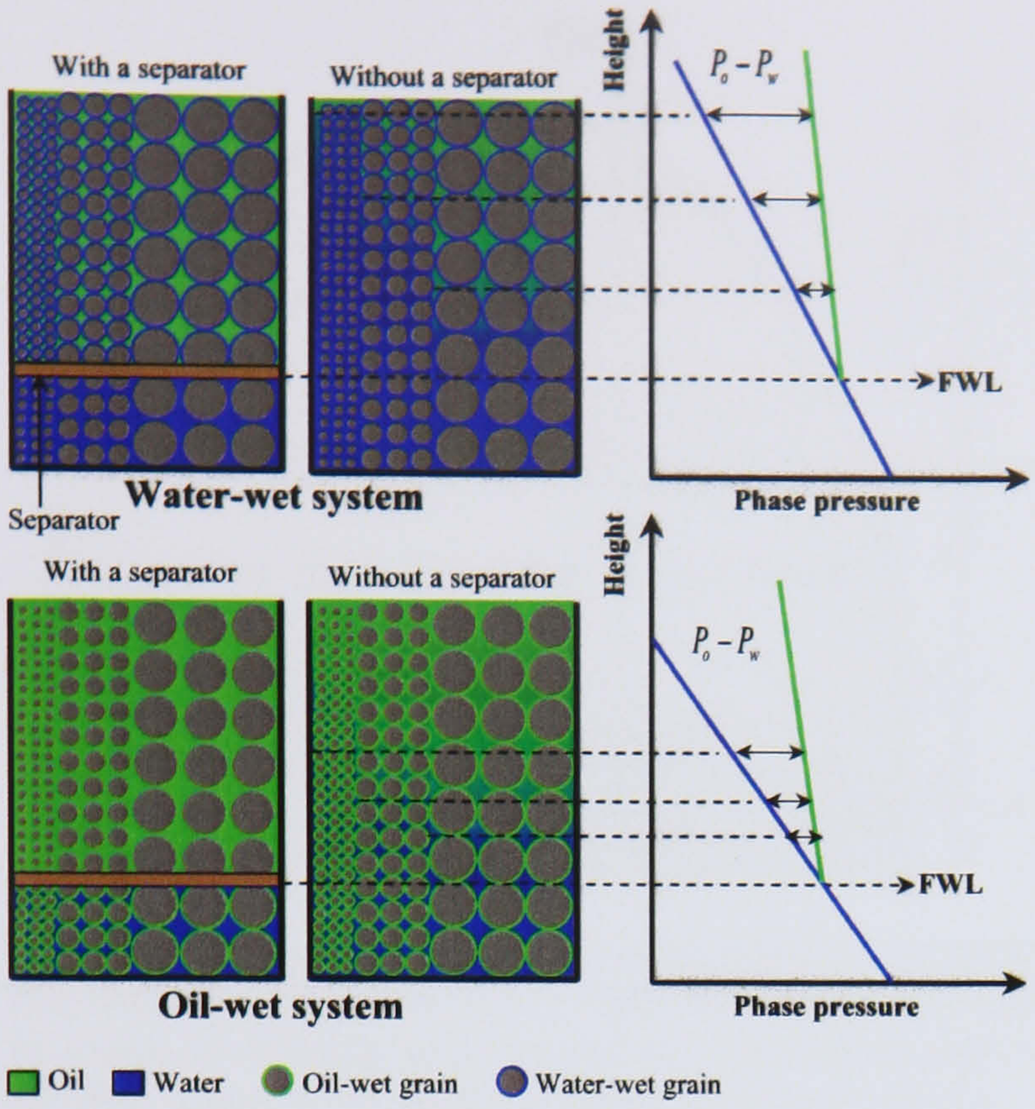

Fig. 3.2. The effect of the pore throat size and wettability on the maximum size to which the wetting phase, water, can rise as a result of the capillary forces caused by the difference in pressure gradients for each immiscible phase. Capillary forces are more dominant in small pore throats than in large ones. Water encounters more resistance to break into pore throats when the grains are oil-wet than when they are water-wet.

There are two basic types of capillary pressures: drainage and imbibition. In drainage process, the non-wetting fluid, oil in this case, displaces the wetting phase, water, while the reverse occurs for imbibition. It is important to emphasise that many rocks have mixed or fractional wettability, see **Appendix B**, so drainage and imbibition should probably be redefined as drainage for the process of oil replacing water, and imbibition for the process for water replacing oil. Generally there is hysteresis in capillary pressure as saturation is varied, making drainage and imbibition curves different. To establish a drainage capillary pressure curve, the wetting-phase saturation is reduced from its maximum to the irreducible value by increasing the capillary pressure from zero to a large positive value. To develop an imbibition capillary pressure curve, the wetting-phase saturation is increased. It is important to note that two distinctly different portions of the imbibition curve can be measured. The first is the spontaneous imbibition curve, which is determined immediately after measurement drainage curve, by decreasing the capillary pressure to zero thus allowing the wetting phase to imbibe, **Fig. 3.3**. The second portion is the forced imbibition curve, where the capillary pressure is decreased from zero to a large negative value. This process changes the contact surface from zero to negative curvature, see **Fig. 3.1**. This curvature is tracked during the measurements by tracking the changes in the contact angle. At the water saturation at irreducible oil, S_{wor}, the lower boundary of the transition zone, *i.e.* the zone where all the present phases can be in simultaneously in a dynamic state, is defined and the imbibition capillary pressure goes to zero, **Fig. 3.3**.

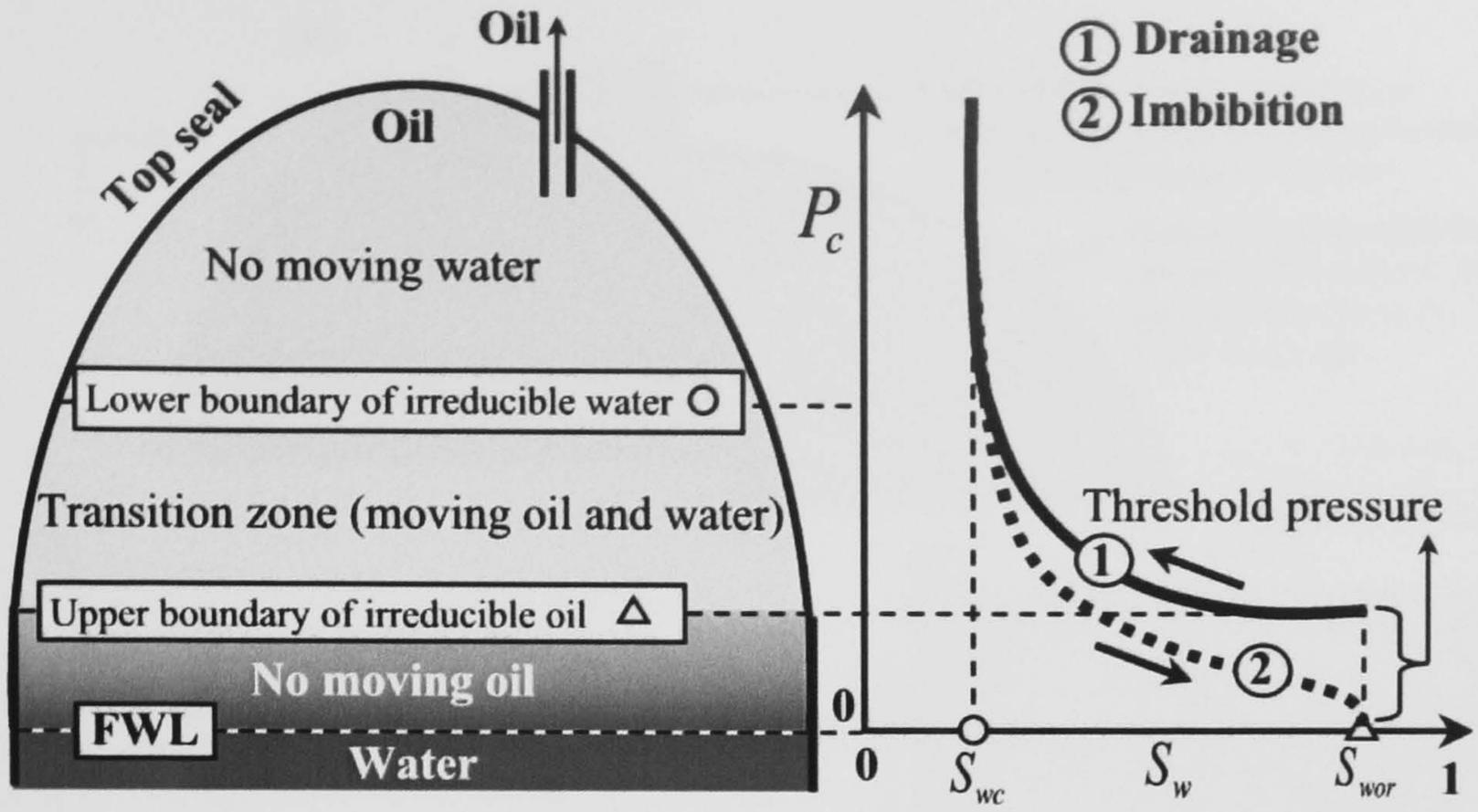

Fig. 3.3. Hypothetical dynamic reservoir and corresponding capillary pressure curves illustrating the relationship between the main saturation boundaries and capillary pressure. Transition zone is where all present phases can be simultaneously in a dynamic state. The existence of the 'no moving water zone' is still a mater of active debate. (Modified from Smith *et al.*, 1999).

3.3. Oil-water flow behaviour across faults

Multiphase flow across faults can have different behaviour to that within undeformed host rocks, because faults can possess different pore throats sizes and therefore different multiphase saturation functions, *i.e.* capillary pressure and relative permeability functions. In this section a detailed description of this flow behaviour across low permeability fault rocks is addressed.

3.3.1. Buoyancy force by the petroleum column height

The conventional way that transmissibility multipliers are formulated (**Chapter 2**) only offers a single-phase treatment when predicting flows across faults. Recent works (*e.g.* Fisher and Knipe, 2001; Manzocchi *et al.*, 2002) suggested that these absolute transmissibility multipliers do not capture the multiphase behaviour of fault rocks in dynamic reservoir modelling. For example, it might be expected that the buoyancy force in the petroleum column would not be sufficient to overcome the threshold pressure (**Chapter 1**) of the fault rock near to the FWL. Here the relative permeability to oil would be expected to be zero (**Fig. 3.4**), which would not be taken into account in conventional methods used to calculate transmissibility multipliers. On the other hand, at greater distances above the FWL the buoyancy force generated by the petroleum column may be sufficient to overcome the threshold pressure of the fault rock. In such a situation the fault rock would have a finite permeability to oil (Fisher *et al.*, 2001).

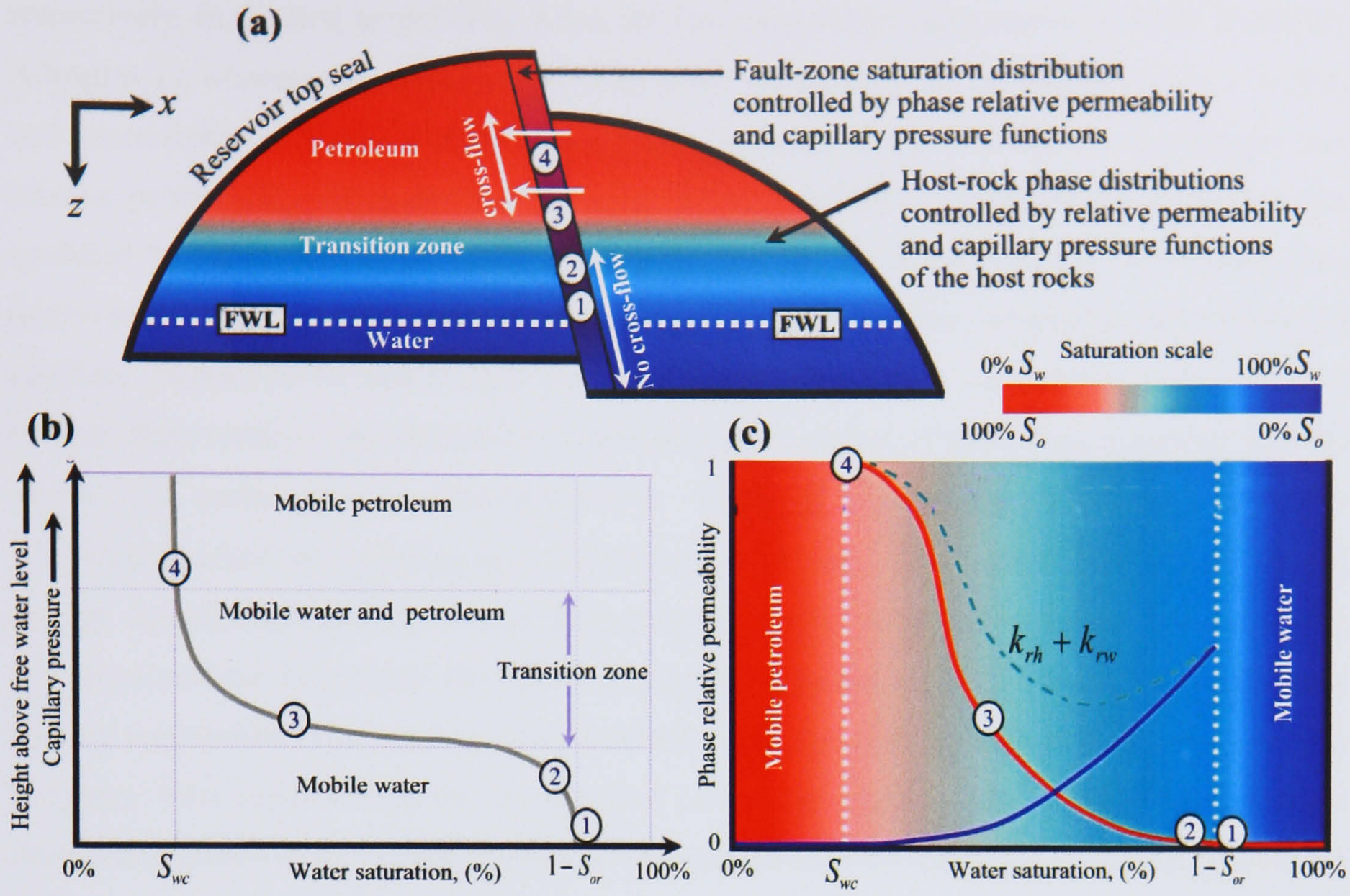

Fig. 3.4. Conceptual model, based on Fisher *et al.*, (2001) for multiphase flow across a fault in a petroleum reservoir. **(a)** The fluid saturations within the reservoir and fault, red for petroleum, blue for water. **(b)** The capillary pressure and **(c)** The *x*-directional water-wet relative permeability curves for the fault rock. The fault has a higher threshold pressure than the reservoir. Close to the FWL (points 1 and 2), the buoyancy force in the petroleum column is not sufficient to overcome the threshold pressure of the fault. Hence, it has zero relative permeability to petroleum. Above point 2 (*i.e.* points 3 and 4) the buoyancy force in the petroleum column is sufficient to overcome the threshold pressure of the fault rock and the fault will have a finite relative permeability to petroleum. Currently methodologies to incorporate fault rock properties using transmissibility multipliers calculated from single-phase permeability measurements (*e.g.* Knai and Knipe, 1998; Manzocchi *et al.*, 1999) do not take account of such effects.

3.3.2. Comparing different representations of faults (Simple simulation example)

Reservoir simulators, *e.g.* **Eclipse 100**™, are used to model the fluid flow behaviour of petroleum reservoirs. The usual strategy involves attempting to reproduce (history match) past and present behaviour in the hope that the models will then be able to predict future performance. They can also be used to understand detailed multiphase flow behaviour across faults by running number of simple synthetic models.

To illustrate the importance of taking into account the multi-phase flow behaviour of faults consider the following tilted (~ 45° to the horizontal axis), 2D (*x*-*z*) model for a water–wet, oil/water system. The cross-section represents 200 ft by 50 ft model simulated using 200 by 100 cells. The model contains a normal fault though its centre, which has a lower permeability and higher threshold pressure than its surrounding host rock. The reservoir has an initial pressure of 5000 psi at the top datum, and the pressure in the rest of the reservoir is distributed according to the gravity-capillary equilibrium. Oil and water viscosities are constant at 5 cP and 1 cP

respectively. In the first model (**Fig. 3.5a**), the fault is included using transmissibility multiplier (**Chapter 2**), whereas the second model (**Fig. 3.5b**) contains a discrete fault as a zone, 1 ft thick and permeability of 1 mD, with its own capillary pressure (ranges between 4 and 60 psi), and relative permeability curve derived from the function defined in Ringrose *et al.* (1993); and modified by Manzocchi *et al.* (2002) for tight rocks, see **§ 3.4.1** for details. The undeformed reservoir is a homogeneous rock with a permeability of 1D. For simplicity, we assume the capillary pressure in the host is zero, *i.e.* water pressure is equal to oil pressure at the oil-water contact. Both models were initiated by mimicking the situation of petroleum migration from its source rock under buoyancy-dominated flow. When oil is expelled from a source rock, it accumulates when encountering an overlying cap-rock seal and a lateral fault with a limited sealing capacity (defined by its capillary pressure curve, which also defines the maximum petroleum column height that the fault can support, Schowalter, 1979). In reality, represented here by the discrete fault model, water-wet fault rocks are impermeable to petroleum until the buoyancy force generated by the accumulated petroleum column is sufficient to overcome the threshold pressure (4 psi) of the fault rock. The transmissibility multiplier treatment ignores the multiphase characteristics of the fault rocks represented in its capillary pressure data. As **Fig. 3.5** shows, the two models behave very differently.

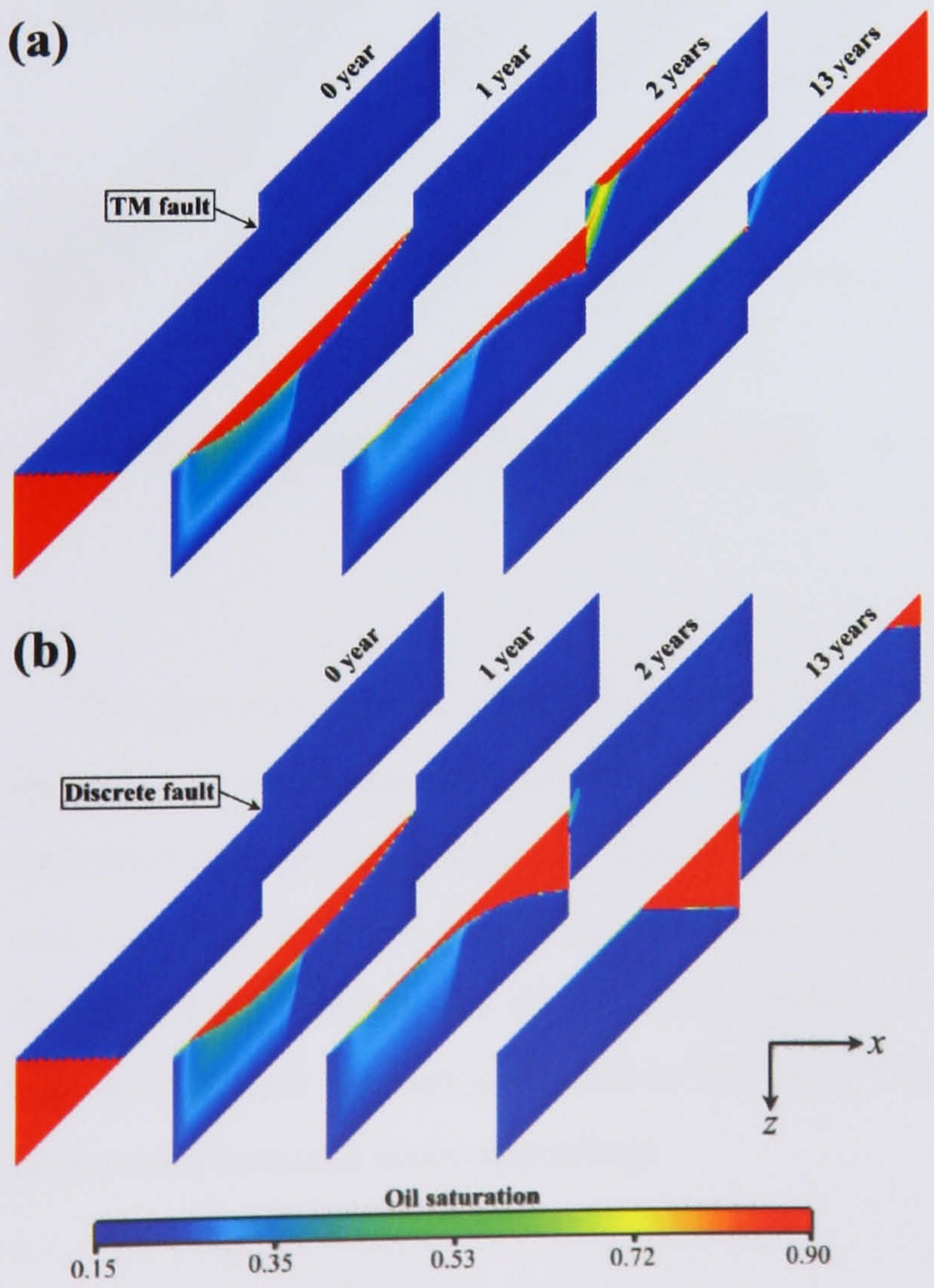

Fig. 3.5. Buoyancy-driven, capillary-resisted oil flow across *TM* fault (a) and a fault material zone (b). The fault zone has different saturation function from its surrounding undeformed materials. Note: the system is closed without injectors or producers.

The discrepancy between the two models becomes less apparent if the flow regime is changed to be more viscous dominated rather than capillary dominated flow by imposing a producer and an injector in the different compartments (**Fig. 3.6**). We imposed a BHP limit of 5000 psi on the producer and 5060 psi on the injector. In this case, fluid viscosity contrast resist the production driven flow, but capillary forces have a negligible effect in resisting such high rate flows. Capillary forces require slow rates to work and therefore they are more apparent in resisting fluid flow in the buoyancy driven flow presented in **Fig. 3.6**.

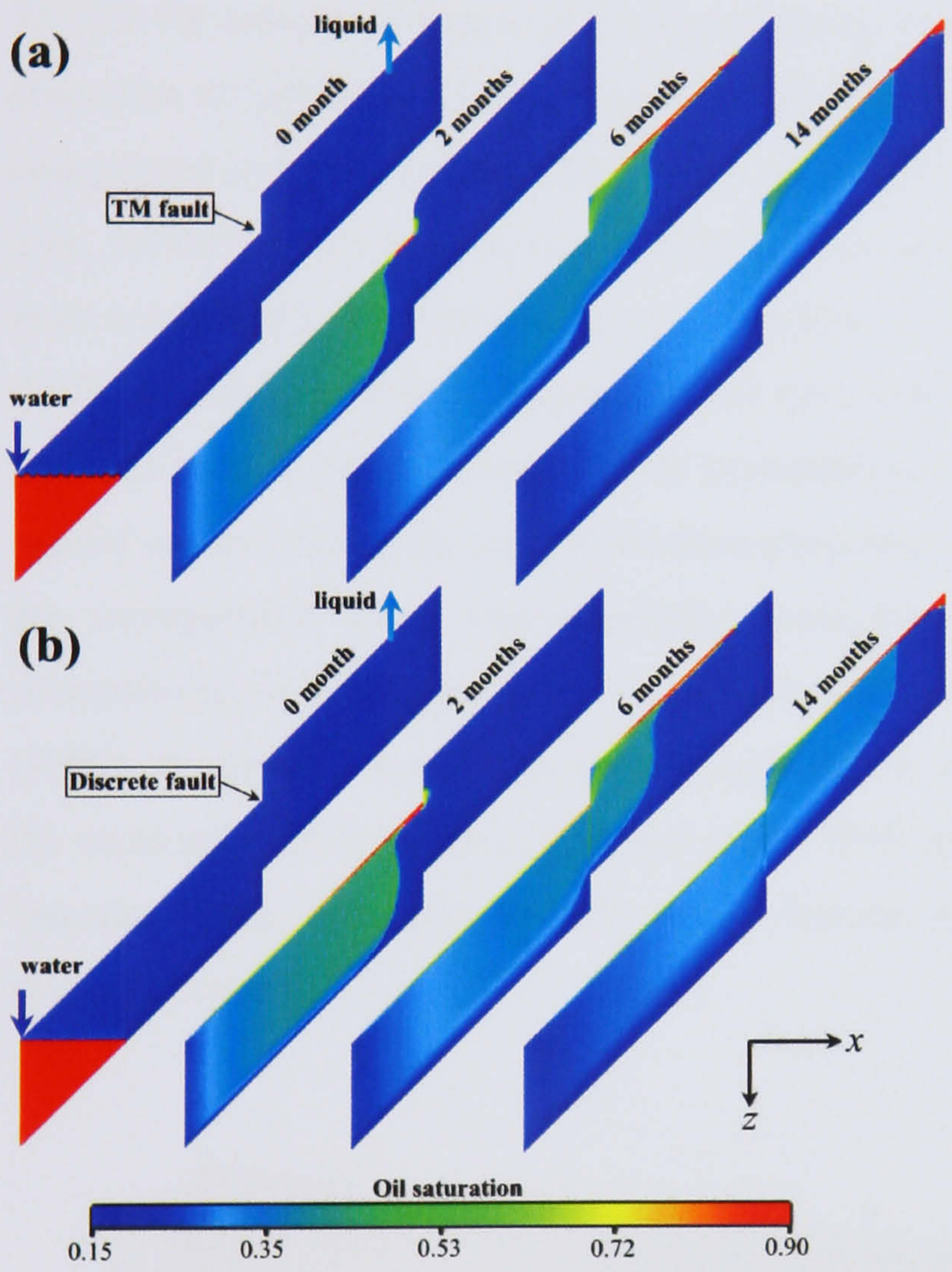

Fig. 3.6. Production-driven flow by applying pressure gradient over short production time-scale. The flow is resisted by fluid viscosities. (a) flow across *TM* fault and (b) flow across a fault material zone (b). The fault zone has different saturation function from its surrounding undeformed materials.

The previous simple simulation tests indicate that it may not always be important to incorporate multiphase properties of fault rocks into production simulation models. It is important to note that if both the fault and the host rock were given similar relative permeability and capillary pressure functions, then transmissibility multiplier representation would have duplicated the result of the discrete fault under the various flow regimes. When the two rocks possess different saturation functions, the need for accounting for the multiphase behaviour of fault rocks becomes more appealing.

3.4. When is multiphase behaviour of faults important?

In this section the key question "*under what circumstances is it better to incorporate the multiphase flow properties of faults into production simulation models than to accurately account for fault rock thickness?*" is addressed for different flow scenarios, fault rock thicknesses, and fault capillary characteristics. Simple box model bi-compartmentalised by a faulted material will be used in addressing this question.

3.4.1. Model Description

To test the relative importance of incorporating fault rock thickness or the multiphase flow properties of fault rocks into production simulation models, some simple flow models have been constructed using the **Eclipse 100™** black oil simulator. The basic model is 2000 ft (*c.* 609.6 m) long, 1000 ft (*c.* 304.8 m) wide and 200 ft (*c.* 61.0 m) thick (**Fig. 3.7**). Two types of model have been constructed. The first incorporates the fault rock discretely using a local grid refinement (LGR) to reduce numerical dispersion (see next section for more details). In this type of model, the fault rock is given unique relative permeability and capillary pressure curves. The second type of model ignores the multiphase flow properties of faults. Instead, the fault rock properties are incorporated using transmissibility multipliers calculated based on the single-phase permeability of the reservoir and fault rock, following the methodology of Manzocchi *et al.* (1999). A common assumption of any upscaling study is that the high-resolution model gives the most realistic result (*e.g.* Cao and Aziz, 1999; Guzmán *et al.*, 1999; Pickup *et al.*, 2000; Darman, 2002). Similarly, we will assume that the model with the local grid refinement gives the correct result.

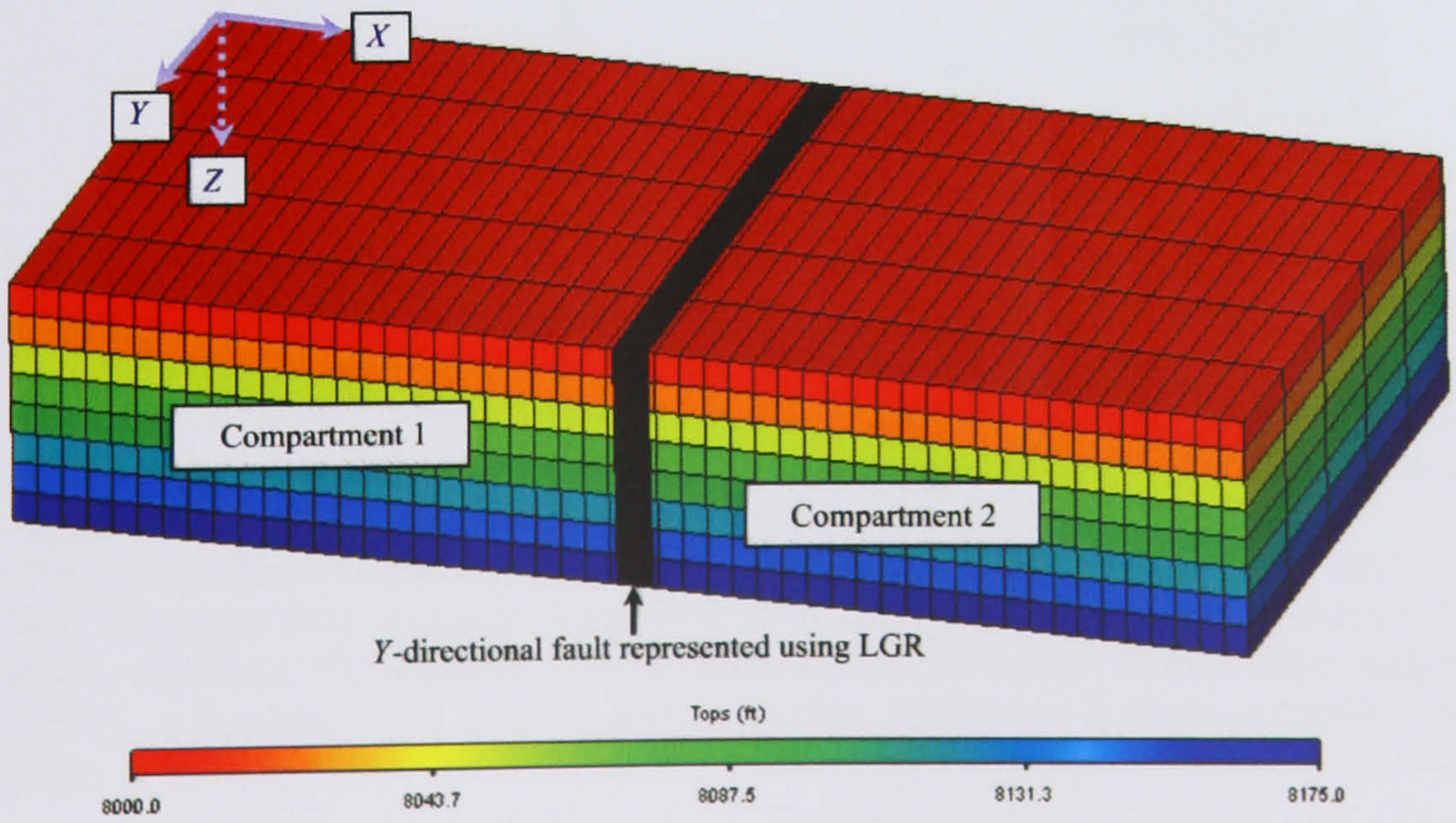

Fig. 3.7. Model geometry with local grid refinement representing a *Y*-directional fault. The fault cuts the entire model, splitting it into two compartments with possible communication. The colour scale represents the depth in feet.

The fault is located along the *y*-direction and divides the model into two compartments (**Fig. 3.7**). The permeabilities of the reservoir and fault rock are assumed to be 1000 mD and 0.01 mD, respectively. Two fault rock thicknesses were modelled, 0.3 ft and 3 ft, which are approximately equivalent to faults with throws of 20 ft and 200 ft, respectively (Manzocchi *et al.*, 1999). For the discrete fault models, two different drainage capillary pressure curves were used. Both curves were linearly scaled from a curve derived using modified empirical relationship between capillary pressure, porosity and permeability as that used by Manzocchi *et al.* (2002), see below. This method follows the functions defined in Ringrose *et al.* (1993) that relate the two-phase properties of host rock to its absolute permeability. The derivation is justified by the similarity in the behaviour between fault rock and host rock when considering the capillary threshold pressure variation with absolute permeability for faulted and undeformed reservoir rock samples from different sources (Manzocchi *et al.*, 2002). **Figure 3.8** gives a summary of available capillary threshold pressure data for faults, normalised for a moderately water-wet system (40 dynes/cm, or 4×10^{-2} N/m) interfacial tension; 30° contact angle), cross-plotted against fault permeability.

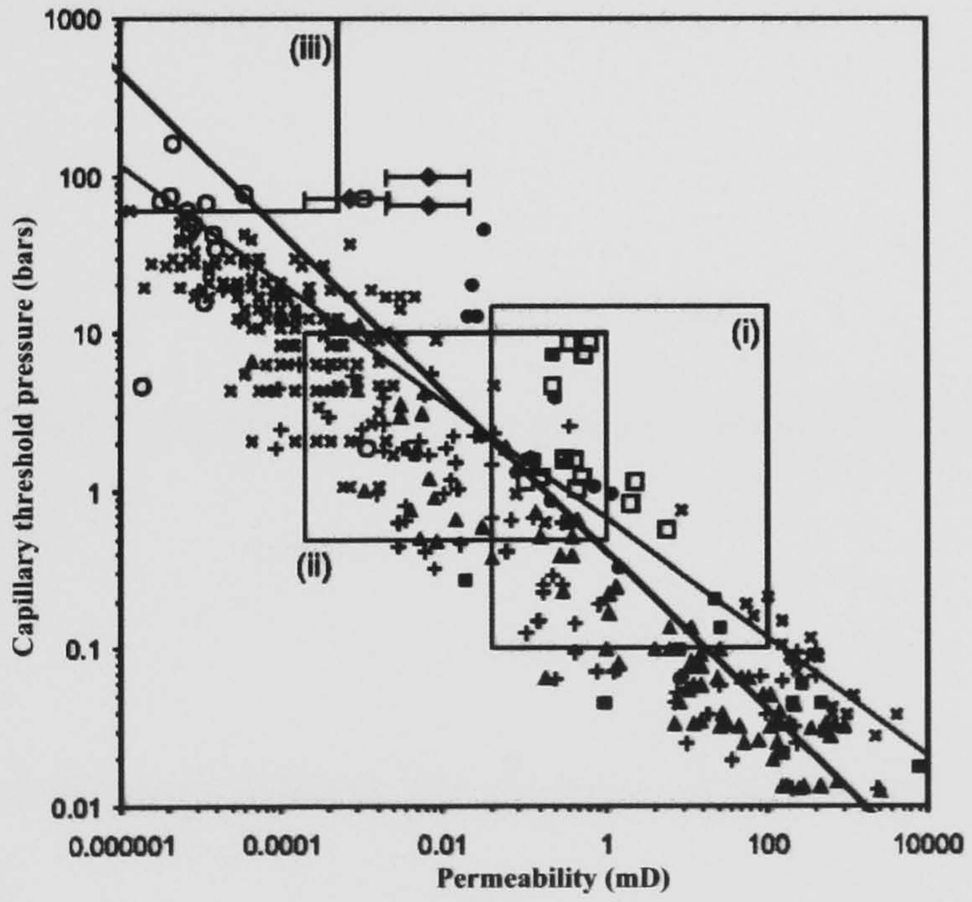

Fig. 3.8. Capillary threshold pressure *vs.* permeability for fault samples (solid symbols) and unfaulted rock samples (crosses and open symbols) from a variety of lithologies. The boxes (Fisher & Knipe 1998) are summaries of data from **(i)** faults in clean sandstone, **(ii)** dirty sandstone and **(iii)** shale-rich fault gouge. The two lines are published model relationships (thinner line from Ringrose *et al.* (1993) and Fisher & Knipe (1998), thicker line from Harper & Lundin (1997)). Capillary threshold pressures have been normalized for a water-wet system with a petroleum–water interfacial tension of 40 dynes/cm, and a contact angle of 30°. Legend: filled triangles and crosses, Sperrevik *et al.* (2002); filled squares, Harper & Lundin (1997); empty squares, Schowalter (1979); filled circles, Gibson (1998); filled diamonds, Fulljames *et al.* (1997); X Ibrahim *et al.* (1970); empty circles, Schlomer & Krooss (1997). After Manzocchi *et al.*, 2002.

Higher permeability faults have threshold pressures similar to undeformed reservoir rocks, and although clay-rich fault-rock values are somewhat higher than unfaulted rock with the same permeability, Manzocchi emphasised that given the scarcity of published capillary threshold

pressure data for low permeability fault-rocks, this observation is tentative. For qualitative modelling purposes, therefore, the relationships between threshold pressure and permeability for both fault rock and undeformed sediments can be considered the same. Manzocchi attributed this conclusion to the similarity of the two lines on the plot, see **Fig. 3.8**, which represent model predictions of capillary threshold pressure for fault-rock (thicker lines; Harper & Lundin, 1997) and for sediments (thinner lines).

The model drainage capillary pressure curve for sediments is derived from the function defined in Ringrose *et al.*, (1993):

$$P_c = C' S_e^{-2/3} \left(\frac{\phi_f}{k_f} \right)^{0.5} \qquad \textbf{3.5}$$

where P_c is the capillary pressure, $C' = 3$ is a conversion factor to give capillary pressure in bars, ϕ_f is porosity, k_f is absolute (single-phase) permeability in mD, and S_e is the effective wetting phase saturation. Here S_e is defined as:

$$S_e = \frac{(S_w - S_{wc})}{(S_{wor} - S_{wc})} \qquad \textbf{3.6}$$

Fault rock porosity has been determined from permeability using the empirical relationship:

$$\phi_f = 0.05 k_f^{0.25} \qquad \textbf{3.7}$$

We change the original function defining the connate water saturation originally defined by Rigrose *et al.* (1993), to:

$$S_{wc} = 0.75 - 10^{-0.6 \exp(-0.5 \log(k_f))} \qquad \textbf{3.8}$$

Manzocchi *et al.* (2002) used a slightly different function for the S_{wc}. As stated by Manzocchi *et al.* (2002), this change, which has no theoretical basis whatsoever, has been made to ensure non-zero effective saturation ranges when derived for lower permeability rocks.

The water and the oil relative permeability (k_{rw} and k_{ro}) curves have been calculated as follows, using the same relationships as Ringrose *et al.* (1993):

$$k_{rw} = 0.3 S_e^3 \qquad \textbf{3.9}$$

$$k_{ro} = 0.85(1 - S_e)^3 \qquad \textbf{3.10}$$

The drainage capillary pressure curve derived using **equation-3.5** is such that the buoyancy force in the petroleum column was sufficient to overcome the threshold entry pressure of the fault rock (see **Chapter 1**). In other words, the fault has a finite relative permeability to oil. Two drainage capillary pressure curves, with capillary pressures straddling the dataset given in **Fig.3.8** for a fault rock permeability of 0.01 mD, were used in this study. The two curves were linearly scaled from an original curve derived using **equation-3.5**. The derived curve was doubled to represent the high capillary curve, and divided by a factor of 80 to represent the low capillary curve. Both capillary pressure curves were well within the limits of those measured from natural fault rocks (Knipe *et al.*, 1997). In all simulations, the undeformed reservoir was given the same capillary pressure curve, which was lower than that used for the fault (**Fig. 3.9**). All of the models contained a single producer, within Compartment 2, which was produced at an initial rate of 1000 barrels/day. Four different models are presented.

- The first model, Model 1, has an injector placed at the opposite side of the fault, which injects fluid into the aquifer at the same rate that fluid is produced (**Fig. 3.10a**).
- The second model, Model 2, has an injector at the same side of the fault as the producer, which injects fluid into the aquifer at the same rate that fluid is produced (**Fig. 3.10b**).
- The third model, Model 3, has no injector. Instead, an analytical aquifer has been incorporated into the model to provide pressure support (**Fig. 3.10c**).
- The fourth model, Model 4, is a gas reservoir produced by gas expansion with a producer situated in Compartment 2 (analogous to Model 3, but without an aquifer).

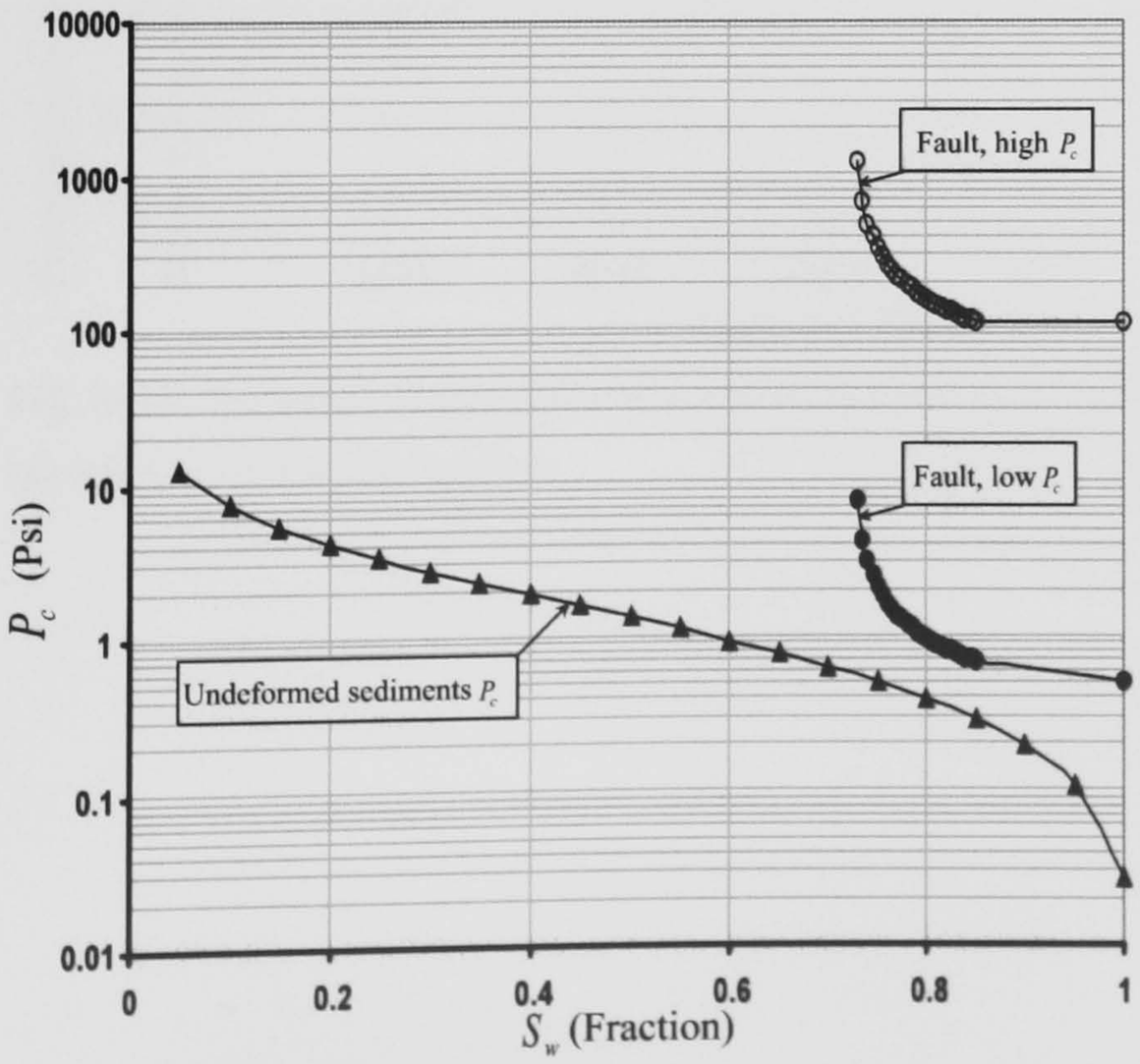

Fig. 3.9. Drainage Capillary pressure (P_c) curves for the undeformed sediment (host rocks) and faulted rock. Each fault was simulated twice using a high- P_c curve, open circles, and a low- P_c curve, solid circles. In all cases the host rock has one P_c curve, solid triangles.

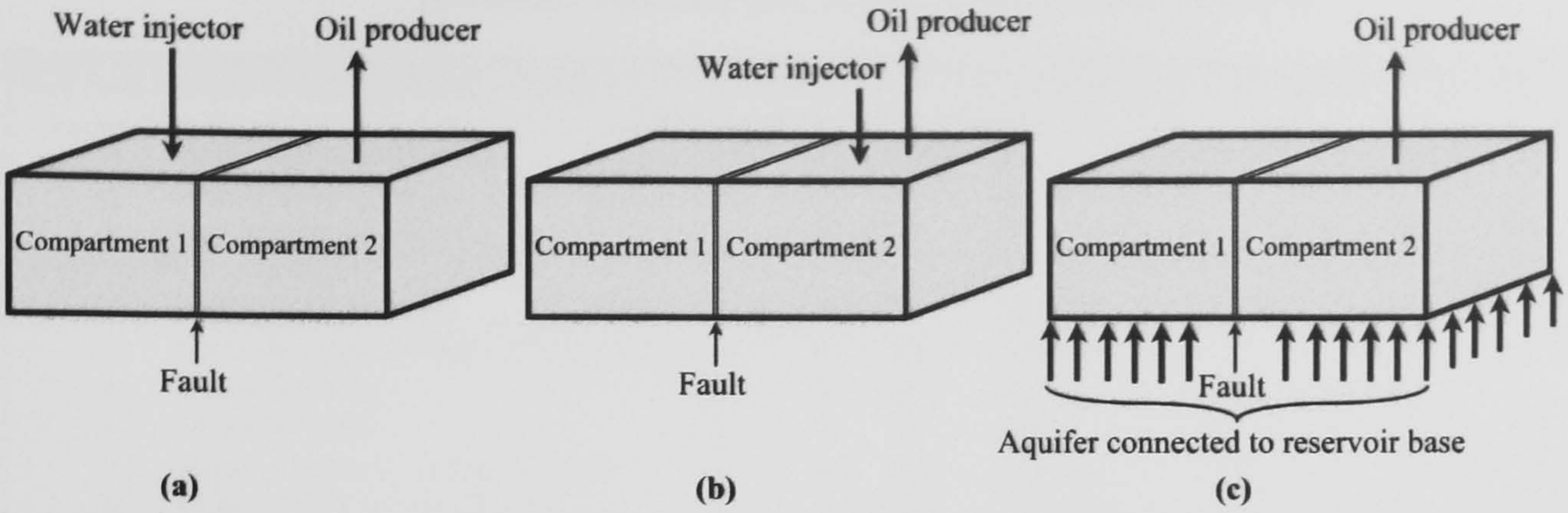

Fig. 3.10. Different model layouts presented in the study. **(a)** Model 1 has a water injector placed at the opposite side of the fault to the oil producer. Water is injected into the reservoir base at the same rate that oil is produced. **(b)** Model 2 has a water injector at the same side of the fault as the oil producer. Water is injected into the reservoir base at the same rate that oil is produced. **(c)** Model 3 has no injector. Instead, an analytical aquifer has been connected to both compartments in the model to provide pressure support. Model 4 (analogous to Model 3, but without an aquifer) has no injector. Instead, gas is produced from a single producer; gas expansion being the main drive mechanism.

Models 1–3 are oil/water systems, whereas Model 4 is a gas/water system. Reservoir geometry, fluid and rock data for Models 1–4 are summarised in **Table-3.1**. **Figure 3.11** shows how gas viscosity and formation volume factor (FVF) change with reservoir pressure for Model 4.

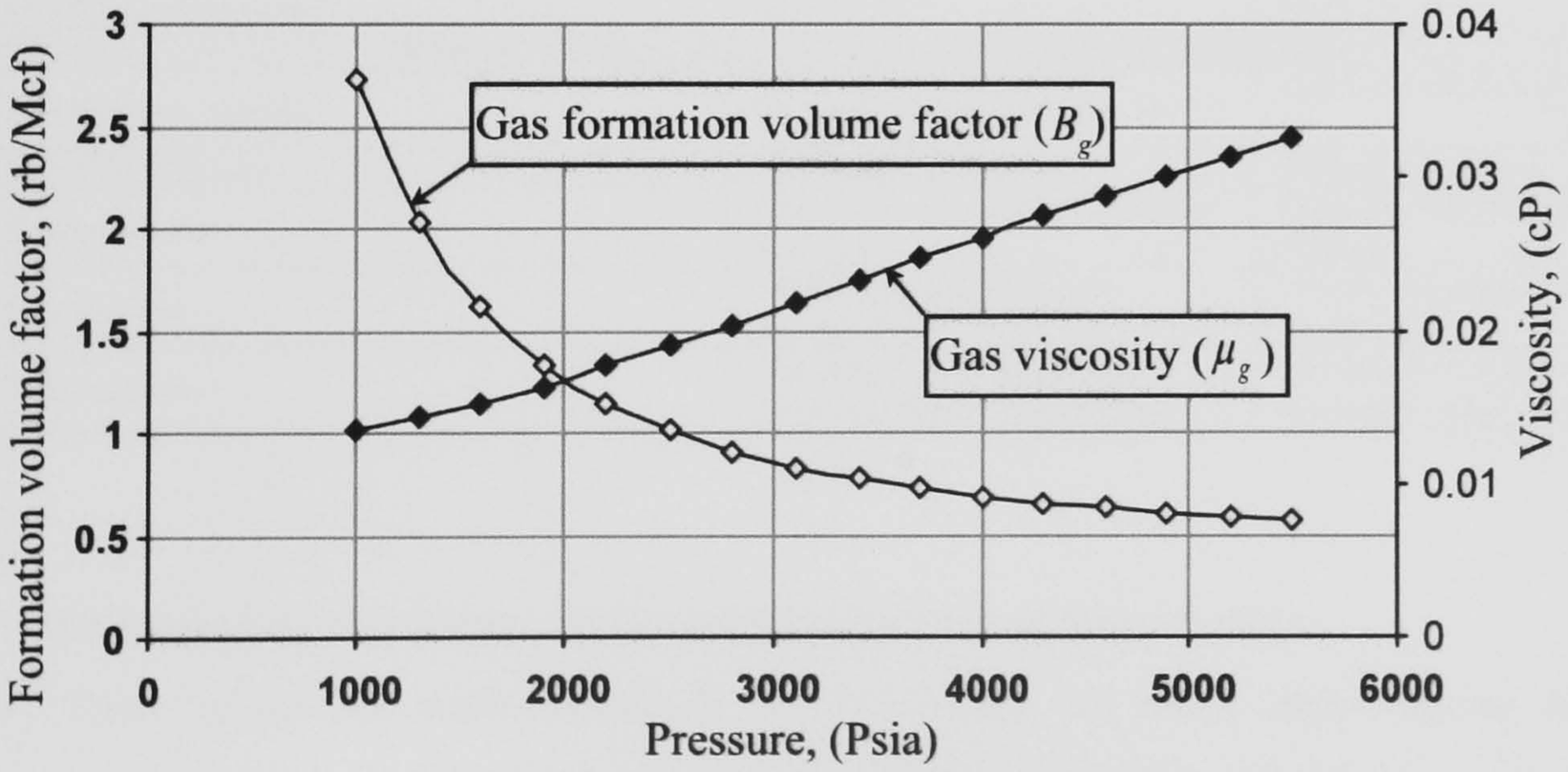

Fig. 3.11. Variation of gas viscosity and formation volume factor with reservoir pressure for Model 4, a gas/water system.

Table-3.1: Reservoir rock, phases, geometry and schedule data for Models 1–3 (oil/water system) and Model 4 (gas/water system)

Item	Models 1-3	Model 4
Phases and rock data (Field units)		
• Reference pressure (RP) • Bubble point pressure • Reference temperature	• 5500 (psia) • 1145 (psia) • 60 (^{0}F)	• 7000 (Psia) • 60 (^{0}F)
Dead oil PVT properties: • Density at stock tank • Formation volume factor (FVF) at RP • Compressibility • Viscosity at RP • Slope of viscosity versus pressure • Slope of FVF versus pressure	 • 53 (lbs/ft^3) • 1.9 (rb/stb) • 2E-5 (psi^{-1}) • 0.8 (cP) • 3E-3 (cP/psia) • 2E-4 (rb/stb/psia)	
Undersaturated water properties: • Density at RP • FVF • Compressibility • Viscosity at RP • Viscosibility at RP	 • 63 (lbs/ ft^3) • 1.02 (rb/stb) • 3E-6 (1/psi) • 0.8 (cP) • 0 (1/psi)	 • 63 (lbs/ft^3) • 1.02 (rb/stb) • 3.8E-6 (1/psi) • 0.3 (cP) • 5.2E-5 (1/psi)
Gas PVT properties: • Density at stock tank • Formation volume factor (FVF) at RP • Viscosity at RP • Slope of viscosity versus pressure • Slope of FVF versus pressure		 • 0.053 (lbs/ft^3) • 0.566 (rb/Mcf) • 0.032 (cP) • See **Fig. 3.9** • See **Fig. 3.9**
Rock properties: • Compressibility at RP	 • 4E-6 (1/psi)	 • 4E-6 (1/psi)
Reservoir and gridblocks geometry data (Field units)		
Number of grid nodes	$50 \times 5 \times 8$	$50 \times 5 \times 8$
Spacing	$DX = 40$ ft $DY = 200$ ft $DZ = 25$ ft	$DX = 40$ ft $DY = 200$ ft $DZ = 25$ ft
Grid type	Cartesian	Cartesian
Grid geometry	Corner point	Corner point
Depth to reservoir top	8000 ft	8000 ft
Reservoir pressure, phases' contacts and schedule data (Field units)		
Initial phases contacts	Oil-water contact (OWC) at 8175 ft	Gas-water contact (GWC) at 8125 ft
Reservoir pressure	5500 psia at 8000 ft	7000 psia at 8000 ft
Production rate	1000 (stb/day) controlled by liquid flow rate	Controlled by BHP upper limit of 1000 psi
Injection rate	100% voidage replacement (Models 1–2)	Primary gas cap expansion drive (no injector)
Time step size	1200 (steps) × 15 (days) (total simulation time = 18,000 days)	180 (steps) ×1.5 (days) (total simulation time = 270 days)

Six individual simulations were conducted for each of these models:

- Two simulations were conducted for 0.3 ft and 3 ft thick faults whose single-phase properties were incorporated using transmissibility multipliers, which were calculated using the same host and fault rock permeabilities as for the other models
- Two simulations were conducted for 0.3 ft and 3 ft thick faults whose multiphase properties were incorporated discretely; in these simulations the fault was given a low threshold pressure.
- Two simulations were conducted for 0.3 ft and 3 ft thick faults whose multiphase properties were incorporated discretely; in these simulations the fault was given a high threshold pressure.

To include the faults discretely in the simulation models, a LGR scheme was used for the middle two cells in the simulation models (**Fig. 3.12a**). LGR cells were added in such a way so as to produce a gradual transition in the cell pore volumes from the fault cells to the host cells. This is done to avoid any numerical instability that may result when placing a fault with low permeability next to a host cell with relatively very high permeability. To test that the LGR scheme used was sufficient to prevent numerical dispersion, we compared the numerical results of a simulated drawdown test in a well situated close to the fault with the analytical solution provided by Yaxley (1987), see **Appendix C** for extended tests on LGR stability. In this test, the pressure output from models with different LGR schemes was compared to the analytical solution. The results achieved a near-perfect match when 120 LGR cells were used for the two parent grid blocks in the middle of the faulted model (see **Fig. 3.12b**).

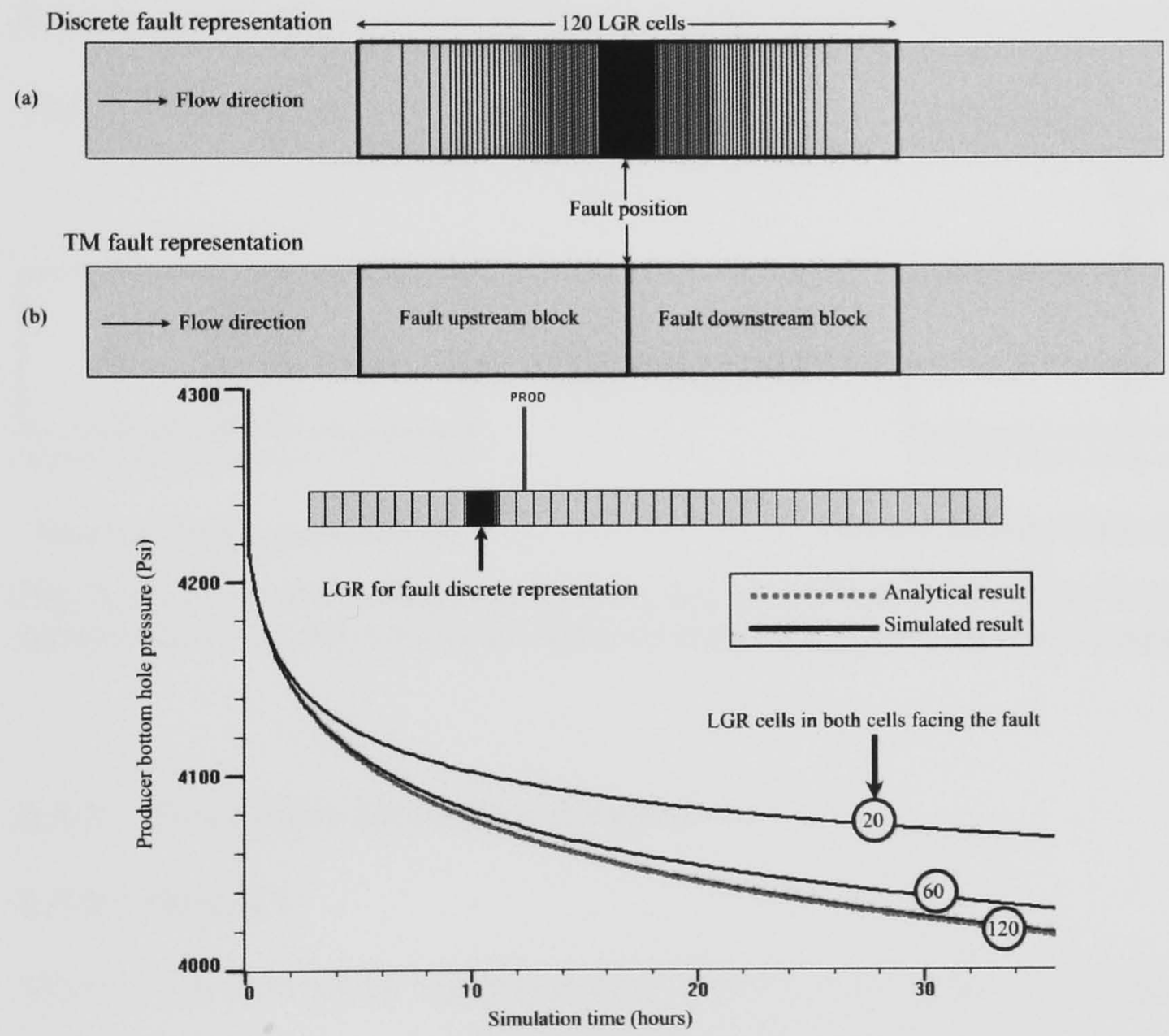

Fig. 3.12. A model providing justification for the choice of the number of LGR cells in the different models used in this study. **(a)** LGR cells are added to the cells adjacent to the fault faces. LGR cells are added in a way, which ensures a gradual transition in the cell pore volumes from the fault cells to the host cells. **(b)** Analytical solutions for a single producer bottom hole pressure (BHP) for a draw down test (Yaxley, 1987) were compared against the same output from a simple 2D reservoir simulation for a single fault using different LGR schemes. The solid lines represent results from different LGR schemes and the doted line is the analytical solution.

Manzocchi *et al.* (1999) showed that the absolute transmissibility multiplier (TM_{abs}) acting between two undistorted cells with different dimensions and properties separated by a fault of constant thickness (**Fig. 3.13**) is given by: (see **chapter 2** for TM_{abs} calculations between distorted cells in corner point geometry)

$$TM_{abs} = \left(1 + \frac{t_f \left(\frac{2}{k_f} - \frac{1}{k_1} - \frac{1}{k_2} \right)}{\frac{L_1}{k_1} + \frac{L_2}{k_2}} \right)^{-1} \qquad \textbf{3.12}$$

where L_1 and L_2 are the cell lengths, k_1 and k_2 are the permeabilities of the undeformed cells, t_f is the cumulative fault rock thickness, and k_f is the fault rock permeability.

In this study, the following data were used:

$L_1 = L_2 = 40$ ft, $k_1 = k_2 = 1000$ mD, and $k_f = 0.01$ mD.

For the cases of $t_f = 0.3$ ft and 3 ft, the corresponding transmissibility multipliers are $TM_{abs} \approx 0.0013$ and $TM_{abs} \approx 0.0001333$, respectively.

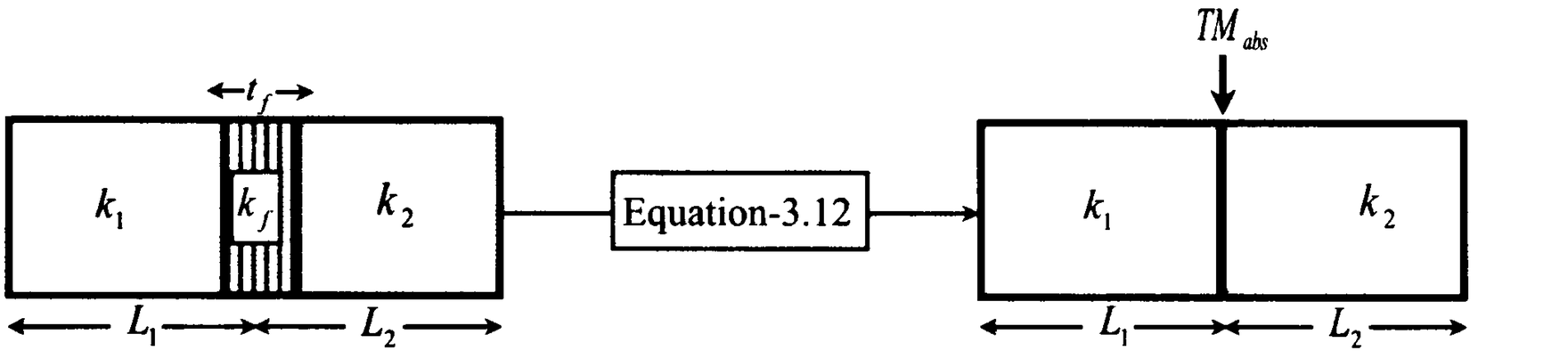

Fig. 3.13. A schematic diagram showing the transformation between the discrete fault representation and the transmissibility multiplier representation using **equaton-3.12**.

3.4.2. Fluid Flow Modelling Results

3.4.2.1 Model 1

Model 1 has an injector and producer at opposite sides of the fault (**Fig. 3.10a**). The injector is perforated in the lower two layers and the producer is perforated in the upper two layers. All simulations predict that most of the oil from the opposite side of the fault (Compartment 1) would be produced (**Fig. 3.14a**). The models in which fault rock properties are included using transmissibility multipliers and the models in which the fault is included discretely with a low threshold pressure all predict similar cumulative oil production profiles, irrespective of whether the fault is 3 ft or 0.3 ft thick. The model in which the fault is given a high threshold pressure predicts that less oil is produced from Compartment 1 than the other models. A rather counter-intuitive result is that the simulations indicate less oil is produced from Compartment 1 when the fault is 0.3 ft thick than when it is 3 ft thick. The physical reason behind this result is that a far higher drawdown occurs in the case of the 3 ft fault (**Fig. 3.14c**) because less water flow

occurs across the fault in the aquifer. The larger drawdown allows higher oil saturations to develop within the fault rock and hence increases its relative permeability.

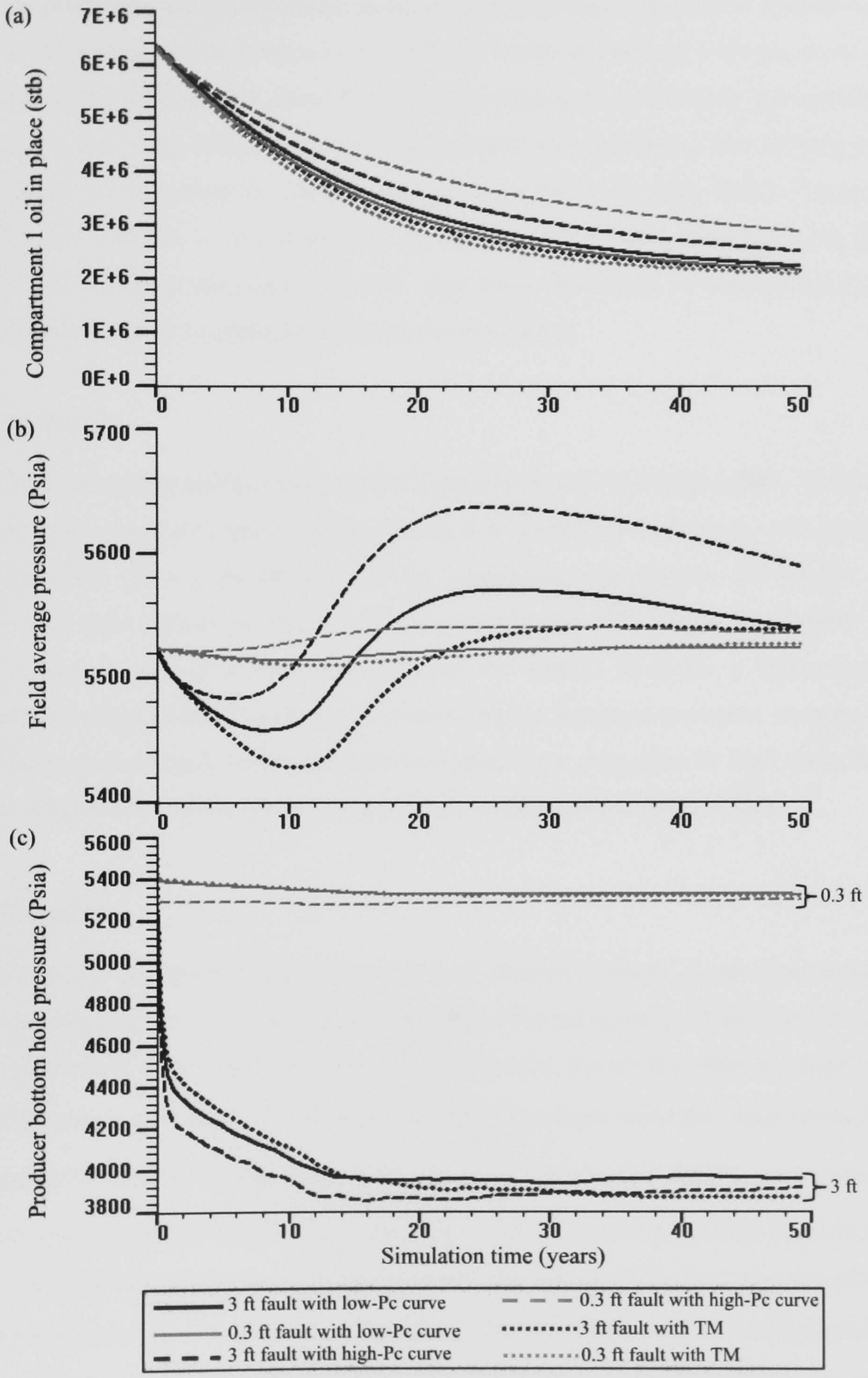

Fig. 3.14. (a) Oil in place in Compartment 1 as a function of simulation time (Model 1). Oil in place is defined as the remaining oil at any instance starting with the original oil in place. **(b)** Field average pressure as a function of simulation time (Model 1). **(c)** Bottom hole pressure in the producer as a function of simulation time (Model 1). High– P_c and low– P_c denote high and low threshold pressures have been used for the fault zone. TM is where fault rock properties were incorporated using transmissibility multipliers.

Large differences exist between the simulation models in terms of their predictions of the field average (**Fig. 3.14b**) and bottom hole pressure within the producer (**Fig. 3.14c**). It appears that the prediction of average field pressures requires that both fault rock thickness and two-phase flow properties are incorporated accurately (**Fig. 3.14b**). The models containing a 3 ft-thick fault all predict similar bottom hole pressures, which are around 1000 psi lower than the models containing a 0.3 ft-thick fault. These results suggest that accurately incorporating fault rock thickness into these models is far more important when predicting bottom hole pressures than accurately incorporating the capillary properties of the faults (**Fig. 3.14c**). The reason for this is that the pressure in the producing block is rapidly drawn down until the threshold pressure of the fault rock has been overcome, after which the rate of movement across the fault is almost independent of its capillary pressure characteristics.

3.4.2.2 Model 2

Model 2 has the injector and producer on the same side of the fault (**Fig. 3.10b**). The injector is perforated in the lower two layers and the producer is perforated in the upper two layers. In all simulations, most oil was produced from the compartment containing the injector and the producer; very little oil was produced from the opposite side of the fault (**Fig. 3.15a**). As with Model 1, there is very little difference between the models in terms of predicting the oil production rate (**Fig. 3.15b**). For the faults with the higher threshold pressures, it seems that it is more valuable to accurately incorporate the two-phase flow properties of fault rocks than their thickness when predicting the bottom hole pressure in the producer (**Fig. 3.15c**).

3.4.2.3 Model 3

Model 3 does not contain an injector; instead, total pressure support comes from an analytical aquifer connected to both compartments (**Fig. 3.10c**). The producer is situated in Compartment 2 and is perforated in the upper two layers. In this model, the results when the fault rock was included discretely with high P_c and when its properties were included using transmissibility multipliers differ greatly. On the other hand, low P_c results are very similar to transmissibility multipliers representations for both fault thicknesses. In particular, the model predicts that only minimal oil would be produced from the opposite side of the fault when the two-phase flow properties are included with high P_c (**Fig. 3.16a**). On the other hand, the model predicts that most oil would be produced from both compartments in the model when fault rock properties are included as transmissibility multipliers (**Fig. 3.16a**). These differences are reflected in both the rate of oil production (**Fig. 3.16b**) and the bottom hole pressure in the producer (**Fig. 3.16c**). Clearly, in this situation it seems that it is more valuable to accurately incorporate the two-phase flow properties of the fault rocks than the fault rock thickness when predicting the bottom hole

pressure in the producer if the fault is high P_c. At low P_c, however, the fault thickness has a bigger effect on petroleum production than it has at high P_c implying that predicting fault rock thickness is more vital when considering petroleum production across low P_c faults.

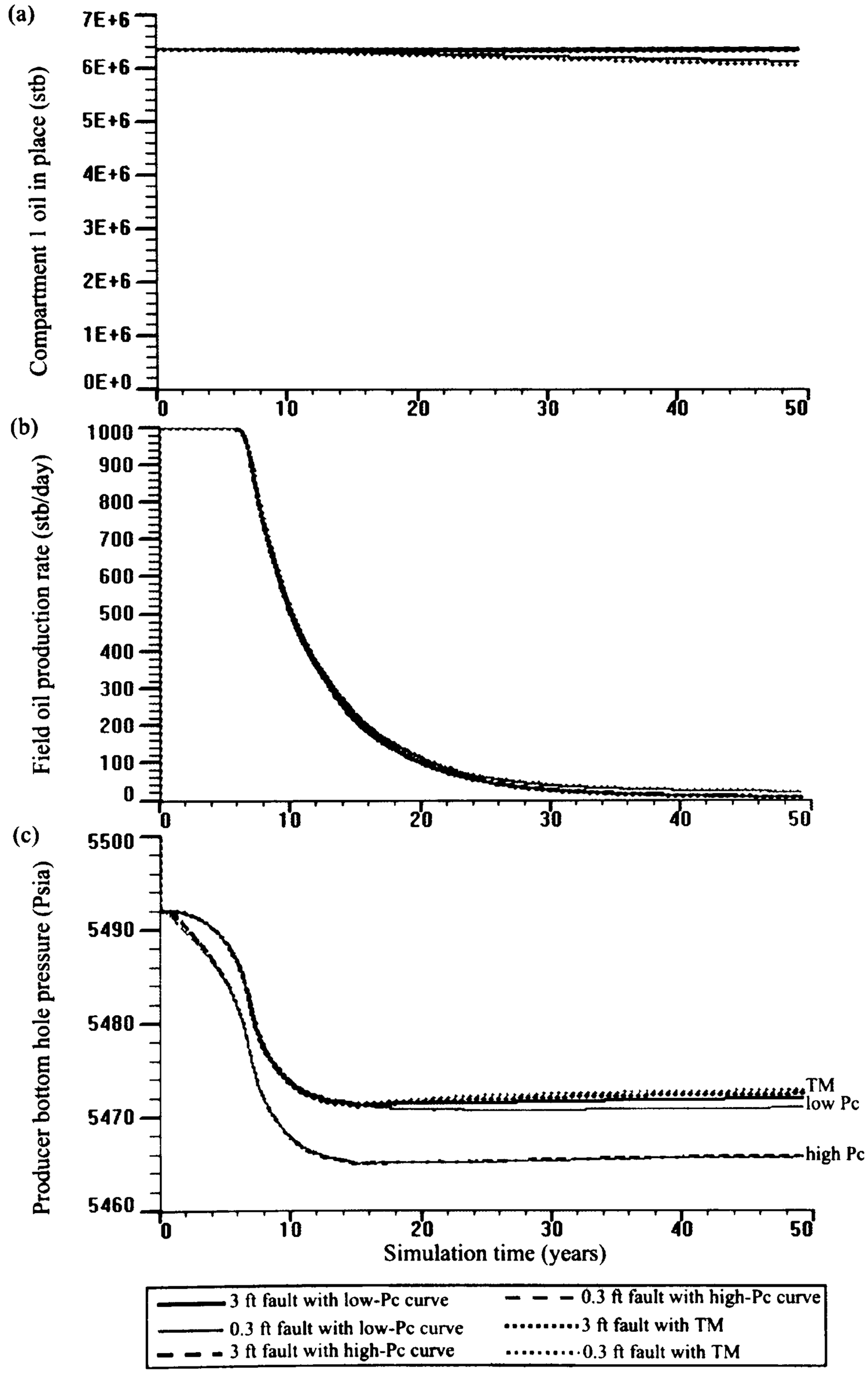

Fig. 3.15. (a) Oil in place in Compartment 1 as a function of simulation time (Model 2). Oil in place is defined as the remaining oil at any instance starting with the original oil in place. **(b)** Field oil production rate as a function of simulation time (Model 2). **(c)** Bottom hole pressure in the producer as a function of simulation time (Model 2). High– P_c and low– P_c denote high and low threshold pressures have been used for the fault zone. TM is where fault rock properties were incorporated using transmissibility multipliers.

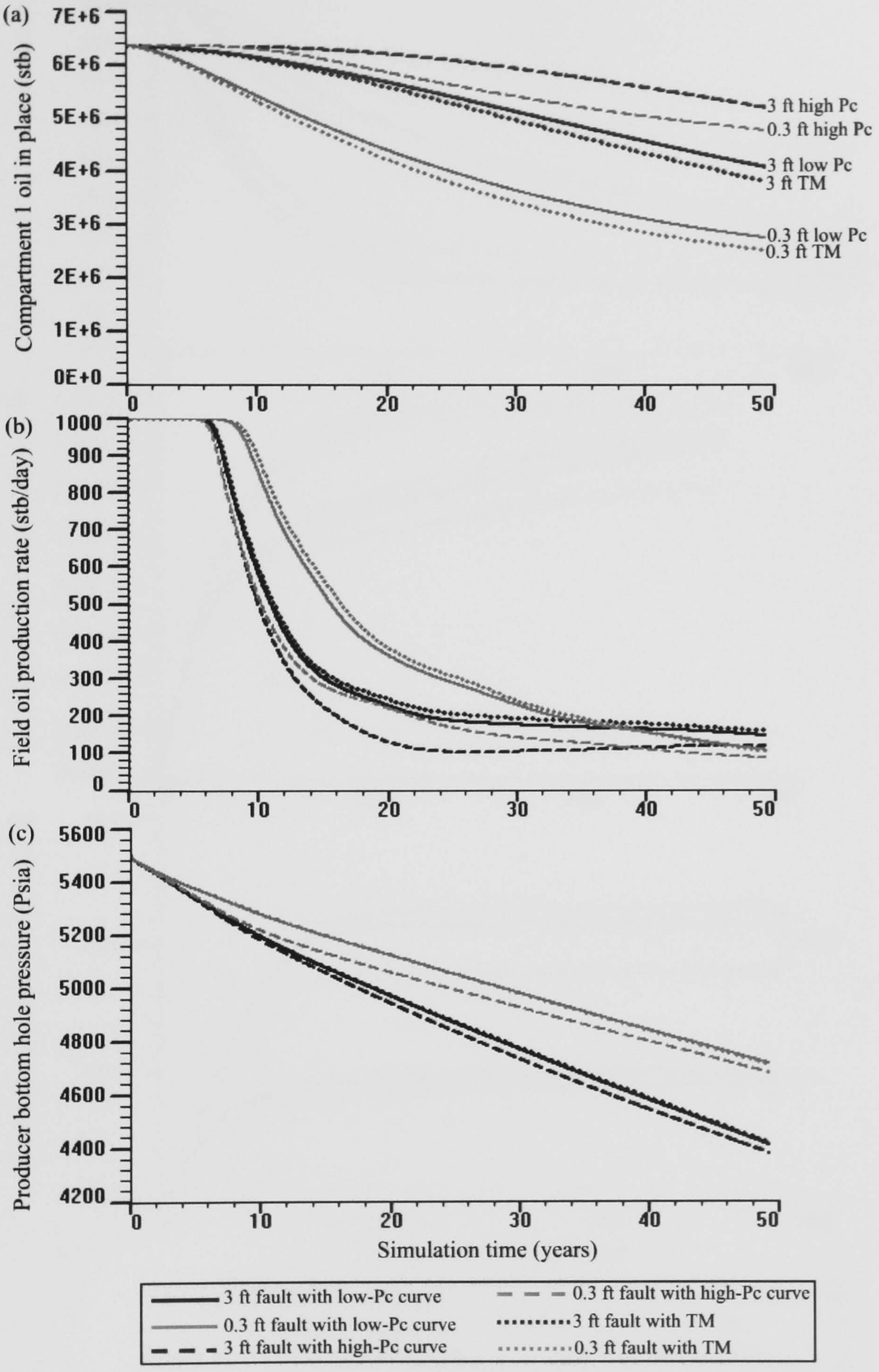

Fig. 3.16. (a) Oil in place in Compartment 1 as a function of simulation time (Model 3). Oil in place is defined as the remaining oil at any instance starting with the original oil in place. **(b)** Field oil production rate as a function of simulation time (Model 3). **(c)** Bottom hole pressure in the producer as a function of simulation time (Model 3). High– P_c and low– P_c denote high and low threshold pressures have been used for the fault zone. TM is where fault rock properties were incorporated using transmissibility multipliers.

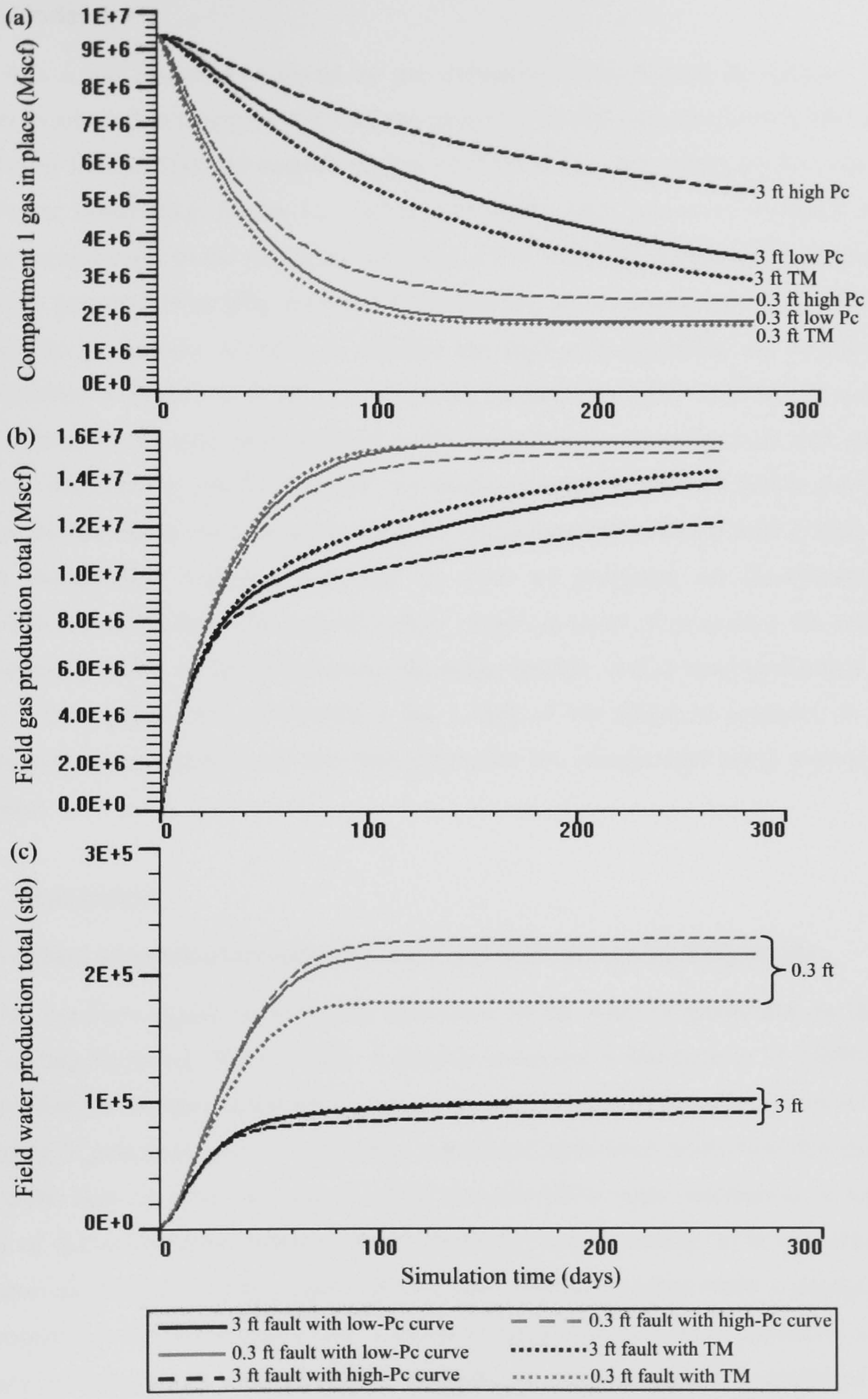

Fig. 3.17 (a) Gas in place in Compartment 1 as a function of simulation time (Model 4). Gas in place is defined as the remaining gas at any instance starting with the original gas in place. **(b)** Field gas production total as a function of simulation time (Model 4). **(c)** Field water production total as a function of simulation time (Model 4). High– P_c and low– P_c denote high and low threshold pressures have been used for the fault zone. TM is where fault rock properties were incorporated using transmissibility multipliers.

3.4.2.4 Model 4

Model 4 is a gas reservoir produced by gas expansion drive without an injector. The gas producer is situated in Compartment 2 of the reservoir. In this case, the bottom hole pressure with a lower limit of 1000 psi controls the gas production rate. The model predicts that, unlike the oil/water system (*e.g.* Model 1), a 0.3 ft fault allows more gas to be produced from the opposite compartment to the producing well than a 3 ft fault (**Fig. 3.17a**) and thus gives more cumulative gas production (**Fig. 3.17b**). The predictions of cumulative gas production do not appear to be particularly sensitive to whether the fault rock properties are included using transmissibility multipliers or as discrete cells when the fault is only 0.3 ft thick. The cumulative gas production is, however, very sensitive to the method of incorporating fault rock properties for a fault thickness of 3 ft. In particular, the model predicts that around half as much gas is produced by the end of the simulation when the threshold pressure of the fault is high and the fault is incorporated discretely compared to when its properties are incorporated using transmissibility multipliers. The opposite effect occurs in terms of predicting the cumulative water production (**Fig. 3.17c**). In particular, the model predicts similar water production profiles for a 3 ft fault independent of whether it has a high or low threshold pressure, or whether capillary pressure is ignored and the fault properties are incorporated using transmissibility multipliers.

3.4.3. Discussion

3.4.3.1 Effect of production/injection on fluid flow across sealing faults

There has not been significant published discussion on the effect of production on fluid flow across sealing faults (*cf.* Watts, 1987). A notable exception is Bjørkum *et al.* (1996), which proposed that the communication between overpressured compartments separated by a fault that was sealing to petroleum prior to production is unlikely (petroleum production was unlikely to result in the flow of petroleum across a fault that has 100% water saturation). A significant amount of discussion does, however, occur internally within industry as to the influence of production on fluid flow across faults. Usually such discussion arises when a change in fault rock properties is needed to gain a history match of production data. More precisely, it is often necessary to increase the transmissibility of faults as more petroleum is produced from a reservoir. In such cases, there is often a debate as to whether the fault has "mechanically broken down" or whether production has resulted in its threshold pressure being overcome. The simulations conducted during this study indicate that this latter mechanism may result in the flow of petroleum across a fault that is sealing prior to production. The physical reason for the change in sealing behaviour is two fold. First, increase in phase pressure of the petroleum in any compartment in which injection is occurring can result in the threshold pressure of the fault rock being overcome. Second, a reduction in the pressure in the compartment in which production is

occurring allows a reduction of phase pressure of the water within the fault allowing the capillary pressure of the fault rock to be overcome (*e.g.* Model 3).

3.4.3.2 Capillary end effect and its play in controlling petroleum flows across high capillary pressure faults

When the rock in a fault has a higher threshold pressure to the surrounding host rock, the water contact may be elevated in the fault and the resulting water saturation will represent a barrier to the cross-fault flow of petroleum. To drive oil though the fault a minimum pressure differential across the fault is required. Once this threshold pressure has been exceeded, flow occurs. Model 1 shows that, starting with a capillary pressure smaller than the threshold entry pressure of the high capillary pressure fault; petroleum has crossed the fault from compartment 1 to compartment 2 (**Fig. 3.14a**) as a result of water injection in compartment 1. However, increasing water saturation in the undeformed sediment rock means reduction in capillary pressure, see **Fig. 3.9**. A key question raised in the face of this fact is 'for a 100% water saturated fault with a high entry pressure, how can oil be forced to cross the fault by increasing water saturation, and thus reducing capillary pressure, in the upstream compartment?' The answer to this question comes from understanding a phenomenon taking place on the boundaries between fault and host rock zones. This phenomenon is termed capillary pressure end-effect. Such effects was first observed by Holditch (1979) when examining the impact of water blocks that form during stimulation on productivity of gas wells.

To illustrate the concept of capillary pressure end-effect, consider a fault region within a host rock (**Fig. 3.18a**). The capillary pressure, P_c, in the fault region is assumed larger than in the host rock. For simplicity, we will assume P_c in the host is zero, *i.e.* water pressure (P_w) is equal to oil pressure (P_o). The P_c in the fault region, which is assumed to range between P_c^{min} and P_c^{max}, causes the water contact to rise. Three scenarios will be addressed, related to pressure variation in the upstream side of the fault, for the threshold pressure in a drainage process, *i.e.* decreasing wetting phase (water), within the fault zone. Concentration is paid on cases in which the P_c in the fault is sufficiently strong for the elevated contact in the fault zone to rise though the reservoir layer being considered – *i.e.* a region just above the host OWC but below the fault OWC, see profile line in **Fig. 3.18a**. At this depth the host contains oil and connate water, or irreducible water S_{wirr}, and the fault contains 100% water. These scenarios are:

- **Threshold pressure blocking** (**Fig. 3.18b**). This is a stable position: oil is mobile in the host, but cannot flow into the fault as the oil phase pressure is higher in the fault. Water is

mobile in the fault but cannot flow out into the host as the water phase pressure is higher in the host.

- **Threshold pressure blocking just before oil starts flowing into the fault** (**Fig. 3.18c**). To cause oil to flow through the fault from left to right, the pressure on the left hand (upstream) side of the fault need to be increased. Suppose that the maximum pressure that is achievable in this compartment was just equal to the P_c^{min} in the fault. This is the maximum pressure difference across the fault that can be held – any increase will enable oil to flow into the fault from the upstream side and water to flow out of the fault from the downstream side.

- **Threshold pressure when oil flow occurs at a steady state** (**Fig. 3.18d**). Suppose the pressure difference is increased above P_c^{min}. Water will flow out of the fault, reducing the water saturation within the fault and allowing oil to flow through the fault material. Note that this causes the capillary pressure in the fault to increase as the water saturation falls. The water saturation falls until a steady state is reached. In the new steady state, the oil pressure must be continuous at both upstream and downstream edges, and the water pressure must be continuous at the downstream edge, as the steady state is reached just as water ceases to flow.

At first it seems that such a state cannot be found – there will always be a capillary pressure difference of P_c^{min} in the fault, yet we need continuity with the oil and water pressures in the downstream host rock, in which the capillary pressure is zero. However, the water saturation at which $P_c = P_c^{min}$ is one for which the oil mobility approaches zero – so the Darcy flow pressure gradient across the region for which the oil mobility approaches zero equalises the oil phase pressure. As a result, a water hold-up region forms at the downstream side of the fault to reduce oil mobility and achieve the required continuity in phase pressures. This is the capillary end-point effect.

The above has only considered the case in which the fault is holding up oil flow (*i.e.* for flow through the reservoir ahead of a displacement front). However, at some point there will be a water inflow as well as an oil inflow. The capillary pressure hold-up at the downstream edge of the fault will not vanish – it is required to allow the oil and water phase pressures to match. However, a similar hold-up distribution of oil will appear in the host rock at the upstream edge of the fault block, see **Fig. 8.19** for an example. This impedes the flow of water and drops the water phase pressure to achieve continuity at the upstream edge of the fault block. The overall effect is that the threshold pressure drop is seen in both phases – although the actual phase pressure variation occurs at one or other of the host rock/fault rock interfaces.

It is the formation of this fault upstream oil zone that can be used to provide an answer to why oil flow occurs across the high capillary pressure fault in Model 1 presented in this study.

The accumulation of oil in this zone forces water saturation in the host rock to decrease further and hence the host capillary pressure to increase to a point where the fault entry pressure is overcome. Without this effect it would be impossible to drive oil across the fault in this particular case unless a mechanical break down takes place.

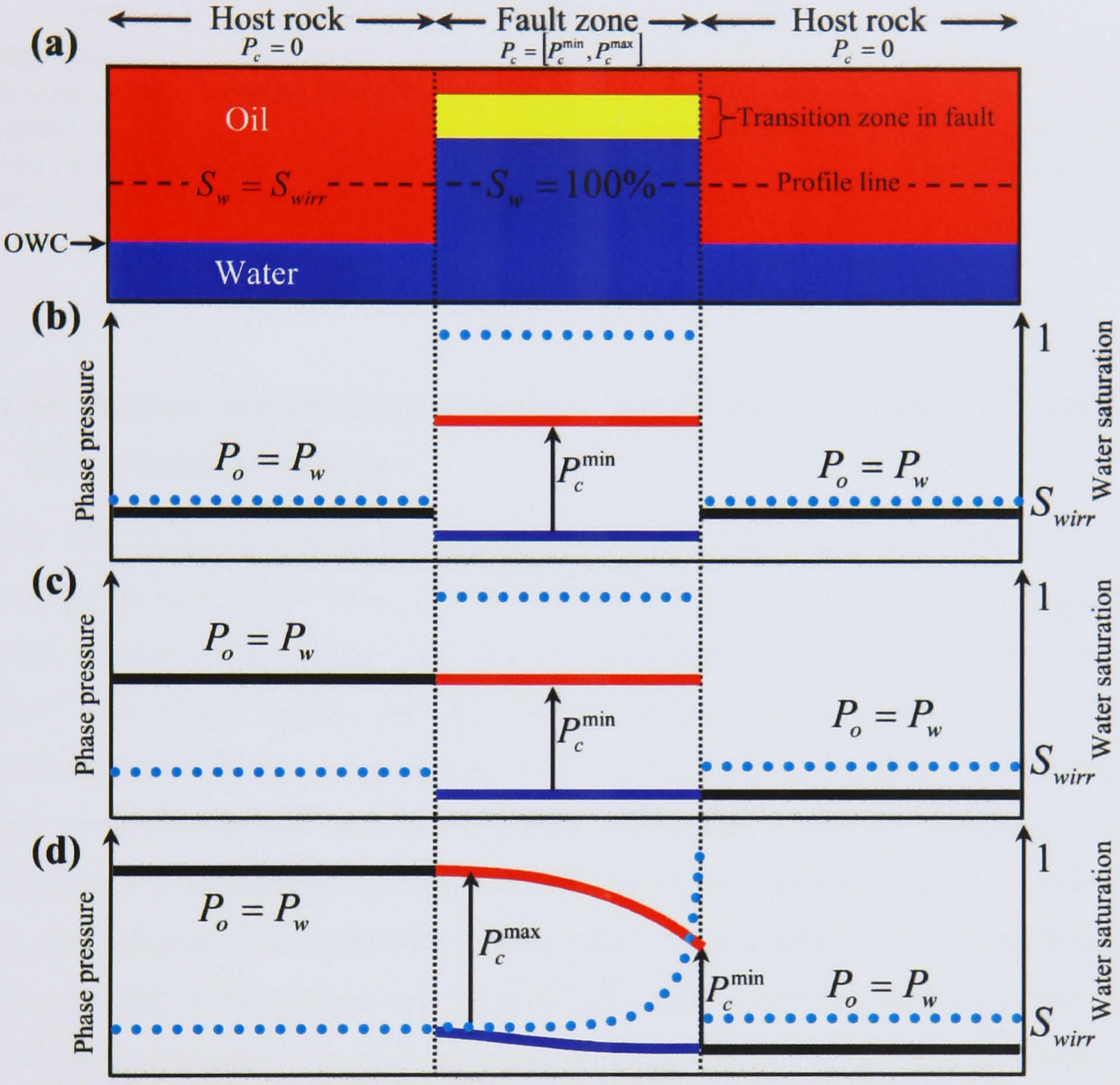

Fig. 3.18. **(a)** A static model showing the elevated water column in the fault zone owing to its capillary pressure characteristics. **(b)** Phase pressures (red solid line is oil pressure, dark blue solid line is water pressure) and water saturation (dotted light blue line) profiles along the profile line shown in **(a)**. **(c)** Changes on phase pressures and saturations when pressure in the left compartment to the fault zone is increased to P_c^{min} in the fault. **(c)** Changes on phase pressures and saturations when pressure in the left compartment to the fault zone is increased to $> P_c^{max}$ in the fault. **(d)** Shows the profiles after a steady state oil flow across the fault zone.

Fig. 3.19. Simulation results showing the oil hold-up region to reduce water mobility in the host and the water hold-up region to reduce oil mobility in the fault. These regions form to achieve phase pressure continuities at both sides of the fault. The results are for water injection on an initially oil saturated, to irreducible water saturation, host rock and 100% water saturation elevated in the fault zone by capillary pressure.

3.4.3.3 Production mechanisms and the incorporation of fault rock properties into simulation models

The main aim of the simulation modelling conducted during this chapter was to provide an answer to the question "*under what circumstances is it better to incorporate the multiphase flow properties of faults into production simulation models than to accurately account for fault rock thickness?*" The results suggest that there are no simple answers to this question. In some circumstances (*e.g.* injector and producer on the opposite sides of a fault), it is clearly more important to accurately take into account fault rock thickness in the simulations. In other circumstances (*e.g.* producing from one side of a fault when pressure support comes from the aquifer), it is clearly more important to incorporate the multiphase flow properties into the simulation. In other circumstances (*e.g.* predicting field pressure when the injector and producer are in different compartments), it is necessary to incorporate both the fault thickness and the two-phase flow properties into the production simulation model. The latter example indicates that, when considering how to incorporate the properties of faults into production simulation models, it is important to identify which are the most important parameters that must be predicted. For example, in Model 1 where the producer and the injector are at opposite sides of the fault, the fault rock thickness had a large impact on prediction of the pressures, whereas the two-phase properties had more of an impact on predicting the oil production rates.

The gas reservoir, Model 4, behaves much differently to the oil models. In particular, for two compartments separated by a thin fault, the high mobility of the gas can replace the need for an injector in the opposite compartment and this is true irrespective of the fault representation (*cf.* Model 3). Overall, the gas model predicts that accounting for fault rock thickness variation is generally more important than incorporating the two-phase properties of the fault rock. Very thick faults, however, are expected to violate this latter rule.

3.5. Conclusions

Dynamic phase pressures and saturations behaviour across low permeability fault zones has been addressed. Faults that possess different capillary characteristics from their surrounding undeformed reservoirs exhibit different flow profiles and must be handled carefully in simulation models. Depending on drive mechanisms and flow regime, incorporating the multiphase flow properties of faults in simulation models has various degrees of importance.

Two-phase fluid flow modelling has been conducted to answer the question "*under what circumstances is it better to incorporate the multiphase flow properties of faults into production simulation models than accurately account for fault rock thickness?*" The results show that in some circumstances accurately determining fault rock thickness does not have a huge impact on the modelling. In these situations, incorporation of multiphase flow properties of fault rocks in production simulations models is far more important. Generally, the relative importance of fault rock thickness and capillary pressure is a function of the relative strengths of viscous forces (*e.g.* those characterised by high flow rates or large length-scales) and capillary forces (*e.g.* those characterised by low flow rates or small length-scales). For example, when predicting bottom hole pressure in Model 1 (with high across-fault flow rates) and Model 2 (with a much lower across-fault flow rates), different conclusions were reached in the case of a high capillary pressure fault. In such cases, Model 1 suggested that fault thickness has more impact than capillary charactersitcs of the fault, whereas Model 2 results suggested that fault capillary pressure had more impact on the results than the fault rock thickness.

It is important to identify which are the most important parameters that need to be predicted when considering how to model faults in flow simulations. It is possible that more work in this area may provide 'rules of thumb' which will indicate which parameters are important to consider when modelling fluid flow in faulted reservoirs. However, each case may be so specific that it is necessary to construct simple numerical models to determine which are the most important parameters to include in full field production simulation models.

As a final conclusion, the present study offers important constraints that should assist in providing 'quality control' on the parameters used to generate history matches of production data. The study also suggests that in many situations the uncertainty in predicting fault rock thickness does not necessarily reduce our ability to model fluid flow in petroleum reservoirs.

Chapter 4

Microstructural and petrophysical properties of fault rocks within the Pierce Field

" Modern fault seal analysis methods use an array of data. These data include seismic, structural and microstructural information from high-resolution core analysis, and well bore and production data to predict fault behaviour and to reduce uncertainty and risk."

Rob Knipe
Director of Rock Deformation Research (RDR) at the University of Leeds

4.1. Introduction

This chapter presents the results of microstructural and petrophysical property analysis conducted on 7 fault rocks and their associated undeformed sandstones from well 23/27-8 in the Pierce Field, North Sea. The chapter is divided into the following parts. The first section (**§ 4.2**) gives an overview of the Pierce Field, North Sea. This section summarises the first and the currently updated fluid flow simulation model of the field. The descriptions outlined and data presented about the Pierce Field are those obtained from Shell. The second part (**§ 4.3** and **§ 4.4**) presents the methodologies and results of microstructural and petrophysical property analyses of 7 fault rocks and their associated undeformed sandstones from well in the Pierce Field. These studies were undertaken as a part of this research to determine the transmissibility multiplier distributions along fault rocks in the Pierce Field and account for the multiphase flow properties of faults in production simulation models. The microstructural and petrophysical properties of individual specimens are described in **Appendix A**. The implications of these results for fluid flow modelling within the Pierce Field is the main theme of the next chapter (**Chapter 5**).

4.2. An overview of the Pierce Field, North Sea

The **Pierce Field** is located in UK blocks 23/22a and 23/27 in the Central North Sea, approximately 265 km from Aberdeen, **Fig. 4.1**. The field comprises the two accumulations of Pierce North and Pierce South discovered 14 years apart by well UK 23/27-3 in 1976 and well UK 23/22a-2 in 1990. The field structure comprises two salt diapirs, which fully penetrate the reservoirs, giving structural dips of up to 70° adjacent to the diapirs.

Each accumulation is associated with a separate salt diapir and has an oil column with a common oil leg and an associated gas cap. The reservoir is a Paleocene-aged basin-floor sandstone draped over two salt-cored structural closures (**Fig. 4.2**). Early in the development,

radial faults around the eastern structure were thought to compartmentalise the reservoir, because oil–water contacts varied significantly across the field (Dennis *et al.*, 1998). Once sufficient pressure data was available, it became apparent that the oil–water contact dip was affected by the regional potentiometric gradient (Dennis *et al.*, 1998). Log and pressure data (**Fig. 4.3**) from 12 wells were used to construct a map of the oil-water contact (OWC). An interesting aspect is the large variation in depth to the OWC across the field, varying by 300 m from west to east (**Fig. 4.4**), which is thought to be caused by a tilted OWC within the Pierce Field. The OWC surface dips to the west with an average gradient of 5° (90 m/km). The OWC tilt is interpreted by Dennis *et al.* (1998) to be due to a hydrodynamic flow from east to west, *i.e.* a hydrodynamic pressure gradient. We can use a very simplified analysis using the steady state Darcy Law to support the interpretation given by Dennis *et al.* (1998). For a steady state flow, the flow rates within both the undeformed sediments and the deformed material is equal, so the pressure ratio across an imaginary boundary within the undeformed sediments and an imaginary boundary within the fault material according to Darcy Law is:

$$\frac{\Delta P_f}{\Delta P_h} = \frac{\Delta L_f}{\Delta L_h}\frac{k_h}{k_f} \qquad \textbf{4.1}$$

where ΔP_f and ΔP_h are, respectively, the pressure differences each across two points covering the entire lengths of the fault material (ΔL_f) and across the undeformed sediment material (ΔL_h). The reservoir is assumed to be homogenous with undeformed sediment permeability of k_h and fault permeability of k_f. For some typical Pierce fault thickness of ~0.3 m, and k_f of ~0.05, and an average k_h of ~10 mD containing one fault every ~1 km (*i.e.* ΔL_h is 1 km), see next sections and **Chapter 5**, $\Delta P_f / \Delta P_h$ is ~3/50. This is saying that a pressure difference of 50 units across the Pierce host material will correspond to a pressure difference of 3 units across a single fault. Using the interpreted average tilt of 90 m/km caused by the hydrodynamic flow, the host material is attributed to a tilt of 90×(50/53) m, or about 84.9 m, whereas the fault can be attributed to a tilt of 90×(3/53) m, or about 5.1 m. Such simple analysis indicates that the contribution of Pierce faults to the observed OWC tilt can be judged very small or even negligible.

The average aquifer pressure gradient is 3 bars/km (approximately 45 psi/km). The gas–oil contact (GOC) is flat because only the water is moving; the oil is stationary in a state of hydrodynamic equilibrium with pressure communication through the oil leg.

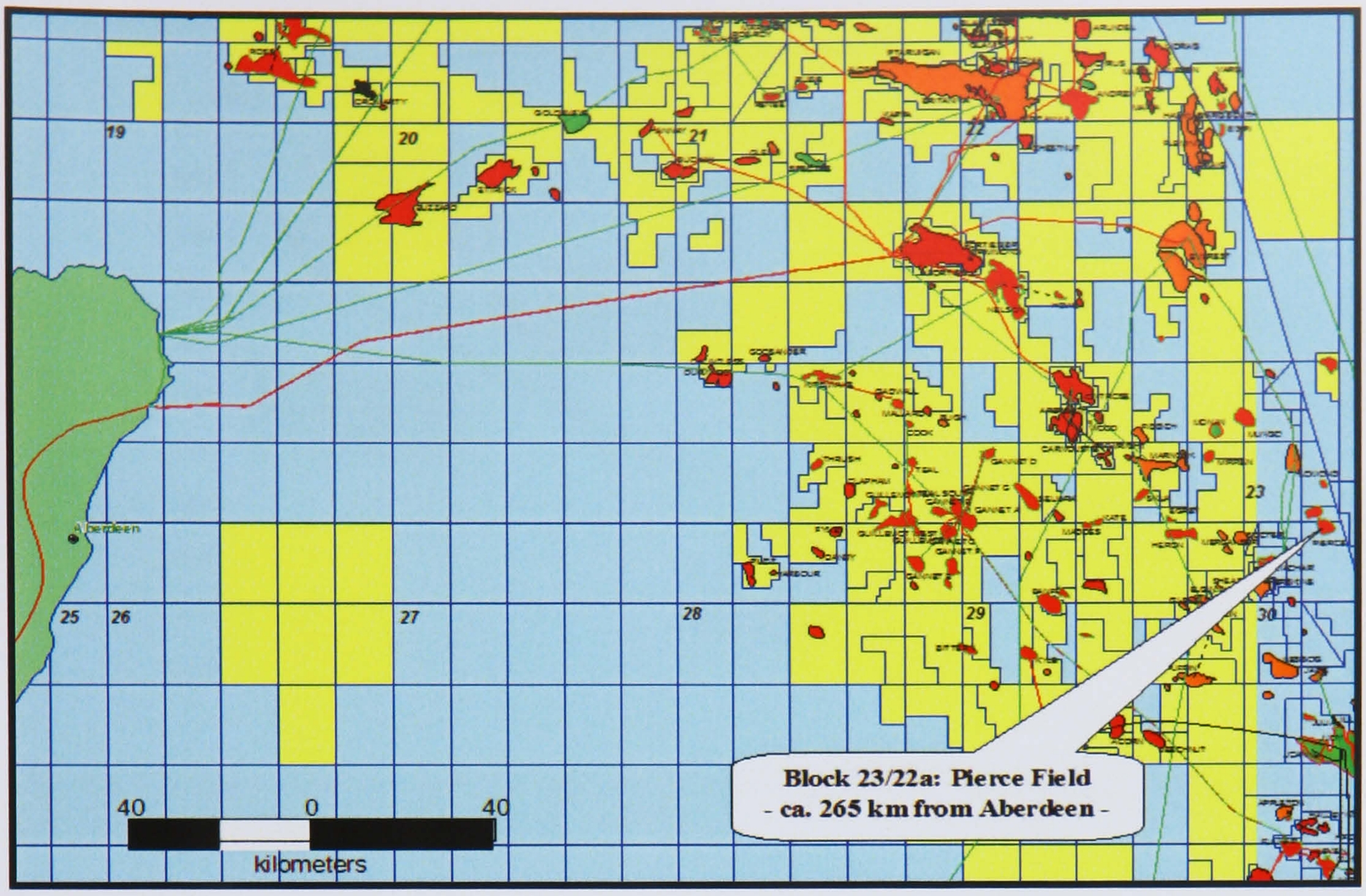

Fig. 4.1. The Pierce Field is located in UK blocks 23/22a and 23/27 in the Central North Sea, approximately 265 km from Aberdeen. The field comprises the two accumulations of Pierce North and Pierce South discovered 14 years apart by well UK 23/27-3 in 1976 and well UK 23/22a-2 in 1990.

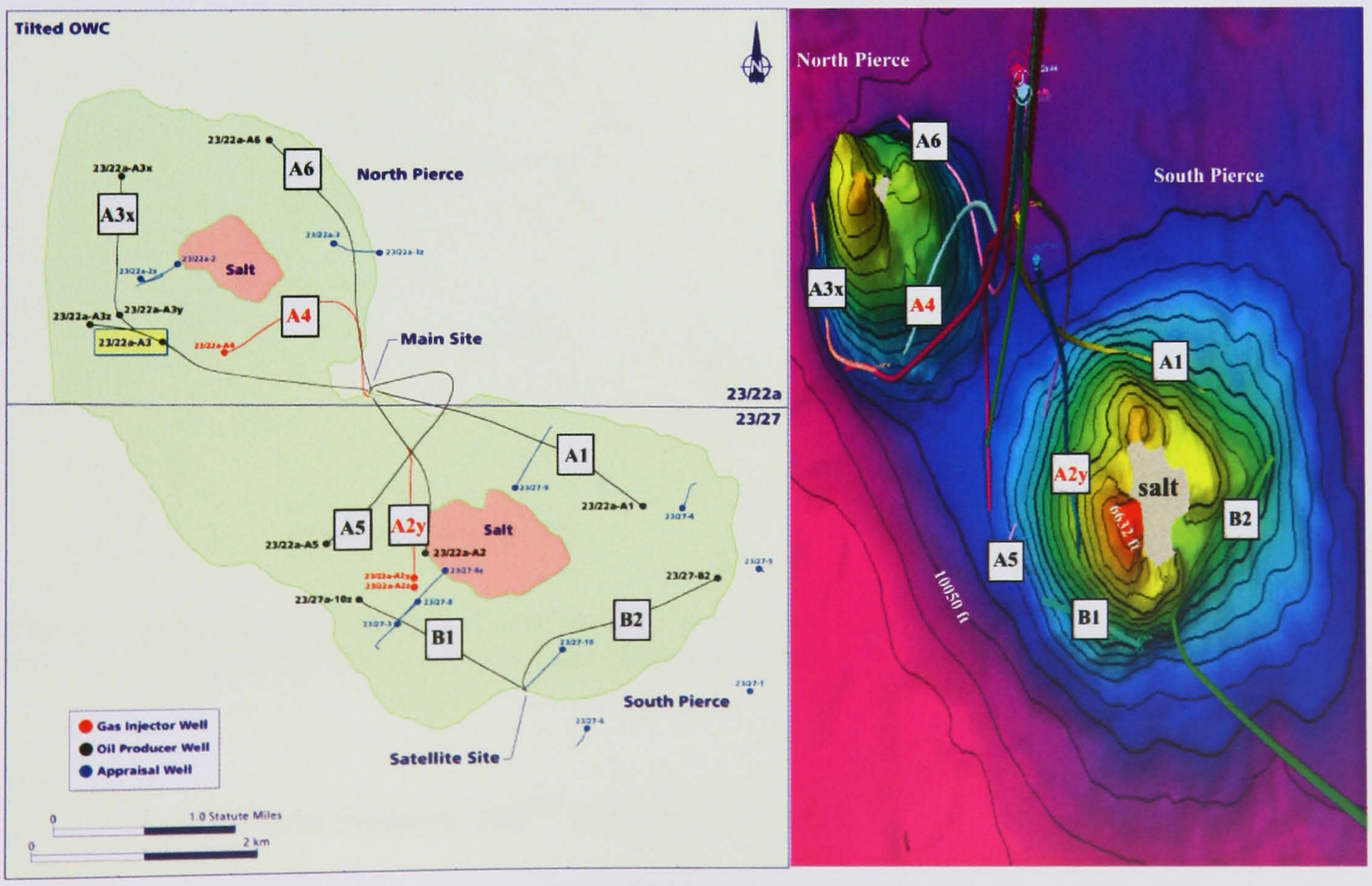

Fig. 4.2. Left: map showing the classification of the wells in the Pierce Field: 6 producers, 2 gas injectors and 13 appraisal wells. Right: 3D view of the deviated wells in the field with depth contours. Red is structure top at about 6632 ft and blue is structure base at about 10050 ft.

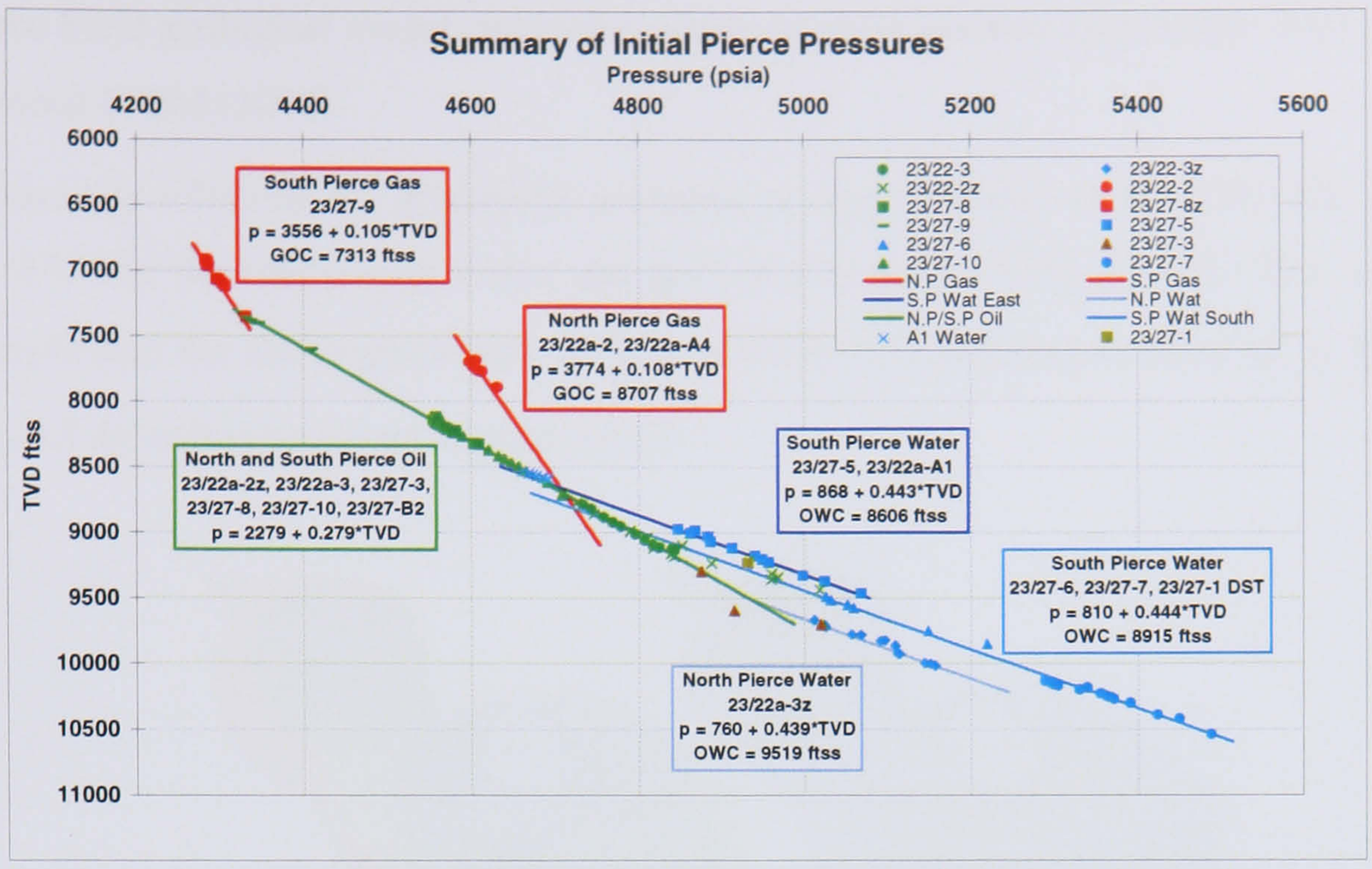

Fig. 4.3. Pressure data (gained from repeat formation tester, RFT, results) suggest that North and South Pierce have separate GOCs and OWCs.

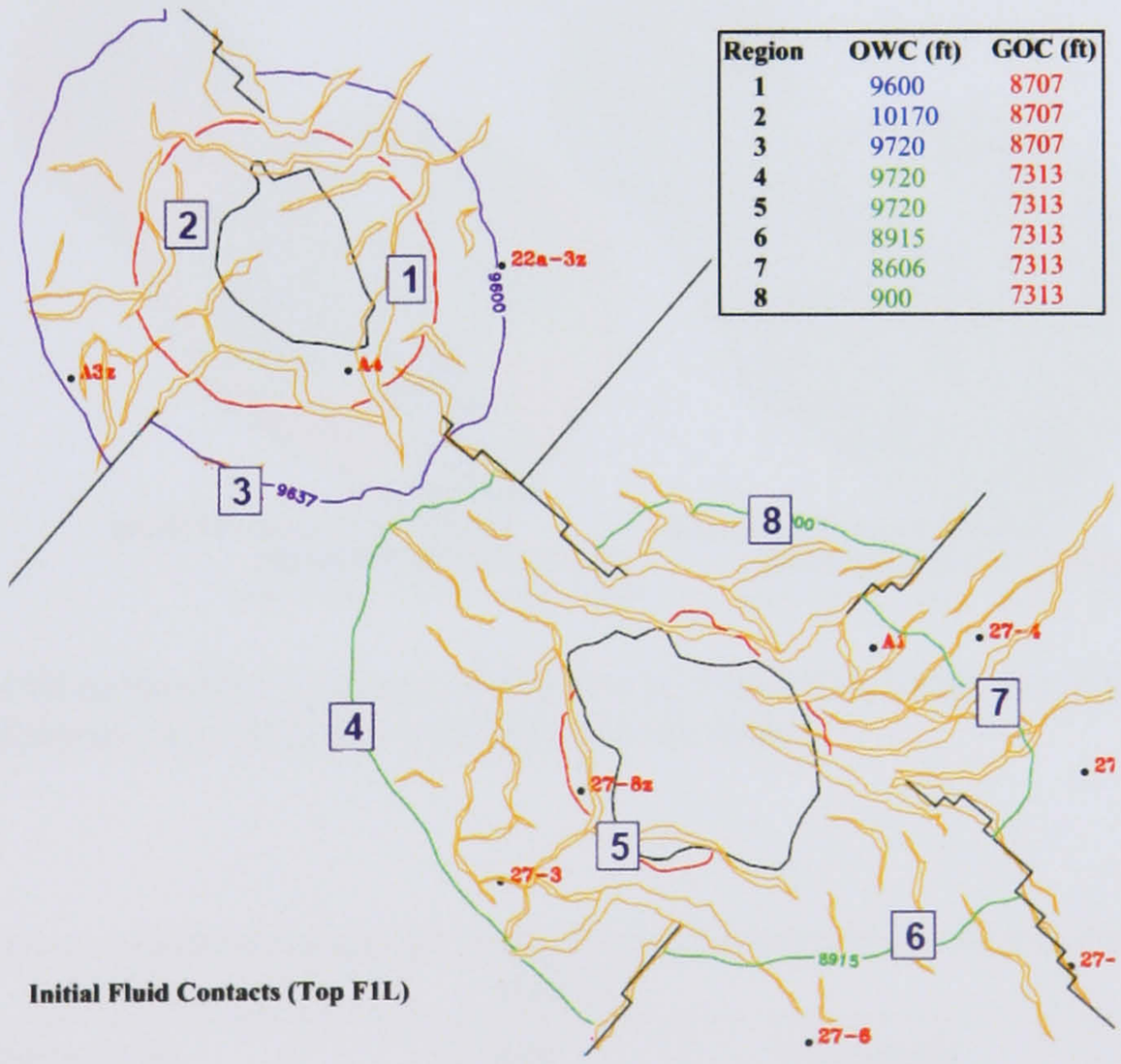

Fig. 4.4. Schematic tilted OWC model for the Pierce Field, indicating the proposed tilted contact. Depths (TVDss) show the variation in the OWC and GOC in each region of the model.

4.2.1. Pierce Field Eclipse 100™ simulation model

The Pierce full field simulation model (FFSM) was updated as part of this study, based on integrated input from all subsurface disciplines, and drawing on a number of pieces of work:

- updated Paleocene reservoir depth maps (August and October 2000);
- Forties fault maps (December 2001);

- Pierce Field geological model and hydrocarbons in place updates (September 2001);
- previous FFSM (2000).

Model layering followed the geological sequence of Upper Forties (F1L, F2U, F2L), Lower Forties (F4) and the intervening shales and poor quality sands (F1U, F3, F5). The simulation model replicated the net-to-gross ratio (NTG), porosity (ϕ) and permeability (k_x), **Table-4.1** and **Fig. 4.5** described by the geological model.

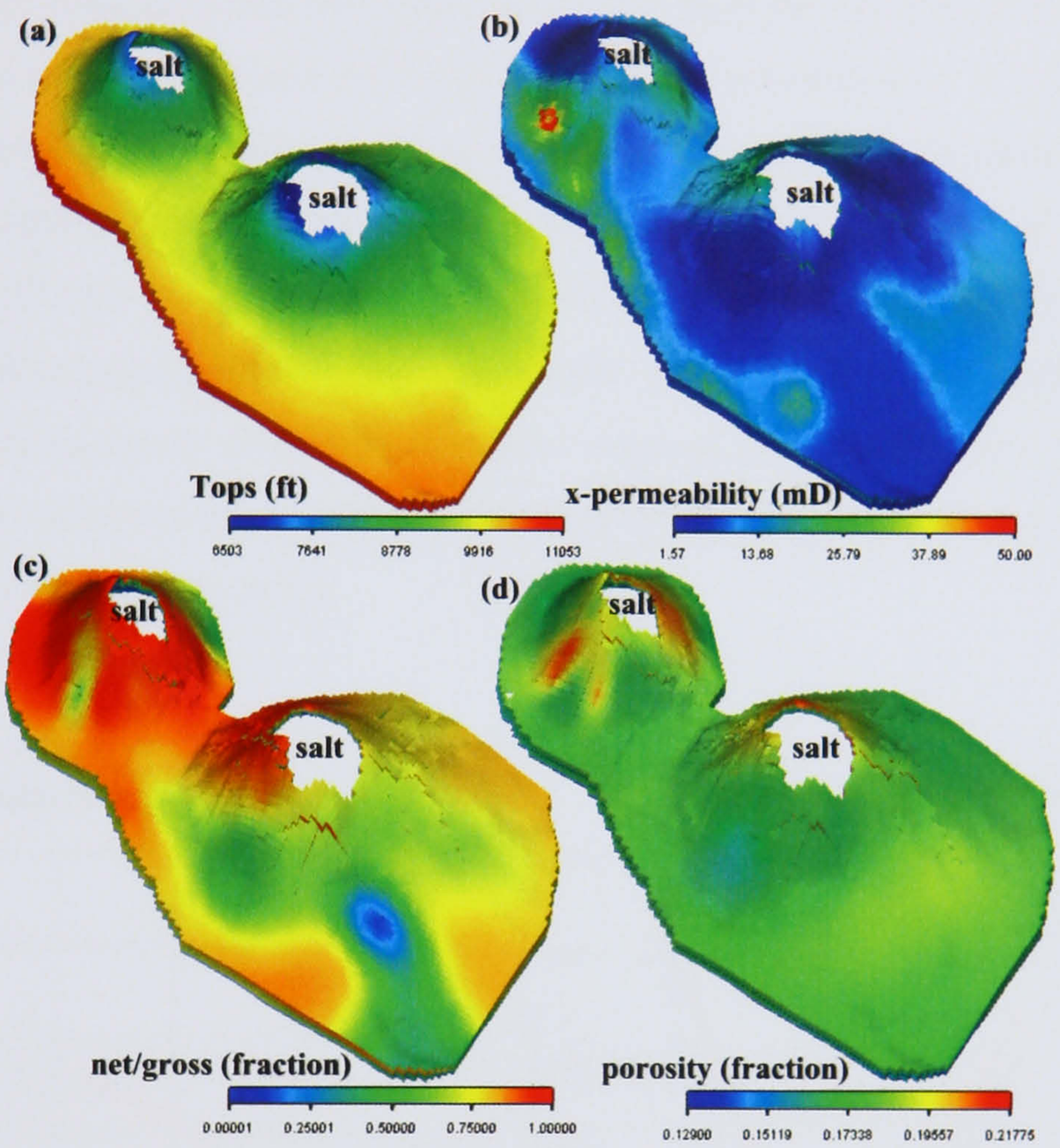

Fig. 4.5. Different cell properties displays of the Pierce Field F1L layer. **(a)** Tops data, **(b)** *x*-directional permeabilities, **(c)** net/gross and **(d)** porosity data.

Table-4.1. Thickness-weighted average petrophysical parameters for the Forties reservoir at Pierce.

Layer	Thickness (ft)			k_x (mD)			ϕ (Fraction)			NTG (Fraction)		
	Min	Max	Mean	Min	Max	Mean	Min	Max	Mean	Min	Max	Mean
1 (F1U)	Shale			Shale			Shale			Shale		
2 (F1L)	0.01	48.88	24.62	3.94	49.27	10.38	0.16	0.21	0.18	0.11	1	0.75
3-4 (F2U)	0.06	103.54	34.76	3.85	30.69	11.01	0.17	0.22	0.19	0.20	0.97	0.71
5-6 (F2M)	3.08	94.69	38.38	3.88	24.39	10.20	0.17	0.22	0.18	0.23	1	0.75
7-8 (F2L)	2.75	72.73	39.29	3.32	32.16	12.08	0.16	0.21	0.18	0.23	0.87	0.69
9 (F3)	0.01	35.42	22.04	1.57	4.28	1.95	0.13	0.20	0.15	0	0.43	0.24
10-13 (F4)	1.92	158.01	44.96	2.74	133.52	8.16	0.15	0.21	0.17	0.25	0.85	0.61
14 (F5)	3.54	72.85	46.34	1.59	2.85	1.98	0.13	0.19	0.15	0.00	0.52	0.21

North and South Pierce share a common oil gradient, but are intersected by different offsets of gas and water gradients. The two GOCs reflect the different gas compositions observed within the gas caps. To resolve the different offsets in water gradients upon initialisation, a localised compartmentalised model with horizontal OWCs was developed. Regional OWCs are made discontinuous across selected fault boundaries in the aquifer to honour initial saturations observed in the exploration and appraisal wells, thus isolating the different observed pressure regimes.

Irreducible water saturation and moveable oil volume data was distributed according to rock quality, with initial water saturations derived from capillary pressure data. A single set of three-phase relative permeability functions was applied across the model, with saturation end-points scaled to the moveable saturation range. The relative permeability curves were generated using Corey exponents (Corey, 1954) adjusted to achieve the closest history match in each region. The oil–water relative permeability curve was initially generated by fitting Corey relationships to end-point laboratory steady-state measurements ('original' curve in **Fig. 4.6**). In April 2003, a new experimentally determined oil–water relative permeability curve ('new' curve in **Fig. 4.6**) was used to replace the original curve.

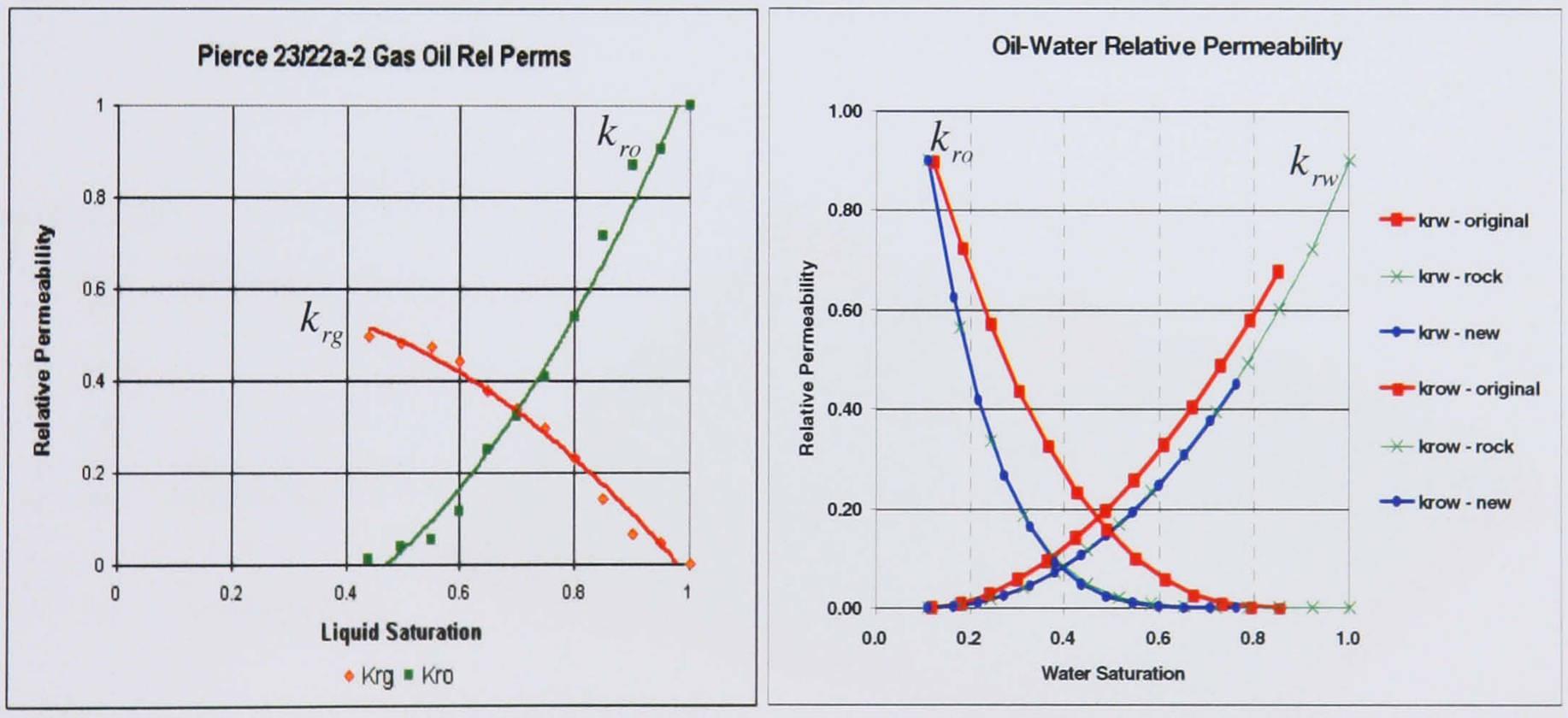

Fig. 4.6. Left: Model input gas–oil relative permeability curves. Right: Model input original and updated (experimentally determined) oil–water relative permeability curves. 'new' curves are the experimentally determined curves, 'rock' curves are those used in the simulation studies after fitting Corey exponents to 'new' curves.

The following data (**Table-4.2**) summarises the simulation model (see **Fig. 4.7** for a grid display of the model):

Table-4.2. Summary of the data input to the Pierce full field simulation model.

Grid dimensions (Nx, Ny, Nz)	130×67×14 (total 121,940 cells)
Active cells	80,619
Cell size	75×75 m with varying thickness (see **Table-4.1**)
k_x, k_y **and** k_z	See **Table-4.1**, $k_y = k_x$, $k_z = 0.1 \times k_x$
Reservoir pressure	Initial average pressure ~ 4600 psia (see **Fig. 4.8B**)
PVT data	At P = 3750 psia: B_g = 0.85 rb/Mcf, μ_g =0.03 cP P_{sat} = 3645 psia, B_{oi} = 1.55 rb/stb, μ_{oi} = 0.19 cP P_{ref} = 5000 psia, B_w = 1.04 rb/stb, μ_w = 0.3 cP
Phase contacts	See **Fig. 4.3** and **Fig. 4.4**
Initial water saturation	S_{wi} = 12% at k_x > 100 mD to 50% at k_x < 1 mD
Saturation functions	See **Fig. 4.6**
Regions	Eight regions around the structure corresponding to observed OWCs
Phases	Oil, water, gas + dissolved gas/vaporised oil
Production and injection	Six producers and two gas injectors (see **Fig. 4.2**). (See **Fig. 4.8 A-B** for field production and injection history)

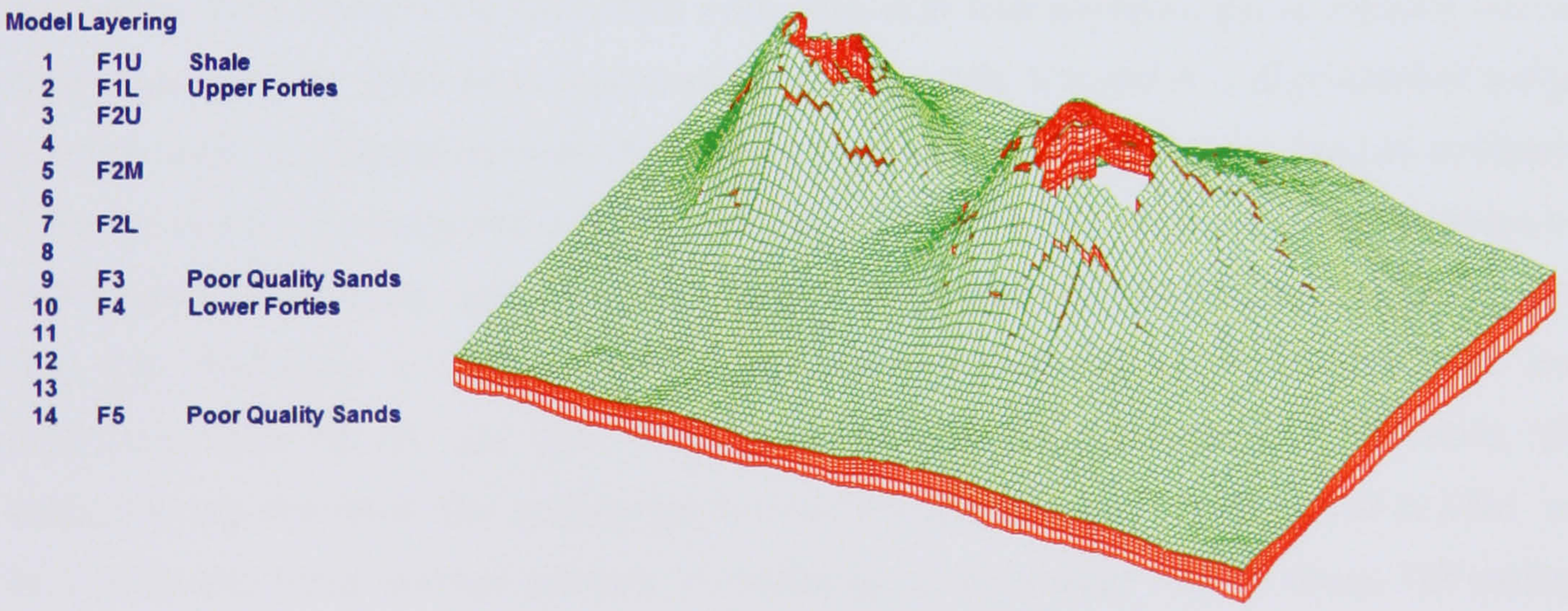

Fig. 4.7. Corner point grid display of the Pierce Field simulation model. The model consists of 14 layers. The compositions of the main Forties are shown on the left. Some Forties are split up into more than one layer for simulation stability and data distribution, *e.g.* phase saturations to honour the tilted OWC. Red lines represent the vertical layering; green lines represent the *x-y* grids.

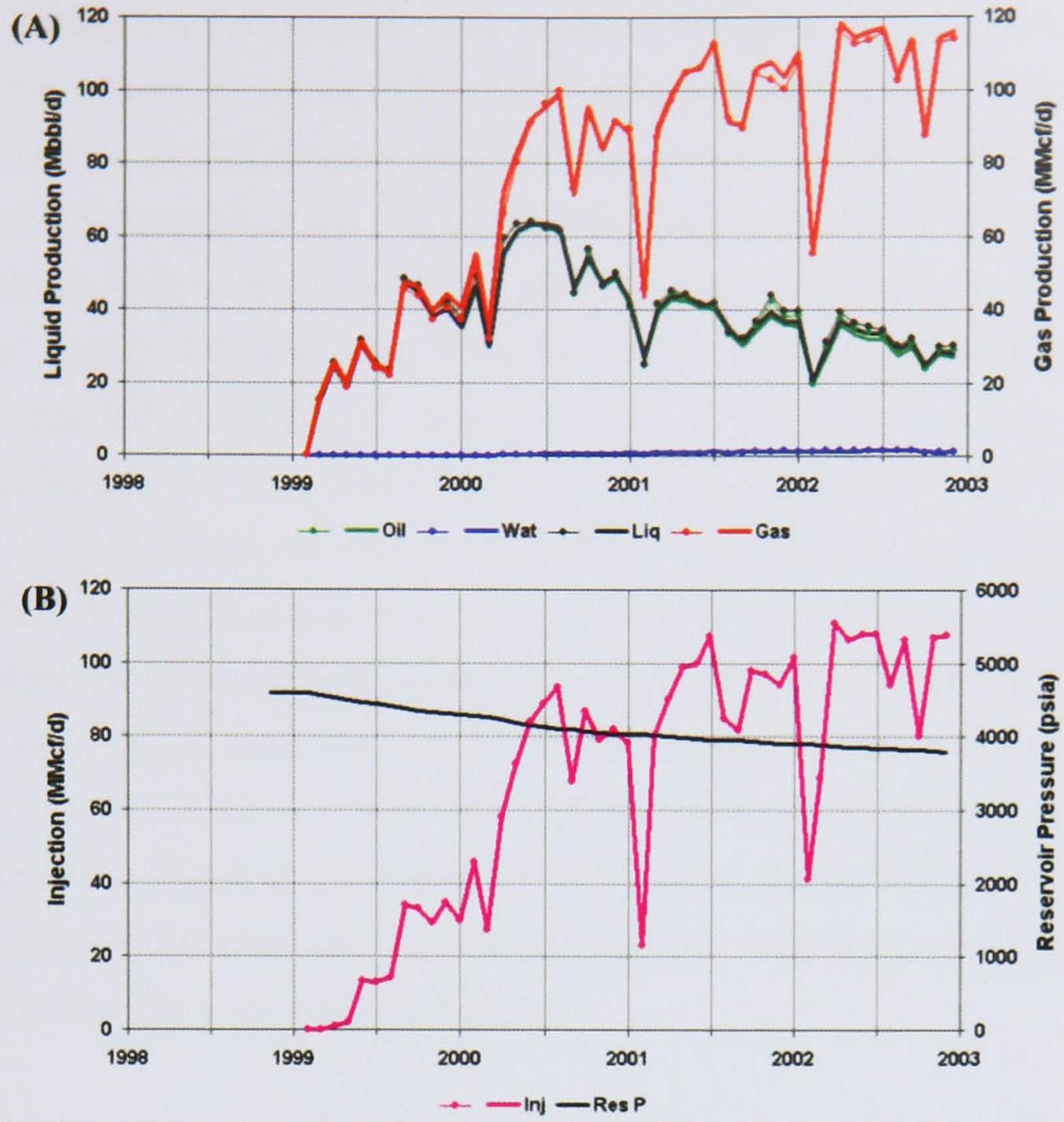

Fig. 4.8. Production **(A)** and injection **(B)** history of the Pierce Field. **(B)** also shows the field average pressure history. Dots are the observed data, continuous lines are the results of Shell's 2003 simulation.

Production from Pierce is via six subsea wells (**Fig. 4.2**) with produced gas re-injected into two subsea gas injectors. With the exception of production wells A3x and A5, all production and gas injection wells functioned normally throughout 2001. A3x was shut in from January to October 2001 due to a subsea safety valve failure, and A5 was shut in for one month due to a subsea tree malfunction. Production and injection started simultaneously at the beginning of 1999 (**Fig. 4.8**). According to 2001 production and injection performance, the field average daily production rates of oil, gas and water productions were, respectively, 37779 stb/d, 95.8 MMscf/d, and 976 stb/d. The average gas re-injection rate during the same period in 2001 was 88.1 MMscf/d. Field average pressure is declining at an average rate of about 180 psi/year, **Fig. 4.8**, indicating that only limited pressure support was available from the aquifer. Producer B2, see **Fig. 4.2**, was the only well that produced significant volumes of water, reaching a water cut of about 16% by end of 2001.

4.2.2. Faults in the Pierce Field

The formation of the two salt domes in the Pierce Field resulted in the formation of radial faults around them with varying degrees of throw and extension. The original field development plan attributed the observed variations in OWC to the presence of sealing radial faults. Recent

development drilling has indicated this early model to be largely incorrect. It has shown that most of the areas of South Pierce are in direct communication, and that most radial faults are not sealing; at worst they provide zones of reduced transmissibility. The only radial faults that have enough vertical displacement to seal (>200 ft) are those that overlie major NW-SE and NE-SW trending basement fault zones. However, in common with other radial faults at Pierce, the displacements rapidly decrease away from the diapir, and it is considered that sealed compartments can only be formed in conjunction with concentric faults (which are far more laterally extensive than the radial faults) and/or stratigraphic trapping elements (**Fig. 4.8**). It is possible that concentric faults are important, yet difficult to image, baffles to fluid flow within the Pierce Field. These faults accommodate most of the vertical strain involved in diapir growth, providing several hundred feet of vertical displacement at a low angle (or parallel) to the steeply dipping beds on the diapir flank. The largest concentric faults are interpreted as forming linked-fault systems, which produce a ring fault around much of the diapir, offset by large displacement radial faults. Such a combination of concentric and radial faults is most likely to create structurally isolated reservoir compartments high on a diapir flank, particularly in areas of the field characterised by a low net/gross reservoir.

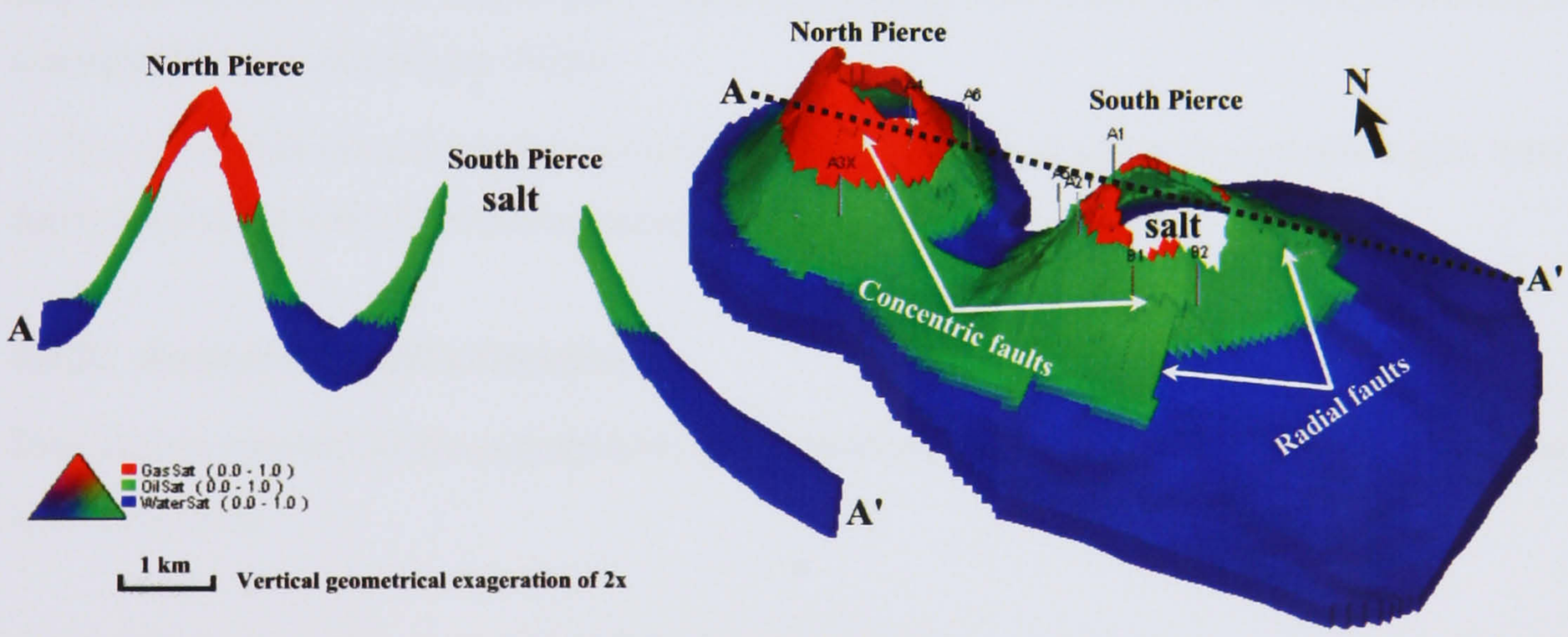

Fig. 4.9. Right: Top view (Top F1L) of the Pierce Field showing the distribution of faults and structure contours of GOCs (green contours) and OWCs (blue contours). Left: A cross-section along A-A' showing the vertical extension of the vertical faults and the initial distribution of phases in the reservoir (blue = water, green = oil, red = gas).

4.3. Microstructural and petrophysical properties of fault rocks from well 23/27-8, Pierce Field

4.3.1. Introduction

This section presents the results of microstructural and petrophysical property analyses of seven fault rocks and their associated undeformed sandstones from the well 23/27-8 in the Pierce Field. These studies were undertaken to determine the transmissibility multiplier distributions along fault rocks in the Pierce Field and account for the multiphase flow properties of these

faults in production simulation models. The main aims of the microstructural and petrophysical property analysis are as follows:

- characterise the microstructure of the reservoir sandstones and deformation features within Pierce;
- determine the permeability and Hg-injection characteristics of the deformed and undeformed sandstones within Pierce;
- identify the deformation processes and sealing mechanisms that have affected the Pierce reservoir;
- constrain the timing of deformation relative to the burial and diagenetic history;
- explore the implications of these core analysis results for fluid flow across faults within the Pierce Field.

4.3.2. Materials studied

A total of 7 fault rocks and their undeformed host rocks were selected from well 23/27-8 for microstructural and petrophysical property analysis. The mineralogies, microstructures and diagenetic histories of the undeformed sandstones and the fault rocks were investigated using a scanning electron microscope (SEM).

The permeabilities and capillary pressures of the undeformed and deformed lithologies were determined using water flow permeametry and Hg-injection porosimetry.

4.3.3. Analytical methodologies

This section summarises the petrographic and petrophysical characterisation methodologies that were employed.

4.3.3.1 Petrographic characterisation techniques

Polished blocks and stubs of fractured surfaces were examined with a CAMSCAN CS44 high performance scanning electron microscope equipped with a secondary electron (SE) detector, a high resolution solid-state four-quadrant back-scattered electron (BSE) detector, a cathodoluminescence (CL) detector and an EDAX energy dispersive X-ray spectrometer (EDS). The SE signal provides topographic information and is therefore extremely useful for investigating the relationships between detrital and authigenic components and establishing their relative timing. The BSE signal is directly proportional to the mean atomic number of the mineral; so phases of different mass have different brightness levels. The BSE signal can be combined with an image analysis system for obtaining quantitative data on mineralogical abundances, grain sizes, porosity and cement distributions. The CL signal is extremely sensitive to trace element abundances and provides information on the growth zonations where different

growth zones incorporate slightly different trace element levels. Some elements (*e.g.* Fe) are known to suppress the luminescence signal, whereas others (*e.g.* Ti and Mn) are known to enhance the signal. Therefore different mineral generations (which have very similar chemical compositions and cannot be differentiated using BSE microscopy or the EDS system) can frequently be identified using cathode luminescence.

The diagenetic history of samples taken from both inside and outside faults are determined and used to establish the timing of deformation in relation to the major diagenetic events. The microstructures of the deformation features were used to assess/identify the active rock deformation mechanisms (*e.g.* diffusive mass transfer, grain fracturing, *etc.*) and the history of deformation. Representative images using BSE and CL are taken from inside and outside of the fault zone as well as traverses across the border zone areas. These images were saved in 8-bit (256 grey levels) digital form, and then imported into an image analysis package. The processing of these images according to the philosophy and approach of Evans *et al.* (1994) yielded estimates of porosity and mineral abundance. This data set is then used to assess the effect of deformation on the porosity/permeability relations, and deformation/diagenetic history of the rock.

4.3.3.2 Mercury injection porosimetry

An investigation of reservoir capillary pressures was conducted using a Micromeretics Autopore II 9220 mercury porosimeter. This equipment is capable of injecting mercury in step-like increments up to pressures of 60,000 psi (~413 MPa) into an evacuated, cleaned and dried core plug or cut sample.

Capillary forces in the reservoir are functions of the surface and interfacial liquid tensions, pore size and shape, and the wetting properties of the rock. In the case of a non-wetting liquid like mercury and assuming cylindrical pores, this relationship is expressed by the Washburn (1921) equation:

$$P_c = -2\gamma\cos(\theta)/r_c \qquad \textbf{4.2}$$

where: P_c is the capillary pressure (dynes/cm^2), γ is the interfacial tension for air–mercury (Hg), θ is the contact angle (in degrees) of Hg in air, and r_c is the radius of the pore aperture (μm) for a cylindrical pore. The interfacial tension of mercury varies with purity. The accepted interfacial tension for air–Hg is 480 dynes/cm^2 (Showalter *et al.*, 1979). The contact angle between clean Hg and the solid containing the pore varies with solid composition, although a value of 140° (or -40° measured from the solid surface to the surface of the non-wetting phase Hg along the anticlockwise direction) is generally accepted (Showalter *et al.*, 1979).

In evaluating seal potential the most important factor is the pressure required to form a connecting filament of non-wetting fluid through the pore space of the sample. As Hg is a non-wetting fluid, pressure must be built up before it displaces the partial vacuum and intrudes into a certain pore size. At a certain pressure, which is dependant on the pore size, the percentage of Hg intruded increases rapidly. This is the threshold pressure and corresponds to a convex upward inflexion point on the Hg-injection curve (Katz and Thompson, 1986, 1987). The Hg-injection curves of samples with sealed sleeves containing both fault rock and undeformed sandstone should have two such inflexions, the first (lower) representing the initially–intruded host lithology and the second (higher) representing the pressure at which the fault seal is breached.

4.3.3.3 Water permeametry

Of all the formation parameters that petroleum geologists employ, permeability is one of the most important. Traditional methods of gas permeability for reservoir appraisal, such as the Hassler sleeve (Hassler, 1942), are unable to measure below ~0.01 mD, and the results below 1 mD are not very accurate because of lateral sealing problems and uncertainties in the Klinkenberg correction (Klinkenberg, 1941). For many applications this is not a significant cause for concern since all lithologies with a permeability below a certain level can simply be considered to have very poor reservoir properties; however, more precise measurements are required for a detailed study of fault seal behaviour.

In this study, hydraulic conductivity tests were performed on fault rock samples and undeformed reservoir sandstones using a custom-designed flow-pump permeameter (Olson and Daniel, 1981; Olsen *et al.*, 1991). This computerised permeameter, which uses an accurate constant-rate-of-flow pump and a highly linear differential pressure transducer, is capable of accurately measuring permeabilities in the range of a few Darcies to a few tens of mD. Permeability measurements are made on 26 mm diameter plugs or across rectilinear blocks oriented perpendicular with respect to the deformation features of interest. The cylindrical cores are fitted into tightly fitting silicone rubber sleeves, whilst the rectilinear samples are confined in polymer sleeves (Zetalabor dental moulding putty) individually moulded to exactly fit the specimen. All samples are de-aired for a minimum period of 24 hours prior to testing. The sleeved samples are placed in a secondary rubber membrane and confined in a triaxial cell at a pressure of ~800 kPa to prevent leakage of permeant down the sides of the sample. A back pressure of 260–270 kPa is also used during testing. Prior to the hydraulic conductivity analysis, any air in the samples and the confining fluid is allowed to equilibrate in order to ensure no destabilising effect on flow rate measurement.

To ensure the validity of the hydraulic conductivity permeability results, the steady-state method was calibrated with the pulse-decay technique of Brace *et al.* (1968). In general, values

derived via steady-state analyses showed excellent correlations with those derived through transient flow analyses in the pulse-decay method. For example, RDR has recently measured the absolute permeability of a cataclastice fault rock from the Hopeman sandstone (near Elgin, Aberdeen coast) using steady-state water permeameter, steady-state gas permeameter and the pulse-decay technique. The results were not identical but pretty encouraging. The results were as follows:

- Steady-state (with water phase) gave 0.003 mD
- Steady-state (with gas phase) gave 0.005 mD
- Pulse decay gave 0.003 mD

This would suggest a maximum error bar for these results of ± 0.002 mD. The match between the steady-state water permeameter (the adopted method in this study) and the pulse-decay technique confirms the validity of the former method.

4.4. Results

4.4.1. Introduction

Microstructural and petrophysical property analyses have been conducted on 7 fault rocks and their associated undeformed sandstones from well 23/27-8 in the Pierce Field. The results of this study are summarised in **Table-4.3** and more detailed information about these results is given in the following sections:

- the diagenesis review is present in § **4.4.2**;
- the deformation features present are summarised in § **4.4.3**;
- the microstructural and petrophysical properties of individual specimens are described in **Appendix A**.

Table-4.3. Microstructural and petrophysical property results for the samples examined from well 23/27-8, Pierce Field.

Well	Sample ID	Top Depth (ft)	Permeability (mD)		Hg-air threshold pressure (psi)		Deformation Features
			Host	Fault	Host	Fault	
23/7-8	1	8270' 8"	9.1		25		Cataclastic fault
	2	8278' 8"	11.7	0.067	25	140	Cataclastic fault
	3	8303'	60.2	0.056	15	170	Cataclastic fault
	4	8305'	63.1	0.010	15	410	Cataclastic fault
	5	8307' 9"					Cataclastic fault
	7	8322'	2.4	0.001	35	750	Calcite cemented fracture
	8	8465' 2"	5.2	0.13	37	270	Cataclastic fault

4.4.2. Diagenesis review

This section briefly reviews the mineralogy and diagenesis of reservoir sandstones from 7 samples that have been examined from well 23/27-8 in the Pierce Field (refer to **Table-4.3** for sample depths). The main aims are to identify the diagenetic processes that operated and assess their relative timing as an aid to assessing the timing of deformation.

The detrital mineralogy of the undeformed sandstones is dominated by quartz, K-feldspar and plagioclase, with subordinate quantities of clay and mica. Most of the sandstones examined are fine grained, and moderately to moderately-well sorted subarkosic arenites.

The main diagenetic processes to affect the mineralogy and poroperm properties of the sandstones were compaction as well as the precipitation of kaolin and quartz. The samples have also experienced the precipitation of K-feldspar, dolomite, albite, calcite and illite. The diagenetic history that has been inferred is summarised schematically in **Fig. 4.10** and each diagenetic process is discussed separately below.

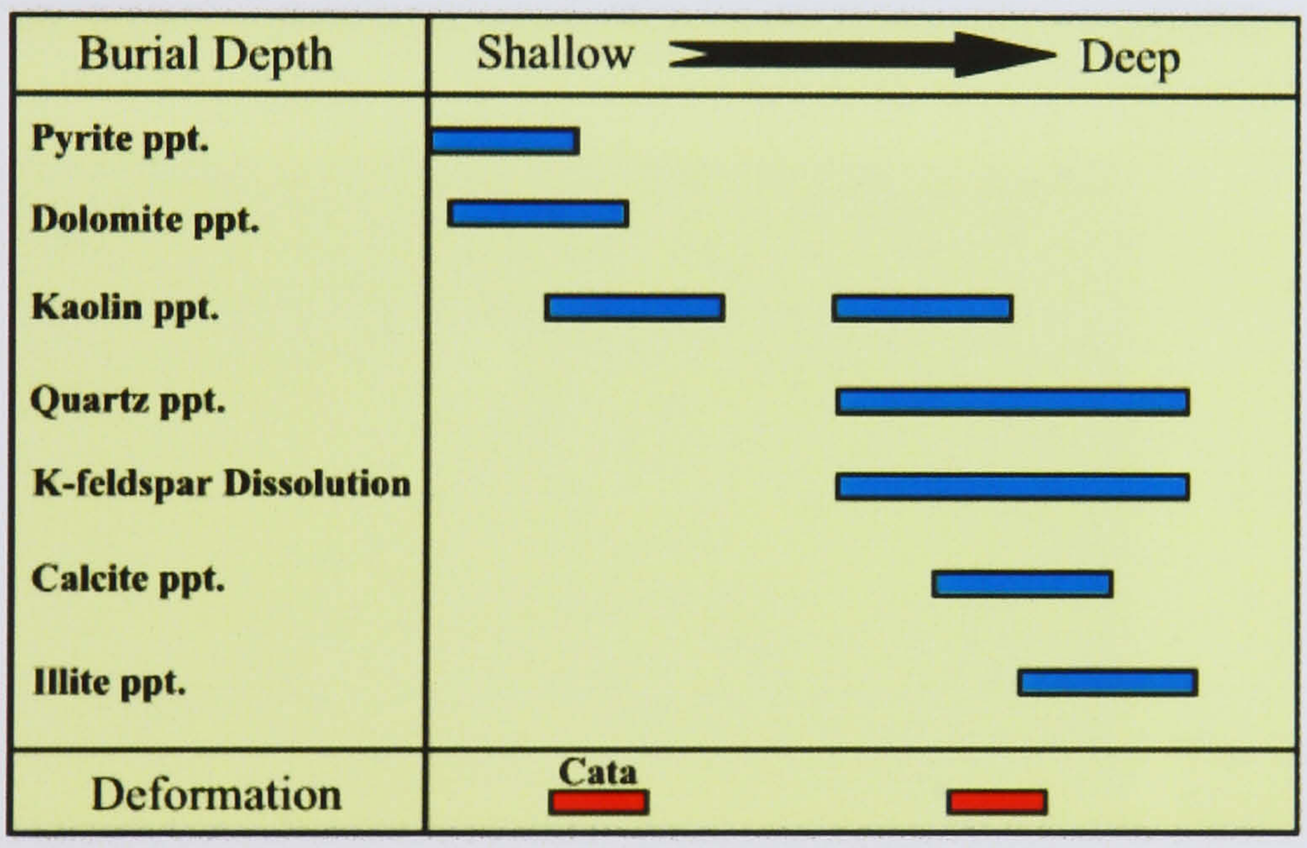

Fig. 4.10. Diagram summarising the diagenetic and deformation history for samples analysed from well 23/27-8 in the Pierce Field (ppt. is precipitation). The later deformation event produced carbonate cemented fractured

4.4.2.1 Mechanical and chemical compaction

The mechanical compaction of sediments, involving grain rearrangement and the crushing of soft lithoclasts, has been discussed by a number of authors (*e.g.* Houseknecht, 1987; Pittman and Larese, 1991; Giles *et al.*, 2000). Operating alone it can reduce the porosity of clay-free, well-sorted sandstones to values of around 30% (Houseknecht, 1987); in clay-rich sandstones it can be more effective. Porosity–depth trends (*e.g.* Ramm, 1992; Ramm and Bjørlykke, 1994) suggest that mechanical compaction occurs in a linear manner until a temperature threshold beyond which chemical compaction dominates (~90 °C in Jurassic sandstones of the North Sea). Overpressuring may decrease the rate of mechanical compaction by reducing the effective stresses at grain contacts. Early cementation can also retard mechanical compaction (Fisher *et*

al., 1999). Chemical compaction (pressure solution) refers to the process of mineral dissolution at stressed grain contacts. In quartzose sandstones, the time–temperature history is probably the most important variable affecting the diffusive mass transfer (DMT) processes involved, with quartz dissolution being very slow at temperatures below 90 °C but significant at higher temperatures. The rate of pressure solution can be enhanced by small concentrations of phyllosilicates at grain contacts.

The sandstones in the samples examined show ample evidence of mechanical compaction, such as the presence of detrital muscovite grains bent around quartz grains. The samples examined have experienced only incipient chemical compaction, probably because they contain only a small concentration of clays between grain contacts.

4.4.2.2 Pyrite precipitation

Authigenic pyrite was observed in many of the samples examined during this study, although it was always found in small quantities (<1%). It most commonly occurs as ~10 μm wide framboids (**Fig. 4.11**) and euhedral grains, which probably grew close to the sediment–water interface as a product of microbially mediated sulphate reduction.

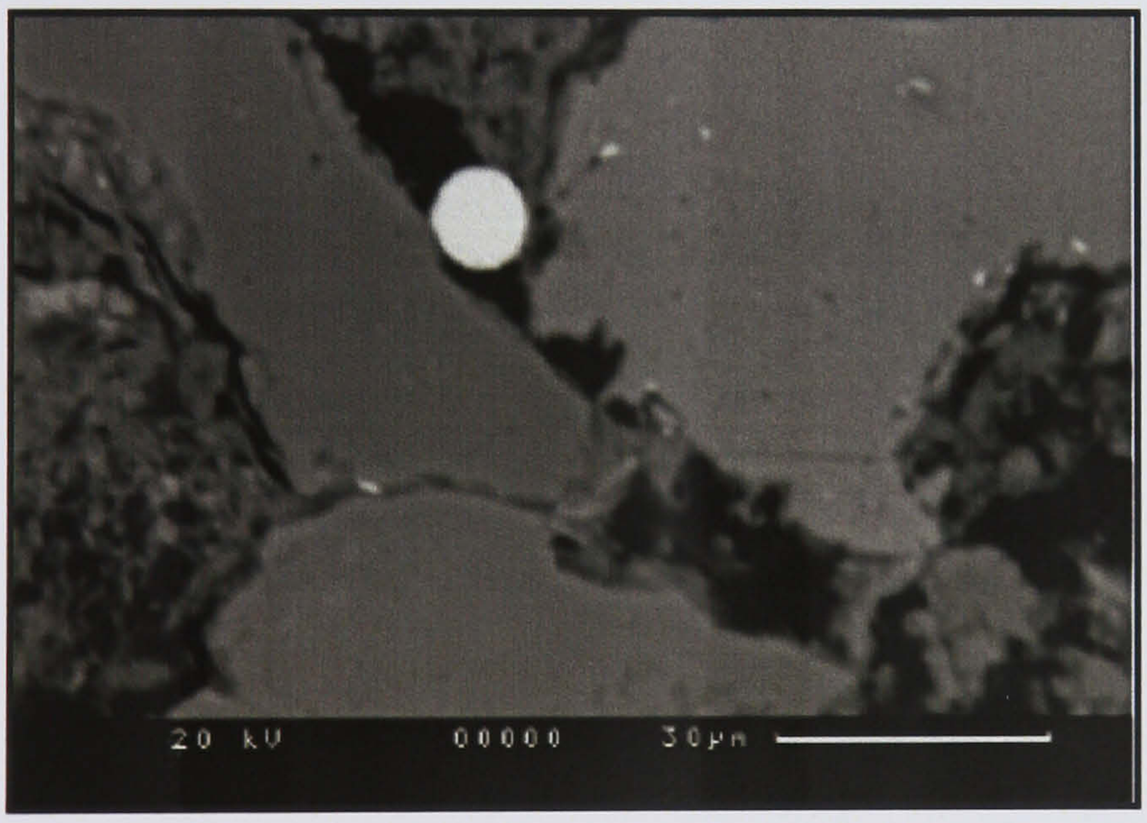

Fig. 4.11. BSE micrographs showing the authigenic fine-grained framboidal pyrite (light phases) in sample 23/27-8.2.

4.4.2.3 K-feldspar precipitation

Authigenic K-feldspar was observed in many samples examined during this study, although it was always found in small quantities (<0.5% of rock volume). It usually occurs as overgrowths of up to 25 μm in width on detrital K-feldspar grains. The authigenic K-feldspar is deformed in the cataclastic faults, indicating that it precipitated at a shallow depth. An early diagenetic origin is consistent with the theoretical results of Bjørlykke and Egeberg (1993) which show that sea water is in thermodynamic equilibrium with K-feldspar at ~10 °C.

4.4.2.4 Dolomite precipitation

Dolomite was only observed in one sample examined during this study (sample 23/27-8.1, depth 8270' 8"), where it occupies <0.5% of the rock volume. In this sample, it occurs as ~20 μm wide, compositionally zoned rhombs (**Fig. 4.12**). The centres of these rhombs have a pure dolomite composition whereas their peripheries are Fe-rich. Dolomite is deformed within the cataclastic fault that cuts this sample, indicating that dolomite cementation pre-dated the cataclastic faulting. It is possible that the dolomite began to precipitate close to the sediment–water interface, although the Fe–dolomite overgrowths probably grew much later after the sediment had become more reduced.

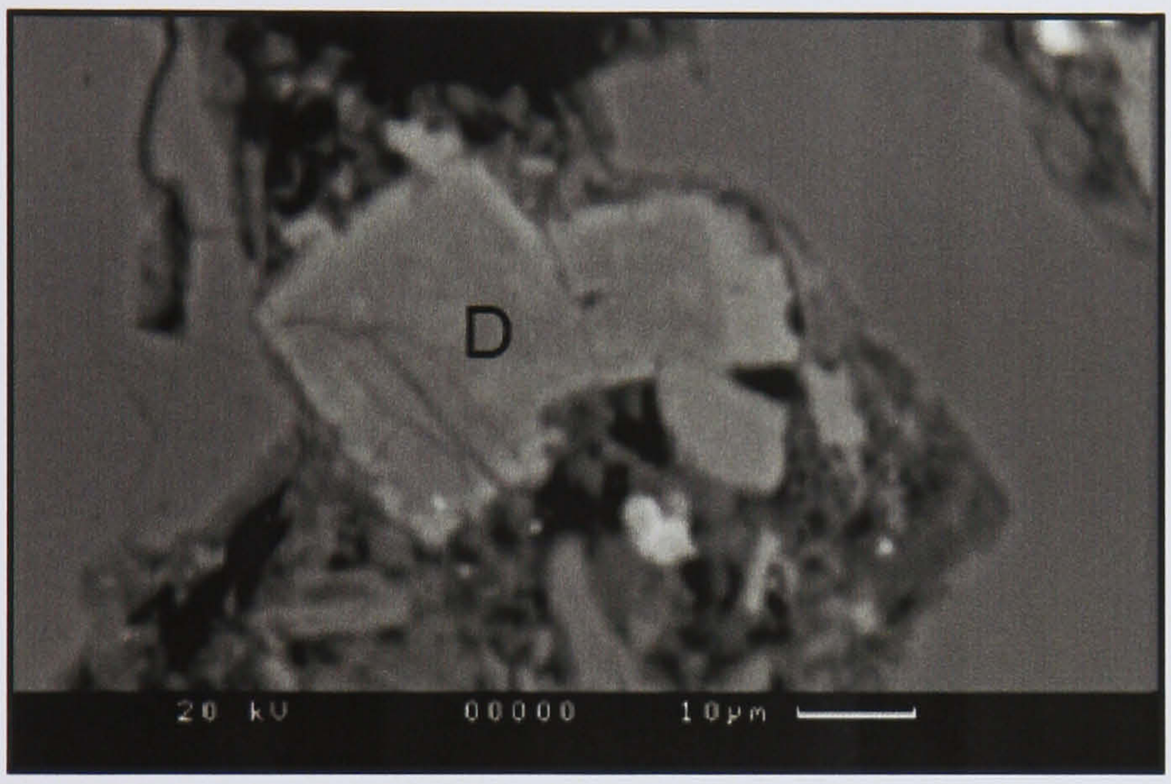

Fig. 4.12. BSE micrographs showing euhedral dolomite (D) in sample 23/27-8.1.

4.4.2.5 Kaolin precipitation

Kaolin is the dominant authigenic clay in all samples examined; its abundance ranges from 4% to ~12% of rock volume. Several generations of kaolin were observed, including vermiform kaolin (**Fig. 4.13**), expanded-mica kaolin (**Fig. 4.13**), microcrystalline kaolin (**Fig. 4.14**), and blocky/pseudo-hexagonal kaolin (**Fig. 4.14**). Studies of the distribution of kaolin within North Sea reservoirs suggest that it is likely that the first three varieties precipitated during shallow burial, whereas the latter variety is a late-stage precipitate (Erhenberg *et al.*, 1993).

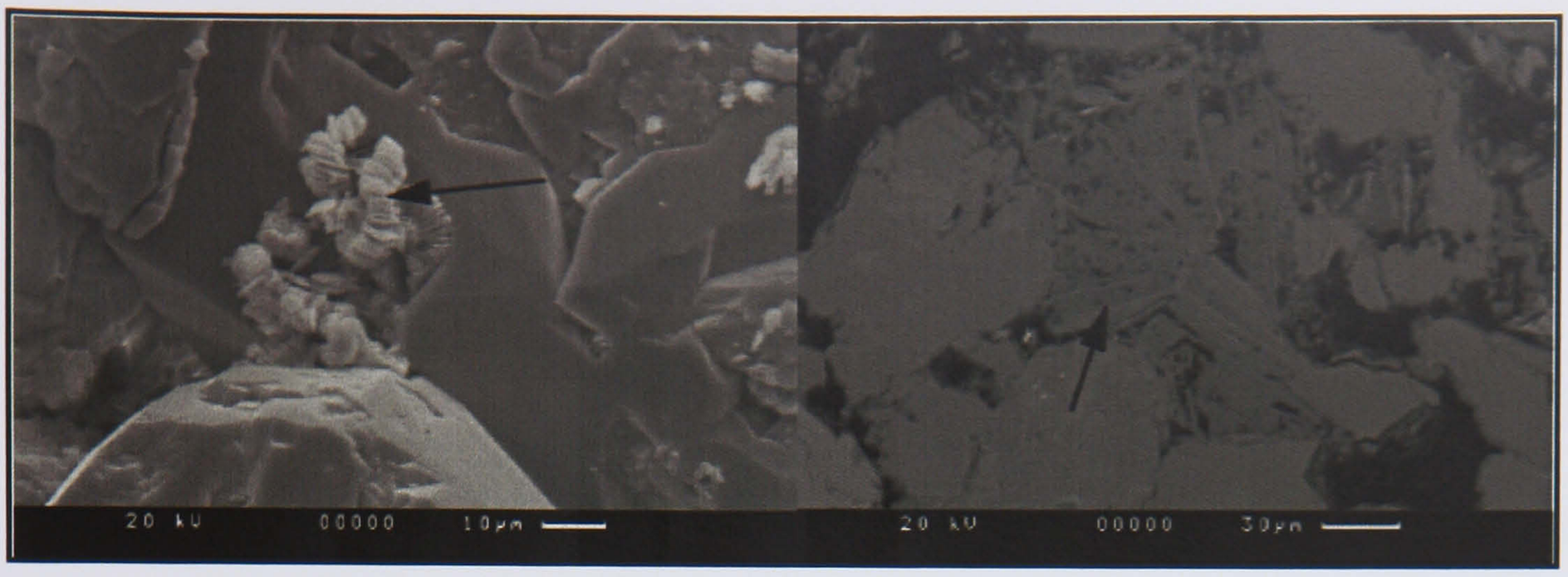

Fig. 4.13. SE (left) and BSE (right) micrographs showing vermiform (left arrow) and expanded mica (right arrow) kaolin in samples from well 23/27-8, Pierce Field.

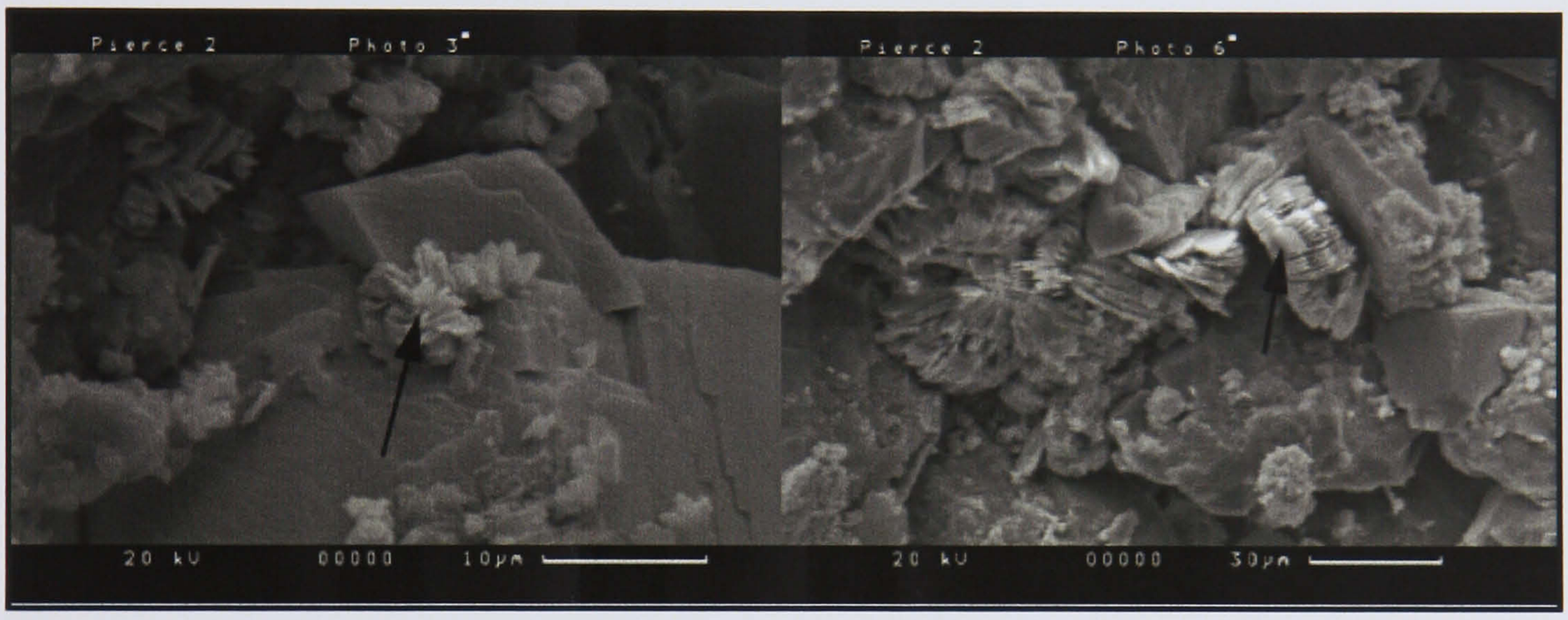

Fig. 4.14. SE micrographs showing microcrystalline (left arrow) and pseudo-hexagonal (right arrows) kaolin in samples from well 23/27-8, Pierce Field.

4.4.2.6 Quartz precipitation

Authigenic quartz is a ubiquitous and volumetrically important component of the sandstones examined. It occurs in mesocrystalline form, as up to 20 µm thick overgrowths on detrital quartz grains (**Fig. 4.15** and **Fig. 4.16**). An image analysis of CL photomicrographs suggests that it typically makes up <5% of the rock volume. The well-developed nature of the quartz overgrowth demonstrates that the sandstones have spent significant amounts of time buried to temperatures beyond ~90 °C (see the following discussions). Silica for quartz cementation was probably sourced locally through grain-contact quartz dissolution. Key factors controlling the abundance of mesocrystalline quartz cement in reservoir sandstones are now quite well understood and include clay content, grain size, mineralogy, hydrocarbon emplacement, and temperature–time history (*e.g.* Bjørlykke and Egeberg, 1993; Giles, 1997; Oelkers *et al.*, 1996; Walderhaug, 1996; Worden *et al.*, 1998; Fisher *et al.*, 2000). These factors are reviewed briefly below.

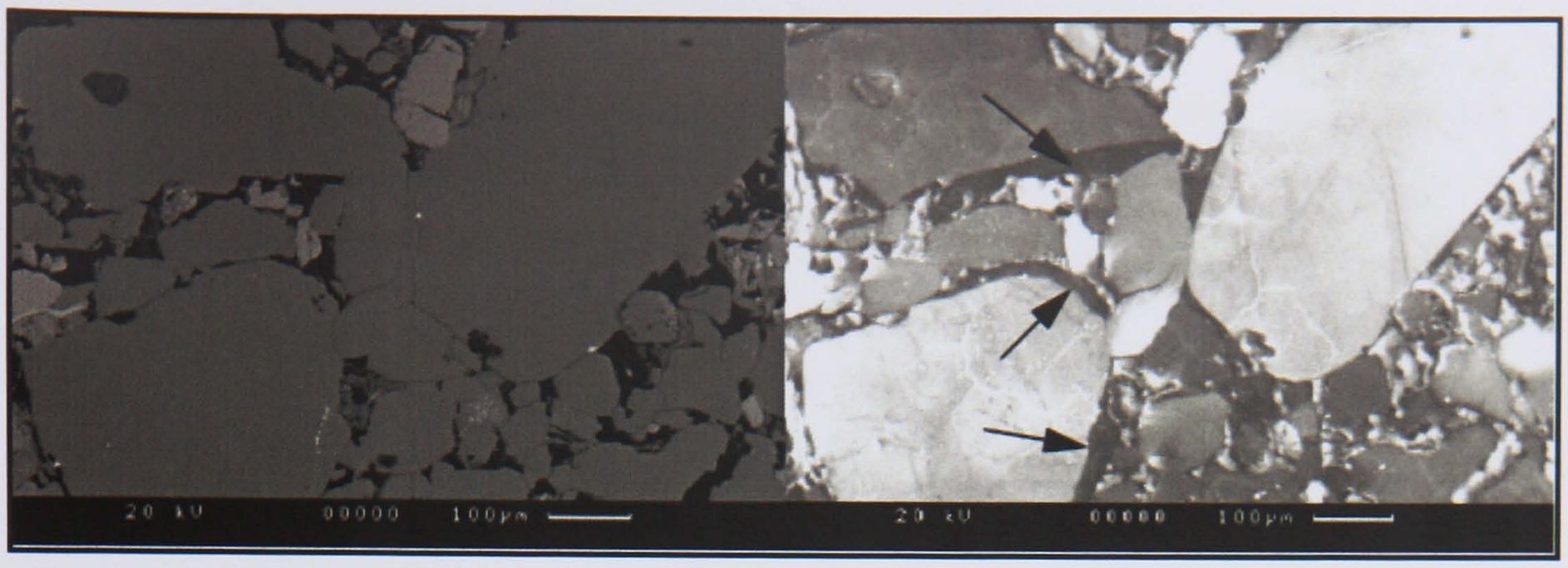

Fig. 4.15. BSE (left) and CL (right) micrographs from the same area of sample 23/27-8.2 showing the authigenic quartz (arrows).

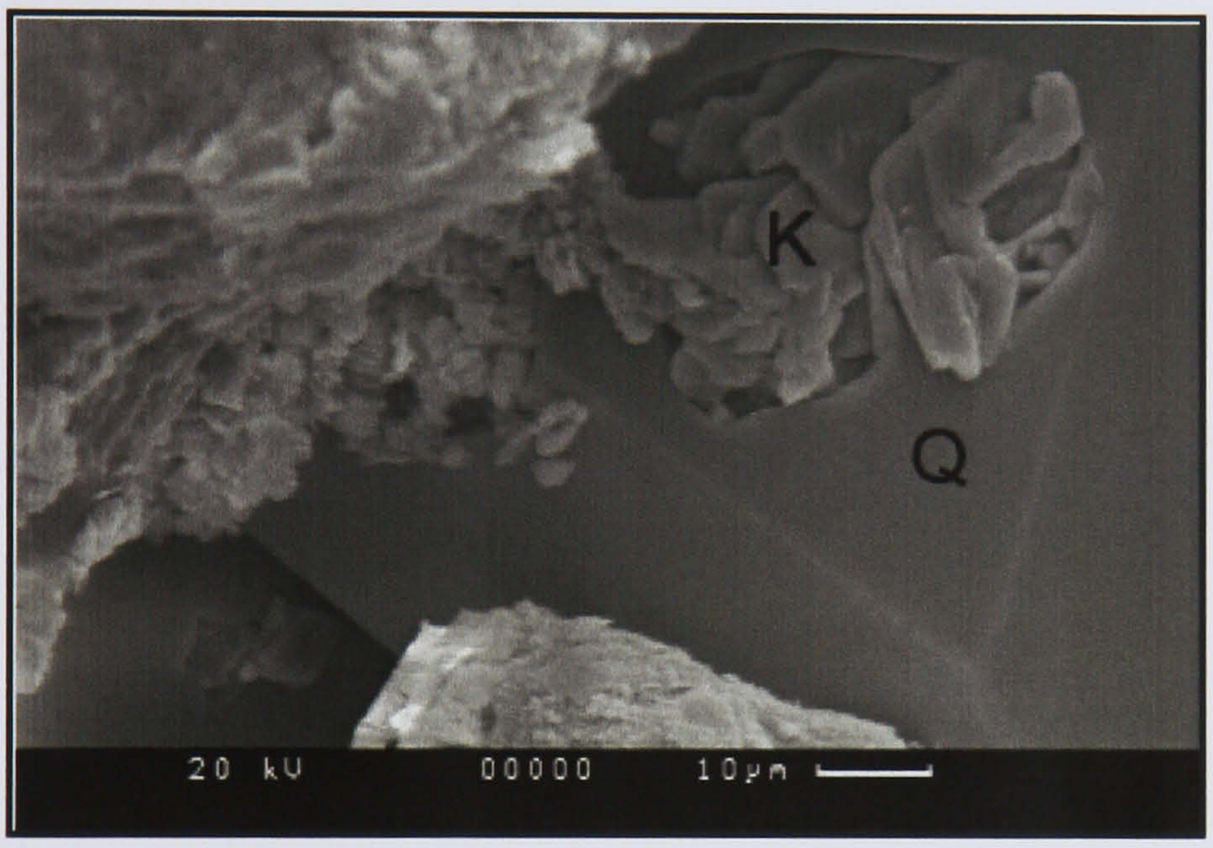

Fig. 4.16. SE micrograph showing authigenic quartz (Q) overgrowing kaolin (K) in sample 23/27-8.2.

Clay content: The presence of clay influences both silica generation and quartz precipitation processes. Low concentrations of clay at grain–grain contacts may increase the rate of quartz dissolution because: (*i*) they enhance the rate of solute diffusion away from stressed dissolution sites due to the presence of enlarged absorbed water films; and/or (*ii*) they locally increase pH and hence quartz solubility. In contrast, high concentrations of grain-coating clays may suppress quartz cementation by: (*i*) retarding solute diffusion to grain surfaces; and/or (*ii*) increasing pH and quartz solubility; and/or (*iii*) blocking nucleation sites.

Grain size: The rate of quartz cementation is often controlled by the quartz surface area, which decreases with increasing grain size in clean sandstones. Fine-grained sandstones are commonly observed to have experienced more quartz cementation than their coarser-grained equivalents.

Sandstone mineralogy: As the quartz surface area often controls the rate of quartz cementation, sandstones with lower concentrations of quartz grains tend to experience less cementation than quartz arenites.

Hydrocarbon emplacement: Whilst quartz cementation may continue subsequent to hydrocarbon emplacement due to solute diffusion through thin adsorbed water films, the rate of solute supply may be reduced, leading to a decrease in the rate of quartz cementation.

Temperature–time history: The rate-governing step in quartz cementation is usually quartz precipitation, which is temperature dependent and not significant until sediments have been buried beyond 90 °C. Quartz cementation should thus be of reduced importance in reservoirs that have not been buried beyond 90 °C. In reservoirs buried beyond this temperature the extent of quartz cementation should be controlled by the temperature–time history.

4.4.2.7 Albite precipitation

Authigenic albite was observed in most samples examined during this study, although it is volumetrically insignificant and occupies <<0.5% of the rock volume. It is likely that the albite is a late-stage precipitate.

4.4.2.8 K-feldspar dissolution

All samples examined had experienced minor K-feldspar dissolution. It is likely that this occurred during deep burial by reaction with kaolin to produce illite (Bjørlkke, 1998).

4.4.2.9 Calcite precipitation

Calcite was only observed in one sample examined during this study (sample 23/27-8.7, depth 8322'). In this sample, the calcite occupies around 17% of the rock volume and occurs as a fracture fill. The calcite overgrows authigenic quartz (**Fig. 4.17**), suggesting it was a late-stage precipitate.

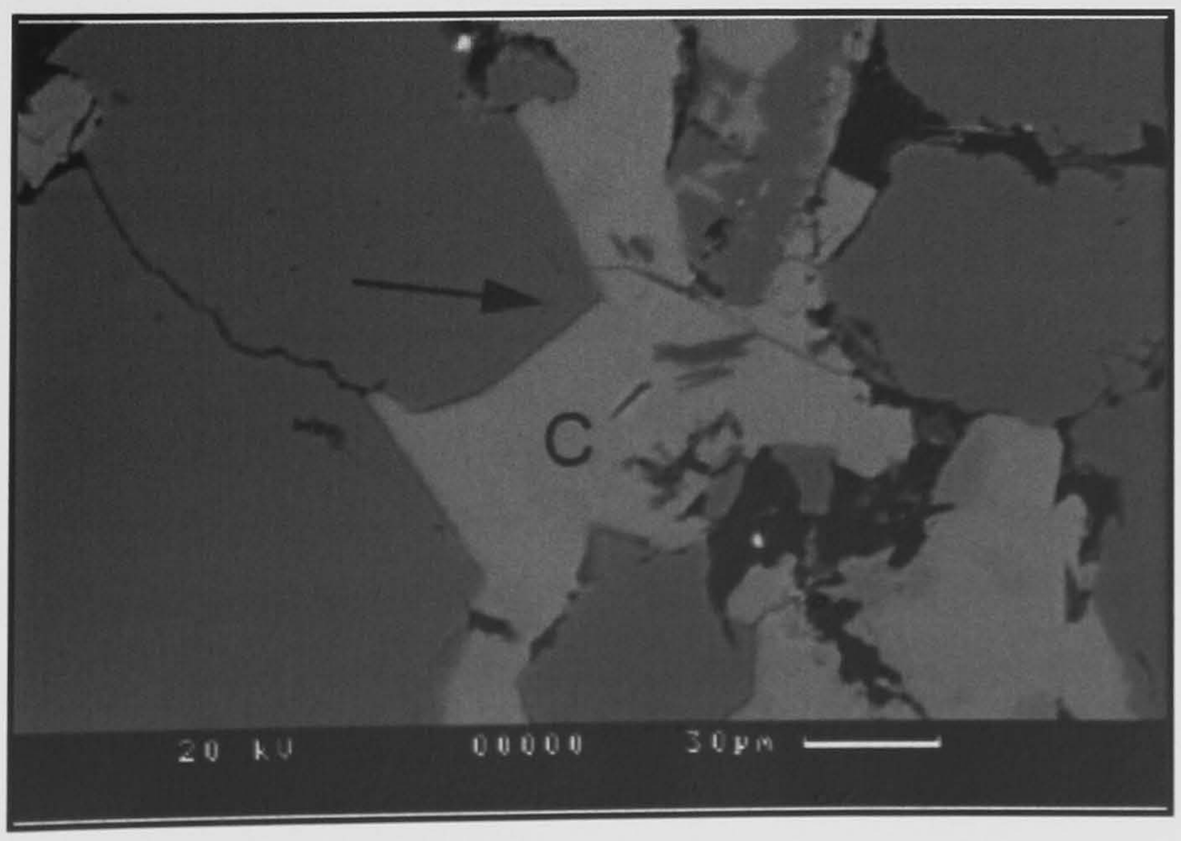

Fig. 4.17. BSE images showing calcite (C) overgrowing authigenic quartz (arrow) in sample 23/27-8.7.

4.4.2.10 Illite precipitation

Authigenic illite was observed in the samples studied, although at an abundance not exceeding 0.5% of the rock volume. The authigenic illite that is present tends to have a hairy morphology (**Fig. 4.18**), which is known to be particularly effective at lowering permeability because of its high surface area to volume ratio. The illite was observed overgrowing authigenic quartz suggesting that it precipitated at a relatively late stage of the geohistory. It is likely that it formed as a product of the dissolution of kaolinite and K-feldspar during deep burial.

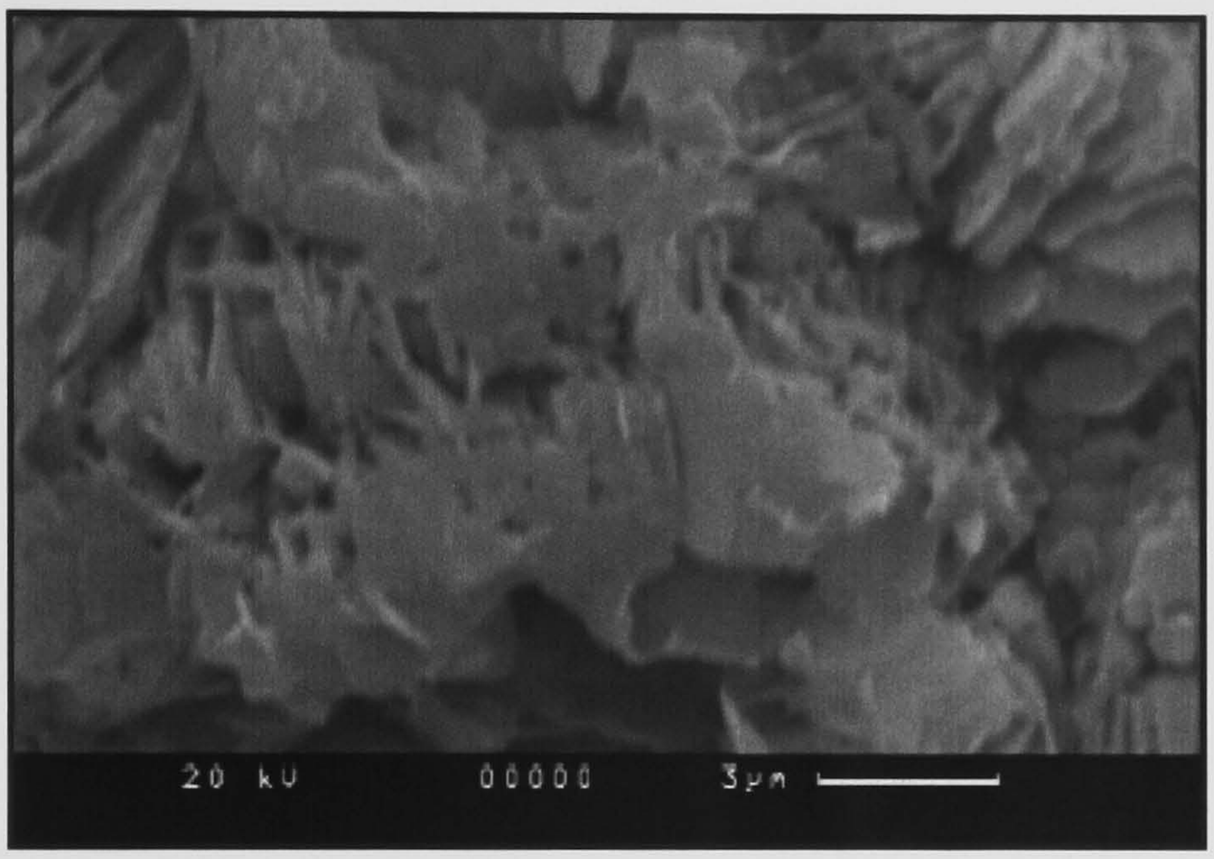

Fig. 4.18. SE images showing the authigenic hairy illite in the sample 23/27-8.2.

4.4.3. Review of deformation feature present

This section provides an overview of the deformation features present in samples from well 23/27-8. The main aims are to: (*i*) review the microstructural characteristics of the fault rocks; (*ii*) identify the processes and mechanisms associated with deformation; and (*iii*) constrain the timing of deformation within the burial history.

The deformation features present in the 7 samples studied include cataclastic fault rocks and calcite cemented fractures. Contextual information for the samples and the results of the SEM are summarised in **Table-4.3**. A review of the microstructure of each type of deformation/seal feature is given in following sections.

4.4.3.1 Cataclastic fault rocks

Fault rocks where the processes of grain fracturing and frictional sliding dominate and induce a reduction in both permeability and porosity are grouped together as cataclastic faults. Fault rocks in which cataclasis is the main process responsible for porosity collapse generally, but not exclusively, develop from clean porous sandstones. The petrophysical properties of cataclastic fault rocks developed from clean sandstones are usually reduced in comparison to the host

sandstones as a result of three processes. Firstly, the reduction in grain size and grain sorting that accompany deformation produce a collapse of macroporosity and allow the grain fragments to be packed more efficiently than in the host sandstone. Secondly, cataclastic faults often experience enhanced quartz cementation following deformation; this cement need not precipitate from exotic fault-related fluids, but instead can be generated by local reactions (*e.g.* grain-contact quartz dissolution) and preferential precipitation within the fault rock due to the presence of clean fracture surfaces. Thirdly, some fault rocks experience enhanced grain-to-grain dissolution following deformation; this process is enhanced by the presence of clays between quartz grain contacts (Fisher and Knipe, 1998; 2001). Cataclastic fault rocks were identified in 6 samples examined during this study. Key observations and conclusions from the SEM studies that were conducted on these samples are summarised below.

- The grain-size reduction experienced by the cataclastic fault rocks is generally small. This suggests that faulting occurred during shallow burial (<1 km depth) rather than deep burial.
- In comparison to the surrounding reservoir, the cataclasites experienced enhanced post-deformation lithification as a result of post-deformation grain-contact quartz dissolution. This process was slightly enhanced within the fault rock because deformation increased the proportion of clay at grain contacts.
- Petrophysical property analyses from four cataclastic faults gave permeability values of 0.01 to 0.13 mD (geometric average = 0.05 mD) and Hg-injection threshold pressures of 140 to 410 psi (average = 250 psi). Photographs showing the typical form of cataclastic faults from well 23/27-8 in hand-specimen are shown in **Fig. 4.19**. A micrograph showing a typical cataclastic fault and its host sandstone from well 23/27-8 are shown in **Fig. 4.20**. Graphs showing typical Hg-injection results from cataclastic faults in well 23/27-8 and their host are shown in **Fig. 4.21**.

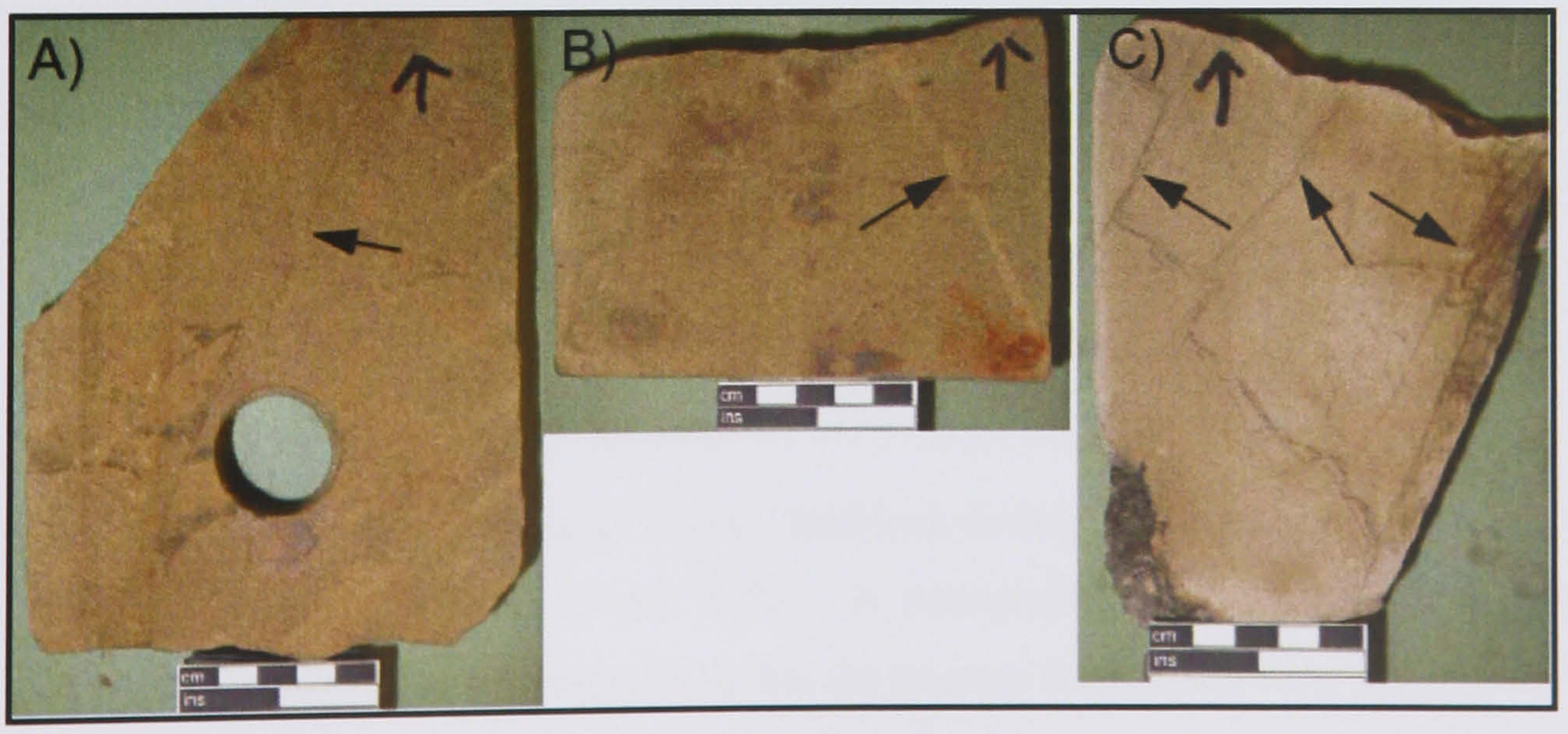

Fig. 4.19. Core photos showing the cataclastic fault rocks (arrows) in samples: **(A)** sample 23/27-8.1 (depth 8270'' 8"); **(B)** sample 23/27-8.2 (depth 8278' 8"); and **(C)** sample 23/27-8.8 (depth 8465' 2").

Fig. 4.20. BSE micrograph showing the undeformed sandstone and the cataclastic fault in sample 23/27-8.4, Pierce Field.

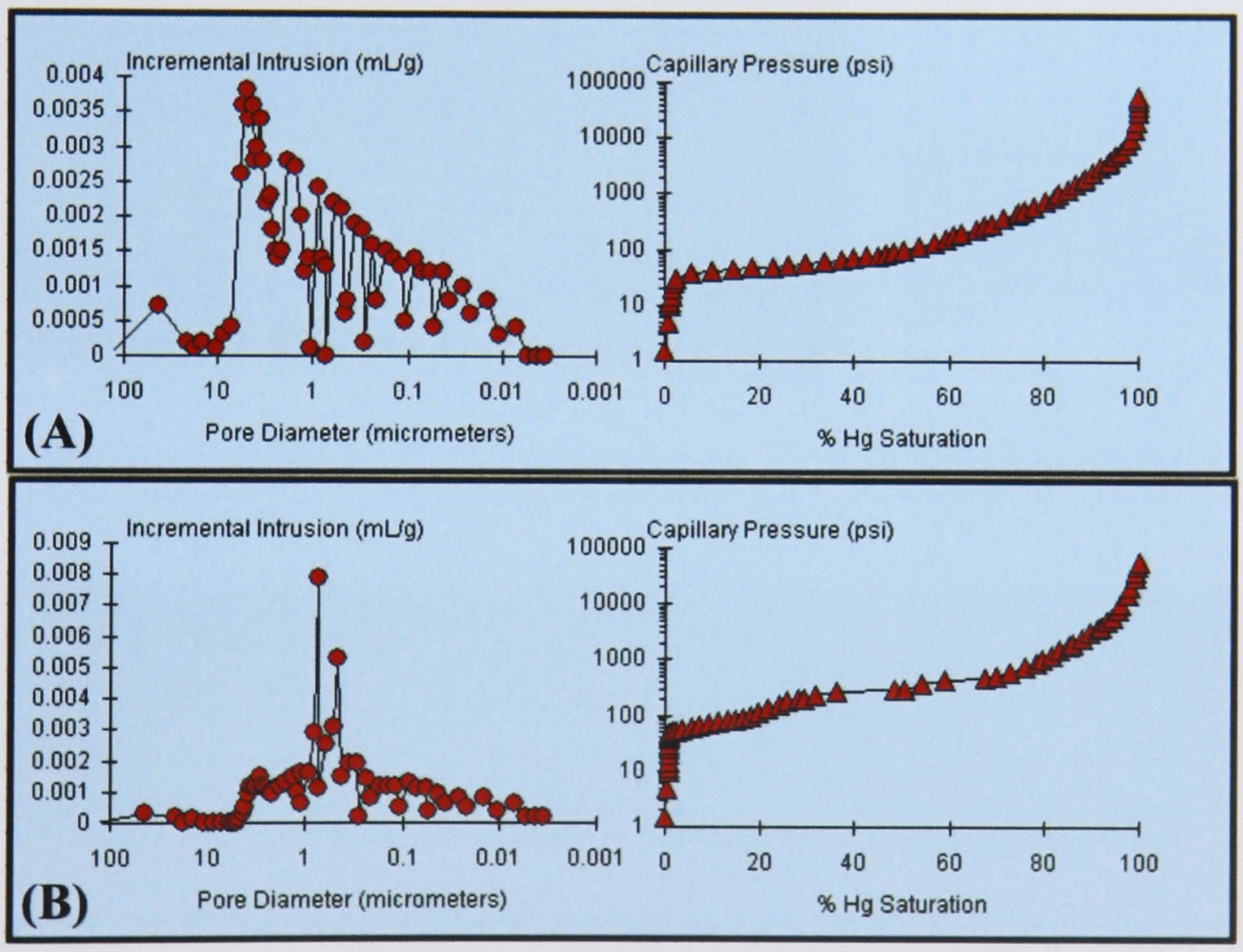

Fig. 4.21. Hg-injection results from **(A)** the undeformed sandstone in sample 23/27-8.8 and **(B)** the fault rock that it contains.

4.4.3.2 Calcite-cemented fractures

The only cemented deformation feature analysed during this study was a calcite-cemented fracture in sample 23/27-8.7 (depth 8322'). A petrographic analysis showed that the calcite overgrows authigenic quartz, suggesting that the fracture formed at a very late stage in the burial and diagenetic history of the reservoir. Petrophysical property analyses showed that the cemented fractures have a permeability of 0.001 mD and a Hg threshold pressure of 750 psi. Clearly, these cemented fractures have very low permeabilities and high Hg threshold pressures,

but it is unlikely that they will be laterally continuous; they are therefore unlikely to influence large-scale fluid flow.

A photograph showing the calcite-cemented fractures from sample 23/27-8.7 in hand-specimen is shown in **Fig. 4.22**. Micrographs showing a typical cataclastic fault and its host sandstone from sample 23/27-8.7 are shown in **Fig. 4.23**. Graphs showing the Hg-injection results from the calcite-cemented fractures in sample 23/27-8.7 and the host sandstone are shown in **Fig. 4.24**.

Fig. 4.22. Core photo showing the calcite-cemented fractures (arrows) in sample 23/27-8.7 (depth 8322')

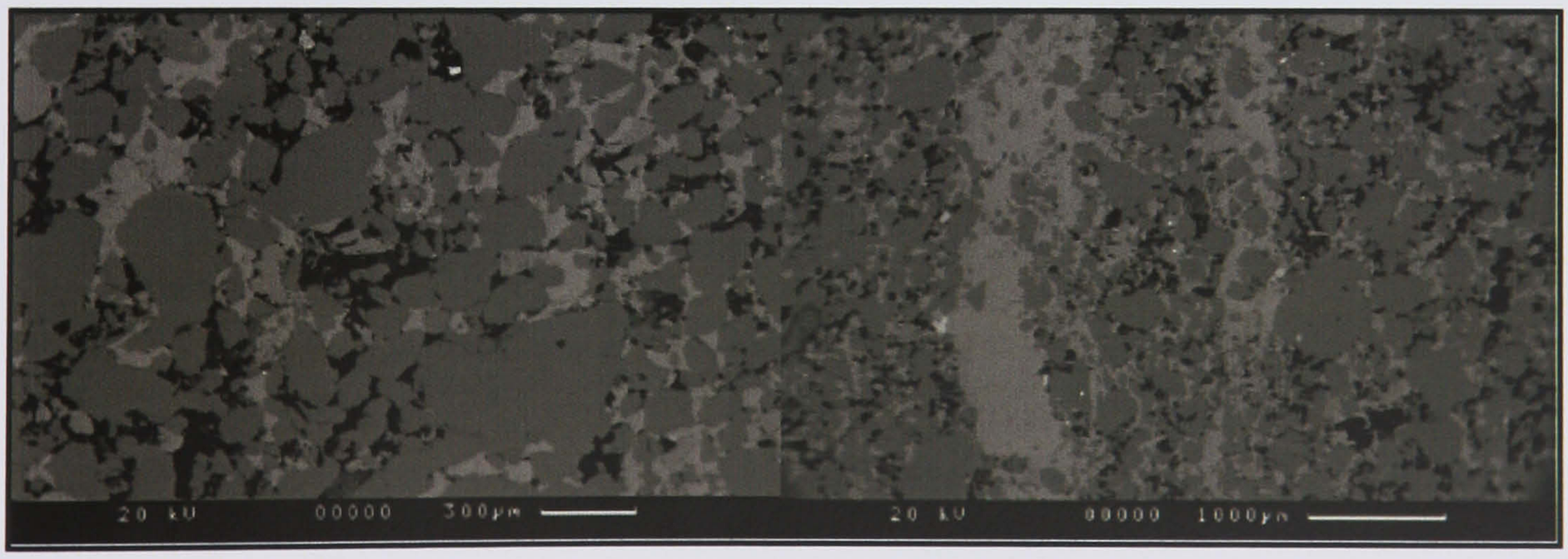

Fig. 4.23. BSE micrograph showing the undeformed sandstone (left) and the calcite-cemented fractures (right) in sample 23/27-8.7, Pierce Field.

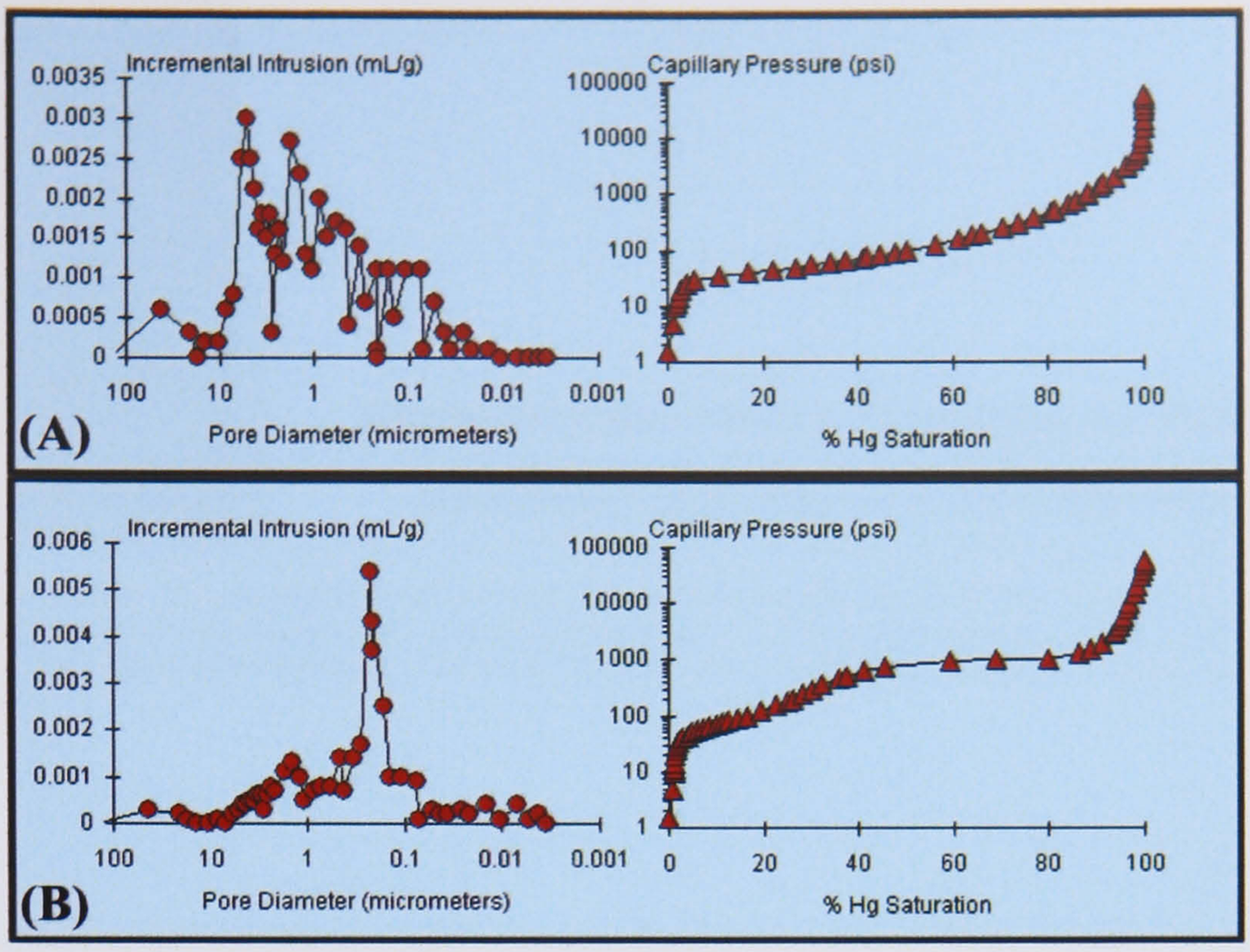

Fig. 4.24. Hg-injection results from **(A)** the undeformed sandstone in sample 23/27-8.7 and **(B)** a calcite-cemented fracture that it contains.

4.5. Conclusions

The deformation features examined during this study have formed at different times during the burial and structural evolution of the reservoir. The characteristics of the deformation features are dependent upon the timing of the fault activity as well as the host rock lithology.

Integration of the diagenetic history and the deformation characteristics has allowed the timing of faulting in individual samples to be established. This provides a platform for the assessment of the fault rock development in the field. The deformation features preserved in the cores can be assigned to different combinations of history involving:

- **Deformation of poorly lithified sediments at moderate burial depths**. The deformation features developed during this period of deformation are characterised by grain-size reductions resulting from cataclasis. These cataclastic faults appear to have formed later than the vermiform kaolin, but before quartz and calcite cement. The moderate grain-size reductions experienced indicate that the deformation features probably formed at burial depths of <1 km.
- **Deformation of lithified sediments during deep burial** resulted in the formation of calcite-cemented fractures. These calcite-cemented fractures appear to have formed later than the quartz cement.

The implications of these microstructural and petrophysical fault property measurements for fluid flow within the Pierce Field are explored in the next chapter (**Chapter 5**).

Chapter 5

Modelling the effects of faulting on fluid flow and simulated impedance within the Pierce Field

" Any attempt to steer the injected water around the reservoir by changing areal rock properties, i.e. permeability and porosity, or introducing areal discontinuity such as faults can be made to produce a history match which may look convincing but will be unrealistic and could lead to damaging development decision being made about such matters at the location of additional wells in the reservoir. "

Lauri Dake
(1941-1999)

5.1. Introduction

After a production simulation model has been constructed, it must be tested to determine whether it can reproduce the previous production behaviour (*i.e.* fluid flow rates, pressures, *etc.*) of the reservoir. Modelling past performance will identify weaknesses in the input parameters to the model, suggest possible modifications and demonstrate the quality of the reservoir description that is eventually accepted before future reservoir performance is modelled. In structurally complex reservoirs (*e.g.* densely faulted), history matching can be a time-consuming and frustrating process due to the large number of parameters that affect performance. Indeed, history matches are inevitably non-unique and therefore the best efforts should be made to ensure that all input parameters are physically/geologically realistic. New technologies are providing increased amounts of data that allow the non-uniqueness in the history match to be reduced. For example, time-lapse (4D) seismic surveys can be used to place constraints on the fluid flow behaviour of reservoirs (Greaves *et al.*, 1987). To use time-lapse seismic effectively, acquisition and processing must be as similar as possible for each survey in the series to ensure that differences can be related to production effects and not merely survey artefacts. The power of this technique lies in its ability to map fluid movements in the lateral and vertical space of the reservoir, thus enabling reservoir engineers to locate unswept zones. A classic example that highlights the usefulness of this technique comes from the Gullfaks Field, North Sea. Two successive 3D seismic surveys taken in 1996 and 1999 over the whole field were used to characterise the reservoir (Evans *et al.*, 2003). The time-lapse evaluations based on these surveys have resulted in several successful drilling targets; proving that this technology has an important role in the reservoir management of the field. Of particular interest for the present study is the possibility of using time-lapse seismic to identify the presence of sealing faults (Lumley and Behrens, 1998; Koster and Gabriels, 2000).

Significant benefit from 4D surveys is gained if the timing between the two seismic acquisitions covers a period of field development within which the results are likely to have a significant effect on well planning. Oil companies aim to gain time-lapse seismic with big residual impedance response in the shortest possible time to achieve an early, reliable reservoir model description. Due to changes in production and injection strategies with time, or non-linear reservoir compaction of the reservoir, the magnitude of the expected impedance residuals may not be proportional to the length of time since the start of production. Initial reservoir models, with acceptable history matches, can be used to predict the timing for optimum forthcoming acquisition by creating a synthetic acoustic impedance response from the fluid flow information. Such initial assessment can be a vital step in quantifying a company's business objectives.

The aim of this chapter is threefold. First, a detailed seal analysis has been conducted on the Pierce Field (see **Chapter 4**) to investigate whether this improves the history match obtained from the production data. Second, the chapter aims to establish if simulated 4D seismic can be used to help calibrate the fault seal analysis. In particular, the chapter aims to identify whether the simulated 4D seismic data has the potential to identify whether the transmissibility multipliers (*TMs*, **Chapter 2**) calculated during the fault seal analysis are more accurate than the ones estimated previously by the operators. Third, the study aims to identify the optimal timing for performing repeat 3D survey, which would have maximum benefit for future development decisions

Five models of the Pierce Field were used and their results were compared. The reservoir models are similar apart from the fault representations. These models comprise:

- **Old-fault *TM* Model**: In this model, fault *TMs* were adjusted and the faults were extended, by editing the *TM* values in the simulation model, in a trial and error manner to improve the match to fluid contacts and production history.
- **New-fault *TM* Model**: In this model, all the faults in the 'Old-fault *TM* Model' were removed and a new fault map was obtained by a direct detection to grid cell throws. Two steps of *TMs* assignment were followed. First, a step-by-step derivation of all faults *TMs* in the Pierce Field was adopted based upon the integration of upscaled properties of the host rock (**Chapter 2**). Second, the fault seal analysis conducted in **Chapter 4** was used to derive new definitions of *TMs* to number of faults in the field. The use of the small-scale features properties as a direct representative to large-scale faults has been intensively argued and experimentally validated to number of field in the work of Fisher and Knipe (2001), see **§2.3.4** in **Chapter 2** for more details. Laboratory measurements of microstructural and petrophysical properties of fault rocks from a single well in the Pierce Field were conducted (see **Chapter 4**) and appropriate *TMs* were derived from permeability and capillary pressure measurements. The derived *TMs* from the measurements conducted were applied to specific

number of faults (faults numbered (1)–(3) in **Fig. 5.2**) in the reservoir that are stated by the reservoir operators in Shell to be the faults that require most careful representations due to their least known behaviour.

- ***TM* Model**: In this model all faults detected directly by grid block throws were given *TMs* calculated using the algorithms in Manzocchi *et al.* (1999) (**Chapter 2**). This latter model is identical to the 'New-fault *TM* Model' except it is not complemented with the fault seal analysis.
- ***TM=0* Model**: In this model all faults detected directly by grid block throws in the model were closed by setting their transmissibility multipliers to zero.
- ***TM=1* Model**: In this model all faults detected directly by grid block throws in the model were opened by setting their transmissibility multipliers to unity.

The '*TM=0*' and '*TM=1*' models are used for fault sensitivity studies representing the two extreme cases of faults behaviour in the field. The chapter starts by defining the 'Old-fault *TM* Model' and the 'New-fault *TM* Model'. Historical production data is then used to compare the reliability of each model. Finally, a synthetic seismic impedance response is generated from both simulation models, using a petro-elastic model based on the Gassmann–Biot theory of elastic wave propagation in a fluid-saturated porous solid (Gassmann, 1951; Biot, 1956). The chapter workflow is summarised in **Fig. 5.1**.

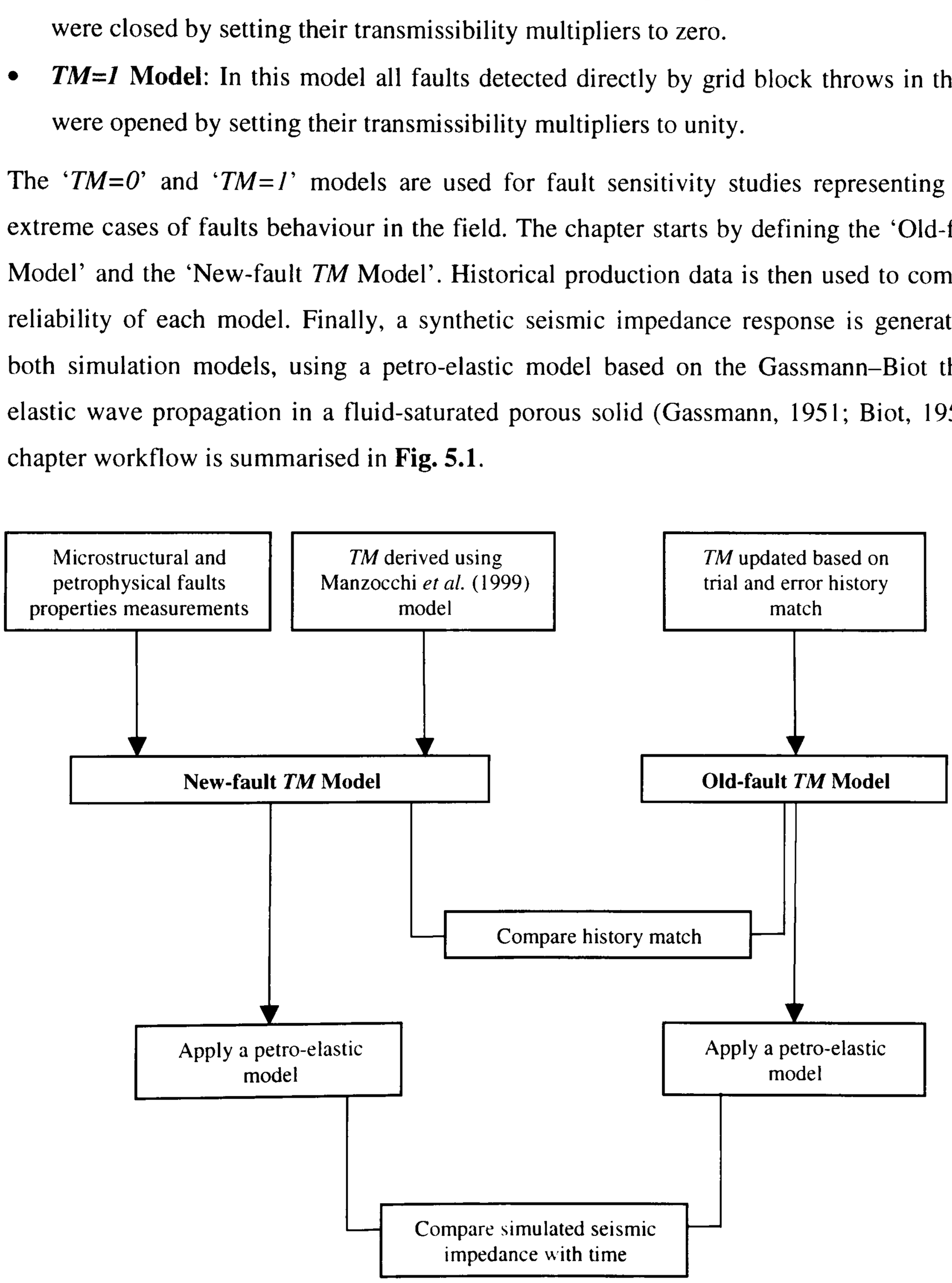

Fig. 5.1. Workflow used in this chapter to address the effects of faults on fluid flow and simulation-generated seismic impedance.

5.2. Old-fault *TM* Model

Since the first history match in 2002, the transmissibility multipliers associated with the faults within Pierce have been tuned and the faults have been extended by simply editing the transmissibilities of number of faults in the field (**Fig. 5.2**) to improve the history match on a trial and error basis. For example, injected free gas was prevented from dominating well B2 (**Fig. 5.2**) by adding a fault with a low transmissibility multiplier (0.05), labelled as fault (1) in **Fig. 5.2**. The resultant history match on the producing gas–liquid ratio (GLR) from well B2 before and after adding fault (1) is shown in **Fig. 5.3**. The addition of the low permeability fault improved the history match at the early stage of reservoir life, but by the end of the simulation it was having the effect of preventing a sufficient quantity of injected gas reaching the well B2.

The 'Old-fault *TM* Model' was supplied by Shell at the start of this project and is a conventional model in which the fluid flow behaviour of the faults is independent of host rock properties or depth, *i.e.* the *TM* for each fault is the same whether the fault cuts water, oil or gas zones. Most of the faults in this model were represented as either completely sealing faults or completely open faults, with few faults having intermediated *TMs* (baffle faults; **Fig. 5.2**).

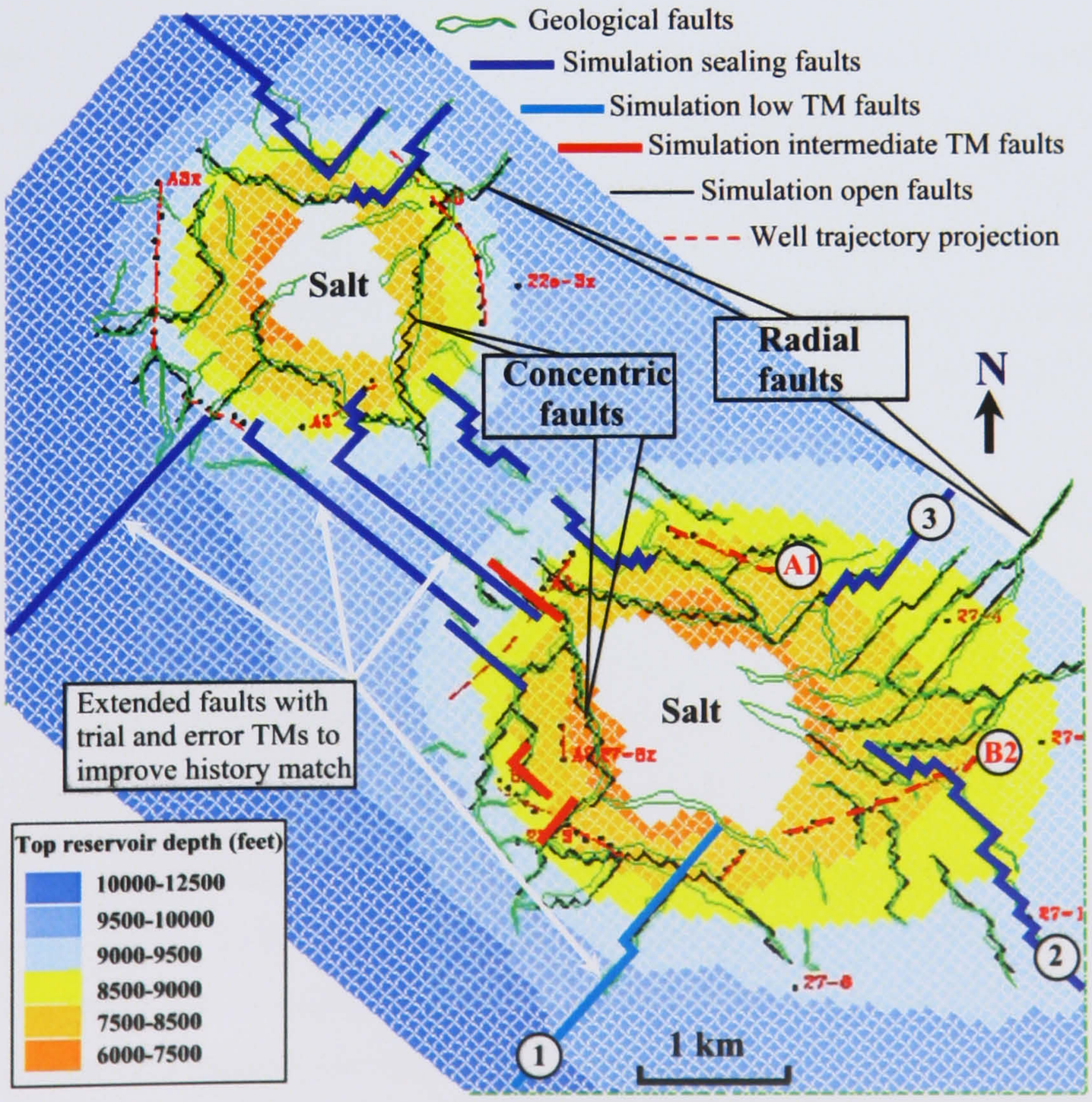

Fig. 5.2. Most of the faults in the field were simulated as open faults, with no resistance to flow (thin black lines). In this study, faults numbered (1)–(3) were given a special treatment and their sealing capacities were varied depending on their relative position with respect to the free water level (FWL), see **§ 5.3.2**.

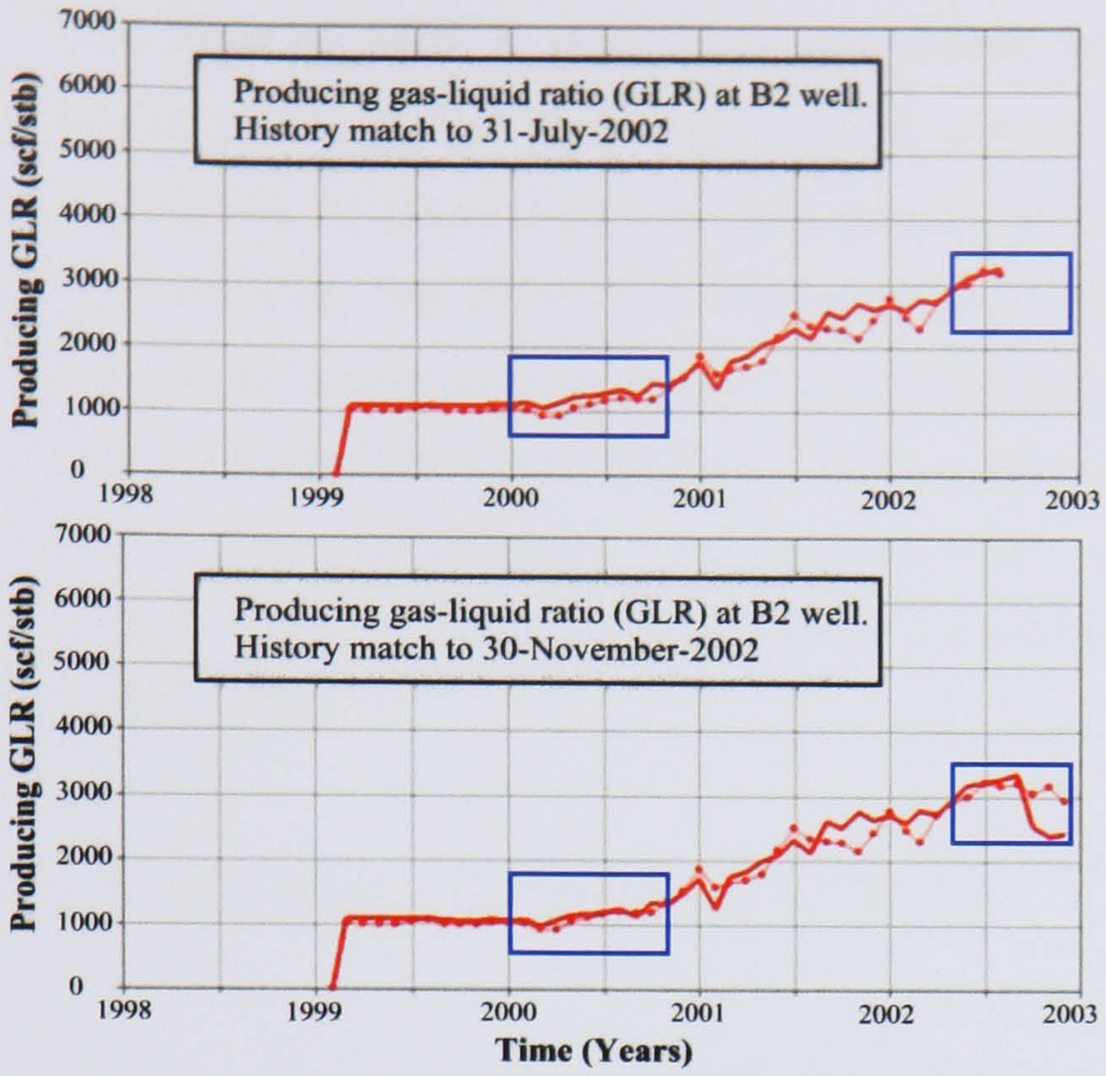

Fig. 5.3. Producing gas–liquid ratio (GLR) at well B2 (**Fig. 5.2**) as a function of simulation time. Top: Before adding a low transmissibility multiplier (TM) fault, fault labelled as (1) in **Fig. 5.2**. Bottom: After adding fault (1) with *TM*=0.05 to prevent injected free gas (gas injected at north-west edge of the south salt dome) from dominating well B2. Connected dots are historical data, continuous thick lines are simulation data.

5.3. New-Fault *TM* Model

5.3.1. Transmissibility multipliers (*TMs*) from empirical relationships

In this model, and also in the '*TM* Model', *TMs* were computed using the methodology of Manzocchi *et al.* (1999). To capture the static properties of fault zones using *TMs*, knowledge of both the permeability and thickness of the fault rock and the undeformed reservoir of the grid blocks immediately adjacent to the fault are required. The *TM* between two cells with different permeabilities juxtaposing a fault with estimated thickness and permeability can be defined as a ratio between the reciprocals of the undeformed cell transmissibilities and the faulted cells transmissibilities (refer to **§ 2.3.5** for detailed equations).

In this model, fault rock thickness, t_f, was estimated from fault displacement using the harmonic average relationship of the observed data compiled by Hull (1988), and data from faults in mixed sandstone/shale sequences in Sinai (Knott *et al.*, 1996), SE Utah (Foxford *et al.*, 1998) and Lancashire, UK (Walsh *et al.*, 1998a), see Manzocchi *et al.* (1999). The harmonic average of these data follow the relationship $t_f = d/170$, where d is the absolute fault displacement. Fault permeability can be estimated based on the clay content of the fault zone (*e.g.* Fisher and Knipe, 2001) using different clay mixing algorithms (**Chapter 1**). The clay content of the fault rock is estimated using algorithms such as the shale gouge ratio (*SGR*), which is the fraction of shale in the sequence that has passed each point on the fault (Yielding *et al.*, 1997; see **§ 2.3.3**). In this study, shale volume was estimated from net/gross assuming that all rock volume in a cell that is not "net" is "shale". Such a treatment gives the maximum shale content and therefore may result in an overestimation of SGR and hence underestimation of the fault permeability.

The value of *SGR* is assumed to approximate the percentage of clay in the fault zone (Yielding *et al.*, 1997). Thus *SGR* can be converted to permeability using experimental determinations of permeability for fault gouges with varying clay content and appropriate geological history (see Fisher and Knipe, 1999, 2001; Manzocchi *et al.*, 1999; Sperrevik *et al.*, 2002). The calibration of Manzocchi *et al.* (1999) indicates that a fault gouge with clay content of approximately 20% will be expected to have a single-phase permeability of between 0.03 and 0.3 mD. They approximated a relationship from an empirical prediction of fault zone permeability as a function of shale content and displacement. This relationship is given by **equation-2.20**:

$$\log k_f = A1 \times SGR - A2 \times \log(d) \times (1 - SGR)^{A3} \qquad \textbf{2.20}$$

where k_f is fault permeability (in mD) and d is fault displacement (in metres). *A1*, *A2*, and *A3*, are empirical constants fit to observed data, typically derived from outcrop and core data. In actual practice, it would be best to apply constant factors that are appropriate for the local field, play, or basin. In this 'New-fault *TM* model' the values suggested by Manzocchi *et al.*, (1999) for *A1*, *A2*, and *A3* of -4, 0.25 and 5, respectively, were used to approximate fault permeability.

Fault rock thickness, clay estimate from *SGR*, permeability and transmissibility multipliers are shown in **Fig. 5.4**. The fault rock thickness takes a maximum value of 2 ft (corresponding to a fault displacement of about 347 ft). As reflected in the fault thickness, fault displacement reduces away from the salt domes for the radial faults. Fault plane maps suggest that concentric faults should have a larger impact on fluid flow than radial faults as a result of the low net/gross around them. The simple mean average transmissibility multiplier of faults in the Pierce Field is about 0.6 (**Fig. 5.4d**). This figure indicates that these faults do not seem to have a large impact on fluid flow, primarily owing to their small throws and low host/fault permeability contrast.

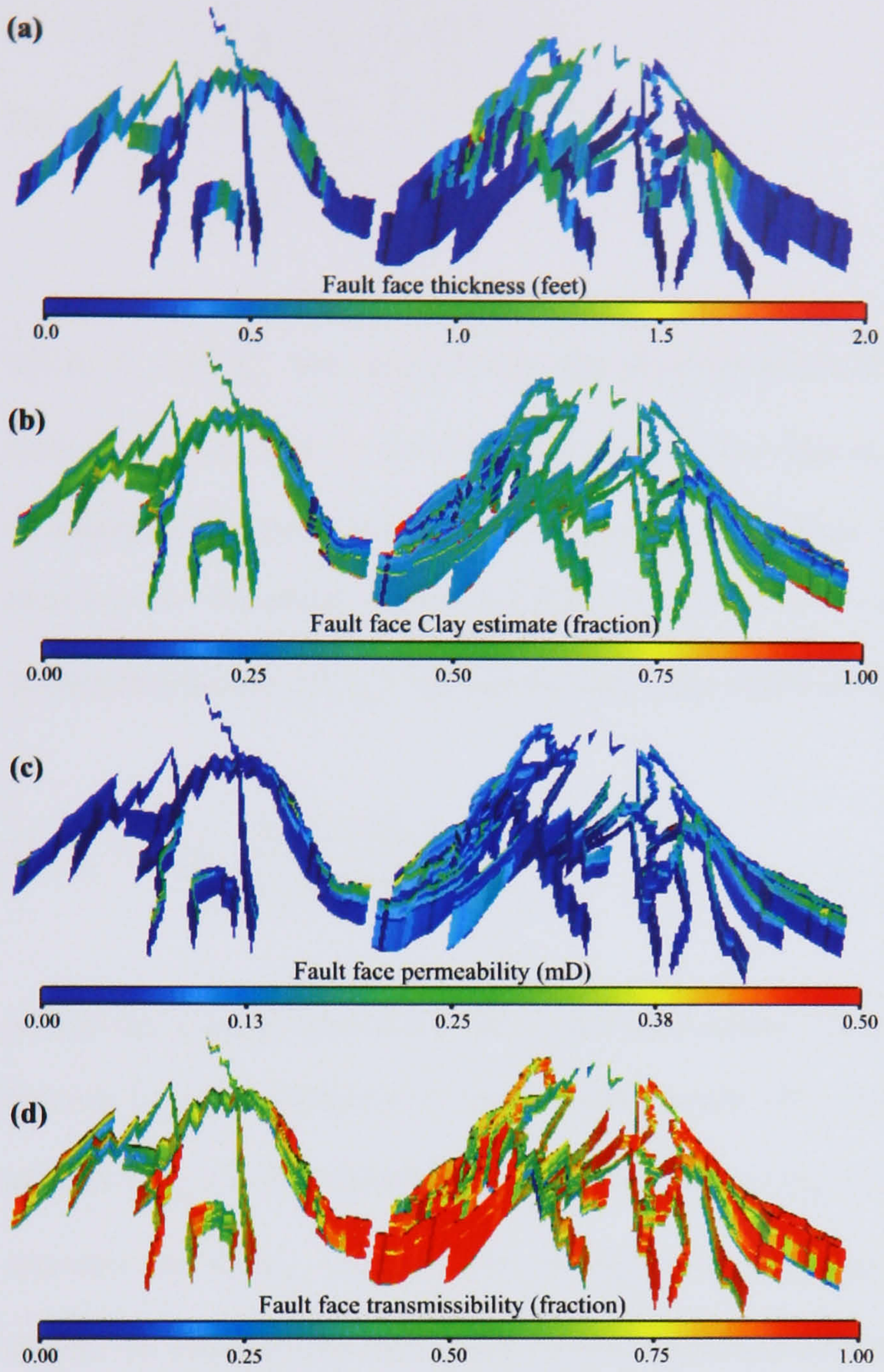

Fig. 5.4. (a) Fault thickness, linearly derived from fault displacement. **(b)** Fault clay estimate from *SGR*. **(c)** Fault permeability, derived from fault thickness and *SGR*, see **equation 2.20**. **(d)** Fault transmissibility multiplier as derived from **equation-2.29**. The derivation follows the methodology of Manzocchi *et al.* (1999). Fault rock thicknesses become thinner radiating away from the salt domes. Concentric faults (see **Fig. 5.2**) have less transmissibility than radial faults. Generally, radial faults become less transmissible with depth.

5.3.2. Transmissibility multipliers (*TMs*) from the microstructural and petrophysical fault property measurements

Microstructural and petrophysical fault property measurements conducted during this study (**Chapter 4**) indicate that cataclasites are the main fault rock type in Pierce and have a geometric average permeability of 0.05 mD and a mean Hg-injection threshold pressure of 250 psi (**Table-4.3**). The average permeability of the undeformed reservoir is around 10 mD (**Table-4.1**). To take into account the presence of a 1 ft thick fault with this permeability within the aquifer in the production simulation model (the grid block width in the simulation model is 75 m (around 246 ft)) would require, according to Manzocchi *et al.* (1999), the use of the following transmissibility multiplier (*TM*) equation of a fault impeded between two units of identical properties and geometries:

$$TM_{abs} = \left(1 + \frac{t_f \left(\frac{2}{k_f} - \frac{1}{k_1} - \frac{1}{k_2} \right)}{\frac{L_1}{k_1} + \frac{L_2}{k_2}} \right)^{-1} \qquad \textbf{5.1}$$

where k_i and k_f are, respectively, the absolute permeabilities of the host units and the fault material, and L_i and t_f are the width of each host unit and the fault width, respectively. A *TM* of around 0.55 must therefore be applied between these adjacent grid blocks. To convert the mercury–air threshold pressure $(P_c)_{Hg}$ value of 250 psi to a subsurface petroleum–water threshold pressure $(P_c)_{hw}$, we use the following equation (Purcell, 1949):

$$(P_c)_{hw} = (P_c)_{Hg} \frac{\gamma_{hw} \cos(\theta_{hw})}{\gamma_{Hg} \cos(\theta_{Hg})} \qquad \textbf{5.2}$$

where the typical laboratory data (see Schowalter, 1979) for hydrocarbon–water interfacial tension (γ_{hw}) is 30 dyne/cm for a contact angle (θ_{hw}) of 0°, and for mercury–air interfacial tension (γ_{Hg}) is 480 dyne/cm for a contact angle (θ_{Hg}) of 40°. With these data, **equation-5.2** converts the $(P_c)_{Hg}$ value of 250 psi Hg-threshold pressure to a subsurface $(P_c)_{hw}$ of around 25 psi. To estimate the maximum vertical hydrocarbon column height, H_{hw}, in feet, above the free water level (FWL) that can be sealed by faults having a threshold pressure $(P_c)_{hw}$ of around 25 psi, we use the following equation (Schowalter, 1979; Watts, 1987):

$$H_{hw} = \frac{(P_c)_{hw}}{0.433(\rho_w - \rho_h)} \qquad \textbf{5.3}$$

where 0.433 is a conversion constant, which also takes into account the effect of gravitational force, and ρ_w and ρ_h are *in-situ* reservoir water and hydrocarbon (in this case oil) densities measured in g/cm^3, respectively. Fluid densities can be estimated from repeat formation tester (RFT) measurements (**Fig. 4.3**). **Equation-5.3** can be re-written in terms of the pressure gradients from the RFT data as follows:

$$H_{hw} = \frac{(P_c)_{hw}}{\Delta_w - \Delta_h} \qquad \textbf{5.4}$$

where Δ_w and Δ_h are water and hydrocarbon RFT gradients measured in psi/ft. According to RFT pressure gradients and the converted subsurface petroleum–water capillary pressure $(P_c)_{hw}$, **equation-5.4** predicts that faults in South Pierce would be able to seal an oil column of about 70 ft. In other words, the results from this study indicate that the faults would be totally sealing to oil for the first 70 ft directly above the FWL within Pierce.

At higher levels above the FWL, we need to take into account relative permeability effects in calculating the transmissibility multipliers that need to be applied to take into account the presence of faults within Pierce. Unfortunately, there have not been any robust studies to measure the multiphase flow properties of faults. As an alternative, proprietary data on the end-point relative permeabilities of low permeability rocks as well as the data from shales generated by Hildenbrand *et al.* (2002) have been used. When compared with the results from a single measurement performed on a tight sandstone sample, it appears that these results are very consistent, showing that rocks with low absolute permeabilities tend to have low relative permeabilities to gas at irreducible water saturation (**Fig. 5.5**).

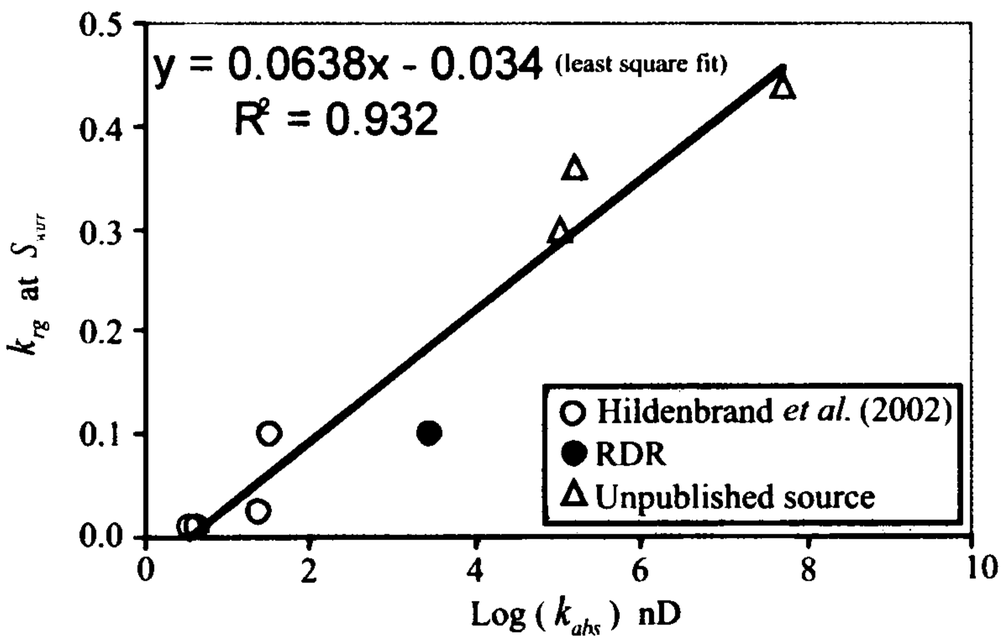

Fig. 5.5. Plot of gas relative permeability, k_{rg}, end points (*i.e.* at irreducible water saturation, S_{wirr}) against absolute permeability from shales (Hildenbrand *et al.*, 2002) and Rock Deformation Research (RDR) sample measurement during this study. To constrain the best fit at relatively higher permeability samples, we used some proprietary data from an unpublished source.

If we assume that once the threshold pressure of a fault rock is overcome (*i.e.* higher than 70 ft above the FWL) its water saturation will be at irreducible values, we can calculate relative *TMs* using the measured absolute permeability (0.05 mD) of the fault and the regression line through the data in **Fig. 5.5**, which gives an end-point gas relative permeability of approximately 0.27. Thus, the required relative transmissibility multiplier can be estimated by modifying **equation-5.1** to the following form:

$$TM_{abs} = \left(1 + \frac{t_f \left(\frac{2}{k_f . (k_{rg})_{S_{wirr}}} - \frac{1}{k_1} - \frac{1}{k_2} \right)}{\frac{L_1}{k_1} + \frac{L_2}{k_2}} \right)^{-1} \qquad \textbf{5.5}$$

Equation-5.5 will be used to take into account the presence of faults within the oil and gas column of Pierce once the petroleum column height is sufficient to overcome the threshold pressure of the fault rock. The assumption regarding the lack of a transition zone within the fault will appear rather counterintuitive to most petrophysicists who are used to low permeability rocks having broad pore-size distributions. However, Hg-injection results indicate that cataclastic faults, as observed within this study, may differ in that they have a narrow range of pore-throat sizes, in which case the transition zone will be very thin.

In summary, the following parameters have been applied to take into account the presence of faults within the Pierce reservoir model. These were applied to those faults thought to have significant effects on fluid flow in Pierce (faults numbered (1)–(3) in **Fig. 5.2**):

- *TMs* calculated using **equation-5.1** were applied to take into account the presence of faults, with average permeability of 0.05 mD, in the aquifer (region 1, **Fig. 5.6**). Host rock permeabilities and geometries are read directly from the simulation model blocks at both sides of each fault. Fault rock thickness is estimated using the harmonic-average relationship between fault-rock thickness and throw (**§ 5.3.1**).
- A transmissibility multiplier of 0 was applied for the first 70 ft above the FWL to take into account the presence of a fault that is totally sealing to oil (region 2, **Fig. 5.6**).
- Relative *TMs* calculated using **equation-5.5** were applied in the reminder of the petroleum column to take into account the relative permeability of the fault rock (region 3, **Fig. 5.6**). These Relative *TMs* were estimated using the measured absolute permeability (0.05 mD) of the fault and the end-point gas relative permeability of about 0.27 that was estimated from the regression line through the data in **Fig. 5.5**. Host rock permeabilities and geometries are read directly from the simulation model blocks at both sides of each fault. Fault rock thickness is estimated using the harmonic-average relationship between fault-rock thickness and throw (**§ 5.3.1**).

The above treatment assumes that the FWL does not change during the simulation. It is important to note, however, that as the simulation progresses, the FWL is likely to change and, therefore, the maximum sealed petroleum column height above the FWL needs dynamic updating. In this study, it is assumed that the FWL change is negligible, and therefore, no dynamic updating is performed.

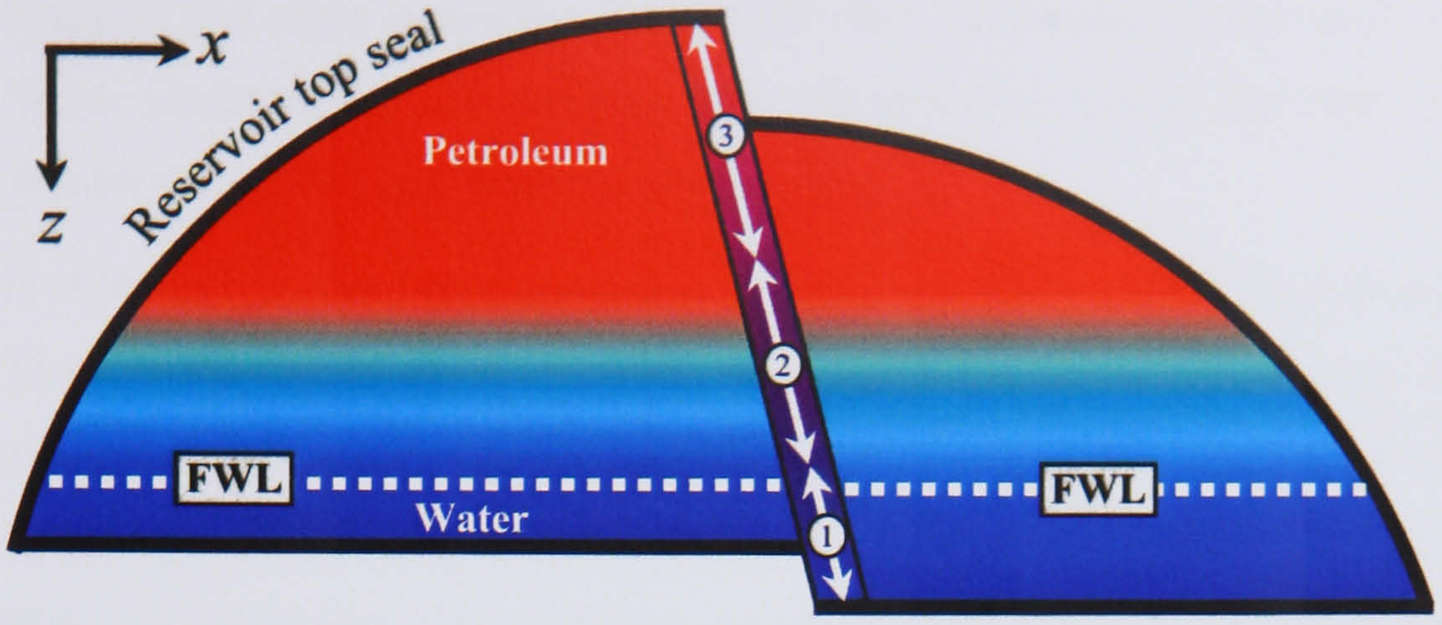

Fig. 5.6. A schematic diagram summarising the input parameters into the Pierce production simulation model. Point 1 is below the FWL and hence the transmissibility multiplier (*TM*) needs to be calculated based on the single-phase permeability of the fault *(i.e.* using **equation-5.1**). Point 2 is above the FWL in the reservoir but at this point the buoyancy force in the oil is not sufficient to overcome the threshold pressure of the fault rock and therefore a *TM* of 0 is applied. At point 3, the fault has a finite relative permeability to oil/gas and a *TM* value is calculated assuming the fault is at irreducible water saturation *(i.e.* using **equation-5.5**).

5.4. Models history match comparison

History matches using the cumulative field gas, oil and water productions have been performed for each model presented in § **5.1** to test their validity. In this study the history match was conducted using production data up to November 2003. **Figure 5.7** and **Fig. 5.8** show that there is a dramatic improvement in history match using the 'New-fault *TM* Model' simulation, especially in the water and oil production data. Gas production data seem to be the least affected data by the different representations of faults whereas water production is the most sensitive to the different representations. The reason for this is twofold. The first is attributed to fault continuity and fluid mobilities. The three treated faults are not continuous in the oil and the gas legs, see **Fig. 5.2**, but are continuous in the water leg. In the Pierce Field, gas is injected at the crest of the reservoir in the gas leg. This injected gas has low viscosities (ranging from 0.01 cP to 0.04 cP). The resultant high mobilities of gas enable it to move around the discontinuous faults and thus they become insensitive to the *TM* values applied to those faults. Pierce Field oil and water have similar range of viscosities (oil viscosities range between 0.5 cP and 0.2 cP and Pierce water average viscosity is about 0.3). With such low range of viscosities, and hence high mobilities, one might expect that these phases to show close behaviour to gas in being able to move around discontinuous faults during the simulated period of production. However, due to the long extension of faults in the oil leg, unlike gas, oil shows some sensitivity to the different fault representations, especially at the end of the simulation time, see **Fig. 5.8**. On the other hand, most of the water is forced to go throw the baffle faults to reach the horizontal production wells in the oil leg above and, therefore, it is the component most affected by the faults. The second reason for the differences in production among the three phases is attributed production wells designs. Production wells are designed to produce oil and/or gas, and therefore production

of these phases in the right quantities is more or less guaranteed if the well controls are honoured. Water production is not designed for, and therefore getting the right match of its production is both the hardest and most revealing factor.

The plots of the two extreme representations of faults, *i.e. TM=1* and *TM=0* models, indicate that the '*TM=0*' is the worst model of water production for this field, whereas the '*TM=1*' Model is among the best models giving almost similar results to the 'New-fault TM Model'. Gas production data do not distinguish even between these two extreme representations of faults, whereas oil production data manifest relatively small differences compared to water production data.

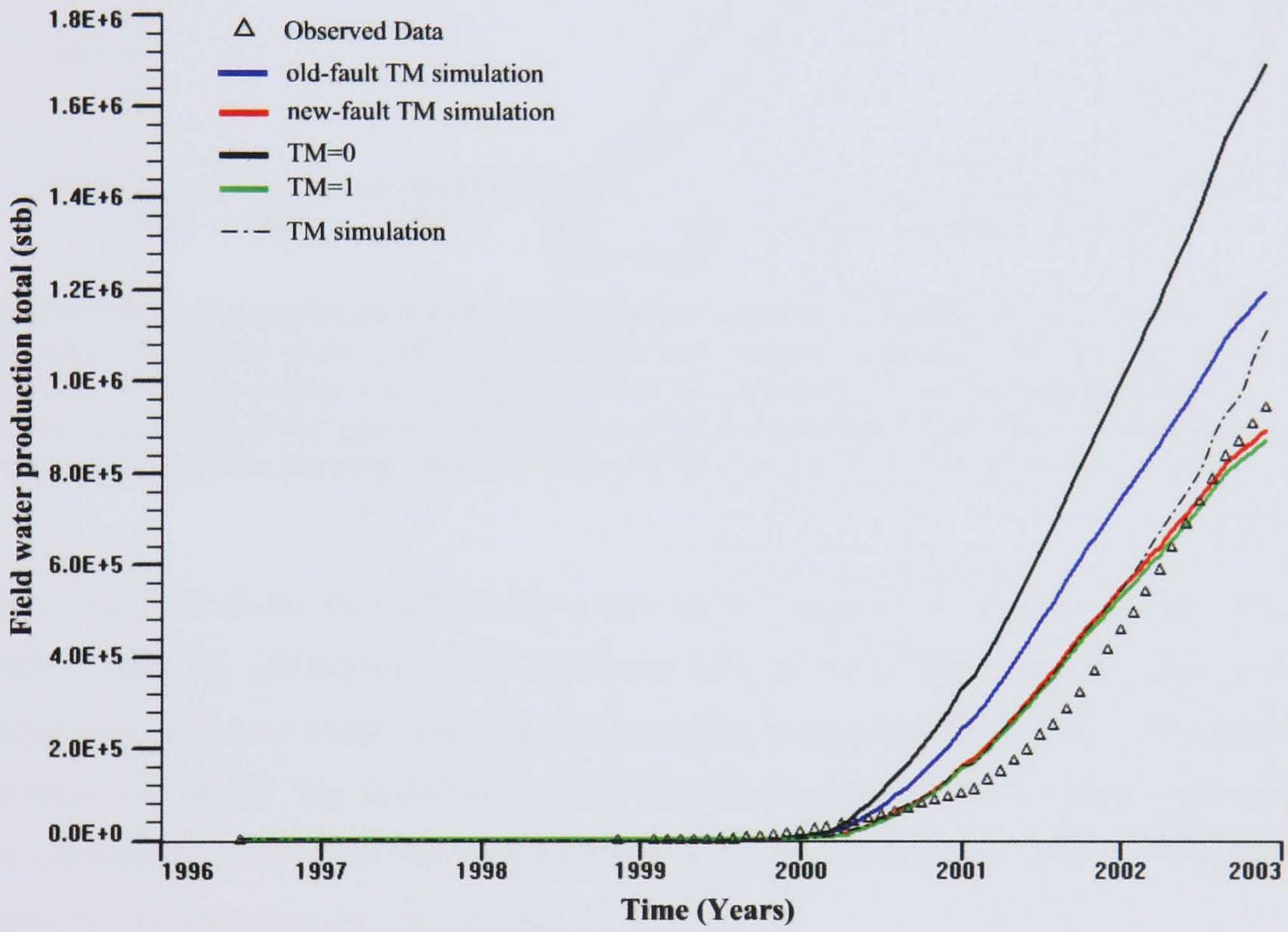

Fig. 5.7. Field water production total as a function of simulation time (in years). The 'Old-fault *TM* Model' (blue line) represents the best history match and results from extending the reservoir faults and using trial and error history match *TMs*. The 'New-fault *TM* Model' (red line) represents the history match results using geologically derived *TMs* ; also faults numbered (1)–(3) (see **Fig. 5.2**) were given a special treatment and their sealing capacities were varied depending on their relative position to the FWL (**§ 5.3.2**). The '*TM* Model' (thin dotted line) represents the history match results using geologically derived *TMs* for all faults in the model. The extreme cases of *TMs* are also shown for comparison purposes.

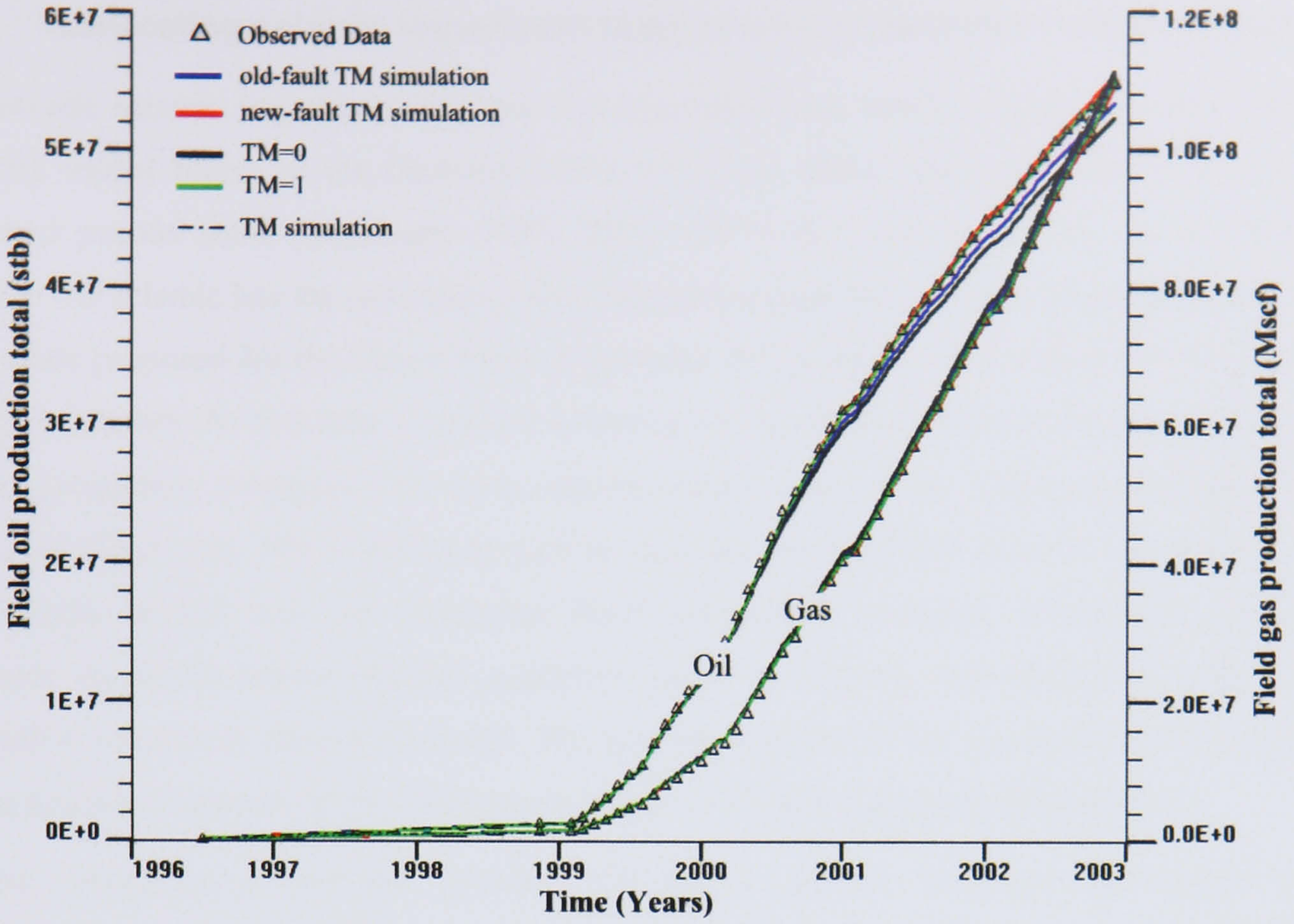

Fig. 5.8. Field oil and gas production totals as a function of simulation time (in years). The 'New-fault *TM* Model' gives an excellent match with observed data for the oil production. Faults do not have a clear impact on gas production because of the high gas mobility. Furthermore, most of the gas accumulation is around faults with high *TMs* (mostly in the top of the reservoir). The extreme cases of *TMs* are also shown for comparison purposes.

While **Fig. 5.3** shows the type of non-unique history match that can result when adding or extending faults by attempting a trial and error history match, **Fig. 5.9** shows the potential improvement in history match gained when including geologically-based faults. Although the 'New-fault *TM* Model' has manifested a clear improvement over the old model, there are still some parameters (*e.g.* water cut and bottom-hole pressures at some wells) which did not improve by implementing this new model.

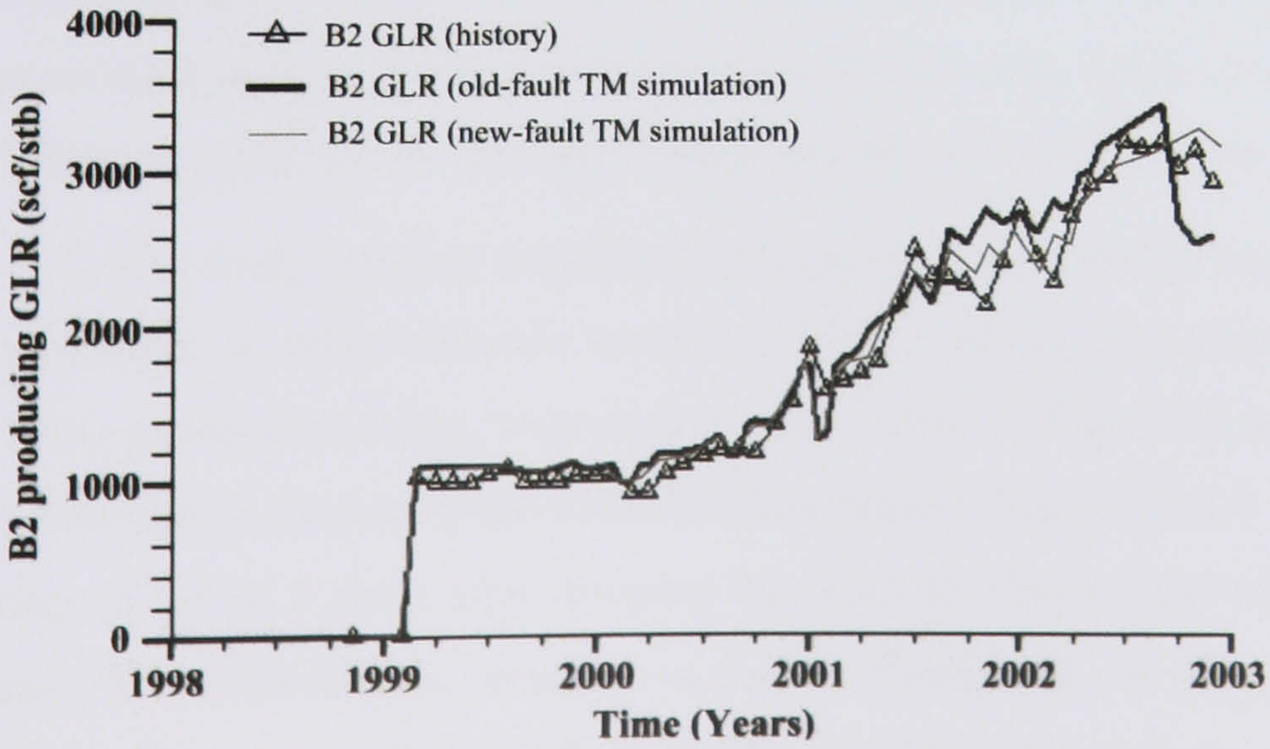

Fig. 5.9. Well B2 (see **Fig. 5.2** for well position) gas–liquid ratio (GLR) history match until the end of 2003. The figure compares the two different faults representations discussed in the text with the observed historical measurement (triangles).

5.5. Generating seismic impedance response from simulation model outputs

A synthetic seismic impedance response was generated from both simulation models, using a velocity model based on the Gassmann–Biot theory of elastic wave propagation in a fluid-saturated porous solid (Gassmann, 1951; Biot, 1956). The purpose of this was to identify whether 4D seismic has the potential to discriminate between the two fault property models that have been proposed for the Pierce Field. If positive, the secondary aim was to use the reliable model to identify the best time to shoot a follow-up survey that would have the most bearing on future production strategies. The petro-elastic model, part of the Geoquest **Eclipse 100**^{TM} simulator (Geoquest, 2003), has been used to generate the simulated acoustic impedance. The petro-elastic model uses the Gassmann fluid substitution equations (Gassmann, 1951) to generate simulated seismic-derived quantities (such as acoustic impedance) in each active gridcell in a reservoir simulation model. The acoustic response of the reservoir is a combination of the acoustic responses of the different rocks and fluids that constitute the reservoir.

The simulations of both the 'Old-fault *TM* Model' and the 'New-fault *TM* Model' were extended to predict the impact that faults have on both reservoir pressure and water cut before, during and after commencing a waterflooding project (**§ 5.5.1**). **§ 5.5.2** presents the theory of the adopted petro-elastic model.

5.5.1. Pierce Field waterflooding project and future prediction

A waterflooding project was implemented on the Pierce Field at the end of 2004 to sweep basement oil, which is not accessed by the current gas re-injection scheme, nor swept by the weak aquifer. The flooding was initiated by two horizontal wells in the western part of the North Pierce salt dome. **Figure 5.10** shows the expected plan of the reservoir development as envisaged by the field operators. The figure shows that, by commencing the waterflooding project, the reservoir is re-energised with a pressure support. This pressure support will assist in accelerating production as higher drawdowns become achievable and in eliminating difficulties associated with production start-up from low-pressure wells. At some point the water injection will be stopped and the gas caps (North and South) produced (gas cap blow-down).

In this study, seismic impedance changes are investigated based on changes in pressure and saturations at three different instances: before, during and after waterflooding, see **Fig. 5.10**. These production stages, indicated by grey circles in **Fig. 5.10**, are referred to as stage 1 (about 1 year before launching the waterflooding project), stage 2 (after 11 years of waterflooding) and stage 3 (about 5 years after stopping the waterflooding project and producing and exporting the gas). The main focus is on which of the two parameters, *i.e.* pressure or water saturation, has the most effect on creating residual seismic features around faults. *TM=1* and *TM=0* models are shown for comparison purpose and no seismic response is created for these models.

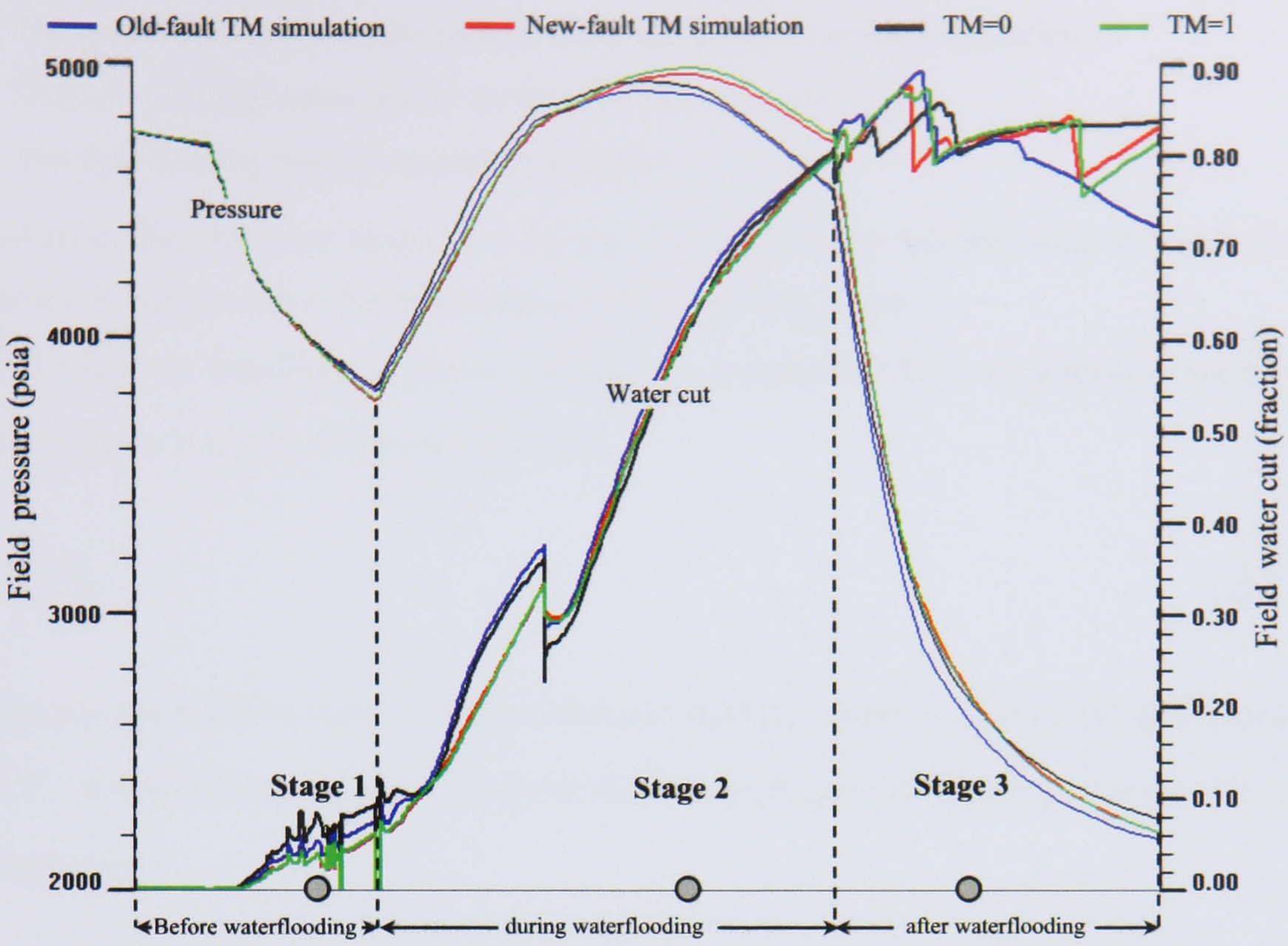

Fig. 5.10. Simulated field average pressure and water cut before, during and after commencing the waterflood project. The difference between the two models does not seem to be considerable in the long run. This study investigates if the impact is similar for the future generated seismic properties. P-wave impedance maps are generated at three different stages (indicated by the grey circles) during the three phases of the reservoir production life. The extreme cases of *TMs* are also shown for comparison purposes.

5.5.2. Velocity model theory

The effective acoustic response of the fluids is calculated from conventional simulation properties (such as pressure, fluid density, fluid saturations and effective porosities). The overall acoustic response of the reservoir is given by combining the effective acoustic response with the acoustic response of the rocks (both frame and minerals). This study uses the petro-elastic model available in **Eclipse 100™** simulator (Geoquest, 2003) to calculate the acoustic response of the reservoir.

The use of the Gassmann fluid substitution equations in the petro-elastic model relies on the following assumptions:

- The seismic frequencies used are sufficiently low (less than 100 Hz), so that the induced pore pressures have equilibrated throughout the pore space (that is, there is sufficient time for the pore volume fluid to flow and eliminate wave-induced pore pressure gradients). This limitation to low frequencies explains why Gassmann's relation works best for very low frequency *in situ* seismic data (<100 Hz) and may perform less well as frequencies increase, such as during sonic wire-line logging ($\sim 10^4$ Hz) and laboratory ultrasonic measurements ($\sim 10^6$ Hz).

- The rock is isotropic (*i.e.* the seismic wave speed is directional independent).
- There is a homogeneous elastic modulus for the minerals present.
- The fluid-bearing rock is completely saturated.

In addition, the fluids are assumed to be not "too" viscous, so that the shear stiffness of the reservoir is entirely due to the shear stiffness of the dry rock frame.

In this study, the impedance to pressure waves, I_p, is computed for every gridcell in the Pierce Field top layer using the following definition:

$$I_p = \rho V_p \qquad \textbf{5.6}$$

where ρ is the effective density of the composite material (fluids and minerals) in the gridcell and V_p is the effective P-wave velocity in the simulation gridcell. The effective velocities are calculated by:

$$V_p = \sqrt{\frac{K + (4G/3)}{\rho}} \qquad \textbf{5.7}$$

where K is the effective bulk modulus of the simulation gridcell and G is the effective shear modulus of the simulation gridcell. The effective bulk modulus of the simulation gridcell is a combination of the effects of the fluids, the frame and the minerals in the gridcell.

The following form of Gassmann's equation is used in the petro-elastic model:

$$K = K_{frame} + \frac{\left(1 - \frac{K_{frame}}{K_m}\right)^2}{\frac{\phi_{eff}}{K_{fluid}} + \frac{(1-\phi_{eff})}{K_m} - \frac{K_{frame}}{(K_m)^2}} \qquad \textbf{5.8}$$

where K_{frame} is the effective bulk modulus of the dry rock frame for this gridcell, K_m is the effective bulk modulus of the minerals in this gridcell, K_{fluid} is the effective bulk modulus of the pore fluid in this gridcell and ϕ_{eff} is the effective porosity of this gridcell.

The overall shear modulus, assuming that the fluids are not too viscous, *e.g.* >200 cP for non-Newtonian oils (Mavko and Nolen-Hoeksema, 1994), is just the shear modulus of the dry rock frame:

$$G = G_{frame} \qquad \textbf{5.9}$$

where G_{frame} is the shear modulus of the dry rock frame for this gridcell. This assumption is quite true for Pierce oil, which has an average viscosity of about 0.2 at reservoir pressure of 3600 psi.

The effective density in a gridcell is given by the effective porosity-weighted average of the fluid density and the mineral density:

$$\rho = \phi_{eff} \cdot \rho_{fluid} + (1 - \phi_{eff}) . \rho_m \qquad \textbf{5.10}$$

where ρ_m and ρ_{fluid} are the effective densities of the minerals and fluids, respectively, in each gridcell. The effective density of the minerals is supplied directly as an input for each petro-elastic region in the simulation model. The density of the minerals in the Pierce Field, as averaged from core sample measurements, is 2.65 g/cc.

The calculation of the effective porosity for a gridcell is based on the porosity at the reference pressure, ϕ_0, in the gridcell and the effects of rock compressibility or rock compaction (depending on which type of pressure effect is present in the model). The petro-elastic model uses a rock model that relates rock effective porosity, ϕ_{eff}, and compressibility by:

$$\phi_{eff} = \phi_0 (1 + X + \frac{X^2}{2}) \qquad \textbf{5.11}$$

where

$$X = C(P - P_{ref}) \qquad \textbf{5.12}$$

and C, P and P_{ref} are the rock compressibility, the pressure and the rock compressibility reference pressure, respectively, for each gridcell. The rock porosity, compressibility and their reference pressures as well as the pressure itself are available within the simulator. The effective fluid density is the saturation -weighted average of the individual fluid component densities:

$$\rho_{fluid} = S_o \rho_o + S_w \rho_w + S_g \rho_g \qquad \textbf{5.13}$$

where $S_{o,w,g}$ is the saturation of oil/water/gas in the gridcell and $\rho_{o,w,g}$ is the density of oil/water/gas in the gridcell. These quantities are also available within the simulator for each gridcell.

Under an isostress situation, *i.e.* pressure equilibration of all the present phases when they are thoroughly mixed at the pore scale, the effective bulk modulus of the mixture of phases is described by the Reuss average (Reuss, 1929) as a saturation-weighted harmonic average of the individual phase bulk moduli, that is:

$$\frac{1}{K_{fluid}} = \frac{S_o}{K_o} + \frac{S_w}{K_w} + \frac{S_g}{K_g} \qquad \textbf{5.14}$$

where $K_{o,w,g}$ is the bulk modulus of the oil/water/gas in the gridcell determined by the phases densities and velocities (see Geoquest (2003) manual for details).

Phase velocities are computed from the gridcell pressure and temperature using empirical relations similar to those summarised by Batzle and Wang (1992), see Geoquest (2003) manual. The Pierce Field temperature varies due to the large petroleum column height and the proximity to salt. RFT data indicate that the temperature is 245 °F at the top of the reservoir, with a gradient of 0.0171 °F/ft.

The rock moduli can often be predicted quite accurately by inserting the effective fluid modulus into Gassmann's relation (Domenico, 1976; Murphy, 1984; Cadoret, 1993; Mavko and Nolen-Hoeksema, 1994).

5.5.3. Petro-elastic model results

The results of the petro-elastic model are presented and discussed via a visual process aided with acoustic impedance maps generated from the velocity model described above. **Figure 5.13** shows water saturation, pressure and P-wave impedance residual maps at three different instances during stage 1, stage 2 and stage 3, see **Fig. 5.10**. These residual maps represent the differences between the 'Old-fault *TM* model' (**Fig. 5.11**) and the 'New-fault *TM* model' (**Fig. 5.12**) at the corresponding stages. At the early stage of production and prior to the waterflooding project, the P-wave impedance residual map, stage 1, seems to have a good correlation with the pressure residual map (see **Fig. 5.13**, top maps). There are high seismic amplitude changes (or seismic features) around faults in South Pierce. At present there are abundant amounts of compressible phases, *i.e.* oil and gas, and these are capable of creating the observed seismic amplitudes even with little change in reservoir pressure. For this reason, one can see that the seismic features are well correlated with the pressure residuals.

The simulations suggest that in stage 2 and after about 11 years of waterflooding, there are almost no seismic features created by faults, irrespective of their representations (see **Fig. 5.13**, middle maps). At this stage of the reservoir life, most of the gas and oil in South Pierce and the saddle region between the two salt domes will have been swept by the flooded water (**Fig. 5.11** and **Fig. 5.12**, middle maps). The absence of the seismic features at this stage can be explained by the phase distribution. The field water cut jumps from about 5% in stage 1 to about 60% in stage 2 (**Fig. 5.10**). The faults would be surrounded by the least compressible phase, water, except at the top of the salt domes. Although the pressure residual is larger than that in stage 1, the seismic features do not correlate with the pressure distribution. The generated seismic impedance is almost identical for both fault representations at this stage, even though the residuals in pressure and saturation are greater than those in stage 1 (**Fig. 5.13**, middle maps).

In stage 3 and 5 years after stopping the waterflooding project and producing and exporting the remaining gas, a big drop in reservoir pressure takes place (**Fig. 5.11** and **Fig. 5.12**, bottom maps). In contrast, there is a small change in water saturation compared to stage 2. This pressure drop allows the light-end hydrocarbons to come out of solution and gas features appear as it drops below its bubble point pressure (see saturation maps in **Fig. 5.11** and **Fig. 5.12** bottom maps). From the stage 3 pressure residual map (**Fig. 5.13**, bottom maps) North Pierce is dominated by a negative pressure residual (light grey). The 'New-fault *TM* Model' predicts more pressure compartmentalisation in North Pierce. On the other hand, South Pierce is dominated by a positive pressure residual (dark grey), meaning that the 'Old-fault *TM* Model' predicts more pressure compartmentalisation in this part of the reservoir. This pressure residual is not well correlated with the P-wave impedance residual. There is, however, some degree of correlation in other parts of the reservoir.

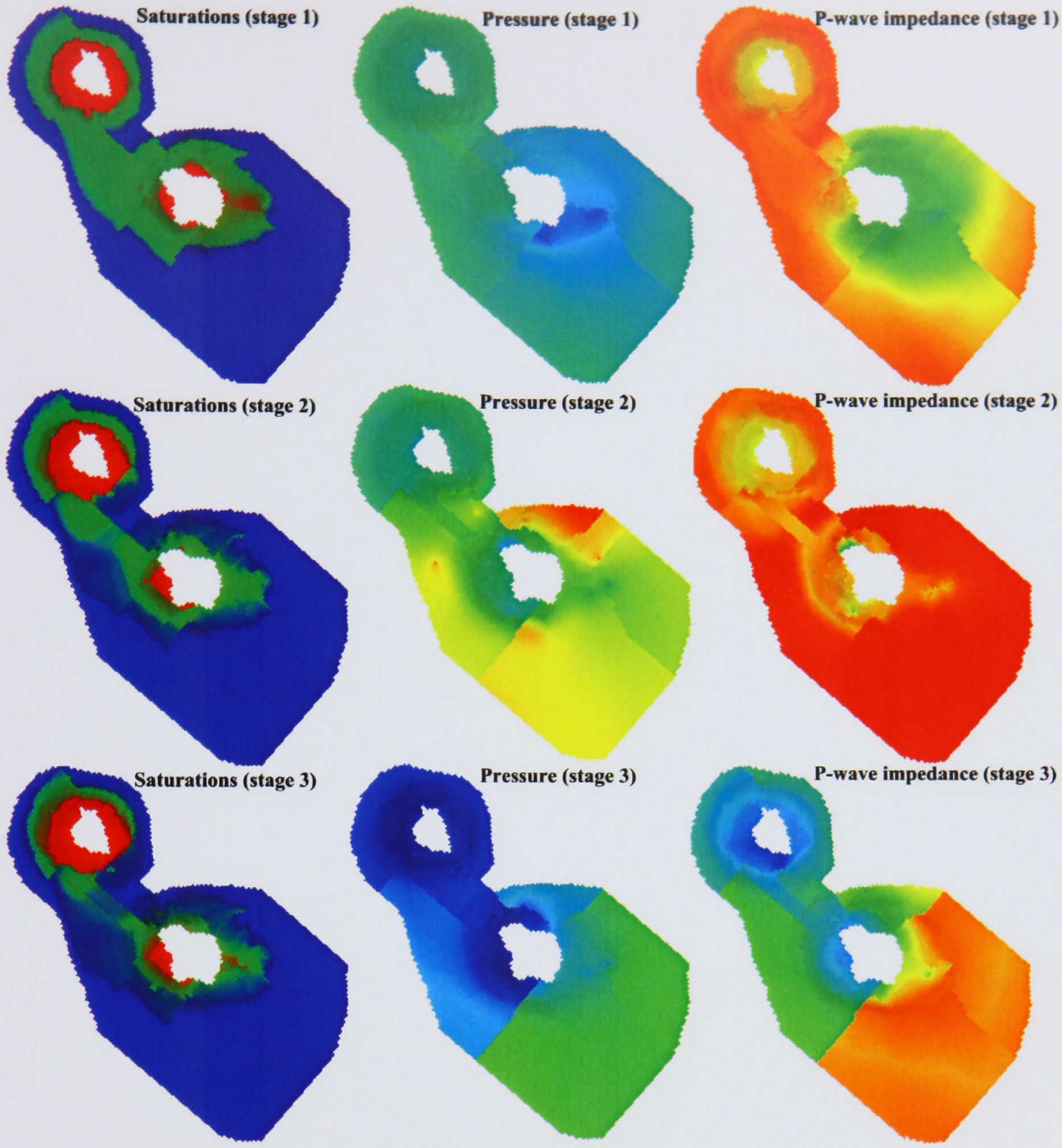

Fig. 5.11. 'Old-fault TM Model' results. Simulated phase saturations (left column), field pressure distribution (middle column) and P-wave impedance (right column) for stage 1 (about 1 year before launching the waterflooding project), stage 2 (after 11 years of waterflooding) and stage 3 (about 5 years after stopping the waterflooding project and producing and exporting the gas).

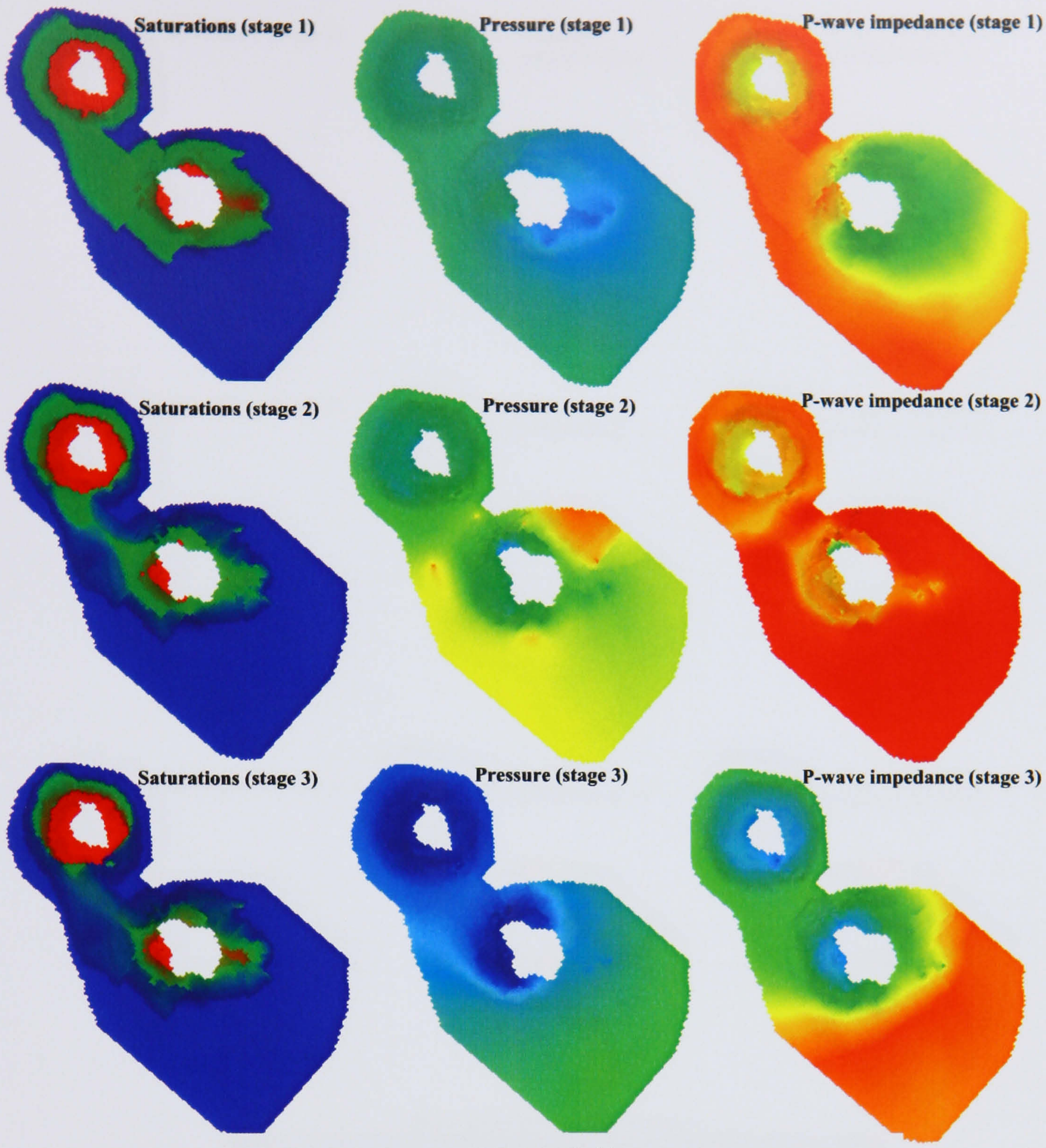

Fig. 5.12. 'New-fault TM Model' results. Simulated phase saturations (left column), field pressure distribution (middle column) and P-wave impedance (right column) for stage 1 (about 1 year before launching the waterflooding project), stage 2 (after 11 years of waterflooding) and stage 3 (about 5 years after stopping the waterflooding project and producing and exporting the gas).

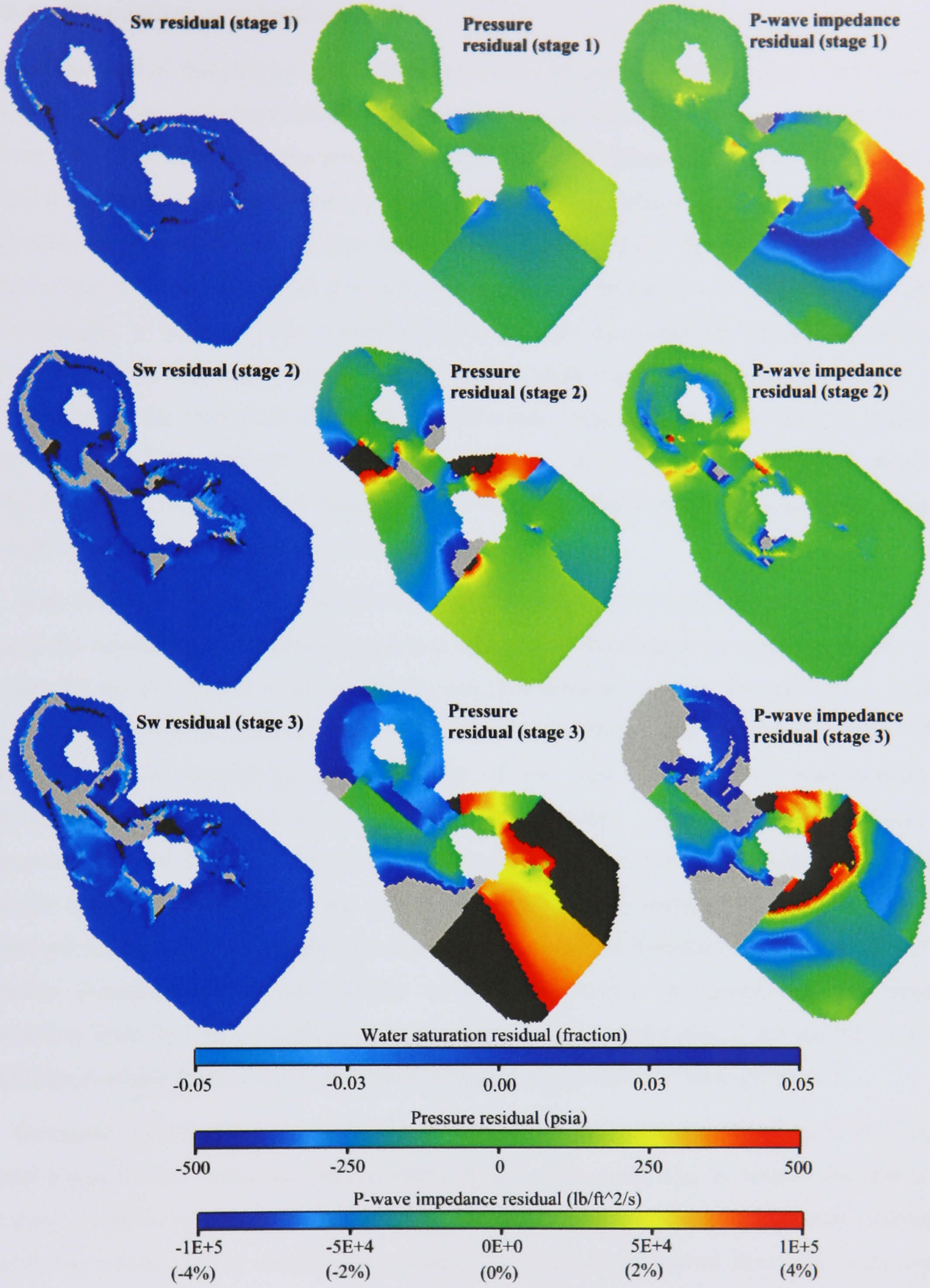

Fig. 5.13. Simulated phase saturation residuals (left column), field pressure distribution residuals (middle column) and P-wave impedance residuals (right column) for stage 1 (about 1 year before launching the waterflooding project), stage 2 (after 11 years of waterflooding) and stage 3 (about 5 years after stopping the waterflooding project and producing and exporting the gas). These residual maps represent the differences between the 'Old-fault TM Model' (**Fig. 5.11**) and the 'New-fault TM Model' (**Fig. 5.12**) at the corresponding simulation times. The light grey colour represents the negative residuals beyond the shown scale, whereas the dark grey colour represents the positive residuals beyond the shown scale. These colours show the areas where the difference is extreme (*e.g.* > ±4% in the P-wave impedance residual).

5.5.4. Discussion and implications

One of the aims of this chapter was to identify whether the generated 4D seismic maps have the potential to discriminate between the two fault property models that have been proposed for the Pierce Field. It is clear from the presented results that the different representations of faults do affect the generated seismic features, despite the fact that they behave similarly when comparing their average production and pressure data (**Fig. 5.10**). Furthermore, the pressure and saturation maps of the two fault models can give different suggestions for future well planning in the field. For example, at stage 2 of the waterflooding (**Fig. 5.11**) the 'Old-fault *TM* Model' predicts unswept-oil zone with high pressure support in the saddle region between the two domes. On the other hand, the 'New-fault *TM* Model' predicts that a large portion of the same oil zone has been swept and the pressure in the region is not as large as the former model suggests (**Fig. 5.12**). The 'Old-fault *TM* Model' results might mislead reservoir engineers in making crucial decision about drilling the wrong well.

With the availability of the real 4D seismic data, which is not the case for this study, one can assess the reliability of each model presented. 4D seismic information provides a powerful tool to identify the distribution of seismic faults, and even subseismic faults, that have some degree of resistance to fluid flow by tracking pressure distributions and front movements. The difficulty lies in quantifying the magnitude of the fault resistance, *i.e.* transmissibility multipliers, from the observed 4D seismic. Conventionally, observed strong residuals in pressures are used to draw a compartmentalisation map of the reservoir without using the 4D seismic information to quantify the sealing behaviour of each detected fault. Correlating the observed seismic features around each fault with the applied transmissibility multipliers of a reliable simulation model can provide valuable information for quantifying the sealing behaviour from the observed 4D seismic. It is important to clarify that, if the real 4D seismic had been available for this study, this latter proposed step could have been performed.

Currently, there is a 3D seismic data set available for the field that was taken in mid-2003, about a year before starting the waterflooding project. This study tries to identify the best time to shoot a follow-up survey that would have the most bearing on future production strategies and to test which method of fault representation is correct. Both models show that, at the early stage of the reservoir development and before commencing the waterflooding project, there is not much change in fluid distribution. Planning a seismic survey at this stage will not show a considerable seismic residual when compared to the 2003 base survey. The waterflooding project causes an abrupt change in both fluid distribution and pressure. Such changes suggest that it is best to shoot a follow-up survey after the waterflooding project. The remaining question is 'How long after the waterflooding should the follow-up survey be conducted?' This question can be simply answered by simulating the seismic variation of the models and comparing the results with the 2003 base seismic map. The results of this process show that the

seismic residual, with respect to the 2003 base survey, increases with time, but after 2007 the increase becomes less apparent. This was also noted at stage 2 presented above (**Fig. 5.12**), where the variation in P-wave seismic distribution across the whole reservoir is the least. Conducting a 3D seismic survey at this stage will not help in giving information about which of the two proposed models is correct because the models show almost identical seismic residuals at this stage (**Fig. 5.13**). Therefore, shooting a follow-up seismic survey in 2007 will give the optimal seismic residual (**Fig. 5.14**) with the base survey and will also help to test the validity of the proposed fault models. The 2007 - 2003 pressure residual map (**Fig. 5.14**) shows an obvious variation in pressures across the reservoir that helps reservoir engineers to answer influential production decisions. A good field example where a similar integrated flow model forecast was successfully used to help schedule a repeat survey is the Weyburn field on the northeast flank of the Williston basin in Southeast Saskatchewan, Canada (Fanchi, 2003).

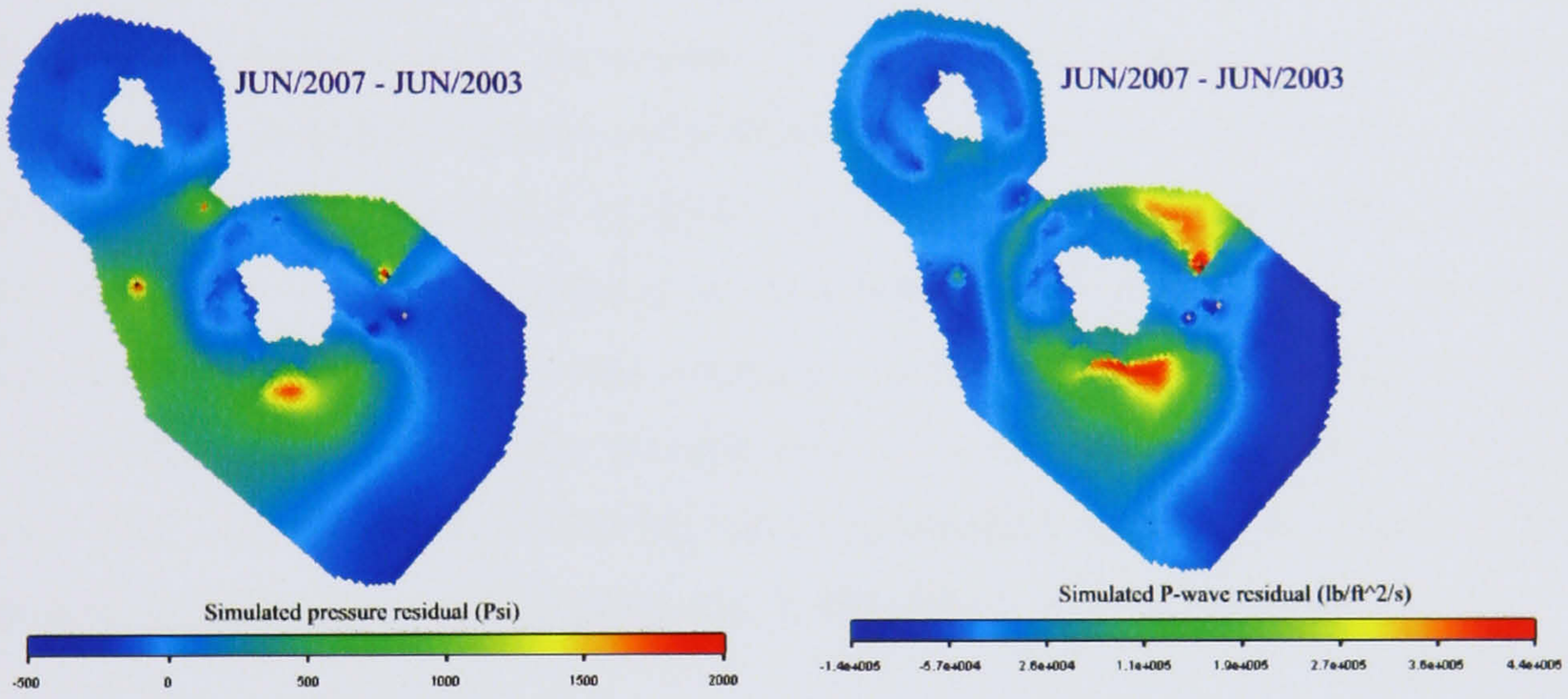

Fig. 5.14. 2007 - 2003 simulated field pressure distribution residuals (left) and P-wave impedance residuals (right) for the 'New-fault *TM* Model'.

5.6. Alternative Model

5.6.1. Model description

The 'New-fault *TM* Model' presented above can raise some issues regarding the relative movement of different phases present in the field. It can be argued that the above modelling of faults can cause some unnatural behaviour of both petroleum and water movement around the treated faults in the 'New-fault *TM* Model'. In particular, the sealing parts of the fault immediately above the FWL may force some petroleum, mainly oil, to flow across the fault within the water leg where the fault should be impermeable to petroleum. Furthermore, this representation may also restrict the movement of water unnaturally in the upper part of the petroleum column and where it is stopped by the sealed parts of the faults in the lower part of

the reservoir. These are important issues and if proved to exist in the previous modelling, the model may be in serious error

One possible way to improve the 'New-fault *TM* Model' and overcome some of the issues raised above is to treat different parts of the reservoir using modified phase relative-permeability curves to control the movement of each phase at each grid block. For example, to restrict the movement of oil below the FWL, the relative permeability to oil can be multiplied by zero for all flows into the fault along this part of the fault. The same process can be performed for the calculated height immediately above the FWL where faults are expected to be completely sealing to petroleum but not to water. At the upper part of the reservoir in the petroleum column, the movement of the petroleum can be treated in a way analogous to that presented in the 'New-fault *TM* Model' but applied to the petroleum relative permeability rather than to the *TMs*. In other words, a more realistic treatment at this part of the fault is to scale the relative permeability curves of the petroleum phases by the estimated end point from **Fig. 5.5**. These two-phase fault-rock effects represented by the relative permeability curves are included as directional irreversible relative permeability curves adjacent to faults in a model where all faults are initially included as geologically-based *TMs* (*i.e.* to the '*TM* Model'). The above representation is applied in a model referred to as the 'Alternative Model'. The way that the relative-permeability curves are attached as directional irreversible curves to the model is summarised in **Fig. 5.15**. Each grid block adjacent to the fault is given one scaled curve (either Curve (1) or Curve (2)) for flows into the fault, and five rock curves (Curve R) in the other five directions. The water relative permeability curve is identical for all fault zones A, B or C corresponding to zones 1, 2 and 3, respectively, in **Fig. 5.6**.

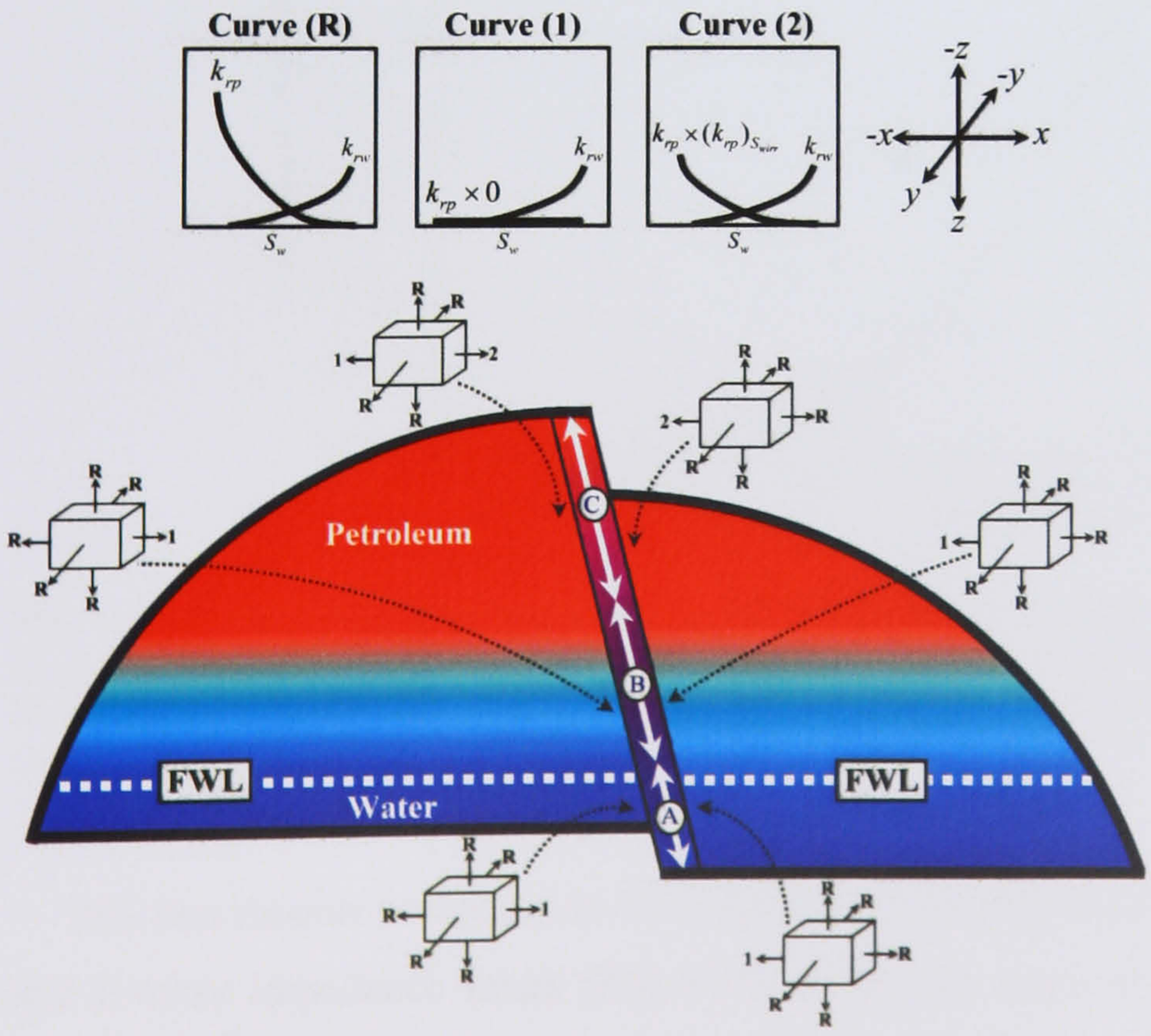

Fig. 5.15. A schematic diagram illustrating how the 'Alternative Model' is created by assigning scaled relative permeability curves to different zones in the fault. Zones A, B and C correspond to regions 1, 2 and 3, respectively, in **Fig. 5.6**.

5.6.2. Model results

In this section the 'New-fault *TM* Model' presented in **§ 5.3** is compared with the 'Alternative Model' presented in **§ 5.6.1**. **Figure 5.16** compares the performance of each model for water production for the current and future developments. Oil and gas productions are not affected by the new representation and their behaviours are almost identical to those shown in **Fig. 5.8**. The figure also plots the performance of the extreme *TM* models for comparison purposes.

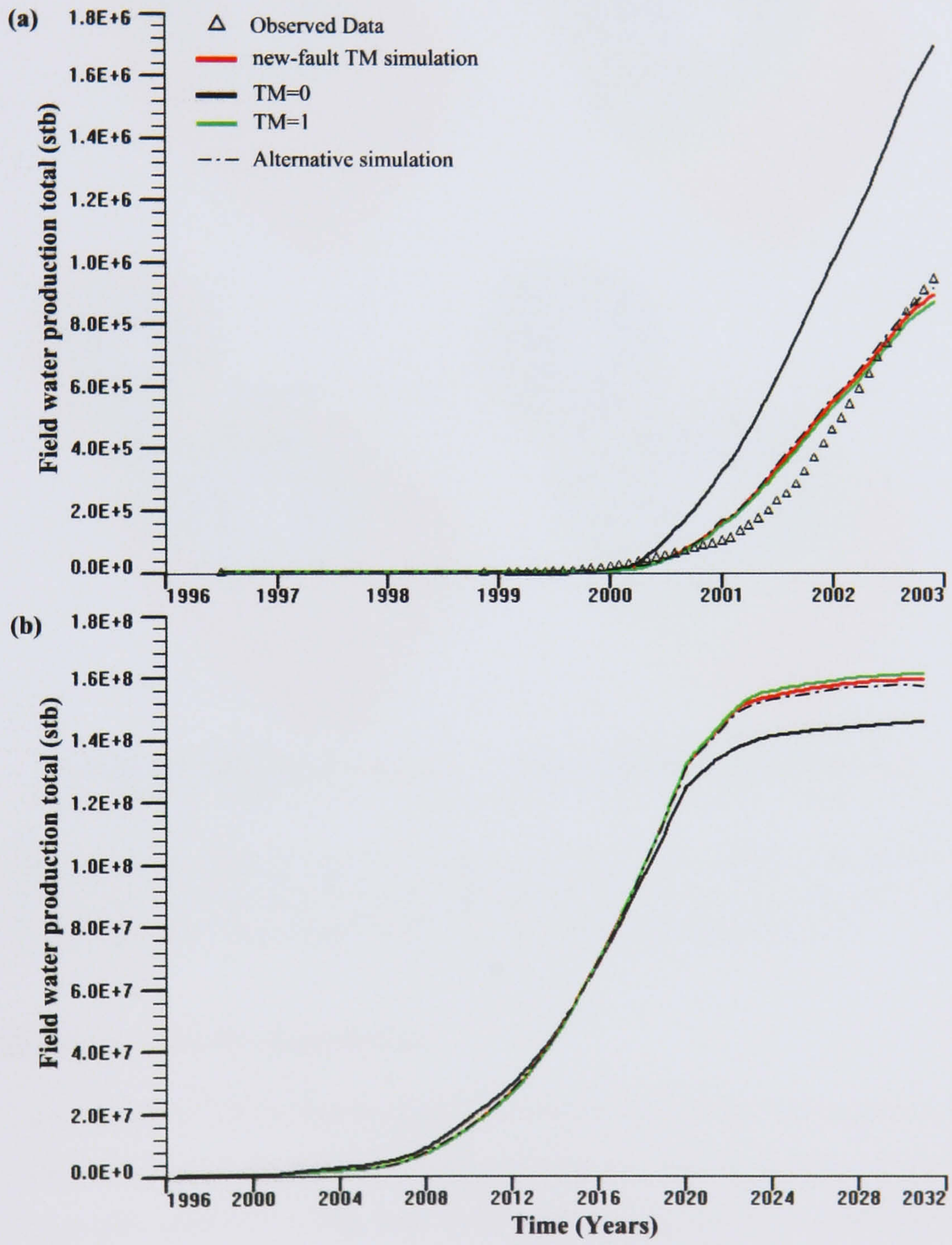

Fig. 5.16. Field water production total as a function of simulation time (in years) for the 'New-fault *TM* Model' (red line) and the 'Alternative Model' (thin dotted line) for **(a)** the current history and **(b)** future prediction. The two models with extreme *TMs* are also shown for comparison purposes.

The two models compared in this section behave almost identically when viewing the water and P-wave impedance maps (**Fig. 5.17**) at the last stage of the field development (Stage 3, corresponding to the year 2028 in **Fig. 5.16**; see **Fig. 5.10** for details). The 'Alternative Model'

is slightly restricting the movement of water around the eastern part of the north dome of the field (rectangular area in **Fig. 5.17**).

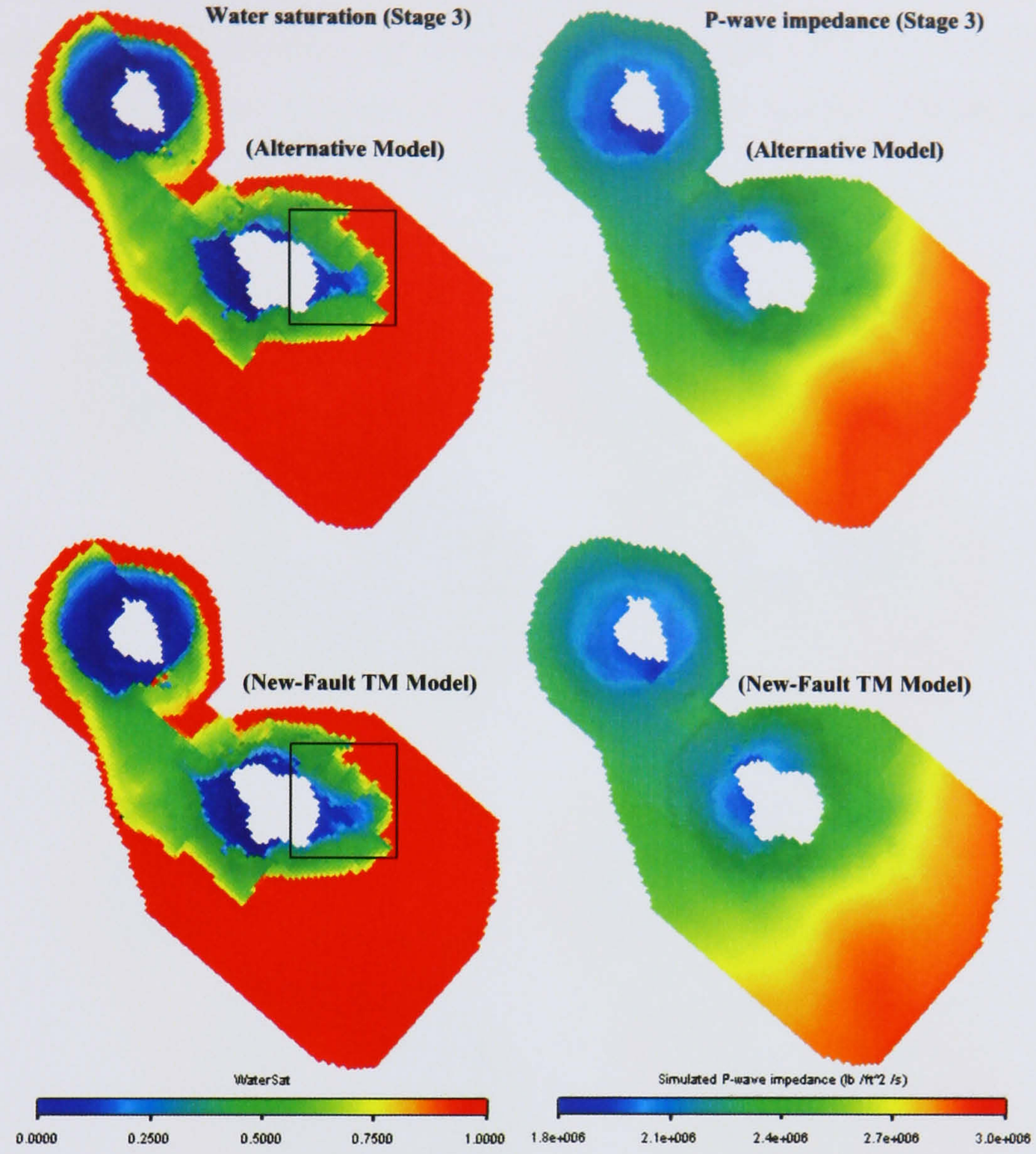

Fig. 5.17. 'New-fault *TM* Model' results versus the proposed 'Alternative Model'. Simulated phase saturations (left column) and P-wave impedance (right column) for stage 3 (about 5 years after stopping the waterflooding project and producing and exporting the gas).

5.6.3. 'Alternative Model' discussion

The results presented in § **5.6.2** comparing the 'New-fault *TM* Model' presented in § **5.3** and the 'Alternative Model' presented in § **5.6.1** indicate that the two models behave very similarly. The water production data depicted in **Fig. 5.16** shows that sealing the faults in the field before the waterflooding project enhances water production, but suppresses the production in the long run after implementing the waterflooding project. The similar behaviour of the three representations, *i.e.* the 'New-fault *TM* Model', the 'Alternative Model' and the '*TM=1* Model', indicates that the current fault model of the Pierce Field is only slightly affected by the different representations. The extreme cases for all the faults in the field, *i.e.* the '*TM=1* Model' and the '*TM=0* Model', do not provide results that would be expected in a field where faults play a major role in affecting fluid flow behaviour. The results also show that the faults are more likely to be open when compared to the current history match. Water saturation and impedance

response maps of the field confirmed that the unnatural fluid movements that the 'New-fault *TM* Model' was expected to exhibit are very unlikely. Most of the conclusions and discussions presented earlier (**§ 5.5.4**) about the simulated 4D seismic changes in the field are still valid since the new representation in the 'Alternative Model' did not show a considerable impact on fluid movements. When comparing the seismic response of the 'Alternative Model', the 2007 response is still the time that can provide the optimal seismic residual. **Figure 5.18** compares the 2007 seismic response with respect to the 2003 base survey.

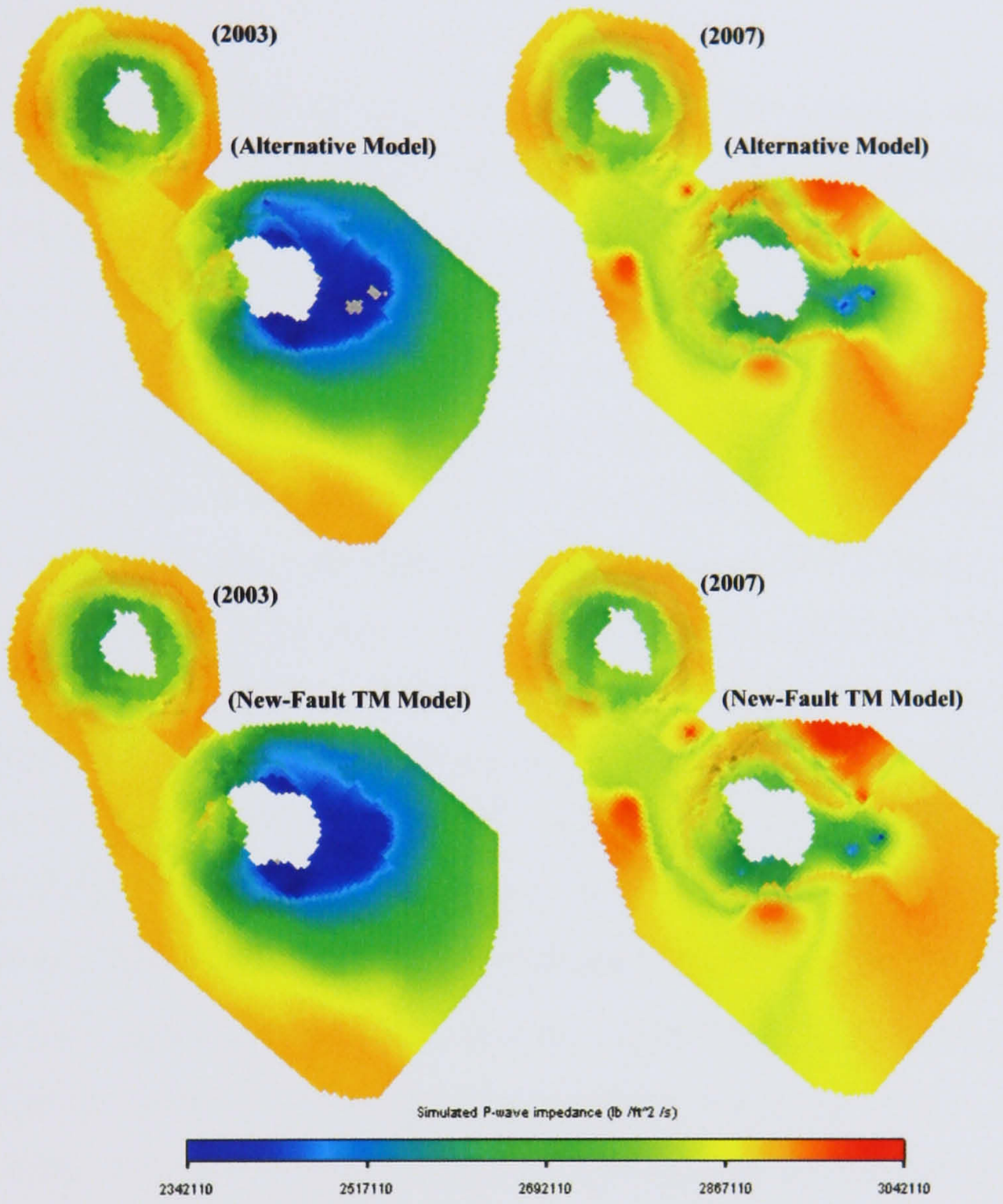

Fig. 5.18. 'New-fault *TM* Model' (bottom maps) results versus the proposed 'Alternative Model' (top maps). Simulated P-wave impedance for the base survey 2003 (left column) and the 2007 survey that shows the optimal residual from the base survey (right column).

Although the 'Alternative Model' presented here appears to be a more realistic alternative model to the 'New-fault TM model', the two models behave almost identically for the Pierce Field faults. There are two possible explanations why the unnatural fluid movements that the 'New-fault *TM* Model' was expected to exhibit did not manifest in the Pierce Field. One reason can be attributed to the relative position of the reservoir base to the FWL. For many of the faults in Pierce the base of the reservoir is more than 70 ft above the FWL, and therefore the only difference between the two representations compared here is the relative transmissibility to

water of the faults. Scaling the fault permeability by the estimated petroleum end point (0.27) in the 'New-fault TM Model' makes the relative transmissibility to water of the faults is approximately four times greater in the 'Alternative Model' than in the 'New-fault *TM* Model'. A factor of four is not expected to make much difference to the overall water flow rates and reservoir pressures, especially for the Pierce Field with the relatively high fault permeabilities (**Fig. 5.4**) derived from the Manzocchi *et al.* (1999) relationships. The second reason can be attributed to the high mobility of oil in the Pierce Field. With such a high mobility, gravitational force can quickly dominate in segregating the water and oil thus allowing them to follow the more natural paths.

To critically compare the two models in a general way, the schematic diagram shown in **Fig. 5.19** can aid in defining the different scenarios for which the two models are appropriate. The figure shows three identical faults with the same sealing capacity. According to the representation in the 'New-fault *TM* Model' (**Fig. 5.19a**), the first fault, labelled F1, will seal for a height above the FWL to the top of the trap. The second fault, labelled F2, has a comparable portion of it sealed above the FWL, whereas the third fault, labelled F3, has only a small portion of itself sealed compared to the petroleum column above. In a dynamic case initiated by water injection in the aquifer, the oil in the extreme left compartment of the 'New-fault *TM* Model' has nowhere to move except in the water leg, whereas it is confined in the 'Alternative Model representation'. For the F1 fault, neither of the two representations may be realistic. In particular, the hydrostatic concept that both models are based on (*i.e.* 70 ft of fault impermeable to oil) is wrong, as viscous forces mean that the capillary pressure in the reservoir can exceed the capillary threshold pressure of the fault close to the FWL, possibly by the same mechanism that was operating in the high P_c Model-1 in **Chapter 3**. However, in the extreme pressure gradients, under high injection for example, the 'New-fault *TM* Model' case could be the most natural case, as oil in reality could be forced through the water leg. This is, however, more likely to occur in the existing oil column (where the capillary pressure in the reservoir is closer to the capillary threshold pressure to start with) than it is in the water leg (where buoyancy forces are contributing nothing to the capillary pressure). Therefore, although for the wrong reason, the 'New-fault *TM* Model' could give simulation results that are closer to the natural case than the 'Alternative Model' as oil can flow through the water leg. However, if this fault (F1) had been modelled as accurately as possible, *e.g.* using discrete grid blocks with independent properties, then much of the oil would naturally flow through the fault above the FWL, but not through the fault in the water leg. The movement across fault F2 in the 'New-fault *TM* Model' can be unnatural for both oil and water as oil might be forced to move through the water leg, and water might be unnaturally restricted to move only in the top part of the model within the petroleum column. Such unnatural behaviour can be overcome in the 'Alternative Model' (**Fig. 5.19b**) by allowing water to move through any part of the fault and restricting the

petroleum movement to the petroleum column. The case of the F2 fault is the one that could demonstrate serious errors in the model in **Fig. 5.19a**. The overall across-fault flow for the F3 fault can be similar in the two models due to the small sealed height in comparison to the petroleum column. For this part of the model, the small sealed part is not capable of forcing the petroleum to move in the water leg and the petroleum will, naturally, move in the upper part. Similarly, water movement is very unlikely to be hindered by the small sealed height, and so the water has more freedom to move either below or above the sealed part. It is this third case of the F3 fault that can provide one explanation for the behaviour observed in Pierce for both models. This discussion, however, assumes that the k_v / k_h ratio is high enough not to significantly hinder vertical flow, which is almost the case in Pierce (see **Table 4-1**), but not in a general case where the k_v / k_h ratio is not favouring vertical flow, *e.g.* multiple horizontal shale layers interbedded within high permeability zone.

(a) Fluid movement in the 'New-fault TM Model'

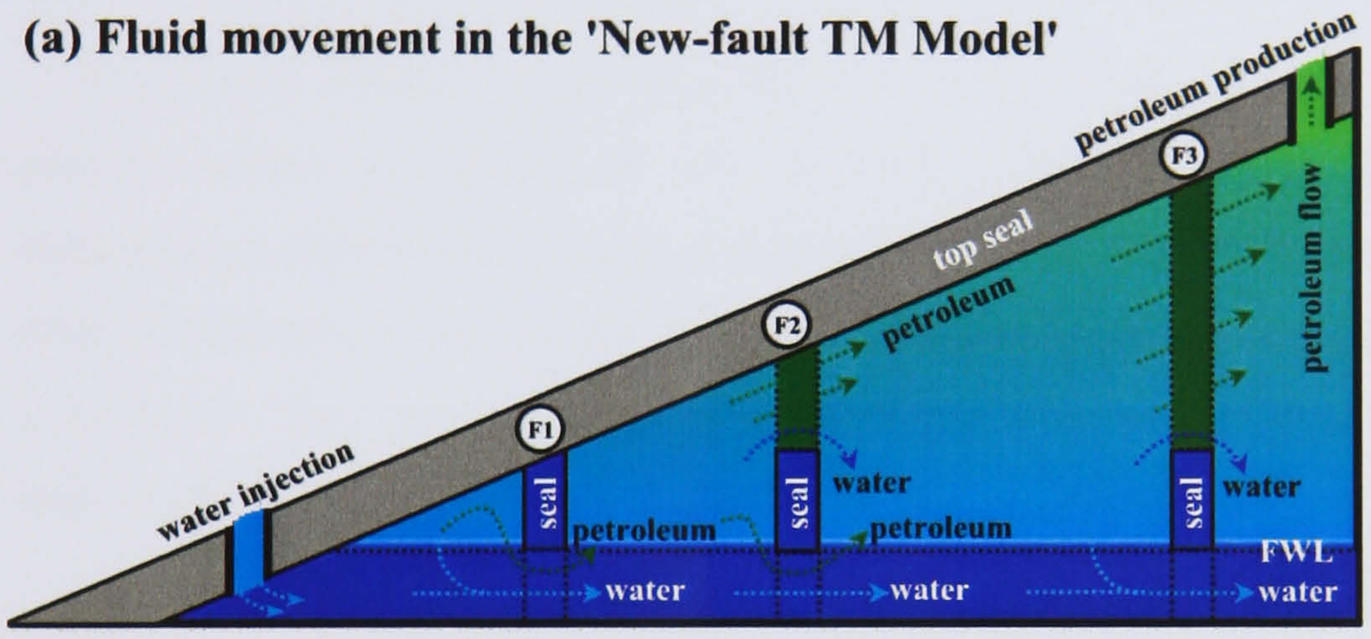

(b) Fluid movement in the 'Alternative Model'

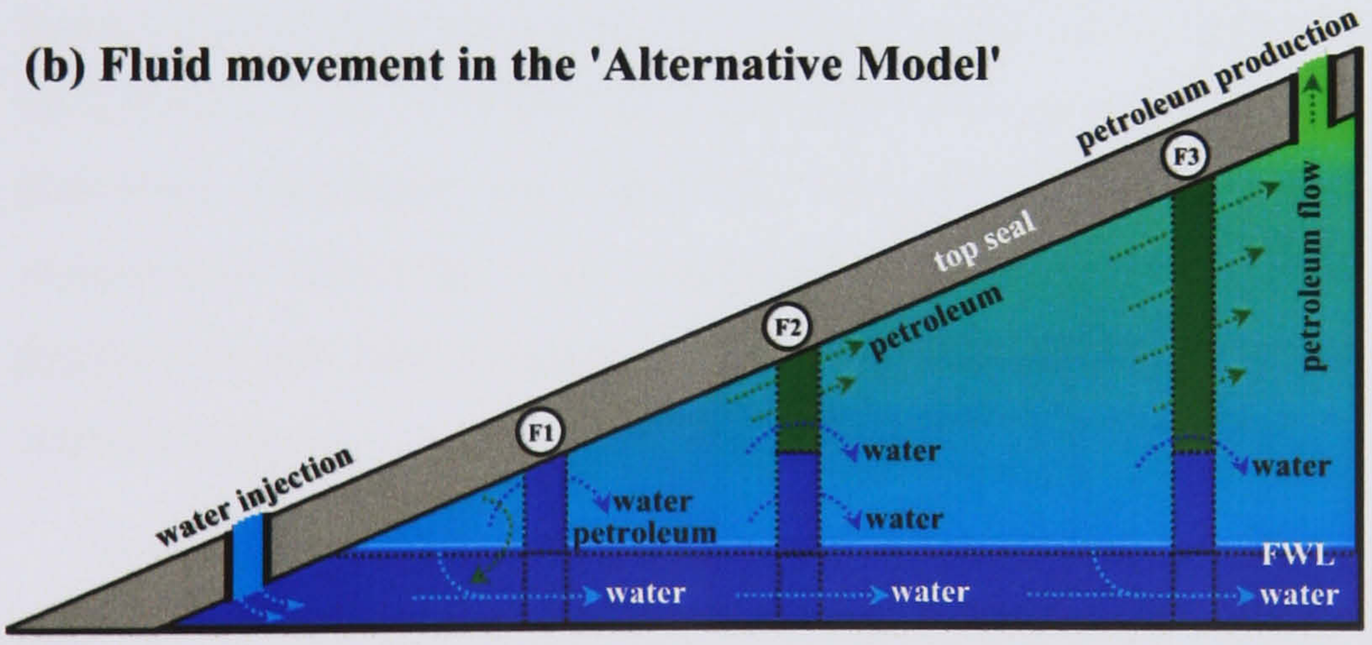

Fig. 5.19. Two models depicting the paths for fluid movement in **(a)** the 'New-fault *TM* Model' and **(b)** the proposed 'Alternative Model'.

5.7. Conclusions

Microstructural and petrophysical fault rock measurements do not only provide a platform for the assessment of fault rock development in the field (**Chapter 4**); here they have been used as a basis for calculating the input parameters required to account for the effect of faults on fluid flow for production simulation models. Different fault representations of the Pierce Field faulted

model were simulated to test the validity of each model by comparing the simulated results against about 8 years of history production data. Changing the fault distributions and fluid flow properties using the conventional method (*i.e.* changing properties by trial and error to gain a history match) can be a misleading process when predicting the future performance of a reservoir. This is because the history matching process is an inevitably non-unique process. Basing fault representations on geological and laboratory studies reduces the expected non-uniqueness in history matches and provides more confidence in the future predicted results. It is worth mentioning that some Pierce faults were originally modelled as sealing to account for the observed differences in FWLs and compartmentalisation across the field. This study of fault rock properties has concluded that completely sealing faults are unlikely in Pierce because average values of measured fault and host rock permeabilities suggest a *TM* of about 0.5 (using an average fault thickness of 1 ft and typical host grid-block geometries from the Pierce simulation model). Faults with such a *TM* value possibly do not affect fluid flow dramatically. Thus, in effect, this study has helped in reservoir characterisation.

Time-lapse seismic studies have the potential to image changes in fluid composition and pressure within the subsurface, thus providing valuable data to history match production simulation models in a more unique manner. Reservoir simulations provide the link between the observed changes in seismic attributes, the produced fluids, and the actual fluid dynamics within a reservoir. This can assist in understanding the past history of the reservoir, and, more importantly, in making the best of its future.

This chapter has illustrated the possible potential hazards that can arise from misrepresenting faults for production simulation modelling. Placing, what could actually be, a false fault based on a forced match of limited historical well data can result in a misleading predicted trapped petroleum distribution and, therefore, can cost a company millions of pounds by drilling unnecessary wells. The work conducted during this study suggests that 4D seismic has the potential to test fault property models, which in turn leads to a more predictive production simulation model.

To overcome some of the limitations, mainly caused by the possibility of some unnatural pathways for different phases in the 'New-fault *TM* Model', an alternative model was proposed based on using scaled directional, irreversible, relative permeability curves to control fluid movement in different parts of the fault. The new 'Alternative Model' gave similar results, and, therefore, similar conclusions to those drawn from the 'New-fault TM Model'. The similarities between the two models can be mainly attributed to the high mobility of petroleum and the small difference both fault representations can cause to the overall water flow rates and reservoir pressures, especially for the Pierce Field with the relatively high fault permeabilities as derived from the Manzocchi *et al.* (1999) relationships.

Chapter 6

Pseudofunctions generation using a simple two-cell model

"Compared to a dry hole, fault seal analysis is an inexpensive technique people can employ to test geological interpretations of fault networks. In a number of companies, fault seal is becoming a necessary task that prospect groups have to go through. At some of the majors, you have to demonstrate that fault seal has been taken into account and analyzed - if appropriate - before drilling is approved"

Graham Yielding

Technology Director at Badleys Geosciences

6.1. Introduction

Upscaling is a mathematical process in reservoir simulation which aims to calculate effective reservoir properties for a coarse-scale grid that usually has blocks several times larger than the fine scale in which the geological and petrophysical descriptions are generated (Christie, 1996; Ewing, 1997). Often reservoir properties are described at small scales (often several million cells) to capture variations observed in cores, logs, geological models and seismic data. However, the resolution of models needed for other applications, such as flow simulations, is much coarser (generally 10000–100000 cells) because the maximum number of grid blocks that can be used is limited by computer resources. Recently, with the advent of more sophisticated gridding algorithms in flow simulators, such as corner point geometry (**chapter 2**) and local grid refinements (**chapter 3**), it is possible to tailor grids to account for complexities, such as faults.

Although single-phase upscaling is fairly well understood (Renard *et al.*, 1997), this is not the case for two-phase upscaling (Pickup *et al.*, 1996). Two-phase upscaling is not merely upscaling static properties, *e.g.* permeability, transmissibility, porosity, *etc.*, but it involves upscaling dynamic properties such as relative permeability and capillary pressure. The effective relative permeability and capillary pressure curves are referred to as dynamic pseudofunctions. The word 'dynamic' implies that these effective properties, or pseudo properties as we refer to them in this chapter, change though time as a function of their saturation dependence. Many different methods for developing pseudo-relative permeability and capillary pressure curves have been reported in the literature (Barker *et al.*, 1997).

A number of recent studies (Barker *et al.*, 1996, 1997; Darman *et al.*, 2001) have reviewed the accuracies and merits of the different two-phase upscaling techniques currently available for

simple heterogeneities. Other studies, *e.g.* Coll *et al.* (2001), compared the accuracy of different pseudofunction methods to predict the effect of more complicated heterogeneities. Most of these studies concluded that the best pseudoisation method to use for a particular problem will depend upon the flow regime, *i.e.* viscous-, gravity- or capillary-dominated flow. For example, steady-state pseudos (Smith, 1991) can be used for capillary-dominated flows, *e.g.* those characterised by low flow rates. On the other hand, dynamic methods are usually used to model the effects of heterogeneities upon viscous-dominated flows, *e.g.* those characterised by high flow rates. In general, many studies characterise the relative importance of viscous, gravity, and capillary forces on reservoir flow in terms of the Bond number (ratio of gravity to capillary forces), gravity number (ratio of gravity to viscous forces) and the capillary number (ratio of capillary to viscous forces). There are many definitions for these dimensionless numbers reported in the literature (*e.g.* de Riz *et al.*, 1997; Sorbie, 1992). In homogeneous reservoirs, the dominant flow regime can be determined from an examination of the relevant dimensionless numbers (*e.g.* Rapoport, 1955; Shook *et al.*, 1992).

This chapter starts by presenting four commonly used dynamic pseudofunctions and evaluates their relative accuracies. Although the evaluation of various dynamic pseudofunctions has been intensively studied by many authors, there are no common guidelines published, as each dynamic pseudofunction is case dependent (see John *et al.*, 1999). Furthermore, the type of upscaling for this specific study is slightly different from that commonly studied in the literature. In particular, in contrast to the common use of complex models for dynamic pseudo-curve generation, simple two-cell models are used in this study to allow us to test as many variables as possible that affect pseudo-curve generation, *e.g.* flow rates, fault rock thickness, host/fault permeability contrast.

Dynamic pseudofunctions are generally used to reduce the size of 3D, multiphase simulation models, *i.e.* directional pseudo-curves are generated for every coarse grid block subjected to flow across any of its faces. Here, we attempt to generate effective pseudo-curves for host cells that are separated by faults with completely different relative permeability and capillary pressure curves. The process is performed to capture flow behaviour across faults without the need to include faults discretely in simulation models. We refer to these generated pseudo-curves as 'fault-pseudo' curves. The chapter will also examine the relative stability of each dynamic pseudofunction tested and outline any associated problem when generating fault-pseudo curves.

6.2. Dynamic pseudofunctions

The four commonly used pseudofunctions are:

- Kyte and Berry (K&B)
- Pore-volume weighted (PVW)

- Weighted relative permeability (WKR)
- Stone

The following sections, **§ 6.2.1** to **§ 6.2.4**, outline the formulation and the main features of each pseudofunction for the purpose of the special upscaling techniques addressed in this study. For a more comprehensive and general review on some of these methods and their use for a more general dynamic upscaling, the reader is referred to the work of Barker and Dupouy (1999), presenting a comparison among five different methods of dynamic pseudo relative permeability, and Baker and Thibeau (1996), reviewing the use of pseudo relative permeability for upscaling. A more general description can also be found in the Schlumberger Geoquest manual of the pseudoisation program (Geoquest, 2003).

6.2.1. Kyte and Berry (K&B)

The Kyte and Berry (1975) method, hereinafter referred to as the K&B method, is one of the most popular methods used to generated dynamic pseudo curves; including both pseudo-relative permeability and pseudo-capillary pressure curves. The method is based on averaging pressures for each coarse grid block and the total flow rates of each phase between each pair of adjacent coarse grid blocks. Fine grid simulation results are used as a direct input into the coarse grid two-phase Darcy law to infer pseudo-relative permeability and pseudo-capillary pressure values at each averaged saturation point. For example, consider a 1D water phase flow along the x-direction in an oil/water system (**Fig. 6.1**).

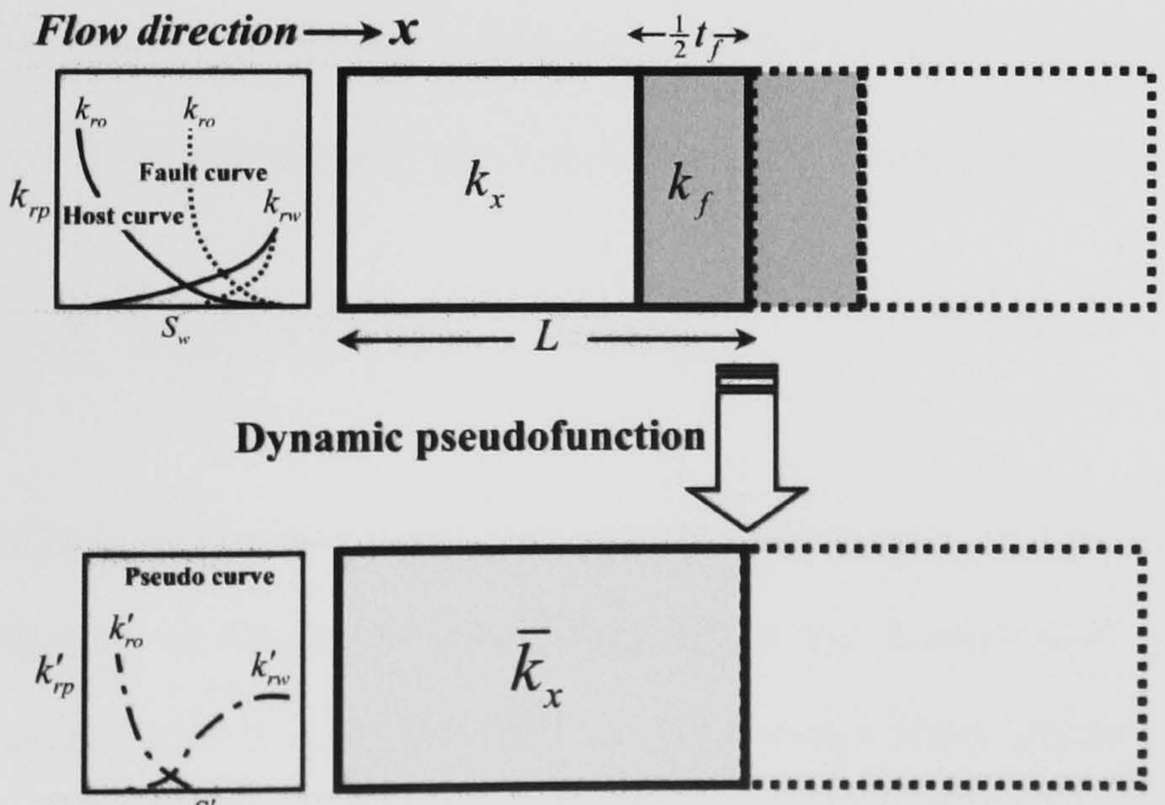

Fig. 6.1. 1D upscaling of faulted cells. Note that only half of the fault thickness contributes to each upscaled coarse grid block

The 'pseudo' relative permeability (k'_{rw}) is defined from Darcy's law as:

$$k'_{rw} = -\frac{\bar{B}_w \bar{\mu}_w \bar{q}_w L}{A \bar{k}_x \Delta \bar{\Phi}_w} \qquad \textbf{6.1}$$

where $\overline{\mu}_w$ and $\overline{B}_w$ are, respectively, the appropriately weighted (usually pore-volume weighted) viscosity and formation volume factor of water in the coarse grid block, A is the cross-sectional area ($\Delta y \times \Delta z$) of the coarse grid block, and L is the centre-to-centre neighbouring coarse grid block distance in the x-direction. For identical host cells each incorporating half of the fault material, L can also be expressed as the total length of each upscaled coarse grid block. Here $\overline{k}_x$ is an appropriately-weighted absolute permeability of the combined host and fault materials between the two upscaled coarse grid blocks, which, for a homogeneous host rock separated by a fault whose thickness is equally divided between the two host cells, is obtained as follows:

$$\overline{k}_x = \frac{L}{\frac{L - \frac{1}{2}t_f}{k_x} + \frac{\frac{1}{2}t_f}{k_f}} \qquad \textbf{6.2}$$

where k_x is the x-directional permeability of the host rock, and t_f and k_f are, respectively, the fault thickness and the x-directional permeability of the fault material. Note that, for situations in which the permeability is heterogeneous, the host permeabilities at both sides of the fault must be considered separately and combined harmonically in the final averaged permeability used in **equation-6.1**. Note also that, for our purpose of upscaling, only half of the fault thickness contributes to each upscaled coarse grid block, see **Fig. 6.1** and **§6.3.3** for more details. The value $\overline{q}_w$ is the appropriate sum of the fine grid flows, and the potential difference ($\Delta\overline{\Phi}_w$) between any two neighbouring coarse grid blocks is estimated from:

$$\Delta\overline{\Phi}_w = \Delta\overline{P}_w - g\overline{\rho}_w\Delta D \qquad \textbf{6.3}$$

where g is the acceleration due to gravity, $\overline{\rho}_w$ is the (usually pore-volume weighted) water density of the coarse grid block, ΔD is the central depth difference between two neighbouring coarse grid blocks, and $\Delta\overline{P}_w$ is the average water phase pressure difference between any two neighbouring coarse grid blocks. The water phase pressure ($\overline{P}_w$) of each coarse grid block is calculated by the weighted average over the central plane of fine grid cells:

$$\overline{P}_w = \frac{\left[kk_{rw}\Delta z(P_w - g\rho_w D)\right]_{i=centre}}{\left[kk_{rw}\Delta z\right]_{i=centre}} \qquad \textbf{6.4}$$

where in the weighting factor ($kk_{rw}\Delta z$), k is the absolute permeability and k_{rw} is the relative permeability to water. Note that the subscript ($i = centre$) means that only the values of the i^{th} fine grid cells that coincide with the centre of the corresponding coarse grid block are used. If, however, the centre coincides with a boundary between two fine grid cells, the average values between these two fine grid cells are used. The corresponding pseudo-capillary ($P_c^{'}$) pressure in each coarse grid block is:

$$P_c^{'} = \overline{P}_w - \overline{P}_o \qquad \textbf{6.5}$$

It has been noted by many authors, *e.g.* Stone (1991) and Barker and Dupouy (1999), that if $\Delta\overline{\Phi}_w$ has the same sign as $\overline{q}_w$ then a negative $k_{rw}^{'}$ arises, and if $\Delta\overline{\Phi}_w$ is zero then $k_{rw}^{'}$ is infinite. Both of these situations can occur, and this is the root of most problems specific to the K&B method (Stone, 1991). John *et al.* (1999) noted that the use of a different weighting factor for each phase in **equation-6.5** means that a non-zero pseudo-capillary pressure can arise when there is no fine grid capillary pressure. Barker and Dupouy (1999) also noted that averaging over the central plane of fine grid cells implies different capillary pressures for different flow directions can result from this pseudoisation method. However, most of the current simulators, *e.g.* **Eclipse 100™**, do not handle the use of directional capillary pressures.

6.2.2. Pore-volume weighted (PVW)

The pore-volume weighted (PVW; Geoquest, 2003) method is similar to the K&B method with the exception that it uses a different average phase pressure weighting. As its name implies, this method uses a pore-volume weighted average over the entire coarse grid block to calculate upscaled pressures. For example, the pore-volume weighted pressure of the water phase in each coarse grid cell is:

$$\overline{P}_w = \frac{\sum_{i=I_i}^{i=I_f} V_i (P_{wi} - g\rho_{wi}(D_i - \overline{D}))}{\sum_{i=I_i}^{i=I_f} V_i} \qquad \textbf{6.6}$$

where the sum is over all the fine grid cells contained within each upscaled coarse grid block between the inlet fine grid cell (i=I_i) and the outlet fine grid cell (i=I_f). $\overline{D}$ is an appropriately averaged central depth of all fine grid cells and V_i is the pore volume of each fine grid cell, which is, for each cell i, defined as:

$$V_i = \Delta x_i \Delta y_i \Delta z_i \phi_i \qquad \textbf{6.7}$$

where ϕ_i is the porosity of the fine grid cell *i*.

A number of authors, *e.g.* Stone (1991); Barker *et al.* (1996) and Barker and Dupouy (1999), view the above formulation of the PVW method, **equation-6.6**, as a clear improvement over the original K&B method, since it overcomes some of the associated problems with the K&B method mentioned earlier. With this definition, the $P_c^{'}$ is the same for all directions and is zero if there is no fine grid capillary pressure. From its definition, this method should allow the fine grid solution to be exactly reproduced on a coarse grid, but the problem of negative or infinite pseudo-relative permeabilities remains (Barker and Dupouy, 1999). In addition, when addressing a similar upscaling case to that considered in this study, *i.e.* a low fault material with high capillary pressure curve embedded within relatively much lower host cells at both sides with low capillary pressure curves (**Fig. 6.1**), Manzocchi *et al.* (2002) noted that the PVW pressure average has the effect of smearing the high capillary pressure region of the fault throughout the upscaled grid block in the upstream side of the fault. Therefore, during typical water flooding, this smearing effect can result in oil flow restriction into the fault upstream grid block from the rest of the upstream side cells.

6.2.3. Weighted relative permeability (WKR)

A very different and less popular method in comparison to the two above-mentioned methods, the weighted relative permeability (WKR; Geoquest, 2003) pseudos concentrate on saturation effects. The method is based on the fact that the dominant effect in determining the flow of a phase between two coarse grid cells is the phase-relative permeability values over the upstream[1] face of the cell (Barker and Dupouy, 1999). Accordingly, the pseudo is defined as a weighted sum of these values. The weighting factor should reflect the relative importance of each fine grid cell, and so is taken as the transmissibility value across the interface to the upstream coarse cell. In this method, the pseudo-relative permeabilities are obtained as follows:

$$k_{rw}^{'} = \frac{(T_x k_{rw})_{i=1_f}}{(T_x)_{i=1_f}} \qquad \textbf{6.8}$$

where T_x is the *x*-directional transmissibility (**Chapter 2**) of the fine grid cell on the outlet face of the upscaled coarse grid block.

These pseudos are rather coarser than the K&B type, as they ignore differences in pressure across various parts of the upstream face (Barker and Dupouy, 1999). In situations that are

[1] Note that the definition of upstream and downstream cells is flow direction dependent (*i.e.* a grid block may act simultaneously as an upstream and downstream cell if the flow of a specific phase reverses direction).

conducive for pseudo generation (large pressure differences dominating gravity effects, and small pressure variations over the coarse grid cells) these give similar results to the K&B approach, but in adverse conditions they will often yield much better results (Coll *et al.*, 1999). The pseudo-capillary pressures are obtained in the same manner as for the PVW pseudos.

6.2.4. Stone

Stone (Stone, 1991) presented a pseudofunction method that is based on an average total mobility in an attempt to avoid calculating phase potential, or average pressures, on the coarser grid, as required by the K&B method. In this method, the fractional flow of the water phase, for example, is matched at the coarse and fine grid boundaries to obtain pseudo-relative permeabilities:

$$k_{rw}^{'} = \bar{\mu}_w \bar{f}_w \bar{\lambda}_t \qquad \textbf{6.9}$$

and

$$k_{ro}^{'} = \bar{\mu}_o (1 - \bar{f}_w) \bar{\lambda}_t \qquad \textbf{6.10}$$

where the average fractional flow of water ($\bar{f}_w$) is:

$$\bar{f}_w = \frac{\bar{q}_w}{\bar{q}_w + \bar{q}_o} \qquad \textbf{6.11}$$

and $\bar{q}_w$ and $\bar{q}_o$ are the flow rates of water and oil, respectively, obtained by summation of the fine grid flows at the interface of the coarse grid block. The averaging of total mobility ($\bar{\lambda}_t$) is only over the outlet face of the coarse grid block:

$$\bar{\lambda}_t = \frac{(T_x \lambda_t)_{i=I_f}}{(T_x)_{i=I_f}} \qquad \textbf{6.12}$$

with

$$\lambda_t = \lambda_w + \lambda_o \qquad \textbf{6.13}$$

and the mobility of the water phase (λ_w) is defined as:

$$\lambda_w = \frac{k_{rw}}{\mu_w} \qquad \textbf{6.14}$$

with the same expression for the oil phase.

In the cases of capillary-dominated and/or gravity-dominated flows, or significant variations in total mobility, the Stone pseudofunction may fail to reproduce the fine grid results on the coarse grid (Barker and Dupouy, 1999). This is because the formulae for obtaining the pseudo-relative permeabilities (**equation-6.9** and **6.10**) neglect the effect of gravity and capillary pressure on the coarse grid. Furthermore, Baker and Fayers (1991) noted that the averaging of total mobility (**equation-6.12**) is only performed over the outlet face of the upscaled coarse grid block, which is inadequate when there are significant variations in total mobility between sub-fine-grid cells.

6.2.5. Other dynamic pseudofunction methods

In addition to the methods outlined above, there are several other ways to generate pseudos that are less commonly used but can reproduce the fine grid solution in some restricted conditions. Total mobility methods, similar to Stone's but using a different definition of the average total mobility, have been proposed by several authors (Baker and Fayers, 1991; Hewett and Behrens, 1991; Christie *et al.*, 1995). In the total mobility method proposed by Christie *et al.* (1995), coarse grid gravity effects are taken into account. The attraction of this method is that it may be useful in some cases where the K&B or the PVW pseudos are unusable (*i.e.* the problem of directional and phase-dependent pseudo-capillary pressures in the K&B and the problem of negative or infinite pseudo-relative permeabilities in the PVW method). Although this method makes a minimum of approximations, it does not guarantee reproduction of the fine grid solution on the coarse grid; negative values of pseudo-relative permeability can occur if the phases are flowing in opposite directions. Furthermore, this method does not usually reproduce average pressure gradients and out-of-range pseudo-relative permeability values (*i.e.* greater than the end points) can occur (Baker *et al.*, 1996). The quasi-steady state method is one in which the permeability of each phase (kk_r) is upscaled (by solution of a Laplace equation, for example) and weighted by the upscaled absolute permeability (Alabert and Corre, 1991; Smith, 1991; Sadd *et al.*, 1995). This method has been shown to be inapplicable in viscous dominated cases, which generally involve displacements of a frontal nature (Barker and Dupouy, 1999). Only when the saturation fronts are favourably smoothed out by capillary forces might the method be reliable (Barker *et al.*, 1996). Other methods that are considered to be a simple variant of the K&B and have essentially the same properties and pros and cons of that method are the method of Jacks *et al.* (1973) and the flux-weighted potential method of Guzman *et al.*

(1994). Dale *et al.* (1997) showed that in 1D, an analytical solution exists for rate-dependent steady-state pseudo-relative permeability and pseudo-capillary pressure functions. Manzocchi *et al.* (2002) noted that Dale's analytical method is potentially appealing; hence fine-scale flow simulation may not be necessary to determine the pseudos.

6.3. Generating pseudofunction curves for low permeability rocks

In this section, pseudofunction curves are generated for low permeability faults (~ 0.001 mD) for an oil/water system. The model used is very simple 1D model consisting of two coarse grid blocks separated by a narrow region of high capillary pressure fault rock. The generated pseudo curves depend on many factors, *e.g.* both fault and host cell geometries, rock permeabilities, net-to-gross ratios, relative permeability and capillary pressure curves, drainage and imbibition processes, fluid properties, and on the across-fault total Darcy flow rates (Manzzochi *et al.*, 2002). In this study, however, only a few of these factors will be examined. The simplicity of the model used, two grid blocks separated by fault material, enables us to vary the tested factors with great ease for the purpose of comparison.

6.3.1. Model description

A 1D, two-phase, oil–water, model was used to upscale the multiphase behaviour, *i.e.* relative permeability and capillary pressure data, of a 3 ft-thick and 0.001 mD-permeability fault zone. The fault is embedded in a host rock with a permeability of 1000 mD. The model geometry is illustrated in **Fig. 6.2**. The water and oil viscosities are 0.5 cP and 5 cP, respectively, and the model is initially water saturated to a residual oil saturation of 0.15. Although this implies that the model has already been swept, this setup was done to map the full range of water saturations in the upstream side of the fault, for the purpose of pseudo-curve generation, by injecting both oil and water (see next section). If the model is initially oil saturated and water is injected, capillary trapping limits the maximum water saturation in the upstream side of the fault to a lower value by trapping oil. The relative permeability and capillary pressure curves were derived using the same empirical relationship between capillary pressure, porosity and permeability as that used by Ringrose *et al.* (1993), for the host rock, and Manzocchi *et al.* (2002), for the fault rock, see **Chapter 3**. Imbibition capillary pressure curves for the undeformed reservoir and fault rock are displayed in **Fig. 6.3**. Local grid refinements, LGRs, are applied around the fault to increase solution accuracy and simulation stability (see **Chapter 3** and **Appendix C**).

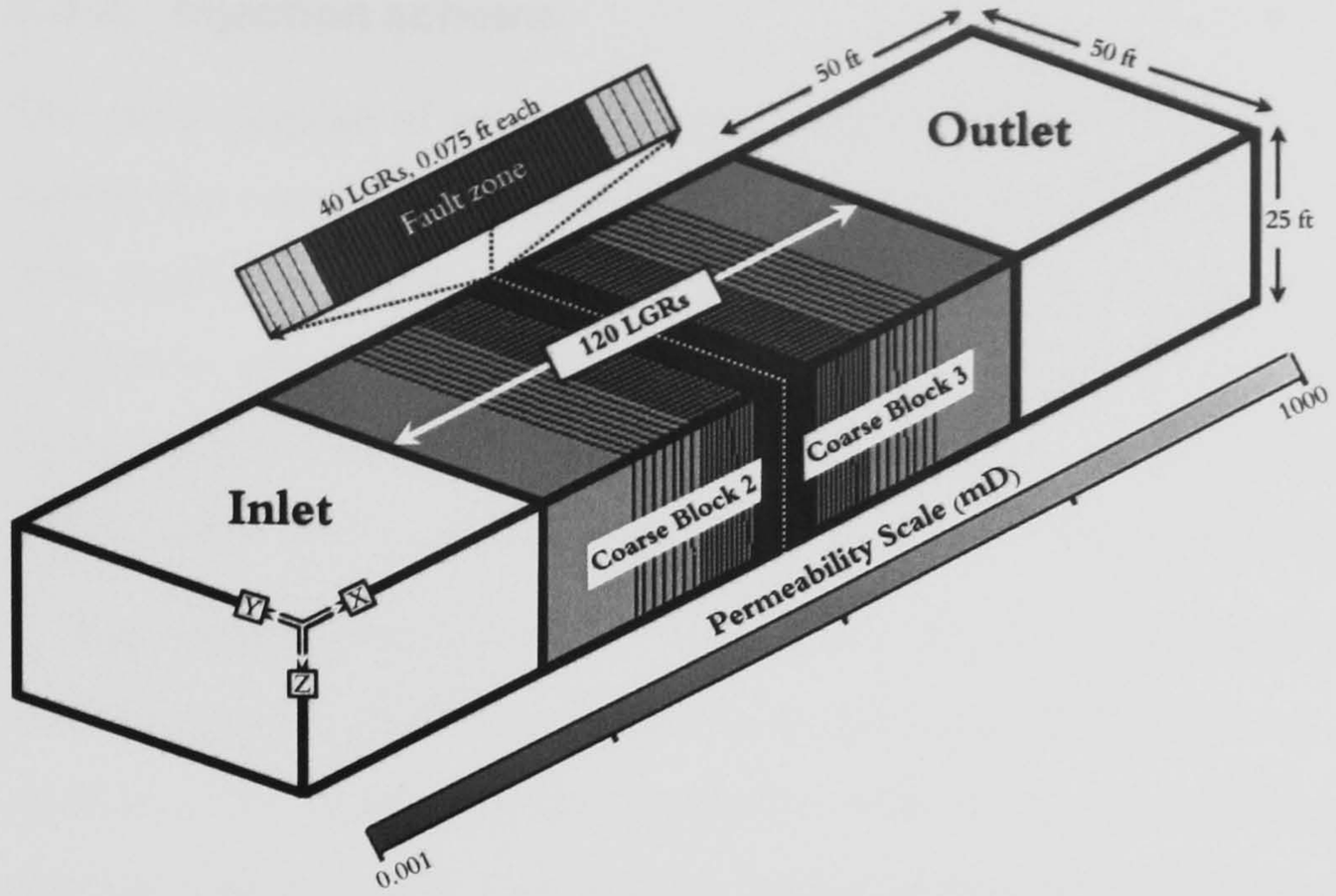

Fig. 6.2. Discrete model geometry

The model inlet is given a very high permeability, but a very low porosity to allow for the inlet end effect. A zero capillary pressure curve is used for the inlet so that no increase in pressure is required for fluid to enter even the smallest pore space in this system. On the other hand, a very large pore volume is used for the outlet to act as an infinite consumer to expelled fluids. The large volume of the outlet cell retains its initial pressure throughout the simulation; this is equivalent to producing fluids from that cell using a well with a bottom hole pressure (BHP) lower limit equal to the outlet pressure. To allow for end effects in this side of the model, a zero capillary pressure curve is used.

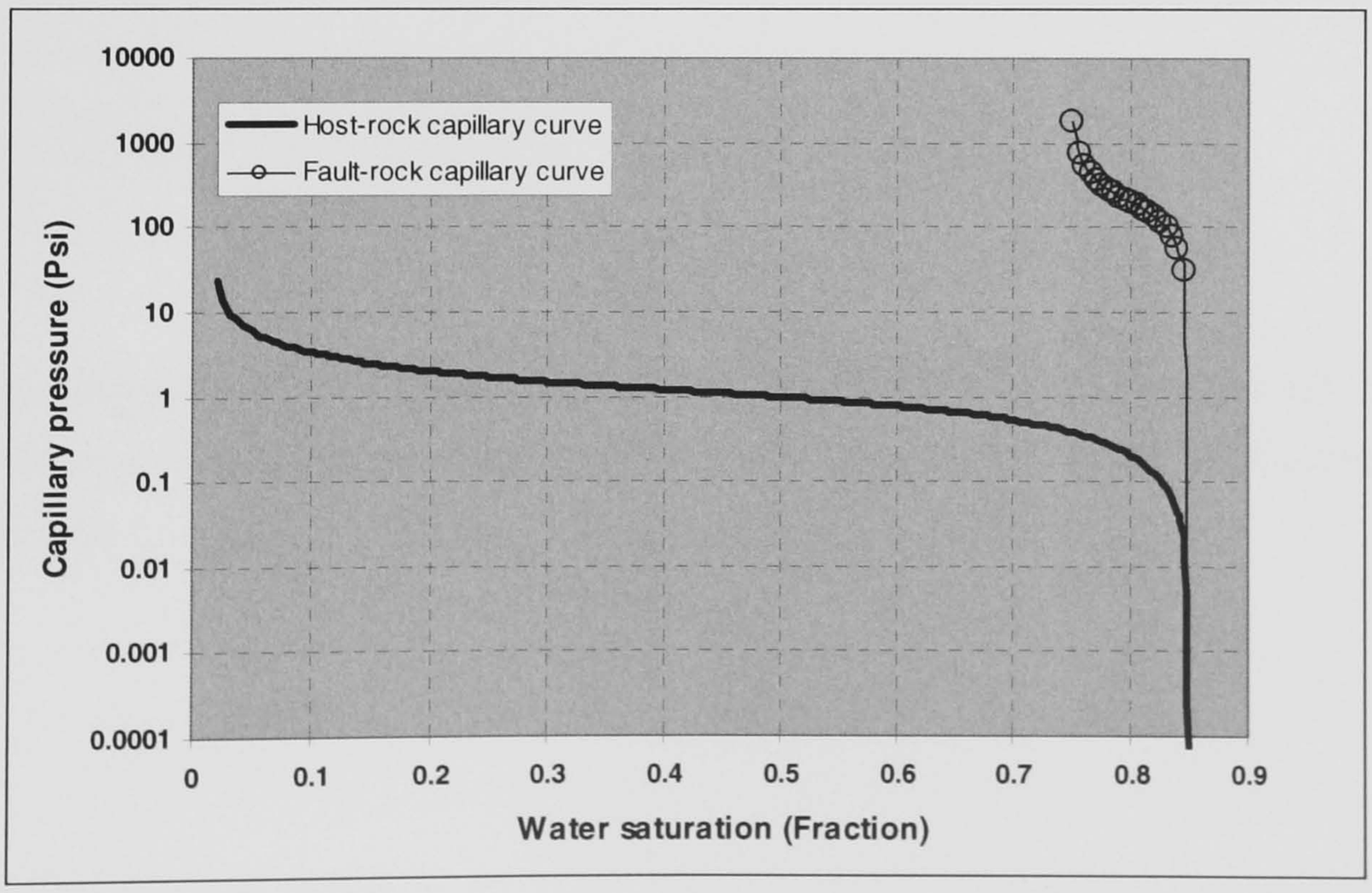

Fig. 6.3. Imbibition capillary pressure curves for the undeformed reservoir and fault rock.

6.3.2. Injection scheme

The main purpose of generating pseudo-curves for fault rocks is to create saturation function curves that carry the characteristics of the multiphase behaviour of fault rocks. These curves are very useful in simulation when modelling the effect of faults on multiphase flow. This usefulness arises from the fact that these curves can be attached to the cells that juxtapose the faults (mainly fault upstream cells) without the need to include the fault zone in the model, which can be a very time consuming process, both for the user and the simulator.

For these generated curves to be standard and useful, they must cover the complete possible saturation range (from irreducible water saturation to residual oil saturation, for an oil/water system). This means that the simulation must be run for enough time to make sure that the average saturation, *e.g.* pore-volume weighted saturations of the fault and the host cells, cover the desired range. To ensure that these saturations are obtained during the simulation run, the relative permeability curve of the upstream fault cell is converted to a corresponding fractional flow curve. The reason this is done becomes clearer when the process of pseudoisation is understood. To construct a single point on the pseudo curve, water saturation is first averaged using pore-volume weighting of both the host and the fault cell saturations. Since the pore volume of the fault rock is much smaller than that of the host rock, the saturation of the latter always domains the weighting. The relative permeability curve of a particular cell enables us to control the saturation in that cell during simulation by controlling the fractional flow. The relative permeability curve of the upstream fault cell is converted to fractional flow using fluid viscosities according to the following equation:

$$(f_w)_{S_w} = \frac{q_w}{q_w + q_o} = 1 \Big/ \left(1 + \frac{(k_{ro})_{S_w}}{(k_{rw})_{S_w}} \times \frac{\mu_w}{\mu_o} \right) \qquad \textbf{6.15}$$

This transformation is shown graphically below, **Fig. 6.4**, for a water-wet relative permeability curve derived using Ringrose's (Ringrose *et al.*, 1993) derivation, for a host rock permeability of 1000 mD.

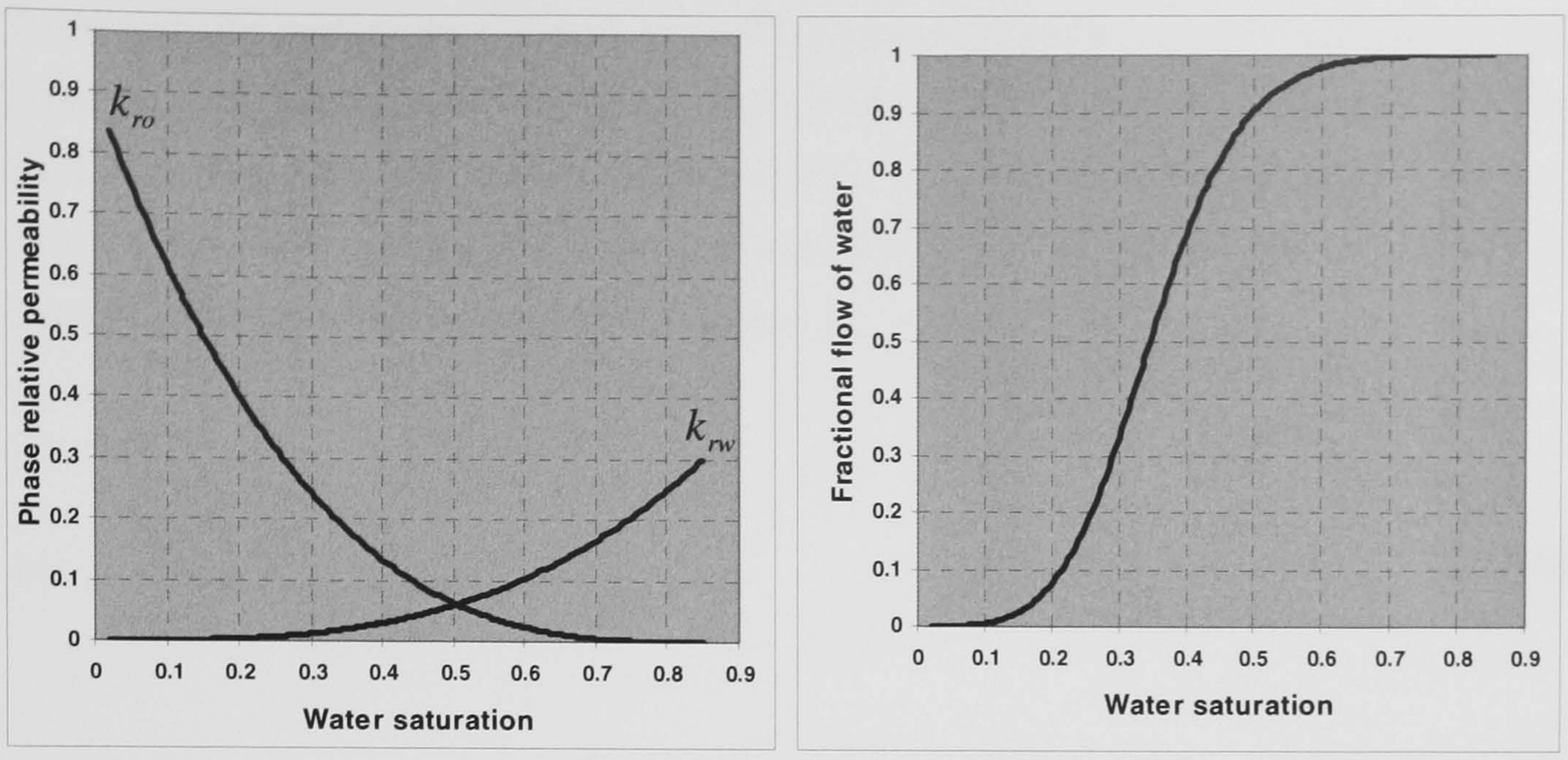

Fig. 6.4. Converting relative-permeability curves to fractional flows using **equation-6.15**

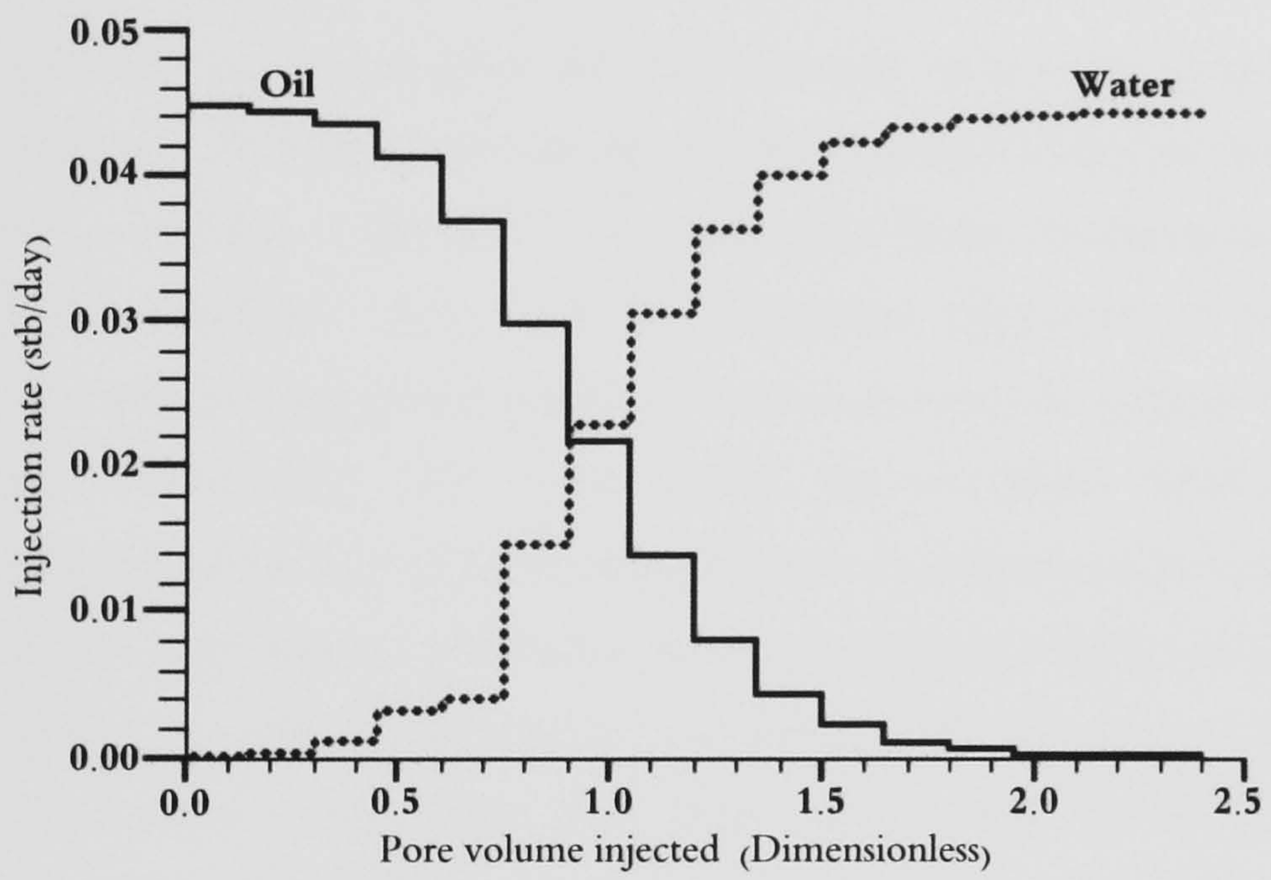

Fig. 6.5. Fractional injection scheme for the model described in **Fig. 6.2**.

The fractional flow curve shown in **Fig. 6.4** can be used to control the saturation range of the generated pseudo-relative permeability curve. For example, the curve shows that using a fractional flow of 0.1 ensures the appearance of a pseudo-relative value at about 0.2 water saturation in the generated pseudo-curve. For this model, this gives a total flow rate of 0.045 stb/day, which corresponds to a lateral Darcy velocity of approximately 2×10^{-4} ft/day for the model shown in **Fig. 6.1**. Ranges of fractional flows are used in the simulation to obtain water saturations at a resolution of 0.05 fraction. The fractional injection scheme is shown in **Fig. 6.5**.

The results of the fine-scale model presented above will be used to generate different pseudocurves, using some of the previously discussed pseudofunctions, that can be used to reproduce the same results in a coarse model without the need to include the fault as a 3D zone.

To compare the performance of each pseudofunction, an upscaled simulation run was performed using the new generated pseudo-curves attached to the upstream side of the fault (*i.e.* coarse block 2 in **Fig. 6.6**). The fault rock permeability and thickness were accounted for in the upscaled run using an absolute transmissibility multiplier, TM_{abs} (**Chapter 2**), derived from these data using the following expression (Manzocchi *et al.*, 1999):

$$TM_{abs} = \left(1 + \frac{t_f \left(\frac{2}{k_f} - \frac{1}{k_1} - \frac{1}{k_2} \right)}{\frac{L_1}{k_1} + \frac{L_2}{k_2}} \right)^{-1} \qquad \textbf{6.16}$$

where L_1 and L_2 are the lengths of the upstream and downstream cells, respectively, that juxtapose the fault, and k_1 and k_2 are the permeabilities of these cells. In this model, the upstream and downstream cells are identical, each with a length of 50 ft and permeability of 1000 mD. With this information, and the fault data presented above, **Equation-6.16** results in a TM_{abs} of about 0.1667×10^{-4}. Conventionally, faults are represented in simulation models using this single-phase TM_{abs} and the multiphase behaviour of faults, which in this study is represented using pseudofunction curves, is completely ignored. We refer to this latter model as the '*TM* model'. The model where the two-phase behaviour is accounted for using pseudofunction curves and TM_{abs}, **Fig. 6.6**, is referred to using the pseudofunction name. It is always important to understand the way simulators handle different representations of a fault, namely the *TM* and discrete representations. One can think of the discrete representation as a combination of two behaviours: static and dynamic. The static part is attributed to the static properties of the fault, *e.g.* permeability, thickness, storage, net-to-gross ratio, *etc.*, all of which can be used to derive the transmissibility across the fault. This is a static treatment because this derived resistance to the transmissibility of fluids between adjacent cells is independent of the saturation history of the phases present. The dynamic part, which is the important part that is usually ignored in the conventional *TM* representation, is the relative movement of the phases present within the fault region as a function of a given wetting phase, *i.e.* relative permeability and capillary pressure curves of the fault zone.

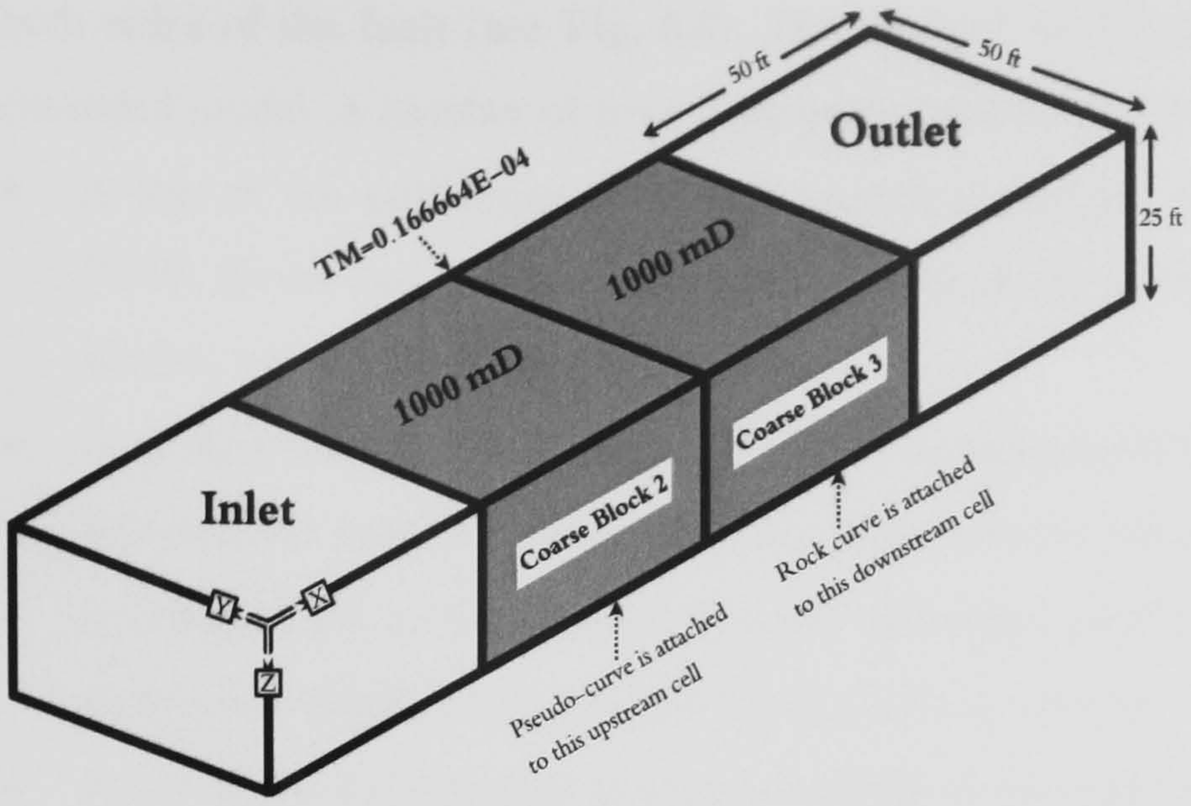

Fig. 6.6. An alternative model geometry to that shown in **Fig. 6.2** to account for faults multiphase behaviour using pseudo-curves.

6.3.3. Different methods of pseudo curves generation

6.3.3.1 Description of tests performed

The dynamic upscaling of pseudofunctions in this study is performed between host and fault material. In this section two different methods of upscaling are compared, namely using half of the fault material or all of the fault material (**Fig. 6.7**). The rectangular area represented by the thick line in **Fig. 6.7** represents the upscaled region in each case. Note that the amount of host rock material is kept identical within each upscaled coarse cell.

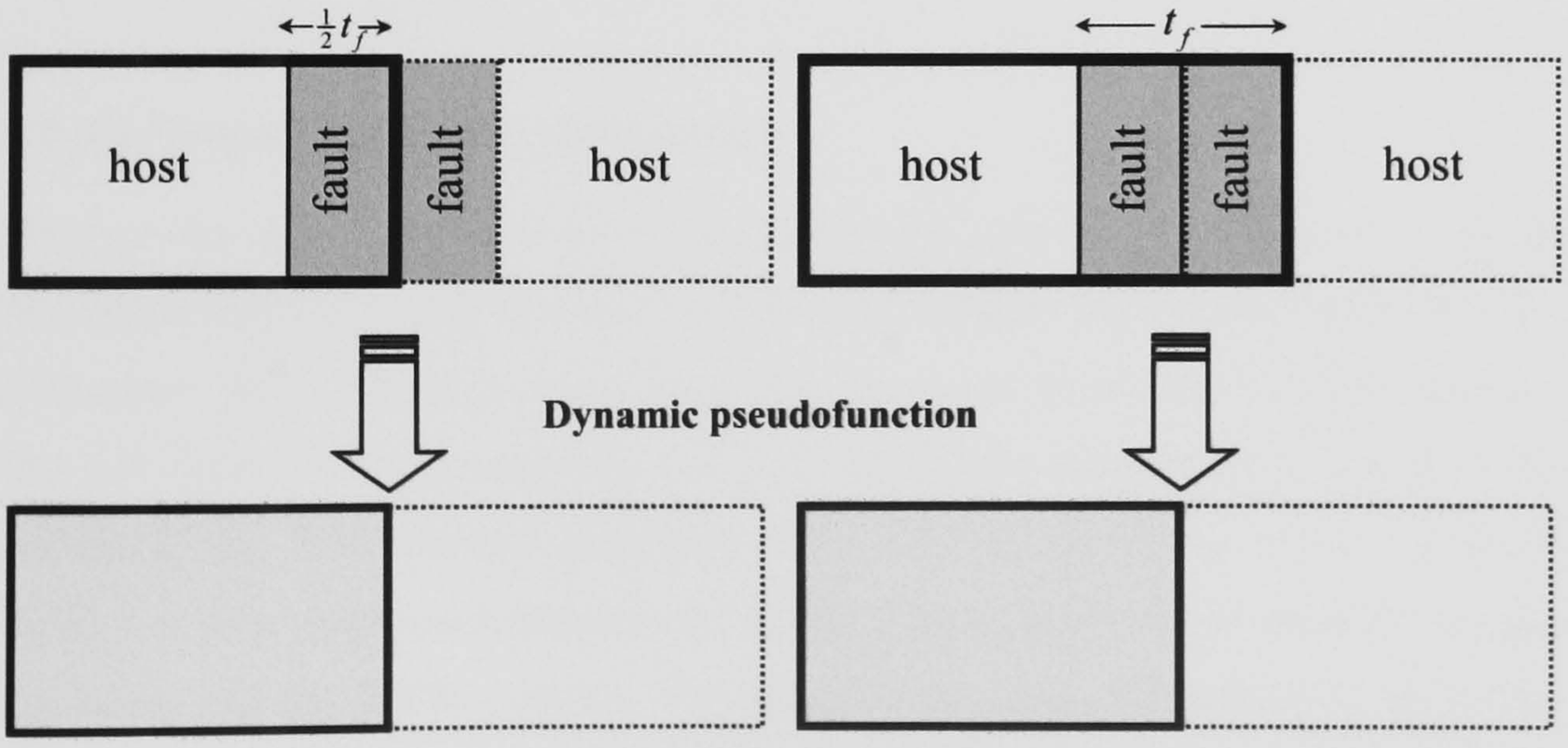

Fig. 6.7. A schematic diagram comparing two possible methods of pseudo generation, namely using half of the fault thickness (left), or using the full-fault thickness (right). Note that the host rock material is identical in each upscaled grid block.

To test the performance of each upscaling method presented in **Fig. 6.7**, the simple two-cell model described in **§ 6.3.1** was run using the injection scheme shown in **Fig. 6.5**. Furthermore, and to test the effects of each upscaling method on further cells in the upstream side of the fault, the model described in **§ 6.3.1** was extended along one direction by adding more host cells at

both sides of the fault (see **Fig. 6.8**). The original model properties are kept unaltered in the extended model. A number of tests were performed on this latter model including the following:

- A test of the performance of each upscaling method shown in **Fig. 6.7** using the K&B, PVW, Stone and WKR pseudoisation methods by comparing the results of the upscaled models with those of the discrete one.
- A comparison of the results of water saturation profiles in the two coarse grid blocks immediately upstream of the fault (*i.e.* Blocks 4 and 3 in **Fig. 6.8**).
- A comparison of the results of water saturation profiles using pseudo capillary pressure curves and unaltered parent grid block capillary curves.
- A test of the performance of each upscaling method shown in **Fig. 6.7** using a realistic water injection scheme with pseudo curves generated from the fractional injection scheme shown in **Fig. 6.5**. Both schemes retain the same total flow rate.

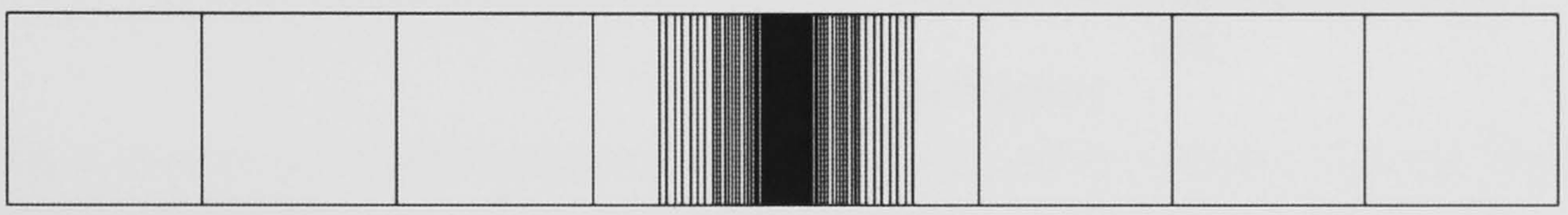

Inlet	Block 2	Block 3	Block 4	Block 5	Block 6	Block 7	Outlet

Fig. 6.8. An extended version of the simple model presented in **§ 6.3.1**.

6.3.3.2 Pseudofunctions comparison

The four dynamic pseudofunctions discussed in this chapter were generated using the results of the simple discrete model described in **§ 6.3.1** as input to the Geoquest pseudoisation program (Geoquest, 2003). Pseudos were generated using the fractional injection scheme shown in **Fig. 6.5**. **Figure 6.9** shows the host and fault rock relative permeability curves and the generated curves for the four different pseudofunctions for each upscaling method shown in **Fig. 6.7**. There is a very good match between the K&B method and the PVW pseudos, and also between the Stone and the WKR pseudos. The different upscaling methods have an influence on the shape of the pseudo relative permeability curves derived using the Stone or WKR methods. On the other hand, those curves generated from the K&B or PVW methods are only slightly affected by the different tested methods of upscaling. Generally, the generated curves using the half-fault thickness method are smoother than those generated using the full-fault thickness upscaling method. The generated pseudo-capillary curves are almost identical for all the four pseudofunctions and they tend to follow the original undeformed sediment curve shown in **Fig. 6.3**. The reliability of each generated pseudo curve will be investigated using the tests described in **§ 6.3.3.1**.

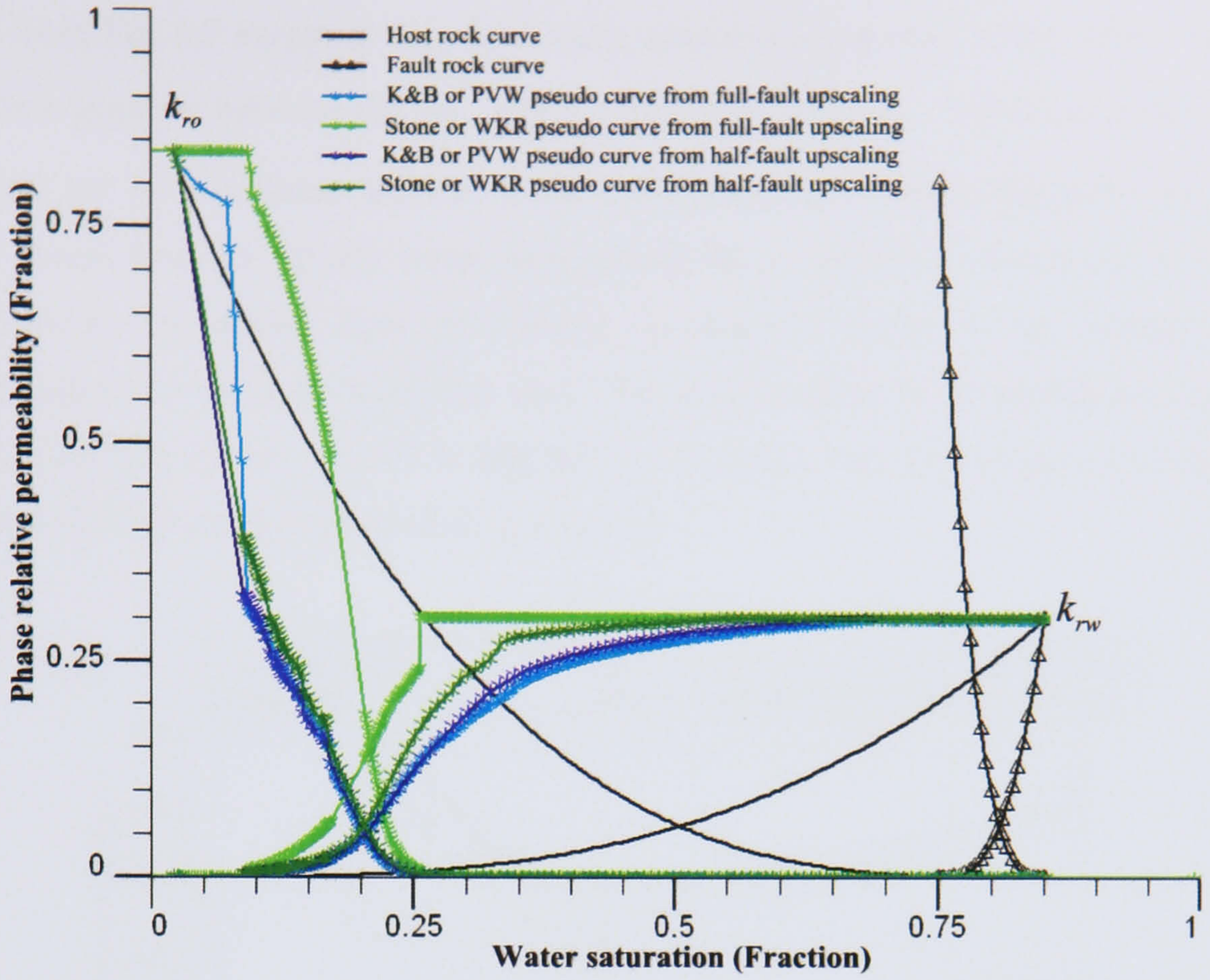

Fig. 6.9. A comparison of different pseudofunctions and upscaling methods. The host and fault curves are also shown.

6.3.3.3 Test results

Figure 6.10 compares the performance of each upscaling method, using the representation shown in **Fig. 6.7**, in duplicating the discrete model results. The results compare average water saturation and pressure in the coarse grid block upstream of the fault for the simple two-cell model described in **§ 6.3.1**. In this test the K&B and the PVW pseudoisation methods were used for each upscaling case. The tested pseudofunctions seem to perform very well using the two upscaling methods. A closer look at the results indicates that upscaling using the half-fault upscaling method gives a slightly closer match to the high-resolution discrete model than using the full-fault upscaling method.

Figures 6.11 to **6.13** show the results obtained over the extended 1D model. The model grid blocks are numbered as in **Fig. 6.8**. Saturation profiles are plotted as a function of model PVI for the coarse blocks 3 and 4 (**Fig. 6.8**). **Figure 6.11** compares the performance of both the K&B and the PVW pseudofunctions for the two upscaling techniques. The results of associating either the pseudo capillary pressure curves ($P_c^{'}$) or the parent grid block (*i.e.* the host grid block) unaltered capillary pressure curve (P_c) with the pseudo-relative permeability curves ($k_{rp}^{'}$) are compared for both the half-fault ($\frac{1}{2}t_f$) and full-fault (t_f) upscaling methods illustrated in **Fig. 6.7**. Note that the results of the K&B and the PVW are virtually identical for each upscaling method when their $k_{rp}^{'}$ curves are associated with the unaltered P_c. This was

expected from **Fig. 6.7** except at very low water saturation (less than ~7%), where differences may become apparent between the $\frac{1}{2}t_f$ and t_f upscaling methods. Similar tests are presented in **Fig. 6.12** but for the Stone and the WKR pseudofunctions. While **Fig. 6.11** and **Fig. 6.12** show the results from an initially water-saturated model subjected to a fractional flow scheme, **Fig. 6.13** shows the results from an initially oil-saturated model to the irreducible water saturation subject to the same total flow rate. The pseudo curves in all models were generated using the fractional scheme shown in **Fig. 6.5**. In all cases, and for comparison purposes, the results from the *TM* and discrete models are shown.

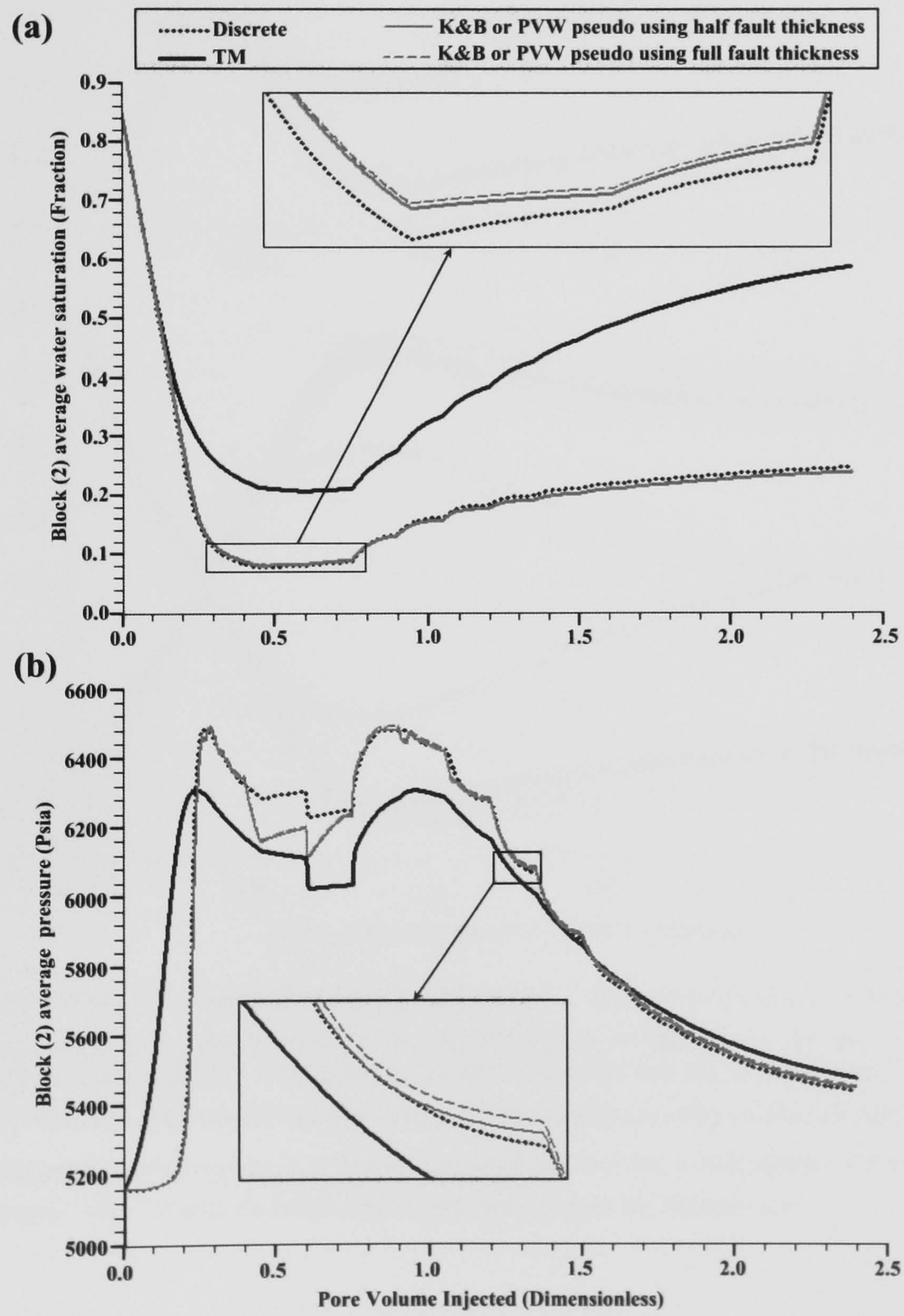

Fig. 6.10. Half-fault upscaling versus full-fault upscaling for a 3 ft thick fault: **(a)** average water saturation and **(b)** average pressure. Discrete and TM results are shown for comparison. The results compare the Block 2 average values for the discrete model (see **Fig. 6.2**) and the TM and pseudo models (see **Fig. 6.6**).

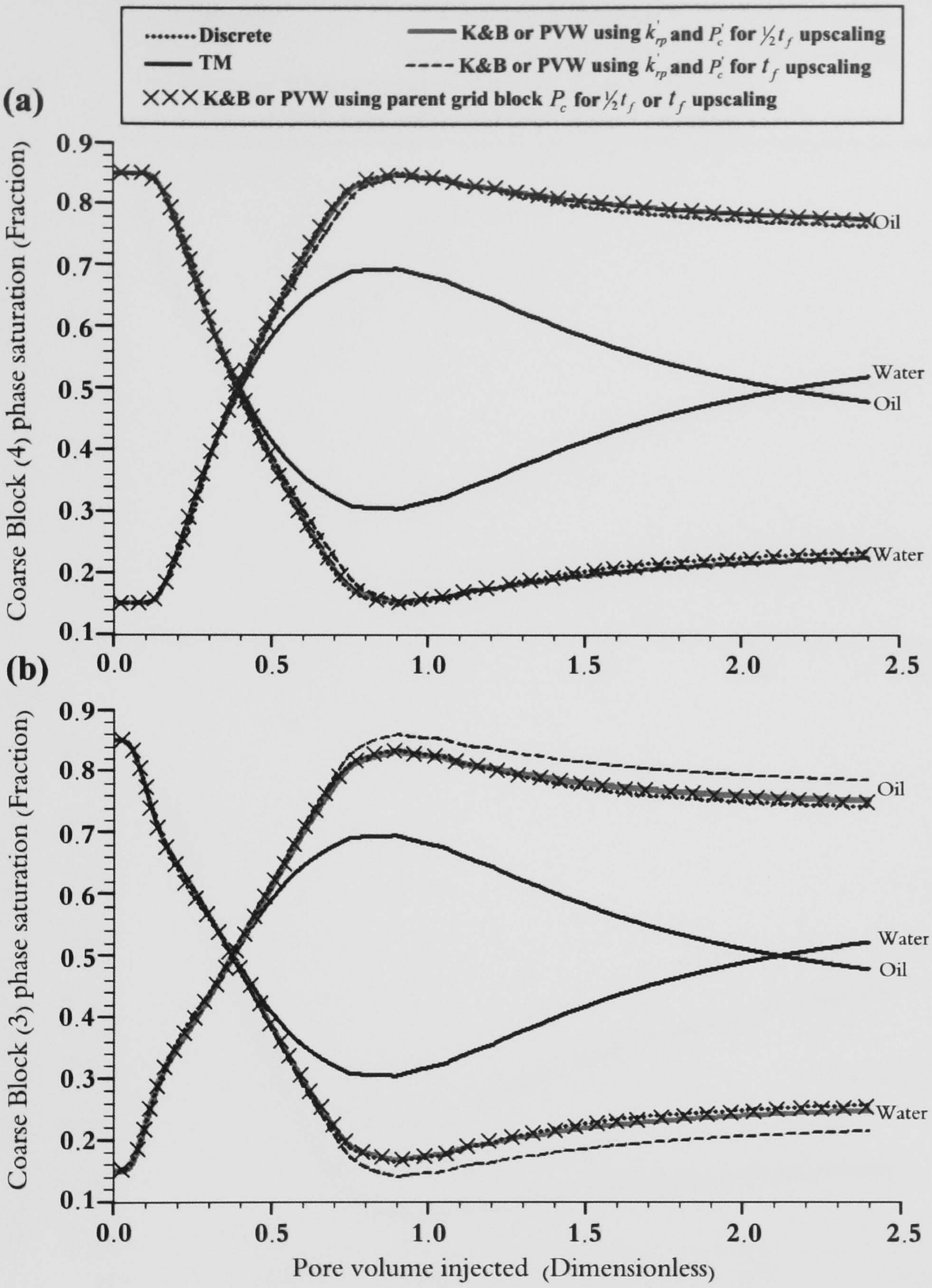

Fig. 6.11. Half-fault ($\frac{1}{2}t_f$) upscaling versus full-fault (t_f) upscaling saturation results for the coarse blocks 4 **(a)** and 3 **(b)** in the extended model shown in **Fig. 6.8** and for the model properties described in **§6.3.1**. The results compare the performance of the pseudo capillary curves ($P_c^{'}$) from the K&B and PVW pseudos and the results of using unaltered parent host block capillary pressure curves (P_c). See the legend and text for a description of the different upscaling tests. The *TM* and discrete results are also shown for comparison.

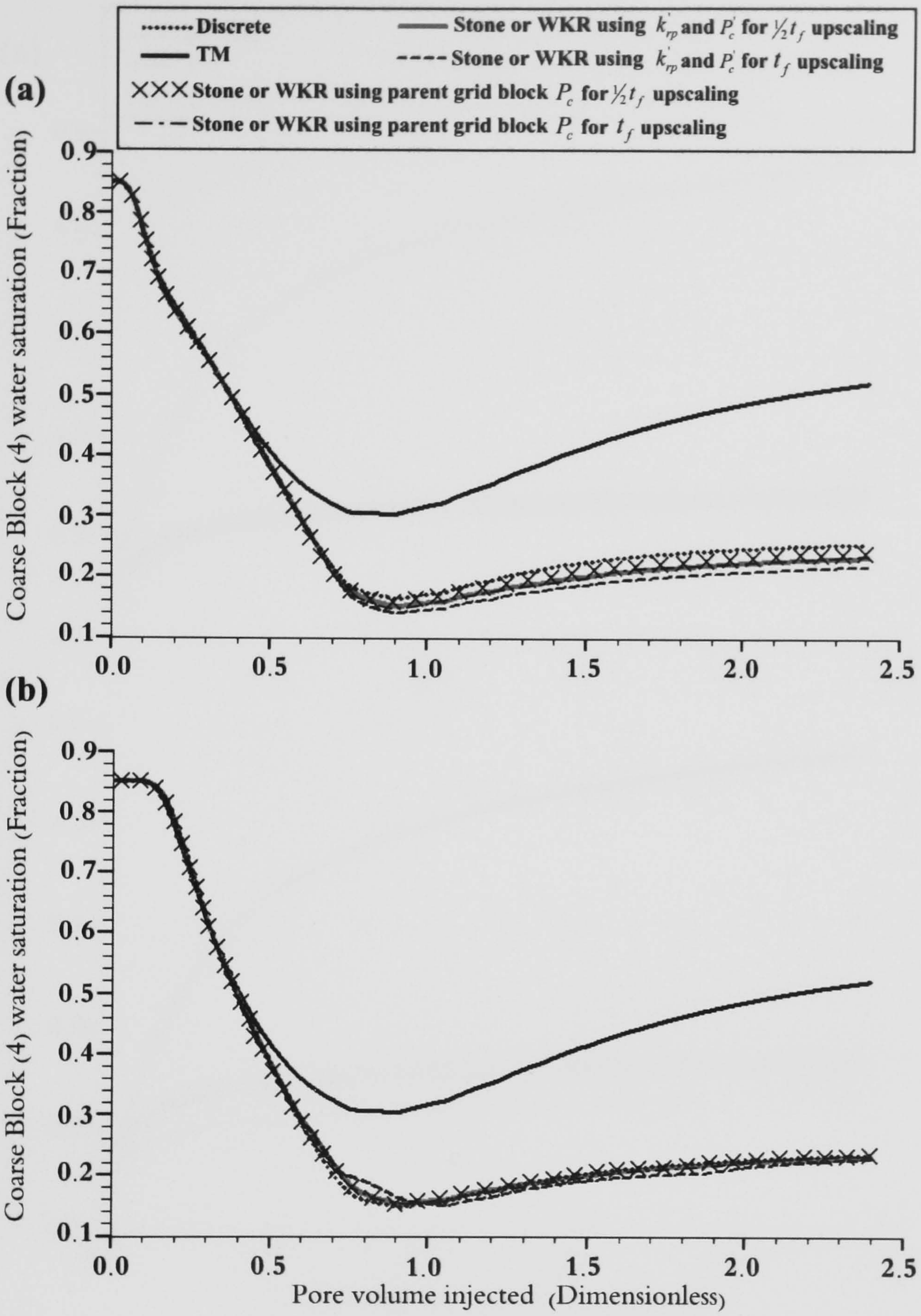

Fig. 6.12. Half-fault ($\frac{1}{2}t_f$) upscaling versus full-fault (t_f) upscaling saturation results for the coarse blocks 4 **(a)** and 3 **(b)** in the extended model shown in **Fig. 6.8** and for the model properties described in **§6.3.1**. The results compare the performance of the pseudo capillary curves ($P_c^{'}$) from the Stone and WKR pseudos and the results of using unaltered parent host block capillary pressure curves (P_c). See the legend and text for a description of the different upscaling tests. The *TM* and discrete results are also shown for comparison. Oil saturation profiles exhibited the same comparisons.

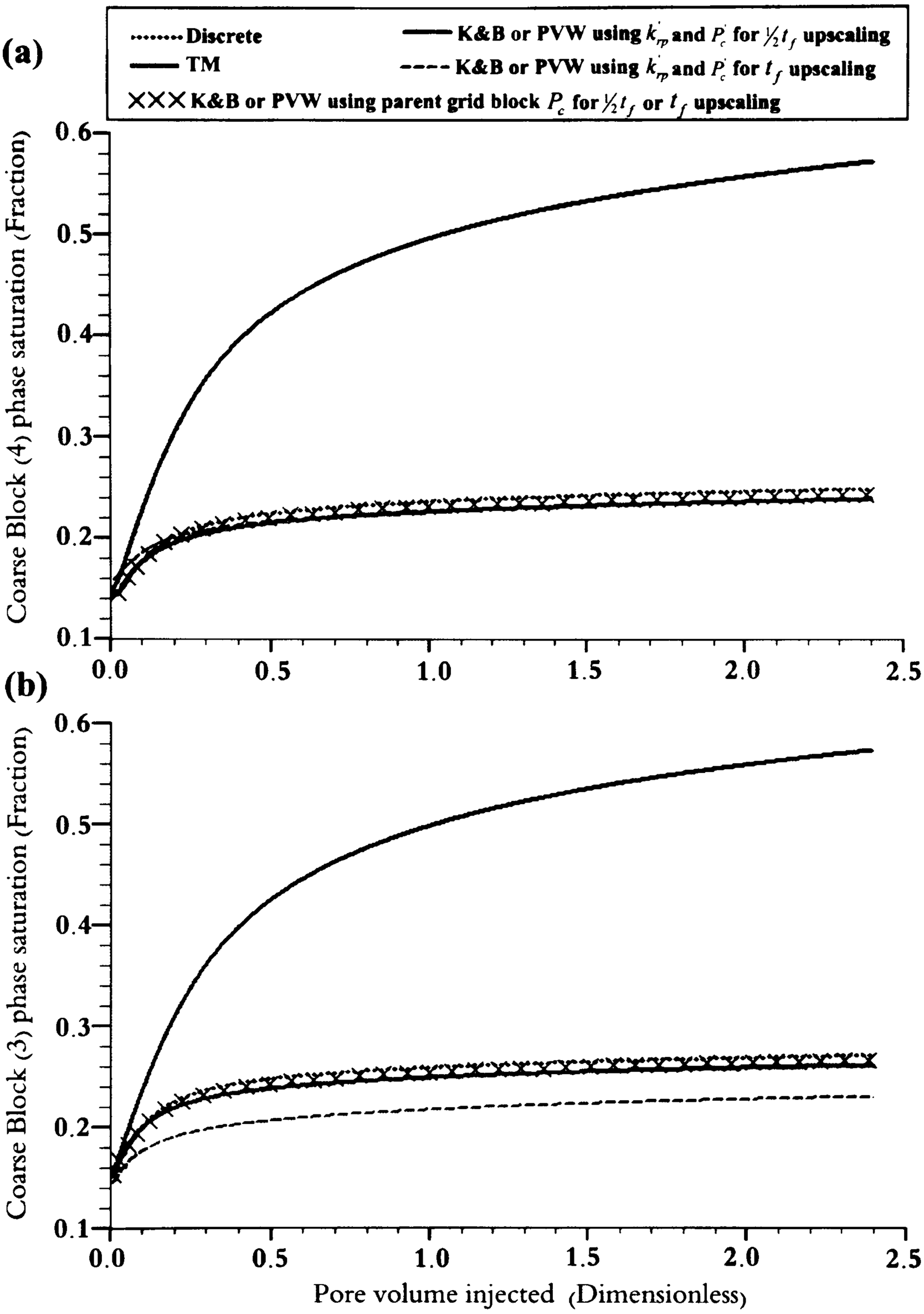

Fig. 6.13. Half-fault ($\frac{1}{2}t_f$) upscaling versus full-fault (t_f) upscaling water phase saturation results for the coarse blocks 4 **(a)** and 3 **(b)** in the extended model shown in **Fig. 6.8** and for the model properties described in **§6.3.1**. The results are for a water flood test on an initially oil-saturated model to the irreducible water saturation. The pseudo curves used are those generated using the fractional flow scheme shown in **Fig. 6.5**. The results compare the performance of the pseudo capillary curves ($P_c^{'}$) from the K&B and PVW pseudos and the results of using unaltered parent host block capillary pressure curves (P_c). See the legend and text for a description of the different upscaling tests. The *TM* and discrete results are also shown for comparison.

6.3.3.4 Test observations

From the results shown in **Fig. 6.10** to **6.13**, the following key observation points can be drawn.

- The match between the discrete and the coarse models is very good for the grid block immediately upstream of the fault, but not as good for the grid block upstream of this latter block. Such results indicate that these sensitivity tests are required not only for the grid block where the pseudo curves are attached, *i.e.* the one immediately upstream of the fault, but must extend to more cells further in the upstream side of the fault. This observation was also noted by Manzocchi *et al.* (2002) when comparing the performance of the K&B and the PVW methods for similar types of tests.
- The K&B and the PVW pseudofunctions seem to perform equally well for a given upscaling method and they give much better results than the Stone or WKR methods, which also give almost identical results for a given upscaling method.
- For all the pseudofunctions tested in the study, using half-fault thickness upscaling gives closer results to the discrete model than full-fault thickness upscaling.
- When using the unaltered host cell capillary pressure curve, instead of the pseudo-generated curve, in conjunction with the pseudo-relative permeability curves, the K&B and the PVW pseudofunctions give almost identical results irrespective of the upscaling method adopted.
- When using the unaltered host cell capillary pressure curve, instead of the pseudo-generated curve, in conjunction with the pseudo-relative permeability curves, the Stone and the WKR pseudofunctions give different results for each upscaling method, with the half-fault method giving better results than the full-fault method.
- The use of the unaltered capillary pressure curve can have a large positive impact on improving the mismatches in those cells further upstream of the fault. Furthermore, the use of the unaltered capillary pressure curve can alleviate the differences between the different pseudoisation methods, *e.g.* between the K&B and the PVW methods.
- The results from using the unaltered capillary pressure curves are very close to those from using pseudo curves. Generally, using the original unaltered capillary pressure curve in conjunction with the pseudo-relative permeability curves generated using the half-fault upscaling method gives the most satisfactory results.
- When extending the upscaling tests to a more realistic water injection scheme, rather than a fractional injection scheme, similar conclusions were drawn regarding the evaluation of the two different upscaling methods and different pseudofunctions for the type of upscaling required for this study.

In summary, the above tests show that using the parent grid block, *i.e.* the host, unaltered capillary pressure in conjunction with the K&B or the PVW pseudo-relative permeability curves generated from the half-fault upscaling method, gives the closest match to the high-resolution

discrete model results. An equally good performance is achieved when using the K&B pseudo-capillary pressure and relative permeability curves generated using the half-fault upscaling method. One point that needs clarification about the use of unaltered parent grid block capillary pressure values is the process of recalculating the pressure values for the new saturation points in the generated pseudo-relative permeability curves. This is a straightforward process in two cases: first, when the saturation points and capillary pressure values are a well-defined function of each other; and second when the saturation points and spacing are identical to those in the original rock curves defining the capillary pressure values. However, neither of these two cases is guaranteed in reality. Capillary pressure values may not be easily related to saturation points via a well-defined function and the required recalculation may require an extrapolation process. The rest of this study adopts the K&B pseudoisation method to test the effects of three main variables affecting the shape of the generated pseudo-relative permeability curves; namely, fault thickness, fault permeability and across-fault Darcy flow rate. The stability and performance of the method within the above tests has favoured the K&B as the method of choice. The use of the parent grid block capillary pressure curves, despite giving excellent results when used with the K&B or the PVW pseudo-relative permeability curves, is not necessary since the K&B $P_c^{'}$ still gives an adequate match. Manzocchi *et al.* (2002) showed that the use of the K&B $P_c^{'}$ gives a very satisfactory result for a similar type of upscaling to that tested in this study.

6.3.4. Pseudo curve resolution

Figure 6.14a compares the performance of each pseudofunction generated using the half-fault thickness for the prediction of the average pressure; **Eclipse 100**^{TM} uses oil-phase pressure to refer to the average pressure, output in the coarse block 2 (see **Fig. 6.6**). The results show that the K&B and PVW pseudos perform much better, in terms of duplicating the discrete results, than the Stone and WKR methods. There is a region of mismatch at a PVI value of about 0.5. From **Fig. 6.10a**, this region corresponds to the lowest water saturation points in the coarse block 2. Thus one can conclude that this mismatch is simply caused by the low resolution of points on the adopted pseudo curves at low water saturation (**Fig. 6.9**). Extra points at low water saturations on the pseudo-curves can be obtained by re-running the discrete simulation, *i.e.* the one that is used to generate the pseudofunctions, starting with a model that is initially oil saturated. Note that this will only generate a few points on the pseudo-curve at low water saturations, but not at high water saturations because of the capillary oil trapping. It should be noted also that total flow rates must be kept fixed for the pseudo-curves to be unique. **Figure 6.14b** shows that the mismatch region can be considerably minimised by running a very refined water injection scheme, with the same total flow rate to that of the fractional scheme. When using a very refined injection to improve the resolution of the generated pseudo curves, the required time steps can be extremely excessive. One of the limitations of the Geoquest

(Geoquest, 2003) pseudoisation program used in this study is that it accepts a limited number of time steps (maximum of 1000). Because of this limitation, it is sometimes difficult to generate a full-saturation pseudo curve when using low flow rates. One way around this, but rather a time-consuming method, is to split the high resolution run, *i.e.* the one that is used to generate pseudofunctions, into more than one run with a limited number of time steps in each run and then combine the generated pseudo curves into one curve. For the sake of simplicity and to allow time to test various variables affecting pseudo-generated curves, lower resolution curves, but ones with a reasonable performance, are used throughout the rest of this study.

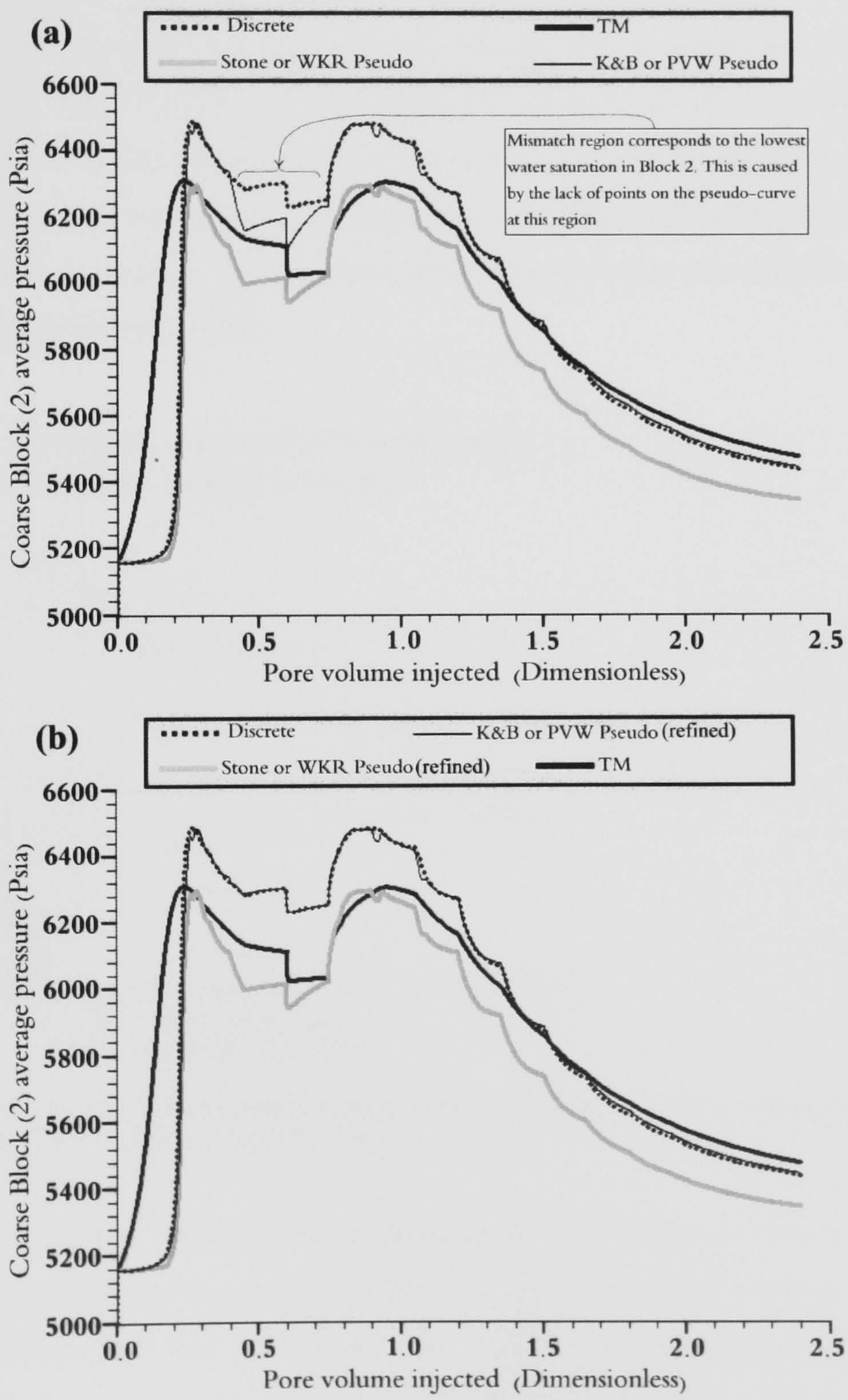

Fig. 6.14. Coarse block 2, see **Fig. 6.6**, average, or oil-phase, pressure for different models: **(a)** before improving the resolution of the generated pseudo curves; **(b)** after improving the resolution of the generated pseudo curves at low water saturations.

6.4. Injection scheme effects on generated pseudo curves

For the same across-fault total flow rate and mobility ratio, there is one unique pseudo-curve even when the weight of each phase flow rate, *i.e.* fractional flow, is changed. Generating pseudo-curves using fractional flows, while keeping the total flow rate constant, only affects the resolution, *i.e.* number of points generated, but not the general shape of the pseudo-curve. This is because some combinations of flow rates do not allow a full saturation sweep in the upscaled blocks to construct the full curve. **Figure 6.15** compares two curves generated using different injection schemes, for the same total flow rate, for the coarse grid block 2 shown in **Fig. 6.6**. Both curves were generated dynamically using the K&B pseudofunction method. One is generated using the fractional flow rate injection schemes shown in **Fig. 6.5**, whereas the other is generated using water injection on an initially oil saturated model to an irreducible water saturation of 15%. Although the points from the two models follow the same path, unlike the former model, the latter does not have enough points to define the full saturation range of the pseudo-curve. This is because the fractional-flow injection rule discussed in **§ 6.3.2** is not obeyed in the water injection model.

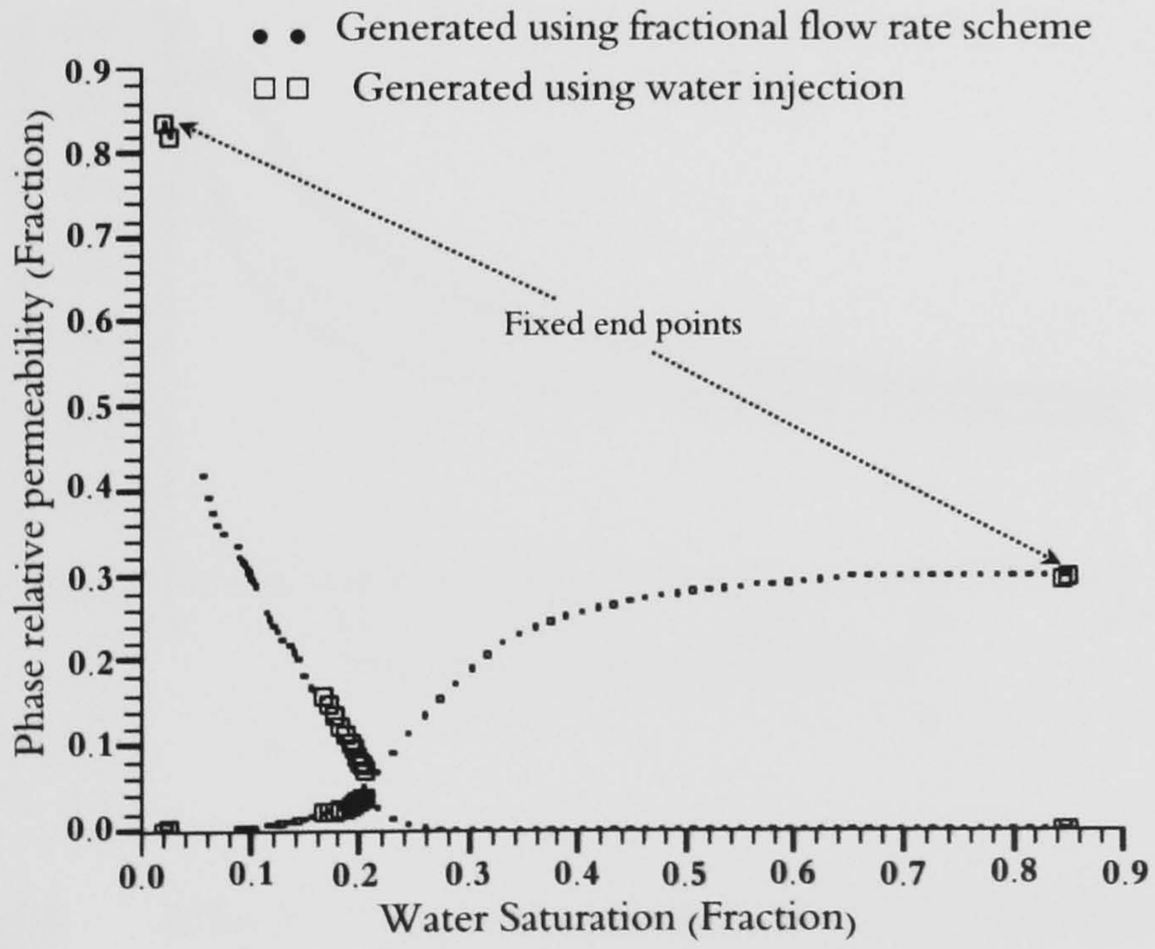

Fig. 6.15. Comparing two pseudo-relative permeability curves generated using different injection schemes with a single total flow rate.

The uniqueness of the full-saturation pseudo-curves arises because they can duplicate the results of high-resolution model runs using different flow schemes but with the same total flow. **Figure 6.16** confirms this fact and shows that pseudo-curves generated from their parent discrete runs, where full-saturation sweep is not reached in the target region, are not able to duplicate the discrete results. However, full-saturation resolution curves, generated using fractional flows, give a much better match to the discrete run. Note that the *TM* results, where fault multiphase behaviour is ignored, are far from being close to the discrete results. This

highlights the need for such pseudo-curves to account for the actual flow behaviour across partially sealing faults.

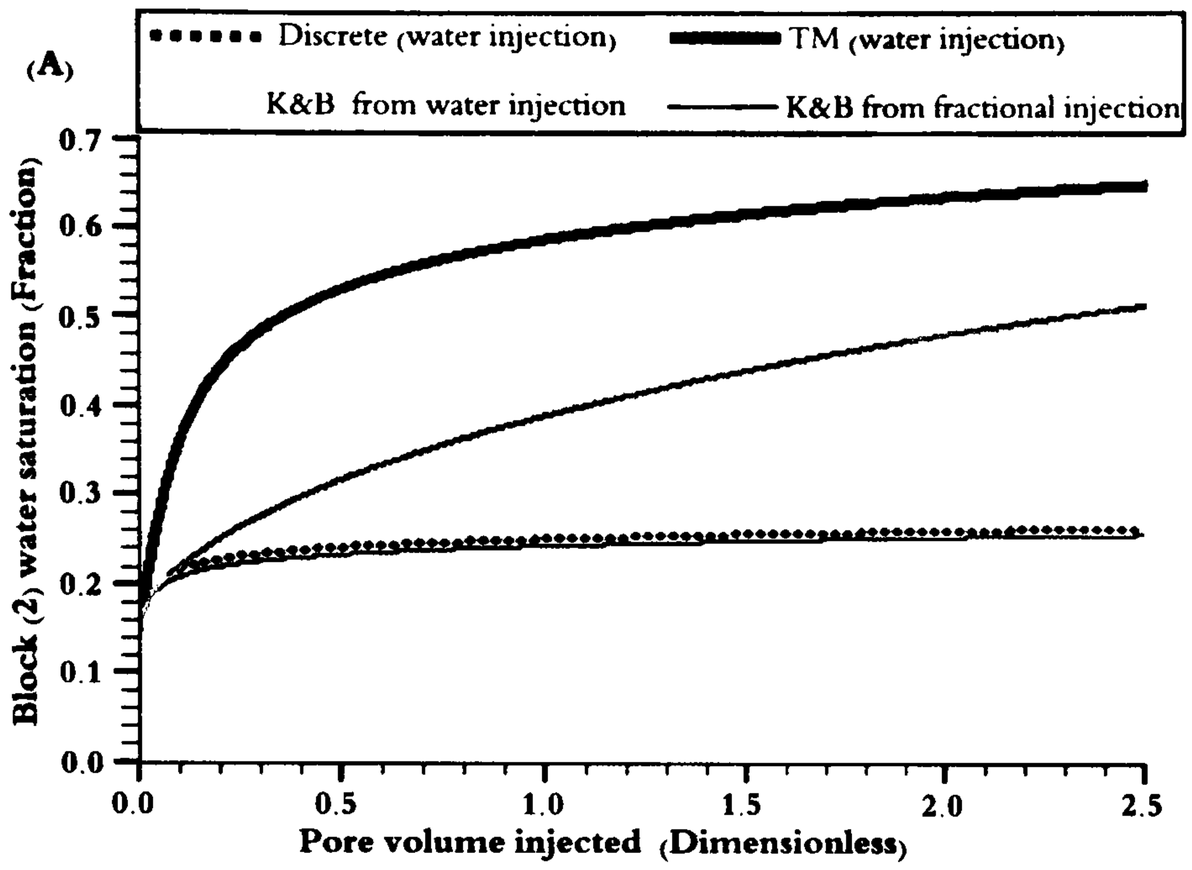

Fig. 6.16A. Comparing the performance of the two pseudo-relative permeability curves shown in **Fig. 6.15** for coarse block 2 average water saturation. The *TM* and discrete results are shown for comparison.

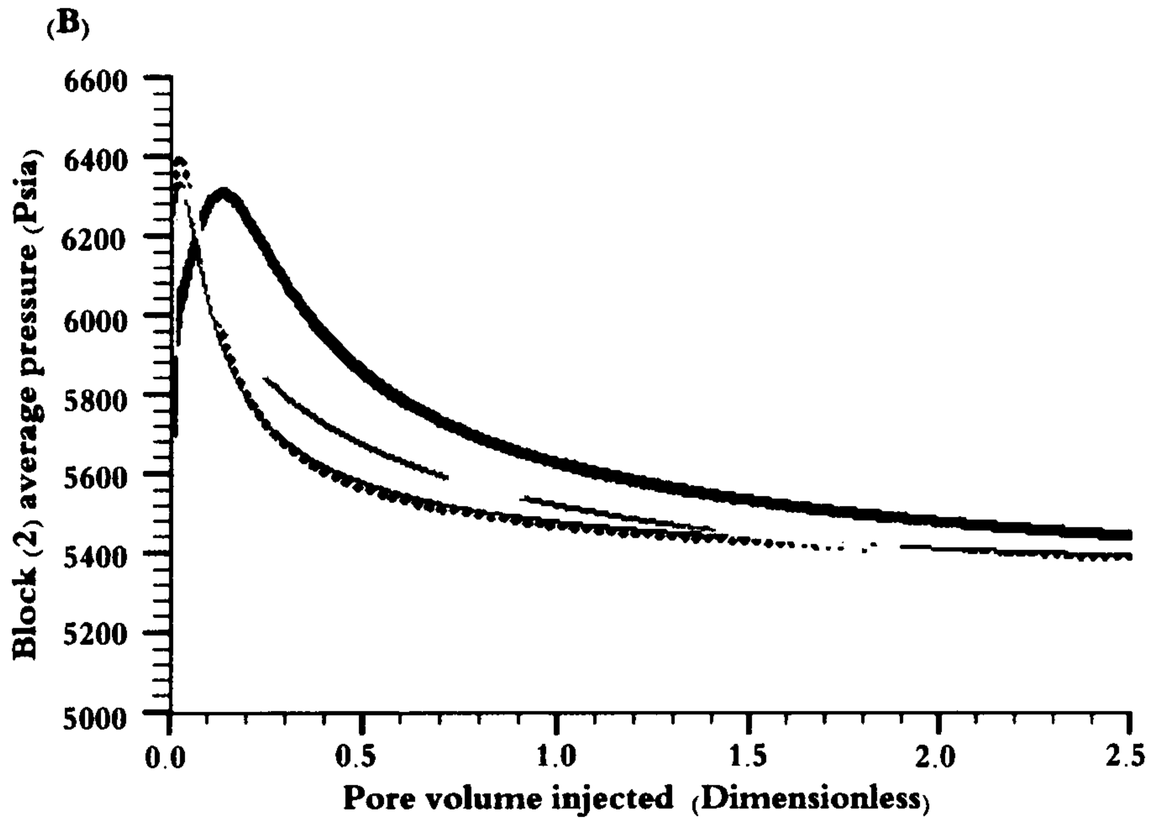

Fig. 6.16B. Comparing the performance of the two pseudo-relative permeability curves shown in **Fig. 6.10** for coarse block 2 average, or oil-phase, pressure. The *TM* and discrete results are shown for comparison. See **Fig. 6.16A** for legend.

6.5 Effects of fault properties on the generated pseudo-curves

In this section, the effects of fault permeability, fault thickness and across-fault Darcy velocity on the shape, resolution and stability of the fault pseudo-generated curves are investigated.

6.5.1. Fault permeability effects

As fault permeability changes, its associated relative permeability and capillary pressure curves also change. In this section we test the shape, resolution and stability of K&B generated pseudo-curves for different fault rocks. Fault zones with varying permeabilities, but single thickness, are used by the K&B pseudo-generation function. The faults are embedded within the same host rock as in the previous models described, *i.e.* a permeability of 1000 mD. Three models are

compared, namely Discrete, *TM* and Pseudo plus *TM*, using the water injection scheme shown in **Fig. 6.5**, with a total flow rate of 0.0005 ft/day, applied to the model shown in **Fig. 6.2**, as the discrete model, and in **Fig. 6.6**, as the *TM* and the Pseudo models. *TMs* are derived using **Equation-6.16** and are summarised in **Table-6.1**.

Table-6.1. *TMs* for different fault permeabilities, k_f , and fixed fault thickness, t_f . The host rock permeability is 1000 mD and the host cell length is 50 ft (**Fig. 6.2**).

t_f **(ft)**	k_f **(mD)**	*TM* **(Dimensionless)**
3	1	0.0164
3	0.1	0.001664
3	0.01	0.000167
3	0.001	0.0000167

The relative permeability and capillary pressure curves for the host rock are fixed for every case. The fault rock relative permeability and capillary pressure curves are derived from the fault permeability and end points (**Chapter 3**). The model fluid properties are those summarised in **§ 6.3.1**. The K&B pseudo-relative permeability curves are shown in **Fig. 6.17**. **Figure 6.18** and **Fig. 6.19** show the performance of each model when predicting coarse block 2, see **Fig. 6.2**, average water saturation and pressure respectively. The results in both figures show that a very good match is obtained between the models with the K&B pseudos and the Discrete Models. The *TM* results for block 2 water saturation are identical for different fault permeabilities (**Fig. 6.19**). The observed pressure mismatch between the K&B and the Discrete Models at about 0.5 PVI (**Fig. 6.19**) can be explained in a similar way to that observed in **Fig. 6.14**.

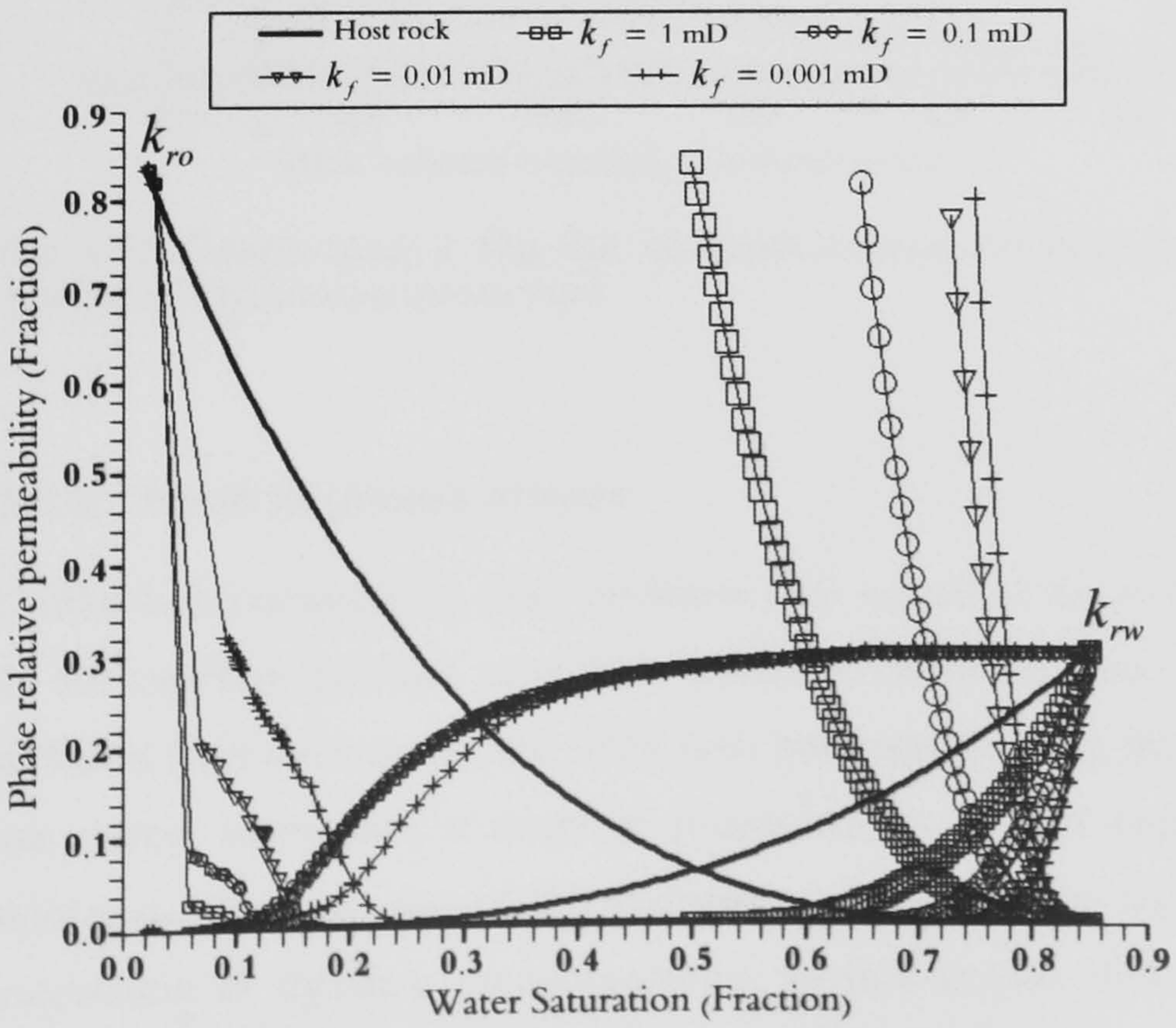

Fig. 6.17. Original fault rock curves (large symbols) and their corresponding K&B pseudo-relative permeability curves (small symbols). The host rock curve is also shown.

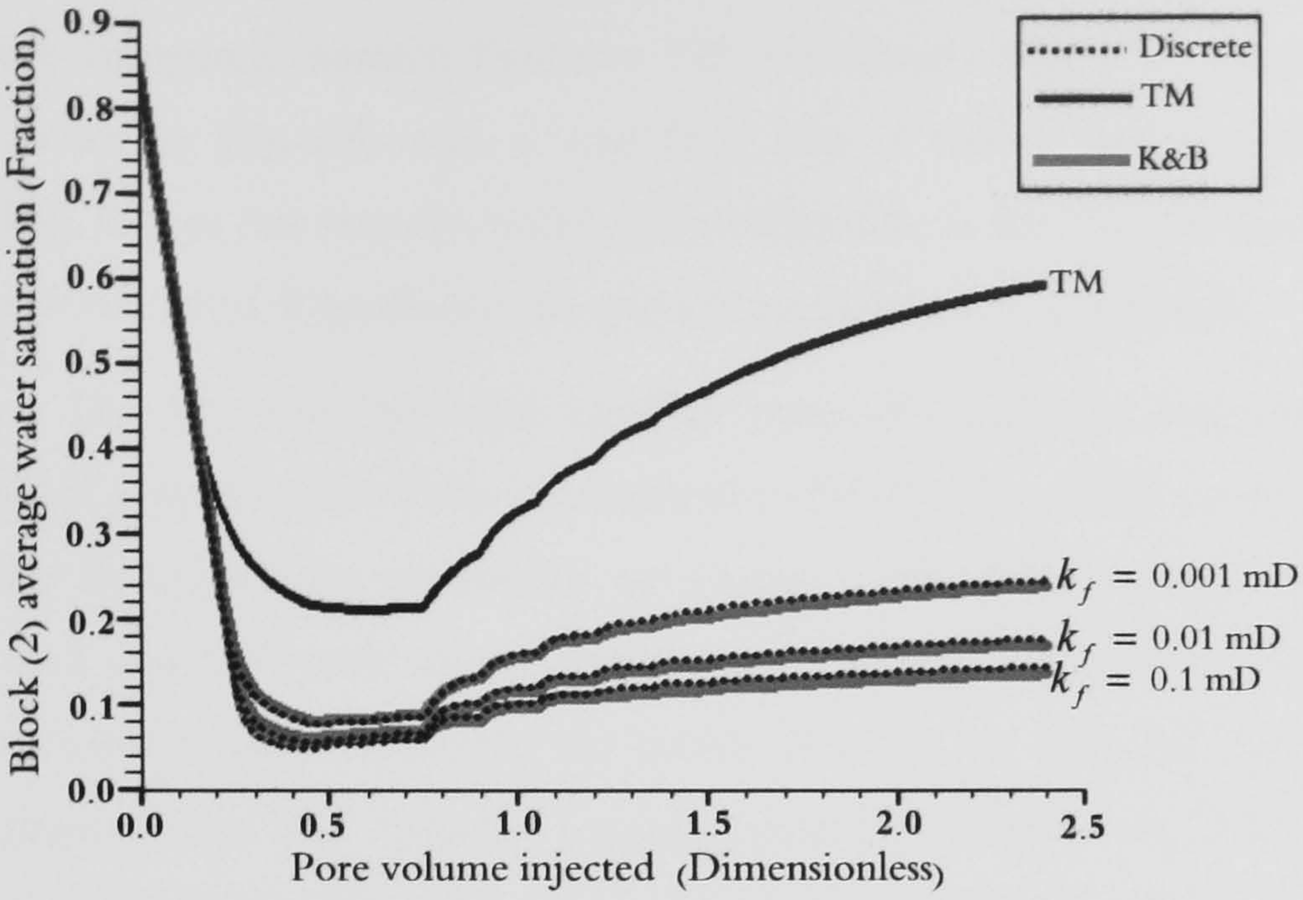

Fig. 6.18. Coarse block 2, **Fig. 6.2**, water average saturation as a function of pore volume injected (PVI) dimensionless time. The *TM* results are identical for different fault permeabilities.

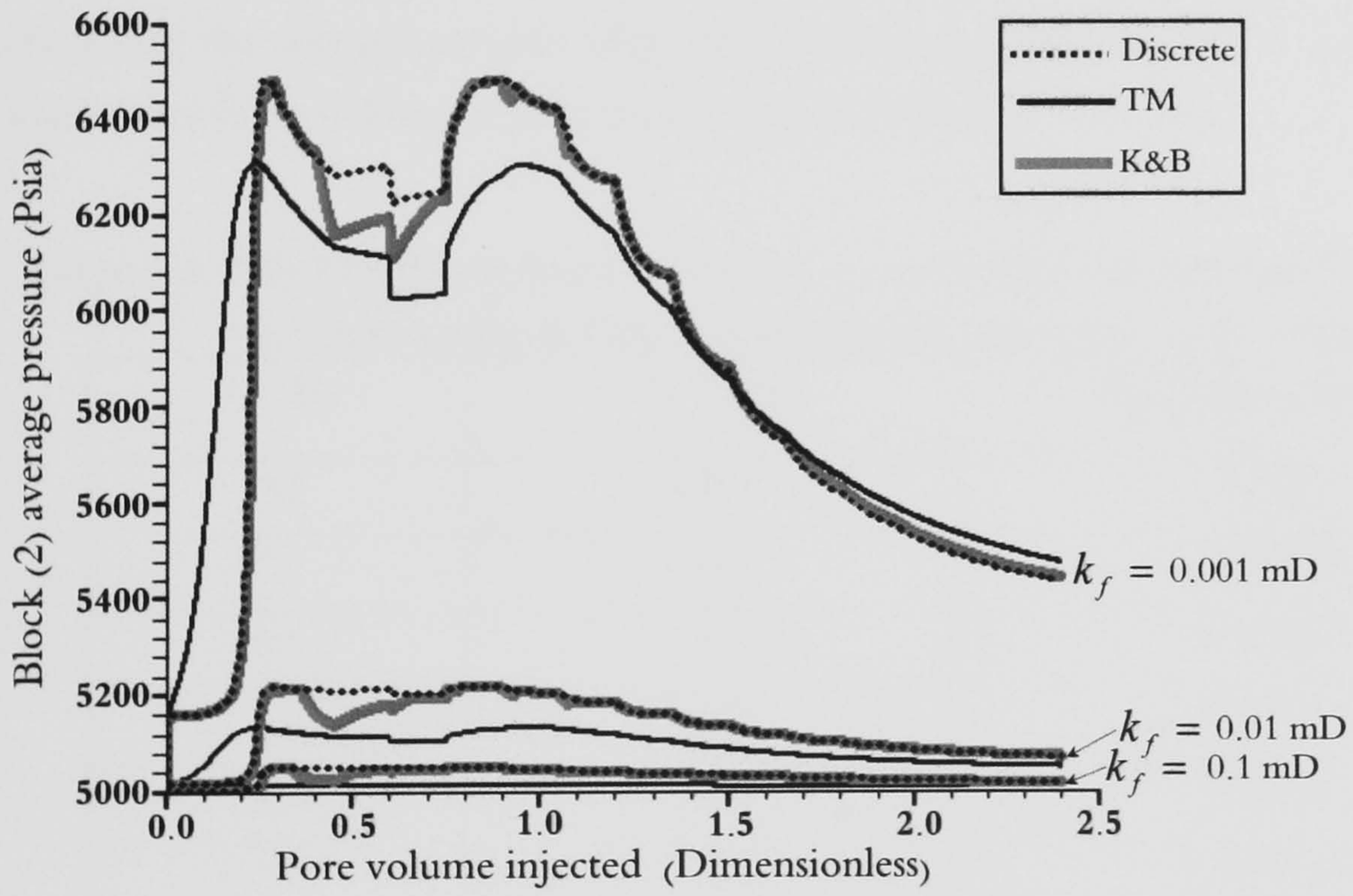

Fig. 6.19. Coarse block 2, **Fig. 6.2**, oil-phase average pressure as a function of pore volume injected (PVI) dimensionless time.

6.5.2. Fault thickness effects

Unlike fault permeability, fault thickness does not affect the shape of the relative permeability or the capillary pressure saturation functions. However, when generating pseudo-curves for different fault thicknesses, but fixed fault permeability using the method described above, one can expect to produce a range of pseudo-curves. This is because changing the fault zone thickness affects the size of the averaged, *e.g.* pore-volume weighted, parameters used in the calculation of dynamic pseudofunctions. In this section, different fault zones with various thicknesses, but a single permeability, are used by the K&B pseudo-generation function. The

faults are embedded within the same host rock, with a permeability of 1000 mD. Three models are compared, namely Discrete, *TM* and Pseudo plus *TM*, using the water injection scheme shown in **Fig. 6.5**, with a total flow rate of 0.0005 ft/day, applied to the model shown in **Fig. 6.2**, as the discrete model, and in **Fig. 6.6**, as the *TM* and the Pseudo models. The *TMs* are derived using **Equation-6.16**, and are summarised in **Table-6.2**.

The host and fault rock capillary pressure curves are those shown in **Fig. 6.9**. The model fluid properties are those summarised in § **6.3.1**. The K&B pseudo-relative permeability curves for different fault thicknesses are shown in **Fig. 6.20** together with the undeformed reservoir rock and fault rock curves. **Figure 6.21** and **Fig. 6.22** compare the results of the three models described when predicting the coarse block 2, see **Fig. 6.2**, average pressure and saturation, respectively. The observed pressure mismatch between the K&B and the Discrete Models at about 0.5 PVI (**Fig. 6.21**) can be explained in a similar way to that observed in **Fig. 6.14**. The *TM* results for block 2 water saturation are identical for different fault thicknesses (**Fig. 6.22**). As the fault thickness increases, the gap between the *TM* and the Discrete results, when predicting the average pressure (**Fig. 6.22**), decreases, indicating that it is more important to account for fault multiphase properties in thin faults than in thick ones.

Table-6.2. *TMs* for different fault thicknesses, t_f, and fixed fault permeabilities, k_f. The host rock permeability is 1000 mD and the host cell length is 50 ft (**Fig. 6.2**).

t_f **(ft)**	k_f **(mD)**	***TM*** **(Dimensionless)**
0.5	0.001	0.0001
1	0.001	0.00005
1.5	0.001	0.000033
2	0.001	0.000025
2.5	0.001	0.00002
3	0.001	0.0000167

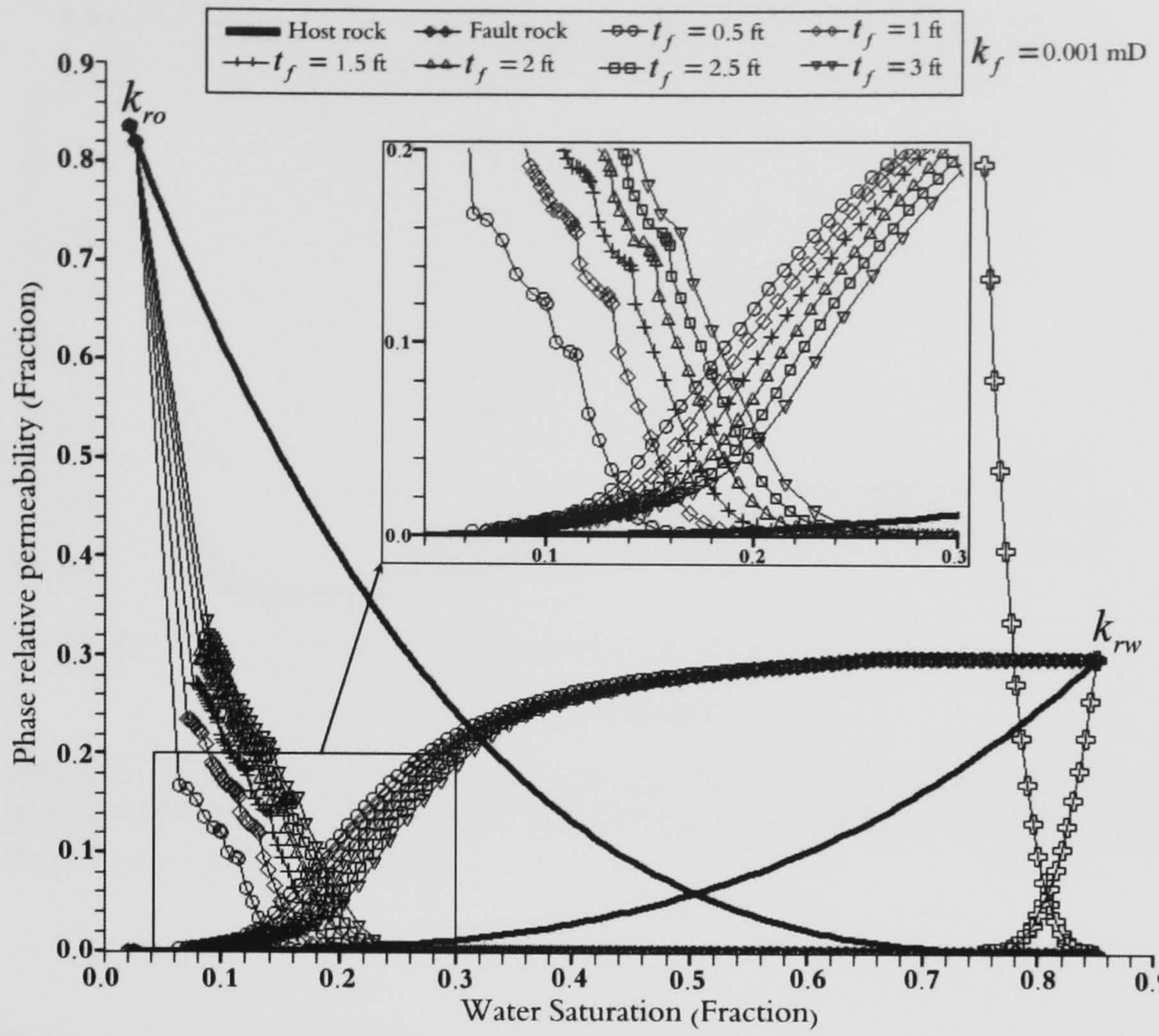

Fig. 6.20. Pseudo-relative permeability curves for different fault thicknesses, see legend, for a 0.001 mD fault rock and 1000 mD host rock. The fault and host rock curves are also displayed.

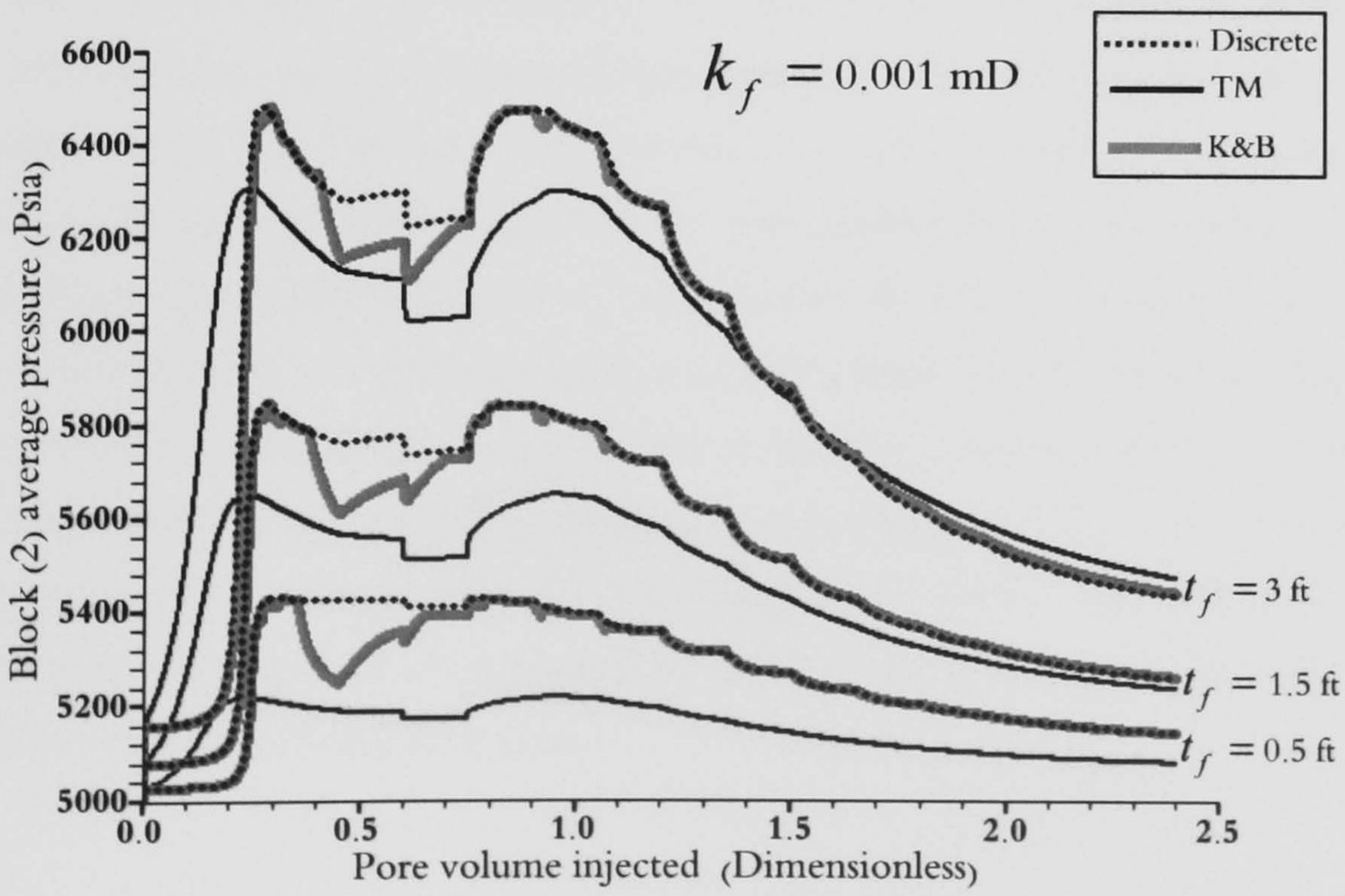

Fig. 6.21. Coarse block 2, **Fig. 6.2**, oil-phase average pressure as a function of pore volume injected (PVI) dimensionless time. Results are for k_f = 0.001 mD.

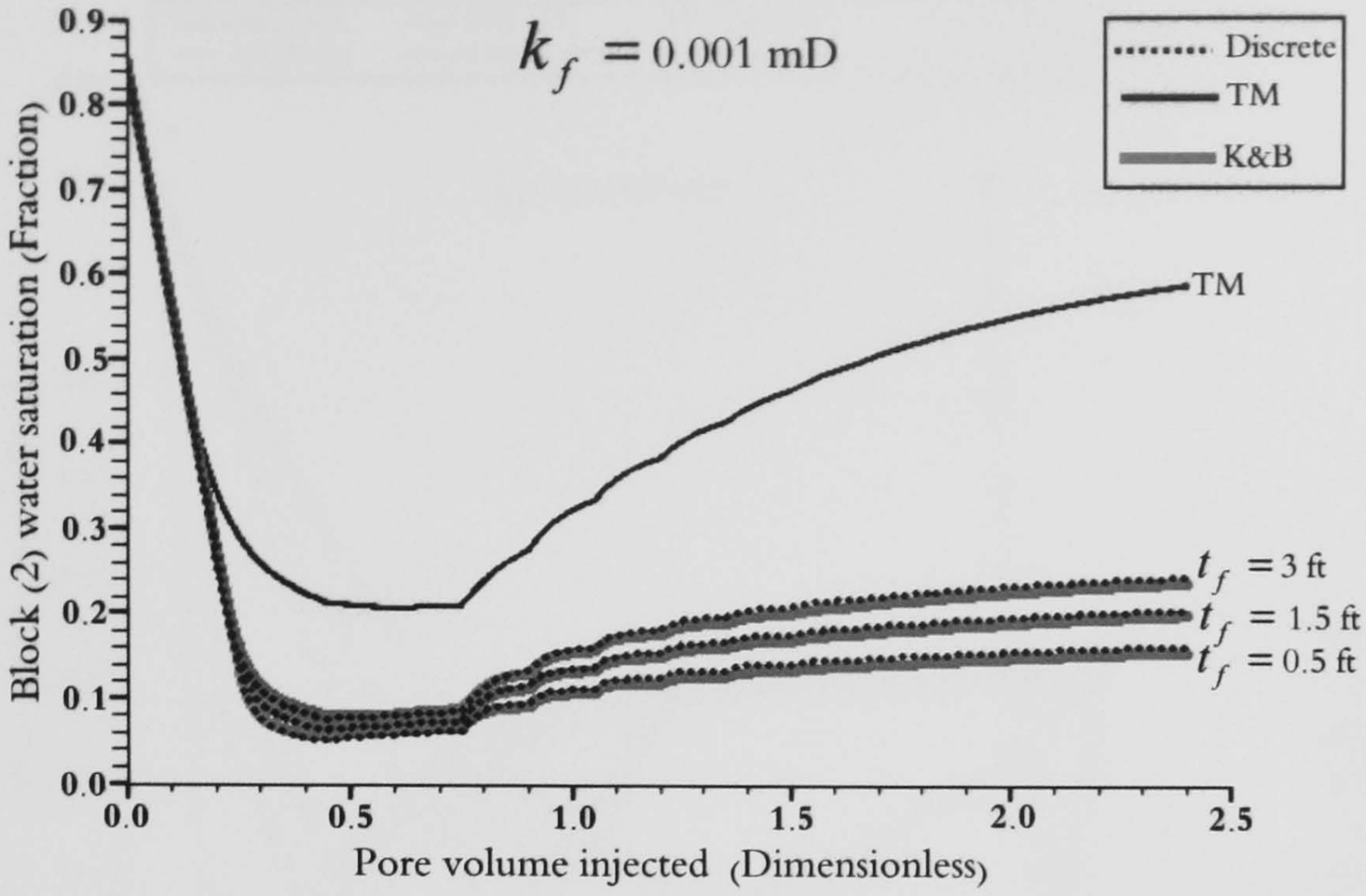

Fig. 6.22. Coarse block 2, **Fig. 6.2**, water average saturation as a function of pore volume injected (PVI) dimensionless time. The *TM* results are identical for different fault thicknesses. Results are for k_f = 0.001 mD.

6.5.3. Flow rate effects

Here the effect of the across-fault flow rate on the shape of the pseudo-generated curves is investigated. Identical models were run using the injection scheme shown in **Fig. 6.5**, except that the total flow rate is different for each model. The effects of different flow rates are addressed for two fault permeabilities, namely 0.001 mD and 0.1 mD, and a single fault thickness of 3 ft. The host rock permeability is always 1000 mD. **Figure 6.23** and **Fig. 6.24** show the resultant K&B pseudo-relative permeability and pseudo-capillary pressure curves for different across-fault lateral Darcy velocities for the 0.001 mD fault. Across-fault lateral Darcy velocities have a significant impact on the shape of the resultant K&B pseudo-relative permeability (**Fig. 6.23**). However, there is almost a negligible effect of different flow rates on the generated pseudo-capillary pressure curves (**Fig. 6.24**). The resultant K&B pseudo-relative permeability curves for different across-fault lateral Darcy velocities for the 0.1 mD fault are displayed in **Fig. 6.25**. Pseudo-capillary pressure curves for the 0.1 mD fault exhibit very little difference for different flow rates.

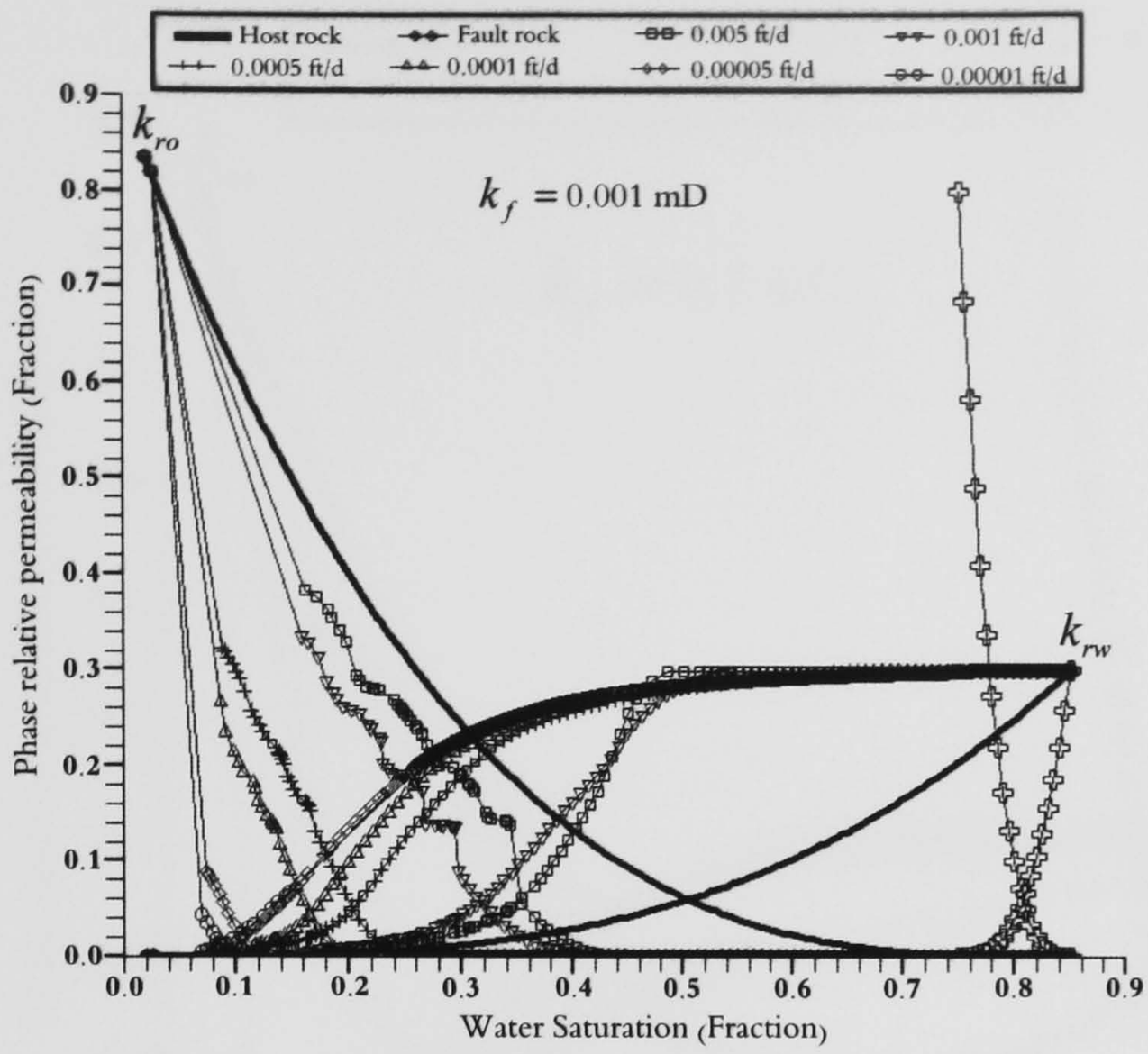

Fig. 6.23. Pseudo-relative permeability curves generated using one injection scheme (**Fig. 6.5**) with different total flow rates. Results are for k_f = 0.001 mD.

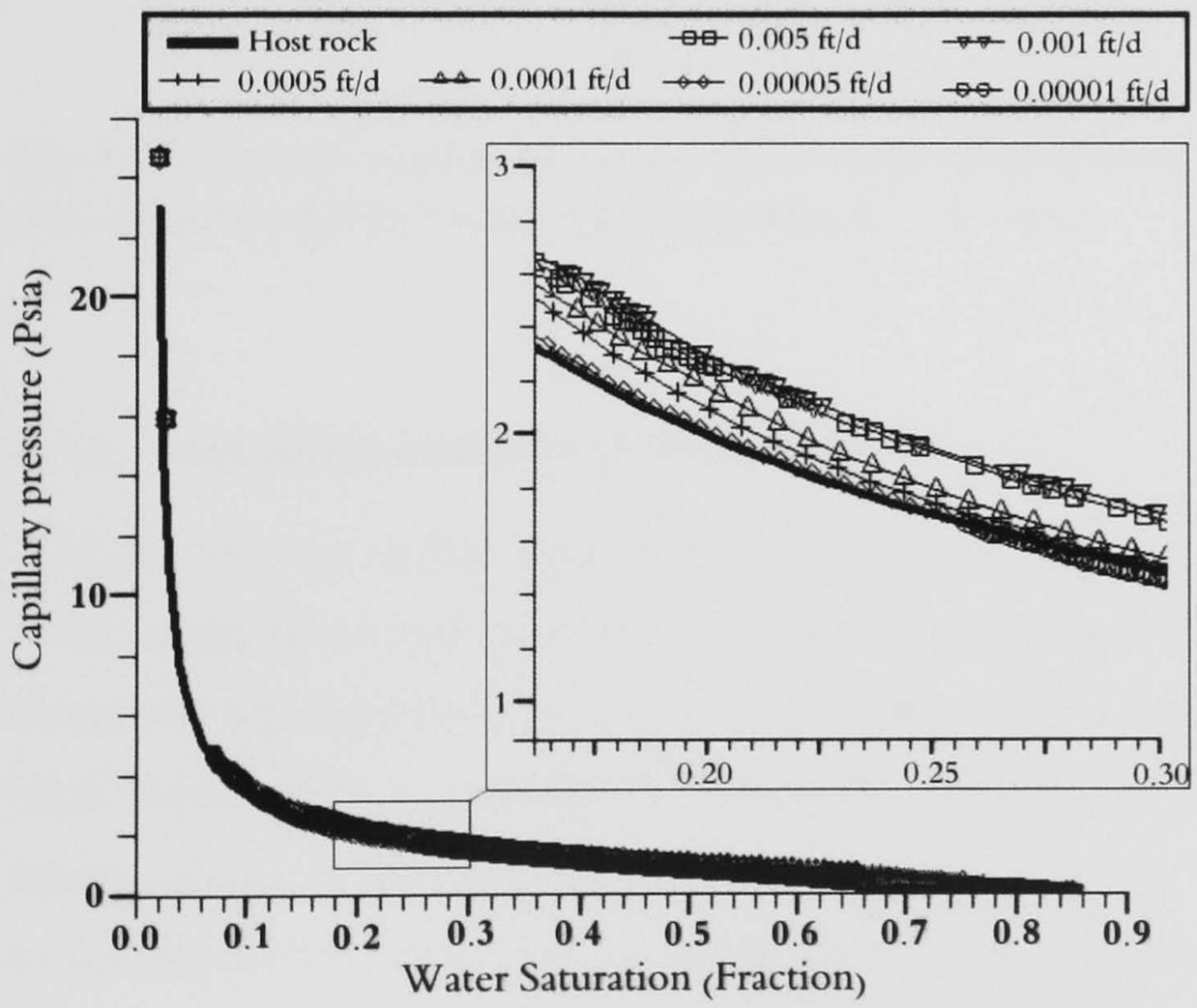

Fig. 6.24. Pseudo-capillary pressure curves generated using one injection scheme (**Fig. 6.5**) with different total flow rates. Results are for k_f = 0.001 mD.

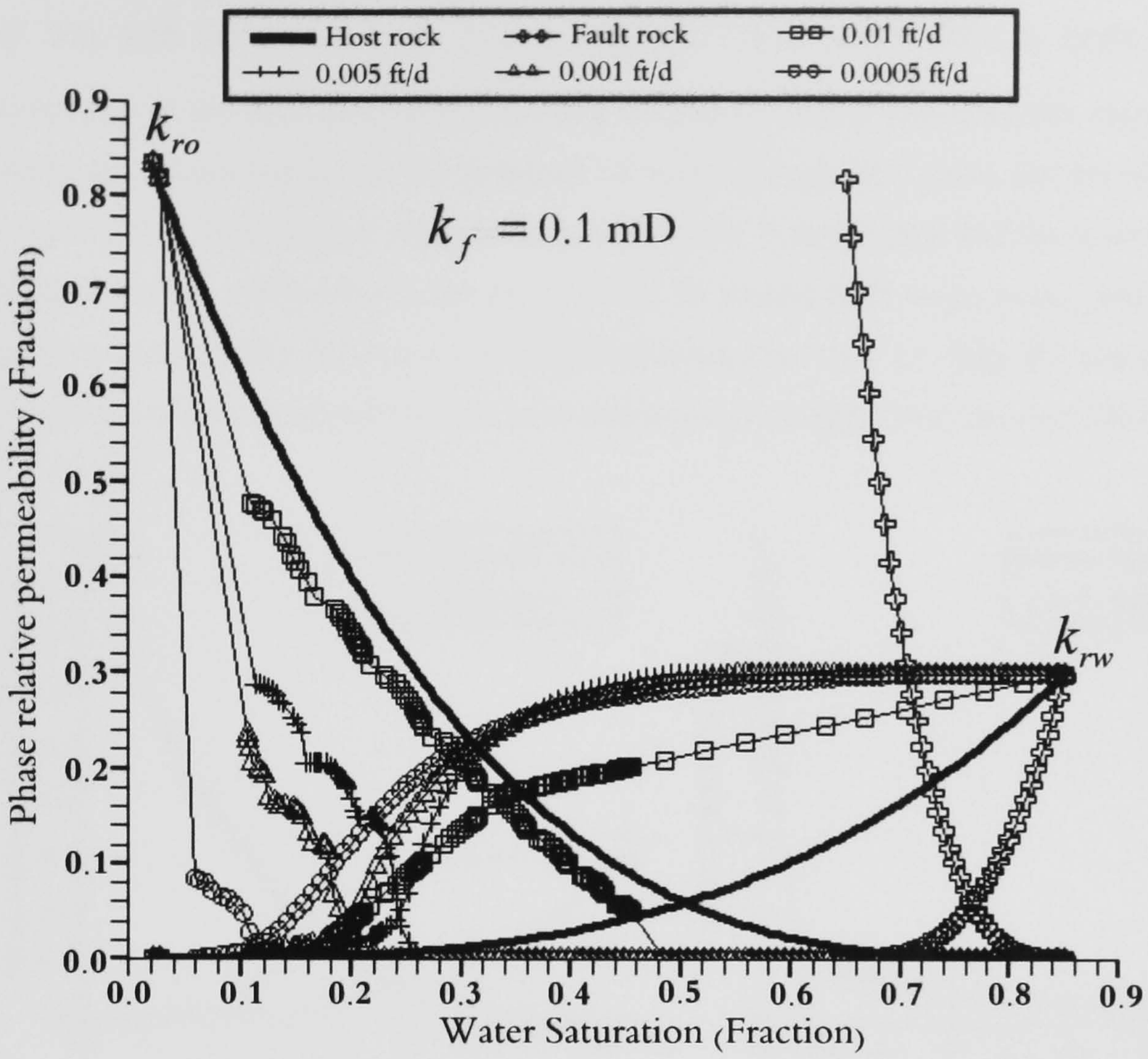

Fig. 6.25. Pseudo-relative permeability curves generated using one injection scheme (**Fig. 6.5**) with different total flow rates. Results are for k_f = 0.1 mD.

6.5.4. Instability under high flow rates

We have seen that as flow rates increase the generated pseudo-curves tend to be similar to those of the undeformed reservoir (refer to **Fig. 6.23** and **Fig. 6.25**). This means that the pseudo-curves become insensitive to the presence of the fault at high flow rates. **Figure 6.26** shows K&B pseudo-curves generated for the coarse grid block 2 shown in **Fig. 6.2**, using the flow scheme shown in **Fig. 6.5**, for a total lateral Darcy velocity of 0.1 ft/day. The fault and host curves are similar to those shown in **Fig. 6.3** and **Fig. 6.9**. The oil pseudo-relative permeability curve is identical to the undeformed sediment curve, but the water pseudo-relative permeability curve differs. **Figure 6.27** and **Fig. 6.28** show the performance of three different representations of faults for the same model described in **§ 6.3.1**, using fault permeabilities of 0.001 mD and 0.1 mD, respectively, and a single fault thickness of 3 ft. Unlike when the flow rates are low (refer to **Fig. 6.18** through **Fig. 6.22**), pseudo-curves generated under high flow rates do not perform well in duplicating the result of the high resolution model, *i.e.* the discrete model. Surprisingly, the *TM* model performs much better that the pseudo model. This means that for high flow rates, *e.g.* > 0.1 ft/day, it is not important to take into account the multiphase behaviour of fault rocks for very low fault rock permeability (*e.g.* k_f = 0.001 mD, see **Fig. 6.27**,

cf. **Fig. 6.28** for $k_f = 0.1$ mD), and using the single-phase *TM* can duplicate the actual behaviour of the fault zone. It is important to mention at this stage that this insensitivity of the generated pseudo-curves to the presence of faults at high flow rates can be attributed to the simple Corey–Brooks-type relationships assumed for both the fault and the reservoir rocks (*e.g.* Ringrose *et al.*, 1993; Manzocchi *et al.*, 2002). In reality, fault rocks could have very different relative permeability behaviour to the undeformed reservoir, *i.e.* they are not expected to be related by simple relationships, and such behaviour under high flow rates may be erroneous.

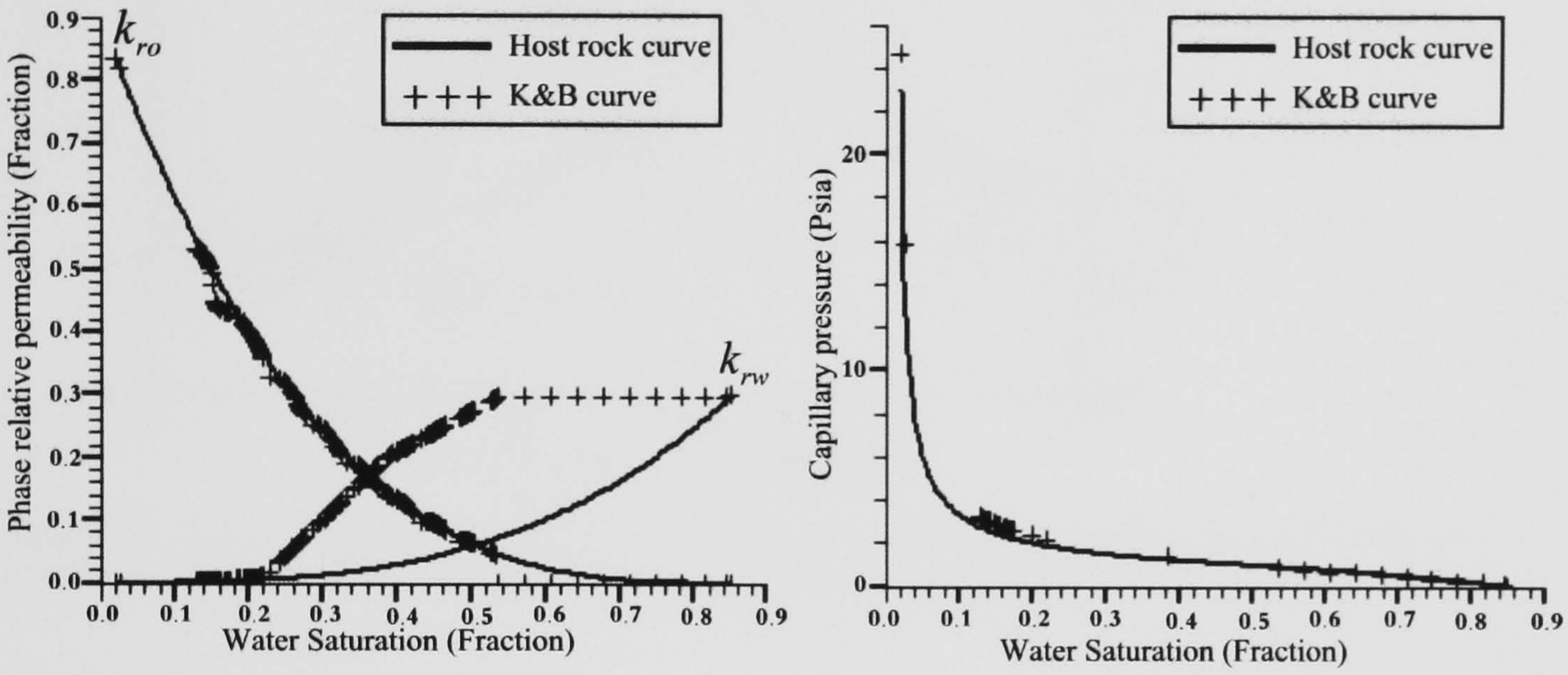

Fig. 6.26. Pseudo-relative permeability curves (Left) and pseudo-capillary pressure curve (Right) generated using a total flow rate of 0.1 ft/day. The host rock curves are also displayed.

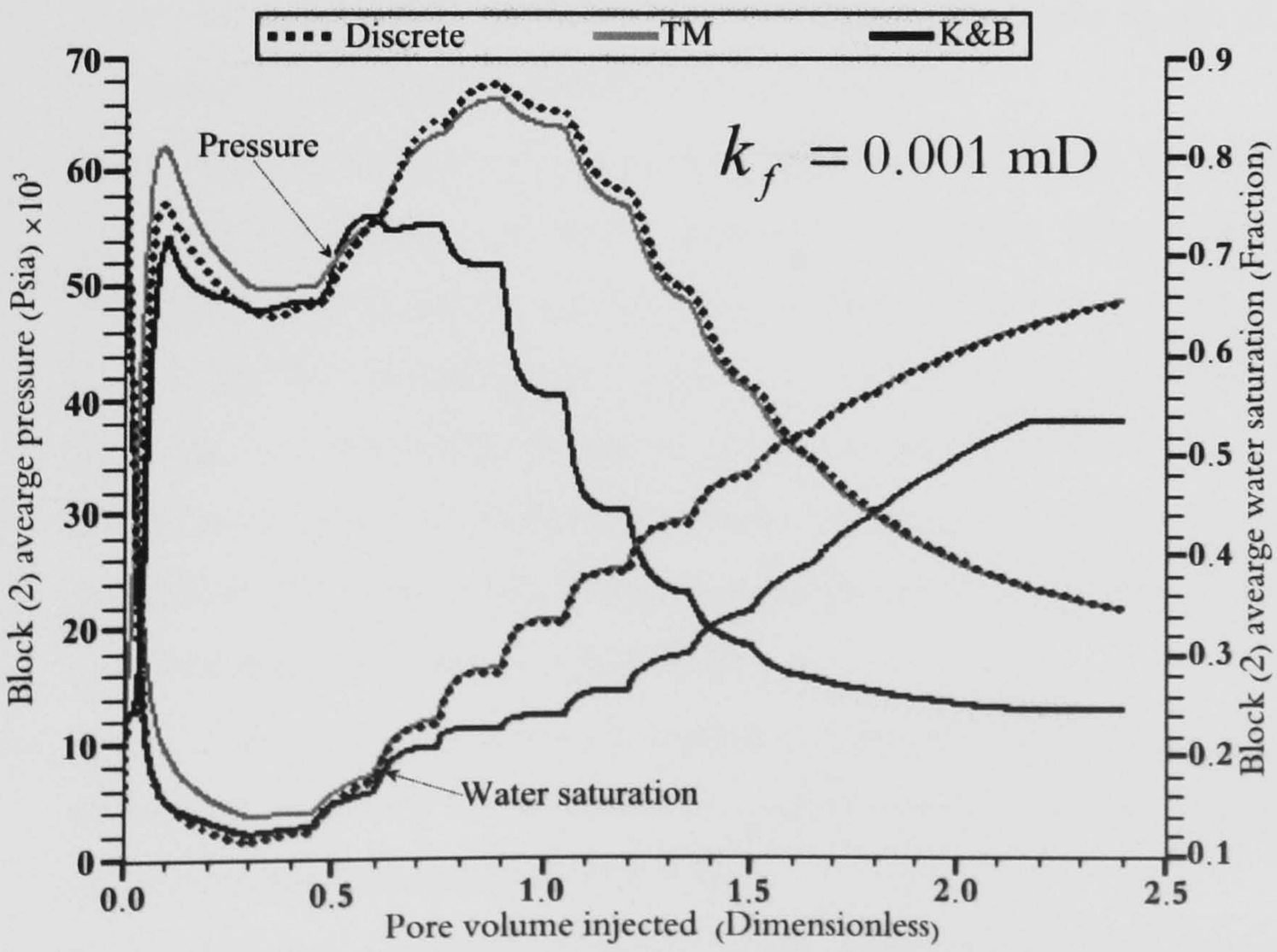

Fig. 6.27. Coarse block 2, see **Fig. 6.2**, average pressure and saturation for a flow rate of 0.1 ft/day across a fault of permeability 0.001 mD and 3 ft thickness.

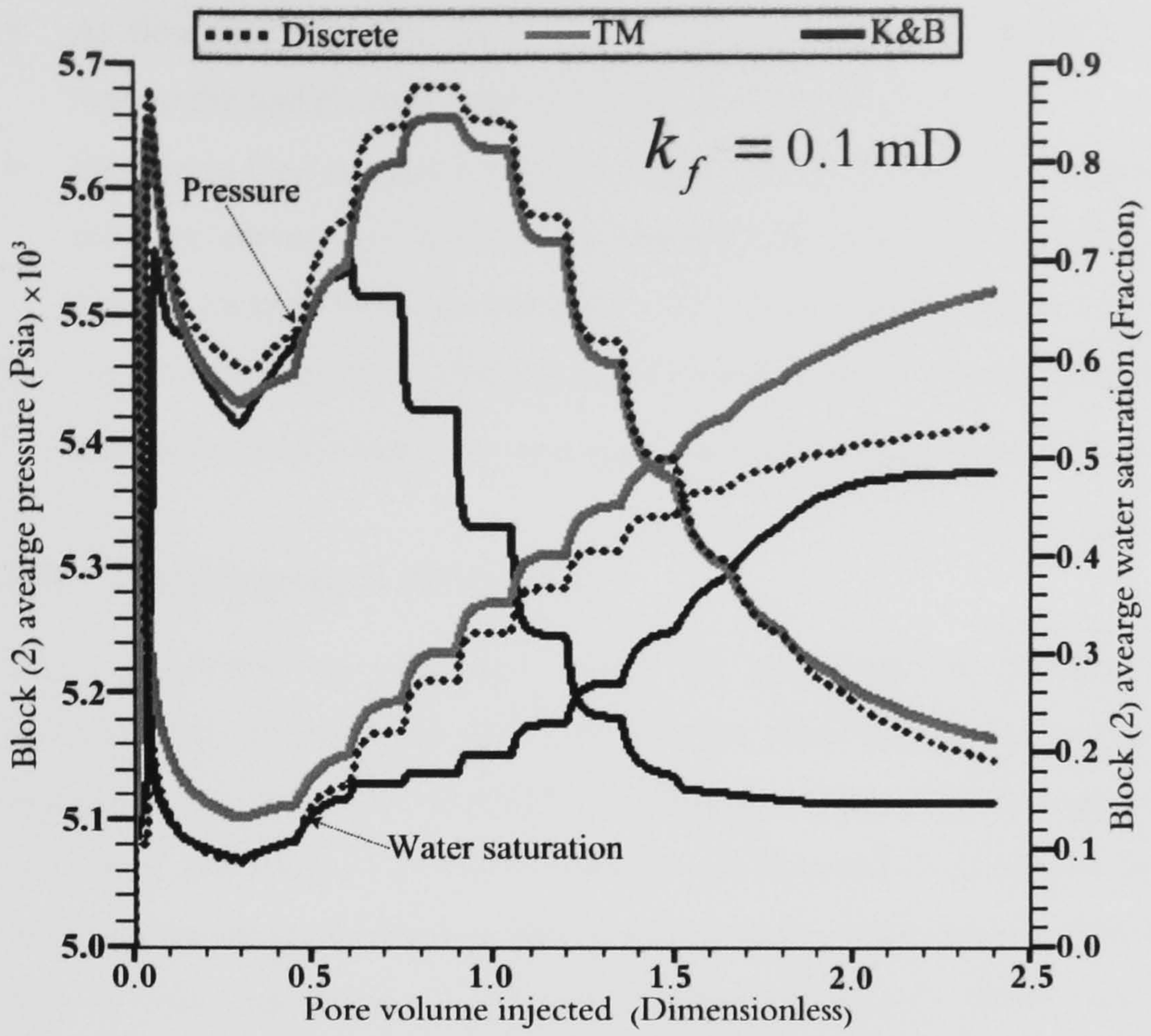

Fig. 6.28. Coarse block 2, see **Fig. 6.2**, average pressure and saturation for a flow rate of 0.1 ft/day across a fault of permeability 0.1 mD and 3 ft thickness.

6.5.5. Observations

The following observations can be summarised from **Fig. 6.12** to **Fig. 6.23** in § **6.5**.

- There are clear trends (see **Fig. 6.17** and **Fig. 6.20**) in the shape of the pseudo-curves generated for varying fault permeability and thickness.
- **Figure 6.18** shows that as the host/fault permeability contrast increases, it becomes more important to account for fault multiphase properties using dynamic pseudo-curves. Generally, for a host/fault permeability contrast of less than 1000, it is unnecessary to account for fault multiphase fluid properties when predicting pressure data for the addressed flow rate, *i.e.* a lateral Darcy velocity of approximately 2×10^{-4} ft/day.
- As the permeability of the faults decreases, it becomes more important to account for their multiphase behaviour when generating pseudo-curves to predict pressure variation in the upstream side of the fault (see **Fig. 6.19**).
- As the thickness of the fault rock decreases, it becomes more important to account for fault multiphase properties when generating pseudo-curves to predict pressure variation in the upstream side of the fault (see **Fig. 6.21**).
- Flow rates have a substantial impact on the shape of pseudo-relative permeability curves, but little impact on the shape of the pseudo-capillary pressure curves (see **Fig. 6.23** and **Fig. 6.24**).

- As flow rate increases, the generated pseudo-relative permeability curves tend to converge toward the undeformed reservoir rock curve, and *vice versa*.
- Increasing flow rate has a negative impact on the accuracy of the generated pseudo-capillary pressure curves, *i.e.* as flow rate increases the generated pseudo-capillary curves tend to diverge away from the undeformed reservoir rock curve, and *vice versa*.
- As flow rate increases, the generated pseudo-relative permeability curves become unstable and suffer from a lack of monotonicity and out of range points (*i.e.* $k_r > 1$ or $k_r < 0$).

6.6. Implication in 3D models

Most reservoirs are simulated using 3D geometries to capture their complexity and heterogeneity. The simplest way to incorporate fault rock properties into production simulation models is to use transmissibility multipliers, *TMs*. Alternatively, pseudo-curves can be generated and attached to those cells that are believed to juxtapose faults from the upstream sides. In the test considered in this section, pseudo-curves are generated individually for every pair of cells that juxtapose a fault in a large 3D model. These tests are conducted for two reasons. Firstly, to test if the generated library of pseudo-curves using the proposed simple two-cell model can approximate the results of fine-grid runs with non-neighbour connections. Secondly, to test the validity of the method on non-trivial, faulted 3D models with a significant amount of heterogeneity. For large 3D models, pseudos are generated for every pair of cells juxtaposed across a fault using the model geometry shown in **Fig. 6.2**.

The adopted workflow is illustrated in **Fig. 6.29**. A slightly different practical workflow proposed for the same purpose, but uses across-fault Darcy flow rates estimated from a single-phase simulation run containing TMs, was also outlined by Manzocchi *et al.* (2002). A high-resolution model, using a discrete representation of faults, is first run to output the fine-scale data for dynamic pseudoisation at every time step. The data is stored in a readable **Eclipse 100™** output file. This discrete model will also be used to validate the results of the upscaled model at the end of the workflow. A simple two-cell model is then used to generate a library of pseudo-curves, using the K&B dynamic pseudofunction. This model is dynamically updated for every across-fault pair of cells in the discrete model. The input to this two-cell model is derived from the pre-stored **Eclipse 100™** output file, where cell geometries, rock properties, initial saturations, pressure, and across-fault fractional flows, including those between non-neighbour connections, can be read. In the new upscaled 3D model, only pseudo-curves generated for the upstream cells to the fault are attached to their corresponding cells in the full-field model and *TMs* are used to account for fault thickness and permeability. This latter model is referred to as the *TM*+Pseudo Model.

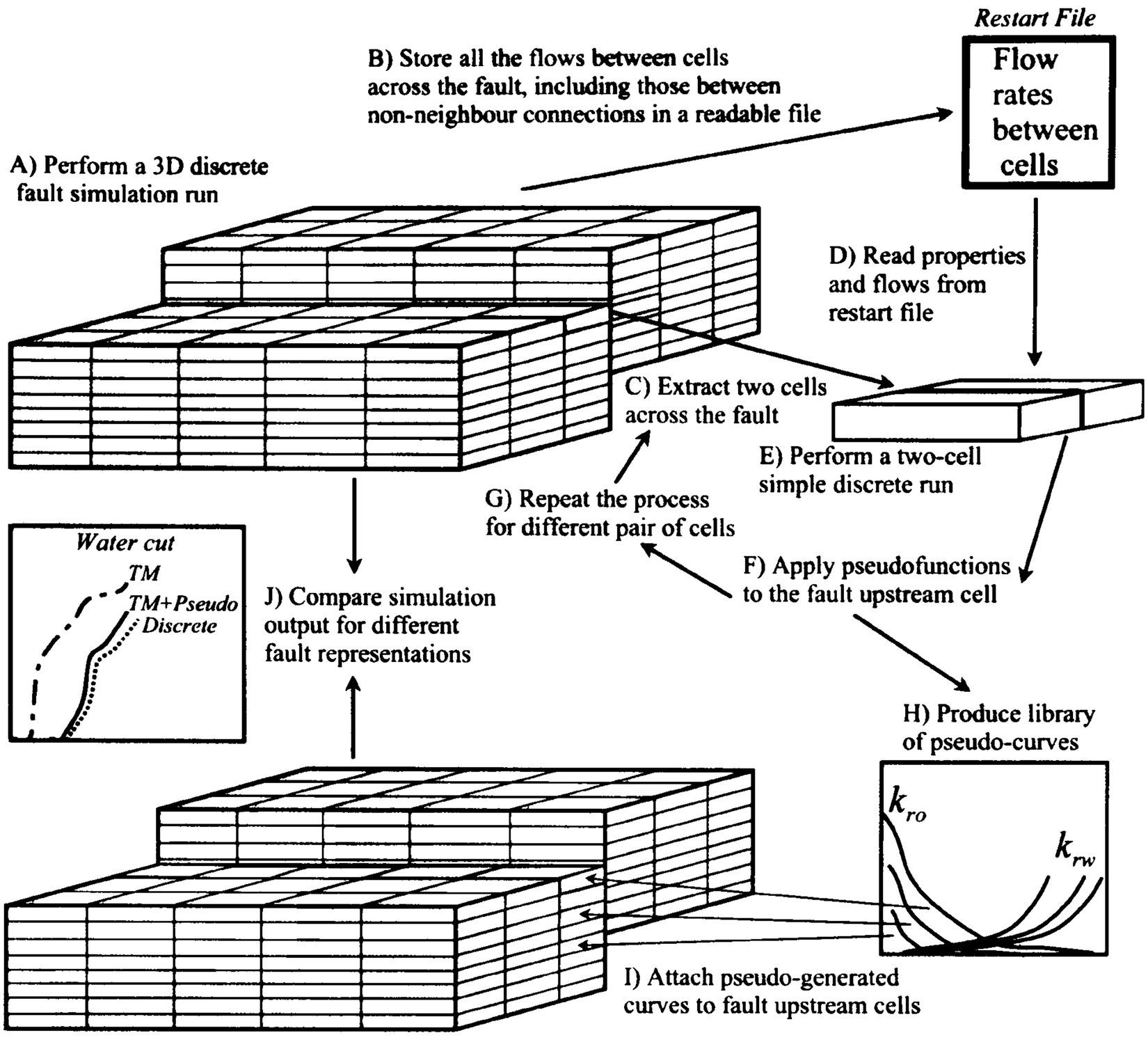

Fig. 6.29. A simplified workflow showing the typical procedures for pseudo generation using a simple two-cell model. Note that if a fault upstream cell is neighboured by two cells in the downstream side, these latter cells are replaced by a single downstream cell in the two-cell model with averaged properties of the two cells. A slightly different practical workflow, using different way of estimating across-fault Darcy flow rates, was proposed in the work of Manzocchi *et al.* (2002).

In the following two sections (**§ 6.7** and **§ 6.8**), two 3D models, homogeneous and heterogeneous, are tested for the validity of the pseudo-generated curves. Each model was constructed in a specific way to put the proposed pseudo-generation method under different severe tests. For each test, we first consider the model where fault fluid flow properties are included using *TMs* and observe its ability to duplicate the discrete model results, which are considered to be a high-resolution true model but computationally expensive, under a range of flow rates. For a case where the *TM* model fails to represent the fault fluid flow properties, a new model, analogous to the *TM* model but supplemented with pseudo-curves for all fault upstream cells, is proposed as a practical model that carries the characteristics of the multiphase fault rock properties.

6.7. Faulted Model-1 (homogeneous case)

6.7.1. Model-1 description

In this section we will investigate whether the simple two-cell model of **§ 6.6** can be used to generate a valid library of pseudo-curves for a pair of faulted cells covering a range of throws. A 3D, two-phase simulation model was constructed and compartmentalised by two vertical faults, the first being 3 ft thick with a permeability of 0.01 mD and a constant throw of 100 ft, and the second a 0.5 ft thick fault with a permeability of 0.1 mD and a constant throw of 20 ft (**Fig. 6.30**). The model contains homogeneous host rock of permeability 1000 mD in the *x*- and *y*-directions, and 100 mD in the *z*-direction. The model description is summarised in **Table-6.3**.

Table-6.3: Reservoir rock, phases, geometry and schedule data for Model-1 (oil/water system).

Item	Model parameters
Phases and rock data (Field units)	
• Reference pressure (RP) • Reference temperature	• 5000 (psia) • 60 (^{0}F)
Dead oil PVT properties: • Density at stock tank • Formation volume factor (FVF) at RP • Compressibility • Viscosity at RP • Slope of viscosity versus pressure • Slope of FVF versus pressure	 • 49 (lbs/ft^3) • 1.9 (rb/stb) • 2E-5 (psi^{-1}) • 2.0 (cP) • 0.0 (cP/psia) • 0.0 (rb/stb/psia)
Undersaturated water properties: • Density at RP • FVF • Compressibility • Viscosity at RP • Viscosibility at RP	 • 63 (lbs/ ft^3) • 1.02 (rb/stb) • 3E-6 (1/psi) • 1.0 (cP) • 0.0 (1/psi)
Rock properties: • Compressibility at RP	 • 4E-6 (1/psi)
Reservoir and grid block geometry data (Field units)	
Number of grid nodes	50 × 5 × 8
Spacing	D*X* = 50 (ft) D*Y* = 50 (ft) D*Z* = 40 (ft)
Grid type	Cartesian
Grid geometry	Corner point
Depth to reservoir top	3000 (ft)
Reservoir pressure, phase contacts and schedule data (Field units)	
Initial phase contacts	Oil–water contact (OWC) at 3400 (ft)
Reservoir pressure	5000 (psia) at 3000 (ft)
Production rate	Varied, **see text**, controlled by liquid flow rate
Injection rate	100% voidage replacement
Time step size	1000 (steps) × 60 (days) (total simulation time = 60,000 days)

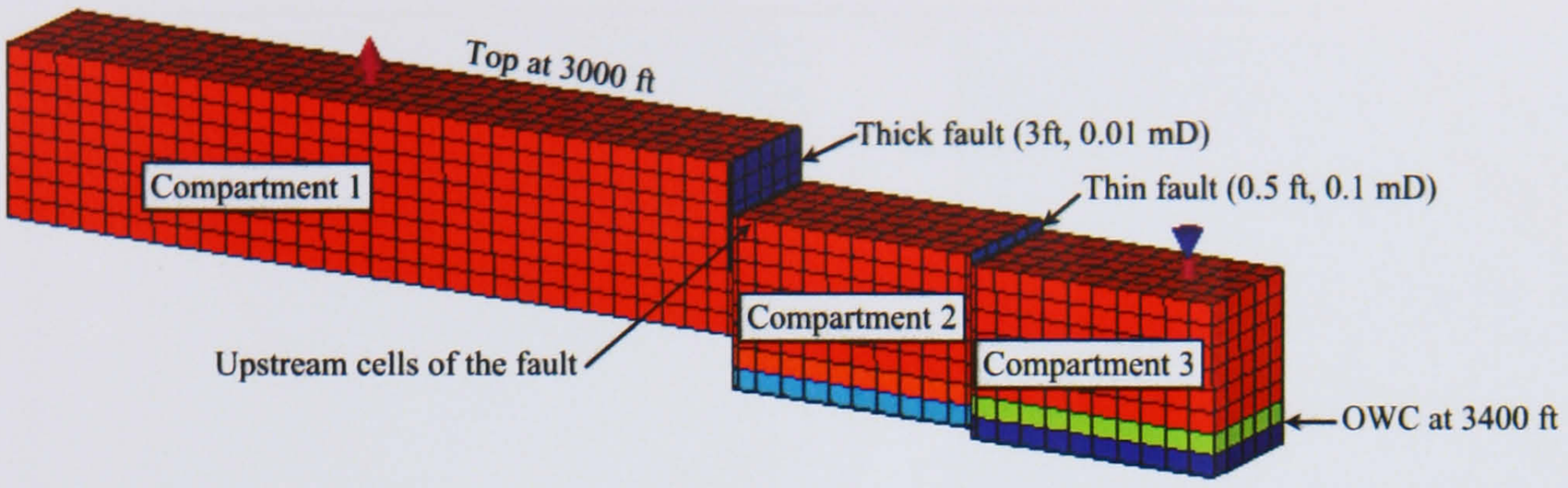

Fig. 6.30. Model-1 geometry and initial OWC. Compartments are labelled for results representation. Note that the faults are along the *y*-direction.

The fluid flow properties for each fault were represented in the simulation using the following three models (all are identical in geometry with a single water injector and an oil producer).

- ***TM* Model**: Faults are represented using transmissibility multipliers. *TMs* for the 3 ft thick and the 0.5 ft thick faults are, respectively, 0.00017 and 0.0099 (calculated using **equation-6.16**, with host rock permeability of 1000 mD).

- **Discrete Model**: Faults are represented with multiphase (imbibition capillary-pressure and relative-permeability curves, **Fig. 6.31**) properties incorporated discretely (curve derivation is analogous to that proposed by Manzocchi *et al.* (2002) for a water-wet, oil/water system, see **Chapter 3**). Local grid refinements are used to define the fault zones and reduce numerical dispersion.

- ***TM*+Pseudo Model**: As well as the *TM* representations, dynamic K&B pseudofunction curves are attached to the upstream cells of the faults, see **Fig. 6.31**, to account for the multiphase behaviour of the fault zone. As the faults are aligned along the *y*-direction, only *x*-directional pseudo-curves are generated (flow is mainly along the *x*-direction and hardly any across-fault flow takes place along the *y*- or *z*-directions).

In addition to the original fault rock and the undeformed reservoir, or host rock, curves, **Fig. 6.31** also shows two pseudo-curves, relative-permeability and capillary-pressure, corresponding to each fault. These are representative curves, *i.e.* averaged curves for each set generated using a mean flow rate for all the across-fault flow rates for every fault. The total number of generated pseudo-curves is 30 curves for the thick fault and 40 curves for the thin fault.

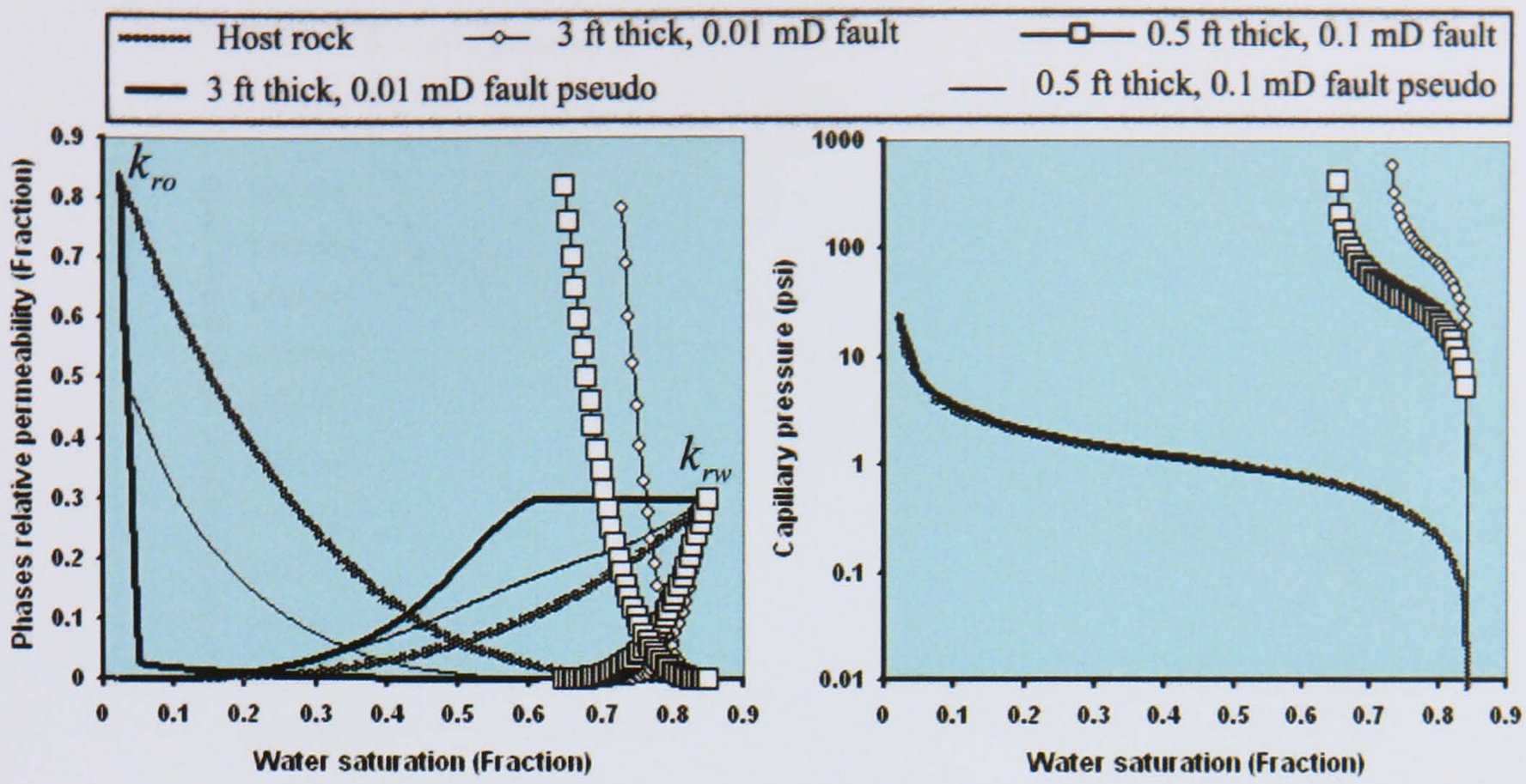

Fig. 6.31. Fault and host rock original curves. The figure also shows representative pseudofunction curves for each set of K&B pseudo-generated curves for both faults, obtained using an across-fault Darcy flow rate of 0.005 ft/day. These curves are attached to the upstream cells of the fault to account for its multiphase behaviour in the simulation model. Note that the pseudofunction capillary-pressure curves are almost identical to the host rock curves.

6.7.2. Fluid flow modelling results

6.7.2.1 TM Model versus Discrete Model for various Darcy flow rates

Figure 6.32 shows the oil in place in compartments 2 and 3 (see **Fig. 6.30**) as a function of the pore volume injected (PVI) into compartment 3 for three different lateral Darcy flow rates (q), namely 0.0005 ft/day, 0.005 ft/day and 0.05 ft/day. These flow rates approximately correspond to well injection rates of, respectively, 5 stb/day, 50 stb/day and 500 stb/day, for the addressed model geometry. The simulation is performed to test the ability of the *TM* Model to duplicate the high-resolution Discrete Model. The *TM* Model results, for all flow rates, show less differences between them than the Discrete Model results do. As the simulation progresses, The *TM* Model results converge together, especially at the end of simulation when the model is dominated by a single-phase flow. At this stage, *i.e.* for single-phase flow, theory predicts that both The *TM* and discrete results should be almost identical. However, the results show that this proves true for compartment 2 results (**Fig. 6.32a**) but not for compartment 3 results (**Fig. 6.32b**). One explanation for this is that the flow out of compartment 3 is affected by both faults, whereas that out of compartment 2 is only affected by one fault. For this reason, capillary trapping phenomena, which only manifest for discrete fault representations, are more dominant for flows out of compartment 3, especially at low flow rates (see **Fig. 6.32b**). The common observation in both plots is that as the flow rate increases, the discrepancy between the discrete and the *TM* fault representations decreases.

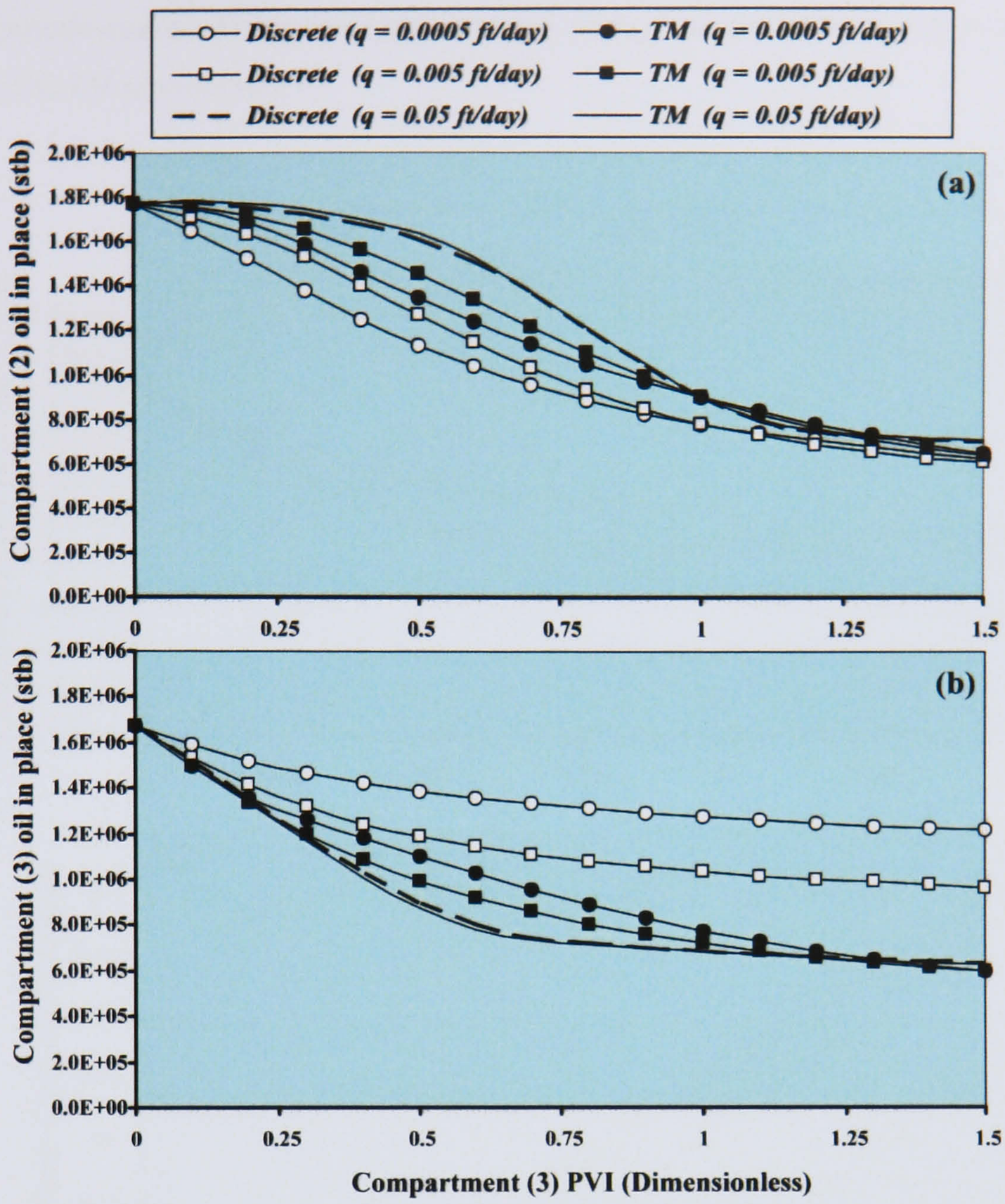

Fig. 6.32. Some simulation results to compare the *TM* and the Discrete Models for different lateral Darcy flow rates: **(a)** Compartment 2 oil in place; **(b)** Compartment 3 oil in place. Results are plotted as a function of compartment 3 pore volume injected (PVI), see **Fig. 6.30**.

6.7.2.2 Model-1 improvement using the K&B pseudo-generated curves

The discrepancy between the *TM* Model and the Discrete Model can be significantly improved by attaching the pseudo-curves to the fault upstream cells in the *TM*+Pseudo Model. The results after applying the full set (70 pseudo-curves in total) and the representative curves (single pseudo-curves for every fault) in the simulation model are shown in **Fig. 6.33**. These results are for the intermediate Darcy velocity of 0.005 ft/day (see **Fig. 6.32**). **Figure 6.33a** shows the compartment 3 remaining oil in place, **Fig. 6.33b** shows the water cut at the producer site (**Fig. 6.30**), and **Fig. 6.33c** shows the field oil production rate. For consistency and comparison purposes, all of the results are plotted as a function of compartment 3 PVI. In **Fig. 6.33b** and **Fig. 6.33c**, the results are plotted starting with a compartment 3 PVI of 0.8 for scaling purposes, as no water breakthrough is observed at the producer until the compartment 3 PVI reaches about 1.01. The *TM* Model results do not reproduce well the results of the 'fine' Discrete Model. All of the plots show a clear improvement in the *TM* Model after supplementing *TMs* with the

generated pseudo-curves. Using the representative curve for each fault produces much better results than the *TM* representation.

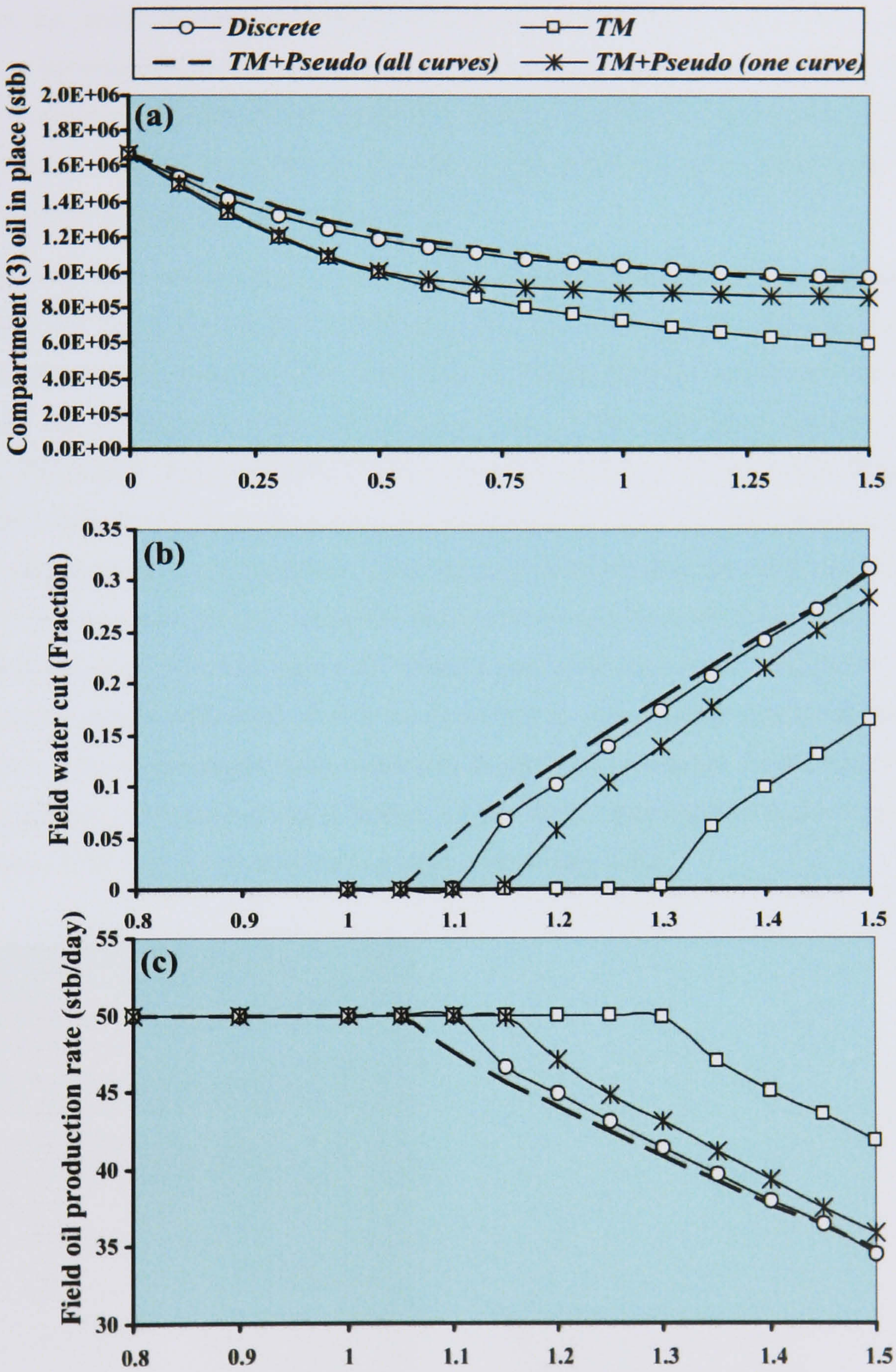

Fig. 6.33. Some simulation results showing the improvement over the *TM* Model when incorporating pseudo-curves in the *TM* simulations for a Darcy velocity of 0.005 ft/day: **(a)** compartment (3) oil in place, **(b)** field water cut, **(c)** field oil production rate. Results are plotted as a function of the compartment (3) pore volume injected (PVI), see **Fig. 6.30**.

6.7.3. Discussion (Model-1)

Flow rates have a very significant impact on the match between the *TM* and the Discrete Models. *TMs* provide a good approximation for the effects of faults on fluid flow under high flow rates, *i.e.* under a viscous driven flow regime. On the other hand, a very significant discrepancy between the two models can result when subjecting the system to low flow rates, *i.e.* under a capillary dominated flow regime (**Fig. 6.32**). For high flow rates, full pseudos might not be needed. It is therefore worthwhile running simple models to test whether or not pseudos are needed before running the full simulation models.

Figure 6.34 shows oil saturation after one pore volume injection (PVI) into compartment 3. Before the water flood hits a fault, no distinction between the models can be observed. As the water front hits the first fault, the *TM* Model starts to exhibit different behaviour from the other two models and the difference becomes more apparent as the flood front crosses the second fault. The *TM*+Pseudo Model seems to approximate the behaviour of the Discrete Model in all of the layers with a very small advance in the flood front (*cf.* layer 8). The *TM* Model predicts less oil being trapped in compartment 3, the injector location, than the other two models. A significant improvement in representing the fluid flow properties of the faults can be achieved by complementing the *TM* simulation with dynamic pseudofunction curves (**Fig. 6.33**). For very large complex faulted reservoirs, it may be necessary to significantly reduce the number of pseudo-curves placed within the final simulation model by grouping the curves and choosing a representative curve for each group (Christie, 1996). These representative curves can improve the accuracy of the fault representation to a large degree (**Fig. 6.33**).

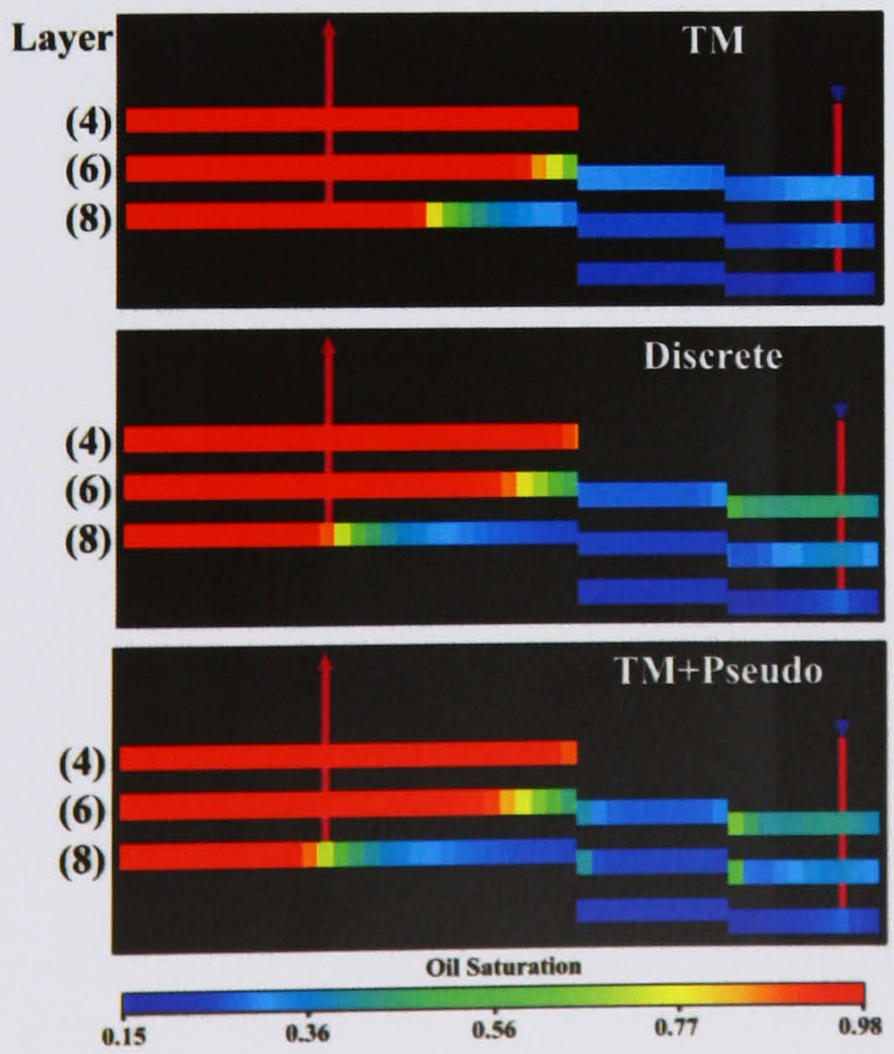

Fig. 6.34. Cross-sectioned (*x-z*) oil saturation maps for different layers in the three fault representations, after about one pore volume injection (PVI) of compartment 3.

6.8. Faulted Model-2 (heterogeneous case)

6.8.1. Model-2 description

The following model will be used to test the effect of permeability heterogeneity on the generated pseudo-curves. A 3D, two-phase simulation model was constructed and compartmentalised by one vertical fault, 3 ft thick with a permeability of 0.01 mD (**Fig. 6.35**). The model contains dipping layers of heterogeneous host rock with permeability ranging from 50 mD to 1047.7 mD in all directions. The fault has a constant throw of 47 ft. The model description is summarised in **Table-6.4**.

Table-6.4: Reservoir rock, phases, geometry and schedule data for Model-2 (oil/water system).

Item	Model parameters
Phases and rock data (Field units)	
• Reference pressure (RP) • Reference temperature	• 5000 (psia) • 60 (^{0}F)
Dead oil PVT properties: • Density at stock tank • Formation volume factor (FVF) at RP • Compressibility • Viscosity at RP • Slope of viscosity versus pressure • Slope of FVF versus pressure	 • 49 (lbs/ft^3) • 1.0 (rb/stb) • 2E-5 (psi^{-1}) • 2.0 (cP) • 0.0 (cP/psia) • 0.0 (rb/stb/psia)
Undersaturated water properties: • Density at RP • FVF • Compressibility • Viscosity at RP • Viscosibility at RP	 • 63 (lbs/ ft^3) • 1.0 (rb/stb) • 3E-6 (1/psi) • 1.0 (cP) • 0 (1/psi)
Rock properties: • Compressibility at RP	 • 4E-6 (1/psi)
Reservoir and grid block geometry data (Field units)	
Number of grid nodes	25 × 25 × 10
Spacing	D*X* = 40 (ft) D*Y* = 40 (ft) D*Z* = 20 (ft)
Grid type	Cartesian
Grid geometry	Corner point
Depth to reservoir top	8000 (ft)
Reservoir pressure, phase contacts and schedule data (Field units)	
Initial phase contacts	Oil–water contact (OWC) at 8227 (ft)
Reservoir pressure	5000 (psia) at 8000 (ft)
Production rate	25 (stb/day) controlled by liquid flow rate
Injection rate	100% voidage replacement
Time step size	1000 (steps) × 30 (days) (total simulation time = 30,000 days)

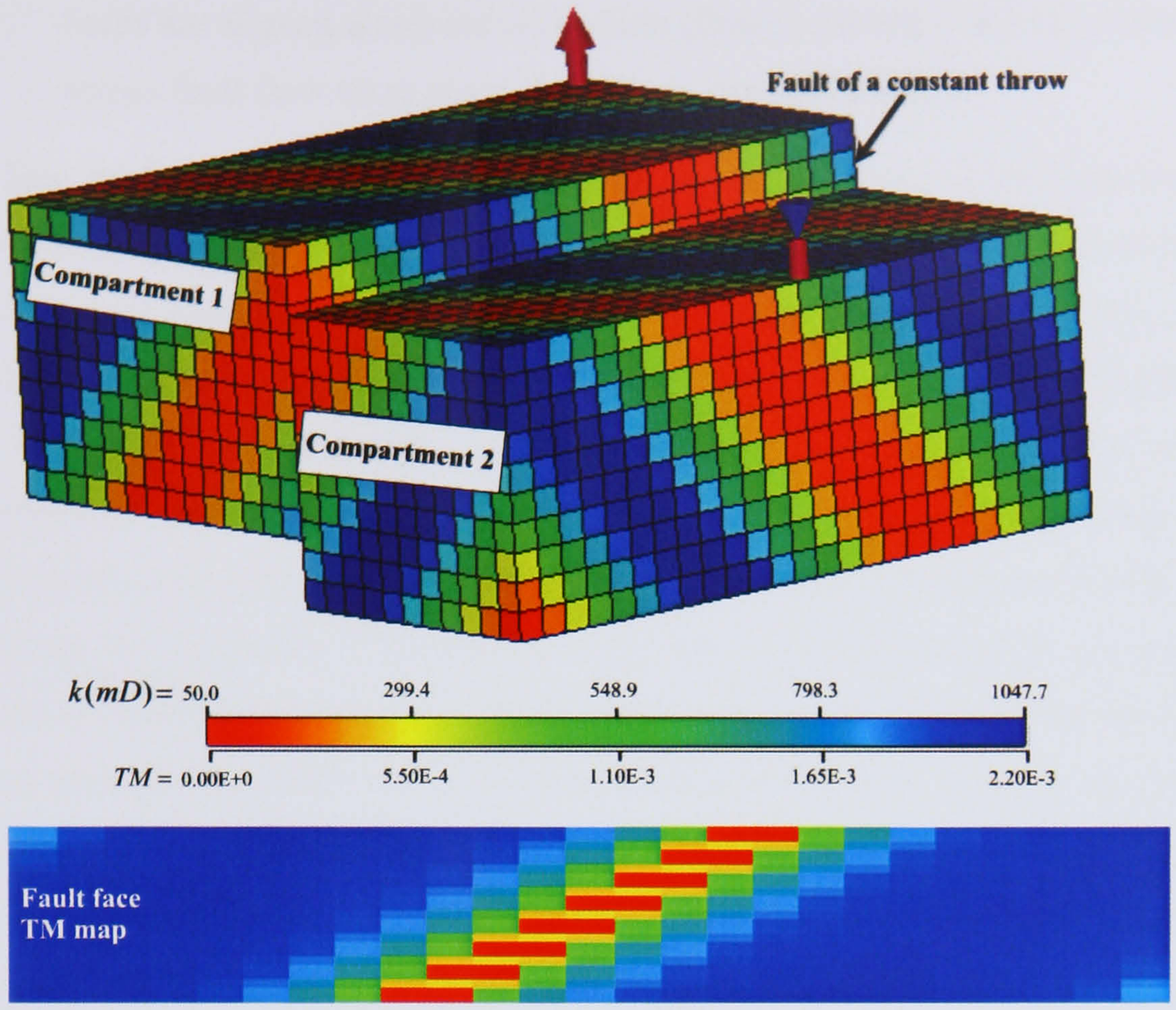

Fig. 6.35. Model-2 permeability distribution and fault face *TMs*. Compartments are labelled for results representation. Note that the fault is along the *y*-direction.

The fluid flow behaviour for each fault was represented in the simulation using the following three models (all are identical in geometry with a single water injector and an oil producer).

- ***TM* Model**: Faults are represented using transmissibility multipliers. *TMs* vary across the fault face (because the host permeabilities vary) and range between 0.00026, forming a dipping slab in the middle of the fault face, and 0.00219, at the extremities of the fault face (**Fig. 6.30**). *TMs* were calculated using **equation-6.16** for a constant fault thickness and permeability, and a host rock with constant geometry but varying permeability.

- **Discrete Model**: The fault is represented using multiphase (imbibition capillary-pressure and relative-permeability curves, similar to those displayed in **Fig. 6.31** for a permeability of 0.01 mD) properties incorporated discretely (curve derivation is analogous to that proposed by Manzocchi *et al*. (2002) for a water-wet, oil/water system, see **Chapter 3**). To simplify the problem, one host rock curve was applied, corresponding to a permeability of 1000 mD, despite the permeability variation. LGRs are used to define the fault zones and reduce numerical dispersion.

- ***TM*+Pseudo Model**: As well as the *TM* representations, dynamic K&B pseudofunction curves are attached to the upstream cells of the faults to account for the multiphase behaviour of the fault zone. Only *x*-directional pseudo-curves are generated because the

faults are aligned along the *y*-direction (flow is mainly along the *x*-direction and hardly any across-fault flow takes place along the *y*- or *z*-directions).

This model requires 200 pseudo-curves to account for the fault multiphase behaviour. To simplify the work of pseudo-generation, only across-fault flows of the middle layer of the fault face were used, thereby reducing the number of generated fault-pseudo curves to 25. Such a simplification is expected to be valid for this model since it is flooded at a low flow rate (25 stb/day, or equivalently, 7×10^{-4} ft/day lateral Darcy velocity across the entire model), and therefore little variation in the flow rates is expected across the model. Note also that this simplification is adopted here because fault properties (thickness and permeability) are constant along the entire face. Care must be taken later when attaching the generated pseudo-curves to the upstream cells of the fault. Each pseudo-curve generated from the central layer is attached to an upstream cell with the same host permeability to that where it was generated from. Flow rates are read from the fine-grid run, or discrete run. These flow rates are the total flow rates including those between non-neighbour connections. Pseudo-curves were generated individually using the simple two-cell model described in **§ 6.3.1**. All cell properties, including rock and fluids, were read from the discrete run output files and were updated for every two-cell model run. This process resulted in a set of 25 K&B pseudo-function curves, **Fig. 6.36**. The variation between the pseudo-curves is mainly attributed to the host rock permeability variation. The pseudo-capillary pressure curves are almost identical to the undeformed rock curve.

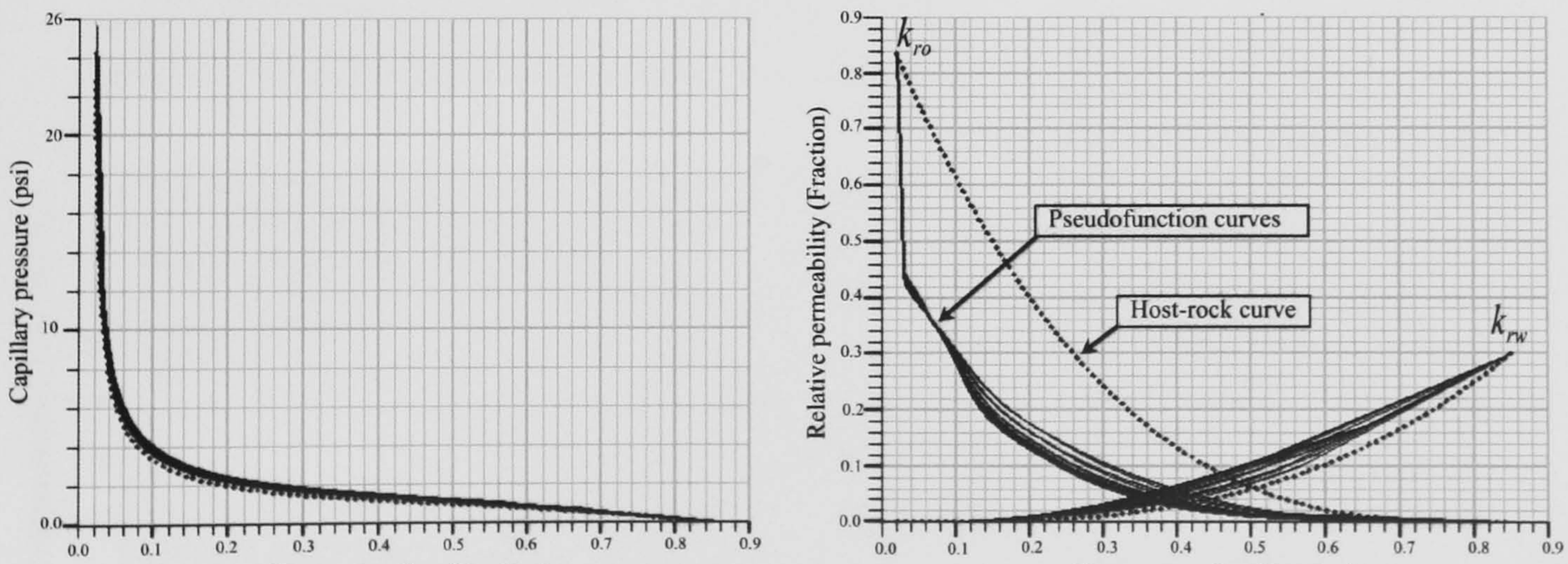

Fig. 6.36. K&B pseudo-generated curves for the middle layer of the fault face shown in **Fig. 6.35**, *i.e.* 25 curves. The undeformed sediment curves (dots) are also shown. The original fault rock curves are similar to those displayed in **Fig. 6.31** for a permeability of 0.01 mD.

6.8.2. Fluid flow modelling results (Model-2)

Figure 6.37 shows some results comparing the performance of the three representations of the fault, namely the Discrete, *TM* and *TM*+Pseudo Models. **Figure 6.37a** shows the compartment 2 remaining oil in place, **Fig. 6.37b** shows the field average pressure and the model producer bottom hole pressure (BHP), and **Fig. 6.37c** shows the field oil production rate and water cut at the producer. For consistency and comparison purposes, all of the results are plotted as a function of compartment 2 PVI (see **Fig. 6.35** for model compartments).

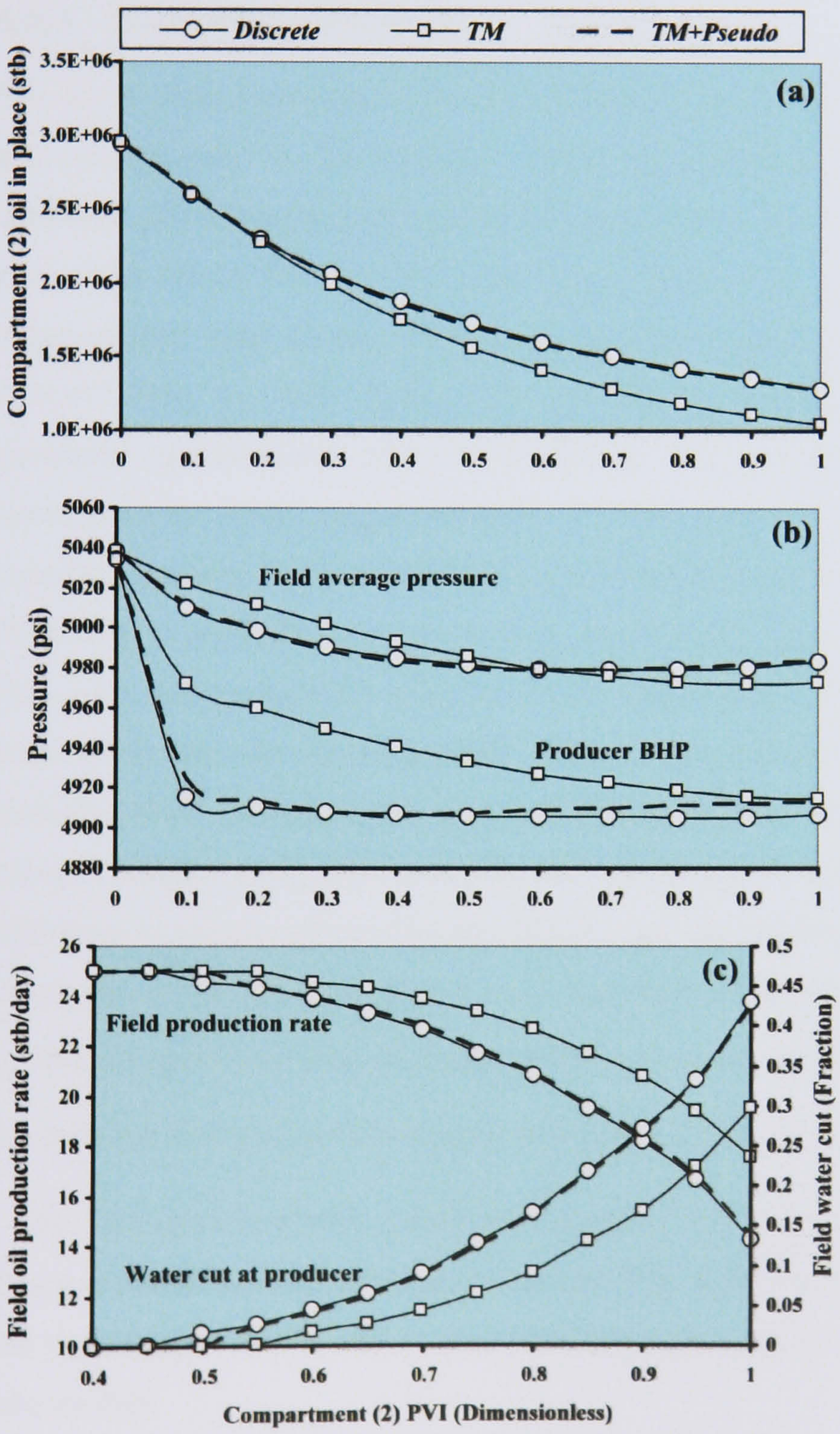

Fig. 6.37. Some simulation results showing the improvement over the *TM* Model when incorporating pseudo-curves in the *TM* simulations: **(a)** compartment (2) oil place, **(b)** field average pressure and producer bottom hole pressure (BHP), **(c)** field oil production rate and water cut. Results are plotted as a function of compartment (2) pore volume injected (PVI), see **Fig. 6.35**.

All of the results in **Fig. 6.37** show an excellent match between the Discrete Model (open circles) and the *TM*+Pseudo Model (dashed lines). An excellent duplication of the Discrete

Model is achievable with upstream fault pseudo-curves, as the petroleum production across the fault (**Fig. 6.37a**) and the phase flows (**Fig. 6.37c**) show. Pressures, as previously shown, are more sensitive to the different fault representations. Even though a very good match between the Discrete Model and the *TM*+Pseudo Model is shown in the pressure plots (**Fig. 6.37b**) the match is not as good for the producer BHP. One possibility is that BHP is usually measured at a single cell in the reservoir, usually the bottom connection cell, and when considering the parameters on a cell-by cell basis, the match is not as good as when considering the average behaviour of the reservoir, *cf.* the average pressure plot (**Fig. 6.37b**).

6.8.3. Discussion (Model-2)

The K&B pseudo-generated curves for Model-2 are very similar and form one group, despite the heterogeneity in the Discrete Model. The differences between the pseudo-curves are attributed to the heterogeneity in the host rock, since across-fault flows are very similar and are very small (about 7×10^{-4} ft/day). The initial tests conducted at the start of this chapter on the effect of flow rates on the resultant pseudo-curves showed that changing the flow rate from 0.5×10^{-4} ft/day to 1×10^{-5} ft/day does not have a considerable impact on the shape of the generated pseudo-curve (refer to **Fig. 6.23**). The host/fault permeability contrast in this heterogeneous model ranges between 10^5 and 5×10^3. As **Fig. 6.17** predicts, this range of contrasts can only cause a small variation between the generated curves, assuming the effect of flow rates is negligible. For this reason, the resultant pseudo-curves for the involved range of flow rates and permeability contrast in this model do not show a significant variation, but it is more likely that the observed small variation is attributed to the permeability heterogeneity. Actually, when performing the simulation using only one single representative curve generated using a simple mean flow rate for the whole set, a reasonably good match between the *TM*+Pseudo Model and the Discrete Model was still achieved. It is worth noting that the shape of the pseudo-curves shows that is more important to include fault multiphase fluid properties to predict oil movement than to predict water movement, because the k_{rw} curves are very similar for both the rock and pseudo-curves, unlike those for k_{ro}.

For this specific model, a very good match of the flood front sweep is observed between the Discrete Model and the *TM*+Pseudo Model (**Fig. 6.38**). As observed in Model-1, see **Fig. 6.34**, the waterfront in this model is also advancing less quickly in the *TM* Model than in the other two models.

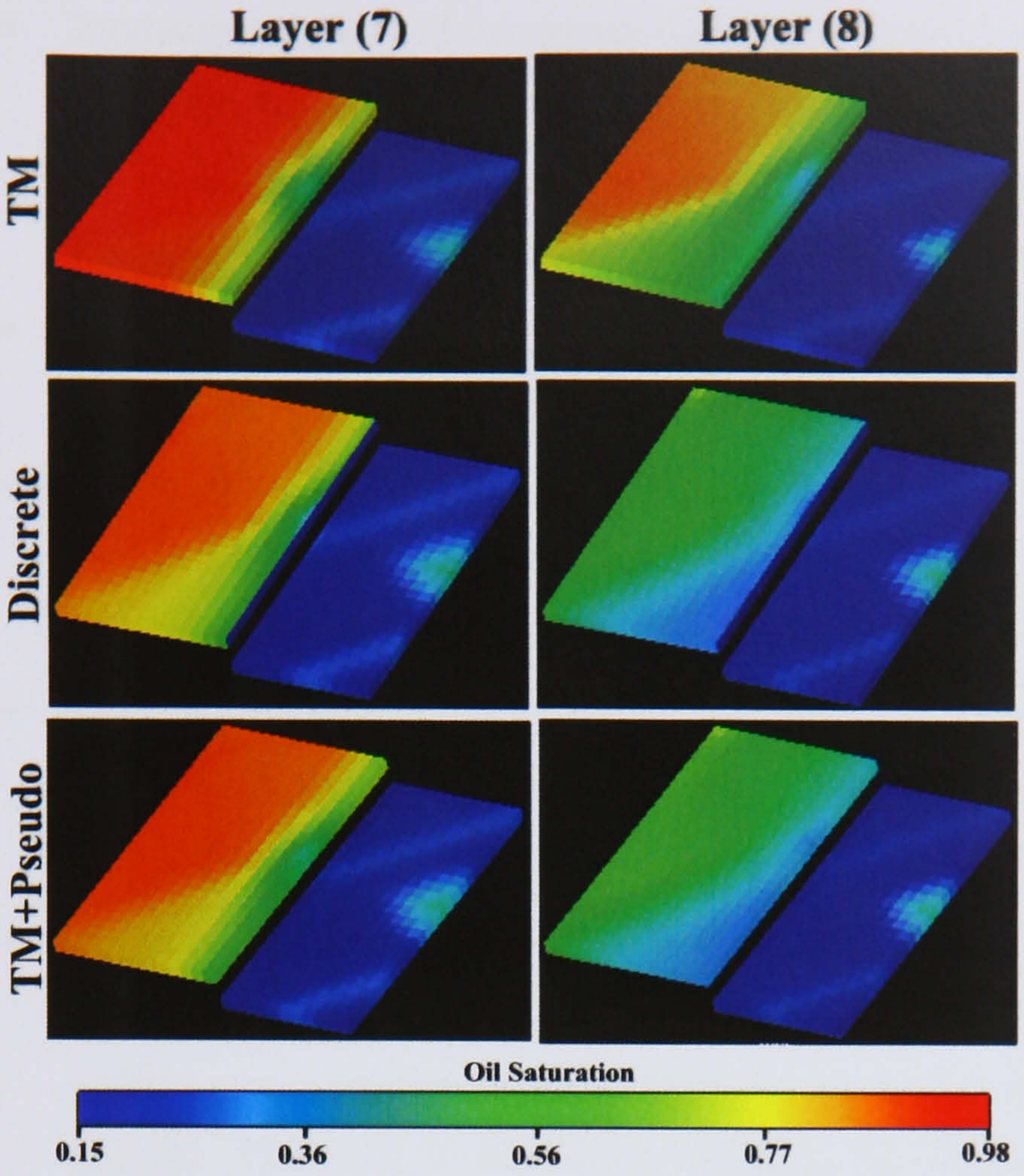

Fig. 6.38. Oil saturation maps for different layers in the three different fault representations, after about 0.75 pore volume injection (PVI) of compartment 2.

6.9. Conclusions and recommendations

In this chapter a simple two-cell model was used to:

- compare between four of the commonly used dynamic pseudofunctions in generating fault pseudo-curves;
- investigate the impact of fault permeability on the shape of the pseudo-generated fault curves;
- investigate the impact of fault thickness on the shape of the pseudo-generated fault curves;
- investigate the impact of across-fault Darcy velocity on the shape of the pseudo-generated fault curves;
- generate fault pseudofunction curves for some 3D faulted models.

These tests were primarily conducted to test the possibility of estimating pseudo-curves without having to run a 'fine-scale' simulation for all fault-juxtaposed cells. The basic approach to achieving this depends on observing cut-off ranges for some parameters that affect pseudo-curves, *e.g.* host/fault permeability contrast, fault thickness, flow rate, below or above which pseudo-generation may or may not be necessary to take into account the multiphase behaviour of some faults.

The study in this chapter has led to the following key conclusion points.

- The K&B and the PVW methods are the best pseudofunctions for generating fault pseudo-curves among the four methods tested in this chapter.

- Producing a library of two-phase fault pseudo-curves is a feasible process when considering a simple two-cell model separated by a fault zone. This library is likely to be very large for 3D simulations of structurally complex reservoirs because there are many single- and two-phase parameters that affect the pseudo-generated curves.
- It is important to generate the full saturation pseudo-curve points in order for the curve to be unique and valid for future use in simulation studies.
- When considering pore-volume weighting, the number of points generated in the pseudo-curves for low-permeability faults can be considered to be controlled by the saturation variation of the fault upstream coarse grid block for each time step.
- To guarantee that a full saturation pseudo-curve is generated, the fault upstream cell rock curve is converted to fractional flows. These fractional flows are then used in the simple two-cell model to guarantee that the desired saturation is reached.
- Pressure data are more sensitive to the shape of the pseudo-curves than the saturation data. Therefore pressure data should be used, whenever available, to validate the generated pseudo-curve. However, it is important to note that this conclusion is boundary-condition specific. The wells in the models tested in this study are controlled by flow rate and the comparisons of pressure, flow rates and oil in place are made at PVI, therefore, of the variables examined, pressure has the most degrees of freedom.
- When investigating the effects of fault thickness and permeability on the generated pseudo-curve, a general trend was observed. This suggests that it may be possible to predict the effect of some intermediate values, or extreme ones. This reduces the need to use a fine-scale simulation model to produce pseudo-curves for all fault rock thicknesses and permeabilities present.
- In contrast to the effects of fault thickness and permeability, the effects of flow rates are difficult to generalise since there was no regular trend was observed between the generated pseudo-curves. However, this conclusion is restricted to the two permeability cases tested in this study. More tests, not only on the three variables examined in this study, are likely to show more conclusive trends, and therefore relationships, to routinely models two phase behaviour of fault rocks using dynamic pseudo-curves. Other variables not modelled in this study include reservoir rock permeability, the oil and water viscosities, the relative permeability and capillary pressures curves, for both drainage and imbibition cycles, of both reservoir and fault and probably the two porosities of both zones (Manzocchi *et al.*, 2002)
- Instability and out-of-range values were obtained when relatively high across-fault flow rates were used to generate pseudo-curves. This problem persisted when trying to improve the model using more refined LGRs (see **Appendix C**) or increasing Newton iterations in the simulator.
- Including the multiphase behaviour of fault rock through pseudo-curve representations becomes less important for high flow rates, or more generally, for viscous dominated flows.

In such cases, using the single-phase representation, *i.e. TM* treatment, gives very satisfactory results. In some cases, accounting for faults using pseudo-curves might deteriorate the actual behaviour of faults in these cases. It is important to mention that two-phase effects need to be taken into account (if only through the end-point values) if the relative-permeability curves of fault rocks are very different from those of the host rock, and not as in this study where it is assumed that the two curves can be correlated using the Corey–Brooks-type relationship. Using measured curves could lead to different conclusions on when the use of pseudo curves is important for different flow regimes. It is possible that more work is required in this specific area to try to generalise the trends of the generated pseudo curves for all the possible variables using measured host and fault curves, rather than correlated curves using relationships like those proposed by Ringrose *et al.* (1997) and Manzocchi *et al.* (2002).

- A workflow was established to generate fault pseudo-curves for 3D faulted models using a simple two-cell model.
- The method outlined in this study for pseudo generation was shown to be very effective as an alternative representation of faults in real simulation models, when tested for different 3D models. The study can be extended and validated to generate a large library of two-phase fault pseudo-curves by varying all possible parameters that affect the shape of the pseudo-curves. Ideally, this library can be linked to an external program, which is in turn linked to a main simulation program. By running a pilot, or sensitivity study to predict the variation of some parameters to which the pseudo-curves are indexed, *e.g.* predicting across-fault flow rates using a single-phase simulation with grid block permeabilities corresponding to the water relative permeability end-point and with water viscosity, as suggested by Manzocchi *et al.* (2002), the external program can be used to automatically link the fault pseudo-curves in its library to the corresponding faulted cells (mainly upstream cells) in the main simulation model.

Chapter 7

In situ generation of dynamic fault pseudo-curves

"The majority of all hydrocarbon-bearing traps are fault-related. In the reservoir management side, where we're coming from, where you may be putting in injectors and producers, we're interested just as much in whether fault analysis shows there's a baffle to flow."

David Hardy

Product Manager at Roxar

7.1. Introduction

In the previous chapters we have shown that the way that transmissibility multipliers, *TMs*, are conventionally used in simulating faulted reservoirs does not take into account the multiphase behaviour of fault rock. **Chapter 2** shows that this static treatment of faults can lead to serious errors when predicting some parameters in a simulation study. This limitation in fault treatment can, however, be improved by using 'fault-rock' pseudo-curves in cells adjacent to faults in simulation models (**Chapter 6**). One of the least known parameters that is required for pseudo-curves generation is the across-fault Darcy velocity. **Chapter 6** presented a simple two-cell model, separated by fault material, where this parameter and other various parameters that affect pseudo-curves can be simply tested within reasonable limits. Such tests can provide a reference library of fault pseudo-curves for reservoir engineers to routinely model the two-phase effects of fault rocks in conventional simulation models. However, due to the large number of variables, considering both fault and host fluid and rock properties and their inter-dependence, this library can be huge, yet feasible to construct (Manzocchi *et al.*, 2002). Furthermore, as noted in **Chapter 6**, this library requires an external program, that is directly linked to the simulator output to automatically assign the correct, or approximately the correct, fault pseudo-curve to each cell adjacent to faults based on the rock properties, fluid properties, and geometries of both the fault and host rocks. Although not completely covered under the scope of this PhD thesis, a brief outline of how to implement the idea of the fault pseudo-curve library generation process is given in **Chapter 6**.

This chapter presents a more practical approach of fault pseudo-curve generation in a faulted simulation model. As is the case in any study, measured data is a key element in this approach. In recent years far more data has been collected on the structure of faults (*e.g.* Harris *et al.*, 2003) and the fluid flow properties of fault rocks (Fisher and Knipe, 1998; 2001). Such

information allows a more sophisticated, geologically reasonable, treatment of faults in production simulation models.

The chapter starts by presenting a new method to generate pseudo-curves using simulation model output in the form of *in-situ* pressures and saturations. Section **7.2** outlines the procedures of the method in a step-by-step basis. The formulation of this model, as explained in **§ 7.3**, is based on the well-known pore-volume weighted (PVW) dynamic pseudofunction (see **Chapter 6**). Section **7.4** discusses some issues that may arise when applying the method to general cases and suggests some possible solutions. Weaknesses and strengths of the proposed method are discussed in **§ 7.5**. The model will be tested on some simple and complex faulted simulation models (**§ 7.6**). Method applicability to real simulation models is briefly discussed in **§ 7.7**.

Fore complexly faulted models, active fluxes, either flows or pressures, can be preserved and the full-field models can be divided into active regions. This makes the handling of faults in each region much easier, and also saves a considerable amount of simulation time since impractical simulation times and/or memory restrictions may arise when all the faults in a densely faulted full-field simulation model are included discretely. **Figure 7.1** shows the performance of the flux boundary condition in a 3D zone of the Pierce Field (see **Chapter 3**). The results show that the reduced run, hereinafter referred to as the 'Use flux' run, gives identical results to the full-field run, hereinafter referred to as 'Dump flux' run, and saves a considerable amount of CPU run time. This procedure of saving flux boundary condition can be generalised and more than one sub-domain can be preserved. This feature of flux preservation will be taken advantage of in this chapter to divide densely faulted models into number of sub-regions and then handle each simple region separately.

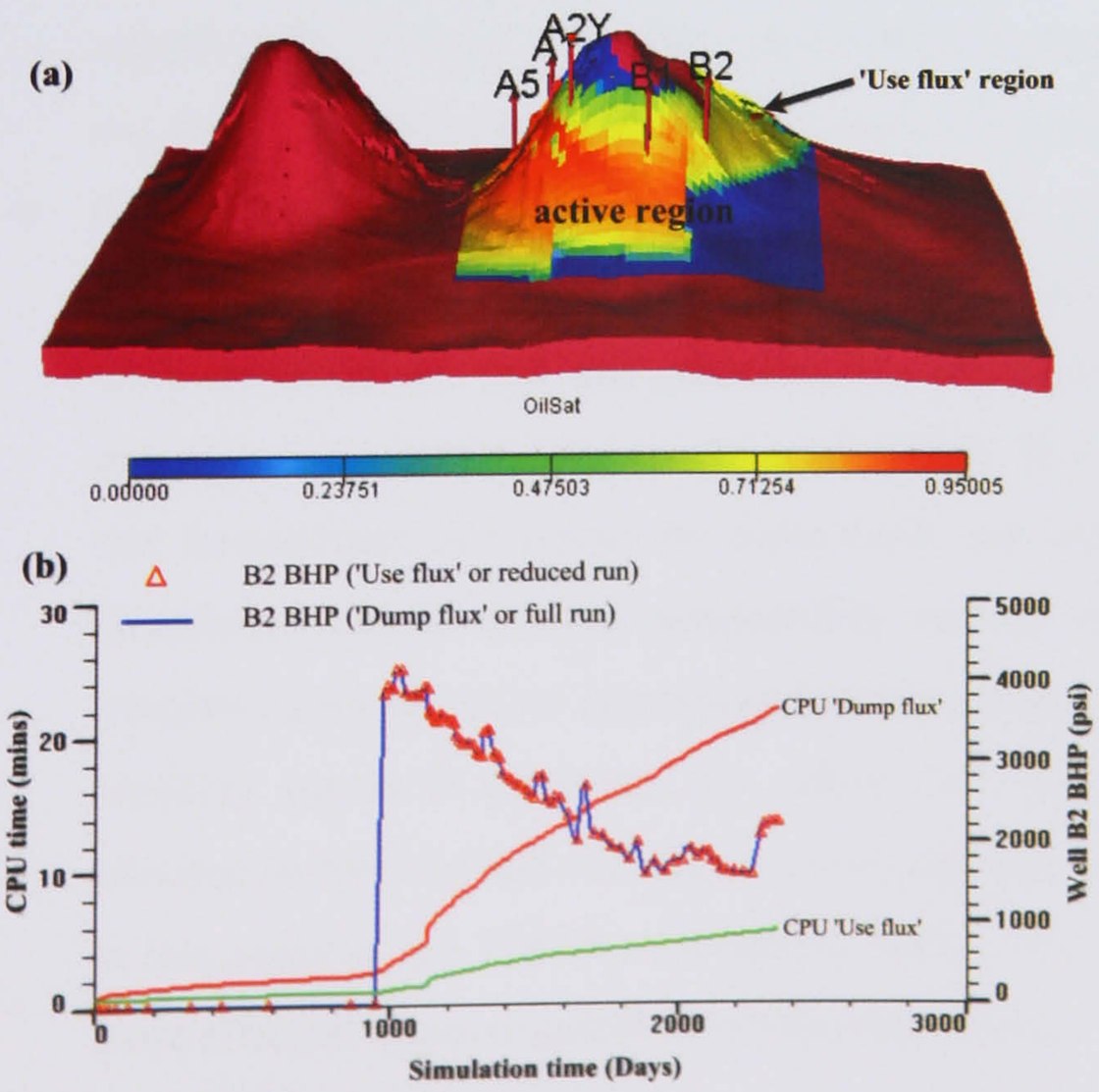

Fig. 7.1. (a) Grid display of the Pierce Field showing the global run grid cells (full-field or 'Dump flux' run) that are used to preserve flux boundary conditions for a chosen region (active region) in a reduced run (or 'Use flux' run). **(b)** The performance of each run in B2 BHP. Note the large difference in the CPU time between the two runs.

7.2. Basic pseudo procedure

The primary objective of pseudo generation in this chapter is to approximate the discrete run results. The same assumption followed in the previous chapters is adopted here, namely that the high resolution model, in which all faults are included discretely, is assumed to give the most realistic results (*e.g.* Cao and Aziz, 1999; Guzmán *et al.*, 1999; Pickup *et al.*, 2000; Darman, 2001), since no observed data is available to provide a comparison. The following steps, see **Fig. 7.2**, are followed in this process of 'fault-rock' pseudo-curve generation.

- Starting with a full-field simulation model (**Fig. 7.2A**), divide the model into sub-domains, *i.e.* flow or pressure inter-connected regions (**Fig. 7.2B**). In this 'Dump flux' run, all of the faults are incorporated using a realistic *TM* representation. Although *TMs* might not represent the correct behaviour of faults when considering multiphase flow, this representation can be improved significantly by varying the *TM* values along faults as a function of phase contacts, see **Chapter 2**. The feature of preserving flux boundary conditions around different regions is available in the **Eclipse 100**^{TM} simulator used in this study.
- For each sub-domain, the following tasks are performed. Firstly, the region is activated using the ACTNUM keyword in the **Eclipse 100**^{TM} data file ('Region section', Eclipse manual, Geoquest, 2003). Secondly, fault zones are included with their independent properties and saturation functions using a stable local grid refinement (LGR) scheme (**Fig. 7.2C**), see **Appendix C**.
- Now generate dynamic 'fault-rock' pseudo-curves, see **§ 7.3**, for every fault-adjacent cell in every active region (**Fig. 7.2D**). As a result, a set of fault pseudo-curves is obtained for each region (**Fig. 7.2E**). These curves, relative permeability and capillary pressure curves, should carry the characteristics of the fault multiphase behaviour. The set of curves may vary significantly in shape depending on how the parameters that control pseudo-curve shape, *e.g.* fault thickness, fault permeability, across-fault Darcy velocities, vary (see **Chapter 6**).
- Next, attach the generated pseudo-curves to their corresponding regions and fault-adjacent cells in the original full-field simulation model based on the *TM* representation (**Fig. 7.2F**). Only those curves that are generated for the fault upstream cells, with respect to flow direction, are relevant (Manzocchi *et al.*, 2002). If a cell acts simultaneously as an upstream and downstream cell across the same fault, see Manzocchi *et al.* (2002) for an example, directional pseudo-relative permeability curves are generated. As the **Eclipse 100**^{TM} simulator does not allow directional functions of pseudo-capillary pressure curves, only one capillary curves is generated per coarse cell. The model where fault pseudo-curve are attached in the full field simulation model together with the *TM* representation is referred to in this study as the *TM*+Pseudo Model. This is the target practical model that is used as a more efficient approximation to the discrete model.

- Finally, to assess the performance of the pseudo-generation code, observed field data are used to compare different fault representations (**Fig. 7.2**). In this chapter, the outputs provided by the discrete model, *i.e.* the high-resolution model, are treated as observed data.

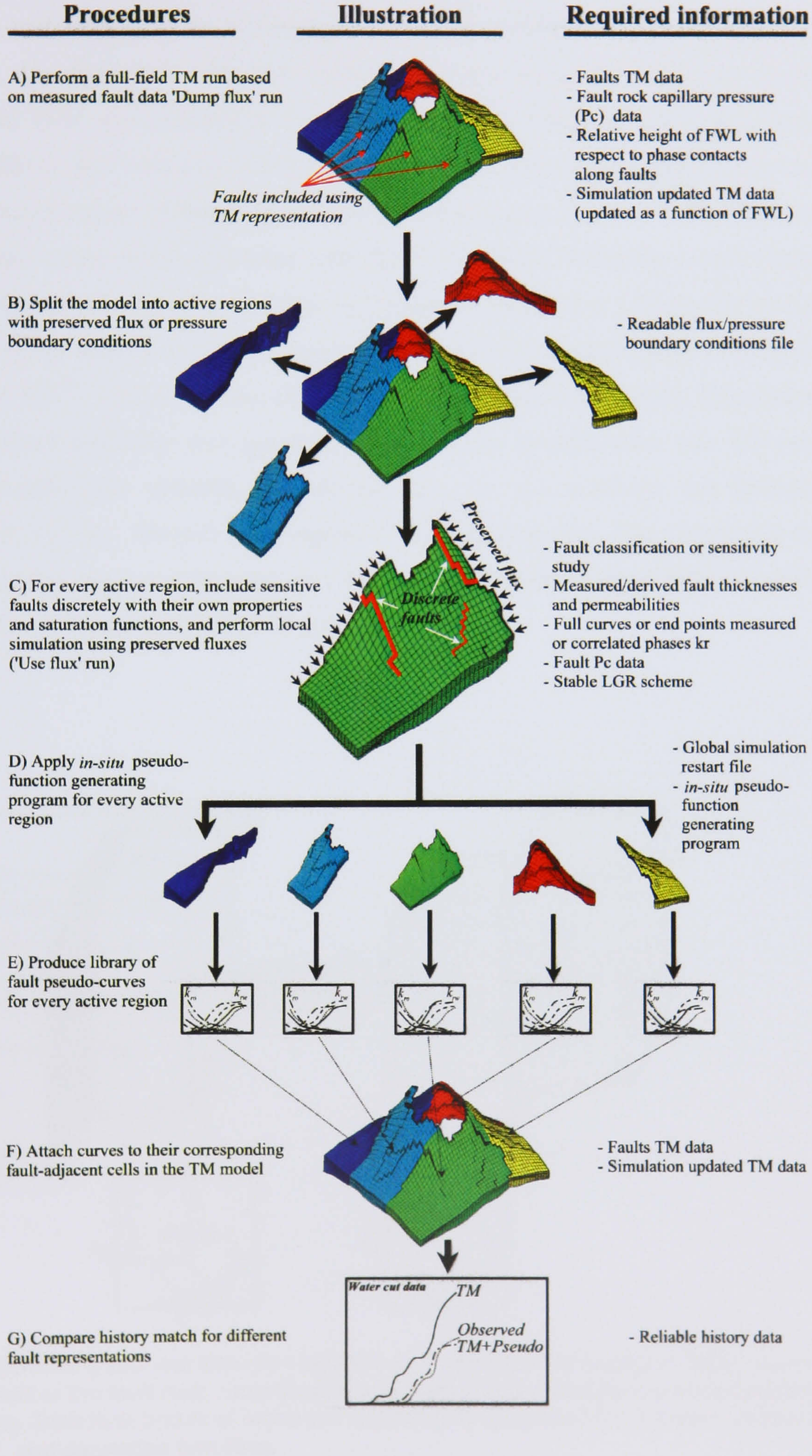

Fig. 7.2. A workflow describing and illustrating the procedures and detailing the required information for *in-situ* fault pseudo-curve generation presented in this chapter.

7.3. Pseudo formulation

This chapter presents the pore-volume weighted (PVW) dynamic pseudofunction formulation for non-neighbour connections. In comparison to the adopted pseudoisation technique in **Chapter 6**, *i.e.* the K&B, the PVW has been chosen in this chapter because it is easier to formulate and implement in software program for complex non-neighbour connections. In particular, this study deals with non-neighbour connection upscaling-technique associated with non-regular local grid refinements (LGRs) to represent faults discretely and, therefore, it is much easier to deal with pore-volume weighting than with central-plane points, as the K&B method would require (**Chapter 6**), to average coarse grid properties. The monotonicity and out-of-range values issues associated with the PVW method (**Chapter 6**) have been dealt with in this study by automatically deleting any generated values that violates the monotonicity or the range of the generated pseudo curves. The input to this pseudoisation process is read from an **Eclipse 100™** simulator output file, or restart file. In this file all of the information about the rock and fluid properties and geometries is stored for pseudoisation use. The pseudoisation process weights and upscales the relevant data, *i.e.* the upstream and downstream fault juxtaposed cell data. The process is repeated for every time step. The formulation described in this section has been implemented, in connection with some **Eclipse 100™** simulator output, into an RDR in-house 'pseudoisation program'.

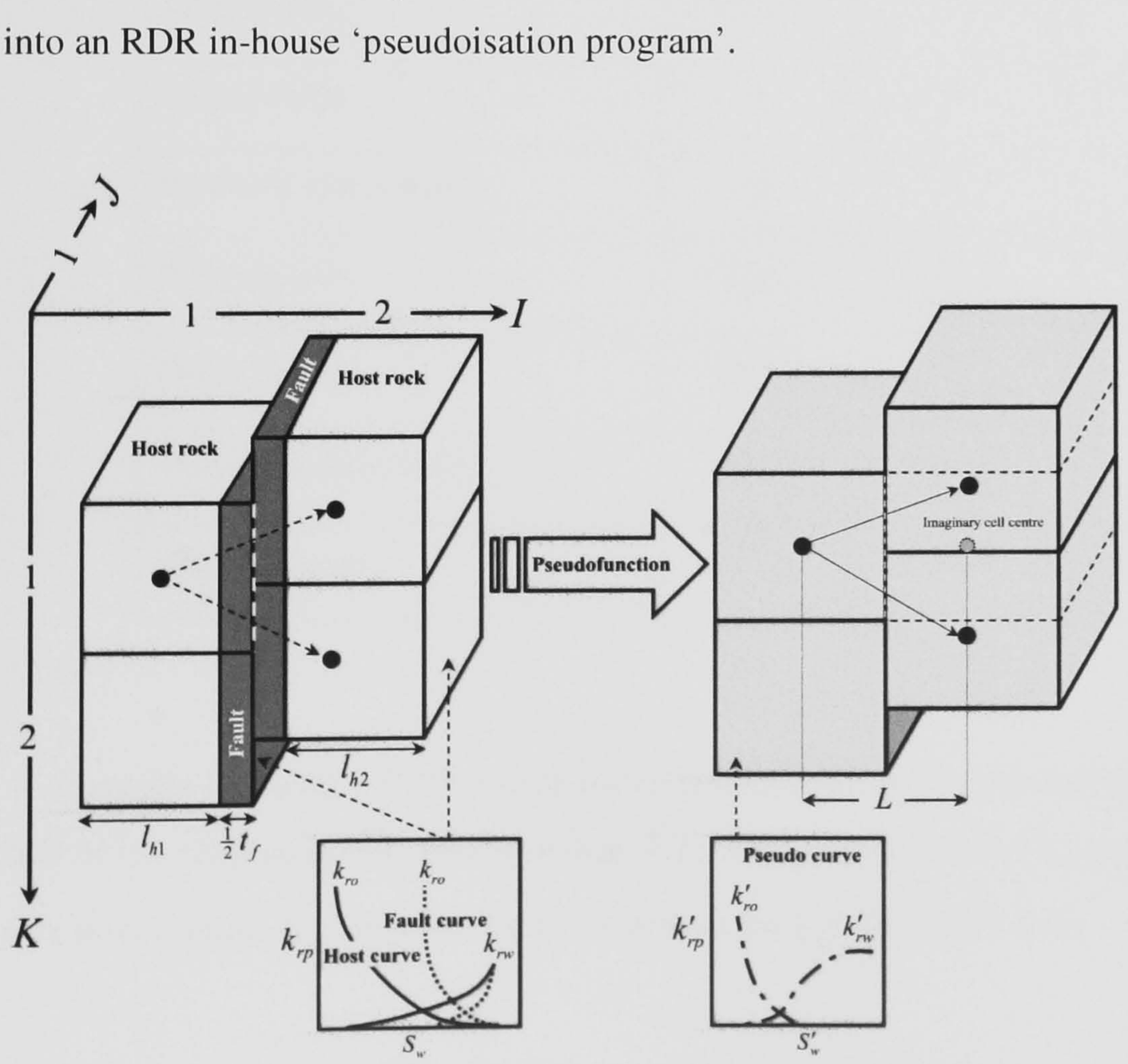

Fig. 7.3. Upscaling process between faulted non-neighbour connections. Each coarse cell contains half of the fault rock. Coordinates within an arbitrary space are used for formulation referencing. Both fault and host rocks are assumed to have their independent properties, see **Table-7.1**, and saturation functions.

Consider the upscaling diagram shown in **Fig. 7.3**. The cells are coordinated within an arbitrary space for formulation reference. Each coarse grid cell contains half of the fault material. Both fault and host rocks have their independent properties, see **Table-7.1**, and relative permeability and capillary pressure curves. The objective of the formulation is to perform *in-situ* PVW pseudoisation for an upstream cell that is attached to one neighbouring coordinate cell, *i.e.* with the same Z-coordinate, and a number of non-neighbouring coordinate cells, *i.e.* with different Z-coordinate, in the downstream side. Note that a given upstream coarse cell can be in contact with more than two coarse cells in the downstream side and not necessarily only two as illustrated in **Fig. 7.3**.

Table-7.1. Rock and phase properties for host and fault cells. The subscripts *h* and *f* refer to host and fault cells, respectively. The subscript *p* refers to the fluid phase, namely either oil or water.

Property	Host rock	Fault rock	Field units
Length	l_h	t_f	ft
Porosity	ϕ_h	ϕ_f	dimensionless
x-permeability	$(k_x)_h$	$(k_x)_f$	mD
Central depth	d_h	d_f	ft
Reservoir pore volume	v_h	v_f	rb
Phase density	$(\rho_p)_h$	$(\rho_p)_f$	lb/ft^3
Phase viscosity	$(\mu_p)_h$	$(\mu_p)_f$	cP
Phase formation volume factor	$(B_p)_h$	$(B_p)_f$	rb/stb
Phase pressure	$(P_p)_h$	$(P_p)_f$	psi

Consider applying a PVW x-directional pseudofunction for the coarse cell (1,1,1), containing half of the fault material, shown in **Fig. 7.3**. The 'pseudo' relative permeability, in field units, of a given phase, k'_{rp}, is given by the common multiphase Darcy Law:

$$\left(k'_{rp}\right)_x = -\frac{1}{1.127\times10^{-3}}\frac{\overline{B}_p\overline{\mu}_p\left(\overline{q}_p\right)_x L}{A\overline{k}_x\left(\Delta\overline{\Phi}_p\right)_x} \qquad \textbf{7.1}$$

where the subscript x indicates the x-direction. The numerical factor in this equation is the Darcy constant conversion factor to field units. L is the magnitude of the vector joining the

centre of the fault upstream coarse block and an imaginary centre of all the downstream coarse blocks that are in contact with the cell to be upscaled in the upstream side of the fault (**Fig. 7.3**). All the downstream coarse blocks are assumed to have centres that position on a common vertical plane. L is then chosen to be a horizontally projected distance, aligning with the upstream coarse block centre, that joins the two centres of the coarse grid blocks at both sides of the fault. For a fault material equally shared between the two coarse grid blocks, L can be simply defined as follows:

$$L = \tfrac{1}{2}(l_{h1} + t_f + l_{h2}) \qquad \textbf{7.2}$$

where l_{h1} and l_{h2} are the host material lengths in the upstream and the downstream coarse blocks at both sides of the fault, respectively.

$(\overline{q}_p)_x$ is the total phase Darcy flow rate out of the upscaled coarse cell along the x-direction. Negative flows, *i.e.* those into the fault upstream cell from the downstream side of the fault, are not included in **equation-7.3**. Note, however, in the case of negative flows and positive flows, *i.e.* flow reversal situation, fault downstream side upscaling will also become a necessity. There are two flows out of the coarse cell (1,1,1), due to the non-neighbour connection, shown in **Fig. 7.3**; one is to the centre of the coarse cell (2,1,1) and the other is to the centre of the coarse cell (2,1,2):

$$(\overline{q}_p)_x = (q_p)_{(1,1,1)\to(2,1,1)} + (q_p)_{(1,1,1)\to(2,1,2)} \qquad \textbf{7.3}$$

Note that the number of flows out of the upstream cells in a given direction depends on the number of neighbour and non-neighbour cells in the downstream side. This number can be more than two, and not necessarily as illustrated in **Fig. 7.3**. A is the cross-sectional area resolved in the direction of flow. This is the contact area between the upstream cell and all the cells it makes contact with in the downstream side. In **Fig. 7.3**, the total contact area when upscaling the coarse cell (1,1,1) is the flow-directional resolved area between cell (1,1,1) and cells (2,1,1) and (2,1,2). We refer to these areas using A_1 and A_2 as follows:

$$A_1 = (A)_{(1,1,1)\to(2,1,1)} \qquad \textbf{7.4}$$

$$A_2 = (A)_{(1,1,1)\to(2,1,2)} \qquad \textbf{7.5}$$

where

$$A = A_1 + A_2 \tag{7.6}$$

To define an upscaled permeability in the x-direction between the upstream and downstream coarse grid blocks, number of steps are followed. First, an upstream coarse block permeability in the x-direction $\left(\bar{k}_x\right)_U$ is defined as a simple harmonic average of the upstream coarse block host permeability, k_{x1}, and fault permeability, k_f:

$$\left(\bar{k}_x\right)_U = \frac{l_{h1} + \frac{1}{2}t_f}{\frac{l_{h1}}{k_{x1}} + \frac{\frac{1}{2}t_f}{k_f}} \tag{7.7}$$

The downstream harmonic permeabilities, $\left(\bar{k}_x\right)_{Di}$, are first defined for each coarse grid block in contact with the upstream coarse block:

$$\left(\bar{k}_x\right)_{Di} = \frac{l_{h2} + \frac{1}{2}t_f}{\frac{l_{h2}}{\left(k_x\right)_{di}} + \frac{\frac{1}{2}t_f}{k_f}} \tag{7.8}$$

where the subscript (di) refers to each downstream host material with a length (l_{h2}). Single downstream coarse block permeability, $\left(\bar{k}_x\right)_D$, can be defined using contact-area weighted permeability of all the downstream coarse cells that are in contact with the cell to be upscaled in the upstream side. Area weighting method is the most direct, and probably, the simplest for this geometrical arrangement. It is important to emphasise that other weighting options, *e.g.* transmissibility or flow rate weighting, could also be used as a more sensible weighting parameters. It is expected that the use of time-dependent weighting parameters, *e.g.* flow rates, can affect the required monotonicity with saturation for the generated pseudo curves. Testing the performance of each weighting technique is, however, beyond the scope of this study.

Considering the upscaling example shown in **Fig. 7.3**, $\left(\bar{k}_x\right)_D$ in the downstream side of the coarse cell (1,1,1) is the contact area-weighted permeability of the coarse cells (2,1,1) and (2,1,2):

$$\left(\bar{k}_x\right)_D = \frac{A_1\left(\bar{k}_x\right)_{D(2,1,1)} + A_2\left(\bar{k}_x\right)_{D(2,1,2)}}{A_1 + A_2} \tag{7.9}$$

Finally, the interface x-directional permeability, $\bar{k}_x$, between the two coarse grid blocks at both sides of the fault used the upscaling **equation-7.1** is defined as a harmonic average of the coarse grid block permeabilities in the upstream side of the fault, $(\bar{k}_x)_U$, and the downstream side, $(\bar{k}_x)_D$:

$$\bar{k}_x = \frac{l_{h1} + t_f + l_{h2}}{\frac{l_{h1} + \frac{1}{2}t_f}{(\bar{k}_x)_U} + \frac{l_{h2} + \frac{1}{2}t_f}{(\bar{k}_x)_D}} \qquad \textbf{7.10}$$

The fluid formation volumes, $\bar{B}_p$, and phase viscosities, $\bar{\mu}_p$, are obtained as a PVW average of the host and fault quantities as follows:

$$\bar{B}_p = \frac{\nu_h \times (B_p)_h + \nu_f \times (B_p)_f}{\nu_h + \nu_f} \qquad \textbf{7.11}$$

$$\bar{\mu}_p = \frac{\nu_h \times (\mu_p)_h + \nu_f \times (\mu_p)_f}{\nu_h + \nu_f} \qquad \textbf{7.12}$$

The phase potential difference, $\Delta\bar{\Phi}_p$, between coarse grid blocks, where flow is possible, is estimated from:

$$\Delta\bar{\Phi}_p = \Delta\bar{P}_p - g\bar{\rho}_p\Delta\bar{D} \qquad \textbf{7.13}$$

where g is the gravity constant, which is, in field units, approximated as 0.00694444, and $\bar{\rho}_p$ is the PVW phase density of each coarse grid block:

$$\bar{\rho}_p = \frac{\nu_h \times (\rho_p)_h + \nu_f \times (\rho_p)_f}{\nu_h + \nu_f} \qquad \textbf{7.14}$$

The pressure and depth data of all the downstream coarse cells, including non-neighbour connections, must be appropriately averaged to define one 'cell' centre, because $\Delta\bar{\Phi}_p$ is defined between two centres across the fault. The value $\Delta\bar{D}$ is the central depth difference

across the fault position. The PVW depth, D, for every coarse cell containing half of the fault material is defined as:

$$D = \frac{v_h \times (d)_h + v_f \times (d)_f}{v_h + v_f} \qquad \textbf{7.15}$$

Note that, when dealing with distorted corner point cells, $(d)_h$ and $(d)_f$ within each coarse cell do not necessarily coincide. One central depth needs to be defined in the downstream side and this depth is taken as the contact area-weighted depth of all the downstream coarse cells that are in contact with the cell to be upscaled in the upstream side. Considering the upscaling example shown in **Fig. 7.3**, the central depth in the downstream side of the coarse cell (1,1,1) is the contact area-weighted depth of the coarse cells (2,1,1) and (2,1,2):

$$D_{(2,1,1),(2,1,2)} = \frac{A_1 D_{(2,1,1)} + A_2 D_{(2,1,2)}}{A_1 + A_2} \qquad \textbf{7.16}$$

where A_1 and A_2 are the contact areas defined by **equations-7.4** and **7.5** respectively.

The pressure differential, $\Delta\overline{P}_p$, is the central phase pressure difference across the fault position. The phase pressure of each coarse cell is given by:

$$\overline{P}_p = \frac{v_h \left(P_p - g\rho_p (d - \overline{D})\right)_h + v_f \left(P_p - g\rho_p (d - \overline{D})\right)_f}{v_h + v_f} \qquad \textbf{7.17}$$

Using an analogous treatment to the depth, a single central phase pressure is defined in the downstream side of the fault using the contact area-weighted pressure of all the downstream coarse cells that are in contact with the cell to be upscaled in the upstream side. For the example shown in **Fig. 7.3**, this central phase pressure is defined as:

$$\left(P_p\right)_{(2,1,1),(2,1,2)} = \frac{A_1 \left(P_p\right)_{(2,1,1)} + A_2 \left(P_p\right)_{(2,1,2)}}{A_1 + A_2} \qquad \textbf{7.18}$$

The pseudo-capillary pressures, P_c', are obtained as the difference between the weighted coarse block phase pressures:

$$P_c' = \overline{P}_o - \overline{P}_w \qquad \textbf{7.19}$$

The same capillary pressures are written out in tables of generated pseudos for each direction, because **Eclipse 100**^{TM} does not use directional capillary pressures.

The above equations are used iteratively by the program for every time step to produce a saturation-dependent table of $k_{rp}^{'}$ and $P_c^{'}$.

7.4. Issues on *in-situ* pseudoisation

There are number of issues that arise, or that one may expect to arise, when applying this *in-situ* pseudoisation process. This section outlines these issues and argues on possible ways of resolving them. These issues include the following.

- One might argue that changing a fault representation from a *TM* model, to a discrete fault with a zone of independent rock and fluid properties and saturation functions can affect the original flux boundary conditions that were generated from the *TM* simulation. To avoid this problem of boundary condition changes, it is always best to choose boundaries with the least flow inter-dependence; those would ideally be boundaries between flow inter-independent regions that are separated by completely sealing barriers over the production life span of the reservoir. Later in the chapter it will be shown that, even when the full field is in dynamic communication, *i.e.* without completely sealing barriers, the proposed pseudoisation method still produces effective results.
- Building discrete models for complexly faulted models can be a tedious and impractical work. The pseudoisation method presented in this chapter does not deal with LGRs generation. The method only uses the output of a discretized model, with manually generated LGRs, after it is simulated using **Eclipse 100**^{TM} simulator. It is important to note that for complexly faulted models, faults discretisation is a huge amount of work when done manually.
- The relative position of the flux boundaries to the fault trajectories is an issue in **Eclipse 100**^{TM} simulator. This simulator does not permit local refinements, which in this study are used to define a fault zone, next to an active flux boundary. Therefore, it is always best to avoid cutting faulted cells with an active flux boundary. Real reservoirs, however, can be too complicated to control, and sometimes one has to divide a full-field simulation model along faults to reduce simulation times. If this latter situation cannot be avoided, one can seal, or use realistic *TM* values, on the extreme connection of a fault with an active flux boundary and resume using LGRs for the remaining trajectory of the fault. This issue, however, should not restrict the use of the method in heavily faulted models; it is the issue of producing stable refinements and availability of multiphase fault data measurements that matter more, and these are the major prerequisites for the method implementation to any reservoir in general.

- Another important issue is the 'future validation of the generated pseudos'. As was shown in **Chapter 6**, pseudo-curves must cover the full possible saturation range in a given reservoir to be valid for future use. The pseudo-curves generated from this *in-situ* method are restricted to the saturation range encountered in the simulation up to the time when they were generated. This means that they may, or may not, cover the full range of saturation, depending on the current saturation history of each grid block in the reservoir. To ensure reliable predictions, one must extend the current simulation run with the future development plans to the required time, and then proceed with pseudo generation.

7.5. Pros and cons of *in-situ* pseudoisation

The pseudoisation method presented in this chapter is very practical for large simulation models. This practicality arises from the fact that this pseudo method reads all the variables that affect fault pseudo-curves *in-situ*. This means that one does not need to worry about the heterogeneity in those parameters that are regarded very crucial in fault pseudo-curve generation, *e.g.* fault thickness, fault permeability, fault imbibition/drainage curves, across-fault Darcy velocity and undeformed reservoir cell properties. Furthermore, most fault detection programs are based on throw detection, *i.e.* they are unable to detect zero-throw subseismic faults without a prior specification by the user. In this program, the user can feed in zero-throw faults where pseudofunctions are to be applied. In addition, the code has been developed to upscale zig-zag faults with directional-dependent fault-pseudo curves. Some pseudoisation programs, *e.g.* Geoquest pseudo program (Geoquest, 2003), do not allow pseudoisation with the use of LGRs or hysteresis options. These limitations do not exist in the use of this *in-situ* pseudoisation code.

On the other hand, there are a number of limitations to this method. In particular, the method is still limited to a two-phase, oil/water system. The extension to three-phase studies should not be tedious in term of coding. However, three-phase behaviour and the shortage of data on laboratory measurements of fault rocks make it difficult to test and extend this work to such systems. Although only the PVW pseudoisation method is applied to this process, other well-known methods, *e.g.* Kyte and Berry (K&B) and weighted relative permeability (WKR), see **Chapter 6**, although more difficult to code, can also be implemented.

7.6. Implication in 3D faulted models

The performance of the *in-situ* pseudoisation method discussed above will be tested on different faulted models. Fault curves, relative permeability and capillary pressure curves, are derived using a method analogous to that described by Manzocchi *et al.* (2002), see **Chapter 5** for details and a derivation. To subject the approach to a severe test, we use a different family of rock curves, *i.e.* the rock and fault curves are not correlated. The following expressions for an

oil/water system rock relative permeability and capillary pressure curves are used (Cao and Aziz, 1999).

The rock phase relative permeability curves are given by:

$$k_{rw} = k_{rw}^{*}\left(\frac{S_w - S_{wc}}{1 - S_{wc} - S_{or}}\right)^{n_w}, \qquad n_w = 3, \qquad k_{rw}^{*} = 0.3 \qquad \textbf{7.20}$$

$$k_{ro} = k_{ro}^{*}\left(\frac{S_o - S_{or}}{1 - S_{wc} - S_{or}}\right)^{n_o}, \qquad n_o = 1.5, \qquad k_{ro}^{*} = 1.0 \qquad \textbf{7.21}$$

The rock oil–water capillary pressure curve is given by:

$$P_c = P_c^{*}\left[\left(\frac{S_w - S_{wc}}{1 - S_{wc} - S_{or}}\right)^{-1/\lambda} - 1\right], \qquad \lambda = 5, \qquad P_c^{*} = 10.0 \qquad \textbf{7.22}$$

Here n_w, k_{rw}^{*}, n_o, k_{ro}^{*}, λ and P_c^{*} are empirical constants, and S_{wc} and S_{or} are the connate water and the residual oil saturations, respectively.

7.6.1. Fault pseudoisation of a zig-zag faulted model

7.6.1.1 Model description

A 3D, two-phase simulation model was constructed and compartmentalised by two vertical, zig-zag faults, namely a 1 ft thick fault with a permeability of 0.01 mD, and a 1 ft thick fault with a permeability of 0.005 mD (**Fig. 7.4**). The model contains homogeneous host rock of permeability 1000 mD along the *x*- and *y*-directions, and 100 mD along the *z*-direction. Each fault has a constant throw, namely 0.7 ft for the 0.01 mD fault, and 4.4 ft for the 0.005 mD fault. The throw values imply that some faulted cells will have more than one flow across them. The model description is summarised in **Table-7.2**.

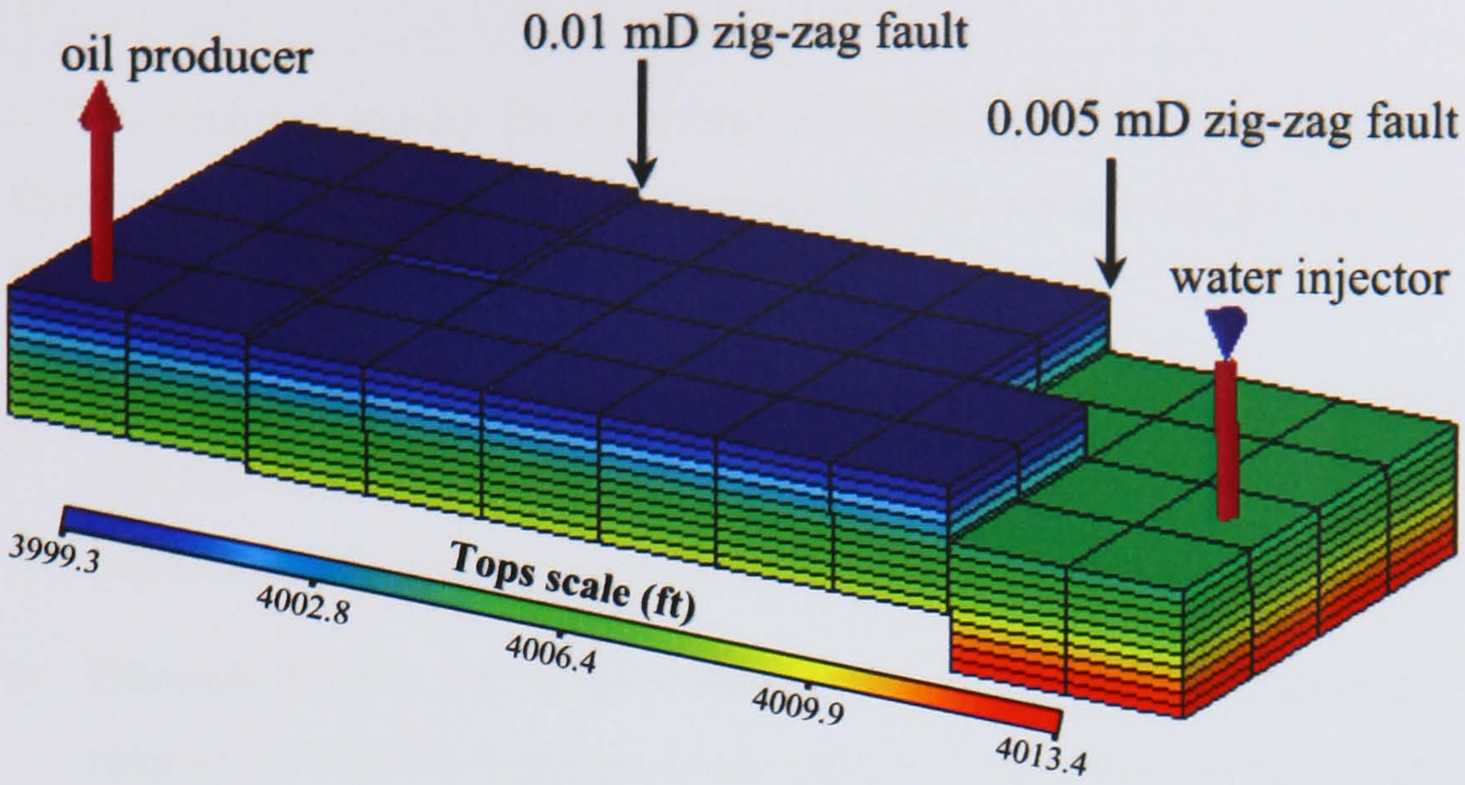

Fig. 7.4. Tops map and well positions for the zig-zag faulted model. Note that the faults are along the *y*- and *x*-directions.

Table-7.2: Reservoir rock, phases, geometry and schedule data for the zig-zag faulted model (oil/water system).

Item	Model parameters
Phases and rock data (Field units)	
• Reference pressure (RP) • Reference temperature	• 5500 (psia) • 60 (^{0}F)
Dead oil PVT properties: • Density at stock tank • Formation volume factor (FVF) at RP • Compressibility • Viscosity at RP • Slope of viscosity versus pressure • Slope of FVF versus pressure	 • 49 (lbs/ft^3) • 1.186 (rb/stb) • 2E-5 (psi^{-1}) • 0.93 (cP) • 0.002 (cP/psia) • 9×10^{-5} (rb/stb/psia)
Undersaturated water properties: • Density at RP • FVF • Compressibility • Viscosity at RP • Viscosibility at RP	 • 63 (lbs/ ft^3) • 1.04 (rb/stb) • 3E-6 (1/psi) • 0.8 (cP) • 0 (1/psi)
Rock properties: • Compressibility at RP	 • 4E-6 (1/psi)
Reservoir and grid block geometry data (Field units)	
Number of grid nodes	$10 \times 4 \times 10$
Spacing	DX = 10 (ft) DY = 10 (ft) DZ = 1 (ft)
Grid type	Cartesian
Grid geometry	Corner point
Depth to reservoir top	3999.3 (ft)
Reservoir pressure, phase saturation and schedule data (Field units)	
Initial water saturation	5 %
Reservoir initial pressure	6000 (psia)
Production rate	20 (stb/day) of liquid rate controlled by BHP limit of 1000 (psia)
Injection rate	100% water voidage replacement controlled by BHP limit of 12,000 (psia)
Time step size	300 (steps) × 1.5 (days) (total simulation time = 450 days)

The sealing capacity for each fault was represented in the simulation using the following three models (all are identical in geometry with a single water injector and an oil producer, **Fig. 7.4**).

- ***TM* Model**: Faults are represented using transmissibility multipliers (*TMs*). *TMs* for the 0.01 mD and the 0.005 mD faults are, respectively, 0.99991×10^{-4} and 0.49998×10^{-4} (calculated using **equation-6.16**, with a host rock permeability of 1000 mD).

- **Discrete Model**: Faults are represented with multiphase (drainage capillary-pressure and relative-permeability curves) properties incorporated discretely. Faults relative permeability and capillary pressure curves are functions of their permeabilities. These curves were derived used those relations presented in **Chapter 3**. Local grid refinements (LGRs), see **Chapter 5**, are used to define fault zones and reduce numerical dispersion.

- ***TM*+Pseudo Model**: As well as the *TM* representations, *in-situ* generated pseudo-curves are attached to the upstream cells of the faults, see **Fig. 7.4**, to account for the multiphase behaviour of the fault zone and for flows strictly across the fault. Original rock curves are still used to account for flows parallel to faults. Some cells were assigned to more than one pseudo relative-permeability curve to account for flow in different directions.

7.6.1.2 *In-situ* pseudoisation procedures

This model was run to test the performance of the *in-situ* pseudo code. For simplicity purposes, no active flux boundaries were applied to this model and all faults were discretised within the global or 'Dump flux' run, *i.e.* the original full-field simulation model. The results for the faulted cells, including the refined cells, were output to a formatted file, called the restart file. This restart file contains all the data required by the pseudo program to perform the required upscaling. There is another file, prepared by the user, which contains the positions of the fault cells. This was done specifically to define apparently zero-throw, *e.g.* pure strike-slip, faults.

For this particular model, the pseudo program resulted in 80 pseudo-curves (**Fig. 7.5**). In this case, the curves are difficult to group for each fault and they exhibit a wide range of variation. Since both faults have the same thickness and fluid properties, this variation can be attributed to the variation in fault permeabilities, and more importantly to the variation in across-fault Darcy velocities. Although the producer and the injector were initially set up to produce and inject at a constant rate, the bottom hole pressure (BHP) limit of the producer was reached very quickly, and the production control changes to the BHP from the early simulation stage. Flow rates can vary significantly when the production is controlled by the BHP, depending on reservoir average pressure variations. It was shown in **Chapter 6** that flow rates have a big effect on the variation in the pseudo-curve shapes. These curves are tabulated for the user to allow their

straightforward inclusion in the *TM*+Pseudo Model. The generated pseudo-capillary curves, on the other hand, show only a small deviation from the original rock curve.

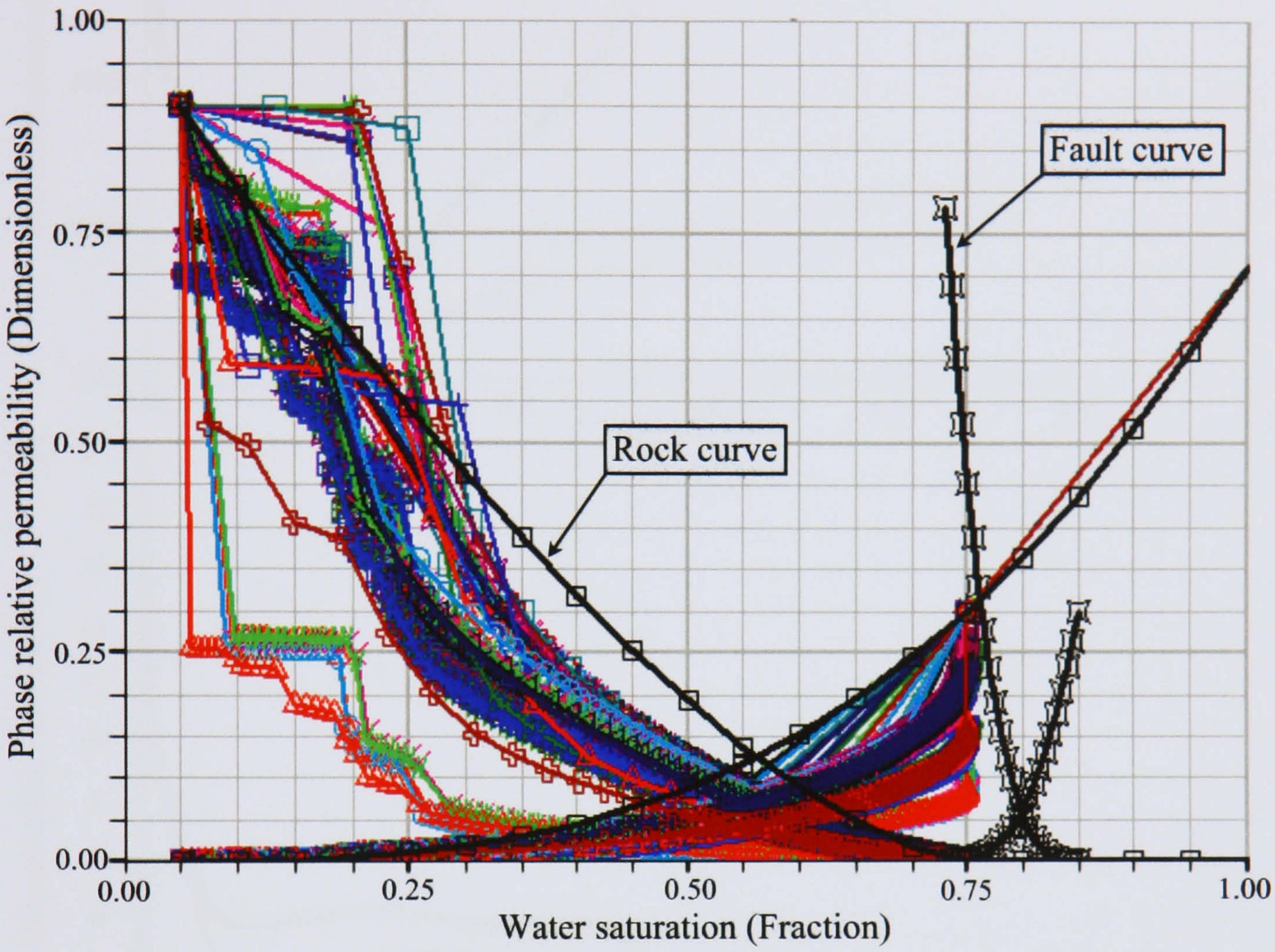

Fig. 7.5. *In-situ* generated pseudo-relative permeability curves in the zig-zag faulted model. The rock and fault curves are also plotted.

7.6.1.3 Fluid flow modeling results

Here the results of the three different models defined in **§ 7.6.1.1** are presented as a function of the widely used measure of dimensionless time, *i.e.* pore volume injection, or PVI. PVI at a particular time is defined as the cumulative volume of water injected up to this time, divided by the total pore volume of the model. The different results for the three fault representations are displayed in **Fig. 7.6**.

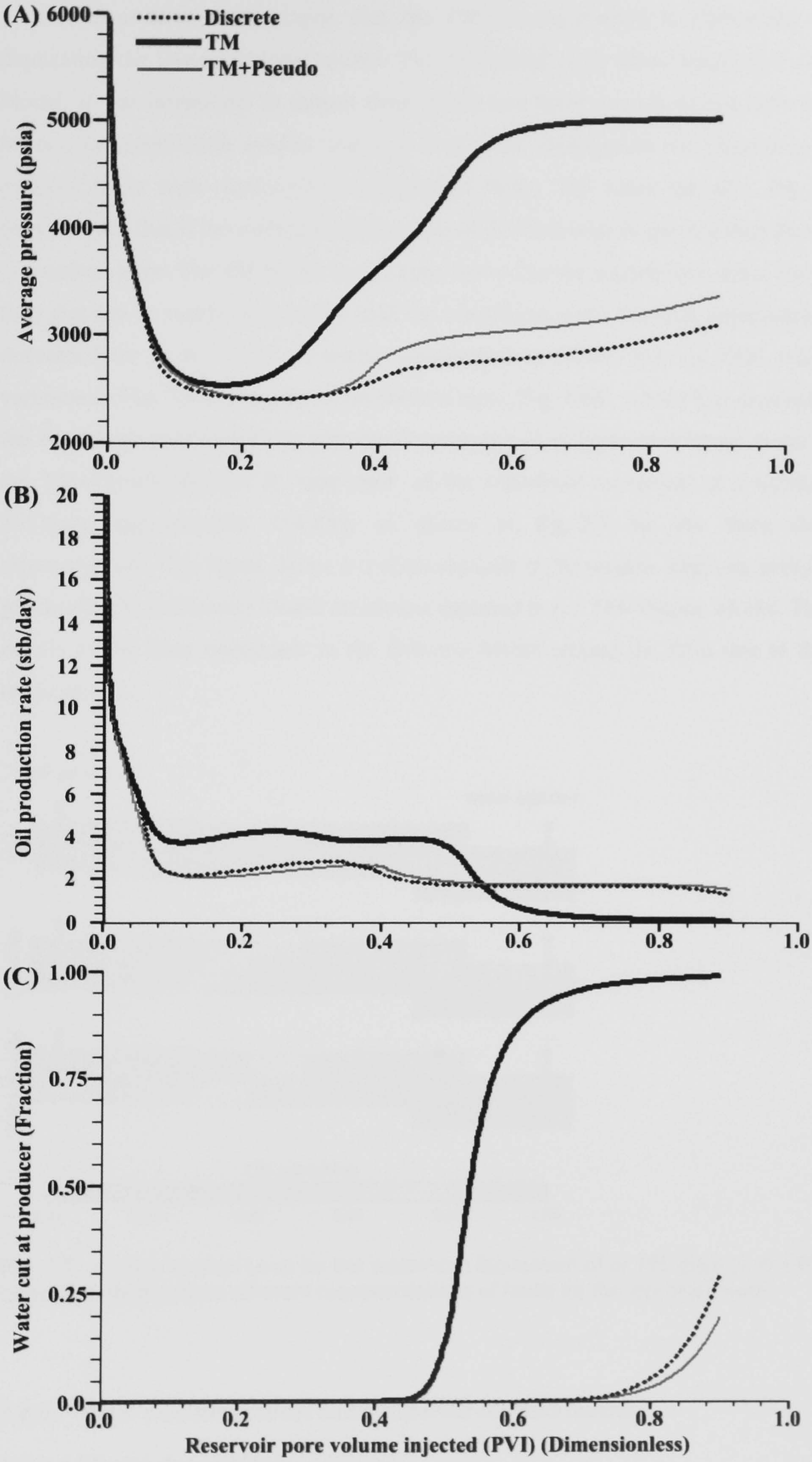

Fig. 7.6. Comparing different outputs for the three fault representations discussed in this section for the zig-zag faulted model: (**A**) field average pressure, (**B**) oil production rate, (**C**) water cut. Results are presented as a function of reservoir PVI.

It is clear from these graphs that the *TM*+Pseudo method is performing very well in duplicating the Discrete Model results. The *TM* Model is far from being close to the Discrete Model. It was intentional to subject these small simulation models to low flow rates, as these factors, *i.e.* small-scale models and low flow rates, demonstrate the importance of capillary trapping under high capillary-force dominated flows. The water cut plot, **Fig. 7.6C**, clearly demonstrates that if the multiphase behaviour of the fault rock is ignored then the model can be in a serious error. The *TM* Model in this case shows that the waterfront reaches the producer at a time that can be nearly 50% earlier than the actual time when the fault multiphase behaviour is accounted for in the model. A similar observation is drawn from the field average pressure variation in **Fig. 7.6A**, whereas oil production rates, **Fig. 7.6B**, exhibit less discrepancy between the three fault representations, and demonstrate excellent agreement between the Discrete and the TM+Pseudo Models. A 'snap shot' of the waterfront movement at a simulation time of 175 days, approximately 0.4 PVI, is shown in **Fig. 7.7** for the three different fault representations. The figure shows x–z cross-sections of the models. One can easily observe that the details of the Discrete Model are almost captured in the TM+Pseudo Model. There are more details of the front movement in the Discrete Model around the fault due to the fault zone refinements.

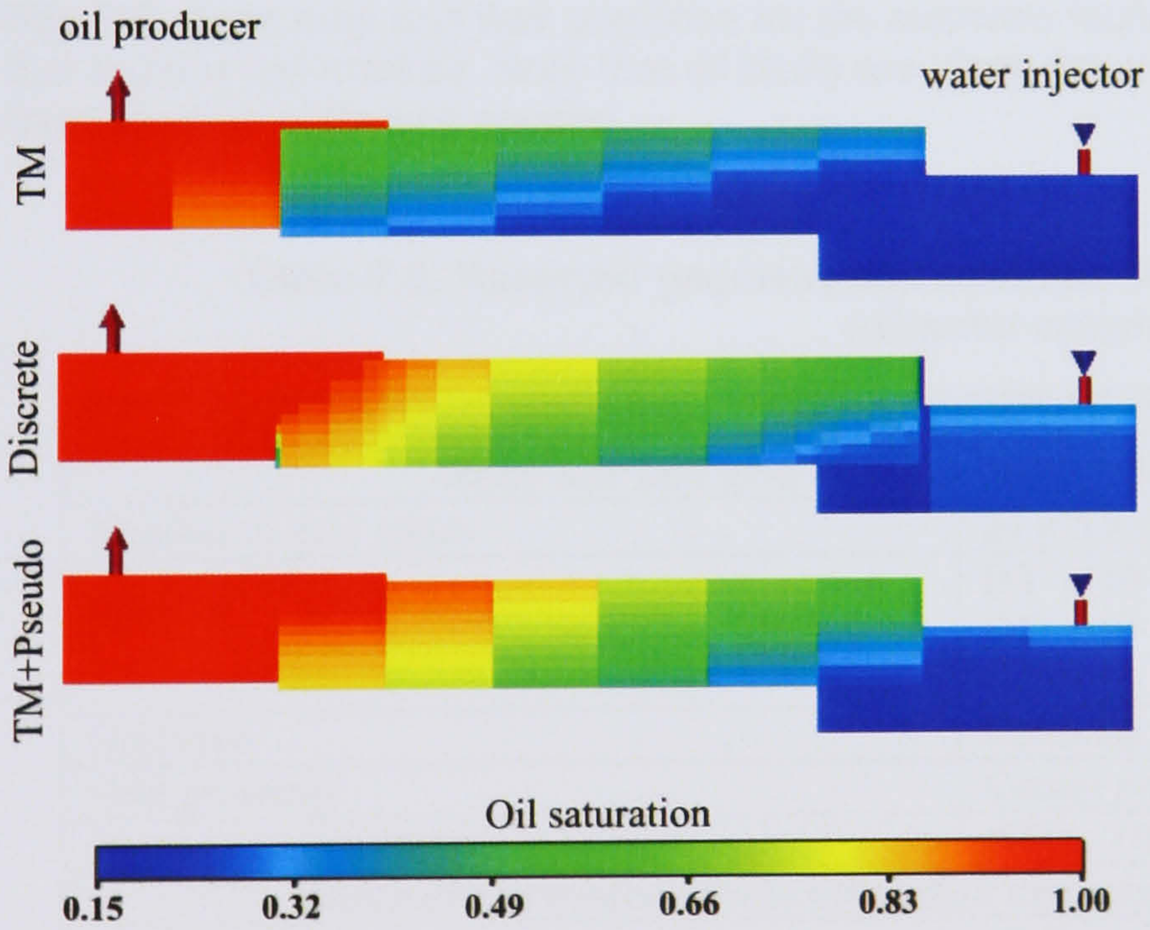

Fig. 7.7. A cross section (x–z) for the waterfront movement after 175 days (*c.* 0.4 PVI) of simulation for the three different representations of faults for the zig-zag model.

7.6.2. Fault pseudoisation of a stepwise faulted model

7.6.2.1 Model description

A 3D, oil/water simulation model was constructed and compartmentalised by four vertical faults to form a stepwise faulted model. All faults have a permeability of 0.01 mD but their

thicknesses range between 0.2 ft and 0.4 ft (**Fig. 7.8**). The model contains homogeneous host rock of 1000 mD along the *x*- and *y*-directions, and 100 mD along the *z*-direction. Each fault has a constant throw of 3.3 ft for the thicker faults, and 1.7 ft for the thinner faults. The throw values imply that some faulted cells will have more than one flow across them. Model phases and rock properties are similar to those tabulated in **Table-7.2**. The model description is summarised in **Table-7.3**.

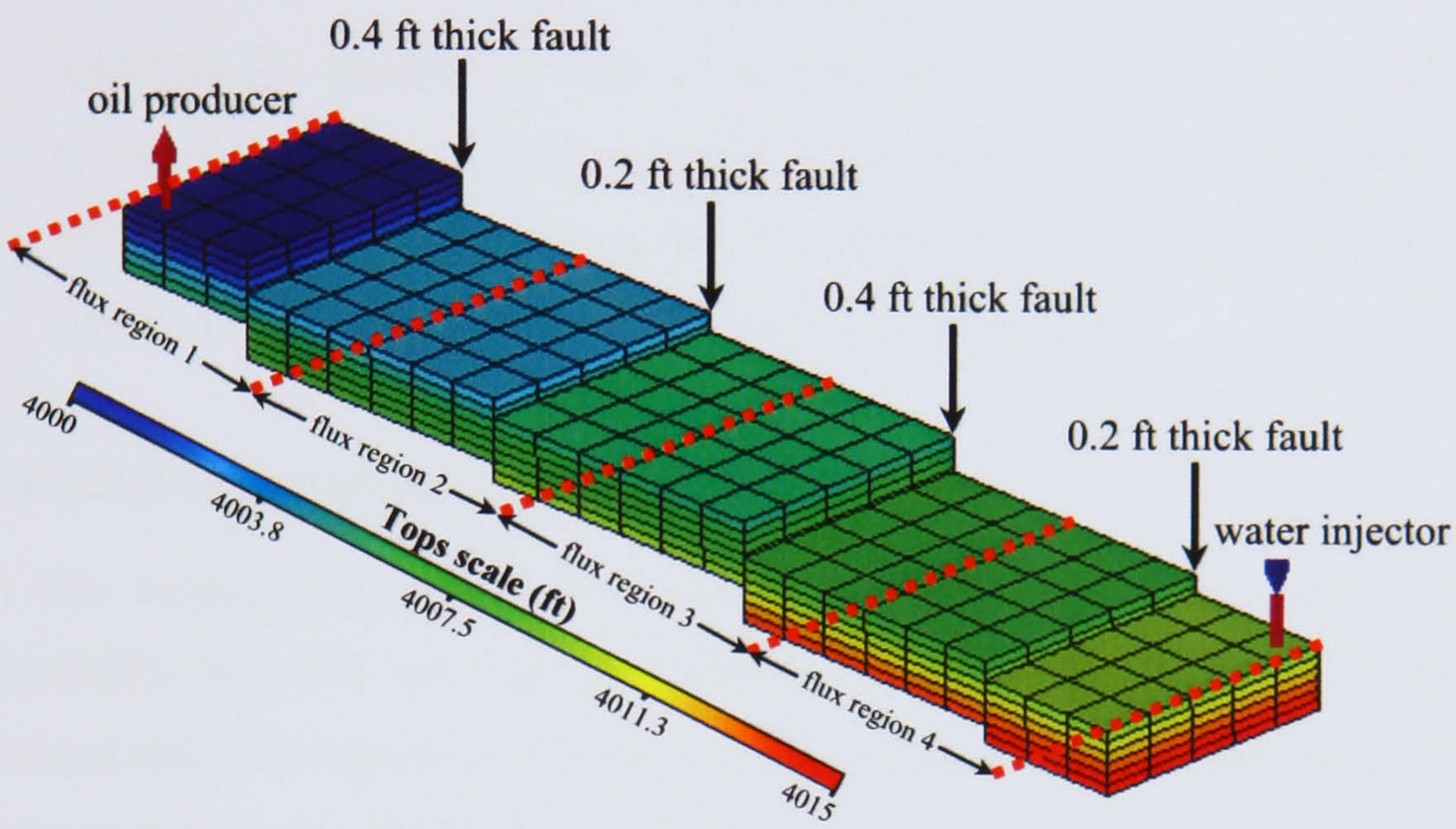

Fig. 7.8. Tops map and well positions for the stepwise faulted model. Boundaries of the active flux regions are marked. Note that all faults are along the *y*-direction. A vertical geometrical exaggeration of 2x was applied.

Table-7.3: Reservoir geometry and schedule data for the stepwise faulted model (oil/water system).

Item	Model parameters
Reservoir and grid blocks geometry data (Field units)	
Number of grid nodes	$24 \times 5 \times 6$
Spacing	$DX = 10$ (ft) $DY = 10$ (ft) $DZ = 1$ (ft)
Grid type	Cartesian
Grid geometry	Corner point
Depth to reservoir top	4000 (ft)
Reservoir pressure, phase saturation and schedule data (Field units)	
Initial water saturation	10 %
Reservoir initial pressure	6000 (psia)
Production rate	20 (stb/day) of liquid rate controlled by BHP limit of 1000 (psia)
Injection rate	100% water voidage replacement controlled by BHP limit of 10,000 (psia)
Time step size	400 (steps) × 1.5 (days) (total simulation time = 600 days)

The sealing capacity for each fault was represented in the simulation using the following three models (all are identical in geometry with a single water injector and an oil producer).

- ***TM* Model**: Faults are represented using transmissibility multipliers (*TMs*). *TMs* for the thick and the thin faults in this model are, respectively, 0.2499×10^{-4} and 0.49976×10^{-4} (calculated using **equation-6.16**, with a host rock permeability of 1000 mD and a single fault permeability of 0.01 mD).

- **Discrete Model**: Faults are represented with multiphase (drainage capillary-pressure and relative-permeability curves) properties incorporated discretely. LGRs are used to define fault zones and reduce numerical dispersion.

- ***TM*+Pseudo Model**: As well as the *TM* representations, dynamic PVW pseudofunction curves are attached to the upstream cells of the faults, see **Fig. 7.8**, to account for the multiphase behaviour of the fault zone and for flows strictly across the fault. Original rock curves are still used to account for flows parallel to faults.

7.6.2.2 *In-situ* pseudoisation procedures

In this model, the pseudoisation procedures outlined in § **7.2** were followed. A full-field simulation was first run with all faults included as *TMs* (*TM* Model). The model was then divided into four regions with preserved active flux boundaries (**Fig. 7.8**). This flux information, generated from the *TM* Model run, is written to a separate flux file, which can then be read by the program for any activated region separately. Every region was then activated and each fault within that region was included discretely (Discrete Model). The simulation CPU time of each active region, each with a discrete fault, is approximately one-forth of the total simulation CPU time for the global run, or the full-field run, with all faults included discretely. The pseudo program was applied separately to each active region to generate fault pseudo-curves. The pseudo-curves from each region were then included in their corresponding fault upstream cells in the full-field *TMs* model (*TM*+Pseudo Model). For this model, 25 fault pseudo-curves were generated for each of the thicker faults, and 15 curves for each of the thinner faults; thus, in total, 80 fault pseudo-curves were generated for all fault upstream cells, see **Fig. 7.9**. Generally, the thin faults give lower pseudo-relative permeabilities to oil than the thick faults. However, this generalisation does not apply to all curves, as some pseudo-curves from the thin faults resulted in higher pseudo-relative permeability to oil than the thick faults. This behaviour, which is different from the one generalised in **Chapter 6**, is attributed to across-fault Darcy velocity variations, as was the case in the zig-zag model, see § **7.6.1.2**.

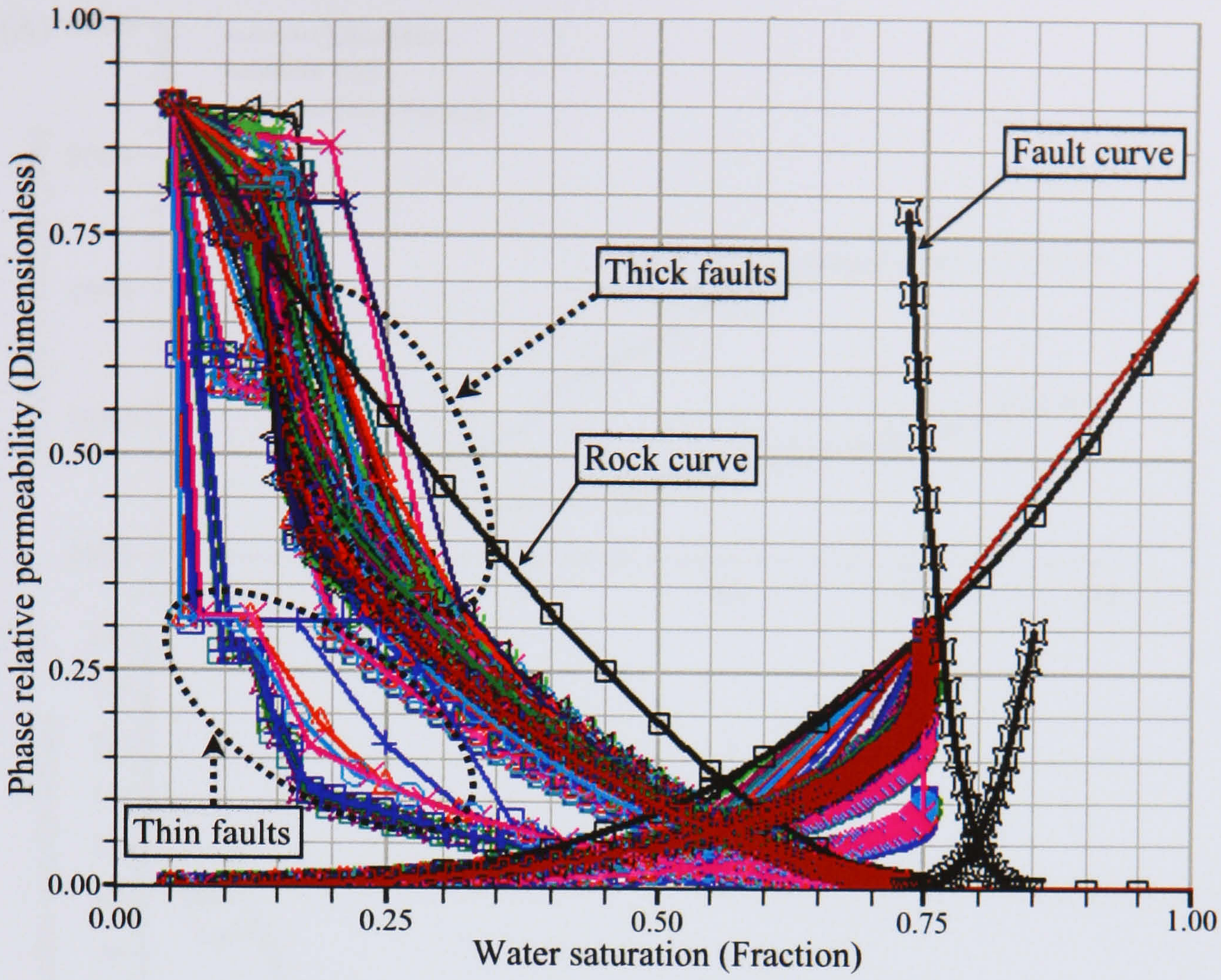

Fig. 7.9. *In-situ* generated pseudo-relative permeability curves in the stepwise faulted model. The rock and fault curves are also plotted.

7.6.2.3 Fluid flow modelling results

The output from the three different fault seal capacity representations is presented in **Fig. 7.10** for (**A**) field average pressure, (**B**) oil production rate, and (**C**) water cut at the producer. All the results are a function of the model pore volume injected (PVI). An exceptionally good match was obtained between the Discrete and the *TM*+Pseudo Models for this particular case. The *TM* representation predicts bigger re-energisation for the model as a result of the waterflooding (**Fig. 7.10A**) and a much sooner water breakthrough at the producer (**Fig. 7.10C**). A 'snap shot' of the water front movement after 200 days, approximately 0.5 PVI, of simulation for the three models is captured in **Fig. 7.11**. The water front advances much quicker in the *TM* Model, indicating that ignoring the multiphase behaviour of fault rock underestimates the sealing capacity of the faults in this model. The front movement in the Discrete Model advances that in the *TM*+Pseudo Model by a very small fraction. The vertical distribution of the saturations behind the front in the Discrete Model is not well captured in the *TM*+Pseudo Model. Generally and globally speaking, these two latter models showed identical performances.

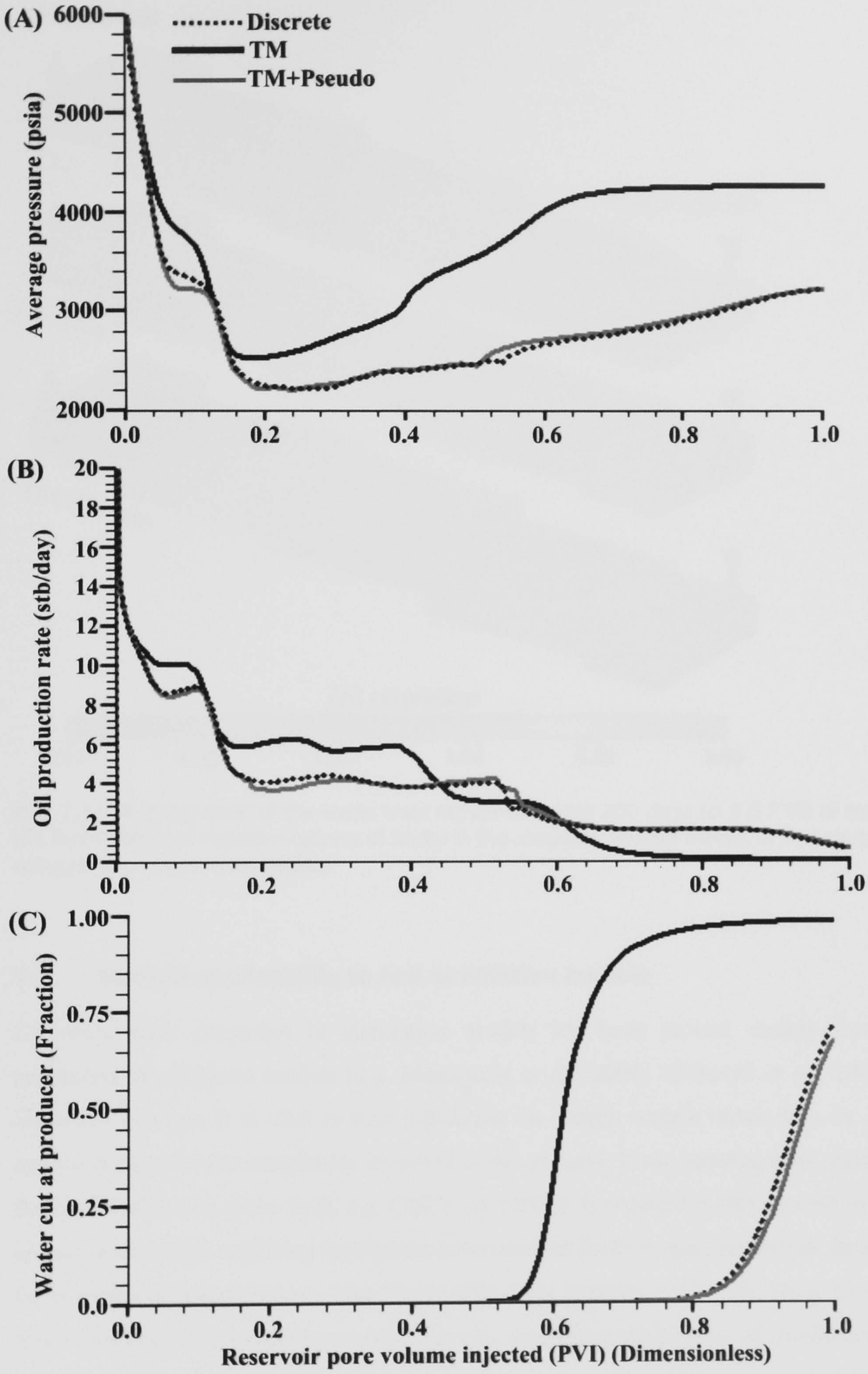

Fig. 7.10. Comparing different outputs for the three fault representations for the stepwise faulted model: (**A**) field average pressure, (**B**) oil production rate, (**C**) water cut. Results are presented as a function of reservoir PVI.

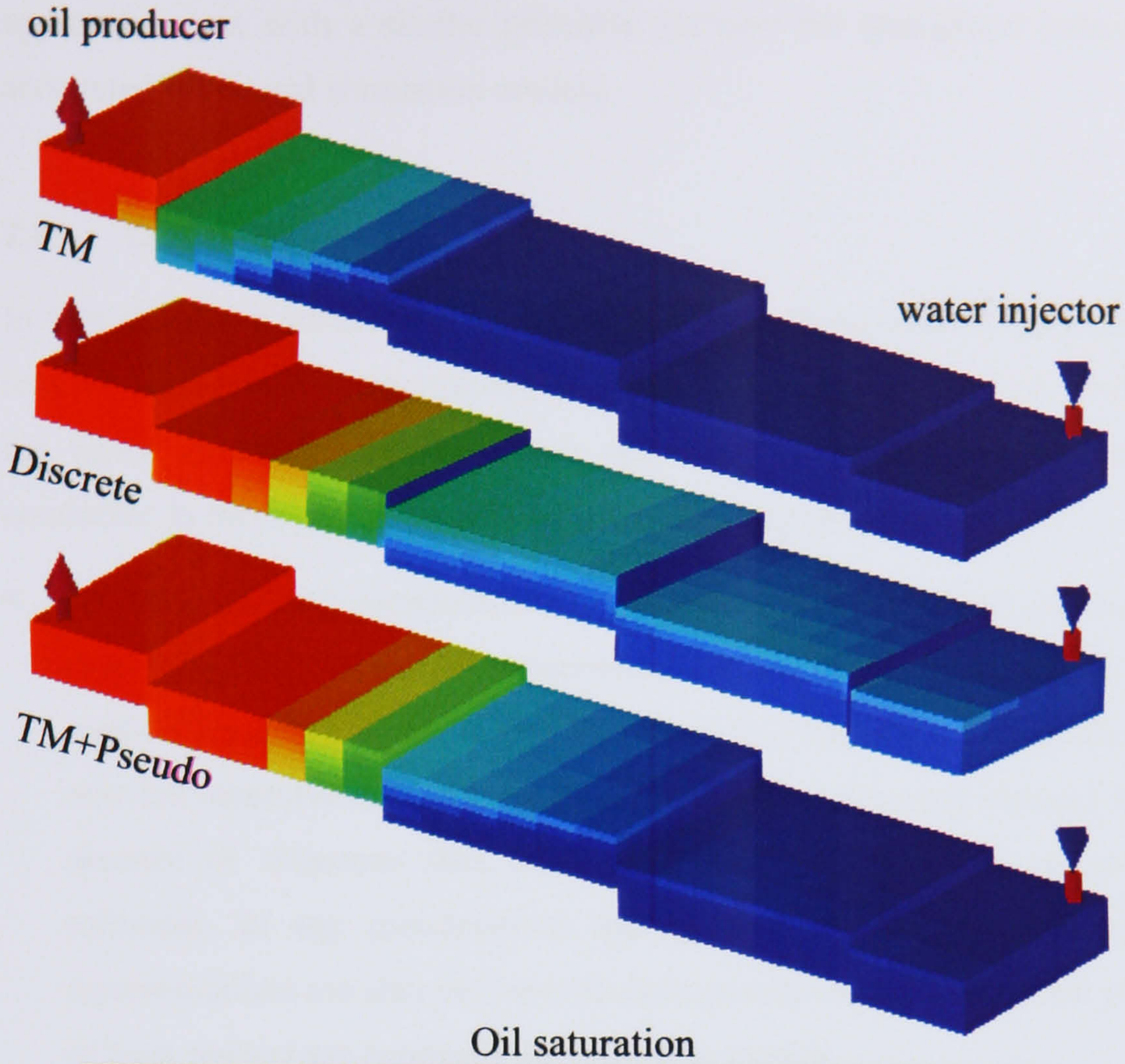

Fig. 7.11. A 'snap shot' of the water front movement after 200 days (*c.* 0.5 PVI) of simulation for the three different representations of faults in the stepwise faulted model. A vertical geometrical exaggeration of 2x was applied.

7.7. Method applicability to real simulation models

Capturing fault properties in simulation models has been proved, mainly through works conducted on synthetic models (*e.g.* Manzocchi *et al.*, 2002; Al-Busafi *et al.*, 2005) to be an important process. It is vital to start validation on simple models rather than on complicated models because of the complexity involved in this process. Understanding flow regimes, even in the local scales of a given field, *e.g.* Coll *et al.* (2000), is required in this process to identify the crucial areas where capturing multiphase behaviour of faults is more important. Real geology is far from being homogeneous, and all possible flow regimes are highly likely to domain in a single real reservoir simulation model. For this recently realised issue of multiphase behaviour of faults, no direct application to real models were tested, primarily owing to models complexity and data limitation. However, the successful application of most simulators can aid in creating high resolution synthetic models, as adopted in this chapter, which can replace the need for observed multiphase behaviour of faults under dynamic conditions. Complexity can be replaced by the detailed understanding of the physical behaviour of the process observed using simple models, which then can be generalised to more geometrically complicated flow models. Previous work, *e.g.* Manzocchi *et al.* (2002) and this work, are offering different practical

approaches, yet with a similar principle, on how the multiphase behaviour of faults can be accounted for in real simulation models.

7.8. Conclusions

In this chapter, a method for including two-phase behaviour of fault-rock properties, namely relative permeability and capillary pressure, in full-field simulation models without including the faults discretely, was presented and tested on some faulted models. From the work conducted in this chapter, the following conclusion pointes are drawn:

- Although all fault pseudoisation methods aim to improve fault representations over the *TM* representations, these latter representations are still very important in the pseudoisation method presented in this study. Therefore, it is important to base the initial faults *TMs* on relevant measured data, *e.g.* using a similar approach to that adopted in **Chapter 4**, or in the absence of measures data, reasonable *TMs* can be based on geologically reasonable estimates. In any pseudoisation method presented so far, including this one, the *TM* representations are also tied up with fault pseudo-curves in the final practical representation of fault multiphase behaviour in simulation models
- The *in-situ* pseudoisation method presented in this chapter takes advantage of the dynamic flux/pressure boundaries in splitting large models into small active regions to allow discrete inclusion of fault zones at a significantly low cost of simulation CPU time. The stepwise faulted Model presented in this study showed that each flux region with LGRs can be run with the cost of one-fourth of the total CPU time required to run the entire model with LGRs. In real models, however, the number of flux regions may not sum up to form the global model, their sum can for various portions of the global model depending on faults distribution. Very large models with few faults clustered in small regions are the ideal models that manifest the usefulness and advantage of using flux regions for the purpose of this study.
- The choice of the active flux boundaries is a vital process in this *in-situ* pseudoisation process and required a general knowledge of the dynamic behaviour of the full-field simulation model.
- Identifying similar faults embedded into regions subjected to the same flow regimes can significantly cut the required work for pseudo-curves generation.
- As shown in the previous chapters, flow rates play an important role in varying the shape of the generated pseudo-curves for the same fault zone.

When applied to different fault scenarios, the presented approach of incorporating two-phase behaviour of faults into production simulation models improved fault representations to a great degree. Therefore, it provides a novel tool and an important development in approaches to

correctly represent faults and their sealing capacities in reservoir simulation models. Nevertheless, the method still has some deficiencies and may require further developments. In particular, the method still has not been generalised to handle models with grid blocks operating simultaneously as upstream and downstream cells. A more important issue is the implementation of a stable LGR schemes to model faults as independent flow zones in heavily faulted reservoirs. This method, which does not handle the discretisation (or refinement) process, requires the flow simulation results of the high-resolution model as a direct input for the pseudoisation procedures. Implementing an automated method for LGRs generation, although being a huge amount of work for faults with variable throws and thicknesses, is still a feasible improvement on the method.

When comparing the merits of the workflow presented in this chapter to that presented earlier in **Chapter 6**, one can see that each workflow can have certain application depending on the size and faults complexity of the simulated model. Although the principal idea of each workflow is the same, **Chapter 7** workflow can be regarded as a general workflow of that presented in **Chapter 6** in the sense that it can be applied relatively quickly to large and more complexly faulted models without the need to handle each pair of cells separately. Furthermore, the method presented in **Chapter 7** overcomes some issues and limitations associated with the use of the current version of **Eclipse**^{TM} pseudoisation program. In particular, unlike the **Eclipse**^{TM} pseudoisation program, this method can handle **(a)** the use of flux boundary regions and **(b)** independent domains of LGRs for fault zones. Furthermore, the current **Eclipse**^{TM} pseudoisation program has a memory and time steps restrictions, *e.g.* it cannot handle large real simulation models and is restricted to accept a maximum of 1000 time steps. The **Chapter 7** method does not have such time steps or memory restrictions.

Chapter 8

Conclusions and future work

"On the exploration side, you're helping to risk traps. You want to know how you might predict the sealing capacity for a particular reservoir and how much hydrocarbon column you could support against that fault and what expected volumes you might have. This is a pre-drill situation. In a development scenario where you've made a discovery, you want to know not just if the faults have compartmentalized the reservoir, but, if so, how many wells you'll need to extract the hydrocarbons. There are a lot of cases where the fault degrades the nice, high permeability around it to form a baffle impacting the sweep pattern and efficiency - for better or worse. Depending on the nature of the baffling, how it's trapped the oil, it could actually improve recovery efficiency. When you pull the core, you must spend time and effort describing the deformation and getting the properties from these faults. Too often, there's a tendency to say there's a fault."

Russell Davies

US Operations Manager at Rock Deformation Research (RDR)

8.1. Conclusions and recommendations

This thesis had two main purposes. First, to investigate the importance of incorporating multiphase fault rock properties into production simulation models. Second, to investigate possible methodologies to incorporate the multiphase flow properties of faults in production simulation models. **Chapter 1** has reviewed fault seal methodologies and their advances and then **Chapter 2** has provided details of how faults are conventionally represented in production simulation models (*i.e.* using transmissibility multipliers (*TMs)* based on a single-phase treatment). It is clear that the traditional way that *TMs* are calculated does not take into account multiphase flow across faults, so **Chapter 3** has used simple box models to begin to investigate when and where it is important to incorporate the multiphase flow properties of fault rocks. In **Chapters 4** and **5** results from microstructural and petrophysical analyses of fault rocks present within a well from the Pierce Field have been analysed and their results have been used to calculate the distribution of *TMs* along the faults. *TMs* were first calculated based on the single-phase permeability values of the fault rocks and undeformed reservoir. An attempt was also made to account for the multiphase flow properties of fault rocks by varying the *TMs* as a function of the position of the fault relative to the free water level. Furthermore, the results of the simulations were used to create time-dependent P-wave impedance maps (or 4D seismics) for different possible *TM* representations. These results were used to identify the optimal time to conduct a follow-up 3D seismic survey to identify unswept compartments at a time that would have a bearing on future production strategies. Finally, **Chapters 6** and **7** used simulation models with various degrees of complexity to test alternative ways of accounting for the multiphase flow properties of faults without their implicit representation as discrete planes

within the full-field production simulation model. On the basis of these studies, the following conclusions and recommendations have been reached.

- In many situations it is probably very important to incorporate the multiphase flow properties of fault rocks into production simulation models of structurally complex reservoirs. As faults cannot generally be included discretely in production simulation models the most obvious way to incorporate their multiphase flow properties is to use dynamic pseudofunctions. The large variations in fault thickness, fault permeability, reservoir permeability and capillary pressure, as well as whether the fault is undergoing drainage or imbibition, potentially means that an unmanageable number of pseudo-relative permeability curves would need to be incorporated into the simulation model. The situation would be eased if a limited number of fault rock thicknesses could be assumed. Numerical modelling was therefore conducted to answer the question '*in which situations is it better to include the multiphase flow properties of fault rocks in production simulation models and when is it better to accurately include fault rock thickness*'? It appears that the answer to this question depends on drive mechanism, well position, and the capillary pressure distribution along the fault, as well on which parameters need to be modelled (*e.g.* bottom-hole pressures, hydrocarbon production rates, water cuts, *etc.*). In the situation where a producer is separated from an injector by a fault with a high capillary pressure, it appears that fault rock thickness has a large influence on predicting the pressure distribution within the field, but has only a slight effect on the oil and water production rates. To model a fault compartmentalised gas reservoir, produced by gas expansion, it appears more important to incorporate the multiphase flow properties of the fault rock to predict whether or not other compartments need to be drilled. It may be beneficial for reservoir engineers to run very simple simulations to identify the most important parameters to include in full-field production simulation models. It is important to emphasise that this conclusion, like most of the other conclusions given in this thesis about the importance of incorporating the multiphase fluid flow of fault rocks for different flow regimes, is based on the assumption that the two curves, *i.e.* undeformed and deformed relative permeability and capillary pressure curves, can be calculated using capillary pressure relationships that were originally derived for use in permeable undeformed sedimentary rocks (*e.g.* Ringrose *et al.*, 1993; Manzocchi *et al.*, 2002). It is important to mention that these conclusions may not be valid if the relative-permeability curves of fault rocks are very different to those calculated using the aforementioned relationships. For example, some recent experimental evidence (RDR, unpublished data) has suggested that the relative permeabilities of low permeability fault rocks could be several orders of magnitude lower than those of high permeability sandstones. If this observation is proven, some attempt will need to be made to take into account these differences within production simulation models.

- It is important to identify the most important parameters that need to be predicted when considering how to model faults in flow simulations. It is possible that more work in this area may provide 'rules of thumb' which will indicate the parameters that are important to consider when modelling fluid flow in faulted reservoirs. However, each case may be so specific that it will always be necessary to construct simple numerical models to determine which are the most important parameters to include in full-field production simulation models.

- The analysis of the microstructural and petrophysical properties of fault rocks from the Pierce Field has confirmed that it is unlikely that fault rocks are responsible for the large differences in the free water level (FWL) that exist across the field. If a fault seal analysis had been conducted earlier, one might have concluded sooner that subsurface hydrodynamics have an important control on petroleum distributions within Pierce. Instead, it was not until 22 years after the initial Pierce discovery (*i.e.* Dennis, 1998) that the importance of hydrodynamics in controlling the different FWLs was appreciated. In that sense, fault seal analysis can be an important part of reservoir characterisation.

- In an attempt to identify the optimal time to conduct a follow-up 3D seismic survey to identify unswept compartments at a time that would have a bearing on future production strategies, the production simulation model for the Pierce Field was run for a variety of possible fault properties. This study has revealed the potential of time-lapse seismic studies to aid reservoir characterisation (particularly the effect of faults on fluid flow) when integrated with simulation modeling. Time-lapse seismic studies have the potential to image changes in fluid composition and pressure within the subsurface, thus providing valuable data to history match production simulation models in a more 'unique' manner. Reservoir simulations provide the link between the observed changes in seismic attributes, the produced fluids, and the actual fluid dynamics within a reservoir. This can assist in understanding the past history of the reservoir, and, more importantly, in making the best of its future. Furthermore, this study has illustrated the possible potential hazards that can arise from misrepresenting faults for production simulation modelling. Placing what could actually be a false fault based on a 'forced' match of limited historical production data can result in a misleading prediction of the trapped petroleum distribution and, therefore, can cost a company millions of pounds by drilling unnecessary wells. The work conducted during this study suggests that 4D seismic has the potential to test fault property models, which in turn leads to a more predictive production simulation model.

- This study has identified that in many situations it may be important to take into account the multiphase flow properties of faults in production simulation models. One possibility is to use dynamic pseudofunctions. There are a number of pseudoisation methods available in the literature. Simple simulation models conducted during this research suggested that the Kyte

and Berry (K&B) and the pore-volume weighted (PVW) methods were better pseudofunctions for generating fault pseudo-curves than other popular methods like the Stone or the weighted relative permeability (WKR) method. Furthermore, simple tests in this study showed that using parent grid block unaltered capillary pressure curves in conjunction with pseudo relative permeability curves from either K&B or PVW is the best choice for pseudoisation process. However, the difficulties in recalculating the parent grid blocks capillary pressure points for each randomly generated pseudo saturation point can favour the use of the full K&B pseudo curves, considering that this latter method virtually gives identical results to the one involving using the unaltered capillary pressure curve. It is important to mention that there are more appealing analytical pseudoisation methods that have been proven to work successfully for an analogous kind of upscaling in heterogeneous cases with different two-phase saturation functions (*e.g.* Dale *et al.*, 1997; Barker and Dupouy, 1999). More tests are required on such analytical methods to confirm their validity in cases where the upscaled saturation functions are very different, *e.g.* undeformed rock next to faulted rock.

- For all the pseudofunctions tested in the study, using half-fault thickness upscaling gives closer results to the discrete model than full-fault thickness upscaling. However, when using the unaltered host cell capillary pressure curve, instead of the pseudo-generated curve, in conjunction with the pseudo-relative permeability curves, the K&B and the PVW pseudofunctions give almost identical results irrespective of the upscaling method adopted.

- Using a simple two-cell model, trends in the shapes of pseudos for different fault rock thicknesses were observed, suggesting that it could be possible to scale the pseudos for intermediate thickness values. This would restrict the number of pseudos that need to be generated for full-field production simulation models. Further tests are still required to establish reliable scaling relationships and to investigate the influence of other variables (*e.g.* viscosity contrasts, shapes of the grid blocks *etc.*) on the number of pseudos that would need to be generated for a full field model.

- In this research, advantage has been taken of the flux-boundary preservation feature available in the **Eclipse 100**^{TM} simulator to outline a possible workflow to apply the proposed method of pseudoisation for real, densely faulted models. Large simulation models can be subdivided into small regions and run separately. Each sub-region can be handled separately, thus making simulation run times more practical, even with a large number of faults included as discrete zones. However, the proposed process for this '*in-situ*' pseudoisation technique can be time consuming when modelling faults discretely (with a local grid refinement) in densely-faulted situations for each of the sub-domains. Further work is required to identify whether code could be written to automatically produce sector

models in which faults are incorporated as discrete planes with an associated local grid refinement.

- Some of the non-trivial faulted models used in this study showed a considerable difference between the fault representations using the conventional, single-phase *TMs*, and the new method of generating pseudo-dynamic curves. This latter representation gives an excellent match with the corresponding high-resolution, fine grid for most of the models addressed. When pseudofunctions are generated, across-fault flow rates are read directly from the high-resolution models without any estimation (*cf.* Manzocchi *et al.*, 2002).

As a final conclusion, the current findings obtained during this research indicate the importance of taking into account the multiphase flow properties of fault rocks for reliable production simulation models. Simple tests, *e.g.* simple two-cell models, have enabled the testing of various flow scenarios and an assessment of the contribution of different parameters, *e.g.* fault rock thickness and permeability, on the importance of this process. More realistic fault measurements are still required to appreciate this for real cases. Measuring full-saturation range relative permeability curves for very tight fault rocks is something that is only just being attempted. Some recently acquired measurements of gas relative permeability end points (*i.e.* k_{rg} at S_{wirr}) conducted on tight faulted rocks (RDR, unpublished data) were found to be as much as two orders of magnitude lower than those predicted by the routinely used Brooks–Corey relations. Analysing the multiphase flow behaviour of fault rocks is likely to be a highly complicated and time-consuming process, which is far from being done on a routine basis in industry. Case studies on producing fields may therefore be required to complement such datasets and assess the robustness of some techniques explored during this research.

8.2. Possible future work

The incorporation of geologically-reasonable fault rock properties into production simulation is only slowly being adopted by the petroleum industry. Furthermore, the consideration of the multiphase flow properties of fault rocks is at the leading edge of the technology and simple attempts at incorporating multiphase flow properties have only been attempted by a small number of operators on a small number of fields. It is therefore easy to see that a huge amount of future work remains to be conducted in this field. In the following section a number of possible future research directions are identified.

8.2.1. Testing on real field examples

All of the technology and many of the workflows presented in this thesis still need testing on real field examples. Firstly, it is necessary to test whether the workflows could be used on full field models; it will be particularly interesting (and challenging) to establish whether the

methodology proposed in **Chapter 7** for including faults as discrete planes, with a local grid refinement, in sector models can be applied to a full field model. Secondly, it is necessary to establish whether the methodologies and workflows can help explain the production history from structurally complex, compartmentalised reservoirs. The second of these tests is, however, easier said than done as history matches are inevitably non-unique and therefore even improving the modelling of production data does not necessarily mean that the methodology is correct. Pursuing other studies such as using 4D time-lapse seismic would undoubtedly play a role in reducing the non-uniqueness and, therefore, accomplishing such demanding tests.

8.2.2. Fault rock multiphase flow property analysis

A major problem with incorporating the multiphase flow properties of faults into production simulation models is that practically speaking there exists no reliable data on the relative permeability of fault rocks. In effect, the derivation of techniques to incorporate the multiphase flow behaviour into production simulation models has accelerated far faster than efforts to measure the relative permeability of fault rocks. Multiphase experiments on tight rocks are limited mainly because they are time consuming and expensive. Given the potential benefits to be gained by accurately modelling the effects of faults on petroleum production it is recommended that a more concerted effort is made to obtain relative permeability measurements from fault rocks.

8.2.3. Capillary end effects and their implications

Simulation models that were run as part of this research project, which indicated that flow through tight fault rocks, with different capillary characteristics from their surrounding host rocks, may create capillary end effects. This effect is related to capillary pressure heterogeneity between different flow units. The effect has been studied by number of authors for different applications. For example, it was first observed by Holditch (1979) when examining the impact of water blocks that form during stimulation on productivity of gas wells. Dale *et al.* (1997) have also included this effect when defining deterministic solution to 1D steady state flowing pressure and saturation functions. The capillary end effect has been described for two-phase flows in **Chapter 3**. Work to further investigate this phenomenon is briefly described in this section for important future implications. In particular, if proved important, capillary end-effects could lay doubt on the validity of assuming complex fault zones can be modelled as single faults with a thickness that is some function of the combined thickness of the small-scale interconnected faults within the fault core and damage zone.

8.2.3.1 Laboratory core simulation test

Three cores were simulated to illustrate the capillary end effect in a gas/water system. The simulation shows a gas-saturated core (with host-rock permeability of 500 mD) flooded with water using differential pressure of 2 bars (~ 29 psi). The inlet cell has a pressure of 3 bars (~ 43.5 psi). To insure that the inlet pressure stays constant, this cell has been given a very high pore volume and permeability. An analogous treatment was applied to the outlet cell with a constant pressure of 1 bar (~ 14.5 psi). The core is initially in pressure equilibrium with the outlet. Each core contains different water-saturated fault zones with a permeability of 1 mD, but with the same effective fault thickness, around its centre. The first core (**Fig. 8.4a**) contains a single zone with 0.6 cm fault material thickness. The second core (**Fig. 8.4b**) contains two zones each has 0.3 cm fault material thickness. The third core (**Fig. 8.4c**) contains three zones each has 0.2 cm fault material thickness. The host material has zero capillary pressure whereas the fault material has capillary pressure curve ranging from 1 to 1.5 bars (entry pressure being 1 bar). Each case was simulated for 12 hours. Initial and final stages are shown in **Fig. 8.4**.

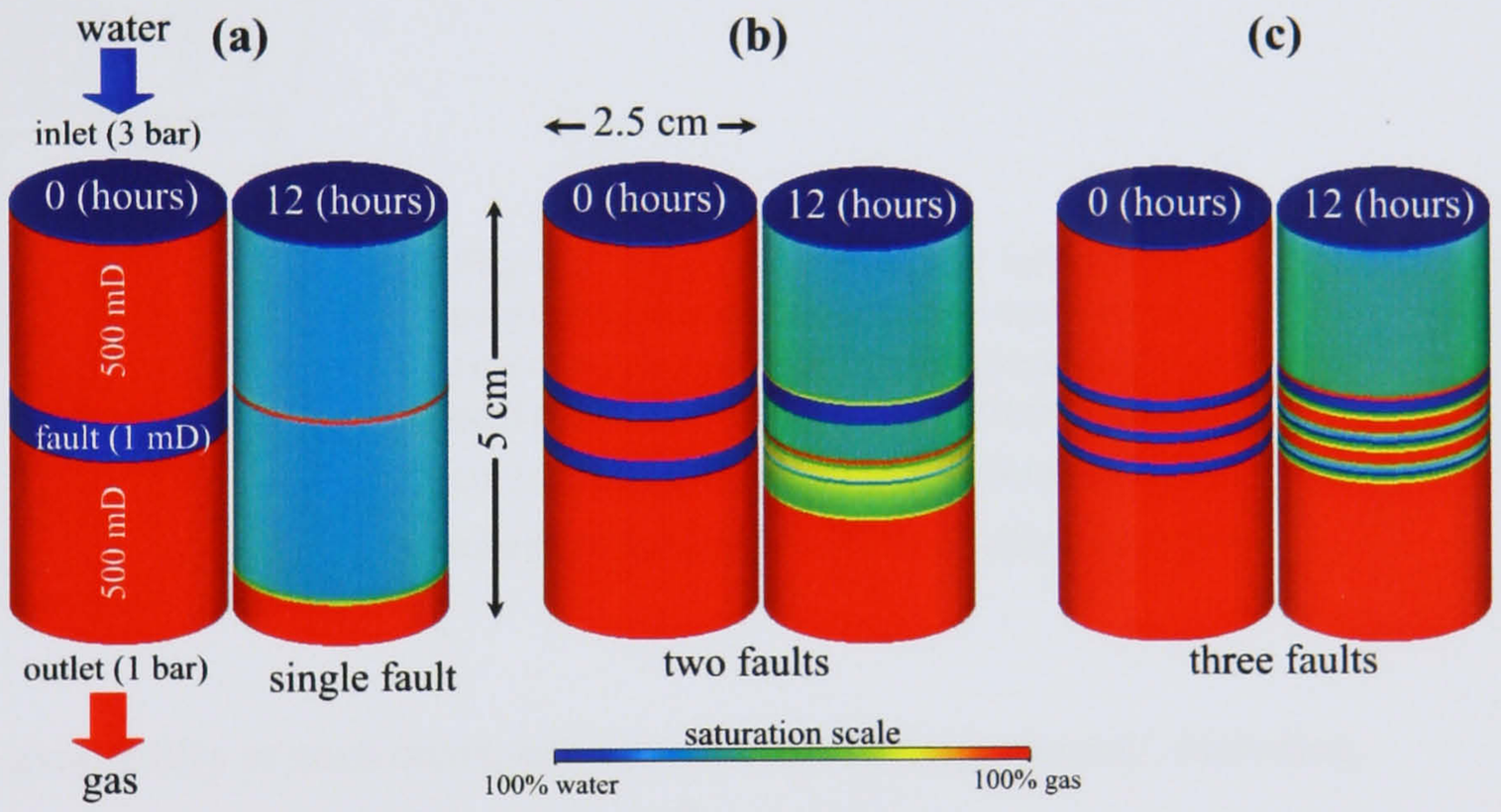

Fig. 8.4. Illustrating the capillary end effect on water sweep speed and efficiency on three identical gas-saturated cores containing different fault zones with identical cumulative fault thickness in each core. See text for details. (a) a core sample with a single fault, (b) a core sample with two faults, (c) a core sample with three faults. Note the differences in the waterfront movement.

The results show different flooding lengths were obtained in each core. The core with a single fault zone is almost completely swept by water (**Fig. 8.4a**). The water sweep length decreases as the fault zone split into more individual faults (compare **Fig. 8.4 a**, **b** and **c**). The capillary end effect has allowed the water-saturated faults to trap some gas behind it in a semi-additive manner, thus reducing the sweep efficiency as going from case **a** to **c** in **Fig. 8.4**.

8.2.3.2 Implications of capillary end effects

The capillary end effect makes a reasonable sense in theory. Future works, however, are required to prove the effect in practice. Laboratory measurements, with the high technology of the computerised tomography (CT) scanner, can provide a visual evidence for this effect. In a highly damaged fault zone, lots of issues can arise if the capillary end effect is proved to be true. For instance, according to this theory, the flow resistance of the effective fault zone will be the semi-additive effect of that of each small fault. The word 'additive' needs some practical proof. Simple measurements, *e.g.* routine steady state laboratory measurements, can contribute a lot to the issue of capillary end effect. The difficulty lies in finding identical cores each of which has different number of faults, of identical properties, but the same cumulative thickness, t_f, in each core (**Fig. 8.5).** One current suggestion is to make these cores using materials with known grain diameters by stacking different lithologies representing host and fault rocks.

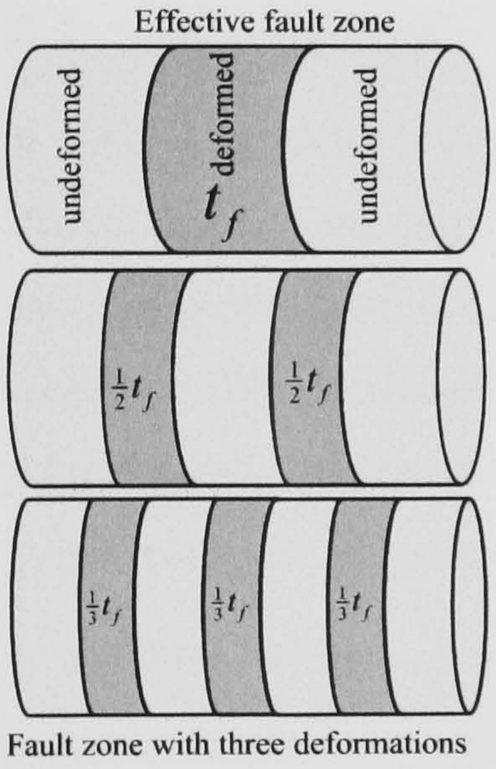

Fig. 8.5. Ideal core samples for testing the proposed theory of capillary end effect. The cores have identical undeformed (light areas) and deformed (dark areas) materials. The cumulative deformations thickness, t_f, is identical for each core fault damage zone.

With the availability of such cores, number of tests can be performed, including:

- Testing the effect of flow rates on the capillary end-point effects.
- Tracking the pressure build up at both sides of the fault damage zone to prove of disapprove the proposed theory, *i.e.* Is the pressure build up proportional to the number of deformation bands or not?
- Drawing number of correlations to help take the effect of fault damage zones into account when simulating reservoir models. For example, finding the effective flow rates that give the same pressure differential across each damage zone with different number of deformations.

The recent work of Christiansen (2005) demonstrates the role of the capillary end effect on gas productivity of leakoff during fracturing and imbibition of water during the productive life of gas wells in low permeability formations.

Appendix A

Microstructure and petrophysical properties of individual specimens from well 23/27-8, Pierce Field

A.1. Introduction

A total of 7 fault rocks and their undeformed host rocks were selected from well 23/27-8 in Pierce Field, North Sea, for microstructural and petrophysical property analysis. The selected samples came from a clay-poor environment and most of which belong to cataclastic fault category. The available samples for this study do not comprise clay-rich samples. The mineralogies, microstructures and diagenetic histories of the undeformed sandstones and the fault rocks were investigated using a scanning electron microscope (SEM).

In this section we present specimen photographs, SEM micrographs and petrophysical property results from individual samples analysed during this study.

A.2. Specimen 23/27-8.1: Cataclastic fault (Depth: 8270' 8" MD)

A hand specimen photograph of sample 23/27-8.1 is shown in **Fig. A.1**. Micrographs showing the general microstructure of the host sandstone and cataclastic fault rock that it contains are presented in **Fig. A.2**. The undeformed sandstone has a permeability of 9.1 mD. Mercury injection results show the host sandstone has a threshold pressure of 25 psi (**Fig. A.3**).

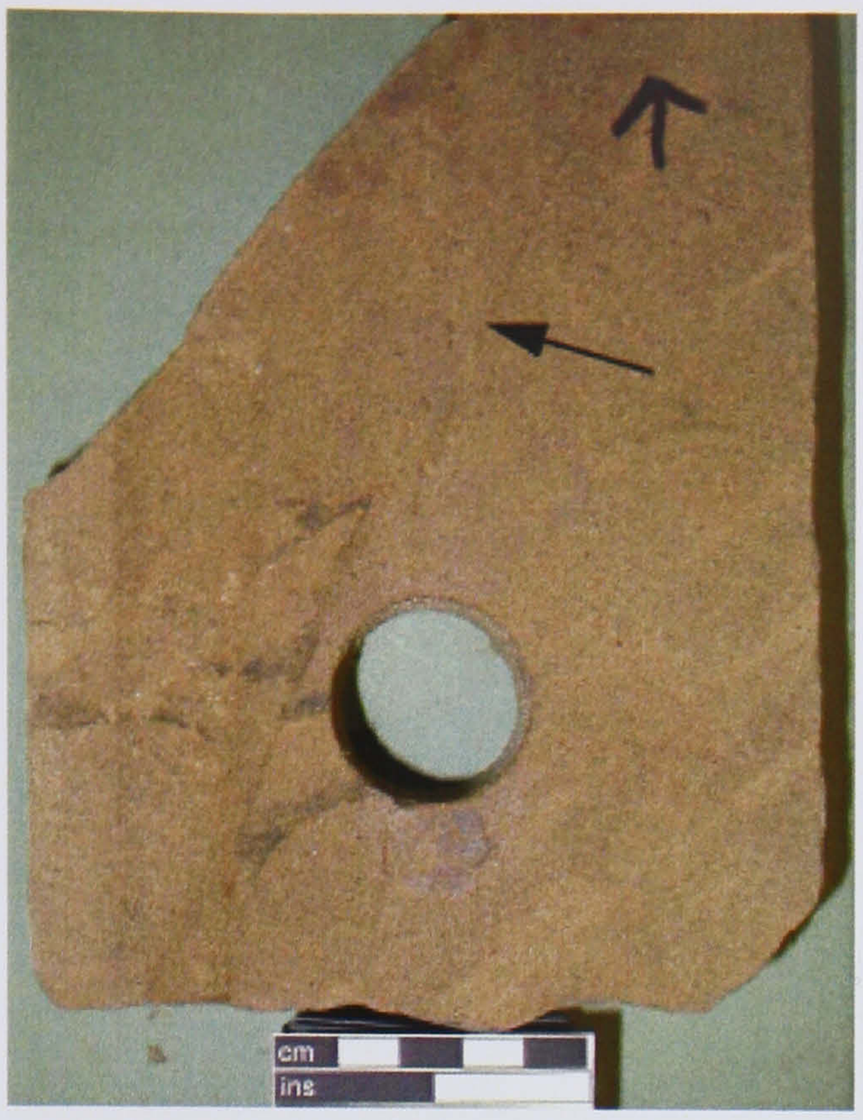

Fig. A.1. Photograph of the hand specimen of sample 23/27-8.1. Note that it contains a thin cataclastic fault (arrow).

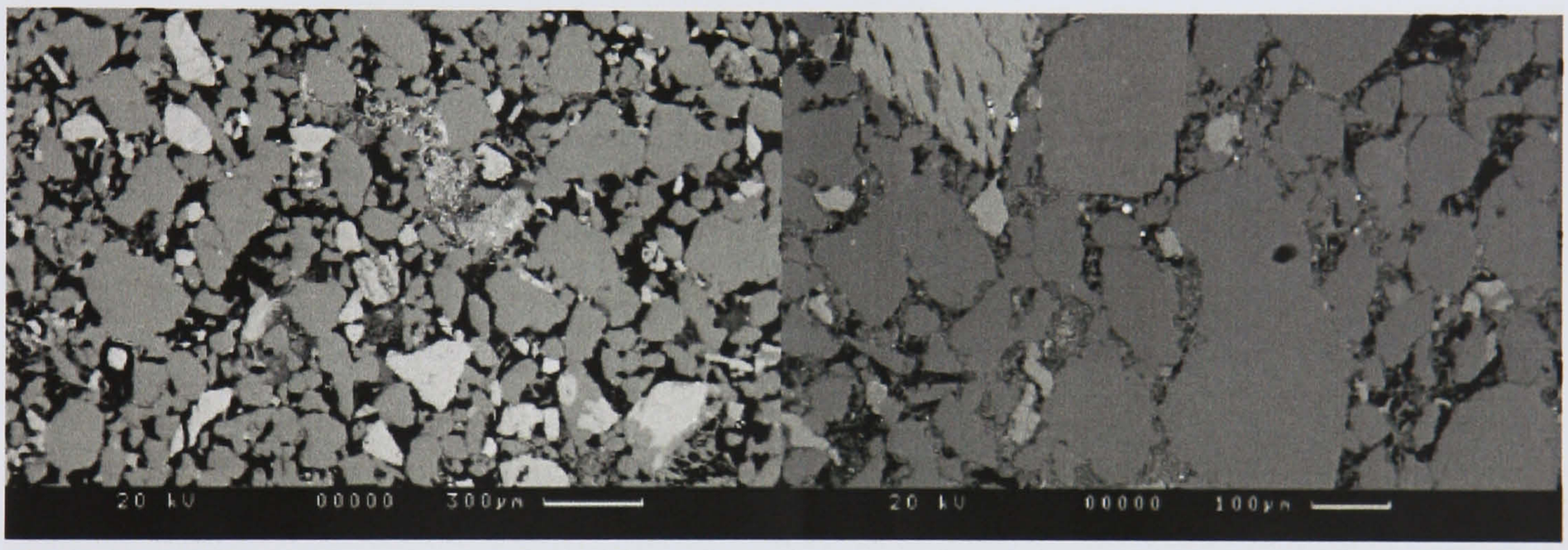

Fig. A.2. BSE micrograph showing the undeformed sandstone **(left)** and the cataclastic fault rock **(right)** in sample 23/27- 8.1.

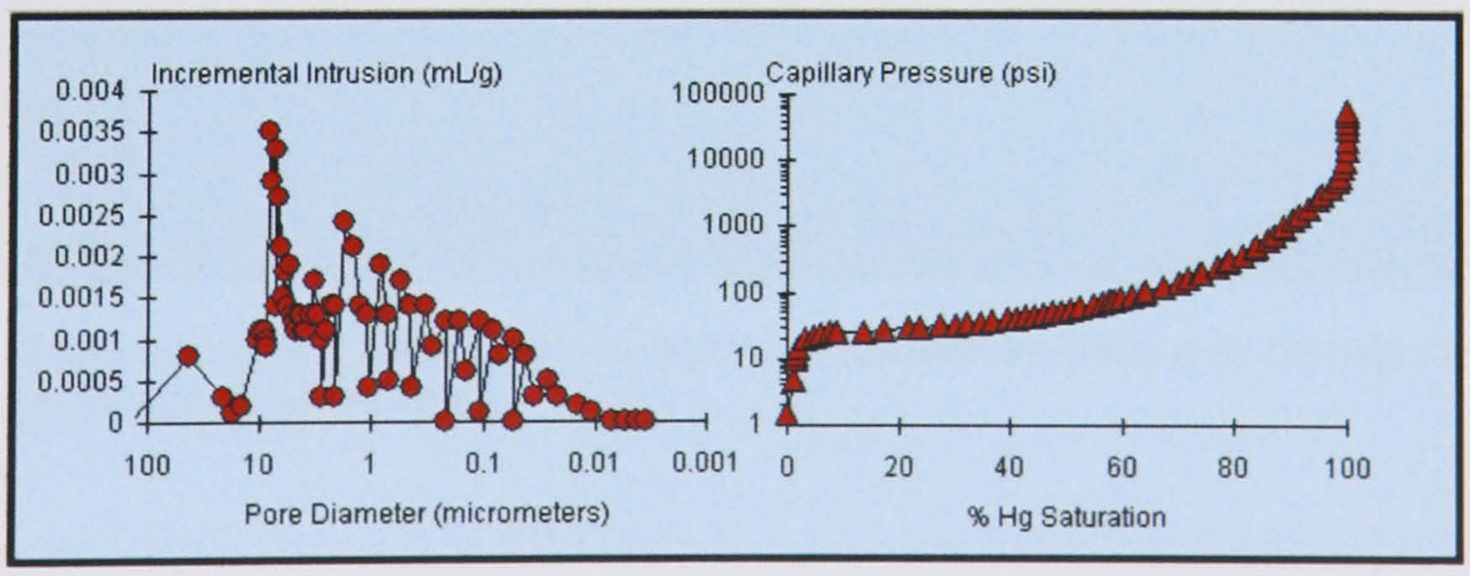

Fig. A.3. Hg-injection results from the undeformed sandstone in sample 23/27-8.1.

A.3 Specimen 23/27-8.2: Cataclastic fault (Depth: 8278' 8" MD)

A hand specimen photograph of sample 23/27-8.2 is shown in **Fig. A.4**. Micrographs showing the general microstructure of the host sandstone and cataclastic fault rock that it contains are presented in **Fig. A.5**. The undeformed sandstone has a permeability of 11.7 mD, whereas the fault rock has a permeability of 0.067 mD. Mercury injection results show the host sandstone has a threshold pressure of 25 psi, whereas the fault rock has a threshold pressure of 140 psi (**Fig. A.6**).

Fig. A.4. Photograph of the hand specimen of sample 23/27-8.2. Note that it contains a thin cataclastic fault (arrow).

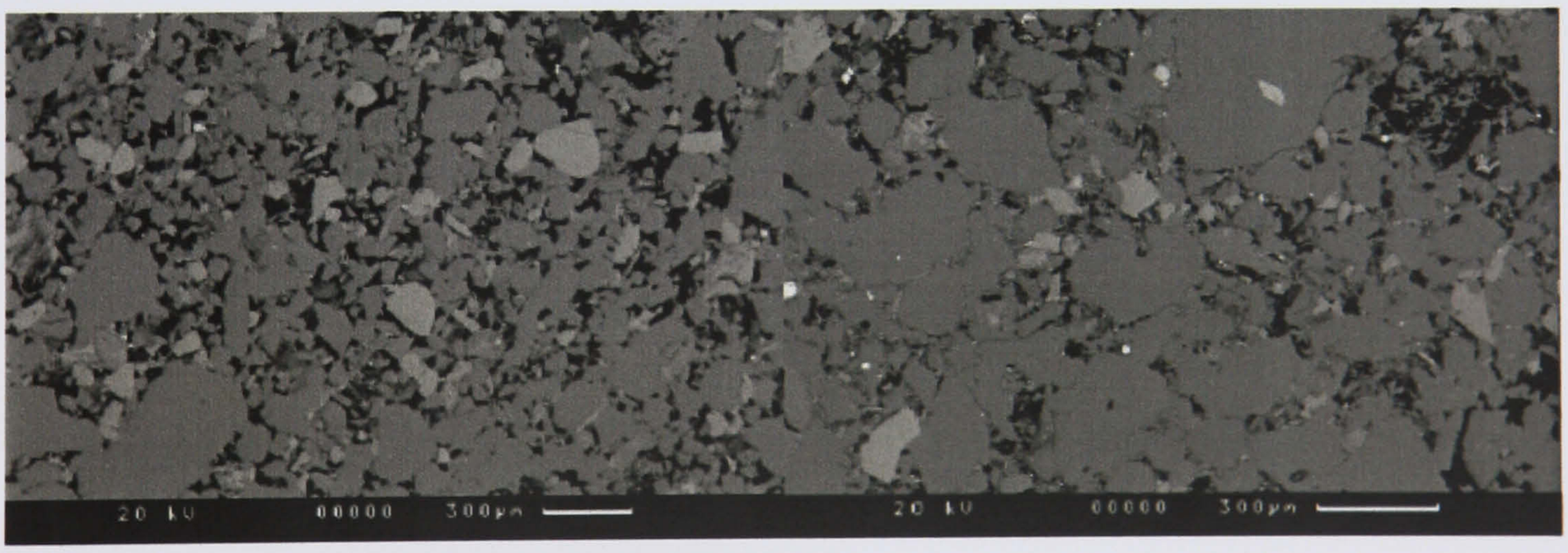

Fig. A.5. BSE micrograph showing the undeformed sandstone **(left)** and the cataclastic fault rock **(right)** in sample 23/27- 8.2.

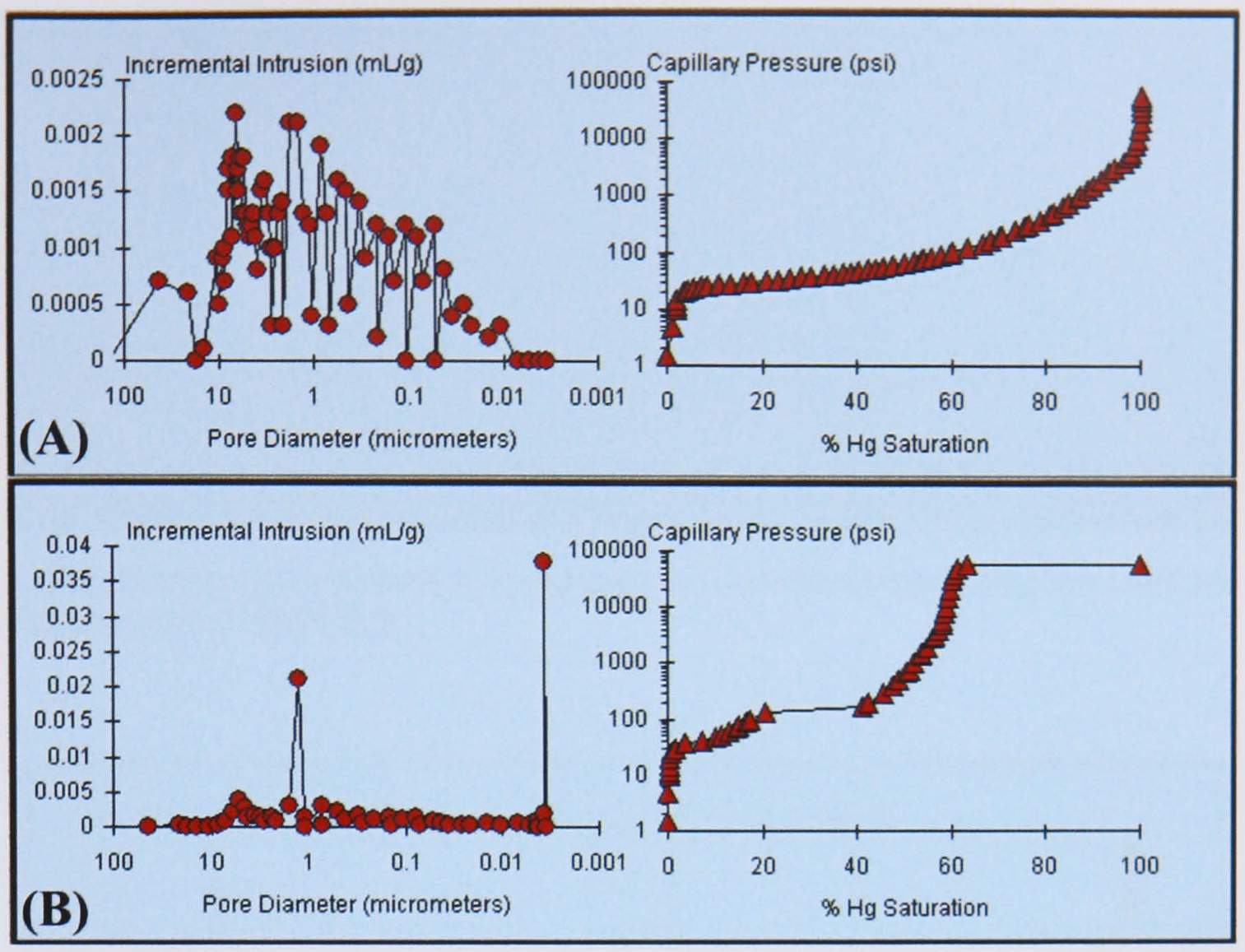

Fig. A.6. Hg-injection results from **(A)** the undeformed sandstone in sample 23/27-8.2 and **(B)** the cataclastic fault that it contains.

A.4 Specimen 23/27-8.3: Cataclastic fault (Depth: 8303' MD)

A hand specimen photograph of sample 23/27-8.3 is shown in **Fig. A.7**. Micrographs showing the general microstructure of the host sandstone and cataclastic fault rock that it contains are presented in **Fig. A.8**. The undeformed sandstone has a permeability of 60.2 mD, whereas the fault rock has a permeability of 0.056 mD. Mercury injection results show the host sandstone has a threshold pressure of 15 psi, whereas the fault rock has a threshold pressure of 170 psi (**Fig. A.9**).

Fig. A.7. Photograph of the hand specimen of sample 23/27-8.3. Note that it contains a thin cataclastic fault (arrow).

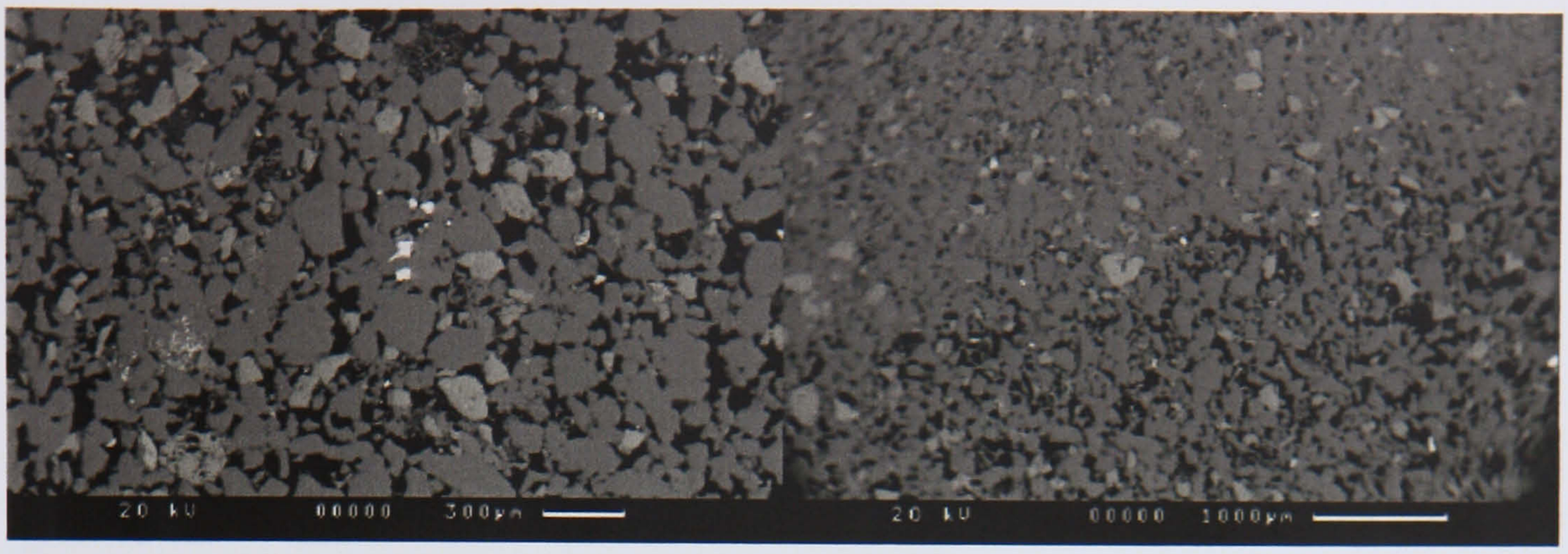

Fig. A.8. BSE micrograph showing the undeformed sandstone **(left)** and the cataclastic fault rock **(right)** in sample 23/27-8.3.

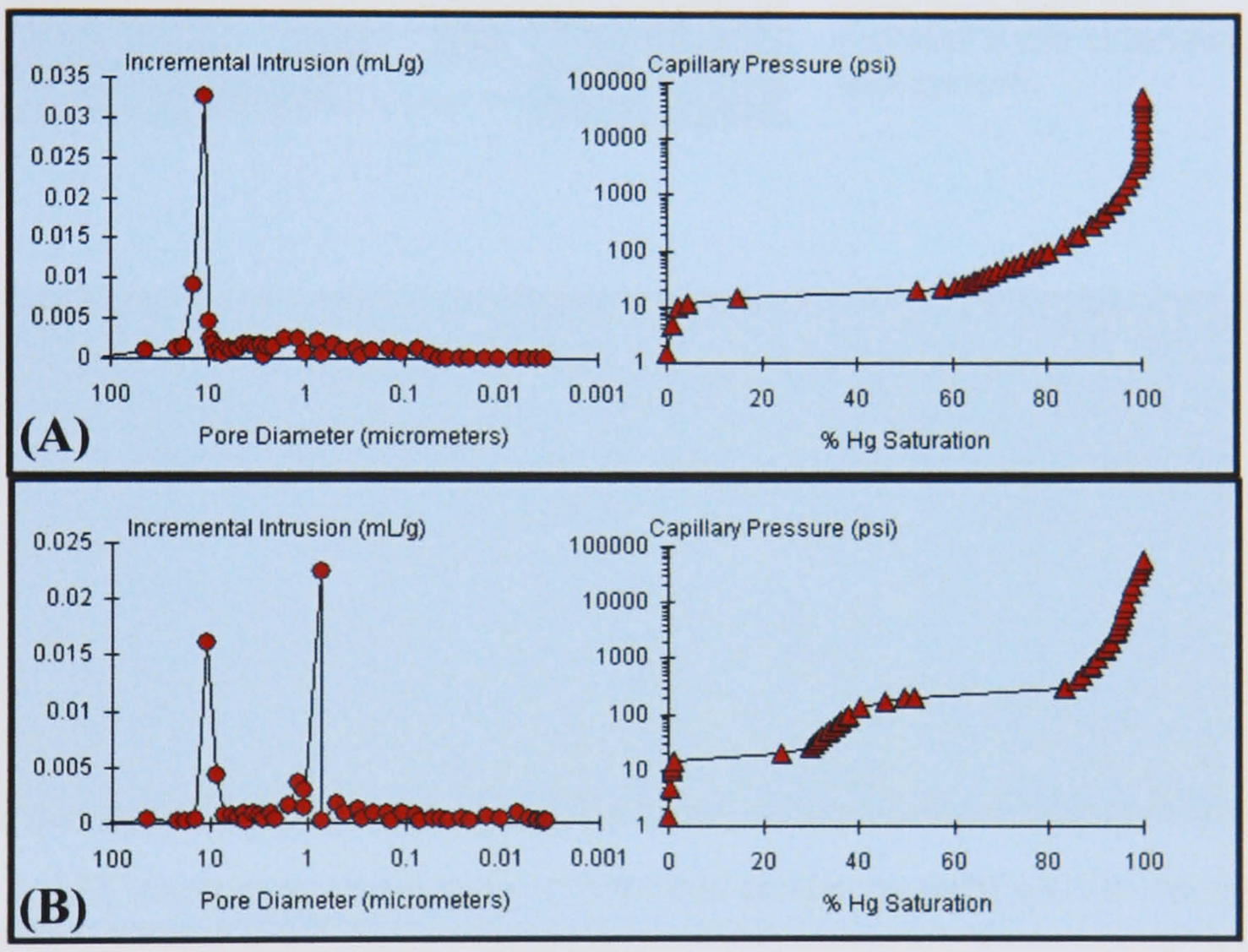

Fig. A.9. Hg-injection results from **(A)** the undeformed sandstone in sample 23/27-8.3 and **(B)** the cataclastic fault that it contains.

A.5 Specimen 23/27-8.4: Cataclastic fault (Depth: 8305' MD)

A hand specimen photograph of sample 23/27-8.4 is shown in **Fig. A.10**. Micrographs showing the general microstructure of the host sandstone and cataclastic fault rock that it contains are presented in **Fig. A.11**. The undeformed sandstone has a permeability of 63.1 mD, whereas the fault rock has a permeability of 0.01 mD. Mercury injection results show the host sandstone has a threshold pressure of 15 psi, whereas the fault rock has a threshold pressure of 410 psi (**Fig. A.12**).

Fig. A.10. Photograph of the hand specimen of sample 23/27-8.4. Note that it contains a thin cataclastic fault (arrow).

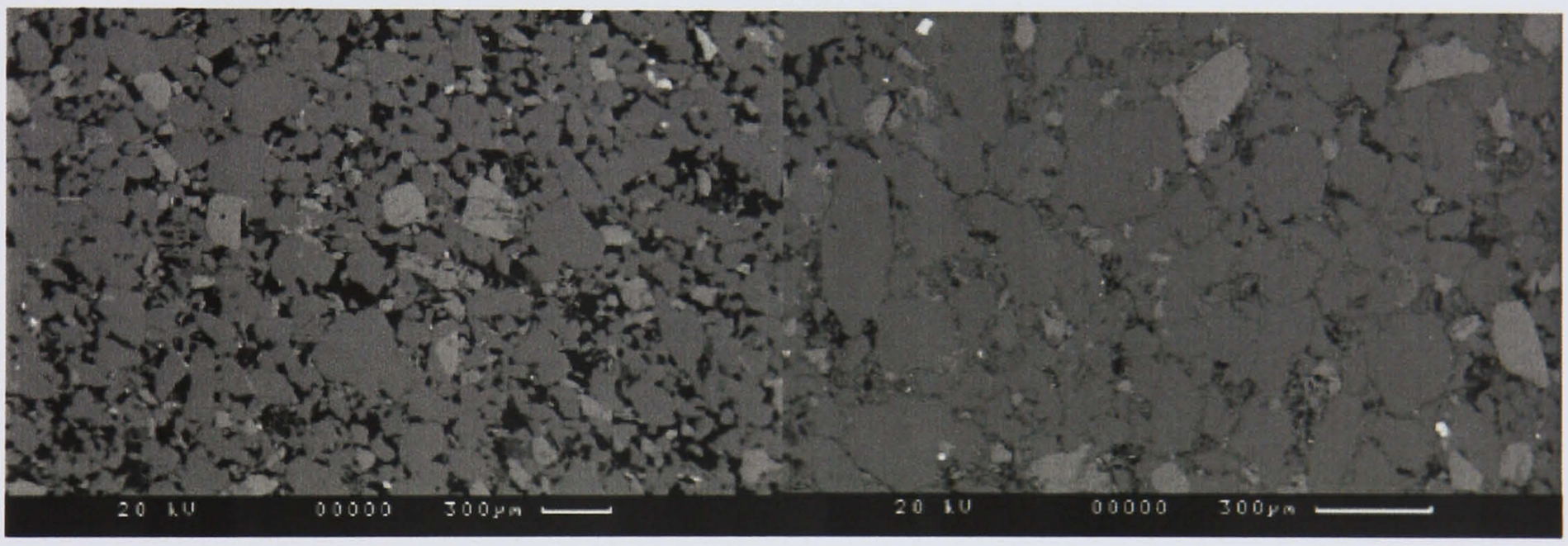

Fig. A.11. BSE micrograph showing the undeformed sandstone **(left)** and the cataclastic fault rock **(right)** in sample 23/27- 8.4.

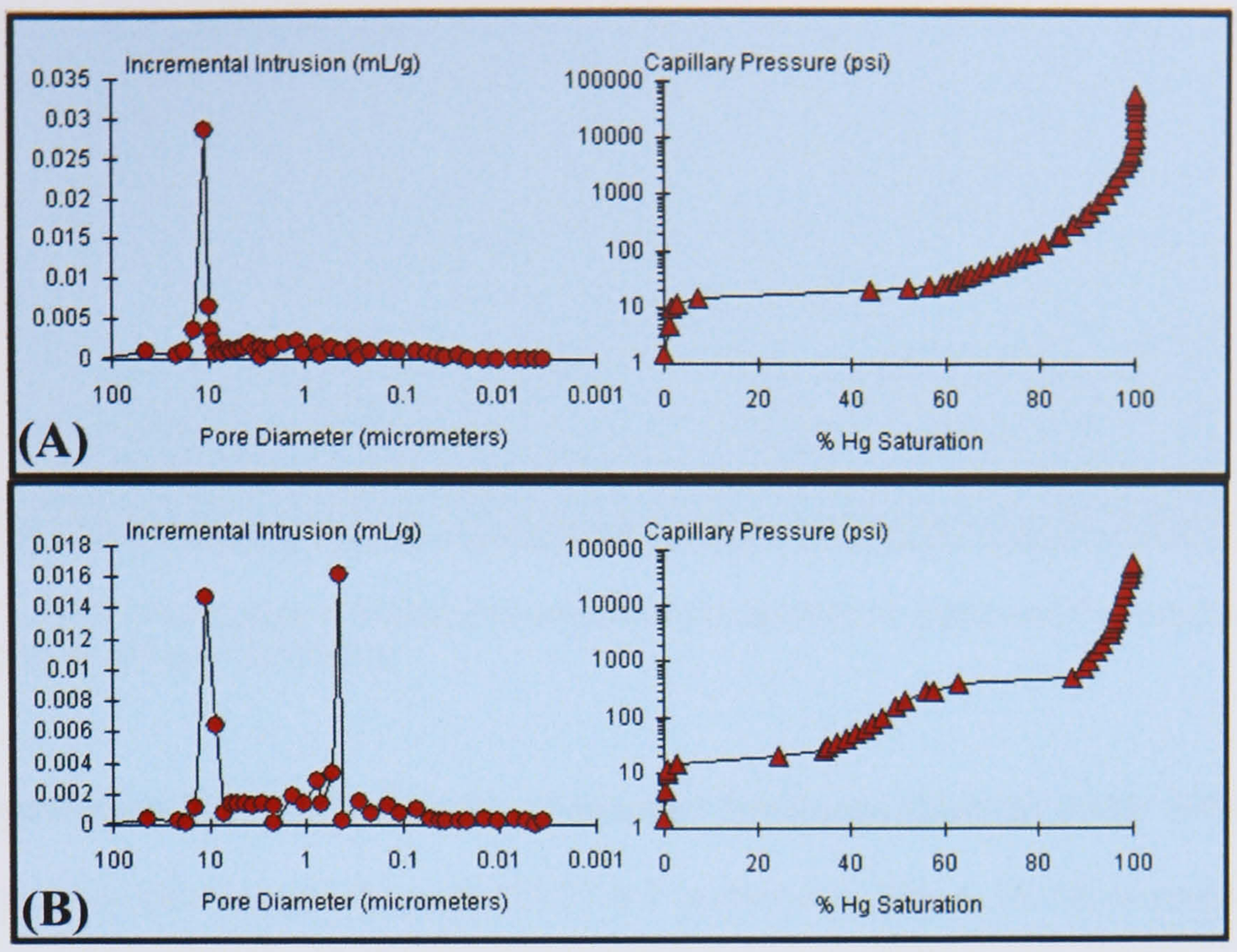

Fig. A.12. Hg-injection results from **(A)** the undeformed sandstone in sample 23/27-8.4 and **(B)** the cataclastic fault that it contains.

A.6 Specimen 23/27-8.5: Cataclastic fault (Depth: 8307' 9" MD)

A hand specimen photograph of sample 23/27-8.5 is shown in **Fig. A.13**. Micrographs showing the general microstructure of the host sandstone and cataclastic fault rock that it contains are presented in **Fig. A.14**.

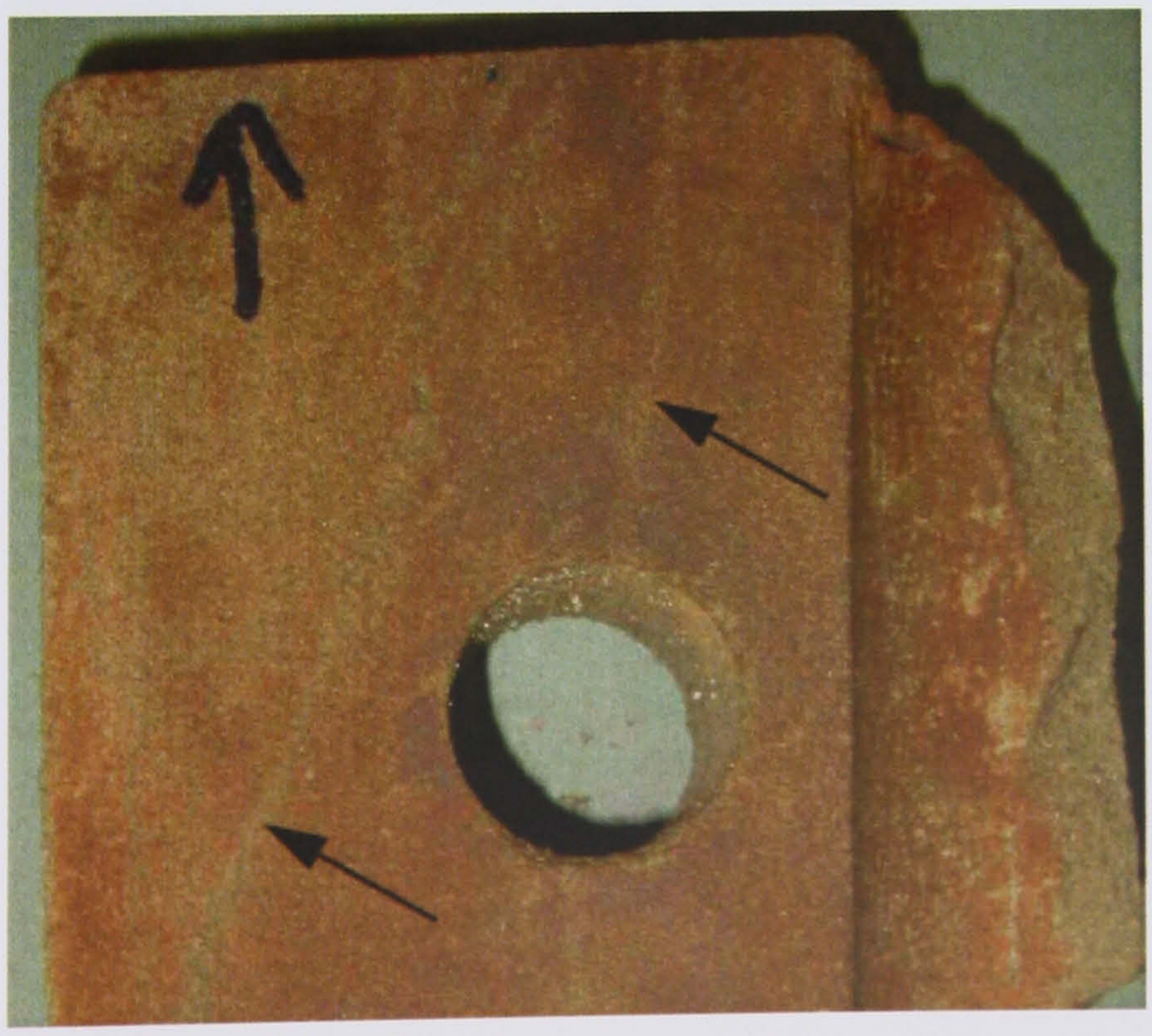

Fig. A.13. Photograph of the hand specimen of sample 23/27-8.5. Note that it contains two thin cataclastic faults (arrows).

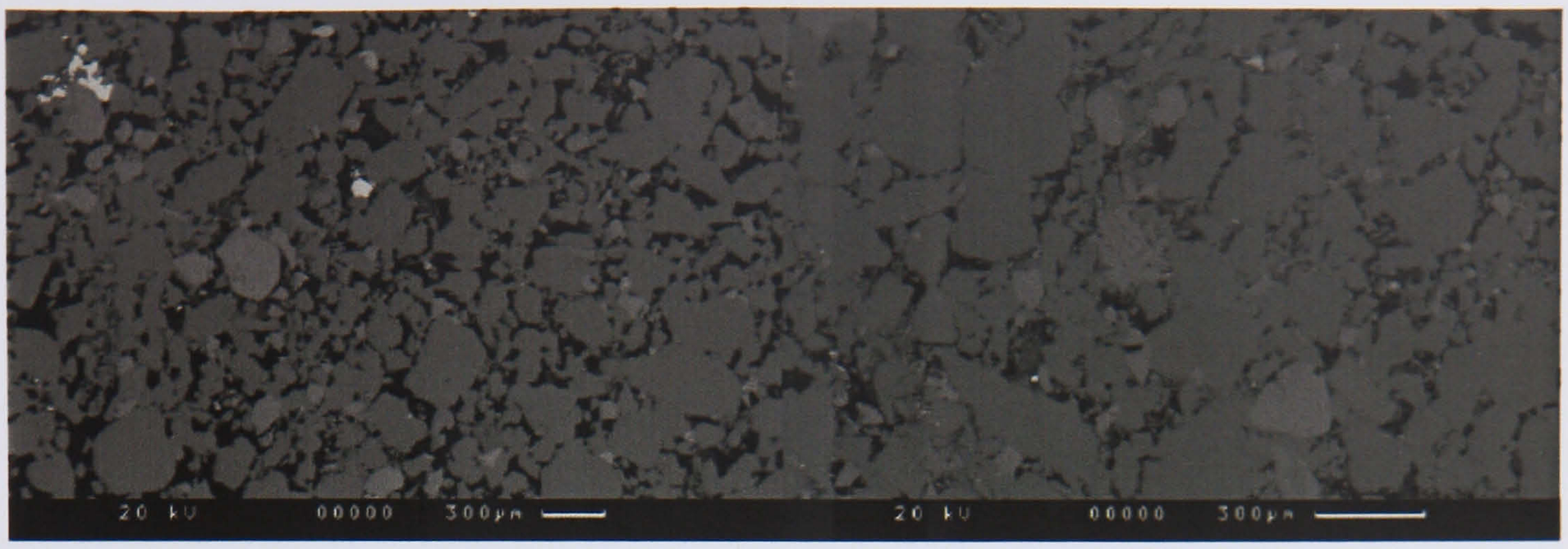

Fig. A.14. BSE micrograph showing the undeformed sandstone **(left)** and the cataclastic fault rock **(right)** in sample 23/27-8.5.

A.7 Specimen 23/27-8.7: Calcite-cemented fractures (Depth: 8322' MD)

A hand specimen photograph of sample 23/27-8.7 is shown in **Fig. A.15**. Micrographs showing the general microstructure of the host sandstone and the calcite-cemented fractures that it contains are presented in **Fig. A.16**. The undeformed sandstone has a permeability of 2.4 mD, whereas the fault rock has a permeability of 0.001 mD. Mercury injection results show the host sandstone has a threshold pressure of 35 psi, whereas the fault rock has a threshold pressure of 750 psi (**Fig. A.17**).

Fig. A.15. Photograph of the hand specimen of sample 23/27-8.7. Note that it contains calcite-cemented fractures (arrows).

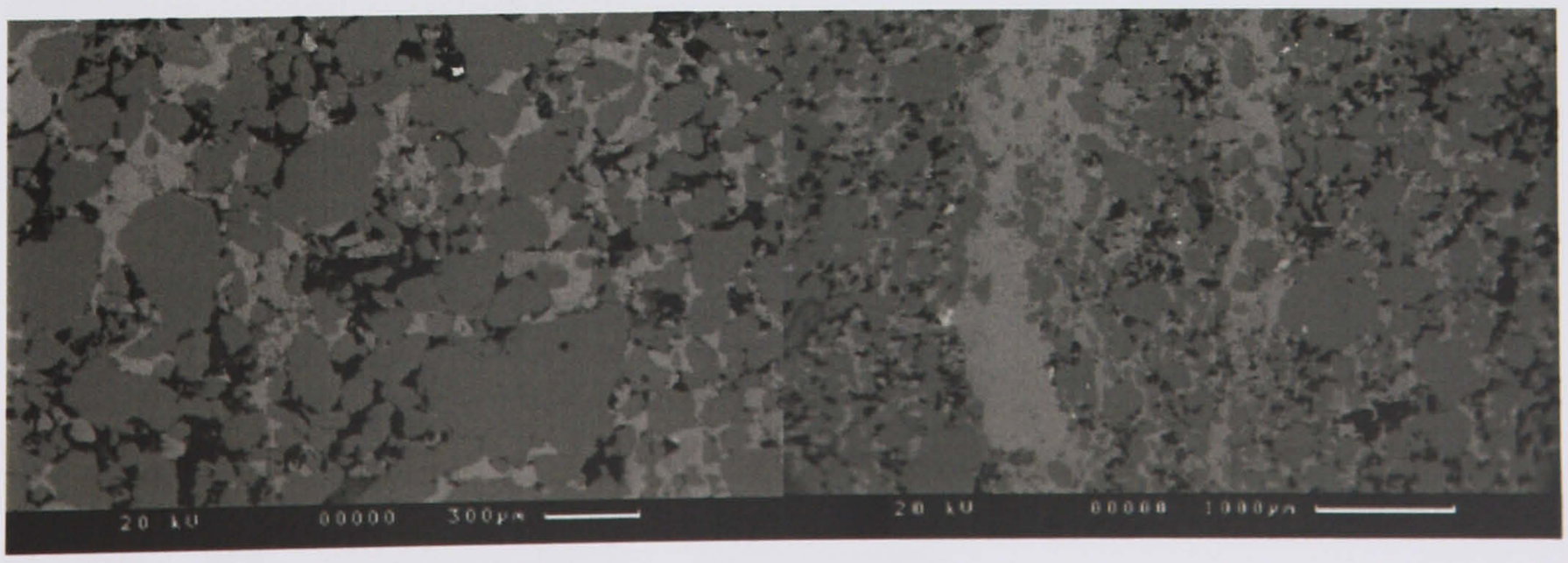

Fig. A.16. BSE micrograph showing the undeformed sandstone **(left)** and the calcite-cemented fractures **(right)** in sample 23/27-8.7.

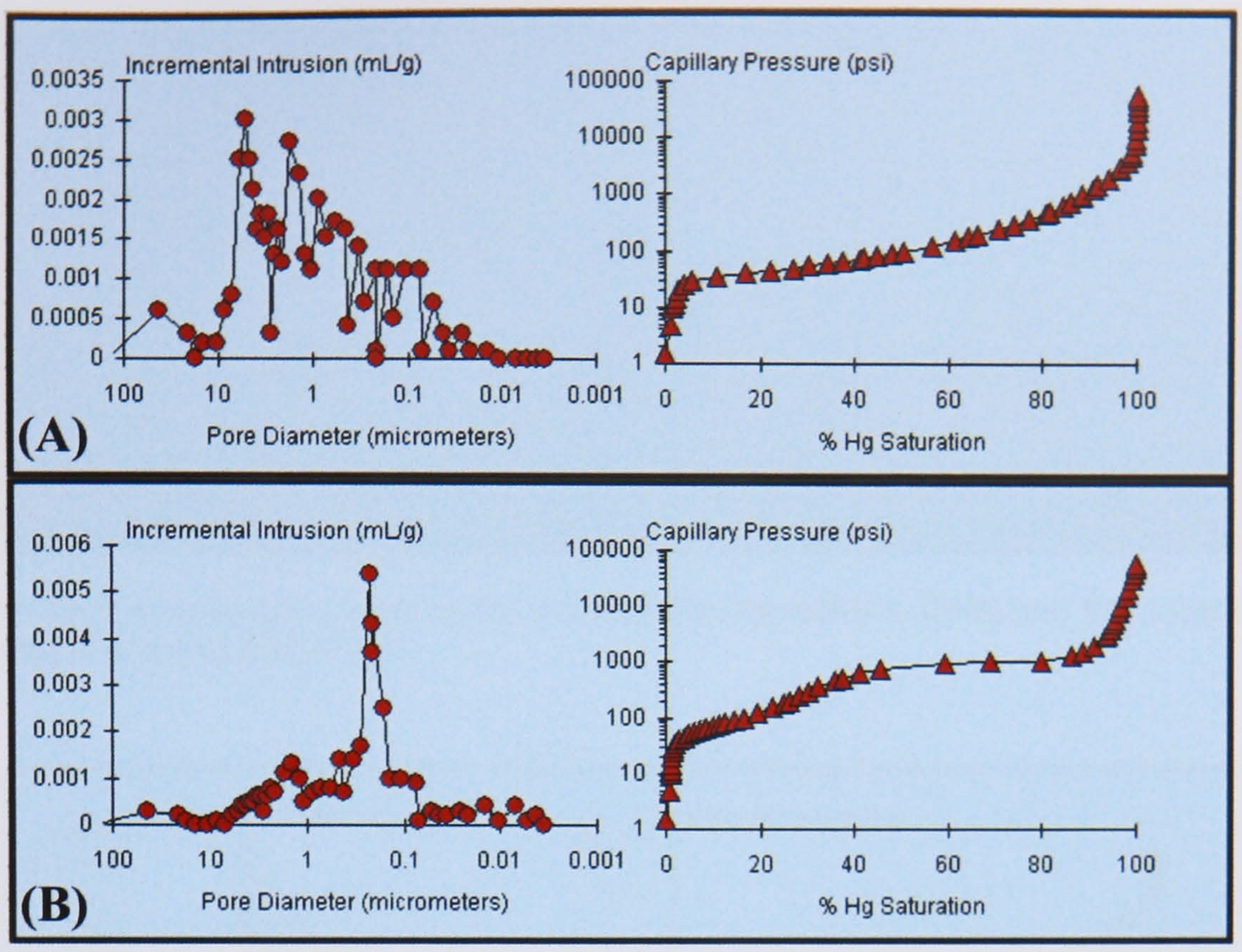

Fig. A.17. Hg-injection results from **(A)** the undeformed sandstone in sample 23/27-8.7 and **(B)** the calcite-cemented fracture that it contains.

A.8 Specimen 23/27-8.8: Cataclastic fault (Depth: 8465' 2" MD)

A hand specimen photograph of sample 23/27-8.8 is shown in **Fig. A.18**. Micrographs showing the general microstructure of the host sandstone and cataclastic fault rock that it contains are presented in **Fig. A.19**. The undeformed sandstone has a permeability of 5.2 mD, whereas the fault rock has a permeability of 0.13 mD. Mercury injection results show the host sandstone has a threshold pressure of 37 psi, whereas the fault rock has a threshold pressure of 270 psi (**Fig. A.20**).

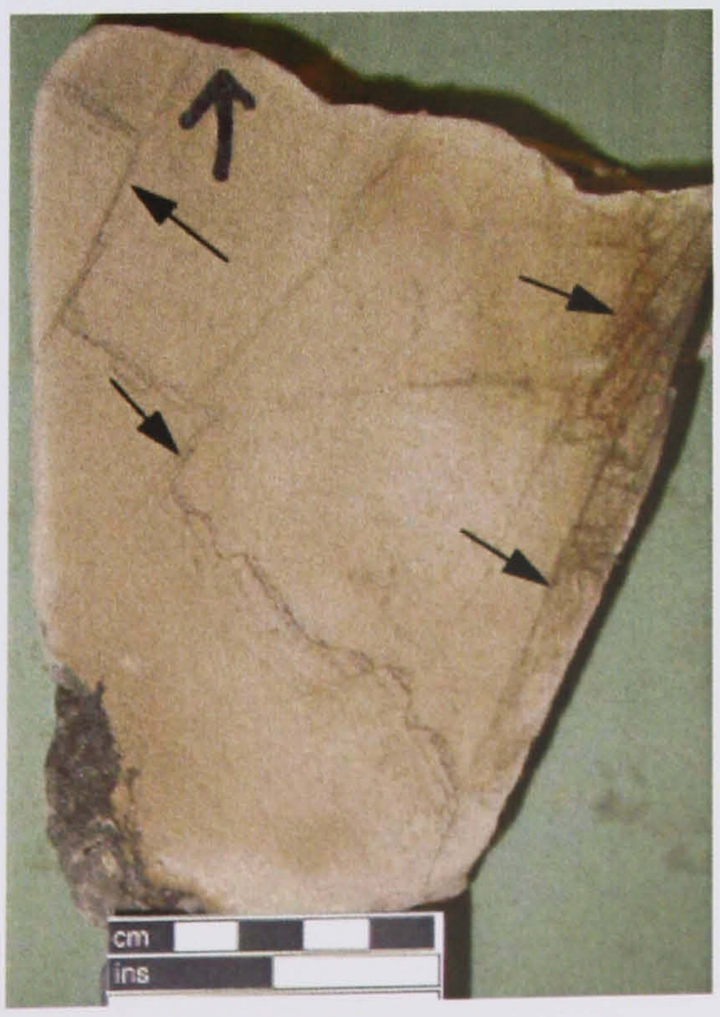

Fig. A.18. Photograph of the hand specimen of sample 23/27- 8.8. Note that it contains thin cataclastic faults (arrows).

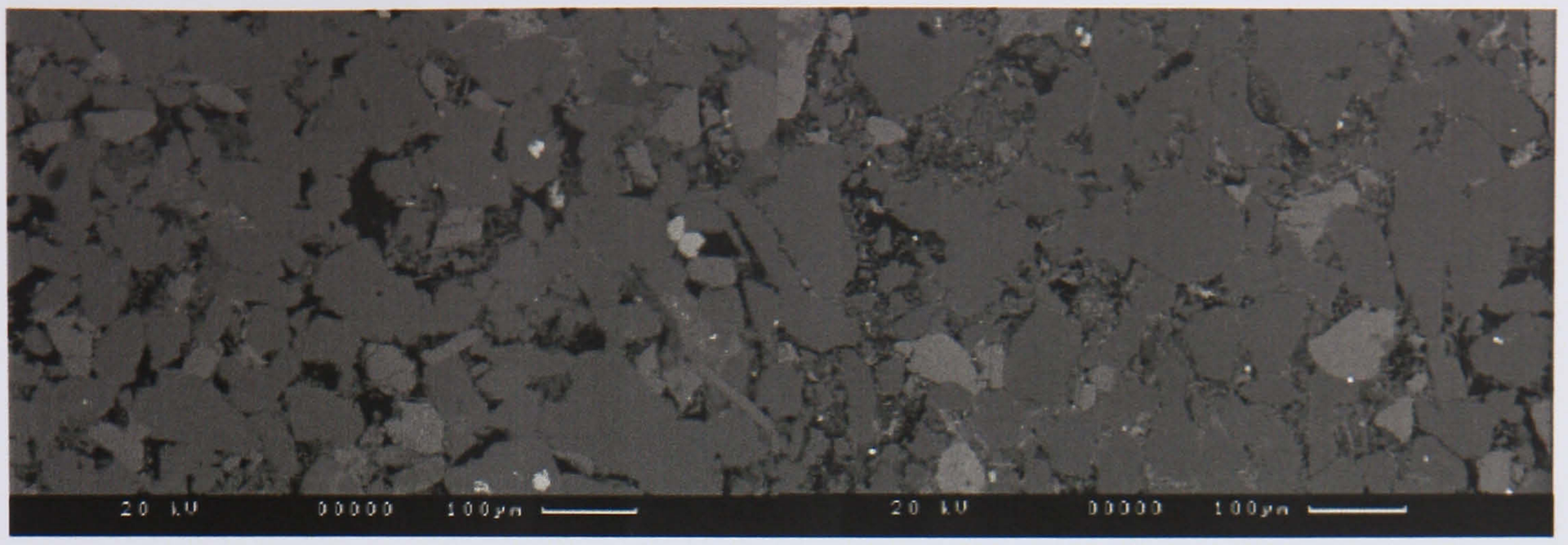

Fig. A.19. BSE micrograph showing the undeformed sandstone **(left)** and the cataclastic fault rock **(right)** in sample 23/27-8.8.

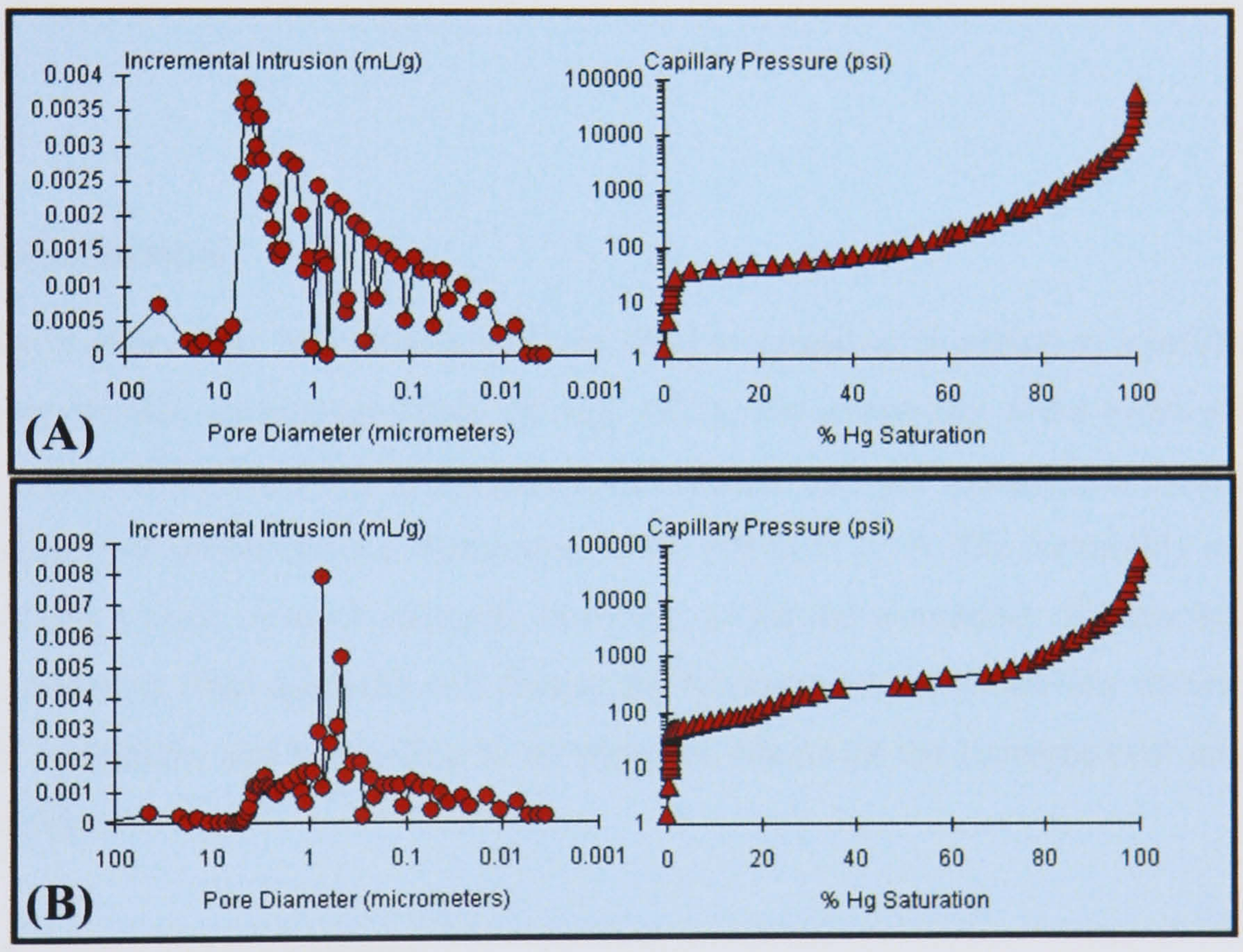

Fig. A.20. Hg-injection results from **(A)** the undeformed sandstone in sample 23/27-8.8 and **(B)** the cataclastic fault that it contains.

Appendix B

Wettability review

B.1. Introduction

Wettability is defined as: "the tendency of one fluid to spread or to adhere to a solid surface in the presence of other immiscible fluids" (Craig, 1971). The wettability of the rocks with respect to liquid phases is known to have a fundamental control on their multi-phase flow behaviour and electrical flow properties (*e.g.* Anderson, 1985, 1986a, b, c, d). The wettability of reservoir rocks has been a topic of much research, however, as yet the wettability of seals has received very little attention. This appendix will discuss the fundamentals of wettability starting with the physics of wettability and proceeding to its variation effects on the pertophysical properties of reservoir rocks.

B.2. Overview of wettability

Sediments invariably become saturated with water soon after deposition. Petroleum may, however, subsequently enter pore spaces as a result of two processes:

- Petroleum may migrate from an external source rock into the pore space.
- Petroleum may be generated in situ by the maturation of solid hydrocarbons.

After the initial migration of hydrocarbon, a thin film (1 to 100 nm) of water will cover the grains present. Components of the crud oil may then, however, interact with the mineral surface causing the thin film to collapse, which may result in an alteration of wettability (*e.g.* Buckley, 1987). Rock surfaces are referred to as water-wet if they have a wetting preference for water as oppose to oil. On the other hand, oil-wet rock surfaces have a wetting preference for oil as oppose to water. Neutral wettability refers to the situation when rock surfaces show little preference to oil. Fractional wettability refers to the situation where some minerals within a rock are oil-wet (Brown and Fatt, 1956), whereas others are water-wet. Mixed-wettability is a term

introduced by Salathiel (1973) to describe a fractional wet rock in which oil-wet surfaces for continuous paths through the large pore spaces. Rocks may therefore be divided into those that have a homogeneous wettability and those that have heterogeneous wettability (**Fig. B.1**).

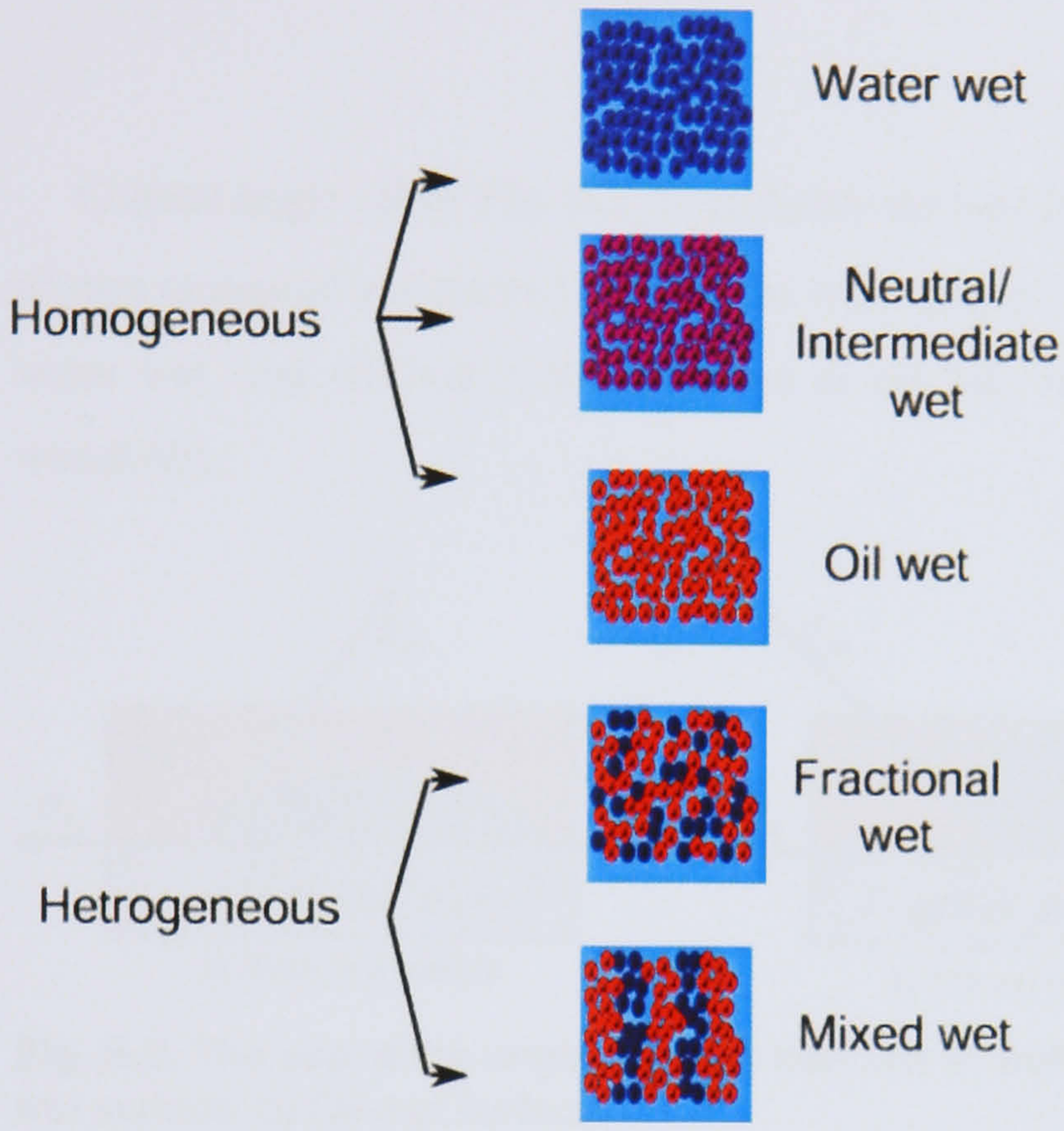

Fig. B.1. Diagram showing the types of wettability commonly encountered within reservoir rocks (based on Robin, pers.com.).

There appear to be a large divergence of opinion regarding the wetting behaviour of petroleum-bearing rocks. For example, most petroleum geologists tend to view siliciclastic rocks as being strongly oil-wet (*e.g.* BjØrkum *et al.*, 1993; BjØrkum *et al.*, 1998). On the other hand, many experts from disciplines such as petroleum engineering, special core analysis and petrophysics are increasingly suggesting that fractional- or mixed-wettability conditions characterise many oil-bearing siliciclastic rocks (*e.g.* Salathiel, 1973). An implication of the same being true of seals is that they would be able to retain less of an oil column by membrane sealing than is often assumed based on the premise that seals are strongly water wetting.

B.3. The physics of wettability

Research into the properties of colloids has provided a significant understanding of the forces between two charged solid surfaces (*e.g.* Derjaguin *et al.*, 1987; Derjaguin, 1989). This research has been reviewed and applied to the wettability of the crud oil-brine rock system by authors such as Hirasaki (1991). A useful conceptual view of wettability that is applicable to the crud oil-brine rock system is to consider the stability of a thin wetting film separating a non-wetting phase from mineral surface (**Fig. B.2**)

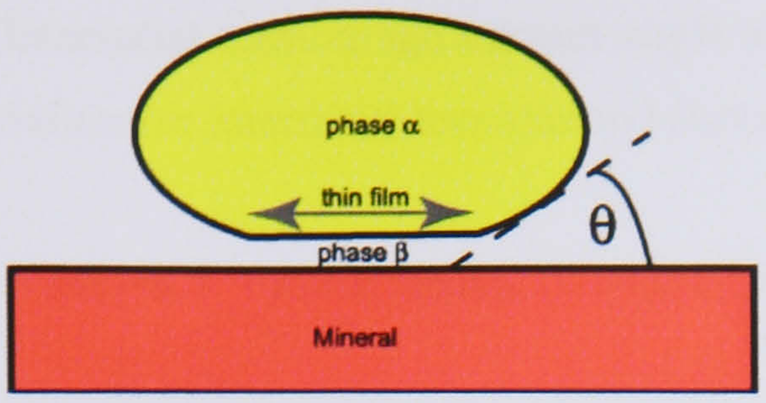

Fig. B.2. Conceptual model of a non-wetting phase (phase α) being separated from the mineral surface by a thin film of a wetting phase (phase β). The contact angle, θ, is the angle which the meniscuc makes when extrapolated back to the mineral surface. (adopted from Basu and Sharma, 1996).

Contact angle (θ in **Fig. B.2**) is probably the best indicator of wettability. Contact angles are always measured and quoted through the water phase. A contact angle of $0^{o}<\theta<75^{o}$ is treated as water wet, and $105^{o}<\theta<180^{o}$ is treated as oil wet; intermediate values are treated as neutral wettability.

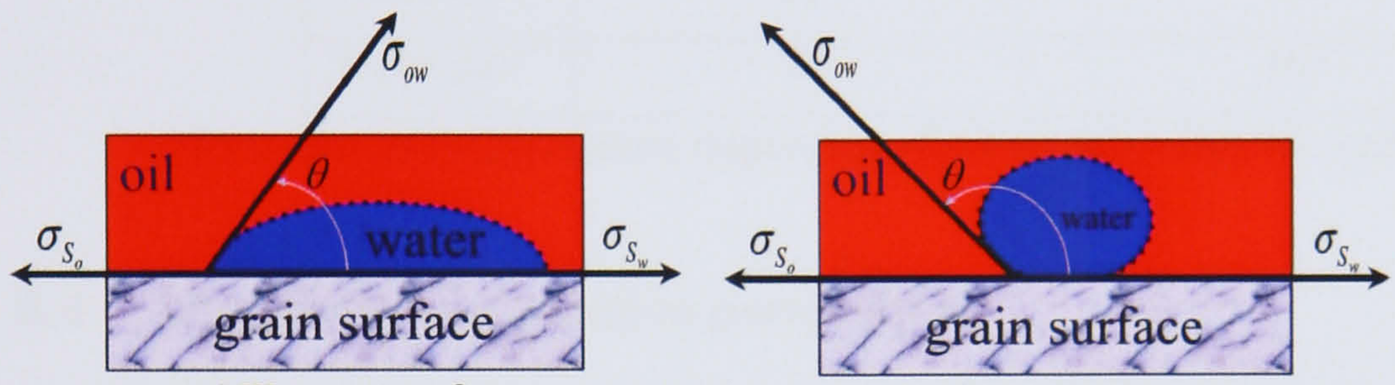

Fig. B.3. The use of the angle θ as an indicator of wettability in an oil/water system. a) Water-wet surface. b) Oil-wet surface.

A drop of water placed on water-wet grain surface behaves differently from a drop of water placed on an oil-wet grain surface. Water-wet surfaces tend to attract the water drop thus making it cover a maximum area of its surface. On the other hand, oil-wet surfaces tend to repel the water drop. In this case, the contact surface area between the water drop and the grain surface is much smaller. This behaviour is illustrated in **Fig. B.3**.

Wettability can be inferred from the contact angle, θ, the angle measured through the aqueous phase and the interfacial tension, σ_{ow}, as shown in **Fig. B.3**. The interfacial tension is measured in laboratory by measuring the following quantities:

- σ_{S_o} = The tension caused by oil
- σ_{S_w} = The tension caused by water
- θ = The contact angle measured from the wetting phase, water

From **Fig. B.3**, the following relation can easily be seen:

$$\sigma_{ow} = \frac{\sigma_{S_o} - \sigma_{S_w}}{\cos(\theta)} \qquad \textbf{B.1}$$

Interfacial tension and contact angle are measured in the laboratory. **Table-B.1** shows typical values for interfacial tensions and contact angles for different systems.

Table-B.1. Typical values for interfacial tensions and contact angles for different systems. After Smith *et al.* (1999).

System	Contact angle (degree)	Interfacial tension (dyne/cm)
Laboratory		
Air-water	0	72
Oil-water	30	48
Air-mercury	140	480
Air-oil	0	24
Reservoir		
Water-oil	30	30
Water-gas	0	50*

*Pressure and temperature dependent. Reasonable value to depth of 5000 ft.

B.4 Wettability and relative permeability

Wetting fluids preferentially occupy the small pore throats in a rock; while non-wetting fluids occupy the large pore throats, thus hinder the movement of the wetting phase during displacement. To understand the concept of wettability and its effects on relative permeability, lets examine the nature of displacement processes that occur in both water and oil wet rocks. **Fig. B.4** shows section of a water-wet rock with pore spaces. The rock is initially saturated with water. If the capillary entry pressure is exceeded, oil invades and displaces water, primary-drainage cycle, to fill the large pore spaces first while water stays in the small pore spaces. The amount of water that cannot be displaced by oil is termed irreducible, or interstitial water saturation, S_{wirr}. This amount fills the small pores and forms a thin film over the rock grains. At this saturation, oil has more freedom to move than water, since it covers the bigger pore spaces, and therefore has high relative permeability, k_{ro}, see **Fig. B.4**.

When the cycle is reversed for the same system to an imbibition cycle, increasing wetting phase saturation, it is impossible to return to the original situation, and the original relative permeability curves cannot be recreated. This phenomenon is termed 'hysteresis' which is also apparent in capillary pressure curves (Anderson, 1995). At start of imbibition, water imbibes along connected films and fills the small pore spaces first. As water saturation increases, water films at pore throats become unstable, causing 'snap off'. At end of imbibition, oil is trapped as isolated blobs in large pores. The isolated amount of oil is termed residual oil saturation, S_{or}. In an oil-water system, the water saturation at this point is given by $1 - S_{or}$. Because these blobs of

oil occupy the large pores, they hinder the movement of water forcing it to have low relative permeability, k_{rw}, at $S_w = 1 - S_{or}$, see **Fig. B.4**.

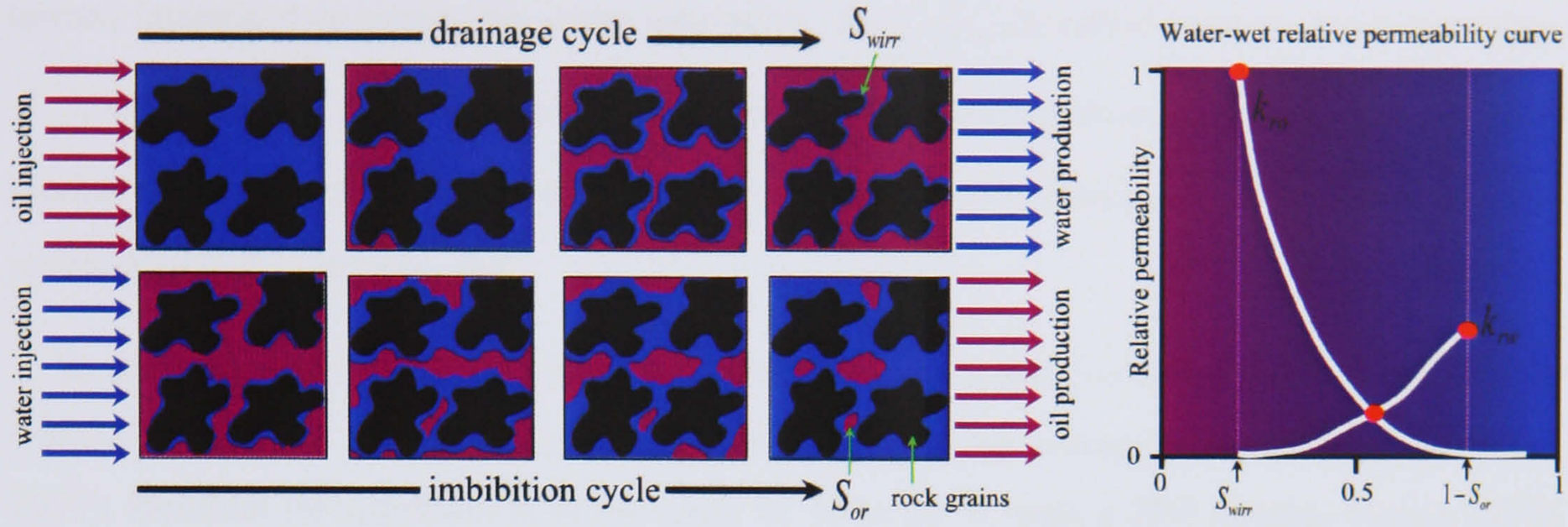

Fig. B.4. **Left**: The gradual processes for the drainage cycle (top left) and imbibition cycle (bottom left) in an immiscible oil-water system. **Right**: The corresponding relative permeability curve for this water-wet system. The horizontal axis represents the increasing water saturation. Theses illustrations are to simplify the general concept of wettability effects on trapped oil and water and do not represent the exact processes that might occur in such systems.

For the case of oil-wet rock, the process is illustrated in **Fig. B.5** for the imbibition cycle. The process starts with a fully oil-saturation system. As the capillary entry pressure (**Chapter 1, 3**) is exceeded, water starts to invade oil but unlike the case in water-wet rocks, it starts to fill the large pore spaces first. As water saturation increases, some oil cannot be swept by the water and it remains trapped in the small pore spaces of the rock forming a thin coat around the rock grains. The remaining unswept oil is termed residual oil saturation, S_{or}. At this saturation, water moves very freely along the centres of large pores and therefore has high relative permeability, k_{rw}, see **Fig. B.5**.

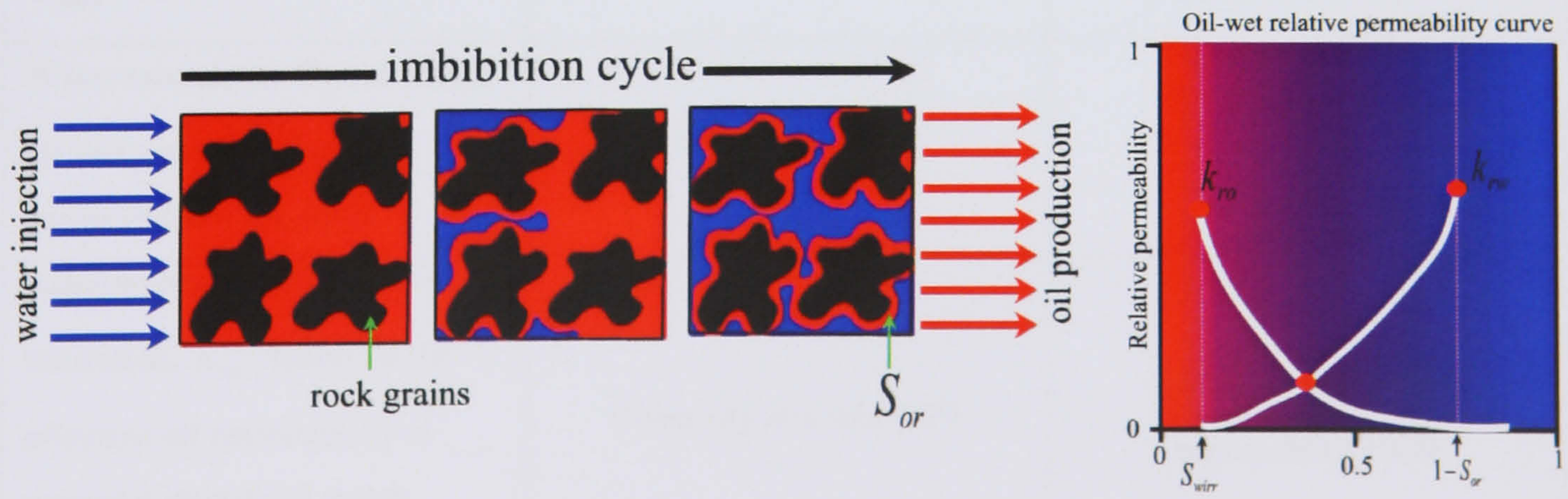

Fig. B.5. **Left**: The gradual processes for the imbibition cycle in an immiscible oil-water system. **Right**: The corresponding relative permeability curve for this oil-wet system. The horizontal axis represents the increasing water saturation. Theses illustrations are to simplify the general concept of wettability effects on trapped oil and water and do not represent the exact processes that might occur in such systems.

When the process is reversed by injecting oil to sweep the water, oil moves to the small pore spaces first and the oil coat around the rock grains grows bigger and bigger. As more oil is injected, water starts to form discrete droplets in the centre of the large pores. These droplets are termed interstitial or irreducible water saturation, S_{wirr}. S_{wirr} is called connate water saturation, S_{wc}, when talking about the same process under reservoir conditions. At S_{wc} water droplets hinder oil movements through the centre of the pores thus causing it to have low relative permeability, k_{ro}, see **Fig. B.5**.

In the preferentially oil-wet case, the irreducible water saturation range is lower than for the water-wet case and is usually between 5 and 30%, with the average being about 15% (Craig 1971). Residual oil saturation is in the range of 10 to 50 %, with a 25% average (Craig 1971), which can be much higher than that encountered in the water-wet systems. Thus, oil-wet reservoirs mean bad news for reservoir engineering when considering the ultimate recovery efficiency with simple miscible flooding techniques. End point ranges and averages are just reversed from the water-wet case. So, although water moves with greater ease in an oil-wet system, the initial oil saturation is generally higher than in a water-wet system. Craig suggested the following rules of thumb, summarised in **Table-B.2**, that could be used to separate the relative permeability behaviour of strongly water-wet and strongly oil-wet rocks based on the shape of their relative permeability curves.

Table-B.2: Craig's rules of thumb for determining wettability, see **Fig. B.3** and **Fig. B.4** for relative permeability curves.

	Water-wet	Oil-wet
Interstitial water saturation S_{wirr}	Usually 20-25%	Generally less than 15% Frequently less than 10%
Water saturation, S_w, at which oil and water relative permeabilities are equal	Greater than 50%	Less than 50%
Relative permeability to water saturation, k_{rw}, based on the effective oil permeability at reservoir interstitial water saturation	Generally less than 30%	Greater than 50% and approaching 100%

Some other general rules for determining wettability were also suggested by Anderson (1986d) as follows:

- In strongly wetted systems, the wetting-phase relative permeability is primary a function of its own saturation; *i.e.* the hysteresis between the wetting phase drainage and imbibition relative permeabilities is much smaller than the non-wetting phase hysteresis.
- In general, at a given saturation, the relative permeability of a fluid is higher when it is the non-wetting phase.

The discussion on wettability is usually restricted to oil and water phases, as it is generally accepted that gas is always a non-wetting phase with regards to both oil and water. The organic background of rocks can be used to classify wettability, for example, a high percentage of carbonates are oil-wet than are sandstones. Perhaps the reason for this stems from the fact that both oil and carbonate rock have organic background

B.5. Wettability alteration

Current theories usually have water in the formation first. Then, at a later time, oil migrates to the formation. Therefore, to make the formation oil-wet, the oil must somehow get the last layer of water, thin film, off of the rock surface. How could this be accomplished? Another theory targets the composition of the oil. Higher API gravity (light) oils will usually tend to be water-wet; whereas, very heavy (low gravity) oils will more often be contained in oil-wet reservoirs. Rock wettability alteration is an ongoing research and has been discussed with deep science in many publications (*e.g.* Anderson, 1986a; Buckley, 1995; Buckley *et al.*, 1996; Kaminsky and Radke, 1997; Yen *et al.*, 1997; Van Duin an Larter, 2001b; Buckley and Wang, 2002). The idea that wettability alteration actually occurs after breakdown of the water film is commonly accepted. Two mechanisms have been discussed that lead to the breakdown of the thin film; it should be emphasized that those two mechanisms are not mutually exclusive and both may contribute to the instability of water films. In the first, a combination of brine and oil chemistry leads to opposite charges developing on the oil/water interface, leading to an attraction between the two interfaces. In the second, the capillary pressure is sufficient to overcome repulsive electrostatic and structural forces leading to a breakdown of the thin film that separates the mineral and oil.

Appendix C

Local grid refinement (LGR) stability tests

C.1. Introduction

Local grid refinements (LGRs) are sub cells within global cells. The LGRs are very useful because they can be added without the need to rebuild simulation models. They are commonly used to conduct more detailed studies in critical regions, such as near-well regions and transition zones. In this study LGRs are used to add faults between global cells. These LGRs can be assigned to independent rock and fluid properties from their parent cells. LGRs can be solved either in-place with the global cells, *i.e.* local timestepping is not used and the local grid is solved fully implicitly with the global grid, or free from the global cells, *i.e.* using local timestepping. This study showed that solving LGRs in place gives more accurate results and stability but this method consumes more CPU time than solving LGRs independently. In this study, LGRs are always solved in-place.

Although they are very useful tool, LGRs require special treatment and the must be used carefully to insure accuracy and stability of a simulation output. Instability in convergence can arise when using LGRs to represent features with large rock and fluid property contrasts compared to their neighbouring cells. For example, when placing a fault with a very small permeability (*e.g.* 0.001 mD) and small thickness (*e.g.* 10 cm) adjacent to a host rock cell with relatively large permeability (*e.g.* 1 D) and a typical size (*e.g.* 50 m wide), any simulator is likely to encounter numerical difficulty, independent of the CPU power of the computer used. Convergence of such problems can be achieved by using extremely small timesteps, which may result in lengthy simulator run-times. Manzocchi *et al.* (2002) stated that these run-times can be shortened and numerical artefacts reduced, if the faults, and the grid blocks adjacent to the faults, are more finely discretized. In this section, LGR stability is tested when placing low

permeability faults in one- and two-phase simulation models. The degree of refinement is analysed and compared to some available analytical solutions.

C.2. Single-phase test

To test that the LGR scheme used was sufficient to prevent numerical dispersion; we compared the numerical results of a simulated drawdown test in a well situated close to the fault with the analytical solution provided by Yaxley (1987). In this test, the pressure output from models with different LGR schemes was compared to the analytical solution. The analytical solution for pressure draw-down in an active well near to a partially sealing fault was given by **equation - C.1** (from Yaxley, 1987):

$$P_{DW} = -\frac{Ei\left(-\frac{r_{dw}^{\ 2}}{4t_{DA}}\right)}{2} - \frac{Ei\left(-\frac{1}{t_{DA}}\right)}{2} - \sqrt{\pi}\alpha_A \int_0^{t_{DA}} \frac{e^{(4z\alpha_A^2+4\alpha_A)} erfc\left(2\alpha_A\sqrt{z}+\frac{1}{\sqrt{z}}\right)}{\sqrt{z}} dz \qquad \textbf{C.1}$$

The analytical solution for pressure build up in an active well near to a partially sealing fault was given by Yaxley as in **equation-C.1**:

$$P_{DS} = P_{DW}(t_{DA_p} + \Delta t_{DA}) - P_{DW}(\Delta t_{DA}) \qquad \textbf{C.2}$$

where:

P_{DW} is well bore pressure during draw-down test (psi),

P_{DS} is well bore pressure following shut-in (psi),

r_{dw} is well bore radius/distance to fault,

Δt is shut-in time (hour),

t_{DA_p} is draw-down time (hour),

α_A is transmissibility ratio, $\alpha_A = \dfrac{k_f}{t_f \dfrac{k}{d}}$ **C.3**

k_f is fault permeability (mD),

k is undeformed reservoir permeability (mD),

d is distance to fault (ft),

t_f is fault thickness (ft),

t_{DA} is dimensionless time, $t_{DA} = \dfrac{0.000264kt}{\phi\mu cd^2}$ **C.4**

ϕ is rock porosity (fraction),

c is rock compressibility (1/psi),

μ is phase viscosity (cP),

t is time (hour) (either $t_{DA_P}, \Delta t, t_{DA_P} + \Delta t$).

The dimensionless time t_{DA} and the pressures, P_{DW} and P_{DS} are converted to the real units when normalised by a rate dependent value (σ):

$$\sigma = \frac{0.708\times10^{-2}\,kh}{q\mu B} \qquad \textbf{C.5}$$

where

h is reservoir thickness (ft),

q is phase production rate (stb/d),

B is phase formation volume factor (rb/stb).

Equations **C.1** and **C.2** were solved for the parameters shown in **Table-C.1**:

Table-C.1: Reservoir Fluid and Rock Data for solving equations **C.1** and **C.2**.

Parameter (Field units)		Value
d	Distance to fault (ft)	249.5
c	Rock compressibility (1/psi)	17E-06
ϕ	Rock porosity (fraction)	0.18
r_w	Well bore radius (ft)	0.5
t_{DA_P}	Draw-down time (hour)	36
μ	Phase (oil) viscosity (cP)	0.9
B	Phase (oil) formation volume factor (rb/stb)	1.2
q	Phase (oil) production rate (stb/d)	10500
p_i	Initial pressure of reservoir (psi)	4500
h	Reservoir thickness (ft)	50
t_f	Fault thickness (ft)	1
k/k_f	Undeformed reservoir /Fault permeability ratio	1E4

Equation-**C.1** was solved for every 0.225 hour. The total number of time steps for a 36-hour draw-down test is given by:

Number of Solutions (Steps) =36/0.225 = 160 P_{DW} solutions.

To compare the result with the **Eclipse 100™** output numerical simulation, we constructed a simple 2D model using the parameters in **Table-C.1**. The partially sealing fault is represented with different number of LGRs so we can assign independent properties and reduce the

numerical problems that might appear when solving the flow equations numerically. The results achieved a near-perfect match when 120 LGR cells were used for the two parent grid blocks in the middle of the faulted model (see **Fig. C.1**).

Using enough number of LGRs is important to insure stable and reliable solution in simulation models with high permeability contrast between fault and host rock. **Fig. C.2** shows that using 120 LGRs in the discrete representation gives a perfect match with the analytical solutions for equations **C.1** and **C.2** even for a high host/fault permeability contrast (k_h / k_f).

Note that in the absence of two-phase rock properties the transmissibility multiplier representation (*TM*) (**Chapter 2**) is always identical to the discrete representation. We will, however, show that this is not the case in the two-phase test (**§ C.3**).

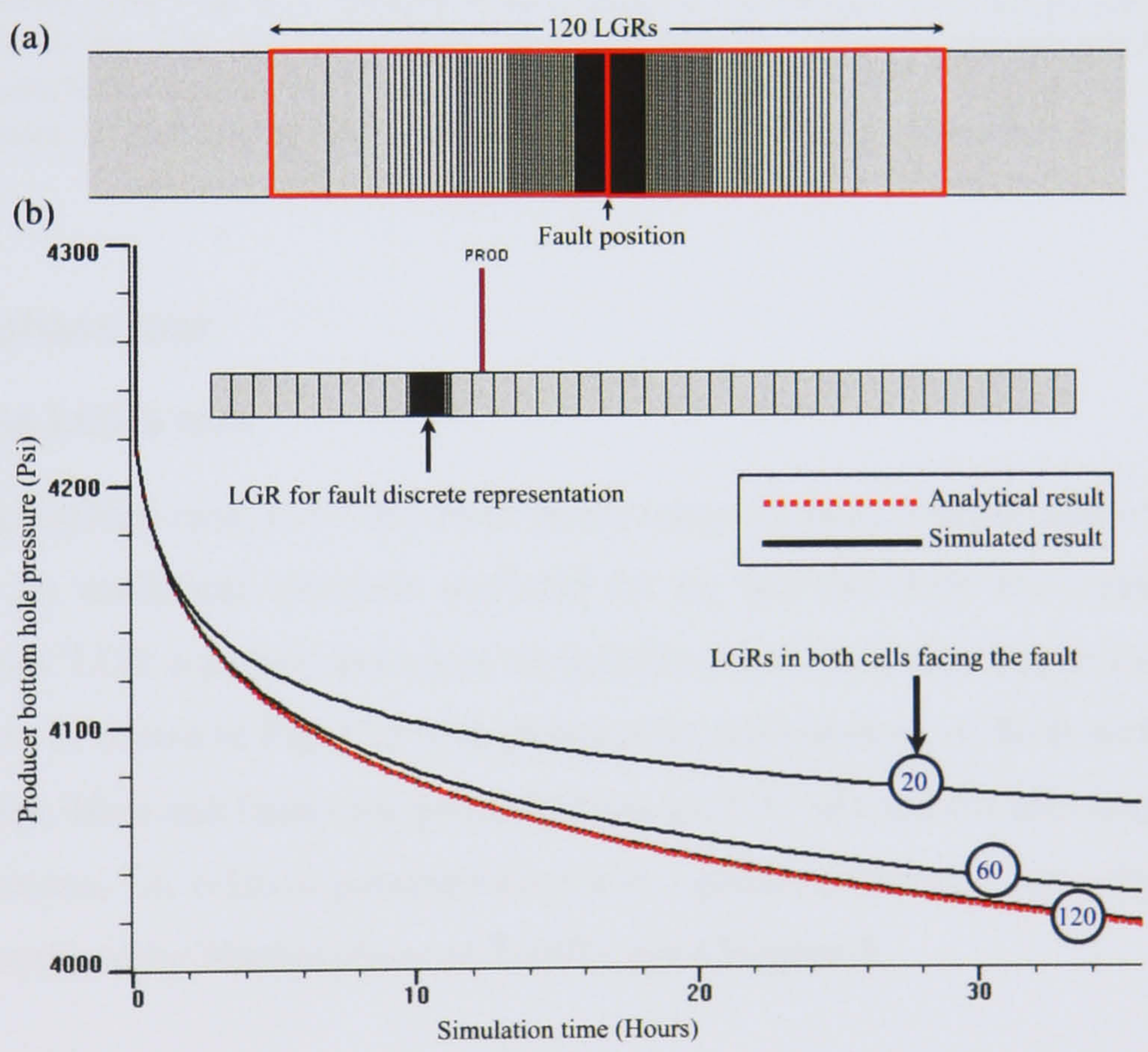

Fig. C.1. A model providing justification for the choice of the number of LGRs. **(a)** LGR cells are added to the cells adjacent to the fault faces. LGR cells are added in a way, which ensures a gradual transition in the cell pore volumes from the fault cells to the host cells. **(b)** Analytical solutions for a single producer bottom-hole pressure for a draw-down test (Yaxley, 1987) were compared against the same output from a simple 2D reservoir simulation for a single fault using different LGR schemes. The solid lines represent results from different LGR schemes and the doted line is the analytical solution.

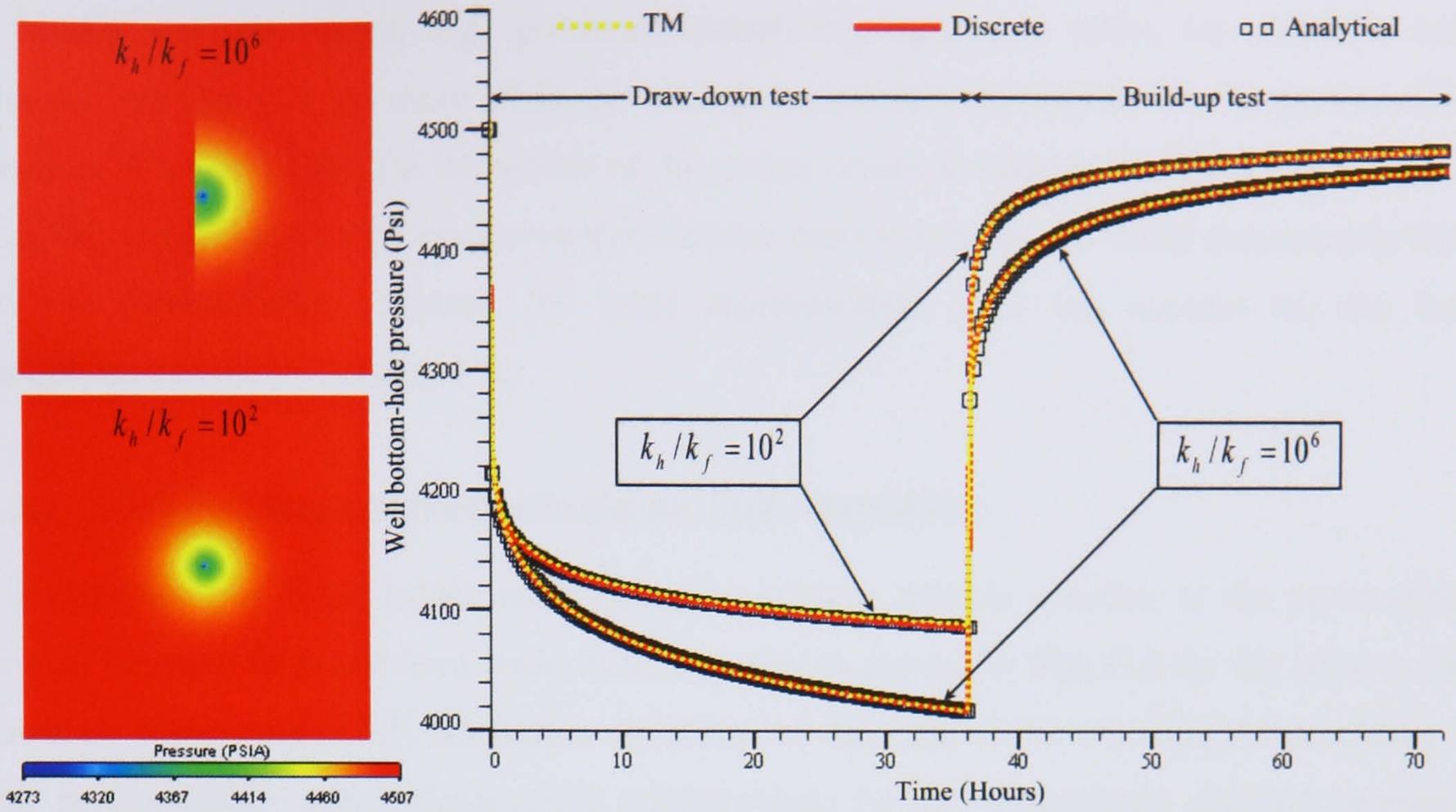

Fig. C.2. Producer, see **Fig. C.1**, bottom-hole pressure behaviour for a single-phase draw-down and build-up tests for *TM* representation (see **Chapter 2**), discrete representation (using 120 LGRs) and analytical results (solution provided by Yaxley, 1987). Figures on the left show reservoir pressure snapshots at end of draw-down test for different permeability contrasts.

C.3. Two-phase test

C.3.1. Simple LGRs test

Unlike the single-phase case, two- and multi-phase cases are more complicated to handle. In this test, there are no analytical solutions available for us, and therefore we compare the results between different LGR schemes and adopt the scheme when the model output ceases to change. Model geometry is shown in **Fig. C.3** with global cells, red boarders, of 50 ft wide, and a central fault of 1 ft thick. Host and fault rock permeabilities are 500 mD and 0.1 mD respectively. Rock saturation functions, *i.e.* relative permeabilities and capillary pressures, were derived using the methodology outlined by Manzocchi *et al.* (2002), see **Chapter 3**.

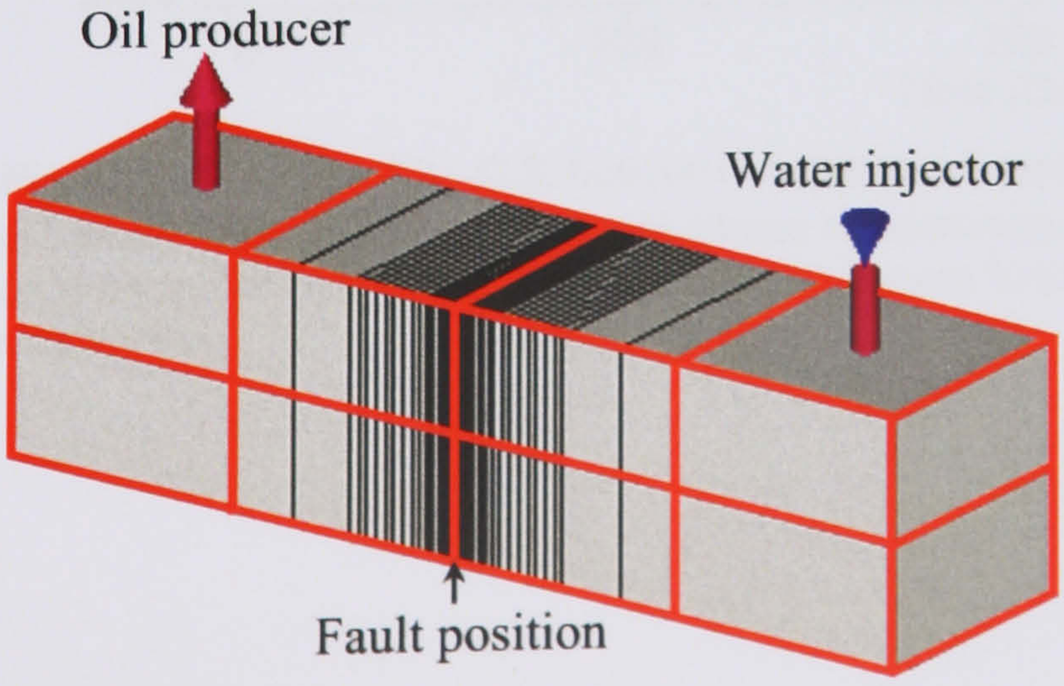

Fig. C.3. Model geometry for a two-phase test on LGR stabilities. LGRs are added to both cells juxtaposing the fault to ensure smooth transition in pore volume, thus reducing numerical dispersion when solving for model outputs numerically.

Model pressure output, *e.g.* producer bottom-hole pressure, varies for different LGR schemes, see **Fig. C.4**. As more LGRs are added, more details are captured in the pressure-time function. After 30 LGRs, the behaviour of the output ceases to change. Unlike the single-phase case, this two-phase simulation shows that discrete representations can differ dramatically from the *TM* representation, because the latter representation does not account for the fault multiphase behaviour (**Chapter 3**).

C.3.2. Permeability contrast effects on LGR stabilities

It is expected that more LGRs are required to achieve reliable solution as the permeability contrast between fault and host rocks increases, this is proved in **Fig. C.5** for the same model described above in **§ C.3.1**. Saturation functions of the fault rocks are changed according to their permeabilities using Manzocchi's relationships. As the permeability contrast increases, more LGRs are required to stabilise the behaviour of the pressure function of the model. In this case, field average pressure is used for the test instead of the producer bottom-hole pressure, which quickly goes below its minimum limit, 1000 psia, for low-permeability faults.

Fig. C.4. Producer, **Fig. C.3**, bottom-hole pressure function behaviour for different LGR schemes. TM , which is the single-phase representation for fault sealing capacity, does not capture the complicated behaviour of the pressure function as the high-resolution discrete models do.

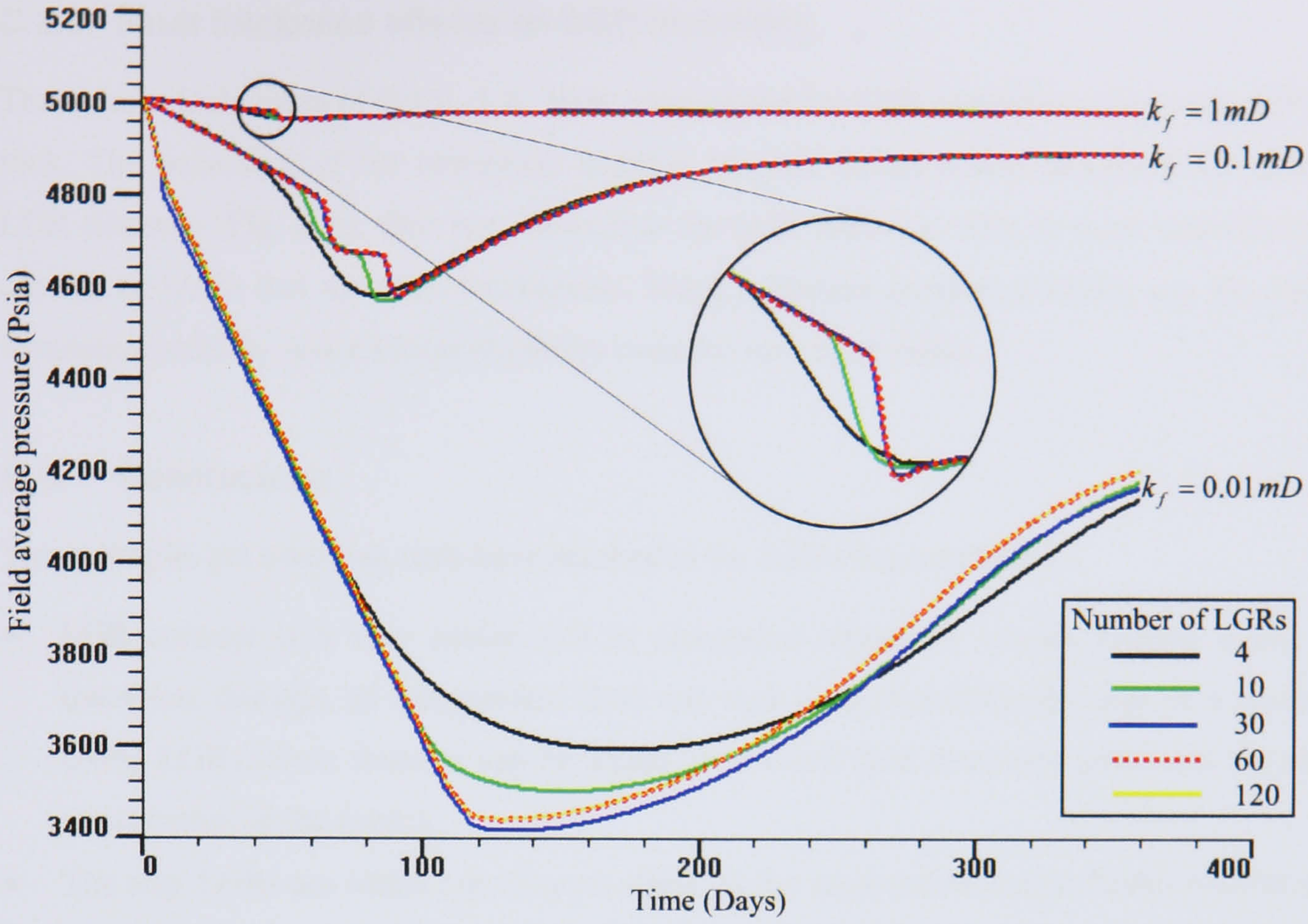

Fig. C.5. Permeability contrast effects on LGR stabilities for the model described in **§ C.3.1**.

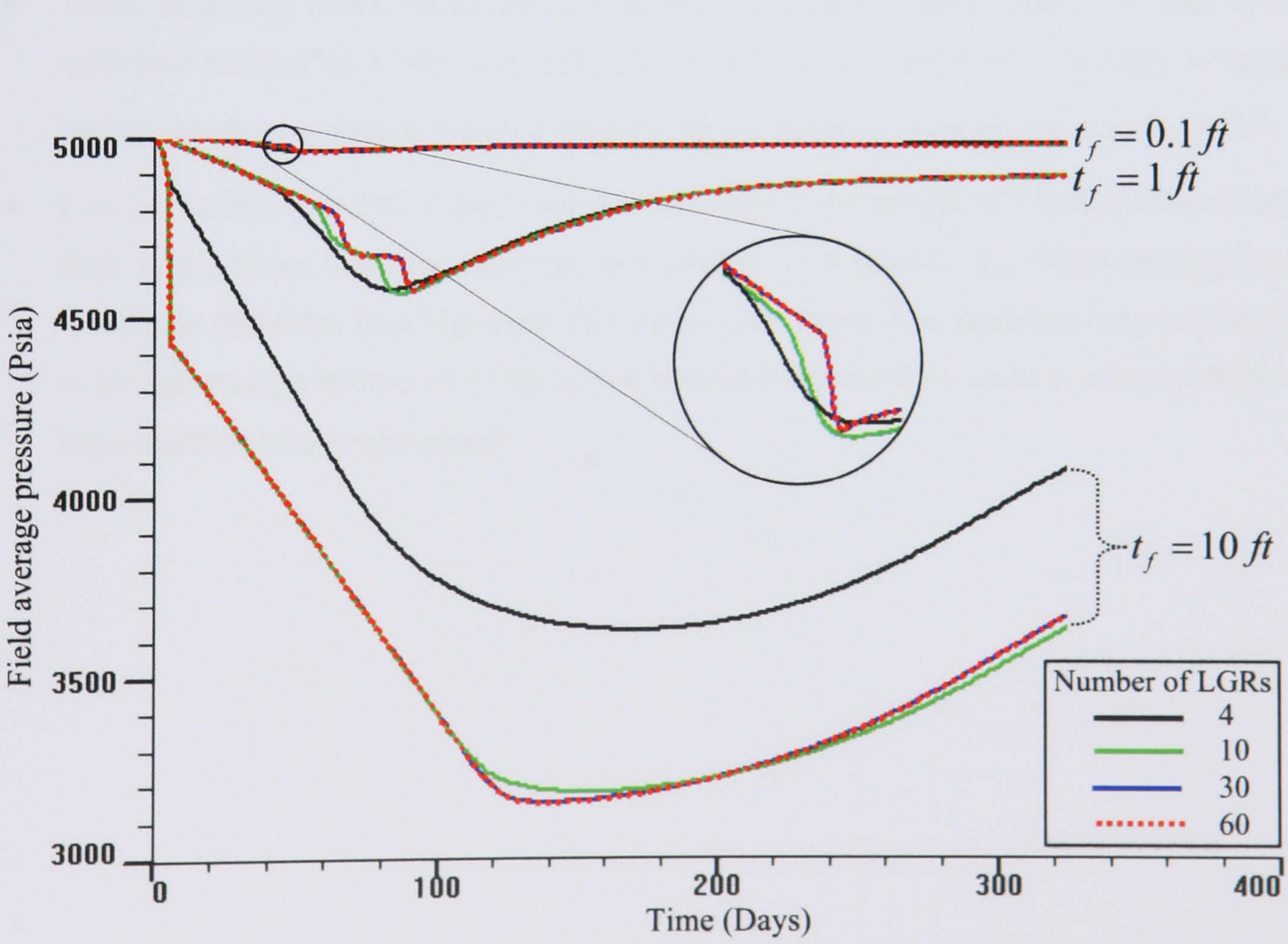

Fig. C.6. Fault thickness effects on LGR stabilities the model described in **§ C.3.1**.

C.3.3. Fault thickness effects on LGR stabilities

Three fault thicknesses of 0.1 ft, 1 ft, 10 ft, were tested for LGR stabilities using a 0.1 mD fault rock. The behaviour of the two-phase average pressure function was compared for different LGR schemes (**Fig. C.6**). This test shows that the thick fault, *i.e.* 10 ft, is more sensitive to the number of LGRs that the other thicknesses. Using sufficient number of LGRs, *e.g.* 60, ensures simulation stability and solution reliability even for very thick faults.

C.4. Conclusions

These simple, yet essential, tests have resulted in the following conclusions:

- LGR concept is a very useful tool in simulation models to specify critical zones, *e.g.* transition, damage, of independent fluid and rock properties from the reset of a reservoir. Using LGRs, these features can be added even when their discovery postpones the initial construction of the model.
- The way LGRs are added can have an effect on the same model output LGRs must be used carefully to ensure smooth transition in pore volume thus avoiding possible numerical dispersion.
- When including faults, single-phase simulation tests have shown that it is vital to use sufficient number of LGRs, *e.g.* 120, added to both cells adjacent to a fault, to ensure perfect match to analytical results even for high permeability contrast, *e.g.* $k_h / k_f = 10^6$.
- Low-permeability and thick faults are very sensitive to the number of LGRs used to define their zones. These, however, converge and stabilise much quicker, *e.g.* when jumping from 4 LGRs to 10 LGRs, than high-permeability and thin faults. It is, therefore, very important to include enough number of LGRs in low-permeability and thick faults to ensure reliable representation of a model output.

References

References

Adamson, A.W. (1982). Physical Chemistry of Surfaces, fourth edition. John Wiley and Sons, New York City.

Albert, F.G. and Corre, B. (1991). Heterogeneity in Complex Turbiditic Reservoir: Impact on Field Development. *Society of Petroleum Engineering,* SPE 22902, presented at the *SPE Annual Technical Conference Exhibition*, Dallas, October.

Al-Busafi, B., Fisher, Q.J., and Harris, S.D. (2005) The importance of incorporating the multiphase flow properties of fault rocks into production simulation models. *Marine and Petroleum Geology*, **22**, 365–374.

Allan, U.S. (1989). Model for hydrocarbon migration and entrapment within faulted structures. *American Association of Petroleum Geologists Bulletin*, **73**, 803–811.

Anderson, W.G. (1985). Wettability literature survey – Part 4: The effects of wettability on capillary pressure, *Society of Petroleum Engineering*, SPE 15271.

Anderson, W.G. (1986a). Wettability literature survey – Part 1: Rock/Oil/Brine interactions, and the effects of core handling on wettability. *Journal of Petroleum Technology* (Oct. 1986).

Anderson, W.G. (1986b). Wettability literature survey – Part 2: wettability measurement, *Society of Petroleum Engineering*, SPE 13933.

Anderson, W.G. (1986c). Wettability literature survey – Part 3: The effects of wettability on the electrical properties of porous media, *Society of Petroleum Engineering*, SPE 13934.

Anderson, W.G. (1986d). Wettability literature survey – Part 5: The effects of wettability on relative permeability, *Society of Petroleum Engineering*, SPE 16323.

Anderson, W.G. (1987). Wettability literature survey-part 4: effects of wettability on capillary pressure. *Journal of Petroleum Technology*, 1283–1300.

Antonellini, A. and Aydin, A. (1994). Effect of faulting on fluid flow in porous sandstones: petrophysical properties. *American Association of Petroleum Geologists Bulletin*, **78**, 181–201.

Aziz, K. and Settari, A. (1979). Petroleum Reservoir Simulation. *Applied Science Publishers*, London, page 398.

Barker, J.W., and Fayers, F.J. (1991). Transport Coefficients for Compositional Simulation with Course Grids in Heterogeneous Media. SPE 22591, presented at the *Society of Petroleum Engineering Annual Technical Conference Exhibition*, Dallas, October and *SPE Advanced Technology Series*, 2 (2), April, 1994.

Barker, J.W. and Thibeau, S. (1996). A critical review of the use of pseudo-relative permeabilities for upscaling. *Journal of Petroleum Technology*, SPE 35491.

Barker, J.W. and Dupouy, P. (1999). An analysis of dynamic pseudo-relative permeability methods for oil–water flows. *Petroleum Geoscience*, **5**, 385–394.

Basu, S. and Sharma, M.M. (1996) Measurement of Critical Disjoining Pressure for Dewetting of Solid Surfaces. *Journal of Colloid and Interface Science*, **181**, 443–455.

Batzle, M., and Wang, Z. (1992). Seismic properties of pore fluids. *Geophys.*, **57**, 1396–1408.

Bentley, M.R. and Barry, J.J. (1991). Representation of Fault Sealing in a Reservoir Simulation: Cormorant Block IV, UK North Sea. *Society of Petroleum Engineers*, SPE 2667.

Bentley, M.R. and Barry, J.J. (1992). Representation of fault sealing in a reservoir simulation: Cormorant block IV, UK North Sea. *Society of Petroleum Engineers*, SPE 22667.

Berg, R.R. (1975). Capillary entry pressure in stratigraphic traps. *American Association of Petroleum Geologists Bulletin*, **78**, 355–377.

Biot, M.A. (1956). Theory of propagation of elastic waves in a fluid saturated porous media. J. Appl. *Phys.*, **33**, 1482–1498.

Bjørkum, P.A., Walderhaug, O, and Aase, N.E., (1993). A model for the effect of illitisation on porosity and quartz cementation in sandstones. *Journal of Sedimentary Research*, **A63**, 1089–1091.

Bjørkum, P.A., Walderhaug, O. and Nadeau, P.H. (1996). Physical constraints on hydrocarbon leakage and trapping revisited. *Petroleum Geoscience*, **4**, 237–239.

Bjørkum, P.A., Walderhaug, O., and Nadeau, P.H., (1998). Physical constraints on hydrocarbon leakage and trapping revisited. *Petroleum Geoscience*, **4**, 237239.

Bjørlykke, K. and Egeberg, P.K. (1993). Quartz cementation in sedimentary basins. *American Association of Petroleum Geologists Bulletin*, **77**, 1538–1548.

Bjørlykke, K. (1998). Clay mineral diagenesis in sedimentary basins; a key to the prediction of rock properties; examples from the North Sea Basin. *Clay Minerals*, **33**, 15–34.

Bouvier, J.D., Kaars-Sijpesteigen, C.H., Kluesner, D.F., Onyejekwe, C.C. and Vander Pal, R.C. (1989). Three-dimensional seismic interpretation and fault sealing investigations. Nun River Field, Nigeria. *American Association of Petroleum Geologists Bulletin*, **73**, 1397–1414.

Brace, W.F., Walsh J.B. and Frangos W.T. (1968). Permeability of granite under high pressure. *Journal of Geophys. Res.*, **73**, 2225 –2236.

Brie, A., Pampuri, F., Marsala, A.F. and Meazza, O. (1995). Shear sonic interpretation in gas-bearing sands. *Society of Petroleum Engineering* Annual Technical Conference and Exhibition, Dallas. SPE 30595.

Brown, A.R., Edwards, G.S. and Howard, R.E. (1987). Fault slicing- a new approach to the interpretation of fault detail: *Geophysics*, **52**, 1319–1327.

Brown, R.J.S., and Fatt, I., (1956). Measurements of fractional wettability of oilfield rocks by the nuclear magnetic relaxation method. *Trans AIME*, **207**, 262–264.

Buckley, J.S., (1987). Influence of electrical surface charges on the wetting properties of crude oils, *Society of Petroleum Engineering*, SPE 16964.

Buckley, J.S. (1995). Asphaltene precipitation and crude oil wetting, *Society of Petroleum Engineering*, advanced technology series, **3**, 53–59.

Buckley, J.S., Liu, Y., Xie, X., Morrow, N.R., (1996). Asphaltenes and crude oil-wetting – the effect of oil composition, *Society of Petroleum Engineering*, SPE 35366.

Buckley, J.S. and Wang, J. (2002). Crude oil and asphaltene characterisation for predicting of wetting alteration. *Journal of Petroleum Science and Engineering*, **33**, 195–202

Bunn, G.F. and Yaxley, L.M. (1986). Design, implementation and interpretation of a 'three-dimensional well test' in the Cormorant field, North Sea. *Society of Petroleum Engineers*, SPE 15858.

Cadoret, T. (1993). Effect de la Saturation Eau/Gas sur les Propriétés Acoustiques des Roches. Ph.D dissertation, University of Paris, VII.

Cao, K. and Aziz, K. (1999). Evalution of pseudo functions. *Journal of Petroleum Technology*, SPE 54589.

Chan, A.W., Zoback' M.D., Finkbeiner, T. and Zinke, J. (2002). Production Induced Faulting and Fault Leakage in Normal Faulting Regions: Examples from the North Sea and Gulf of Mexico. *American Association of Petroleum Geologists*: pathways of hydrocarbon migration, faults as conduits or seals.

Christiansen, R. (2005). Capillary end effects and gas production from low permeability formations. Paper presented at the International Symposium of the *Society of Core Analysis*, Toronto, Canada, 21-15 August.

Christie, M.A., Mansfield, M., King, P.R., Barker, J.W. and Culverwell, I.D. (1995). A Renormalisation-Based Upscaling Technique for WAG Floods in Heterogeneous Reservoirs. *Society of Petroleum Engineering* SPE 29127, presented at the 13th Symposium on Reservoir Simulation, San Antonio, Texas, 12–15 February.

Christie, M.A. (1996). Upscaling for reservoir simulation. *Journal of Petroleum Technology*, **1**, 1004–1010.

Coll, C., Muggeridge, A.H., and Jing, X.D. (2000). Regional Upscaling: A New Method to Upscale Waterflooding in Heterogeneous Reservoirs for a Range of Capillary and Gravity Effects. *Society of Petroleum Engineering* SPE 74139 presented at the 2000 SPE/DOE *Improved Oil Recovery Symposium*, Tulsa, 3–5 April.

Cordazzo, J., Maliska, C.R. and da Silva, A.F.C. (2002). Interblock transmissibility calculation analysis for petroleum reservoir simulation. Presented in the 2nd Meeting on Reservoir Simulation, Buenos Aires, November 5-6.

Corey, A.T. The interrelation between gas and oil relative permeabilities. Producer Monthly (November 1954), 38–41.

Craig, F.F. (1971). The Reservoir Engineering Aspects of Waterflooding, *Society of Petroleum Engineers*, Monograph Series, **3**, Dallas, Texas, 1971.
Crawford, B.R. (1989). Experimental fault sealing: shear band permeability dependency on cataclastic fault gouge characteristics. In: Coward, M.P. Johnson, H. and Daltaban, T. (*eds.*) Structural Geology in Reservoir Characterisation. *Geological Society*, London, Special Publications, **127**, 27–44.
Dahlberg, E.C. (1982). Applied hydrodynamics in petroleum exploration. New York, Springer-Verlag, 161p.
Dale, M., Ekrann, S., Mykkeltveit, J. and Vernovsky, G. (1997). Effective relative permeabilities and capillary pressures for one-dimensional heterogeneous media. *Transport in porous media*, **26**, 229–260.
Darman, N.H., Pickup, G.E., and Sorbie, K.S. (2001). The Calculation of Pseudo Functions Using Potential Averaging Methods. SPE 66377 presented at the 2001 *Society of Petroleum Engineering Reservoir Simulation Symposium*, Houston, 11–14 February.
Darmen, N.H., Pickup, G.E. and Sorbie, K.S. (2002). A comparison of two-phase dynamic upscaling methods based on fluid potentials. *Computational Geosciences*, **6**, 5–27.
de Riz, L. and Muggeridge, A.H. (1997). Will Vertical Mixing Improve Oil Recovery for Gravity-Dominated Flows in Heterogeneous Reservoirs? *Society of Petroleum Engineering*, SPE 37996 presented at the 1997 *SPE Reservoir Simulation Symposium*, Dallas, 8–11 June.
Dennis, H., Baillie, J., Holt, T. and Wessel-Berg, D. (1998). Hydrodynamic activity and tilted oil-water contacts in the North Sea. *NPF* Conference. Haugesund. September 1998.
Deraguin, B.V., Churaev, N.V. and Muller, V.M. (1987). Surface forces, Consultants Bureau, New York City.
Deraguin, B.V. (1989). Theory of Stability of Colloids and Thin Films, Consultants Bureau, New York City.
Domenico, S.N. (1976). Effect of brine-gas mixture on velocity in an unconsolidated sand reservoir. *Geophys.*, **41**, 882–894.
Downey, M.W. (1984). Evaluating seals for hydrocarbon accumulations. *American Association of Petroleum Geologists Bulletin*, **68**, 1752–1763.
Ehrenberg, S.N., Aagaard, P., Wilson, M.J., Fraser, A.R., and Duthie, D.M.L. (1993). Depth-dependent transformation of kaolinite to dickite in sandstones of the Norwegian continental shelf. *Clay Minerals*, **28**, 325–352.
Evans, J., Hogg, A.J., Hopkins, M.S. and Howarth, J.R. (1994). Quantification of quartz cements using combined SEM, CL, and image-analysis. *Jurnal of Sedimentary research*, **64**, 334–338.
Evans, D., Graham, C., Armour, A. and Bathurst, P. (2003). The Millennium Atlas: Petroleum Geology of the Central and Northern North Sea. Published by the *Geological Society of London*.
Ewing, R.E. (1997). Aspects of upscaling in simulation of flow in porous media. *Adv Water Res*, **20**, 349–358.
Fanchi, J.R. (2003). Estimating geomechanical properties using an integrated flow model. *Society of Petroleum Engineering*, SPE 83730.
Farmer, R.T. and Hillier, A.P. (1991). The Barque Field, Blocks 48/13a, 18/14, UK North Sea. From Abbotts, I.L. (*ed.*), 1991, United Kingdom Oil and Gas Fields, 25 Years Commemorative Volume, *Geological Society Memoir*, **14**, 395–400.
Firoozabadi, A., Ramey, H.J. (1988). Surface tension of water-hydrocarbon systems at reservoir conditions: *Journal of Canadian Petroleum Technology*, **27**, 41–48.
Fisher, Q.J. and Knipe, R.J. (1998). Fault sealing processes in siliciclastic sediments. *In:* Jones, G., Fisher, Q.J. and Knipe, R.J. (*eds*) Faulting, Fault Sealing and Fluid Flow in Hydrocarbon Reservoirs. *Geological Society*, London, Special Publications, **147**, 117–134.
Fisher, Q.J., Casey, M., Clennell, M.B. and Knipe, R.J. (1999). Mechanical compaction of deeply buried sandstones. *Marine and Petroleum Geology*, **16**, 605–618.
Fisher, Q.J., Knipe, R.J. and Worden R. (2000). The microstructure of deformed and undeformed sandstones from the North Sea: its implications for the origin of quartz cement. *In*. Morad. S and Worden, R (*eds.*) Quartz cement: origin and effects on hydrocarbon reservoirs. *International Association of Sedimentology*, Special Publication.
Fisher, Q.J. and Knipe, R.J. (2001). The permeability of faults within siliciclastic petroleum reservoirs of the North Sea and Norwegian Continental Shelf. *Marine and Petroleum Geology*, **18**, 1063–1081.
Fisher, Q.J., Harris, S.D., McAllister, E., Knipe, R.J. and Bolton, A.J. (2001). Hydrocarbon flow across sealing faults: theoretical constraints. *Marine and Petroleum Geology*, **18**, 251–257.
Fisher, Q.J., Casy, M., Harris, S.D. and Knipe, R.J. (2003). Fluid-flow properties of faults in sandstone: The importance of temperature history. *Geological Society of America*, **31**, 965–968.
Fisher, Q.J. (2005). Recent advances in fault seal analysis as an aid to reservoir characterization and production simulation modelling. Presented at the 14th Europec Biennial Conference held in Madrid, Spain, 13-16 June 2005. *Society of Petroleum Engineers*, SPE 94460.

Foxford, K.A., Walsh, J.J., Watterson, J., Garden, I.R, Guscott, S.C. and Burley, S.D. (1998). Structure and Content of the Moab Fault Zone, Utah, USA, and its Implications for Fault Seal Prediction. *Geological Society Special Publications*, **147**, 87–103

Freeman, B., Yielding, G., Needsham, D.T. and Badley, M.E. (1998). Fault seal prediction : the Gouge Ratio method. Structural Geology in Reservoir Characterisation, *Geological Society Special Publication*, London, **127**, 19-25.

Freeman, S.R., Harris, S.D. and Knipe, R.J. (2005). Fault seal mapping–incorporating geometric and property uncertainty. *Geological Society of London*, Special Publication on Geological Modelling, in press.

Fristad, T., Groth, A., Yielding, G. and Freeman, B. (1997). Quantitative fault seal prediction - A case study from Osberg Syd. In: Møller-Pedersen, P. and Koestler, A.G. (eds) Hydrocarbon Seals: Importance for production and exploration. *Special Publication of the Norwegian Petroleum Society*, **7**, 107–124.

Fulljames, J.R., Zijerveld, L.J.J., Franssen, R.C.M., Ingram, G.M. and Richard, P.D. (1996). Fault seal processes, *in Norwegian Petroleum Society, eds.*, Hydrocarbon seals- importance for exploration and production (conference abstracts): Oslo, *Norwegian Petroleum Society*, p. 5.

Fulljames, J.R., Zijerveld, L.J.J. and Franssen, R.C.M.W. (1997). Fault seal process: systematic analysis of fault seals over geological and production time scales. *In:* Møller-Pedersen, P. and Koestler, A.G. (*eds*) Hydrocarbon Seals: Importance for exploration and production. *Norwegian Petroleum Society* Special Publications, **7**, 51–60.

Gassmann, F. (1951). Über die Elastizität poröser Medien. *Vier. Der Natur. Gesellschaft in Zürich*, **96**, 1–23

Geoquest (2003). *Eclipse 100 Version 2003 Technical Description*, Schlumberger.

Gibson, R.G. (1996). Sealing capacity of pressure-sealing fault zones in siliciclastic strata. Faulting, Fault Sealing and Fluid Flow in Hydrocarbon Reservoirs: Abstracts, University of Leeds, Sep. 23–25.

Gibson, R.G. (1998). Physical character and fluid flow properties of sandstone-derived fault zones. *In:* Coward, M.P., Daltaban, T.S. and Johnson, H. (*eds*) Structural Geology in Reservoir Characterisation. *Geological Society*, London, Special Publications, **127**, 83–98.

Giles, M. (1997). Diagenesis and its impact on rock properties: A Quantitative Perspective. Kluwer, pp 520.

Giles, M.R., Indrelid, S.L., Beynon, G.V. and Amthor, J. (2000). The origin of large scale quartz cementation: Evidence from large datasets and coupled heat-fluid-mass transport modelling. *In*: Quartz cementation in oil field sandstones (*eds.* by S. Morad and R. H. Worden), *Spec. Publs. Int. Ass. Sediment.*

Goldthorpe, W.H. and Chow, Y.S. (1985). Unconventional Modelling of Faulted Reservoirs: A Case Study. *Society of Petroleum Engineers*, SPE 13526.

Gontijo, R.C., Souza Cruz, C.E., Caldas, J.L.L., Arienti, L.M. and D'Avila, R.S.F. (2005). Structurally Controlled Sand-Rich Gravity Deposits of the Jubarte Oil Field (BRazil Deep Seds - Deep-Water Sedimentation on the Southeast Brazilian Margin Project). *American Association of Petroleum Geologists* Annual Convention (June 19–22, 2005).

Greaves, R.J. and Fulp, T.J. (1987). Three-dimentional seismic monitoring of an enhanced oil recovery process, *Geophysics*, **52**, 1175–1187.

Guzman, R.E., Giordano, D., Fayers, F.J., Godi, A. and Aziz, K. (1994). The Use of Dynamic Pseudo Functions in Reservoir Simulation. Presented at the 5th International Forum on Reservoir Simulation, Muscat, Oman, December 10–14.

Guzmán, R.E., Giordano, D., Fayers, F.J., Godi, A. and Aziz, K., (1999). Evaluation of dynamic pseudofunctions for reservoir simulation. *Journal of Petroleum Technology Journal* **4**, March, 37–46.

Hardman, R.F.P. and Booth, J.E. (1991). Structural interpretation of hydrocarbon traps sealed by basement normal fault block faults at stable flank of foredeep basins and at rift basins: *American Association of Petroleum Geologists Bulletin*, **73**, 813–840.

Harper, T.R. and Lundin, E.R. (1997). Fault seal analysis: reducing our dependence on empiricism. *In:* Møller-Pedersen, P. & Koestler, A.G. (*eds*) Hydrocarbon Seals: Importance for exploration and production. *Norwegian Petroleum Society* Special Publications, **7**, 149–164.

Harris, D., Yielding, G., Levine, P., Maxwell, G., Rose, P.T. and Nell, P. (2002). Using shale gouge ratio (SGR) to model faults as transmissibility barriers in reservoirs: an example from the Strathspey Field, North Sea. *Petroleum Geoscience*, **82**, 167–176.

Harris, S.D., McAllister, E., Knipe, R.J. and Odling, N.E., (2003). Predicting the three-dimensional population characteristics of fault zones: a study using stochastic models. *Journal of Structural Geology*, **25**, 1281–1299

Hassler, G.L. (1942). Method and apparatus for permeability measurements. *U.S. Patent*, **2**, 345–935.

Hawett, T.A. and Behrens, R.A. (1991). Scaling Laws in Reservoir Simulation and their Use in a Hybrid Finite-Difference /Streamtube Approach to Simulating the Effects of Permeability Heterogeneity. *In:*

Lake, L.W., Carroll, H.B., and Wesson, T.C., (eds) *Reservoir Characterisation II.* Academic Press, San Diego, 402–441.
Hegre, T.M., Dalen, V. and Henriquez, A. (1986). Generalised transmissibility for distorted grids in reservoir simulation. *Society of Petroleum Engineers*, SPE 15622 presented at the 61st Annual Technecnical Conference and Exhibition (New Orleans, Oct. 5–8).
Hildenbrand A., Schlömer, S. and Krooss, B.M. (2002). Gas breakthrough experiments on fine-grained sedimentary rocks. Geofluids, **2**, 3–23.
Hirasaki, G.J. (1991). Wettability: fundamentals and surface forces, *Society of Petroleum Engineering*, Formation Evaluation, **6**, 217–226.
Holditch, S.A. (1979). Factors affecting water blocking and gas flow from hydraulically fractured gas wells. *Journal of Petroleum Technology*, 1515-1524.
Houseknecht, D.W. (1987). Assessing the relative importance of compactional processes and cementation to the reduction of porosity in sandstones. *American Association of Petroleum Geologists Bulletin*, **71**, 633–642.
Hubbert, M.K. (1953). Entrapment of petroleum under hydrodynamic conditions: *American Association of Petroleum Geologists Bulletin*, **37**, 1954–2026.
Hull, J. (1988). Thickness–displacement relationships for deformation zones. *Journal of Structural Geology*, **10**, 431–435.
Ibrahim, M.A., Tek, M.R. and Katz, D.L. (1970). Threshold pressure in gas storage. *American Gas Association*, Arlington.
Jacks, H.H., Smith, O.J.E. and Mattax, C.C. (1973). The Modelling of Three-Dimensional Reservoir with a Two-Dimensional Reservoir Simulator– The Use of Dynamic Pseudo Functions. *Society of Petroleum Engineering Journal*, June, 175.
James, W.R., Fairchild, L.H., Nakayama, G.P., Hippler, S.J. and Vorlijk, P.J. (2004). Fault-seal analysis using a stochastic multifault approach. *American Association of Petroleum Geologists Bulletin*, **88**, 885–904.
Jev, B.I., Kaars-Sijpesteign, C.H., Peters, M.P.A.M, Watts, N.W. and Wilkie, J.T. (1993). Akaso Field, Nigeria: use of integrated 3-D seismic, fault-slicing, clay smearing and RFT pressure data on fault trapping and dynamic leakage: *American Association of Petroleum Geologists Bulletin*, **77**, 1389–1404.
John, W., Barker, W. and Philippe, D. (1996). An Analysis of Dynamic Pseudo-Relative Permeability Methods for Oil-Water Flows. Presented at *the 5th European Conference on the Mathematics of Oil Recovery*, Leoben, Australia, 3-6 September. *Petroleum Geoscience*, **5**, 385–394.
Kaminsky, R. and Radke, C.J. (1997). Asphaltenes, water films, and wettability reversal, *Society of Petroleum Engineering*, **2**, 485–493.
Katz A.J. and Thompson, A.H. (1986). Quantitative prediction of permeability in porous rock. *Phys. Rev.* **B34**, 8179–8181.
Katz A.J. and A.H. Thompson (1987). Prediction of rock electrical conductivity from mercury injection measurements. *J. Geophys. Res.* **92**, 599–607.
Klinkenberg, L.J. (1941). The permeability of porous media to liquids and gasses. Drilling and Production Practice, 200–213.
Knai, T.A. (1996). Faults impact on fluid flow in the Heidrun Field. In: Faulting, Fault sealing and Fluid Flow in Hydrocarbon Reservoirs, University of Leeds, Leeds, **75**. (Abstract).
Knai, T.A. and Knipe, R.J. (1998). The impact of faults on fluid flow in the Heidrun Field. In Jones, G., Fisher, Q.J. and Knipe, R.J. (*eds.*), Faulting, fault sealing and fluid flow in hydrocarbon reservoirs. *Geological Society* (London) Special Publications, **147**, 269–282.
Knipe, R.J. (1997). Juxtaposition and seal diagrams to help analyse fault seals in hydrocarbon reservoirs. *American Association of Petroleum Geologists Bulletin*, **81**, 187–195.
Knipe, R.J., Fisher, Q.J., Jones, G., Clennell, M.B., Farmer, A.B., Kidd, B., McAllister, E., Porter, J.R. and White, E.A. (1997). Fault Seal Prediction Methodologies, Applications and Successes. *In*: Moller-Pedersen, P., & Koestler A.G. (Eds.) Hydrocarbon seals - Importance for Exploration and Production. *NPF* Special Publication, **7**, 15–38.
Knipe, R.J., Freeman, S., Harris, S.D. and Davies, R.K. (2004). Structural uncertainty and scenario modelling for fault seal analysis. Proceedings of the *American Association of Petroleum Geologists* Annual Convention Abstracts, 18th–21st April, Dallas, Texas, **13**, paper A77.
Knott, S.D. (1994). Fault seal analysis in the North Sea: *American Association of Petroleum Geologists Bulletin*, **77**, 778–792.
Knott, S.D., Beach, A., Brockband, P.J., Brown, J.L., McCallum, J.E., and Weldon, A.L. (1996). Special and Mechanical Controls on Normal Fault Populations, *Journal of Structural Geology*, **18**, 359–372.
Koster, K. and Horvei, A. (2000). Reservoir monitoring of the Draugen field through time-lapse seismic and it's business impact. *Journal of Petroleum Technology*, SPE 87300.
Kyte, J.R. and Berry, D.W. (1975). New Pseudo Functions To Control Numerical Dispersion. *Journal Society of Petroleum Engineering* (August 1975) 269.

Lehner, F. K., and W. F. Pilaar (1996). On a mechanism of clay smear emplacement in synsedimentary normal faults, *in Norwegian Petroleum Society, eds.*, Hydrocarbon seals-importance for exploration and production (conference abstracts): *Norwegian Petroleum Society*, Oslo, p. 4.

Lerche, I., and Thomson, R.O. (1994). Hydrodynamic of oil and gas. New York, Plenum Press, 308p.

Lia, O., More, H., Tjelmel, H., Holden, L. and Egel, T. (1997). Uncertainties in reservoir production forecasts. *American Association of Petroleum Geologists Bulletin*, **81**, 775–802.

Lindsay, N.G., Murphy, F.C., Walsh, J.J. and Watterson, J. (1993). Outcrop studies of shale smear on fault surface. *International Association of Sedimentologists* Special Publication, **15**, 113–123.

Lumley, D.E., and Behrens, R.A. (1998). Practical issues of 4D seismic reservoir monitoring: What an engineer needs to know. SPE *Reservoir Evaluation and Engineering*, December 1998, 528–538.

Manzocchi, T., Walsh, J.J., Nell, P. and Yielding, G. (1999). Fault transmissibility multipliers for flow simulation models. *Petroleum Geoscience*, **5**, 53–63.

Manzocchi, T., Heath, A.E., Walsh J.J. and Childs, C. (2002). The representation of two-phase fault-rock properties in flow simulation models. *Petroleum Geoscience*, **8**, 119–132.

Mavko, G., and Nolen-Hoeksema, R. (1994). Estimating seismic velocities in partially saturated rocks. *Geophys.*, **59**, 252–258.

Mavko, G., Mukerji, T. and Dvorkin, J. (1998). The rock physics handbook: tools for seismic analysis in porous media. Cambridge University Press.

Murphy, W.F., III, Winkler, K.W., and Kleinberg, R.L. (1984). Contact microphysisces and viscous relaxation in sandstones, in *Physics and Chemistry of Porous Media*, D.L. Johnson and P.N. Sen, eds. *American Institute of Physics*, New Yourk, 176–190.

Naruk, S.J., Dula, W.F., Busch, J.P., Couzens-Schultz, B.A., Garmezy, L., Griffiths, H., Gunst, A.M., Hedlund, C.A., McAllister, E., Onyeagoro, U.O., Ozumba, B.M. and Younes, A. (2002). Common characteristics of proven sealing and leaking faults.

Oelkers, E.H., Bjørkum, P.A. and Murphy, W.M. (1996). A petrographic and computational investigation of quartz cementation and porosity reduction in North Sea sandstones. *American Journal of Science*, **296**, 420–452.

Olsen, H.W., Gill, J.D., Willden, A.T. and Nelson, K.R. (1991). Innovations in hydraulic conductivity measurements. In Procs. *Transportation Research Board* 70th Annual Meeting, Washington D.C. paper 910367.

Olson, R.E. and Daniel, D.E. (1981). Measurement of the hydraulic conductivity of fine grained soils. *In*: Zimmie, T.F. and Riggs, C.O. (*eds*). Permeability and Groundwater Contaminant Transport, *American Society for Testing of Materials, STP*, **746**, 18–64.

Ottesen Ellevest, S., Knipe, R.J., Olsen, T.S., Fisher, Q. and Jones, G. (1998). Fault controlled communication in the Sleipner Vest Field, Norwegian Continental Shelf: detailed quantitative input for reservoir simulation and well planning. In: Jones, G., Fisher, Q.J. and Kinpe, R.J. (*eds*) Faulting, Fault Sealing and Fluid Flow in Hydrocarbon Reservoirs. *Geological Society*, London, Special Publications, **147**, 283–297.

Ozkaya, S.I. and Minton, K.R. (2005). Fractured reservoir characterization using dynamic data in a carbonate field, Oman. *Society of Petroleum Engineering*, SPE 93312.

Pickup, G.E. and Sorbie, K.S. (1996). The scaleup of two-phase flow in porous media using phase permeability tensors. *Society of Petroleum Engineering Journal*, **1** (4), 369–381.

Pickup, G., Ringrose, P.S. and Sharif, A. (2000). Steady-state upscaling: from lamina-scale to full field scale. *Journal of Petroleum Technology*, SPE 62811.

Pittman, E. D. and Larese, R. E. (1991). Compaction of Lithic Sands: Experimental Results and Applications. *Bulletin of the American Association of Petroleum Geologists*, **75**, 1279–1299.

Ponting, D.K. (1989). Corner point geometry in reservoir simulation. Proc. 1st European Conference on the *Mathematics of Oil Recovery*, Cambridge, P.R. King (*eds*), Clarendon Press, Oxford, 45–65.

Purcell, W. R. (1949). Capillary pressure-their measurements using mercury and the calculation of permeability there from: AIME *Petroleum Trans.*, **186**, 39–48.

Ramm, M., 1992. Porosity-depth trends in reservoir sandstones: offshore Norway. *Marine and Petroleum Geology*, **9**, 553–567.

Ramm. M and Bjørlykke. K. (1994). Porosity depth trends in reservoir sandstones - assessing the quantitative effects of varying pore-pressure, temperature history and mineralogy, norwegian shelf data. *Clay minerals*, **29**, 475–490.

Rapoport, L.A. (1955). Scaling Laws for Use in Design and Operation of Water-Oil Flow Models," *Trans., AIME*, **204**, 143.

Renard, P. and de Marsily, G. (1997). Calculating Equivalent Permeability: A Review. *Adv. in Water Resour.* **20**, 253.

Reuss, A. (1929). Berechnung der Fliessgrenzen von Mischkristallen auf Grund der Plastizitätsbedingung für Einkristalle, *Zeitschrift für Angewandte Mathematik und Mechannik*, **9**, 49–58.

Ringrose, P.S., Sorbie, K.S., Corbett, P.W.M and Jensen, J.L. (1993). Immiscible flow behaviour in laminated and cross-bedded sandstones. *Journal of Petroleum Science and Engineering* , **9**, 103–124.

Ringrose, P.S. and Corbett, P.W.M (1994). Cotrols of two-phase fluid flow in heterogeneous sandstones. In J. Parnell. Geofluids: Origin, migration and evolution of fluids in sedimentary basins. *Geological Society* (London) Special Publications, **78**, 141–150.

Roof, J.D. (1970). Snap-off of oil droplets in water-wet pores. *Society of Petroleum Engineers Journal*, **10**, 85–90.

Saad, N., Cullick, A.S., and Honarpour, M.M. (1995). Effective Relative Permeability is Scale-Up and Simulation. *Society of Petroleum Engineering*, SPE 29592, presented at the *Joint Rocky Mountain Regional Meeting and Low Permeability Reservoirs Symposium*, Denver, 20–22 March.

Salathiel, R.A. (1973). Oil recovery by surface film drainage in mixed–wettability rocks. Journal of Petroleum Technology, 1216–1224.

Sammon, P.H. (2000). Calculation of convective and dispersive flows for complex corner point grids. *Society of Petroleum Engineers*, Computer Modelling Group, Ltd. SPE 62929.

Schlomer, S. & Krooss, B.M. (1999). Experimental characteristics of the hydrocarbon sealing efficiency of cap rocks. *Marine and Petroleum Geology*, **14**, 565–580.

Geoquest (2003). Schlumberger *Eclipse 100*^{TM} *Version 2003 Technical Description.*

Schowalter, T.T. (1979). Mechanics of secondary hydrocarbon migration and entrapment. *American Association of Petroleum Geologists Bulletin*, **63**, 723–760.

Shook, M., Li, D. and Lake, L. (1992). Scaling Immiscible Flow Through Permeable Media by Inspectional Analysis," *In Situ*, **16**, 311.

Smith, C.R., Tracy, G.W. and Farrar, R.L. (1999). Chapter 2 in applied reservoir engineering. *Oil and Gas Consultants International* Publication, Tisla, **2**, 8–46.

Smith, D.A. (1980). Sealing and non-sealing faults in Louisiana Gulf Coast salt basin: *American Association of Petroleum Geologists Bulletin,* **64**, 145–172.

Smith, D.A. (1966). Theoritical consideration of sealing and non-sealing faults: *American Association of Petroleum Geologists Bulletin,* **50**, 363–374.

Smith, E.H. (1991). The Influence of Small-Scale Heterogeneity on Average Relative Permeability. *In*: Lake, L.W., Carroll, H.B. and Wesson, T.C., (eds) *Reservoir Characterisation II.* Academic Press, 52–76.

Sneider, R.M., and Neasham, J. (1993). Comparison of seal capacity determination (SCD) from cores with SCD's from cuttings of the same interval, *in* Ebanks, J., Kaldi, J., and Vavra, C., *eds.*, Seals and Traps: A Multidisciplinary Approach: *American Association of Petroleum Geologists*, Hedberg Research Conference, unpublished abstract.

Sorbie, K.S. (1992). Flow Regimes in Miscible Displacement in Heterogeneous Correlated Random Fields. *Society of Petroleum Engineering*, SPE 24140 presented at the 1992 *SPE Symposium on Enhanced Oil Recovery*, Tulsa, 22–24 April.

Sperrevik, S., Gillespie, P.A., Fisher, Q.J., Halvorsen, T. & Knipe, R.J. (2002). Empirical estimation of fault-rock properties. *In:* Koestler, A.G. & Hunsdale, R. (*eds*) Hydrocarbon Seal Quantification. *Norwegian Petroleum Society* Special Publications, 11.

Stegemeier, G.L. (1977). Mechanisms of Entrapment and Mobilization of Oil in Porous Media, in Improved oil Recovery by Surfactant and Polymer Flooding, Shah, D. O. and Schechter, R. S. ed., *Academic Press*, New York.

Stone, H.L. (1970). Probability model for estimating three-phase relative permeability. *Trans AIME* (*Journal of Petroleum Technology*), **249**, 214–218.

Stone, H.L. (1991). Rigorous Black Oil Pseudo-Functions. *Society of Petroleum Engineering*, SPE 21207 presented at the SPE *Symposium on Reservoir Simulation*, Anaheim, California, 17–20 February.

van Duin A.C.T and Larter, S. (2001b). A computational chemical study of penetration and displacement of water films near mineral surfaces. *Geochemical Transactions*, 6.

Vavra, C.L., Kaldi, J.G. and Sneider, R.M. (1992). Geological application of capillary pressure: a review: *American Association of Petroleum Geologists Bulletin,* **76**, 840–850.

Vrolijk, P., James, B., Myers, R., Maynard, J., Sumpter, L. and Sweet, M. (2005). Reservoir connectivity analysis—Defining reservoir connections and plumbing. *Society of Petroleum Engineering*, SPE 93577.

Walderhaug, O. (1996). Kinetic modelling of quartz cementation and porosity loss in deeply buried sandstone reservoirs. *Bulletin of American Association of Petroleum Geologists*, **80**, 731–745.

Wallts, N.L. (1987). Theoretical aspects of cap-rock and fault seals for single and two-phase hydrocarbon columns. *Marine and Petroleum Geology*, **4**, 274–307.

Walsh, J.J., Watterson, J., Heath, A.E. and Childs, C. (1998a). Representation and scaling of faults in fluid flow models. *Petroleum Geoscience*, **4**, 241–251.

Washburn, E.W. (1921). Note on a method of determining the distribution of pore sizes in a porous material: *Proceedings of the National Academy of Science*, **7**, 115–116.

Watts, N.L. (1987). Theoretical aspects of cap-rock and fault seals for single and two phase hydrocarbon columns. *Marine and Petroleum Geology*, **4**, 274–307.

Weber, K.J., Mandl, G., Pilaar, W.F., Lehner, F. and Precious, R.G. (1978). The role of faults in hydrocarbon migration and trapping in Nigerian growth faults: *10th Annual offshore Technology Conference Proceedings*, **4**, 2643–2653.

Worden, R.H., Oxtoby, N.H. and Smalley, P.C. (1998). Can oil emplacement prevent quartz cementation in sandstone? *Petroleum Geoscience*, **4**, 129–137.

Yan, J., Plancher, H., and Morrow, N. (1997). Wettability changes induced by Adsorption of Ashphaltenes, *Society of Petroleum Engineering*, SPE 37232

Yaxley, L.M. (1987). Effect of a partially communicating fault on transient pressure behaviour. *Society of Petroleum Engineers*, Formation Evaluation, 590–598.

Yielding G., Freeman, B. and Needham, D.T. (1997). Quantitative fault seal prediction. *American Association of Petroleum Geologists Bulletin*, **81**, 897–917.

Yielding, G., Overland, J.A. and Byberg, G. (1999a). Characterisation of fault zones in the Gullfaks Field for reservoir modelling. In: Fleet, A.J. and Boldy, S.A.R. (*eds*) Petroleum Geology of Northwest Europe: Proceedings of the 5th Conference. *Geological Society*, London, 1177–1185.

Yielding, G.,Øverland, J.A. and Byberg, G. (1999). Characterisation of fault zones for reservoir modeling: an example from the Gullfaks field, northern North Sea. *American Association of Petroleum Geologists Bulletin*, **83**, 925–951.

Yielding, G. (2002). Shale Gouge Ratio: calibration by geohistory. *In*: Koestler, A.G. and Hunsdale, R. (*eds*) Hydrocarbon Seal Quantification. NPF Special Publications, *Elsevier*, Amesterdam, 1–5.